PB81-122210

Second Symposium on the Transfer and Utilization of Particulate Control Technology
Volume II. Electrostatic Precipitators

Denver Research Inst., CO

Prepared for

Industrial Environmental Research Lab.
Research Triangle Park, NC

Sep 80

U.S. Department of Commerce
National Technical Information Service
NTIS

United States
Environmental Protection
Agency

Industrial Environmental Research
Laboratory
Research Triangle Park NC 27711

EPA-600/9-80-039b
September 1980

PB81-122210

Research and Development

EPA

Second Symposium on the Transfer and Utilization of Particulate Control Technology

Volume II. Electrostatic Precipitators

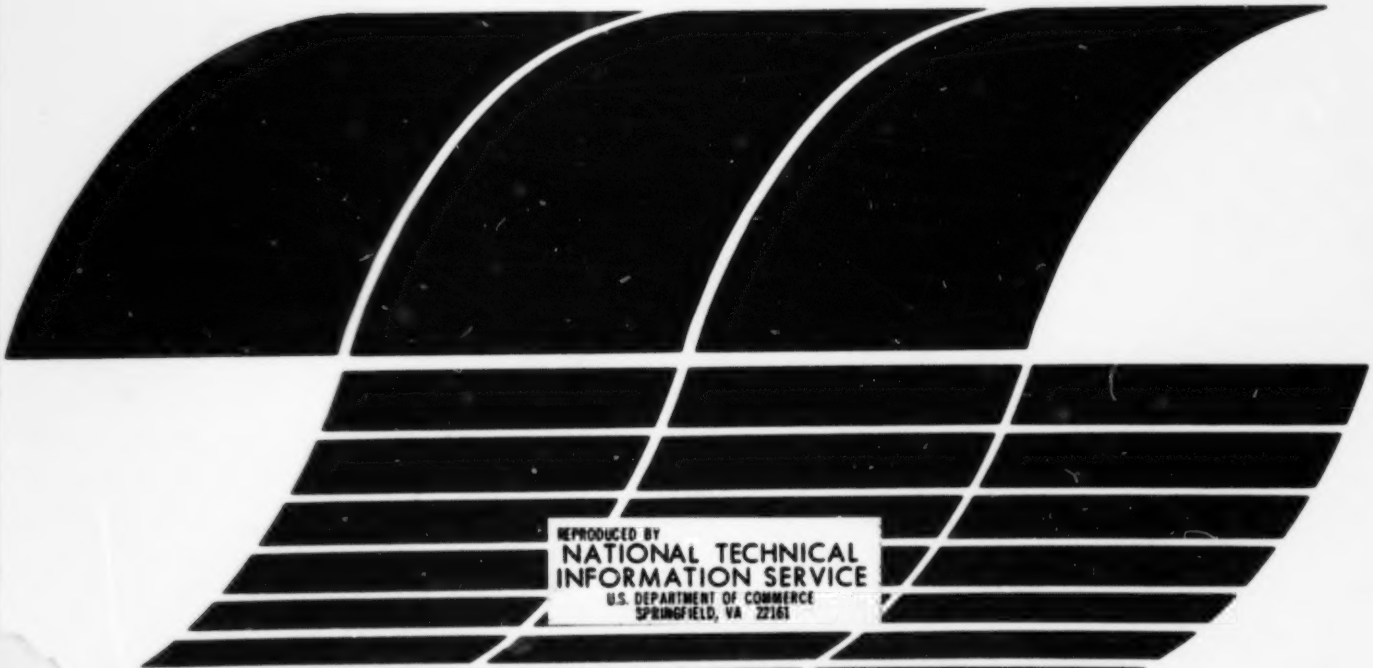

REPRODUCED BY
NATIONAL TECHNICAL
INFORMATION SERVICE
U.S. DEPARTMENT OF COMMERCE
SPRINGFIELD, VA 22161

RESEARCH REPORTING SERIES

Research reports of the Office of Research and Development, U.S. Environmental Protection Agency, have been grouped into nine series. These nine broad categories were established to facilitate further development and application of environmental technology. Elimination of traditional grouping was consciously planned to foster technology transfer and a maximum interface in related fields. The nine series are:

1. Environmental Health Effects Research
2. Environmental Protection Technology
3. Ecological Research
4. Environmental Monitoring
5. Socioeconomic Environmental Studies
6. Scientific and Technical Assessment Reports (STAR)
7. Interagency Energy-Environment Research and Development
8. "Special" Reports
9. Miscellaneous Reports

This document is available to the public through the National Technical Information Service, Springfield, Virginia 22161.

TECHNICAL REPORT DATA
(Please read Instructions on the reverse before completing)

1. REPORT NO. EPA-600/9-80-039b	2. IERL-RTP-1062	3. RECIPIENT'S ACCESSION NO. PB81 122210
4. TITLE AND SUBTITLE Second Symposium on the Transfer and Utilization of Particulate Control Technology (Denver, July 1979) Vol. II. Electrostatic Precipitators		5. REPORT DATE Sept. 1980 Issuing Date. 6. PERFORMING ORGANIZATION CODE
7. AUTHOR(S) F.P. Venditti, J.A. Armstrong, and Michael Durham		8. PERFORMING ORGANIZATION REPORT NO.
9. PERFORMING ORGANIZATION NAME AND ADDRESS Denver Research Institute P.O. Box 10127 Denver, Colorado 80210		10. PROGRAM ELEMENT NO. EHE624 11. CONTRACT/GRANT NO. R805725
12. SPONSORING AGENCY NAME AND ADDRESS Industrial Environmental Research Laboratory Office of Research and Development U.S. Environmental Protection Agency Research Triangle Park, NC 27711		13. TYPE OF REPORT AND PERIOD COVERED Proceedings; 6/79-6/80 14. SPONSORING AGENCY CODE EPA/600/13

15. SUPPLEMENTARY NOTES
IERL-RTP project officer is Dennis C. Drehmel, MD-61, 919/541-2925. EPA-600/7-79-044a thru -044d are proceedings of the 1978 symposium.

16. ABSTRACT

The proceedings document the approximately 120 presentations at the EPA/IERL-RTP-sponsored symposium, attended by nearly 800 representatives of a wide variety of companies (including 17 utilities). The keynote speech for the 4-day meeting was by EPA's Frank Princiotta. The meeting included a plenary session on enforcement. Attendees were polled to determine interest areas: most (488) were interested in operation and maintenance, but electrostatic precipitators (ESPs) and fabric filters were a close second (422 and 418, respectively). Particulate scrubber interest appears to be waning (288). Major activities of attendees were: users, 158; manufacturers, 184; and R and D, 182. Technical presentations drawing great interest were the application of ESPs and baghouses to power plants and the development of novel ESPs. As important alternatives to ESPs, baghouses were shown to have had general success in controlling coal-fired power plant emissions. When operating properly, baghouses can limit emissions to <5 mg/cu nm at pressure drops of <2 kPa. Not all baghouse installations have been completely successful. Both high pressure drop and bag loss have occurred (at the Harrington Station), but these problems appear to be solved.

17. KEY WORDS AND DOCUMENT ANALYSIS

a. DESCRIPTORS		b. IDENTIFIERS/OPEN ENDED TERMS	c. COSATI Field/Group	
Pollution	Scrubbers	Pollution Control	13B	07A
Dust	Flue Gases	Stationary Sources	11G	21B
Aerosols		Particulate	07D	
Electrostatic Precipitators		Baghouses	13I	
Filters			14G	
Fabrics			11E	

18. DISTRIBUTION STATEMENT Release to Public	19. SECURITY CLASS *(This Report)* Unclassified	21. NO. OF PAGES 537
	20. SECURITY CLASS *(This page)* Unclassified	22. PRICE

☆ U.S. GOVERNMENT PRINTING OFFICE: 1980--657-165/0158

EPA-600/9-80-039b
September 1980

SECOND SYMPOSIUM ON THE TRANSFER AND UTILIZATION OF PARTICULATE CONTROL TECHNOLOGY

VOLUME II. ELECTROSTATIC PRECIPITATORS

by

F.P. Venditti, J.A. Armstrong, and Michael Durham

Denver Research Institute
P.O. Box 10127
Denver, Colorado 80210

Grant Number: R805725

Project Officer

Dennis C. Drehmel
Office of Energy, Minerals, and Industry
Industrial Environmental Research Laboratory
Research Triangle Park, NC 27711

INDUSTRIAL ENVIRONMENTAL RESEARCH LABORATORY
OFFICE OF RESEARCH AND DEVELOPMENT
U.S. ENVIRONMENTAL PROTECTION AGENCY
RESEARCH TRIANGLE PARK, NC 27711

DISCLAIMER

This report has been reviewed by the Industrial Environmental Research Laboratory-Research Triangle Park, North Carolina, Office of Research and Development, U.S. Environmental Protection Agency, and approved for publication. Approval does not signify that the contents necessarily reflect the views and policies of the U.S. Environmental Protection Agency, nor does mention of trade names or commercial products constitute endorsement or recommendation for use.

ABSTRACT

The papers in these four volumes of Proceedings were presented at the Second Symposium on the Transfer and Utilization of Particulate Control Technology held in Denver, Colorado during 23 July through 27 July 1979, sponsored by the Particulate Technology Branch of the Industrial Environmental Research Laboratory of the Environmental Protection Agency and hosted by the Denver Research Institute of the University of Denver.

The purpose of the symposium was to bring together researchers, manufacturers, users, government agencies, educators and students to discuss new technology and to provide an effective means for the transfer of this technology out of the laboratories and into the hands of the users.

The three major categories of control technologies - electrostatic precipitators, scrubbers, and fabric filters - were the major concern of the symposium. These technologies were discussed from the perspectives of economics; new technical advancements in science and engineering; and applications. Several papers dealt with combinations of devices and technologies, leading to a concept of using a systems approach to particulate control rather than device control. Additional topic areas included novel control devices, high temperature/high pressure applications, fugitive emissions, and measurement techniques.

These proceedings are divided into four volumes, each volume containing a set of related session topics to provide easy access to a unified technology area.

CONTENTS

Page

VOLUME I CONTENTS viii
VOLUME III CONTENTS ix
VOLUME IV CONTENTS xvi

Section A - Fundamentals

COLLECTION EFFICIENCY OF ELECTROSTATIC PRECIPITATORS BY NUMERICAL SIMULATION 1
E.A. Samuel

THE EFFECTS OF CORONA ELECTRODE GEOMETRY ON THE OPERATIONAL CHARACTERISTICS OF AN ESP 31
G. Rinard, D. Rugg, W. Patten and L.E. Sparks

THEORETICAL METHODS FOR PREDICTING ELECTRICAL CONDITIONS IN WIRE-PLATE ELECTROSTATIC PRECIPITATORS 45
R.B. Mosley, J.R. McDonald and L.E. Sparks

LATERAL PROPAGATION OF BACK DISCHARGE 65
S. Masuda and S. Obata

THEORETICAL MODELS OF BACK CORONA AND LABORATORY OBSERVATIONS 74
D.W. VanOsdell, P.A. Lawless and L.E. Sparks

CHARGE MEASUREMENTS ON INDIVIDUAL PARTICLES EXITING LABORATORY PRECIPITATORS 93
J.R. McDonald, M.H. Anderson, R.B. Mosley and L.E. Sparks

OPTIMIZATION OF COLLECTION EFFICIENCY BY VARYING PLATE SPACING WITHIN AN ELECTROSTATIC PRECIPITATOR 114
E.J. Eschbach and D.E. Stock

INTERACTION BETWEEN ELECTROSTATICS AND FLUID DYNAMICS IN ELECTROSTATIC PRECIPITATORS 125
S. Bernstein and C.T. Crowe

PARTICLE TRANSPORT IN ELECTROSTATIC PRECIPITATORS . . . 146
G. Leonard, M. Mitchner and S.A. Self

Section B - Operation and Maintenance

THE "HUMAN ELEMENT" - A PROBLEM IN OPERATING PRECIPITATORS 168
W.J. Buchanan

ELECTROSTATIC PRECIPITATORS - ELECTRICAL PROBLEMS AND SOLUTIONS 173
R.K. Raymond

Page

ELECTRODE CLEANING SYSTEMS: OPTIMIZING RAPPING ENERGY AND RAPPING CONTROL 189
M. Neundorfer

COMPOSITION OF PARTICULATES--SOME EFFECTS ON PRECIPITATOR OPERATION 208
J.D. Roehr

INCREASING PRECIPITATOR RELIABILITY BY PROPER LOGGING AND INTERPRETATION OF OPERATIONAL PARAMETERS - AN OPERATORS GUIDE 219
P.P. Bibbo and P. Aa

ELECTROSTATIC PRECIPITATORS - START-UP, LOW LOAD, CYCLING, AND MAINTENANCE CONSIDERATIONS 242
F.A. Wybenga and R.J. Batyko

ELECTROSTATIC PRECIPITATOR EMISSION AND OPACITY PERFORMANCE CONTROL THRU RAPPER STRATEGY 256
W.T. Langan, J.H. Oscarson and S. Hassett

RAPPING SYSTEMS FOR COLLECTING SURFACES IN AN ELECTROSTATIC PRECIPITATOR 279
H.L. Engelbrecht

LOW POWER ELECTROSTATIC PRECIPITATION - A LOGICAL SOLUTION TO COLLECTION PROBLEMS EXPERIENCED WITH HIGH RESISTIVITY PARTICULATE 296
J.H. Umberger

Section B - Advanced Design

HIGH INTENSITY IONIZER TECHNOLOGY APPLIED TO RETROFIT ELECTROSTATIC PRECIPITATORS 314
C.M. Chang and A.I. Rimensberger

BOXER-CHARGER - A NOVEL CHARGING DEVICE FOR HIGH RESISTIVITY DUSTS 334
S. Masuda and H. Nakatani

PRECIPITATOR ENERGIZATION UTILIZING AN ENERGY CONSERVING PULSE GENERATOR 352
H.H. Petersen and P. Lausen

PRECHARGER COLLECTION SYSTEM - DESIGN FROM THE LABORATORY THROUGH FIELD DEMONSTRATION 369
M. Nunn, D. Pontius, J.H. Abbott and L.E. Sparks

Page

TOWARDS A MICROSCOPIC THEORY OF ELECTROSTATIC PRECIPITATION 374
C.G. Noll and T. Yamamoto

ION CURRENT DENSITIES PRODUCED BY ENERGETIC ELECTRONS IN ELECTROSTATIC PRECIPITATOR GEOMETRIES 391
W.C. Finney, L.C. Thanh and R.H. Davis

EXPERIMENTAL STUDIES IN THE ELECTROSTATIC PRECIPITATION OF HIGH-RESISTIVITY PARTICULATE 399
J.C. Modla, R.H. Leiby, T.W. Lugar, and K.E. Wolpert

PILOT PLANT TESTS OF AN ESP PRECEDED BY THE EPA-SoRI PRECHARGER 417
L.E. Sparks, G.H. Ramsey, B.E. Daniel and J.H. Abbott

Section C - Industrial Applications

PILOT PLANT/FULL SCALE EP SYSTEM DESIGN AND PERFORMANCE ON BOF APPLICATION 427
D. Ruth and D. Shilton

THE SELECTION AND OPERATION OF A NEW PRECIPITATOR SYSTEM ON AN EXISTING BASIC OXYGEN FURNACE 441
D. Ruth and D. Shilton

CONTROL OF FINE PARTICLE EMISSIONS WITH WET ELECTROSTATIC PRECIPITATION 452
S.A. Jaasund

TUBULAR ELECTROSTATIC PRECIPITATORS OF TWO STAGE DESIGN 469
H. Surati, M.R. Beltran and I. Raigorodsky

PRESENT STATUS OF WIDE-SPACING TYPE PRECIPITATOR IN JAPAN 483
S. Masuda

LOW FREQUENCY SONIC CLEANING APPLIED TO ELECTROSTATIC PRECIPITATORS 502
S.B. Smith and J.A. Schwartz

AUTHOR INDEX 514

VOLUME I

CONTROL OF EMISSIONS FROM COAL FIRED BOILERS

Section A - Electrostatic Precipitators

COST AND PERFORMANCE OF PARTICULATE CONTROL DEVICES FOR LOW-SULFUR WESTERN COALS 1
R.A. Chapman, D.P. Clements, L.E. Sparks and J.H. Abbott

CRITERIA FOR DESIGNING ELECTROSTATIC PRECIPITATORS . . . 15
K. Darby

EVALUATION OF THE GEORGE NEAL ELECTROSTATIC PRECIPITATOR 35
R.C. Carr

EPA MOBILE ESP HOT-SIDE PERFORMANCE EVALUATION 56
S.P. Schliesser, S. Malani, C.L. Stanley and L. E. Sparks

PRECIPITATOR UPGRADING AND FUEL CONTROL PROGRAM FOR PARTICULATE COMPLIANCE AT PENNSYLVANIA POWER & LIGHT COMPANY 80
J.T. Guiffre

MODIFICATION OF EXISTING PRECIPITATORS TO RESPOND TO FUEL CHANGES AND CURRENT EMISSION REGULATIONS. 100
D.S. Kelly and R.D. Frame

PERFORMANCE OF ELECTROSTATIC PRECIPITATORS WITH LOAD VARIATION. 117
W.T. Langan, G. Gogola and E.A. Samuel

FLY ASH CONDITIONING BY CO-PRECIPITATION WITH SODIUM CARBONATE 132
J.P. Gooch, R.E. Bickelhaupt and L.E. Sparks

PREDICTING FLY ASH RESISTIVITY - AN EVALUATION 154
R.E. Bickelhaupt and L.E. Sparks

SO_3 CONDITIONING FOR IMPROVED ELECTROSTATIC PRECIPITATOR PERFORMANCE OPERATING ON LOW SULFUR COAL 170
J.J. Ferrigan, III and J. Roehr

DOES SULPHUR IN COAL DOMINATE FLYASH COLLECTION IN ELECTROSTATIC PRECIPITATORS? 184
E.C. Potter and C.A.J. Paulson

ANALYSIS OF THERMAL DECOMPOSITION PRODUCTS OF FLUE GAS CONDITIONING AGENTS 202
R.B. Spafford, H.K. Dillon, E.B. Dismukes and L.E. Sparks

VOLUME I CONTENTS (Cont.)

Page

BIOTOXICITY OF FLY ASH PARTICULATE 224
A.R. Kolber, T.J. Wolff, J. Abbott and L. E. Sparks

Section B - Fabric Filters

FABRIC FILTERS VERSUS ELECTROSTATIC PRECIPITATORS 243
E.W. Stenby, R.W. Scheck, S.D. Severson, F.A. Horney and D.P. Teixeira

DESIGN AND CONSTRUCTION OF BAGHOUSES FOR SHAWNEE STEAM PLANT 263
J.A. Hudson, L.A. Thaxton, H.D. Ferguson, Jr., and N. Clay

OPERATING CHARACTERISTICS OF A FABRIC FILTER ON A PEAKING/CYCLING BOILER WITHOUT AUXILIARY PREHEAT OR REHEAT. 297
W. Smit and K. Spitzer

OBJECTIVES AND STATUS OF FABRIC FILTER PERFORMANCE STUDY 317
K.L. Ladd, R. Chambers, S. Kunka and D. Harmon

START-UP AND INITIAL OPERATIONAL EXPERIENCE ON A 400,000 ACFM BAGHOUSE ON CITY OF COLORADO SPRINGS' MARTIN DRAKE UNIT NO. 6 342
R.L. Ostop and J.M. Urich, Jr.

DESIGN, OPERATION, AND PERFORMANCE TESTING OF THE CAMEO NO. 1 UNIT FABRIC FILTER 351
H.G. Brines

EXPERIENCE AT COORS WITH FABRIC FILTERS - FIRING PULVERIZED WESTERN COAL 359
G.L. Pearson

FABRIC FILTER EXPERIENCE AT WAYNESBORO. 372
W.R. Marcotte

A NEW TECHNIQUE FOR DRY REMOVAL OF SO_2. 390
C.C. Shale and G.W. Stewart

SPRAY DRYER/BAGHOUSE SYSTEM FOR PARTICULATE AND SULFUR DIOXIDE CONTROL, EFFECTS OF DEW POINT, COAL AND PLANT OPERATING CONDITIONS 410
W.R. Lane

SELECTION, PREPARATION AND DISPOSAL OF SODIUM COMPOUNDS FOR DRY SO_x SCRUBBERS. 425
D.A. Furlong, R.L. Ostop and D.C. Drehmel

VOLUME I CONTENTS (Cont.)

Page

HIGH VELOCITY FABRIC FILTRATION FOR CONTROL OF COAL-FIRED BOILERS 432
J.C. Mycock, R.A. Gibson and J.M. Foster

EPA MOBILE FABRIC FILTER - PILOT INVESTIGATION OF HARRINGTON STATION PRESSURE DROP DIFFICULTIES 453
W.O. Lipscomb, S.P. Schliesser and V.S. Malani

PASSIVE ELECTROSTATIC EFFECTS IN FABRIC FILTRATION . . . 476
R.P. Donovan, J.H. Turner and J.H. Abbott

A WORKING MODEL FOR COAL FLY ASH FILTRATION. 494
R. Dennis and H.A. Klemm

Section C - Scrubbers

PARTICULATE REMOVAL AND OPACITY USING A WET VENTURI SCRUBBER - THE MINNESOTA POWER AND LIGHT EXPERIENCE . . 513
D. Nixon and C. Johnson

PERFORMANCE OF ENVIRONMENTALLY APPROVED NLA SCRUBBER FOR SO_2 529
J.A. Bacchetti

DESIGN GUIDELINES FOR AN OPTIMUM SCRUBBER SYSTEM. . . . 538
M.B. Ranade, E.R. Kashdan and D.L. Harmon

TESTS ON UW ELECTROSTATIC SCRUBBER FOR PARTICULATE AND SULFUR DIOXIDE COLLECTION 561
M.J. Pilat

EPA MOBILE VENTURI SCRUBBER PERFORMANCE 570
S. Malani, S.P. Schliesser and W.O. Lipscomb

THE RESULTS OF A TWO-STAGE SCRUBBER/CHARGED PARTICULATE SEPARATOR PILOT PROGRAM 591
J.R. Martin, K.W. Malki and N. Graves

AUTHOR INDEX 616

VOLUME III

PARTICULATE CONTROL DEVICES

Section A - Scrubbers

Page

FLUX FORCE/CONDENSATION SCRUBBER DEMONSTRATION PLANT IN THE IRON AND STEEL INDUSTRY 1
R. Chmielewski, S. Bhutra, S. Calvert, D.L. Harmon, J.H. Abbott

COLLECTION CHARACTERISTICS OF A DOUBLE STAGE SCRUBBER TO ELIMINATE THE PAINT MIST FROM A SPRAY BOOTH 16
T. Isoda and T. Azuma

APPLICATION OF SLIPSTREAMED AIR POLLUTION CONTROL DEVICES ON WASTE-AS-FUEL PROCESSES 25
F.D. Hall, J.M. Bruck, D.N. Albrinck and R.A. Olexsey

EVALUATION OF THE CEILCOTE IONIZING WET SCRUBBER 39
D.S. Ensor and D.L. Harmon

DEMONSTRATION OF A HIGH FIELD ELECTROSTATICALLY ENHANCED VENTURI SCRUBBER ON A MAGNESIUM FURNACE FUME EMISSION 61
M.T. Kearns and D.L. Harmon

DROPLET REMOVAL EFFICIENCY AND SPECIFIC CARRYOVER FOR LIQUID ENTRAINMENT SEPARATORS 81
J.H. Gavin and F.W. Hoffman

AN EVALUATION OF GRID ROD FAILURE IN A MOBILE BED SCRUBBER 95
J.S. Kinsey and S. Rohde

OPERATION AND MAINTENANCE OF A PARTICULATE SCRUBBER SYSTEM'S ANCILLARY COMPONENTS 104
P.A. Czuchra

LOWERING OPERATING COSTS WHILE INCREASING THROUGHPUT AND EFFICIENCY OF REACTORS AND SCRUBBERS 117
R.P. Tennyson, S.F. Roe, Jr. and R.H. Lace, Sr.

OPTIMIZING VENTURI SCRUBBER PERFORMANCE THROUGH MODELING 127
D.W. Cooper

THE IMPACT OF HUMIDIFICATION CHAMBER PHYSICS ON WET GAS CLEANUP SYSTEMS 145
D.P. Bloomfield, M.L. Finson, G.A. Simons and K.L. Wray

VOLUME III CONTENTS (Cont.)

Page

IMPROVING THE EFFICIENCY OF FREE-JET SCRUBBERS 162
D.A. Mitchell

Section B - Fabric Filters

HIGH VELOCITY FIBROUS FILTRATION 171
M.J. Ellenbecker, J.M. Price, D. Leith and M.W. First

THE EFFECT OF DUST RETENTION ON PRESSURE DROP IN A HIGH VELOCITY PULSE-JET FABRIC FILTER 190
M.J. Ellenbecker and D. Leith

ROLE OF FILTER STRUCTURE AND ELECTROSTATICS IN DUST CAKE FORMATION 209
G.E.R. Lamb and P.A. Costanza

PRESSURE DROP IN ELECTROSTATIC FABRIC FILTRATION 222
T. Ariman and D.J. Helfritch

EXPERIMENTAL ADVANCES ON FABRIC FILTRATION TECHNOLOGY IN JAPAN - EFFECTS OF CORONA PRECHARGER AND RELATIVE HUMIDITY ON FILTER PERFORMANCE 237
K. Iinoya and Y. Mori

BAGHOUSE OPERATING EXPERIENCE ON A NO. 6 OIL-FIRED BOILER 251
D.W. Rolschau

NEW FABRIC FILTER CONCEPT PROVEN MORE FLEXIBLE IN DESIGN, EASIER TO MAINTAIN, AND UNSURPASSED FILTRATION 260
B. Carlsson and R.J. Labbe

EPRI'S FABRIC FILTER TEST MODULE PROGRAM: A REVIEW AND PROGRESS REPORT 270
R.C. Carr and J. Ebrey

Section C - Granular Beds

ELECTROSTATIC ENHANCEMENT OF MOVING-BED GRANULAR FILTRATION 289
D.S. Grace, J.L. Guillory and F.M. Placer

ELECTRICAL AUGMENTATION OF GRANULAR BED FILTERS 309
S.A. Self, R.H. Cross and R.H. Eustis

VOLUME III CONTENTS (Cont.)

Page

THEORETICAL AND EXPERIMENTAL FILTRATION EFFICIENCIES IN ELECTROSTATICALLY AUGMENTED GRANULAR BEDS 344
G.A. Kallio, P.W. Dietz and C. Gutfinger

AEROSOL FILTRATION BY A CONCURRENT MOVING GRANULAR BED: DESIGN AND PERFORMANCE 363
T.W. Kalinowski and D. Leith

DEEP BED PARTICULATE FILTRATION USING THE PURITREAT (TM) PROCESS 382
L.C. Hardison

Section D - Novel Devices

PILOT-SCALE FIELD TESTS OF HIGH GRADIENT MAGNETIC FILTRATION 404
C.H. Gooding and C.A. Pareja

EXPERIENCES WITH CONTROL SYSTEMS USING A UNIQUE PATENTED STRUCTURE 416
G.C. Pedersen

ELECTROSTATIC EFFECTS IN VORTICAL FLOWS 429
P.W. Dietz

CONDENSATIONAL ENLARGEMENT AS A SUPPLEMENT TO PARTICLE CONTROL TECHNOLOGIES 439
J.T. Brown, Jr.

Section E - Specific Applications

WELDING FUME AND HEAT RECOVERY - THE PROBLEM, THE SOLUTION, THE BENEFITS 448
R.C. Larson

PARTICULATE REMOVAL CONSIDERATIONS IN SOLVENT EMISSION CONTROL INSTALLATIONS 472
E.A. Brackbill and P.W. Kalika

ARSENIC EMISSIONS AND CONTROL TECHNOLOGY - GOLD ROASTING OPERATIONS 484
J.O. Burckle, G.H. Marchant and R.L. Meek

CONTROL OF SALT LADEN PARTICULATE EMISSIONS FROM HOGGED FUEL BOILERS 508
M.F. Szabo, R.W. Gerstle and L. Sims

AUTHOR INDEX 526

VOLUME IV

SPECIAL APPLICATIONS FOR AIR POLLUTION MEASUREMENT AND CONTROL

Section A - High Temperature High Pressure Applications

Page

FUNDAMENTAL PARTICLE COLLECTION AT HIGH TEMPERATURE AND PRESSURE 1
R. Parker, S. Calvert, D.C. Drehmel and J.H. Abbott

PARTICULATE COLLECTION IN A HIGH TEMPERATURE CYCLONE . . 14
K.C. Tsao, C.O. Jen and K.T. Yung

EVALUATION OF A CYCLONIC TYPE DUST COLLECTOR FOR HIGH TEMPERATURE HIGH PRESSURE PARTICULATE CONTROL 30
M. Ernst, R.C. Hoke, V.J. Siminski, J.D. McCain, R. Parker and D.C. Drehmel

CERAMIC FILTER TESTS AT THE EPA/EXXON PFBC MINIPLANT . . 42
M. Ernst and M.A. Shackleton

HOT GAS CLEAN-UP BY GLASS ENTRAINMENT OF COMBUSTION BY-PRODUCTS 64
W. Fedarko, A. Gatti and L.R. McCreight

THE A.P.T. PxP DRY SCRUBBER FOR HIGH TEMPERATURE AND PRESSURE PARTICULATE CONTROL 84
R.G. Patterson, S. Calvert and M. Taheri

GAS CLEANING UNDER EXTREME CONDITIONS OF TEMPERATURE AND PRESSURE 98
E. Weber, K. Hübner, H.G. Pape and R. Schulz

PROGRESS ON ELECTROSTATIC PRECIPITATORS FOR USE AT HIGH TEMPERATURE AND HIGH PRESSURE 126
G. Rinard, D. Rugg, R. Gyepes and J. Armstrong

REDUCTION OF PARTICULATE CARRYOVER FROM A PRESSURIZED FLUIDIZED BED 136
R.W. Patch

COMPARATIVE ECONOMIC ANALYSIS OF SELECTED PARTICULATE CONTROL SYSTEMS FOR ADVANCED COMBINED CYCLE POWER PLANTS 154
J.R. Bush, F.L. Blum and P.L. Feldman

CONCLUSIONS FROM EPA'S HIGH TEMPERATURE/HIGH PRESSURE CONTROL PROGRAM 170
D.C. Drehmel and J.H. Abbott

VOLUME IV CONTENTS (Cont.)

Section B - Fugitive Emissions

Page

WATER SPRAY CONTROL OF FUGITIVE PARTICULATES: ENERGY AND UTILITY REQUIREMENTS 182
D.P. Daugherty, D.W. Coy and D.C. Drehmel

THE CONTROL OF DUST USING CHARGED WATER FOGS 201
S.A. Hoenig

SPRAY CHARGING AND TRAPPING SCRUBBER FOR FUGITIVE PARTICLE EMISSION CONTROL 217
S. Yung, S. Calvert, and D.C. Drehmel

CONTROL OF WINDBLOWN DUST FROM STORAGE PILES 240
C. Cowherd, Jr.

THE CONTRIBUTION OF OPEN SOURCES TO AMBIENT TSP LEVELS 252
J.S. Evans and D.W. Cooper

FUTURE AREAS OF INVESTIGATION REGARDING THE PROBLEM OF URBAN ROAD DUST 274
E.T. Brookman and D.C. Drehmel

STATUS OF CONNECTICUT'S CONTROL PROGRAM FOR TRANSPORTATION-RELATED PARTICULATE EMISSIONS 291
J.H. Gastler and H.L. Chamberlain

NEW CONCEPTS FOR CONTROL OF FUGITIVE PARTICLE EMISSIONS FROM UNPAVED ROADS 312
T.R. Blackwood and D.C. Drehmel

DEVELOPMENT OF A SAMPLING TRAIN FOR THE ASSESSMENT OF PARTICULATE FUGITIVE EMISSIONS 321
R.L. Severance and H.J. Kolnsberg

SECONDARY NEGATIVE ELECTRON BOMBARDMENT FOR PARTICULATE CONTROL 333
W.E. Stock

Section C - Measurement and Analysis

HIGH TEMPERATURE AND HIGH PRESSURE SAMPLING DEVICE USED FOR PARTICULATE CHARACTERIZATION OF A FLUIDIZED BED COAL GASIFICATION PROCESS 338
S.P. Tendulkar, J. Pavel and P. Cherish

ON-STREAM MEASUREMENT OF PARTICULATE SIZE AND LOADING 351
E.S. VanValkenburg

VOLUME IV CONTENTS (Cont.)

Page

ANALYSIS OF SAMPLING REQUIREMENTS FOR CYCLONE OUTLETS 368
M.D. Durham and D.A. Lundgren

ELECTROSTATIC EFFECTS ON SAMPLING THROUGH UNGROUNDED PROBES 387
W.B. Giles and P.W. Dietz

OPTICAL PARTICULATE SIZE MEASUREMENTS USING A SMALL-ANGLE NEAR-FORWARD SCATTERING TECHNIQUE 396
J.C.F. Wang

IN-STACK PLUME OPACITY FROM ELECTROSTATIC PRECIPITATOR SCRUBBER SYSTEMS 411
L.E. Sparks, G.H. Ramsey and B.E. Daniel

TI-59 PROGRAMMABLE CALCULATOR PROGRAMS FOR IN-STACK OPACITY 424
S.J. Cowen, D.S. Ensor and L.E. Sparks

UTILIZATION OF THE OMEGA-1 LIDAR IN EPA ENFORCEMENT MONITORING 443
A.W. Dybdahl and F.S. Mills

EFFECTS OF PARTICLE-CONTROL DEVICES ON ATMOSPHERIC EMISSIONS OF MINOR AND TRACE ELEMENTS FROM COAL COMBUSTION 454
J.M. Ondov and A.H. Biermann

A SOURCE IDENTIFICATION TECHNIQUE FOR AMBIENT AIR PARTICULATE 486
E.J. Fasiska, P.B. Janocko and D.A. Crawford

PARTICLE SIZE MEASUREMENTS OF AUTOMOTIVE DIESEL EMISSIONS 496
J.D. McCain, and D. Drehmel

CONTROL STRATEGIES FOR PARTICULATE EMISSIONS FROM VEHICULAR DIESEL EXHAUST 508
M.G. Faulkner, J.P. Gooch, J.R. McDonald, J.H. Abbott and D.C. Drehmel

AN EVALUATION OF THE CYTOTOXICITY AND MUTAGENICITY OF ENVIRONMENTAL PARTICULATES IN THE CHO/HGPRT SYSTEM . . 524
N.E. Garrett, G.M. Chescheir, III, N.A. Custer, J.D. Shelburne, Catherine R. De Vries, J.L. Huisingh and M.D. Waters

AUTHOR INDEX 536

COLLECTION EFFICIENCY OF ELECTROSTATIC PRECIPITATORS BY NUMERICAL SIMULATION

BY:

Eric A. Samuel
Buell Emission Control Division
Envirotech Corporation
Lebanon, Pennsylvania 17042

ABSTRACT

A numerical simulation code has been developed to analyze the coupled electro-aerodynamic phenomena within an electrostatic precipitator operated in both the positive and negative corona modes. The space charge and current densities, as well as the static and space charge components of the electric field, are first obtained using the known cross-sections for ionization and negative ion formation. Data includes the effects of fluid flow. The above quantities (except the static field) are then corrected in a subsequent iteration for the presence of dust particles of known size distribution, charged predominantly by the field charging mechanism. The precipitator collection efficiency is calculated from the trajectories of the charged dust particles. For theory comparison, the collection efficiencies of model precipitators were measured by light-scattering techniques using oil drops as test particles. The variation of efficiency with wire-to-wire spacing will be discussed as a case study.

1. INTRODUCTION

Introduction

The sizing of electrostatic precipitators for a given application is conventionally based on statistics drawn from performance data on existing precipitators for that application. Such an approach will yield a reliable sizing criterion only if the performance data base includes a sufficiently large number of units. The method, however, is limited for sizing precipators for new applications and for design improvement. Computer-assisted modeling of the precipitation process is an alternative sizing procedure which overcomes the above limitation.

In this paper, we discuss a computer program which simulates the important physical phenomena within an idealized electrostatic precipitator (to be defined below) without the use of differential equations. Obtained by simulation are the corona space charge density in the presence of air flow, the charging of particulates and their subsequent drift in the total electric field, the effect of the interaction among charged particulates (the concentration effect and, eventually, the collection efficiency) by number density of the idealized precipitator containing N wires in the gas flow direction. Also described in the paper are the results of experiments performed using laser light scattering techniques to test the predictions of the computer simulation. Because of the good agreement between theory and experiment within the assumptions of an idealized precipitator, our simulation code has the potential of becoming the starting point for a computer model which includes the effects of non-ideal behavior in industrial precipitators.

In order to demonstrate the use of our simulation code in design improvement, we discuss as a case study the effect of varying one geometric parameter; namely, the wire-to-wire spacing on the performance of the idealized precipitator. We have found that for a given plate-to-plate spacing, there is an optimum value of the wire-to-wire spacing. The efficiency maximum, however, is not very sharp. The above finding, which we also confirmed experimentally, is significant since it suggests that an increase in the number of wires per gas passage over the current industry standard will result in increased performance with the same plate area even though the wire-to-wire spacing is smaller than the optimum value.

An Idealized Electrostatic Precipitator

Figure 1 shows a cross-sectional view of the studied model precipitator to establish the scaling of the wire spacing (2L) to plate spacing (2W) ratio. The precipitator extends to a height H perpendicular to the plane of the page such that $L/H<<1$. The electrodes are of smooth conducting sheets at the uniform ground potential. The corona wires are under sufficiently large tension and assumed to be free of oscillations in order to maintain uniform distances to adjacent wires and plates. (See Reference 1 for the analysis of the wire oscillation.) The wire diameter D is chosen so that the ratio, D/W, is in the same range as that for industrial precipitators; i.e., $D/W \sim 3 \times 10^{-2}$.

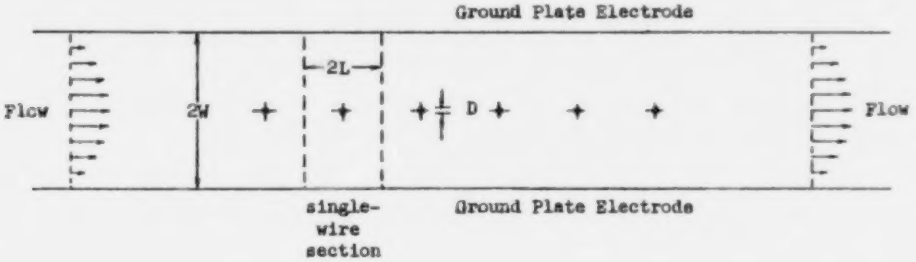

Figure 1. A top view of the model precipitator. The wires and plates extend to a height H, normal to the plane of the figure.

The inlet of the precipitator consists of a long, leading section of parallel plates without wires. The mean flow speed is comparable to those of industrial precipitators. However, the flow Reynolds number is kept smaller than the critical value for transition to turbulent flows by keeping the plate spacings smaller than the industrial values. As a result of these restrictions, the flow acquires the fully developed Poiseuille profile upstream of the first corona wire. Depending on the wire spacing, the flow may recover the Poiseuille profile downstream of a wire before encountering the next wire, and so on. The exit also has a long trailing section of parallel plates without wires to insure the desired flow field characteristics. The flow field has been measured in great detail by photographing tracer particles under illumination by an argon ion laser beam.

The host medium is synthetic air consisting of 80% nitrogen and 20% oxygen at room temperature and one atmosphere. The corona operating current is chosen in the range about a factor of 5 above the industrial range of around 20 μA/ft of a corona wire. The corresponding potential difference depends sensitively on the ratio L/W for small spacings, and this is included in the analysis.

Polydispersed oil droplets have been used for this study. Measurement shows a Nukiyama-Tanasawa distribution of the respirable range with the maximum at 0.3 μm in radius. The particulate number density ranges from 10^4 through 10^8 particles/cm^3.

The precipitator is operated under clean electrode condition, both in experiment and simulation in order to insure reproducibility. This is also necessary because of difficulty in modeling the so-called aging of the precipitator.

The corona operates in both the positive and negative D.C. corona mode. Arcing and current modulation are assumed to be absent. In experiment, this is realized by using current limiting techniques with high voltage power supplies.

The differences between the idealized precipitator and industrial precipitators obviously are numerous. The industrial precipitators have the following additional features.

(a) Considerable level of turbulence in the flow due to higher Reynolds number and the baffles and gaps in the ground plate.

(b) Substantial thickness of weakly conducting dielectric layers of collected particulates on all electrodes.

(c) Frequent arcing between wires and plates, and the so-called back corona resulting from breakdowns in the dielectric layers.

(d) Large amplitude oscillations of wires.

(e) Re-entrainment of collected particulates during removal by rapping of the plates.

(f) Complex shapes and the interior structures of particulates.

(g) Contamination of the flue gas by a large number of gaseous combustion products which affect space charge formation.

(h) Deliberately added conditioners to influence conductivity and adhesion properties of particulates.

(i) Full wave rectified but unfiltered power supplies.

(j) Higher operating gas temperature, and pressure variations.

(k) Large fluctuations in the particulate number density at the inlet.

(l) Sedimentation of particulates.

(m) Particulate agglomeration.

Once agreement between theory and experiment is established for the idealized precipitator, the non-ideal effects listed above can be included in the computer program; one at a time, starting with the most significant. Experiments must be designed to test the predictions of the program after inclusion of each non-ideal effect.

An Outline of the Paper

Particulate precipitation takes place in a precipitator in the following manner. The particulate is carried into the precipitator by its surrounding fluid element at the local flow speed. (Particulates in the respirable size range follows the streamlines accurately, except around the corona wire where the inertia effect is strong. See Reference 2 for detailed analyses.) Upon entering the corona field of the first wire, the particulate acquires charges in the form of ions or electrons. The corona creates a region of positive ions by electron impact ionization of air molecules (positive corona), or negative ions by attachment of electrons to molecules (negative corona) around the wire. The particulate, now polarized in the electric field of the high voltage wire, attracts the ions and electrons. Thermal fluctuations of the ions and particulate, regardless of the wire electric field, also contributes to charging. In principle, the charging continues throughout the particulate motion until the Coulomb repulsion of the acquired charge can hold off further diffusion of ions and attraction by polarization.

As the amount of electrical charge on the particulate increases, the Coulomb force on the particulate begins to accelerate it against the drag of the fluid. A terminal velocity results in the direction of the local electric field line, while the velocity along the streamline persists. The eventual particulate trajectory evolves out of the competition between these two velocity components, which in turn change according to how the particulate trajectory is unfolded.

Since the maximum amount of charge depends on the particulate size, electric field strength, and space charge density, the particulate may not reach the ground plate within the distance 2L. If it does not, the drifting can continue in subsequent sections until the particle reaches the plate or leaves the precipitator still entrained in the flow.

In finer details, the trajectory of the particulate depends on other surrounding particulates; whereas, the space charge density is modified by the spatial and size distribution of the particulates and the flow field. In short, precipitation results from a set of strongly coupled physical processes. The present investigation systematically separates individual processes, and then combines them and evaluates the effects of their coupling on the precipitation efficiency.

In Chapter 2, we describe calculations of the space charge density and electric field everywhere in a two-dimensional section defined by 2L and 2W, with a corona wire located at the center (see Figure 1). It includes detailed descriptions of such calculations for both the positive and negative corona in the presence of the flow field. A check of our numerical simulation technique is described, which calculates a coaxial positive D.C. corona and compares the result with the analytical solution from Poisson's equation. In this test, of course, the flow has been turned off.

In Chapter 3, we discuss particulate trajectory calculations for a single-wire precipitator, including the charging process and the effects of the particulate number density and size distribution. Extensions to multi-wire precipitators are described next. The results of the multi-wire calculations are then compared with the Deutsch equation. A framework for reducing a single-wire efficiency from a multi-wire precipitation efficiency is formulated, which becomes the basis for analyzing the scaling of wire-to-plate spacing ratio. We then present the experimental results for the collection efficiencies of several multi-wired research precipitators obtained by light scattering techniques, and discuss the scaling of the L/W ratio on the basis of both experimental and theoretical data. Concluding remarks are given in Chapter 4.

2. CALCULATION OF SPACE CHARGE DENSITY AND ELECTRIC FIELD FOR A PLATE-WIRE CORONA WITH TRANSVERSE FLOW

Introduction

Prior to treating the fundamental processes that sustain the positive and negative corona in air, we first obtain expressions for the electric potential and the electric field in the region between the wire and the plates using the method of conformal transformations. This method is advantageous because the expressions are in closed forms and are easily extended to the case of a multi-wire precipitator.

Electrons play the central role in initiating and sustaining both the positive and negative corona. In describing the positive and negative corona, especially the negative corona, knowledge of the average electron energy in an electric field is essential because it determines the rates that ions are generated either by electron impact ionization of air molecules or by electron attachment. It is generally known that the drift speed of an electron is proportional to the electric field strength over a large range of electric fields and gas densities. This is because an electron can be accelerated in the field until the energy gain of the electron becomes equal to the energy loss by collisions with molecules. When the molecules are monatomic, the electron-molecule collisions are mostly elastic. When the gas molecules are polyatomic, as in air, the electron-molecule collisions are more often inelastic and the average electron energy evaluation requires attention to the specific molecular structure. A detailed analysis is given in Reference 1. A simplified procedure for calculating the average electron energy in polyatomic gases is discussed.

We will then discuss the main processes that operate in a positive corona and the way these processes are simulated in our computer code. A similar discussion follows for the negative corona. In both simulations, we assume that air consists of 80% nitrogen and 20% oxygen only, and ignore other trace gases. In the negative corona, it is assumed that only oxygen molecules can form stable, long-lived negative ion species. The cross-sections for both ionization and negative ion formation by electron impact are taken from the literature. The mobilities of nitrogen and oxygen ions are also known.

In the numerical code for the corona, we also include the effect of fluid flow. Analytically, one has to solve Poisson's equation, the continuity equation and the Navier-Stokes equation simultaneously. Since this approach is rather laborious, the flow field is measured instead, and the space charge calculation carried out in that flow field. Due to the relatively low corona current range, the influence of the corona wind on the flow field can be neglected. The ability to include the effects of flow in this way is one of the chief advantages of our numerical code.

In each simulation, the corona current and voltage are inputs. This means prior knowledge of the corona characteristics. They are obtained from measurement using the actual multi-wire research precipitator. We note that the current-voltage characteristic depends on the wire spacing as well as the wire radius, plate spacing and electrode materials. Generally, the characteristic curve is parabolic near the corona threshold.

A detailed description of the algorithms used in the numerical code is given next. This is followed by a discussion of the methods by which we verify that the results of our numerical simulations are consistent with the fundamental laws of physics. The final section contains a discussion of the salient features of the electric field distribution within a precipitator.

The Solution of Laplace's Equation for the Plate-Wire-Plate Geometry

A solution to Laplace's equation in to independent variables x and y can be formulated in terms of analytic functions of a comples variable since the real and imaginary parts of such functions are harmonic. Details of the calculation using the theory of complex variables for the potential $\phi(x,y)$ within a plate-wire precipitator, sketched in Figure 1, is given in Reference 3. The result is:

$$\phi(x,y) = -\lambda \sum_{p=0}^{N-1} \ell n \left(\frac{A_p - B}{A_p - B}\right),$$

where $A_p = \cosh \pi(y-2pL)/2W$ and $B = \cos(\pi x/2W)$. The x and y components of the electric field, $\vec{E}$, are obtained from $\vec{E} = -\operatorname{grad} \phi(x,y)$:

$$E_x(x,y) = \frac{\lambda\pi}{W} \frac{B\sqrt{1-B^2}}{A_p^2 - B^2}$$

$$Ey(x,y) = \frac{\lambda\pi}{W} \frac{A_p\sqrt{1-A_p^2}}{A_p^2 - B^2} \qquad (2)$$

The Average Electron Energy in the Electric Field

Evaluation of the average electron energy $\xi(E)$ in the electric field of strength $\vec{E}$ is, in general, very complicated and requires attention to the details of energy losses during the Coulomb acceleration of the electrons. The energy losses stem from (1) elastic collisions with molecules in which transfer of a small fraction of the electron kinetic energy to a target molecule takes place, (2) inelastic collisions with molecules in which an electron gives up a fixed amount of energy to a molecule and the molecule becomes excited internally. A proper accounting of the inelastic collisions can be done in principle but it requires full knowledge of the molecular energy levels of a given target molecule and the probability of an electron-molecule collision resulting in excitation to each molecular energy level.

An approximate, but considerably more detailed, analysis of $\xi(E)$ in air is described in Reference 1. We have found that for consideration of both ionization and electron attachment in the corona of air, the maximum distance of ten collisional mean free paths is a good compromise for the distance of electron acceleration beyond which further acceleration is offset by inelastic energy losses. Thus, throughout the space charge density calculation, we calculate the average electron energy as:

$$\xi(E) = 10\lambda o e E, \quad \lambda o = (n\ \sigma)^{-1} \tag{3}$$

where n is the number of target molecules per unit volume and λo is the cross-sectional area of the target molecule. An experimental confirmation for the rather gross simplification of equation (3) exists in that the radius of the ionization zone calculated using equation (3) agrees with laboratory measurements.

The Positive Corona

The positive corona is initiated by residual electrons in the gas, created by cosmic rays. This electron moves towards the wire at positive high voltage with respect to the plates and reaches the ionization zone around the wire where $\xi(E)$ exceeds the ionization potential of molecular oxygen ($\Delta\xi_I = 12.5$ eV). ($\Delta\xi_I$ for molecular nitrogen is 15.7 eV.) An ionizing collision produces a positive ion of the target molecule and an additional electron. This results in electron multiplication or avalanche. In this way, after traversing several ionization mean-free paths, the electrons multiply in number, until at the wire the total corona current is carried entirely by electrons.

The electron multiplication factor, α, for an electron passing through the entire ionization zone is simply given by the total number of ionizing collisions over R_I, the radius of the ionization zone:

$$\alpha = 2^{\int_{D/2}^{R_I} dr/\lambda_I} \tag{4}$$

where $\lambda_I = [n\sigma_I(\xi)]^{-1}$. $\sigma_I(\xi)$ is the ionization cross-section and depends on the electron energy $\xi(E)$, thus becoming position dependent.

Of course, the ions are accelerated too, but due to their large mass, their drift velocity remains much smaller than the electrons. For this reason, the space charge density, inside and outside the ionization zone, is determined by the ions. While the total corona current is carried entirely by electrons at the wire, outside the ionization zone it is carried entirely by the positive ions which are produced in the ionization zone.

In the simulation, we divide a single wire section of the multi-wire precipitator into a 20 bin x 20 bin mesh and calculate the x and y components of the electrostatic field of Equation (2) at centers of the 400 cells. The charge per unit length of the wire, λ, is obtained from the boundary condition that the potential at $r=D/2$, is the corona voltage, V_c, as given by the power supply. D is the wire diameter.

The space charge density and the electric field due to the space charge are then obtained as follows: The corona current is represented by a certain number 2 Δn, of line charge packets introduced into the field at the outer surface of the ionization zone in a time interval Δt. Each charge packet is assigned a number of elemental charges amounting to the magnitude of q. Δn, Δt and q are related by:

$$2q\frac{\Delta n}{\Delta t} = i_c \tag{5}$$

where i_c is the corona current. The actual values of Δn and Δt are chosen as a compromise between the computing time and the desired accuracy of the result. The charge packets are created within the ionization zone and their exact departure point on the surface of the zone is determined randomly by a random number generator. While the charge packets are long lines parallel to the wire and interact among themselves as line charges, their motion is governed by the rules of single ions because the ions in a packet are not bound to each other. We assume that negative ion production within the ionization zone by electron attachment is negligible.

The positive ion packets created in a time step as well as all previously created positive ion packets are initially moved under the influence of the electrostatic field due to the wires and the flow field. The local flow velocity is vectorially added to the electrostatic drift velocity of an ion to get the total ion velocity. At every few time steps, the ion packets are frozen at the closest grid points and the electric field, due to all of the ion packets and their images at the plates, are calculated and added to the electrostatic field of the wires. The charge packets are then allowed to move during the next time interval Δt in this new, total electric field coupled to the flow field. At the end of the interval, the field is recalculated. The iteration is continued until a steady state is reached; i.e., when the total number of ion packets in the region between wire and plate is constant and $2\Delta n$ packets per time step are collected at the plates on the average. The steady state total electric field due to the ion packets, and the spatial distribution of the ion packets (i.e., the space charge density), are averaged over several iterations and retrieved in IBM cards for use in the second phase of the simulation.

The Negative Corona

Since the algorithms and numerical techniques for simulating the negative plate-wire corona are essentially the same as for the positive corona, we will only describe how the physical processes are taken into account in the simulation. When the wire is maintained at a potential negative with respect to the plates, the positive ions move toward the wire and electrons, and the negative ions move toward the plates held at zero potential. The negative corona is initiated by stray electrons in the ionization zone. As the electrons move outward along the field lines, they will produce more electrons in the ionization zone.

As these electrons leave the ionization zone, their average energies will progressively decrease because of the decreased electric field strength. The electrons reach a region where their energies are in the range favored for the dissociative attachment reaction:

$$O_2 + e^- \rightarrow O + O^-$$

There are many reactions by which these O^- ions can form neutral molecules, electrons, or other negative ions. We assume, however, that the attachment rate is large enough to ignore depletion of the O^- ions by secondary reactions. Some electrons reach still another region in which their energies are suitable for the direct attachment reaction:

$$O_2 + e^- \rightarrow O_2^-$$

Again, the electrons, because their mobilities are so much larger than those of ions, do not contribute to the space charge density. But they induce the formation of negative ions which do contribute to the space charge. Our consideration of only dissociative and direct attachment to oxygen molecules to the exclusion of all other negative ion producing reactions is by no means an accurate picture. Many other negative ion species such as O_3^-, NO^-, NO_2^-, have been detected. It is expected that inclusion of the most abundant negative ions is adequate to yield a representative field due to the negative ion space charge density in the precipitator.

The simulation proceeds as follows. $2\Delta n$ packets of electrons per time interval, Δt, are produced at the surface of the wire. The charge carried by a packet is initially given by γq, where q satisfies Equation (5). The factor, γ, is related to the rate of the electron multiplication in the ionization zone. The electron packets are moved within the ionization zone radially along field lines. The ionization zone is divided into 20 concentric rings and 16 equally-spaced radial lines, superimposed in the 20 x 20 mesh field of the single wire section, as shown in Figure 3. A grid point in the ionization zone has the polar coordinates (r, θ):

$$r(i) = (\Delta r/2)\,(2i - 1),\quad i = 1, \ldots, 20$$
$$\theta(j) = (\Delta\theta/2)\,(2j - 1),\quad j = 1, \ldots, 16, \qquad (6)$$

where $\Delta r = (R_I - D/2)/20$ and $\Delta\theta = \pi/8$.

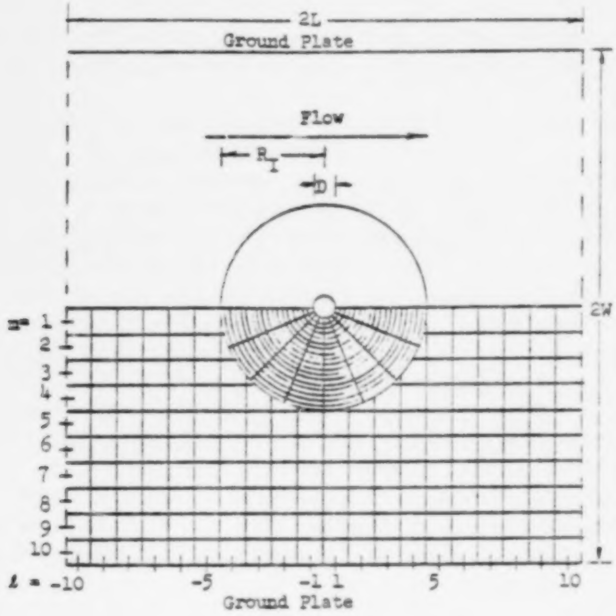

Figure 2. The plan for division of the ionization zone and the 20x20 rectangular mesh field of the plate-wire-plate corona.

As an electron packet passes each ring, the number of ionizing mean-free paths in the annulus between successive rings is calculated, assuming the field to be uniform over the annulus. The number of additional electrons produced in this annulus is $2^{1/\lambda_I}$. To include this increase in the number of electrons, the charge on an electron packet is increased by $2^{1/\lambda_I}\gamma q$, instead of increasing the number of electron packets. The electron packet, in passing the annulus, also leaves behind $(2^{1/\lambda_I} -1)$ of positive ions.

The positive ions created in this way are randomly distributed around the grid point closest to the position of the electron packet. Each electron packet is moved until it reaches the edge of the ionization zone. The value of the charge, when the charge packet arrives at the ionization zone edge, is compared with the q of Equation (5). The factor γ is initially started at a low value, say, 10^{-5}, and is successively doubled until the electron packet, which left the wire surface with a charge , arrives at the edge of the ionization zone with the charge q. That is, γ is increased during the iteration self-consistently until one satisfies the relationship:

$$\gamma\alpha = 1 \qquad (7)$$

The electron packets are now moved outside of the ionization zone along field lines. As they cross a line of centers of the cells or grid line of constant x, their average energy is calculated from Equation (3) and the number of negative ion packets they produce by attachment to molecules is calculated using the known cross sections. The negative ion packets formed along each step are randomly distributed in the cell where the grid point is located.

Thus, each timestep consists of moving $2\Delta n$ electron packets, randomly formed on the surface of the wire, through the ionization zone while increasing in the amount of charge per packet up to q or through the remaining space to the plates with a fixed amount of charge q per packet. In the same timestep, the positive and negative ions created during all preceding timesteps are also moved. At regular time intervals, the electric field due to the positive ions is calculated. Since the radius of the ionization zone is small compared to L or W, the contribution from the positive ions inside the ionization zone is calculated in the form of the increasing shielding of the charge on the corona wire $(-\lambda)$. A symmetric distribution of the positive ions around the wire is assumed for this purpose. The field due to the negative ion packets is found by the same image charge method as for the positive corona. The calculations are continued until steady state is reached. By keeping track of the average number of times an electron packet crosses a given grid point (ℓ,m) in Δt, we can obtain the current density $\vec{J}(\ell,m)$, of electrons at the grid point. Again, the total current density is given by the electrons while the space charge density is by the ions. Note that the flow velocity is again added vectorially to the electrodynamic drift velocity in order to determine the total ion velocity.

For the purpose of calculating the rate at which particulates are charged in the precipitator, we retrieve from the simulation code and store the negative ion space charge density $\rho^-(\ell,m)$, the total electric field $\vec{E}(\ell,m)$ and the ratio $J(\ell,m)/E(\ell,m)$. The ratio $J(\ell,m)/E(\ell,m)$ is equal to $\rho_e(\ell,m)\ k_e$ where $\rho_e(\ell,m)$ is the electron space charge density and k_e is the electron mobility. The product $\rho^-(\ell,m)k^-$ is also stored, where k^- denotes the negative ion mobility.

Computer Algorithms for the Simulation Code

Definition of Grid Points. A grid point refers to the center of a cell and is identified by indices (ℓ,m). Its x and y coordinates are:

$$x(\ell) = (2\ell-1)a_x/2 \qquad \text{and} \qquad y(m) = (2m-1)a_y/s \tag{8}$$

where $a_x = W/10$ and $a_y = L/10$

Electrostatic Field of the Wires. In order to commence on the calculation of the x and y components of the electrostatic field due to the wires, we first determine λ, the charge per unit length of the wire, from the corona voltage V_c and Equation (5). From the λ-value, the x and y components of the electric field, $E_x(\ell,m)$ and $E_y(\ell,m)$ are calculated at each of the 400 grid points using Equation (2).

Algorithm for Moving Charge Packets. The x and y coordinates of all charge packets at the current iteration (x_1, y_1), and the iteration immediately preceding (x_0, y_0) are stored in the program. A charge packet is created randomly within the ionization zone at a point (x_0, y_0). In the same time step it is created, the packet is moved by the algorithm:

$$x_1 = x_o + v_x(x_o)\ \Delta t$$
$$y_1 = y_o + v_y(y_o)\ \Delta t \qquad (9)$$

In subsequent time steps, the packet is moved by the slightly different algoritym:

$$x_2 = x_o + v_x(x_1)(2\Delta t)$$
$$x_3 = x_1' + v_x(x_2)(2\Delta t) \qquad (10)$$

and so on, where

$$x_1' = x_o + [v_x(x_o) + v_x(x_1)]\Delta t/2$$

The same is done to calculate the y- components.

The velocities of equations (9) and (10) are determined as follows:

$$v_x(x,y) = k_1\ [E_x(\ell,m) + E_x'(\ell,m)]$$

$$v_y(x,y) = k_1\ [E_y(\ell,m) + E_y'(\ell,m)] \qquad (11)$$

where k_1 is the mobility of the positive or negative ions, $E_x\ (\ell,m)$ and $E_y(\ell,m)$ are the components of the electrostatic field of the wires alone, and $E_x'(\ell,m)$ and $E_y'(\ell,m)$ are the space charge field components. Since the ions move from the high field region near the wire to the low field region near the plates, Equation (11) is designed to correct for initial overestimation of the displacement of the ion packet in the preceding time step.

Electric Field Due to the Space Charge Density. This particular segment of the calculation takes up most of the processing time in a typical run. At regular time intervals, the ion packets throughout the region between the wire and the plates are frozen and assigned to the nearest grid points in order to find the distribution of the number of the charge packets, $Q(\ell,m)$. The space charge density is then obtained:

$$\rho(\ell,m) = Q(\ell,m)\ q/a_x a_y \qquad (12)$$

Figure 4 illustrates the method of calculating the space charge electric field in a single wire section of the precipitator. The section is divided into four quadrants labeled I, II, III, and IV. Let us consider two charge packets at grid points (ℓ,m) and (n,k). For the two real positive charge packets in quadrant I, we show two real positive charge packets that can always be found in quadrant II from the symmetry about the plane of wires. Also shown are the image packets on the bottom side of the lower conducting plate, which is labeled as quadrant V. Of the infinite number of image charges that exist for the pair of the parallel conducting plates, we consider only those images closest to the charge packets in quadrants I to calculate the field in the quadrant of interest.

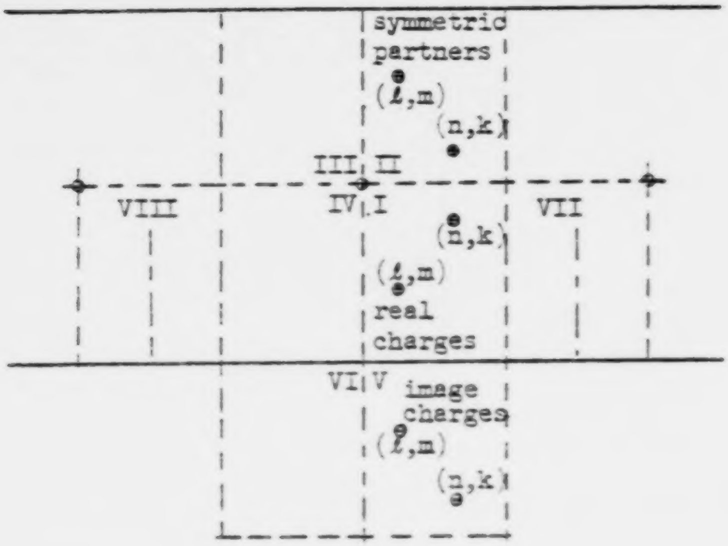

Figure 3. The arrangement of image and symmetric partner charge packets for two ion packets in a plate-wire corona section.

The electric field at the grid point (ℓ,m) of Quadrant I is calculated from five charge packets: the real packet at (n,k) in Quadrand I, its symmetric partner in Quadrant II and its image in Quadrant V; both the symmetric partner in Quadrant II and the image packet in Quadrant V of the real charge packet located at the grid point (ℓ,m). Writing out the x and y components of the electric field, we have

$$E'_x(\ell,m) = 2q \frac{a_x(\ell-n)}{a_x^2(\ell-n)^2 + a_y^2(m-k)^2}$$

$$+ \frac{a_x(2N_o + 1-\ell-n)}{a_x^2(2N_o+1-\ell-n)^2 + a_y^2(m-k)^2} + \frac{a_x(\ell+n-1)}{a_x^2(\ell+n-1)^2 + a_y^2(m-k)^2}$$

$$+ 2q \frac{1}{a_x(2\ell-1)} + \frac{1}{a_x(2N_o-1-2\ell)} \qquad (13)$$

and

$$E'_y(\ell,m) = 2q \frac{a_y(m-k)}{a_x^2(\ell-n)^2 + a_y^2(m-k)^2}$$

$$- \frac{a_y(m-k)}{a_x^2(2N_o+1-\ell-n)^2 + a_y^2(m-k)^2} + \frac{a_y(m-k)}{a_x^2(\ell+n-1)^2 + a_y^2(m-k)^2} \quad ,(14)$$

where N_o is the number of bins in L or W; i.e., $N_o = 10$ in this case. Notice that the charge packets are infinitely long lines of charges. One can similarly determine the field components at the grid point (n,k). The total space charge field due to all charge packets in the entire region is found by summing all individual charge packet contributions of the type shown above.

When the corona wires are close together; i.e., L/W ~1, it is necessary to include the field due to the space charge in the neighboring sections also. To ease the use of computer processing time, we make the approximation that most of the contribution to the field in Quadrant I comes from the space charge in the left half of Quadrant VII of the section to the right, and that in Quadrant IV from the right half of Quadrant VIII of another section on the left. Expressions of Equations (13) and (14) are easily adapted to include the effect of the space charge in the neighboring sections.

The Flow Field. In this work, we use the velocity flow field obtained experimentally using the tracer particle method. The experimental setup and technique are given in Reference 1. Results for a single wire precipitator are shown in Figures 4(a) and 4(b). The x and y components of the velocity, respectively, are shown in a dimensionless form. Since only the y component of the velocity exists upstream and far downstream from the wire and it obeys the Poiseuille law, the velocity scale on the graphs is determined by requiring that the flow rate for unit plate spacing is unity; i.e.,

$$u_o \int_{-1}^{1} (1 - x^2)\, dx = 1,$$

Or, $u_o = 3/4$. Thus, the maximum value of the y component of the normalized velocity is 0.75. The actual velocities for a given flow rate are obtained by multiplying the normalized velocities by Q/HW, where Q is tne volume flow rate.

It can be seen from Figures 4(a) and 4(b) that recovery of the flow downstream of the wire to the Poiseuille profile requires a distance comparable to the plate spacing (2W). This holds for the full range of laminar flows we have considered in the present study. As a result, the multi-wire flow field

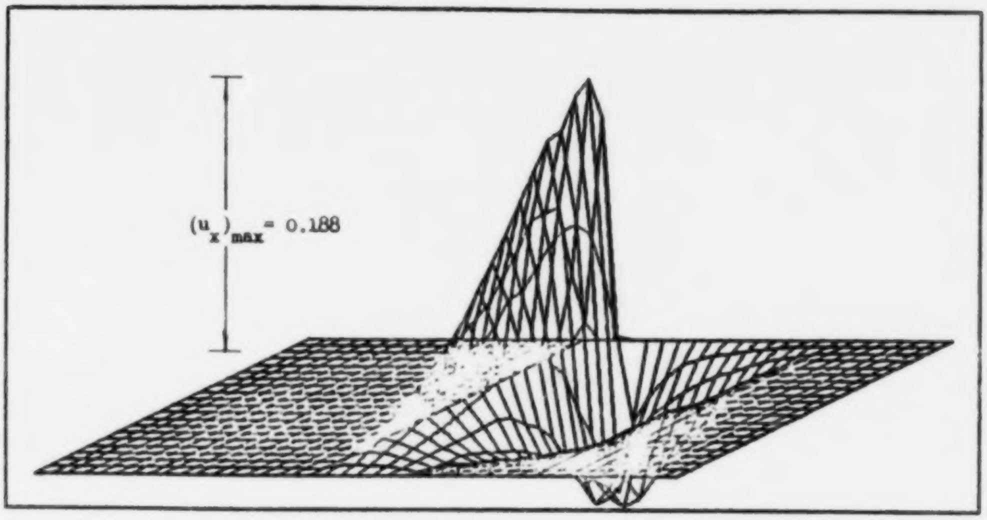

Fig. 4(a). The measured laminar velocity flow field for a single-wire precipitator section. The normalized x-component.

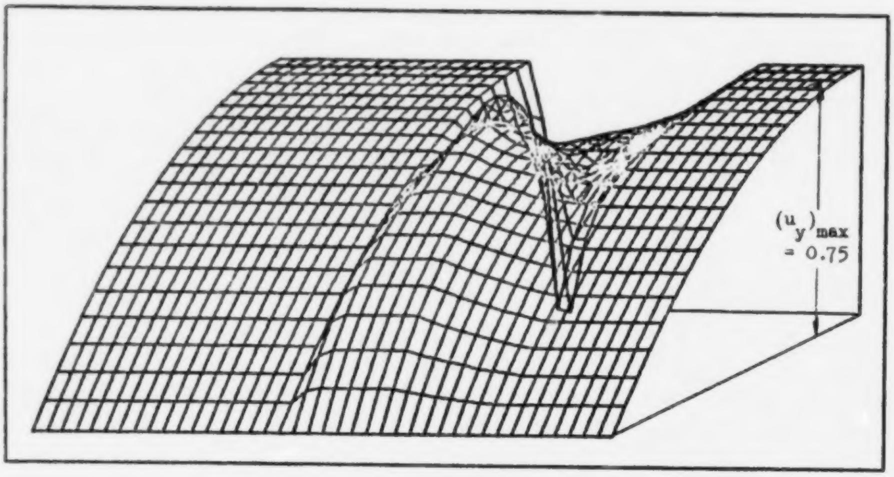

Fig. 4(b). The measured laminar velocity flow field for a single-wire precipitator section. the normalized y-component.

is obtained by simply piecing together the single-wire flow field for all values of L/W considered here. The practice should be reasonable down to L/W = 1, but below this the accuracy of the simulation suffers noticeably as will be seen later.

Verification of the Simulation Code. The algorithms used in our numerical code are checked by two methods. The first method verifies that the continuity equation is satisfied. The second method compares the electric field and space charge density given by the analytical solution of Poisson's equation for a positive coaxial corona configuration with those obtained by the simulation. In the first case, the checking is done computationally by verifying that all the charge packets crossing planes parallel to the plate electrodes of the plate-wire-plate corona add up to the total corona current. In fact, this check is made routinely while the simulation is in progress. Details of the second check are given in Reference 3. The agreement between the analytical results and those by numerical simulation is extremely good outside the ionization zone, and this is taken as evidence that our numerical code is consistent with the fundamental laws of electro-magnetism and kinetic theory.

A Discussion of the Calculated Electric Field. Generally, the electrostatic field of the wire decreases monotonically as one goes away from the wire, while the space charge electric field increases as one approaches the plates. In addition, the space charge field shows two peaks; one on the upstream side of the wire and another on the downstream side. The downstream field is of flightly larger magnitude than the upstream. The latter feature is due to the streaming of ions at the local flow velocities.

The most interesting aspect of the results shown has to do with the fact that the electric field near the plate electrodes gets most of its contribution from the space charge density. This means that the final collection of particulates depends to a large extent on the space charge field, and it underscores the importance of those molecular species susceptible to ionization (positive corona) or electron attachment (negative corona) in electrostatic precipitation.

3. CALCULATION OF THE EFFICIENCY OF A MULTI-WIRE ELECTROSTATIC PRECIPITATOR

Introduction

In this phase of calculation, the charging of initially uncharged dust particles is considered and their subsequent trajectories in the precipitator are calculated. From these trajectories, the collection efficiency of the precipitator is determined. In this chapter, we first discuss the rate at which a dielectric sphere becomes charged in the corona field.

The size distribution function of test particulates -- namely, oil droplets produced by an atomizer used in our experiments -- will be discussed, together with the way the size distribution is incorporated in the calculations. The latter discussion will include a description of how the effect of charged particulates is accounted for in the space charge density and the electric field (the concentration effect). The procedure for obtaining the collection efficiency of a single-wire precipitator is given, followed finally by the procedure for obtaining the collection efficiency of a multi-wire precipitator.

The Charging Rate of Particulates

Particulate charging is usually discussed for two mechanisms: charging by polarization of particulates in the electric field, commonly known as ion bombardment charging, and charging by thermal motion of ions, commonly known as diffusion charging. A rigorous theory includes both mechanisms and gives quite different results than shown here.[1]

An approximation considered in Reference 2 gives the following result for the rate of field charging of a dielectric sphere of radius R:

$$q_s(t) = q_s(\infty)\ (1 - e^{-t/t_c})$$

$$\text{where } t_c = (2ne_o\ n_o^+ k^+)^{-1} \quad \text{and } q_s\ (\infty) = \frac{1}{2}\ \frac{3\varepsilon}{\varepsilon_1 + 2\varepsilon_o} R^2 E_o \qquad (15)$$

n_o being the ion density far away from the dust particle, e_o being the electronic charge, k^+ being the mobility of the ions and ε_o, ε being the dielectric constant of the fluid and material of the sphere. The relaxation time, t_c, is of the order 10^{-4} seconds under conditions considered here, and this justifies the instantaneous charging of the particulates to $q_s(\propto)$ in the simulation.

Charging by diffusion involves collisions of ions with the target particulate by random notion of ions and subsequent adhesion due to attraction by their image charges. The size distribution of the particulates considered in the present study can be shown to be in the range where field charging predominates. We, therefore, ignore diffusion charging in our study.

The Particulate Size Distribution Function

The particulates used for the present study have been the droplets of heavy mineral oil produced by an atomizer. By measuring the sedimentation velocities of several hundred oil droplets, the size distribution of the oil droplets has been obtained previously in our laboratory.[2] A least-squares fit of the experimental distribution to the Nukiyama-Tanasawa distribution has been made:

$$F(R) = A\ R^2 \exp\ (-BR^s) \qquad (16)$$

where $B = 2R^{-s}/s$, $s \approx 1$ and $R_m = 2.58 \times 10^{-5}$ cm. R_m is the particulate radius at which the distribution function has a maximum.

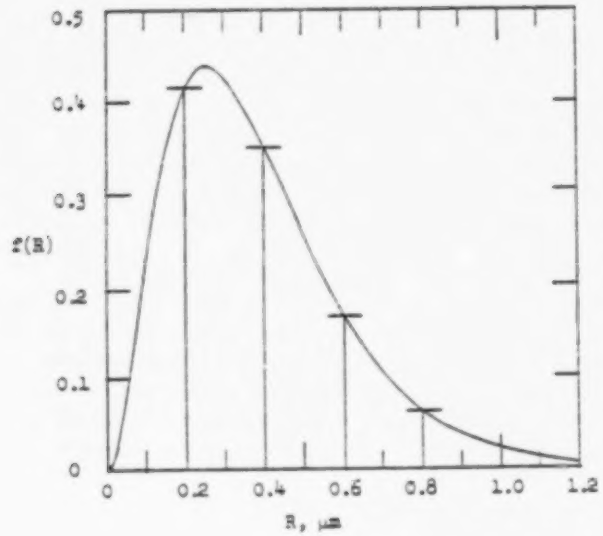

Fig. 5.

The measured particulate size distribution function and a discretized fit. The vertical axis gives the normalized probability of finding a particulate of given radius.

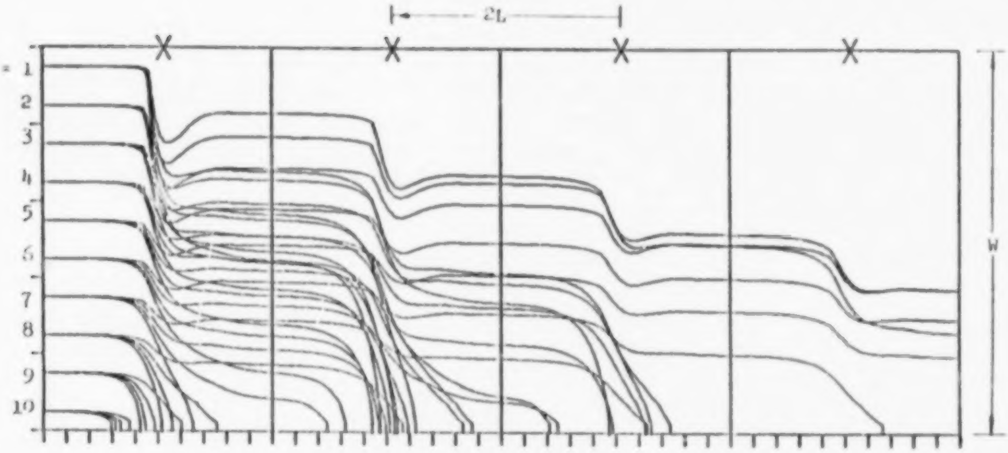

Fig. 6. Calculated particulate trajectories over four single-wire precipitator sections for L/W = 3, $i_c^+ = 33\ \mu A$/wire, $Q = 660\ cm^3$/sec and $n_p(0) = 10^7\ cm^{-3}$. Four different size particulates are introduced at each inlet position. Notice that the largest of them reaches the plate first.

In our calculations, we have approximated the measured distribution with a histogram containing only 4 size divisions, as shown in Figure 5. This approximation was dictated by the limited computer memory space. In the histogram, the probabilities of finding particles with radii 2×10^{-5}, 4×10^{-5}, 6×10^{-5} and 8×10^{-5}cm are 0.418, 0.354, 0.167 and 0.060, respectively. We denote these probabilities by f_1, f_2, f_3 and f_4, respectively. In order to simulate a random array of different size particulates in space, a random number generator is employed. Since all numbers between 0 and 1 are produced with equal likelihood by the random number generator, it is first decided which of the four ranges, 0 to f_1, f_1 to $f_1 + f_2$, $f_1 + f_2$ to $f_1 + f_2 + f_3$, and $f_1 + f_2 + f_3$ to 1, a given random number belongs to. When this number lies in the ith range (i = 1,2,3,4), a particulate of the ith radius is called out into the precipitator under simulation. The distribution of particulate sizes produced in this way indeed becomes identical with the histogram of Figure 5 when averaged over a large number of particulates. The particulate number density in the flow, of course, is determined by how frequently such particulates are called out, each by a newly generated random number.

A Single Wire Precipitator

From a given flow rate, Q, the maximum flow velocity, u_o, of the Poiseuille profile is determined by $u_o = Q/HW$. The normalized velocity flow field discussed in Chapter 2 is multiplied by u_o in order to establish an actual flow field for the full simulation.

Initially uncharged particulates are introduced at the entrance of the first stage (y = -L) as packets in much the same manner as in the corona field calculation. Each packet of particulates contains the same number of uniform-size particulates arranged along the z-axis (i.e., the wire axis). The number of particulates per unit length of a packet, δn_z, is given as follows:

$$Qn_p = 2\frac{\Delta N}{\Delta t} H \, \delta n_z \tag{17}$$

where n_p is the number density of the particulates and ΔN is the number of packets introduced in the inlet region between x = 0 and x = W at y = -L in a time interval Δt.

W, half of the precipitator inlet width, is divided into ten sections. During each time interval ΔN packets are introduced into the sections sequentially; i.e., the first packet enters the first section closest to the symmetry plane, the second packet enters the second section, and so on, until the (ΔN)th packet has been introduced. In the next time step, the first packet is introduced in the section next to that which the (ΔN)th packet entered in the preceding time interval. When all ten entrance sections have been used, subsequent packets are introduced sequentially, starting with the first section.

Using the procedure outlined earlier, each particulate packet is identified with one of the four diameters in the histogram of Figure 5, such that the size distribution of the particulate packets is the same as in the histogram. While δn_z is the same for all particulate packets, the electric charge they carry will depend not only on the radius of the particulates in a packet, but also on their starting positions as well as their current positions in the precipitator.

Whenever a particulate packet enters a region, where the space charge is greater than one tenth the charge density corresponding to one ion packet per cell (i.e., $Q(\ell,m) \geq q/10\ a_x a_y$, where q is the charge carried per ionic packet in the corona simulation program), we assume that each of the particulates of the packet is instantaneously charged, according to Equation (15), provided that $\Delta t >> t_c$.

The particulate packets introduced in a time step and all the previously introduced packets are moved in the precipitator using the algorithms outlined in Chapter 2. Initially, a packet moves in a space charge free region and follows the streamlines. Once the packet reaches a region in which the space charge density is non-zero, as measured by packets/cell, each particulate within it is given $q_s(\infty)$ corresponding to the local field strength.

Upon charging, the motion of a packet becomes coupled to both the flow field and the corona field. The packet behaves according to the mobility of a single particulate in the form of

$$k_p = q_s(\infty)/6\pi\eta R \tag{18}$$

because each particulate of the packet individually experiences the Coulomb force and the Stokes drag, both of the same magnitude but opposite directions during steady state motion. During each time step, the charge on the particulates within the packet is compared with $q_s(\infty)$ of the new field and the packet is allowed to have the higher of the two charge values. This practice is justifiable for motions toward increasing as well as decreasing field strength.

At regular time intervals of a chosen number of Δt's, the electric field, due to the particulates, is recalculated and added to the total corona field. During recalculation of the field, the particulate packets are frozen on the grid points closest to them, as in the corona field simulation. The field due these packets are calculated according to the same procedure as outlined in Chapter 2 by the image charge method. Since each particulate in a packet carries a charge $q_s(\infty)$, the packet has an effective charge per unit length of $q_s(\infty)\ \delta n_z$.

The calculation is continued until the total number of particulate packets within the precipitator section is constant; i.e., a steady state is reached. At this stage, the packets introduced during a chosen number of Δt's are tagged, and the calculations are continued until all of the tagged packets either end up on the plates, meaning collection, or exit the precipitator. By keeping track of the total number of the tagged packets introduced and the numbers of those packets that are collected according to particulate size, we can calculate the collection efficiency for each of the four size as well as the overall efficiency representative of the full size distribution.

For later use in calculations for multi-stage precipitators, the x-coordinates at the precipitator exit ($y = + L$) of those uncollected particulates are stored in a 10 by 4 array, according to their starting positions and sizes. Because the exit positions fluctuate due to fluctuations in the electric field, stemming from variations in the spatial arrangement of charged particulates, we only store the exit positions averaged over those particulates that have been tagged at the inlet.

When calculating the efficiency for single section precipitators with varying L/W ratio, it becomes necessary to change Δt. Whenever such a change is made, we also change the number of particulate packets introduced per time step so that the rate, $\Delta N/\Delta t$, is the same for all L/W ratios. In this way, δn_z, the number of particulates per unit length of the packet along the z-axis is not changed, and this allows the direct comparison of the efficiencies among single section precipitators of different L/W ratios.

When the particulate number density n_p in the precipitator reaches sufficiently high values, the electric field due to the charged particulates become comparable to the electric field due to the ionic space charge. When this condition prevails, the ionic space charge distribution has to be recalculated in order to allow for the presence of the charge particulate field. This is accomplished by freezing the electric field due to the charged particulates at values obtained from the steady state precipitation simulation, and re-running the simulation of the corona field against this background charged particulate field. The corona field obtained from this iteration is employed in the final simulation for particulate trajectories and the collection efficiency.

It has been found that for particulates of the size distribution which are predominantly in the sub-micron range, the charged particulate field remains smaller than the ionic space charge field for $n_p < 10^7$ cm^{-3}. For densities of 5×10^7 cm^{-3} or higher, some readjustment of the ionic space charge distribution becomes necessary.

A Multi-wire Precipitator

We calculate the collection efficiency of a multi-wire precipitator by performing exactly particulate trajectory calculations for the first two sections and inferring from the results the exit positions of particulates for subsequent sections. From the first section calculations, we obtain for uncollected particulates not only their exit positions $XIT_1(n_1,n_2)$, but also their charges $q_1(n_1,n_2)$ and mobilities $k_{p1}(n_1,n_2)$ with which they exit the first section. Note that each of these leads to a 10 x 4 array of numbers because there are ten first section entrance positions (n_1) and four particulate radii (n_2). The subscript 1 denotes the first section of the precipitator. In the second section calculation, the particulates enter with the same charges and mobilities at the same x-positions as they exit the first section with. ΔN, the rate at which the particulate packets are introduced, is the same as in the trajectory calculation for the first section, except that only those uncollected packets from the first section are used. In other words, the particulate number density decreases in subsequent sections as it should. When a steady state is reached with the number of packets in the section, those packets introduced during a certain number of Δt's are tagged and the calculation is continued until all of the tagged packets either are collected or leave the second section.

From this calculation, we obtain the exit positions for the second section $XIT_2(1,n_1,n_2)$, of those particulate packets which entered the first section at the entry position designated by n_1 and with a radius designated by n_2. The first index, 1, signifies the exit positions computed for the packets having the same charges as at the exit of the first section. At this point, two additional calculations are performed in order to obtain the second section exit positions of the packets with one-half and twice the original charges. The resulting exit positions are designated by $XIT_2(2,n_1,n_2)$ and $XIT_2(3,n_1,n_2)$, the index 2 standing for half charges and the index 3 standing for double charges. The exit positions for subsequent sections are obtained by linear interpolation of these three 10 x 4 arrays of exit positions, according to the charge and exit position of each packet at the exit of the preceding section.

When the number density of particulates is high enough to influence the ionic space charge distribution, the interpolation involves one more variable; namely, the number density of particulates at the exit of the preceding section. The first two section simulations are done for two densities, one at 10^7 and another $10^8 cm^{-3}$, for this purpose. Even for very high first section densities, such an interpolation is needed only for the first few sections of the multi-wire precipitator.

The above procedure is repeated for all succeeding sections until each particulate packet has either hit the plates or exits the entire multi-wire precipitator. By carrying out this procedure for many particulates representative of the size distribution, we obtain the collection efficiency as a function of particulate size and also as a function of the number of the single-wire sections.

The Relationship Between the Single-Wire and Multi-Wire Precipitator Efficiency

In the manner prescribed in the preceding discussion, it is simple to determine the efficiency $\eta(1)$ of a single-wire precipitator. Here, we are interested in expressing the efficiency of a multi-wire precipitator in terms of the efficiencies of constituent single-wire sections. If N_o particulates enter the multi-wire precipitator per unit time, the number of particulates that leave the first single-wire section per unit time is

$$N_1 = N_o[1 - \eta_1(1)]$$

where the subscript i of $\eta_i(1)$ denotes the single-wire section number.

Similarly, the number after the Nth section is

$$N_N = N_o \mathop{\pi}_{i=1}^{N} [1 - \eta_i(1)] \qquad (19)$$

The collection efficiency of the N-wire precipitator is obtained from Equation (19) as follows:

$$\eta(N) = (N_o - N_N)/N_o$$

$$= 1 - \mathop{\pi}_{i=1}^{N} [1 - \eta_i(1)] \qquad (20)$$

Once $\sim(N)$ is known as a function of N, it is possible to determine $\eta_i(1)$ as a function of the section number i by best fitting Equation (20) to the data.

If $\eta_i(1)$ is assumed to be the same for all sections, Equation (20) reduces to

$$\eta(N) = 1 - [\ 1 - \eta_1(1)]^N \qquad (21)$$

which is an analog of the Deutsch equation[4]. Equation (21) becomes identical to the Deutsch equation in the limit of large N:

$$\eta^D(N) = 1 - e^{-\eta_1^D(1)\ N} \qquad (22)$$

Where N is integer values of y/2L and $\eta_1^D(1) = \omega\frac{A}{q}$,

and A is the plate area per single section of the precipitator and ω the average drift in a direction velocity perpendicular to the plates Q is the flow rate.

As will be seen in the following section, the notion of uniform single-wire efficiency is incorrect for multi-wire precipitators. The Deutsch equation, which is based on such a notion as well as other simplifying assumptions, naturally fails to represent the behavior of the multi-wire precipitator.

A Discussion of the Results from the Numerical Simulation

Trajectories of forty particulates of four different sizes are displayed in Figure 6 for L/W = 3, $i_c^{\pm}$ = 33 μA/wire, Q = 660 cm^3/sec and $n_p(0) = 10^7$ cm^{-3}. Four different size particulates introduced at each inlet position are seen to drift toward the plate at different speed; the largest being the fastest as expected from the mobility consideration. Notice that the figure has been compressed along the direction of the flow in order to display the trajectories for four consecutive single-wire sections. We emphasize that these particulates have been selected and followed out of approximately one thousand particulates present in the field of each section at any given time.

The figure concisely sums up how a multi-wire precipitator behaves. Those particulates near the plate are collected rather quickly, thus contributing strongly to the collection efficiency of the first two sections. The space charge density is large, as is the space charge field strength in the region near the plate. There is a stretch of distance where the particulates introduced in the middle between the plate and the plane of wires drift toward the plate, but the drift is not enough to effect collection. Thus, the efficiency is low. In the next few sections, the efficiency increases due to the arrival of those particulates at the plate. Collection of the particulates introduced nearer to the plane of wires takes place slowly over a long stretch of sections. The electric field strength can be very high in this band of space very near the wires, but the space charge density is very low. At the same time, the flow velocity is the highest in this band and the streamlines are such that the charged particulates are quickly taken out of the strong field region at each wire. The net result is these particulates take a long flow time to reach the region where the collection is favorable.

Figure 7 shows the collection efficiency as a function of the number of single-wire sections for the case of $L/W = 3$, $i_c^+ = 33\ \mu A$/wire, $n_p\ (0) = 10^7\ cm^{-3}$ and $Q = 660\ cm^3/sec$. The efficiency $\eta(N)$ is shown for each particulate size as well as for the full distribution. As expected, $\eta(N)$ cannot be represented by a uniform single-wire efficiency function of Equation (21) or Equation (22). In Figure 8, we show $\eta_i(1)$ as a function of the section number i, obtained by smooth curve fitting $\eta(N)$ of Equation (20) to the data displayed in Figure 7. It is interesting to observe that in each case of four different size categories as well as the full distribution, the single-wire efficiency for the first section is larger than for the immediately following ones. Of course, the fact that $\eta_i(1)$ eventually becomes unity is the inevitable consequence of the property of Equation (20). That is, $\eta(N)$ cannot become unity for finite values of N without one or all of $\eta_i(1)$'s becoming unity.

The effect the particulate number density has on the precipitation efficiency is seen quantitatively in Figure 9. $\eta(1)$ and $\eta(2)$ are shown for three values of n_p for a precipitator with $L/W = 3$, $i_c^+ = 33\ \mu A$/wire and $Q = 660\ cm^3/sec$. This phenomenon, which we call the concentration effect, has its origin in the Coulomb repulsion of charged particulates in the corona field. As the number density is increased sharply, their repulsion becomes significant and drives the particulates toward the plates. The net result is a considerable increase in the efficiency.

Comparison of Theoretical Predictions with Experiment

In order to make an objective test of the results from the simulation, a series of measurement has been carried out of the particulate collection efficiency in 6-wire model precipitators. Altogether, five separate 6-wire precipitators have been used. All have exactly the same wires and dimensions except that the wire spacing (2L) varies from one unit to another to give the wire-to-plate spacing ratio L/W of 3/4, 1,2,3 and 4, respectively. The collection efficiency is measured by a light-scattering method at the He-Ne laser, as well as argon ion laser wavelengths. Experimental details

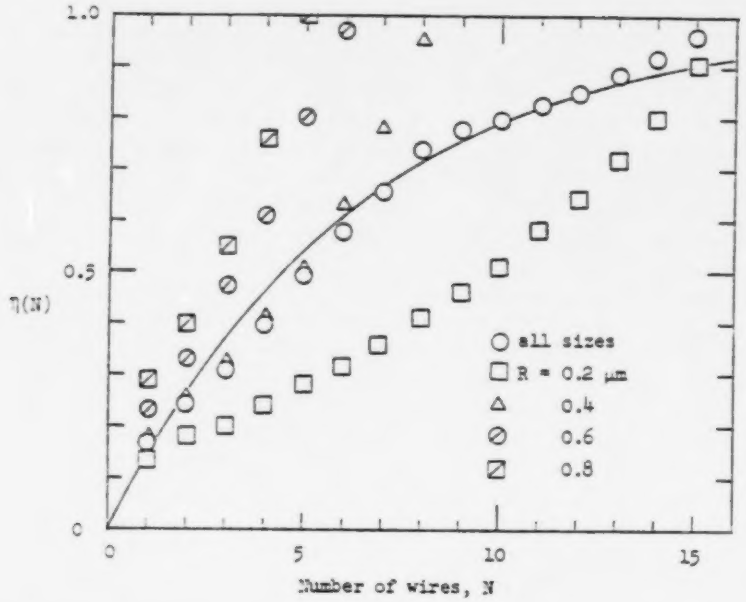

Fig. 7. $\eta(N)$ vs. N for L/W = 3, i_c^+ = 33 μA/wire, Q = 660 cm^3/sec, and $n_p(0) = 10^7$ cm^{-3}. Also shown are $\eta_R(N)$ for four different values of R: R = $2x10^{-5}$, $4x10^{-5}$, $6x10^{-5}$ and $8x10^{-5}$ cm. $\eta(N)$ of eq.(21) is plotted with $\eta(1) = 0.145$ for comparison.

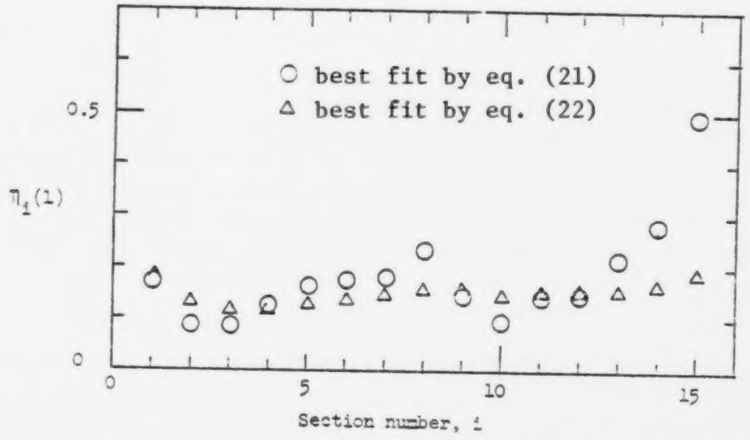

Fig. 8. $\eta_i(1)$ vs. the section number i, as obtained by best fitting eqns. (20) and (21) to the data of Fig. 7.

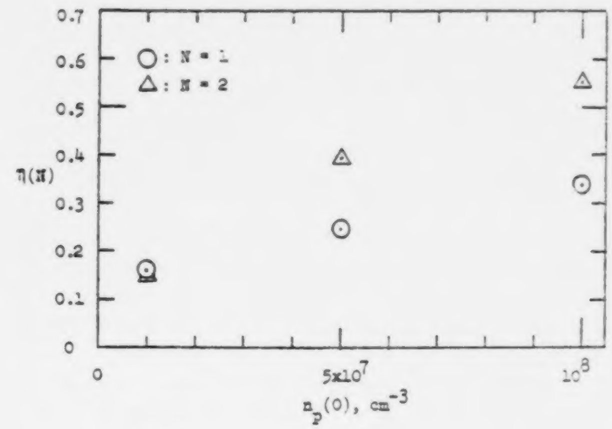

Fig. 9.
$\eta(1)$ and $\eta(2)$ for three values of the particulate number density at the inlet, $n_p(0)$, for $L/W = 3$, $i_c^+ = 33\mu A$/wire and $Q = 660$ cm^3/sec.

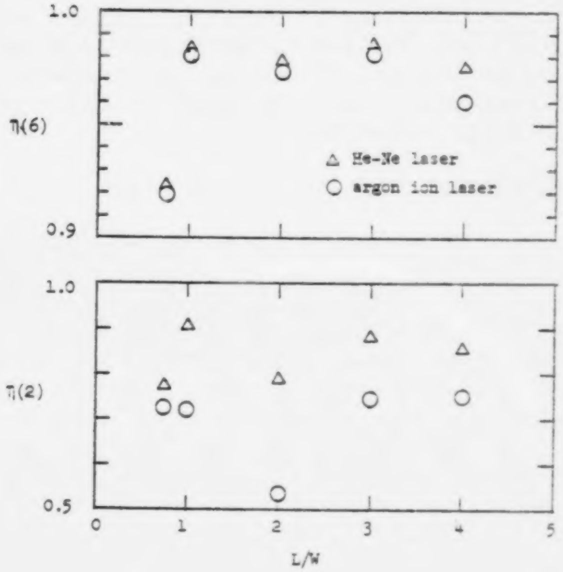

Fig. 10.
Measured $\eta_R(2)$ and $\eta_R(6)$ vs. L/W of the model precipitators operating at $i_c^+ = 33$ μA/wire and $Q = 660$ cm^3/sec. Both He-Ne and ArI laser data are shown.

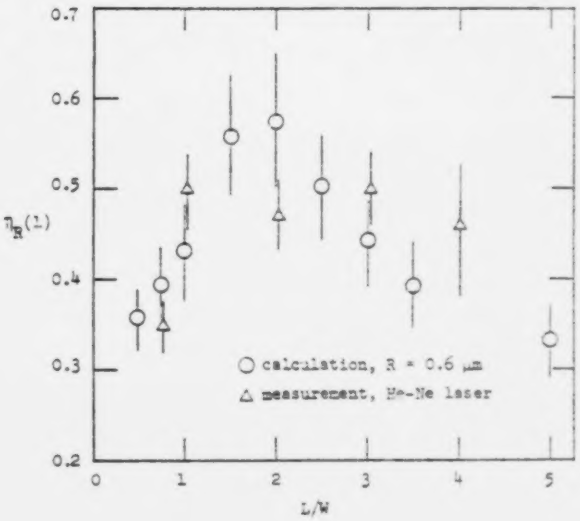

Fig. 11.
Calculated and measured $\eta_R(1)$ vs. L/W for $Q = 660$ cm^3/sec, $i_c^+ = 33$ μA/wire and $R = 0.6$ μm. $\eta_R(1)$ has been obtained from $\eta_R(6)$ by eq. (21). Note that $n_p(0)$ is 10^7 and 10^6 cm^{-3} for theory and experiment respectively, but this difference has no effect here.

may be found in Reference 3. In the following, we compare the experimental results with the theoretical predictions. In the final section, the scaling of the efficiency as a function of the L/W ratio is analyzed on the basis of data from both experiment and numerical simulation.

The large majority of particulates used for this study are considerably smaller in radius than the wavelength of the He-Ne laser (6328Å) and those of the argon ion laser (4880 and 5145 Å). Studies of light scattering (5) show that the total cross-section is the largest at the He-Ne wavelength of 6328 Å for particulates of 0.59 μm (microns). At the Ar ion wavelengths of 4880 and 5145Å, the largest total scattering cross-section is found for particulates of 0.49 μm. Figure 10 displays a plot of measured total efficiencies at the end of 2 sections, $\eta_R(2)$ and at the end of 6 sections, $\eta_R(6)$, versus the L/W ratio at Q=660 cm^3/sec., obtained with both the He-Ne and ArI laser; i.e., for R=0.59 and 0.45μm. A comparison of the above data with those from numerical simulation in Figure 11 demonstrate a good agreement between theory and experiment in the case of precipitator operation in the positive corona mode.

The Variation of the One-wire Efficiency with the Wire-to-plate Ratio

Figure 11 shows the experimental verification of the theoretically predicted existence of an optimum value of the wire-to-plate ratio, L/W, for a given flow rate. This optimum L/W ratio may be understood as arising from the competition between two effects: larger L/W ratios give higher efficiencies because of larger treatment times, while smaller L/W ratios give higher efficiencies because of higher charging and collecting fields. From this explanation, it is clear that the optimum L/W ratio will be different for different flow rates. The significant fact is that the one-wire efficiency maximum is somewhat shallow, which means that over a large range of L/W, the one-wire efficiency can be regarded as approximately constant. The above finding leads to the important conclusion that it is the number of wires per gas passage rather than the plate area which determines the collection efficiency of the precipitator.

4. CONCLUDING REMARKS

In the preceding chapters, we have described a versatile and powerful technique of numerical simulation ideally suited to solve a class of coupled kinetic-electro aerodynamic problems found in large-scale electrostatic precipitators. A narrowly definable problem of the scaling of the wire-to-plate spacing ratio has been identified and analyzed by this technique. An independent experiment has been designed and carried out to confirm the conclusions from the numerical simulation. A good agreement between the simulation and experiment has been demonstrated.

The existence of an optimum wire-to-plate spacing ratio constitutes a new and basic finding. Our understanding of the physics of the phenomenon appears reasonable. While the analysis has been limited to the idealized precipitators and to the positive corona configuration, it is most likely that this optimal behavior is in effect in all sizes and variations of the plate-wire precipitator. Detailed analysis has also been made for the negative corona configuration. It shows the same optimal behavior as for the positive corona. The negative corona results are not presented here because the efficiencies predicted from the numerical simulation fail to agree with the experimental data on an absolute scale. This is due in large part to the lack of reliable and detailed data on collision cross sections for various electron sttachment processes in air.

This study has revealed in anatomical detail how the electrostatic precipitation process takes place and, thereby, established the roles of various operating parameters or features in terms of their influence on the collection efficiency. An example is the concentration effect. Another is the way the space charge density affects the precipitation efficiency. Its primary role is not in the particulate charging rate as commonly thought, but in contributing to the total electric field strength near the plate where the electrostatic field of the wire is weak and the particulates must gain significant drift speed for final collection by virtue of high field strength. Charging of the particulates takes place elsewhere, near the precipitator inlet where the space charge density is generally low. It is noted that the assumption we adapted of instant charging becomes questionable only in very small precipitators such as our model units operating at the highest rate quoted. Its reasonableness improves drastically for large scale precipitators.

Another basic finding of rather subtle nature is the role the particulate size distribution function plays in influencing the collection efficiency. We have seen in Chapter 3 that the single wire efficiency can be broken down to its dependence on the particulate size. Careful examination of numerically generated trajectories shows that the makeup of the nearest neighbor particulates of a test particulate strongly influences the eventual course of its trajectory. This leads to the observation that the single wire efficiency for a given particulate size depends in a significant way on the full-size distribution function of the particulates in the precipitator. This effect contributes, in part, to the position dependence of the single wire efficiency.

One can now ask how much one can improve the efficiency of an N-wire precipitator by optimizing the wire-to-plate spacing ratio. Judging from the results of Chapter 3, it is reasonable to anticipate 10 to 15% improvement in the single-wire efficiency. Assume now for the sake of simple estimation that $\eta(1)$ is constant throughout the precipitator. In Table 1

TABLE I. $\eta(N)$ as calculated from Equation (21) for several values of $\eta(1)$ and N

$\eta(1)$	$\eta(20)$	$\eta(30)$	$\eta(50)$
0.06	0.710	0.844	0.955
0.07	0.766	0.887	0.973
0.08	0.811	0.918	0.985
0.09	0.848	0.941	0.991
0.10	0.878	0.958	0.995

We list values of $\eta(N)$ for five different values of $\eta(1)$ and three of N. A 14% increase in $\eta(1)$ from 7 to 8%, for example, results in a 6% increase in $\eta(20$ from 76.6% to 81.1% and only a 1% increase in $\eta(50)$from 97.3% to 98.5%. The results of Table I also indicate the extent of efficiency enhancement that may be expected by increasing the number of wires per gas passage. This simply illustrates the magnitude of the task in making the necessary improvement in the actual N-wire precipitator efficiency. It also underscores the optimization of the wire-to-plate spacing ratio as one area where a few precious percent can be gained in the total efficiency.

This study benefited a great deal from discussions with Peter Sincerny and Yong Kim of Lehigh University and William Langan, Gordon Gogola and John Modla of Buell/Envirotech. Olga Garnet's help with the manuscript is deeply appreciated.

References

1. Kim, Y. W. Electrostatic Precipitators I. Wire Oscillation, Particulate Charging Rates, Flow Field and Imparity Effects", Physics of Fluids Technical Report No. 26, Department of Physics, Lehigh University (1978).

2. Kim, Y. W. An Analytical Consideration of the Particle Inertia Effect with an Application to Aerosol Sampling Efficiency Calculation, Physics of Fluids Technical Report No. 24, Department of Physics, Lehigh University (1974).

3. Kim, Y. W. and E. A. Samuel. Electrostatic Precipitators II. The Efficiency and Wire-to-Plate Spacing Ratio, Physics of Fluids Technical Report No. 27, Department of Physics, Lehigh University (1978).

4. Rose, H. E. and A. J. Wood. An Introduction to Electrostatic Precipitation in Theory and Practice. Constable and Company, Ltd, London (1956).

5. Kerker, M. The Scattering of Light and Other Electromagnetic Radiation, Academic Press, New York (1969).

THE EFFECTS OF CORONA ELECTRODE GEOMETRY ON THE OPERATIONAL CHARACTERISTICS OF AN ESP

by

George Rinard, Donald Rugg and Whitney Patten
Denver Research Institute
Denver, Colorado 80208

and

Leslie Sparks
Industrial Environmental Research Laboratory
Environmental Protection Agency
Research Triangle Park, North Carolina

ABSTRACT

Experiments were run in a pilot scale electrostatic precipitator (ESP) to determine the effects of corona wire-to-wire spacing on the operating conditions. Tests were run, using a reentrained low sulfur fly ash at both hot- and cold-side conditions. The effects of varying wire-to-wire spacing were determined. Results are given which show that varying wire spacing at cold-side conditions has little operational effect on the ESP while improved efficiency can be obtained at hot-side (low resistivity) conditions by reducing wire spacing. The increased efficiency results from a higher average operating voltage. The effects of back ionization are clearly demonstrated by a set of experiments in which dust was selectively removed from the wires or plate. These tests show that the lower operating voltage caused by back ionization is a combined effect of high resistivity dust on both the wires and plate.

THE EFFECTS OF CORONA ELECTRODE GEOMETRY ON THE OPERATIONAL CHARACTERISTICS OF AN ESP

INTRODUCTION

An electrostatic precipitator (ESP) collecting ash with high electrical resistivity must be operated at low corona current density to avoid back ionization. Usually this means that the operating voltage will also be very low. If the operating voltage for a given current density could be increased, ESP performance should improve. It is well known that changes in the geometry of the corona electrode will alter the clean plate VI characteristics. Either an increase in the size of the corona wires or a decrease in the spacing between the wires will result in an increased corona onset voltage and higher voltages for a given current density (White, 1963). If the dirty plate VI characteristics of an ESP could be modified to give the same result, improved ESP performance could result.

Experiments were conducted on a pilot scale ESP at EPA's Industrial Environmental Research Laboratory, Research Triangle Park, to determine the effects of corona electrode geometry on the clean and dirty plate operating characteristics of an ESP collecting high resistivity dust. The results of these tests, regarding how the electrode geometry affected the electrical characteristics, efficiency and opacity, are given below.

Experimental Procedure

The pilot scale ESP is a one lane wire duct ESP and is fully described by Lawless et al. (1979). There are four electrical sections consisting of two 1.2 m square collector plates. The plate-to-plate spacing for these experiments was 22.9 cm. Temperature is controllable from ambient to 400°C by means of propane burners. A draft fan provides air flow. The aerosol used in these experiments was fly ash which was injected through sandblast guns. This method of injection produced a stable test aerosol.

The test procedure included variation of electrical conditions and corona wire-to-wire spacing, and measurement of mass efficiencies at both cold-side and hot-side temperatures utilizing a low sulfur ash. Tests were also performed to determine the relative effect, on VI characteristics, of ash on the plates and the wires.

The resistivity of the fly ash, as measured in the laboratory, is given in Figure 1. The laboratory measurement for 150°C agrees well with *in situ* measurements.

Sections 1 and 2 of the ESP had 0.32 cm corona wires spaced at 22.9 cm. Section 3 and 4 had 0.32 cm wires spaced at 7.62 cm.

This work was supported under Grant R805733 through the EPA's Industrial Environmental Research Laboratory, Research Triangle Park, North Carolina.

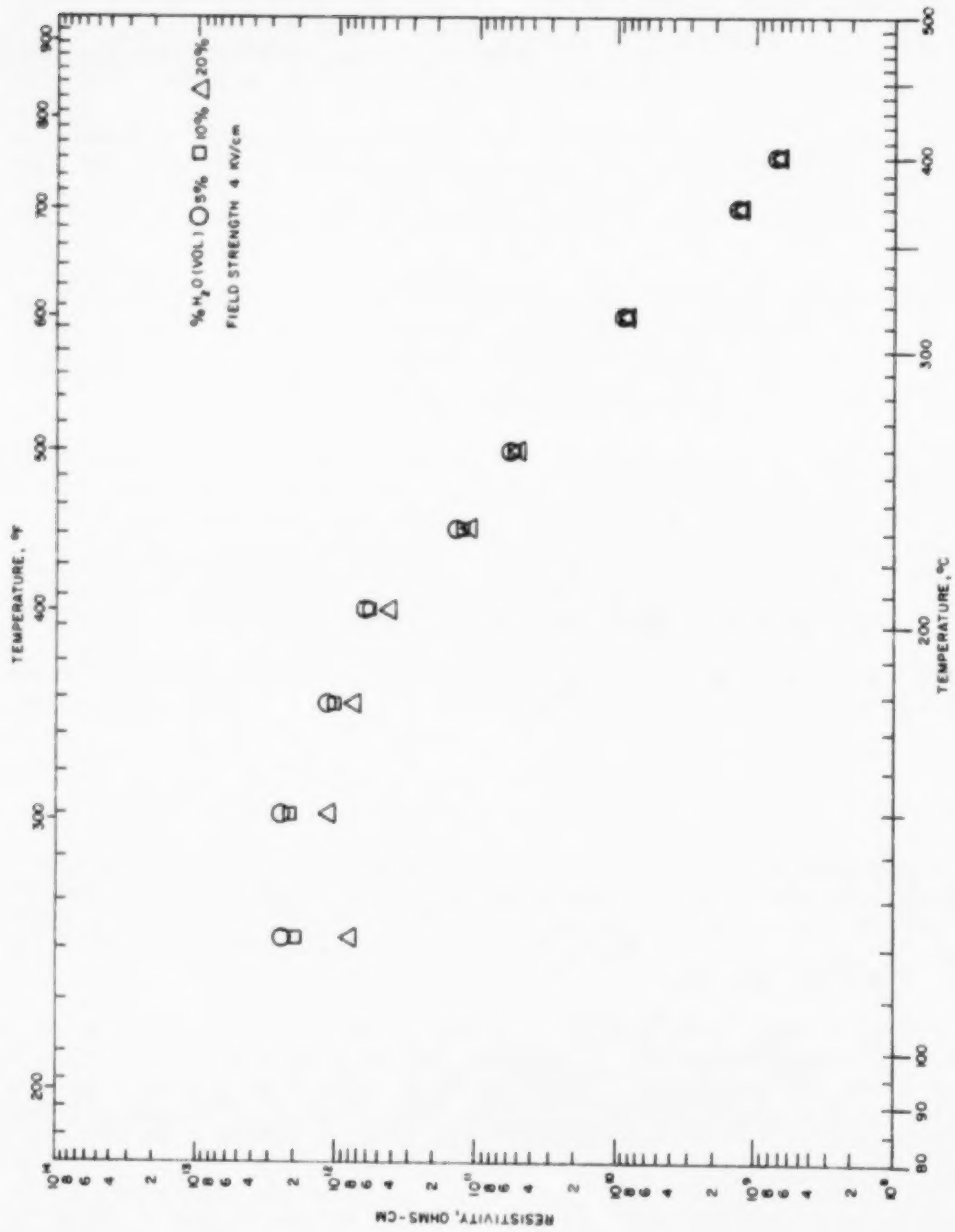

Figure 1. FLY ASH RESISTIVITY

RESULTS

Previous tests had shown that the mechanical condition of the ESP is good and thus there is no section to section variation in electrical conditions for a given wire-to-wire spacing. This was verified in these experiments, i.e., the electrical conditions in any sections with the same wire-to-wire spacing were the same under all operating contions.

Clean-plate/clean-wire (CP/CW) and dirty-plate/dirty-wire (DP/DW) VI curves for Section 1 (22.9 cm wire spacing) at 148°C are shown in Figure 2. The corona onset voltage is much lower for the DP/DW case. Also note that the current for a given voltage is much higher in the DP/DW case.

CP/CW corona onset voltage and DP/DW VI curve for Section 3 (7.62 cm wire spacing) are shown in Figure 3. In this case the corona onset voltage for DP/DW case is much less than corona onset for clean conditions. Also note that the DP/DW VI curve is similar to the DP/DW VI curve for Section 1 (Figure 2) although the CP/CW curves are much different.

Also shown in Figures 2 and 3 are the operating points for Sections 1 and 3 for two levels of current density. The current was manually controlled around the two set points. The data were obtained from the data printout for the ESP which printed operating conditions once every minute. The operating points for both sections drift but are essentially the same and are independent of wire spacing. Curves similar to those in Figures 2 and 3 but for hot-sides (350°C) are shown in Figures 4 and 5.

For hot-side conditions the operating point was much more stable and remained very close to the CP/CW characteristics for each of the four sections. For the 22.9 cm wire-to-wire spacing, while operating at a current of about 1 mA, the voltage remained in the vicinity of 26 kV. However, for the 7.62 cm wire-to-wire spacing while operating at the same current the voltage was maintained in the vicinity of approximately 33 kV.

Comparisons of these four figures indicate that at cold-side temperatures the ultimate operating point of the precipitator is nearly independent of the corona electrode geometry. However, while operating under hot-side conditions, the operating point was quite dependent upon the corona electrode geometry.

Figure 6 shows the change in precipitator operating voltage as a function of temperature for a constant operating current of 1.5 mA. As can be seen, the operating voltage for both 7.62 and 22.9 cm wire-to-wire spacing is very nearly the same and is independent of electrode geometry for temperatures in the range of 148°C to 204°C. However, the operating voltage for 7.62 cm wire-to-wire spacing is about 8 kV higher than that for the 22.9 cm wire-to-wire spacing in the temperature range above 260°C. In this range the operating characteristics are very nearly those of CP/CW. In the range of 204°C to 260°C the operating voltage is somewhat lower than would be expected from the CP/CW characteristics for both 7.62 cm and 22.9 cm wire-to-wire spacing. At around 233°C the operating voltage for the 7.62 wire-to-wire spacing makes a dramatic jump of approximately 5 kV.

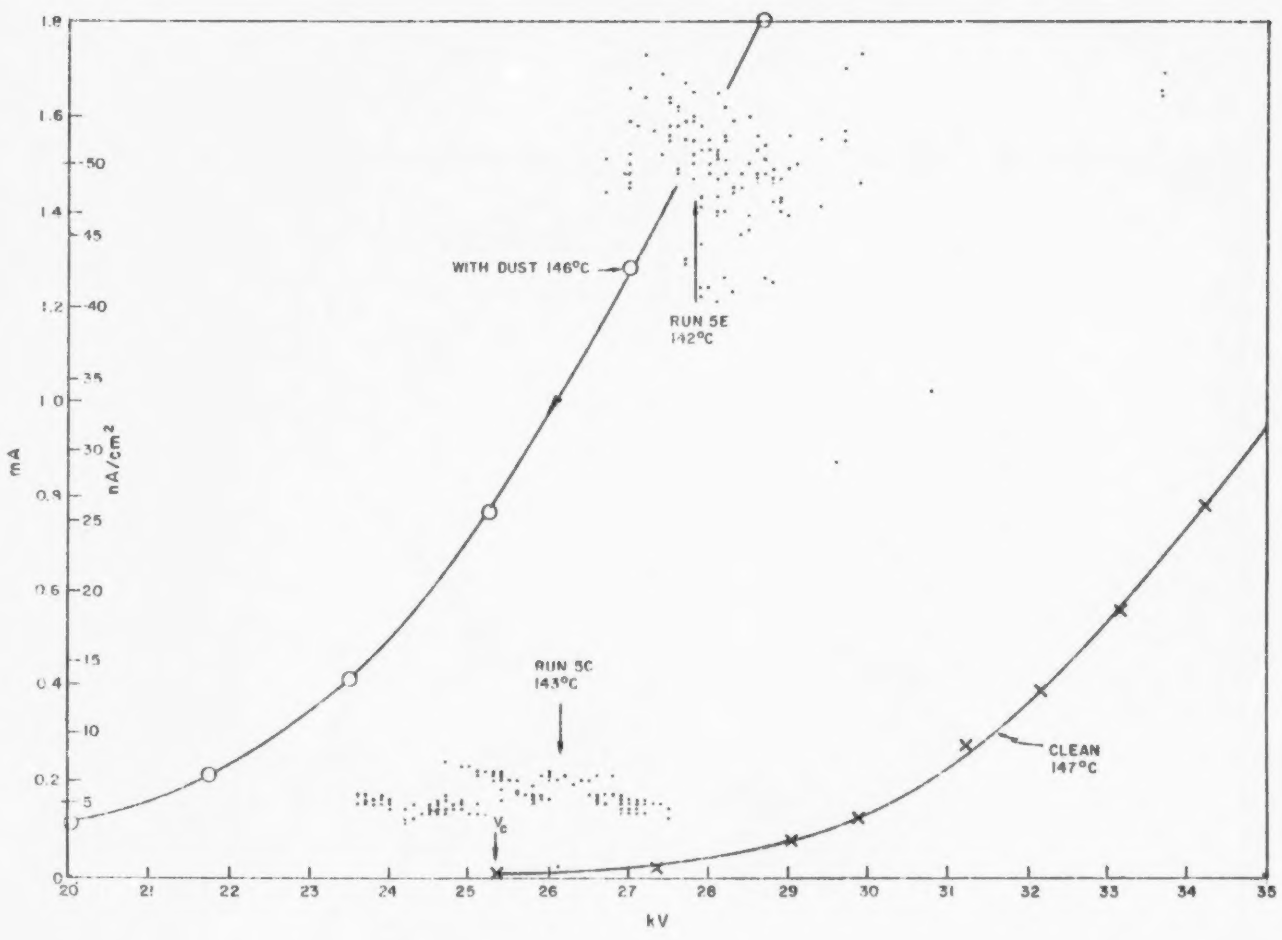

Figure 2. OPERATING CHARACTERISTICS OF SECTION 1
WITH 22.9 cm SPACING AT COLD-SIDE TEMPERATURES

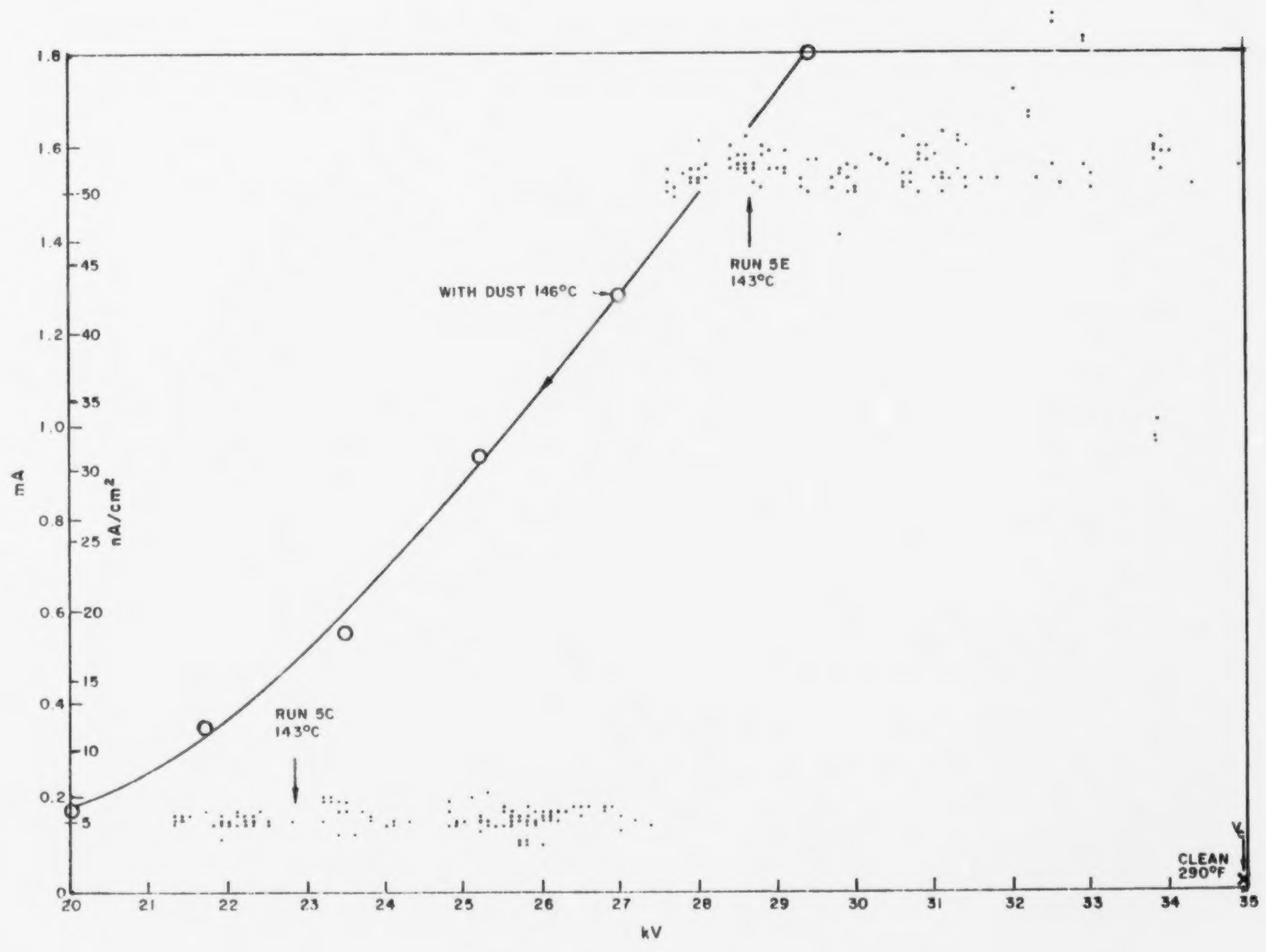

Figure 3. OPERATING CHARACTERISTICS OF SECTION 3
WITH 7.62 cm WIRE SPACING AT COLD-SIDE TEMPERATURES

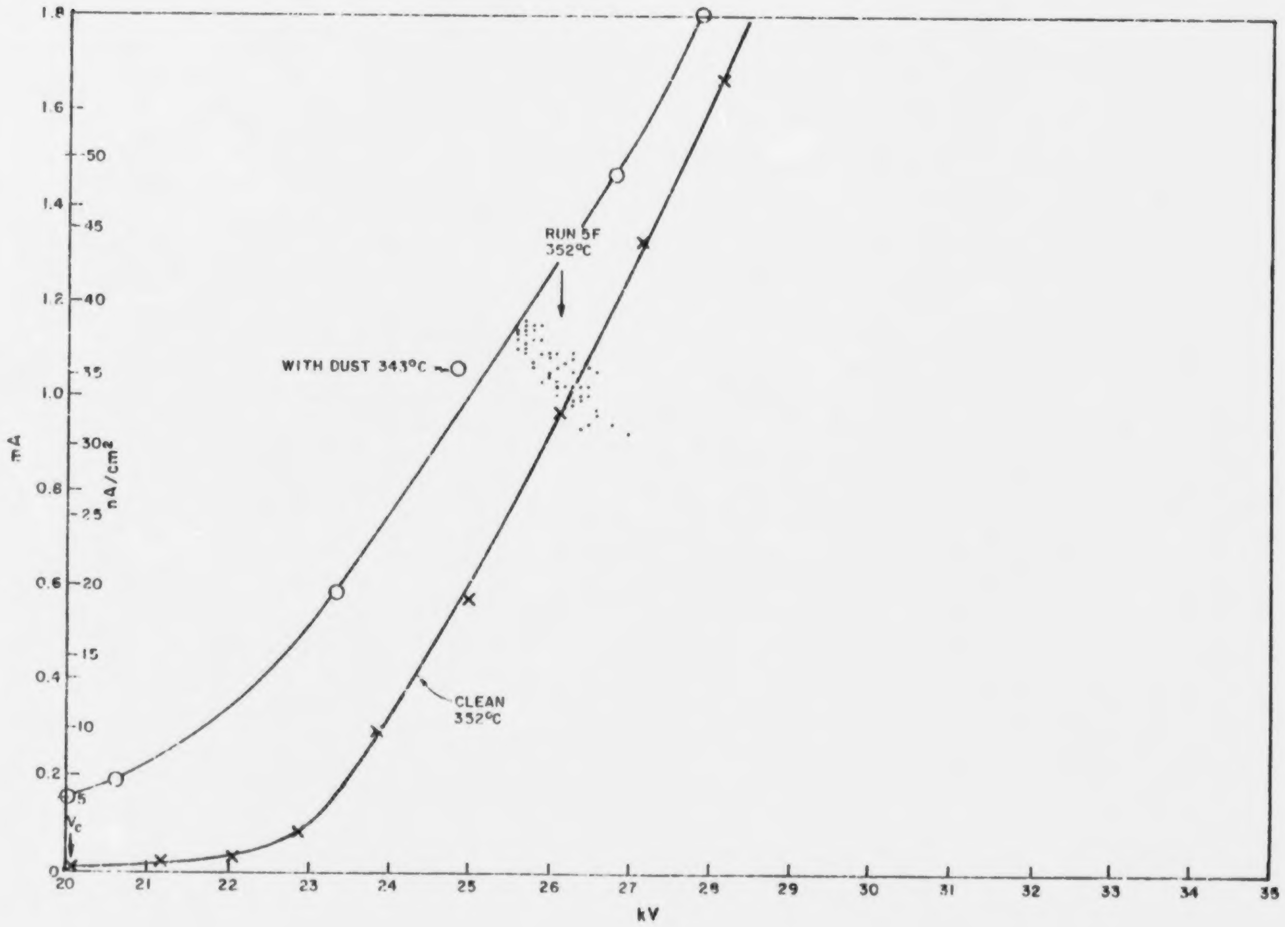

Figure 4. OPERATING CHARACTERISTICS OF SECTION 1 WITH 22.9 cm WIRE SPACING AT HOT-SIDE TEMPERATURES

It is evident from Figure 6 that the operating characteristics of the precipitator in the temperature range of 148°C to 204°C are determined primarily by the high resistivity of the dust (approximately 10^{12} ohm-cm). At 148°C the operating points for 7.62 wire-to-wire spacing and 22.9 cm wire-to-wire spacing very nearly coincide. As the temperature is increased above 148°C the operating voltage for the precipitator increases as the dust resistivity decreases. In the temperature range 204°C to 260°C the dust resistivity becomes low enough (approximately 10^{11} ohm-cm) so that it is no longer the predominant effect. As the temperature is increased beyond this range the operating voltage decreases due to the decreased density of the air at the higher operating temperature. Similar results were obtained by Tachibana et al. (1978) in tests where the voltage rather than current was maintained constant as temperature was increased.

Figure 7 gives the voltage current characteristics of a section of the precipitator with 7.62 cm wire-to-wire spacing and without dust on the wires and/or the plates. These characteristics were all obtained at cold-side temperatures at around 148°C. To obtain these characteristics, the ESP was opened after several hours of operation with dust and either plates or wires were cleaned. Then the ESP was closed and operated with no reentrained dust.

The corona onset voltage for DP/DW is about 12 kV lower than that of CP/CW. This voltage difference was maintained between these two curves as the current increased. As the voltage was decreased for DP/DW the current decreased more slowly, resulting in hysteresis in the operating characteristics. The corona onset voltage for dirty-plate/clean-wire (DP/CW) is very nearly the same as that for CP/CW. As long as the operating voltage for DP/CW was maintained slightly above corona onset, stable operating conditions could be maintained. However, as the voltage was increased beyond this point the current increased abruptly and the voltage started to decrease. As the voltage was decreased the current remained rather high resulting in considerable hysteresis for this situation. For the clean-plate/dirty-wire (CP/DW) case the corona current started at a voltage below 25 kV. The current for this situation then increased up into the range of about 38 kV. At this voltage, the corona current increased abruptly with voltage. As the voltage was decreased from the point of maximum current, very little hysteresis was observed. Other investigators suggest that high resistivity dust on the discharge electrode wire will decrease the corona current (Robinson, 1971) which is not consistent with the data in Figure 7. The effect of a high resistivity coating on the wires is not fully understood. It is clear that the dust affects the roughness factor but other mechanisms also appear to be involved.

Figure 8 gives the results of mass efficiency measurements as a function of the average voltage of all four of the precipitator electrical sections for the period of time that the mass samples were taken. The four efficiency measurements in Group I are for 22.0 cm wire-to-wire spacing in all four electrical sections while the precipitator is operating at cold-side temperatures. The three efficiency measurements in Group II are for the same precipitator configuration except when operating at hot-side temperatures. The efficiencies for hot-side conditions were considerably higher than for cold-side conditions. In both cases the efficiency was greatly increased by the increase in operating current and

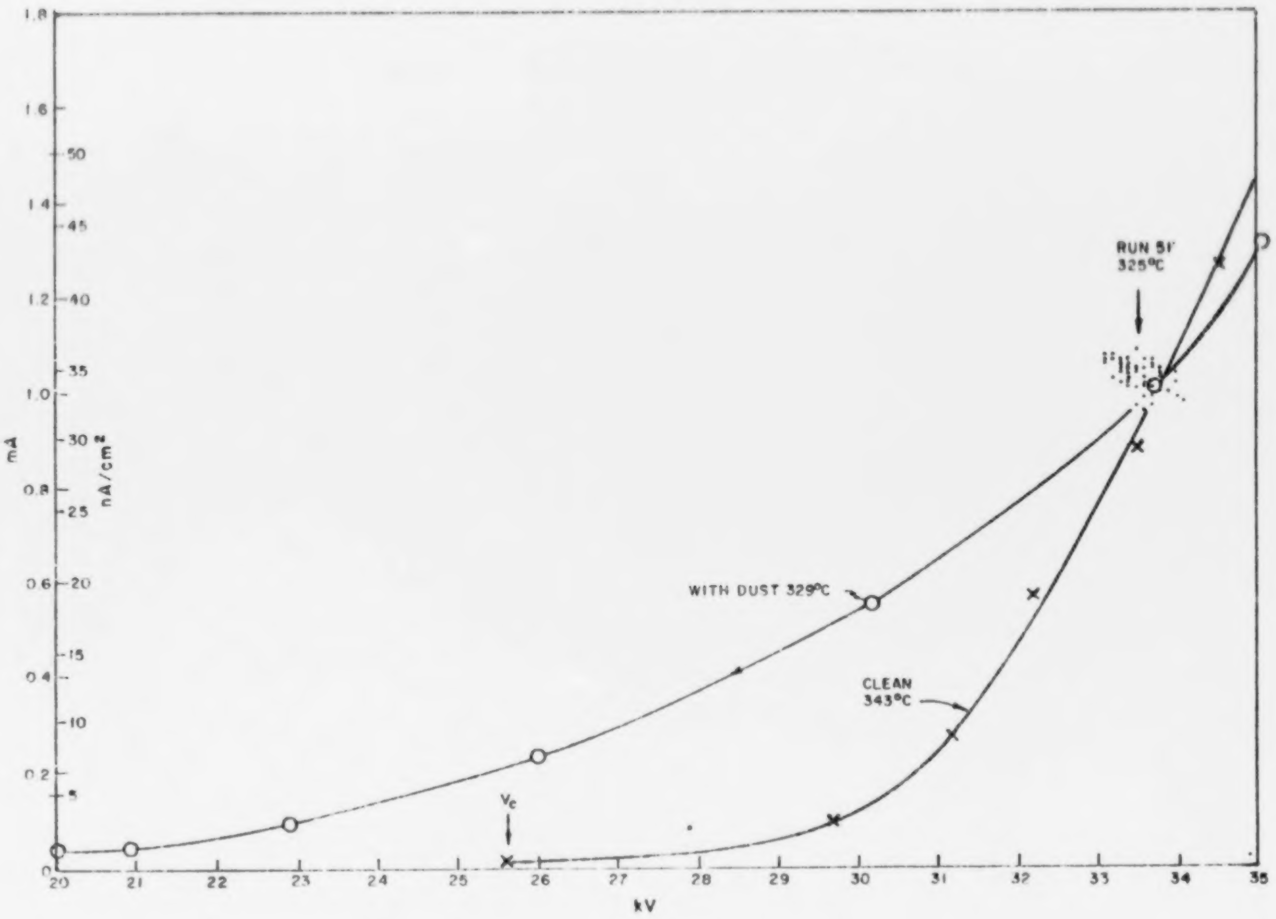

Figure 5. OPERATING CHARACTERISTICS OF SECTION 3
WITH 7.62 cm WIRE SPACING AT HOT-SIDE TEMPERATURES

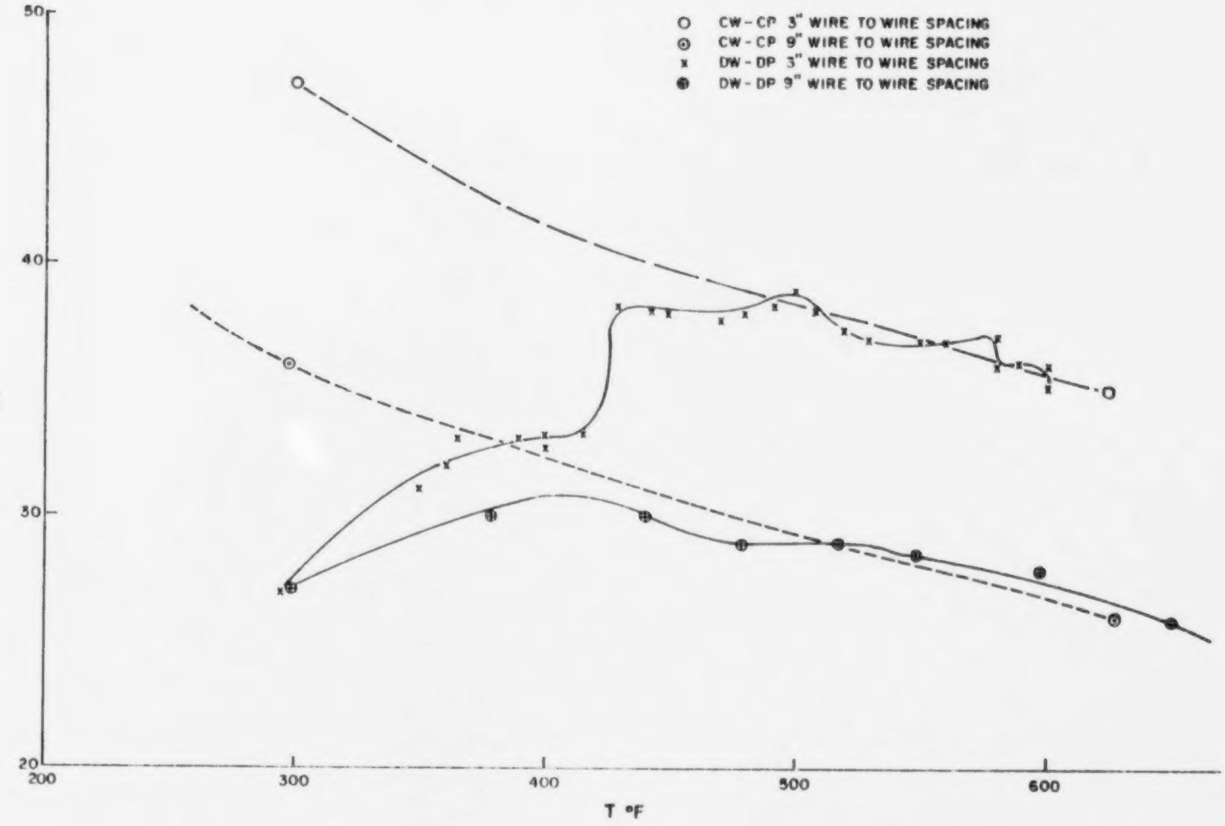

Figure 6. OPERATING VOLTAGE vs TEMPERATURE
FOR CONSTANT CURRENT OF 1.5 mA

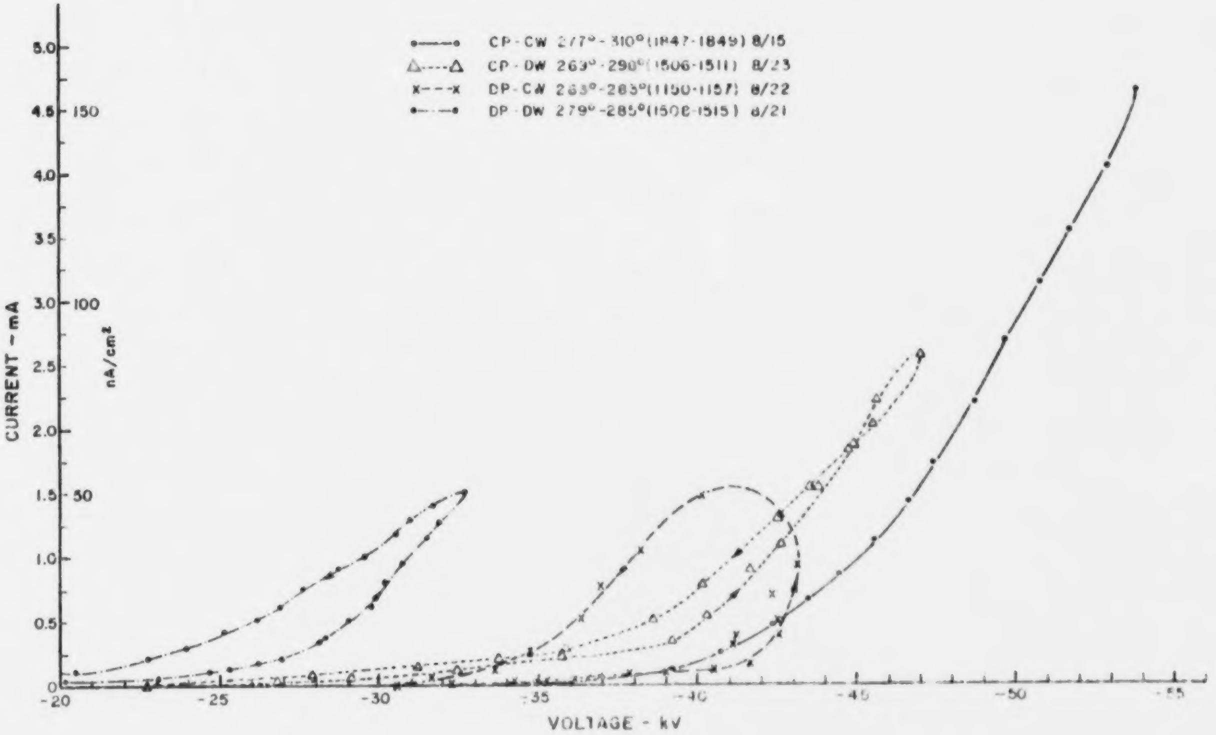

Figure 7. VOLTAGE/CURRENT CHARACTERISTICS WITH/WITHOUT DUST ON WIRES AND/OR PLATE

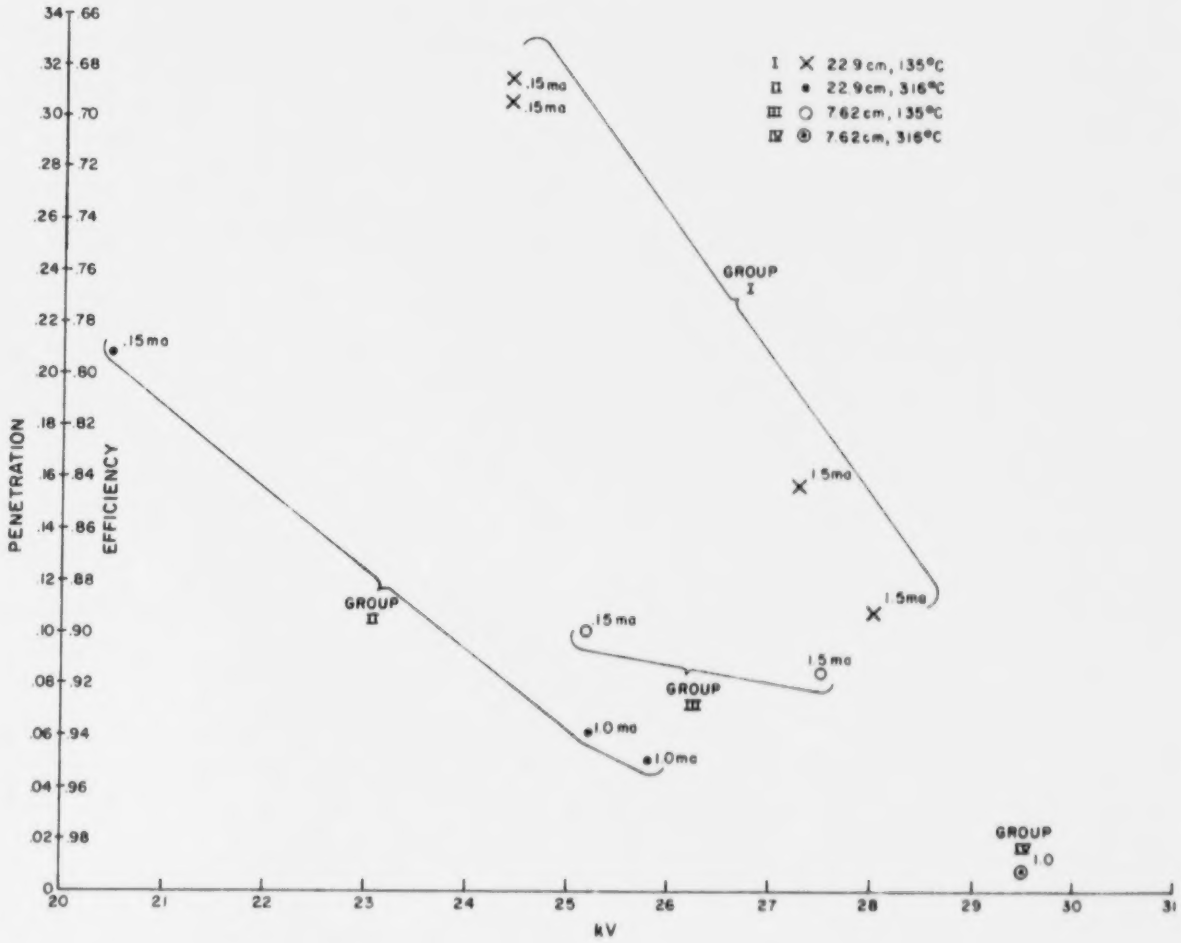

Figure 8. EFFICIENCY & PENETRATION vs
AVERAGE VOLTAGE DURING MASS SAMPLE RUNS

the resultant increase in voltage. The two mass efficiency measurements in Group III are for the precipitator with 22.9 cm wire-to-wire spacing in the first two electrical sections and 7.62 cm wire-to-wire spacing in the last two electrical sections. In this case, the efficiency was not dramatically increased by the tenfold increase in current. However, the ESP was somewhat cleaner during the test at 1.5 mA and may have influenced the efficiency measurement at this current level. The mass efficiency measurement in Group IV was for the same precipitator configuration except while operating under hot-side conditions. This resulted in the highest efficiency of all tests made.

Opacity measurements were made during all runs using a plant process visiometer (PPV). The opacity varied directly in all tests with efficiency.

DISCUSSION OF RESULTS

From the results given in the previous section, the following is evident:

Cold-Side Temperatures

1. At these temperatures the dust electrical resistivity is high (10^{12} ohm-cm) and the predominant effect is back ionization. Thus, the steady state operating voltage is very nearly independent of the electrode geometry.

2. Back ionization onset is caused by a combination of the dust on the wires and the dust on the plates. When the wires are clean and the plates are dirty, VI characteristics are similar to clean conditions for low operating currents. However, when there is dust on the wires, corona onset occurs at a much lower voltage causing back ionization to occur and the steady state operating point to be maintained at a much lower voltage.

3. The beneficial effects of corona electrode geometry can be realized only if the corona electrodes can be maintained essentially dust free.

4. Wire spacing of 7.62 cm appears to offer some advantage with regard to efficiency of dust collection for high resistivity dust when operating at low current levels. However, further tests are indicated.

5. Theoretical understanding of why dust on the wire is so important is lacking. Roughness factor explanations are insufficient especially in light of hot-side temperature results.

Hot-Side Temperatures

1. The operating point for the precipitator is determined primarily by the wire-to-wire spacing of the corona electrode.

2. Higher operating voltage and resultant higher efficiency can be obtained by decreasing wire spacing.

3. Dust on the wires has little effect.

CONCLUDING REMARKS

Some improvements in efficiency may be obtained at cold-side temperatures by using closer wire spacing. However, the improvement is not dramatic and the electrical operating conditions are practically unchanged by decreasing wire spacing.

At hot-side temperatures the operating voltage and efficiency can both be increased by closer wire spacing.

It is apparent from these tests that back ionization once started, becomes more important than corona wire spacing in determining the electrical operating conditions. It is also apparent that the dust on the corona wires plays an important role in the formation of back ionization.

REFERENCES

1. Lawless, P.A., B.E. Daniel, and G.H. Ramsey. "Characterization of the EPA/IERL-RTP Pilot-Scale Precipitator." EPA 600/7-79-052, February 1979.

2. Robinson, M., Air Pollution Control, Part I, Ed. W. Strauss, Wiley-Interscience, NY, 1971.

3. Tachibana, N., Y. Matsumoto, and N. Sakamoto. "Vanishing Temperature of Back Corona with High Resistivity Fly Ash in Hot-Side Precipitation." CSIRO Conference on Electrostatic Precipitation, August 1978.

4. White, H.J. Industrial Electrostatic Precipitation. Addison-Wesley, Reading, MA, 1963.

THEORETICAL METHODS FOR PREDICTING ELECTRICAL CONDITIONS IN WIRE-PLATE ELECTROSTATIC PRECIPITATORS

by

Ronald B. Mosley
Jack R. McDonald
Southern Research Institute
2000 Ninth Avenue South
Birmingham, Alabama 35205

and

Leslie E. Sparks
Industrial Environmental Research Laboratory
Environmental Protection Agency
Research Triangle Park, North Carolina 27711

ABSTRACT

A new semi-empirical, approximate theory for predicting electrical conditions is described. In the approximate theory, analytical expressions are derived for calculating voltage-current characteristics and electric potential, electric field, and space charge density distributions. Comparisons of numerical and approximate solutions over a wide range of possible precipitator geometries and electrical operating points indicates that for practical purposes the approximate theory can be used in lieu of the more rigorous numerical theory. This saves large amounts of computer time and makes possible hand calculator usage. Recent *in situ* gaseous ion mobility data which are needed in the models are presented. For coal fired power plants, the reduced effective ion mobility in positive corona is found to be 1.6 times that for negative corona. Approaches for describing particulate space charge effects in the gas and electrical conditions in the collected particulate layer are briefly discussed.

THEORETICAL METHODS FOR PREDICTING ELECTRICAL CONDITIONS IN WIRE-PLATE ELECTROSTATIC PRECIPITATORS

INTRODUCTION

An accurate representation of the electrical conditions in an electrostatic precipitator is one of the most crucial steps in developing a mathematical model of the electrical precipitation process. A realistic model must describe the electrical properties of both the gaseous region of the precipitator and the dust layer collected on the plates. The model should be capable of describing the electrical properties, not only of the clean gas with ionic charge carriers, but also of the dust-laden gas in which the charged particles alter the electrical processes. In order to model the current-voltage characteristics of the clean gas it is necessary to know the mobility of the ionic charge carriers. For this reason, some in situ measurements of effective ion mobilities are presented. An approach for incorporating the space charge effects of particles into the model is discussed. An approach for describing the electrical properties of the dust layer is also presented.

APPROXIMATE SOLUTION FOR SPACE CHARGE LIMITED CURRENTS IN WIRE-DUCT PRECIPITATORS

Development of Equations

In order to model the behavior of an electrostatic precipitator, it is necessary to compute the electric field and potential in the interelectrode space. In one mathematical model[1] of the electrostatic precipitation process, a relaxation method is used to solve Poisson's equation coupled with the charge transport equation. This numerical procedure[2] requires a great deal of computer time. An analytic solution would be very advantageous in circumventing this difficulty. Since an exact solution does not seem probable, an approximate solution is appropriate.

Using a conformal mapping technique, Cooperman[3] demonstrated that the electrostatic potential in the interelectrode space of a wire-duct precipitator with 2N+1 corona wires can be written as

$$V_s(x,y) = V_{st} \sum_{m=-N}^{N} \ln \left| \frac{\cosh \pi (y-2ms_y)/2s_x - \cos(\pi x/2s_x)}{\cosh \pi (y-2ms_y)/2s_x + \cos(\pi x/2s_x)} \right| \qquad (1)$$

with

$$V_{st} = -\frac{s_x \quad E_0}{\pi \, \mathrm{Sin}(\pi a_0/2s_x)} \left\{ \sum_{m=-N}^{N} \frac{\cosh\,(m\pi s_y/s_x)}{\cosh^2(m\pi s_y/s_x) - \cos^2(\pi a_0/2s_x)} \right\}^{-1} \tag{2}$$

where

E_0 = the electric field at the surface of the wires (V/m),
a_0 = radius of the wires (m),
s_x = wire-to-plate spacing (m),
s_y = half wire-to-wire spacing (m).

Figure 1 shows the region of the precipitator that is of interest. The origin is taken at the wire, while x is measured toward the plate and y is measured toward an adjacent wire. When a current flows in the presence of space charge, equation 1 does not apply. This solution can be used to advantage, however, in obtaining an approximate solution for the dynamic case in which the current is space charge limited. Suppose a steady current flows under the action of an applied potential for the case illustrated in Figure 1. The electrical configuration will be simplified by using the principle of superposition. Contributions to the potential will be separated and described below.

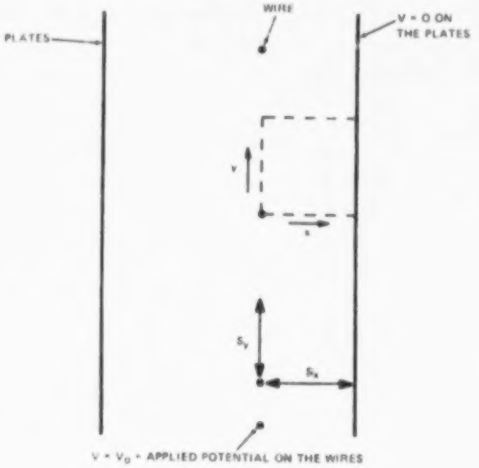

Figure 1. Wire-duct precipitator.

First consider just the electrodes. For a negative corona, the wire will be charged negatively while the plates will be charged positively. The charge on the plates will exceed the magnitude of the charge on the wire by an amount equal to the quantity of negative space charge in the interelectrode space. The negative charge on the wires coupled with an equal amount of positive charge on the two plates constitutes a situation similar to the static case of Cooperman. Mathematically, the solution for this case is identical in form to the electrostatic case, but the amount of charge on the wires is not necessarily the same as when the current is zero. Suppose that a small increase in the electric field at the surface of the wire gives rise to a large increase in the number of electrons emitted from the wire during the corona discharge. The field at the surface of the wire when a current flows, then would be nearly the same as Peek's value of the field required for corona start. In this case, the charge on the wire will be computed in terms of Peek's condition[4] on the field at the wire. The static-like solution would then be completely determined. It remains to specify the contributions to the potential from the negative space charge coupled with an equal amount of positive charge on the plates and from the corona discharge process itself. These last contributions must be approximated since closed-form solutions are not available.

The primary considerations to be used in obtaining approximate solutions will be the apparent symmetry of the arrangement. For example, the equipotential lines near the discharge wires look very much like those for a wire-cylinder geometry,[1] while the equipotential lines near the plates look very much like those for a parallel plate geometry.[5,6] Using these observations, it will be assumed that the space charge near the wire is distributed in the same manner as that in a wire cylinder geometry, and that the space charge near the plate is distributed in the same manner as for a parallel plate geometry. These two space charge distributions along with their associated surface charges are illustrated in Figures 2 and 3, respectively. Potentials computed from these two geometries will be matched at some point (x=R, where R is the radius of the cylinder of charge) in the interelectrode space to yield continuity of potential. The electric field is also required to be continuous at the matching point.

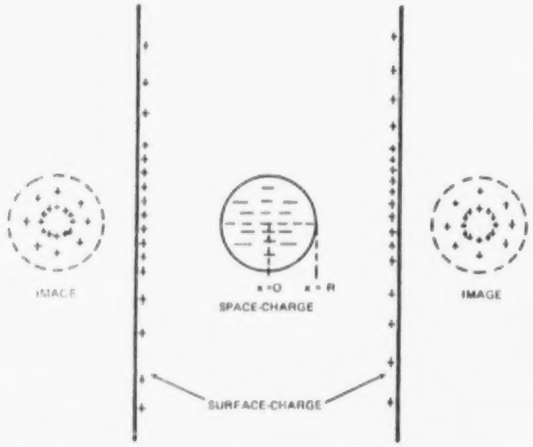

Figure 2. Cylindrical distribution of space-charge with associated surface-charge.

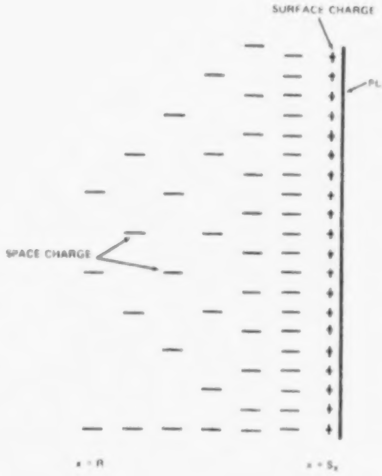

Figure 3. Parallel plane distribution of space-charge.

The contributions to the potential by the corona region will be assumed to be small. According to Loeb,[7] the potential drop across the ionization region of a corona is essentially independent of the current. The effect of the corona on the field at the surface of the wire at corona start is included in the measurement of Peek's field since the measurement is made with a minimum steady current. Based on the above discussion, it is assumed that the only role which the corona plays is to supply ions to carry the current in the interelectrode space.

Negative charge distributed uniformly in planes parallel to the plate which has an equal amount of positive charge, as shown in Figure 3, will yield a potential given by

$$V = -\frac{2}{3}\left(\frac{2J}{b\varepsilon_0}\right)^{\frac{1}{2}}\left[(S_x - R)^{3/2} - (x - R)^{3/2}\right] \tag{3}$$

where

J = current density (A/m^2),
b = ion mobility (m^2/V-sec),
ε_0 = permittivity of gas (A sec/Vm),
R = point at which the solutions are to be matched.

In this same region, near the plate, the potential produced by the cylinder of negative charge coupled to an equal amount of positive charge on the plates must be taken into account. For points which lie outside the cylinder of charge shown in Figure 2, the solution will be the same as for a line of charge at the center with the same quantity of charge as contained in the cylinder. This problem has a solution similar to the electrostatic case mentioned before. When all 2N+1 wires are considered, the contribution to the potential for x greater than R will be

$$V = V_1 \sum_{m=-N}^{N} \ln\left[\frac{\cosh\pi(y-2ms_y)/2s_x - \cos(\pi x/2s_x)}{\cosh\pi(y-2ms_y)/2s_x + \cos(\pi x/2s_x)}\right] \tag{4}$$

where V_1 depends on the amount of charge in the cylinder.

At points inside the cylinder of charge, the potential due to the other wires is given by an expression which is identical to equation (4) except that the term for m=o is absent. To this we must add the potential due to the charge inside the cylinder as well as that due to the two images shown in Figure 2. To obtain the potential due to the negative space charge in the cylindrical distribution, we subtract the electrostatic solution for a wire and cylinder with no space charge from the solution of the same wire and cylinder with space charge.[8] The two images are used to account for the coupling of the space charge in the cylinder with the associated charge on the plates. The potential at a point inside the cylinder due to space charge and the two images is given by a complicated expression of x and y. This expression can be identified in the equation for the potential shown in the appendix. Mathematical expressions for the total potential as well as for the x and y components of the electric field are presented in the appendix.

Comparisons of Approximate Model with Numberically Integrated Solutions and Experimental Observations

In general, the agreement of the approximate model with the numerically integrated solution is found to be quite good. Table 1 summarizes the comparison between the approximate model and the numerical solution for a wide range of geometrical parameters and current densities. Columns 1, 2, and 3 list the corona wire radius, the wire-to-plate spacing, and the half wire-to-wire spacing, respectively. While most combinations of geometrical parameters in this table are typical of industrial electrostatic precipitators, examples of both close and wide wire spacing are shown. Both large and small corona wires are represented and a considerable range of plate spacings is given. Column 4 lists the current densities that were used. The values of current density were chosen to represent both moderate and relatively high space charge situations. Column 5 gives the percent difference in applied voltage for the approximate and numerically integrated solutions. Column 6 gives the percent difference in the average electric field at the plate. Column 7 gives the maximum percent difference in the potential profiles. Columns 8 and 9 give the maximum percent differences in the x-component and the y-component respectively of the electric field profiles. Column 10 gives the maximum percent difference in the charge density profiles.

In the approximate model, one is free to choose the position (x=R) at which to match the functions derived from the two different symmetries. For the calculations shown in Table 1, R was choosen to be $0.975S_x$. This corresponds to using only a few millimeters near the plate in which the space charge is distributed according to the rectangular geometry of a parallel plate arrangement. The reason for using such a small volume with rectangular symmetry is that it tends to over estimate the electric field near the plate. That is, the parallel plate solution predicts too large an effect due to space charge. The fact that rectangular symmetry plays such a small role in the space charge contribution to the profiles does not necessarily contradict the observations made earlier that the equipotential lines near the plate reflect a strong influence of planar geometry. The planar character of the equipotential lines is largely provided by the static-like solution which accounts rigorously for much of the charge on the plates. In all cases the approximate model agrees well with the numerically integrated solution for zero current. This case, of course, corresponds to the electrostatic solution at conditions for corona start, the limit in which the approximate model becomes exact.

Predictions of the approximate model as well as those of the numerical solution are compared with some experimental results of Penney and Matick[6] in Figures 4, 5, and 6. An effective ion mobility of 1.8×10^{-4} m^2/V-sec in the approximate model yields voltage-current curves which predict the experimental operating conditions to within one percent. These voltage-current curves along with the numerically integrated ones are shown in Figure 4. Figure 5 shows a comparison of the potential profiles along a line connecting the wire with the plate. The approximate model agrees with this measured potential profile to within 3 percent. A comparison of the potential profiles along a line connecting a point midway between two wires with the plate is shown in Figure 6. The approximate potential is as much as 15 percent larger than the measured

Table 1. COMPARISON OF APPROXIMATION AND NUMERICALLY INTEGRATED SOLUTION

Wire Radius (10^{-3} m)	Wire Plate Distance (m)	Half Wire-to-wire Distance (m)	Current Density (nA/cm^2)	Percent Difference In Applied Voltage	Percent Difference In Field At The Plate	Max. % Difference In Potential Profiles	Max. % Difference In x-component of field[1]	Max. % Difference In y-component of field[2]	Max. % Difference In Charge Density Profiles[3]
1.1906	0.127	0.03175	10	1	6	2	12	400	23
1.1906	0.127	0.03175	100	3	12	5	12	400	32
1.1906	0.127	0.0635	10	0	8	3	12	100	18
1.1906	0.127	0.0635	100	2	9	8	11	320	12
1.1906	0.127	0.127	10	3	1	8	12	53	8
1.1906	0.127	0.127	100	1	0.1	11	5	118	10
1.1906	0.127	0.15875	20	2	5	12	10	30	19
1.1906	0.127	0.15875	100	2	6	13	16	40	22
1.1906	0.200	0.0635	20	3	1	7	15	60	24
1.1906	0.200	0.0635	80	4	6	2	7	50	10
3.00	0.127	0.0635	20	2	4	2	7	50	10
3.00	0.127	0.0635	100	2	2	4	9	50	12
0.500	0.127	0.0635	10	3	9	4	15	300	14
1.016	0.1143	0.07348	20	1	3	3	9	40	9
1.016	0.1143	0.07348	200	2	1	6	10	80	15
0.1524	0.1143	0.07348	5	22	6	22	18	300	6
0.1524	0.1143	0.07348	180	9	10	9	16	213	13

---

[1] Points closer than two diameters to the wire and points near the plane connecting the centers of the wires with the plates have been neglected.

[2] Even though the percent difference in the y-components of the electric field seems quite large in some cases, the absolute error is relatively unimportant because the y-component is much smaller than the total field for nearly all such cases.

[3] Some points very near the plates and some near the centers of the wires have been neglected.

potential along this line. The approximate potential is 10 percent larger than the numerically integrated potential along this same line. The apparent reason for this disagreement lies in the large current density used. A large current density corresponds to the large space charge limit where the approximation is expected to be less accurate. Also, this region, between the wires, is where the approximate model is expected to be least accurate. It should be noted that moderate errors in the potential profile in this region (between the wires) have little influence on the predicted electrical operating conditions of the precipitator device. The value of 1.8 x 10^{-4} m^2/V-sec used for effective mobility is consistent with measured values of ion mobility in negative corona discharges in air. It may be concluded that the predictions of the approximate model agree quite well both with the numerically integrated solutions and with experimentally measured electrical properties of precipitator devices.

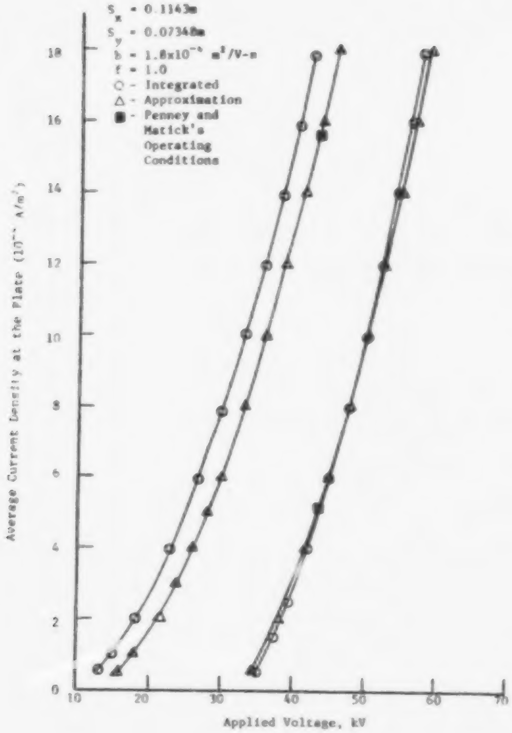

Figure 4. Theoretical voltage-current curves for the geometries used by Penney and Matick.[6]

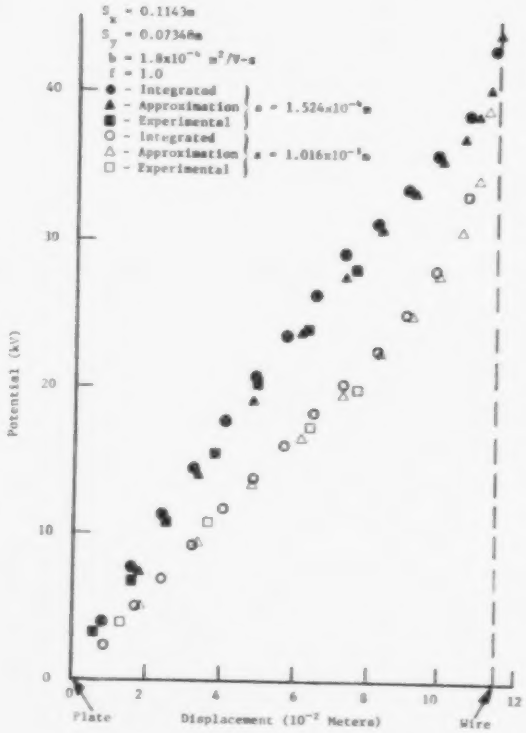

Figure 5. Theoretical and experimental potential profiles along a line from a wire to the plate.

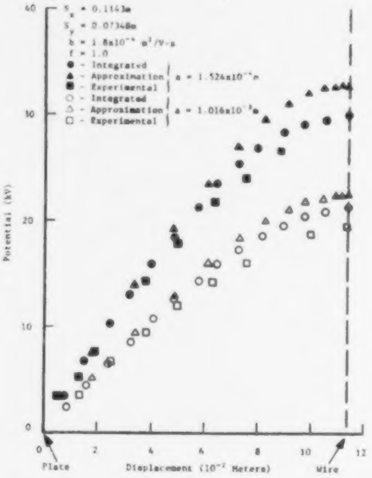

Figure 6. Theoretical and experimental potential profiles along a line from a point midway between two wires to the plate.

MEASURED EFFECTIVE ION MOBILITIES

The effective mobility of ions created in a corona discharge can strongly influence the current-voltage characteristics of the discharge device, the electric field distribution in the gaseous region, and the particle charging process. Thus the effective ion mobility can have a significant effect on particle collection efficiencies in an electrostatic precipitator. In general, the effective ion mobility depends on the temperature, pressure, and composition of the gas, as well as on the electric field strength. Consequently, for purposes of modeling electrostatic precipitators, it is important to obtain *in situ* measurements of effective ion mobility in industrial flue gases. The technique is based on a measured current-voltage curve obtained for corona discharge in a wire-cylinder geometry. Both the instrument and the method of measurement have been described elsewhere.[8] Some representative measurements from three different plants are summarized in Table 2. Plant A is a gold smelter, while Plants B and C are coal fired power plants. It will be noted that the chemical analysis of the gas in Plant A is quite different from the other two plants. It is also apparent that the positive reduced mobility experiences a greater variation from one plant to another, as well as for different conditions at the same plant than does the negative reduced mobility. It is generally the case that the effective mobility of positive ions is more sensitive to small variations in the gas composition than the mobility of the negative ions.

The reduced effective mobilities for both negative and positive coronas are somewhat smaller than previously reported.[8] In filtered flue gas, the reduced effective mobility for positive corona is found to be about 1.6 times greater than for negative corona. Larger ratios were observed in previous measurements. The measurements in this paper were made at pressures near that

[redacted]

Table 2. ION MOBILITY FIELD TEST DATA

Run ID[1]	Temp. °C	Absolute Pressure mm Hg	Effective Mobility K_e cm²/v-s	Reduced Effective Mobility K_0 cm²/v-s	Multiple Correlation Coefficient	Average Reduced Effective Mobility $\bar{K}_0$ cm²/v-s	Volume Percent			PPM		Maximum Voltage kV	Maximum Current Density µA/cm²	Maximum Average E/p V/cm-Torr
							H_2O	O_2	CO_2	SO_2	SO_3			
PLANT A														
13NG	184	701	2.76	1.52	0.964	1.20	6.0	18.7	0.0	10^4	6.0	22	0.88	7.3
14NG	185	701	2.24	1.23	0.984		6.0	18.7	0.0	10^4	6.0	21	0.69	6.9
15NG	185	701	1.96	1.08	0.975		6.0	18.7	0.0	10^4	6.0	21	0.69	6.9
16NG	185	701	2.15	1.18	0.984		6.0	18.7	0.0	10^4	6.0	21	0.70	6.9
17NG	185	701	2.10	1.15	0.990		6.0	18.7	0.0	10^4	6.0	22	0.79	7.3
18NG	185	701	1.89	1.04	0.970		6.0	18.7	0.0	10^4	6.0	22	0.69	7.3
19PG	186	701	2.55	1.40	0.992	1.38	6.0	18.7	0.0	10^4	6.0	20	0.54	6.6
20PG	186	701	2.61	1.43	0.989		6.0	18.7	0.0	10^4	6.0	20	0.56	6.6
21PG	186	701	2.48	1.36	0.995		6.0	18.7	0.0	10^4	6.0	20	0.55	6.6
22PG	186	701	2.39	1.31	0.997		6.0	18.7	0.0	10^4	6.0	21	0.66	6.9
23PG	186	701	2.55	1.40	0.990		6.0	18.7	0.0	10^4	6.0	20	0.54	6.6
24PG	186	701	2.49	1.37	0.987		6.0	18.7	0.0	10^4	6.0	20	0.53	6.6
PLANT B														
01NG	125	735	2.10	1.39	0.996	1.30	(No Gas Analysis)					40	8.1	12.9
02NG	133	735	2.07	1.35	0.997		(No Gas Analysis)					38	7.0	12.3
03NG	141	735	2.10	1.34	0.974		(No Gas Analysis)					37	6.4	11.9
04NG	142	735	1.97	1.26	0.997		(No Gas Analysis)					33	4.6	10.6
05NG	143	735	1.91	1.21	0.997		(No Gas Analysis)					33	4.5	10.6
06NG	143	735	1.93	1.23	0.997		(No Gas Analysis)					31	3.8	10.0
02PG	142	732	3.30	2.09	0.997	2.08	(No Gas Analysis)					24	2.5	7.8
03PG	144	732	3.16	1.99	0.998		(No Gas Analysis)					24	2.6	7.8
04PG	144	732	3.23	2.04	0.998		(No Gas Analysis)					24	2.5	7.8
05PG	144	732	3.39	2.14	0.997		(No Gas Analysis)					24	2.6	7.8
06PG	144	732	4.27	2.69	0.997		(No Gas Analysis)					23	2.2	7.5
PLANT C (NO ADDITION OF CONDITIONING AGENTS)														
140PG	146	597	4.17	2.14	0.992	2.08	10.5	4.5	14.7	593	0.5	20	2.1	7.9
141PG	146	597	4.07	2.08	0.996		10.5	4.5	14.7	593	0.5	20	2.1	7.9
142PG	146	597	3.99	2.04	0.998		10.5	4.5	14.7	593	0.5	20	2.1	7.9
143PG	146	597	4.11	2.10	0.998		10.5	4.5	14.7	593	0.5	20	2.0	7.9
144PG	146	597	3.98	2.04	0.997		10.5	4.5	14.7	593	0.5	20	2.1	7.9
145PG	146	597	4.07	2.08	0.998		10.5	4.5	14.7	593	0.5	19	1.7	7.5
146NG	146	597	2.89	1.48	0.998	1.47	10.5	4.5	14.7	593	0.5	30	5.6	11.9
147NG	146	597	2.87	1.47	0.998		10.5	4.5	14.7	593	0.5	30	5.4	11.9
148NG	146	597	2.87	1.47	0.997		10.5	4.5	14.7	593	0.5	30	5.4	11.9
149NG	146	597	2.84	1.45	0.997		10.5	4.5	14.7	593	0.5	30	5.4	11.9
150NG	146	597	2.86	1.46	0.997		10.5	4.5	14.7	593	0.5	29	5.0	11.5
151NG	146	597	2.85	1.46	0.997		10.5	4.5	14.7	593	0.5	30	5.5	11.9
PLANT C (7 PPM SO_3 INJECTED)														
242NG	146	597	2.92	1.49	0.998	1.47	10.5	4.5	14.7	593	7.0	29	4.9	11.5
243NG	146	597	2.81	1.44	0.997		10.5	4.5	14.7	593	7.0	28	4.4	11.1
244NG	146	597	2.91	1.49	0.997		10.5	4.5	14.7	593	7.0	28	4.4	11.1
245NG	146	597	2.94	1.50	0.996		10.5	4.5	14.7	593	7.0	28	4.3	11.1
246NG	146	597	2.96	1.52	0.996		10.5	4.5	14.7	593	7.0	28	4.3	11.1
247NG	146	597	2.70	1.38	0.997		10.5	4.5	14.7	593	7.0	28	4.2	11.1
248PG	146	597	4.79	2.45	0.996	2.46	10.5	4.5	14.7	593	7.0	21	2.8	8.3
249PG	146	597	4.77	2.44	0.998		10.5	4.5	14.7	593	7.0	21	2.8	8.3
250PG	146	597	4.81	2.46	0.998		10.5	4.5	14.7	593	7.0	21	2.8	8.3
251PG	146	597	4.81	2.46	0.997		10.5	4.5	14.7	593	7.0	21	2.8	8.3
252PG	146	597	4.91	2.51	0.996		10.5	4.5	14.7	593	7.0	20	2.3	7.9
253PG	146	597	4.80	2.46	0.998		10.5	4.5	14.7	593	7.0	20	2.3	7.9
PLANT C (100 lbs/hr Na_2CO_3 INJECTED)														
284NG	157	597	2.99	1.49	0.999	1.49	10.5	4.5	14.7	593	0.5	34	7.6	13.5
285NG	158	597	3.02	1.50	0.999		10.5	4.5	14.7	593	0.5	33	7.0	13.1
286NG	160	597	2.99	1.48	0.999		10.5	4.5	14.7	593	0.5	31	6.0	12.3
287NG	161	597	2.98	1.47	0.999		10.5	4.5	14.7	593	0.5	31	6.0	12.3
288NG	161	597	3.04	1.50	0.999		10.5	4.5	14.7	593	0.5	32	6.0	12.7
289NG	163	597	3.04	1.49	0.999		10.5	4.5	14.7	593	0.5	31	5.9	12.3
290PG	157	597	4.96	2.48	0.997	2.50	10.5	4.5	14.7	593	0.5	20	2.4	7.9
291PG	157	597	4.76	2.38	0.998		10.5	4.5	14.7	593	0.5	20	2.3	7.9
292PG	157	597	5.00	2.49	0.998		10.5	4.5	14.7	593	0.5	20	2.4	7.9
293PG	157	597	5.03	2.51	0.998		10.5	4.5	14.7	593	0.5	20	2.4	7.9
294PG	157	597	5.12	2.55	0.998		10.5	4.5	14.7	593	0.5	20	2.4	7.9
295PG	157	597	5.18	2.58	0.997		10.5	4.5	14.7	593	0.5	20	2.4	7.9

---

[1] The Run ID's are coded in the following manner: The first 2 or 3 digit number is the run number at that test location. The first letter indicates the polarity of the corona (P or N). The second letter, G, indicates that the measurement was made in filtered flue gas.

of the flue gas, while the previous measurements were made at reduced pressures. The differences in these sets of measurements are attributed primarily to the differences in pressure. The values of effective mobility reported in this paper are believed to be more representative of ions in industrial flue gases.

SPACE CHARGE EFFECTS OF PARTICLES

The effects of charged particles on the electrical properties of an electrostatic precipitator can be taken into account by the use of the effective mobility concept. For the case in which both ions and charged particles contribute to the electrical conditions in the interelectrode space, the two transport equations and Poisson's equation can be reduced to a system of equations which is identical in form to the system of equations applicable to ions alone. This system of equations differ from the case of ions alone in that effective values of current density, mobility and charge density are used. The effective current density is given by

$$J_{eff} = b_{eff} \, (J_i/b_i + J_p/b_p) \tag{5}$$

where

b_{eff} = effective mobility (m^2/V-s),
b_i = ion mobility (m^2/V-s),
b_p = particle mobility (m^2/V-s),
J_i = ion current density (AMP/m^2),
J_p = particle current density (AMP/m^2).

The effective mobility is defined in the usual way

$$b_{eff} = (b_i\bar{\rho}_i + b_p\bar{\rho}_p)/(\bar{\rho}_i + \bar{\rho}_p) \tag{6}$$

where

$\bar{\rho}_i$ = average ion charge density (c/m^3),
$\bar{\rho}_p$ = average particle charge density (c/m^3).

The effective charge density is given by

$$\rho_{eff} = \rho_i + \rho_p \quad . \tag{7}$$

For given values of effective current density and effective mobility, the potential, electric field, and effective charge density can be computed in the same manner as for ions alone. It is then a matter of choosing a value of effective current density at the plate which corresponds to the correct value of the actual current density. Since the correct value of the effective current density at the plate depends on the effective mobility and the average field which, in turn, depend on the charge on the particles, it will be necessary to iterate on the effective mobility. If the particle current density is neglected in comparison with the ion current density, the following algorithm could be used for a given particle mass loading and known size distribution.

1. Specify the current density (hold fixed).
2. Compute the potential and charge density for the clean gas. These values will be used to compute an initial estimate of the charge on the particles.
3. Compute the average particle mobility and the effective mobility.
4. Compute the effective current density.
5. Compute new potentials, fields and effective charge densities.
6. Compute the average ion density from the effective charge density.
7. Compute the new charge on the particles.
8. Compute new values of average particle mobility and effective mobility.
9. Repeat steps 4 through 8 until the effective mobility does not change significantly.

AN APPROACH FOR DESCRIBING ELECTRICAL PROPERTIES OF PRECIPITATED DUST LAYERS

Background

Once a dust layer is deposited on the collection electrodes of an electrostatic precipitator, the negative corona current must pass through the particulate layer to the grounded collection electrode. The average electric field in the particulate layer (E_{Ave}) can be increased to the point that the layer breaks down electrically. When this breakdown occurs, one of two possible situations will ensue. If the average electrical resistivity of the particulate layer is moderate ($\sim$0.1-1.0x10^{11} ohm-cm), the applied voltage may be sufficiently high so that a spark will propagate across the interelectrode space. The rate of sparking will determine the operating electrical conditions in such a circumstance. If the average electrical resistivity of the particulate layer is high (>10^{11} ohm-cm), the applied voltage may not be high enough to cause a spark to propagate across the interelectrode space. In this case, the particulate layer will be continuously broken down electrically and will discharge positive ions into the interelectrode space. This condition is called back corona or back discharge. The effect of these positive ions is to reduce the amount of negative charge on the particles in the gas stream due to bipolar charging which in turn reduces the space charge component of the electric field. Both the magnitude of particle charge and the rate of particle charging are affected adversely by back corona. Useful precipitator current is therefore limited to values which occur prior to electrical breakdown whether the breakdown results in sparkover or back corona. At the present, no comprehensive theoretical model is available to describe the electrical conditions in the collected particulate layer. This type of model is needed in order to develop a complete model for electrostatic precipitation and in order to provide a fuller understanding of the physical mechanisms which produce the observed electrical phenomena.

In this paper, a theoretical approach for describing the electrical characteristics of precipitated dust layers is proposed and discussed. The macroscopic electrical properties of the dust layer are described by coupling the current transport equation and Poisson's Equation. The electrical breakdown of the dust layer is attributed to enhanced values of the local electric field due to the combined effects of polarization in the dielectric layer and the contribution to the electric field from the space charge distribution in the layer.

Models formulated from the proposed approach offer the potential of providing the following information:

(1) voltage-current characteristics of the particulate layer,
(2) electric field, electric potential, and charge density distributions in the particulate layer,
(3) average electrical resistivity and positional dependence of resistivity,
(4) electrical force holding the layer to the collection electrode,
(5) prediction of the average electric field strength at the onset of electrical breakdown of the layer, based on a designated value of breakdown strength, and
(6) prediction of what types of conditioning agents will be beneficial in reducing the resistivity of the particulate layer.

In one commonly accepted picture of electrical breakdown of the dust layer, the gas trapped in the interstitial space breaks down electrically.[9,10] This breakdown results from the acceleration of free electrons to the gas ionization velocity which produces an avalanche condition similar to that at the corona electrode. Experimental measurements show that particulate layers may experience electrical breakdown at average electric field strengths across the layers of approximately 5-15 kV/cm.[11,12] For temperatures and pressures encountered in precipitators, it takes an electric field strength of approximately 15-30 kV/cm to cause electrical breakdown of the gas.[13] This suggests that locally high electric fields must exist in the particulate layer to produce breakdown of the gas in the layer.

Polarization Effect

The effect due to polarization can be estimated by treating the layer as a collection of spherical particles all of the same size and arranged in a cubic array. The problem is then to evaluate the effect of placing dielectric spheres in an applied electric field. For a parallel plate capacitor arrangement of metal electrodes containing a dielectric material, the polarization charge induced on the surface of the dielectric is neutralized by charge flowing in an external circuit. The local electric field inside the volume of such a dielectric is computed by combining the contributions from all the dipoles of the particles with the applied electric field. Figure 7 shows the physical arrangement and nomenclature that will be utilized in estimating the effect due to polarization. A calculation of these effects has been presented by the present authors.[14]

Space Charge Effect

The effect of space charge on the macroscopic electric field can be investigated by solving the problem involving the transport of charge carriers through the particulate layer. A simplified model is proposed in order to demonstrate that space charge effects can result in a significant enhancement

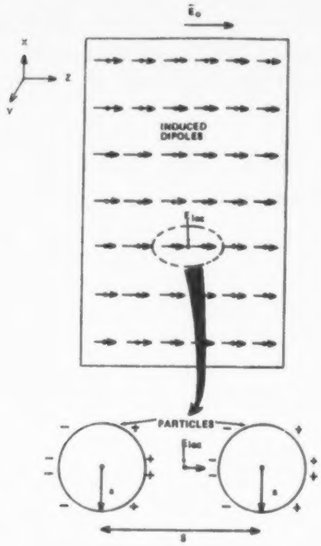

Figure 7. Polarization of particles in the layer.

of the electric field in the particulate layer. In this model, we assume that only one species carries the charge and that the gradient term in the transport equation can be neglected for all values of x. For a detailed calculation see reference 14. When polarization and space charge effects are combined, the maximum local electric field strength (E_{loc}) in the layer is given[14] by

$$E_{loc} \approx 1.5 \; [1 + 1.25 \; (K-1)] \; E_{Ave} \; . \tag{8}$$

This relationship depends on the dielectric constant (K) of the layer or, more specifically, of the individual particles. Since, in the case of fly ash particles, the dielectric constant may vary over a certain range from one source to another, it is desirable to compute the maximum electric field strength as a function of dielectric constant. The average value of the electric field for which breakdown will occur can also be computed as a function of dielectric constant by specifying a breakdown strength (E_B) for the trapped gas. For illustrative purposes, the breakdown strength of the gas will be assumed to be that of air (approximately 30 kV/cm at $T_0 = 293°K$ and $P_0 = 760$ mm Hg). It will also be assumed that the breakdown strength of the gas at any arbitrary temperature (T) and pressure (P) can be obtained by multiplying 30 kV/cm by the quantity $(T_0 \cdot P)/(T \cdot P_0)$. Table 3 shows the results of calculations for several cases of interest. Notice that the description of dielectric breakdown obtained from the simplified model presented here is consistent with observed phenomena.

If the dielectric constant and the average resistivity of a particular fly ash are measured in the appropriate environment, then a practical upper bound on the operating current density can be established to avoid dielectric breakdown. If the dielectric constant is known, we can compute the average

Table 3. AVERAGE ELECTRIC FIELD AT BREAKDOWN FOR VARIOUS DIELECTRIC CONSTANTS, TEMPERATURES, AND PRESSURES

	E_B = 30 kV/cm at 293°K, 760 mm Hg		E_B = 20.8 kV/cm at 422°K, 760 mm Hg		E_B = 11.4 kV/cm at 616°K, 608 mm Hg	
K	E_{loc}/E_{Ave}	E_{Ave} for Breakdown (kV/cm)	E_{loc}/E_{Ave}	E_{Ave} for Breakdown (kV/cm)	E_{loc}/E_{Ave}	E_{Ave} for Breakdown (kV/cm)
1	1.50	20.00	1.50	13.90	1.50	7.60
2	3.38	8.88	3.38	6.15	3.38	3.37
3	5.25	5.71	5.25	3.96	5.25	2.17
4	7.13	4.20	7.13	2.92	7.13	1.60
5	9.00	3.33	9.00	2.31	9.00	1.27
6	10.88	2.76	10.88	1.91	10.88	1.05
7	12.75	2.35	12.75	1.63	12.75	0.89
8	14.63	2.05	14.63	1.42	14.63	0.78
9	16.50	1.82	16.50	1.26	16.50	0.69
10	18.38	1.63	18.38	1.13	18.38	0.62

electric field required for breakdown from equation (8). The current density corresponding to this average electric field would constitute the upper bound on the operating current. The condition which must be satisfied in order to avoid breakdown is

$$qJ < E_{Ave}/\rho \qquad (9)$$

where E_{Ave} is computed for breakdown.

SUMMARY

An approximate model for computing current-voltage characteristics in a wire-plate precipitator has been presented. This model uses a rigorous solution for the paired charges of opposite sign on the electrodes. The contributions to the potential and electric field from space charge are approximated. Near the wires these approximations are based on cylindrical symmetry while near the plates the approximations are based on rectangular symmetry. The predictions of this approximate model agree quite well both with the numerically integrated solutions and with experimental results.

Values of effective ion mobilities were measured at three different industrial plants. The values of reduced effective mobilities for negative corona ranged from 1.2 to 1.5 $m^2/V\text{-}s$. Values of reduced effective mobilities for positive corona ranged from 1.4 to 2.5 $m^2/V\text{-}s$. The positive mobility was found to exceed the negative mobility by a factor of about 1.6. A method for obtaining a self-consistent solution which incorporates the effects of charged particles is proposed. This method is based on an effective current density, an effective mobility, and an effective charge density. Iterations on the effective mobility are required to obtain self-consistency.

A method for computing the electrical properties of the dust layer is proposed. The approach is to solve the electrical transport equation coupled with Poisson's equation. Electrical breakdown fields in the layer are computed in terms of an enhancement by space charge and by dielectric polarization of the particles in the layer. The combination of space charge and polarization are shown to give a sufficient enhancement of the average electric field to explain electrical breakdown of trapped gas in the layer.

ACKNOWLEDGMENT

This work was supported by the Industrial Environmental Research Laboratory, U.S. Environmental Protection Agency, Research Triangle Park, North Carolina, under Contract Nos. 68-02-2193 and 68-02-2683, Dr. Leslie E. Sparks, Project Officer.

REFERENCES

1. McDonald, J. R. A Mathematical Model of Electrostatic Precipitation: Revision 1. Volume 1, Modeling and Programming. EPA-600/7-78-111b, U.S. Environmental Protection Agency, Research Triangle Park, North Carolina, June 1978.

2. McDonald, J. R., W. B. Smith, H. W. Spencer III, and L. E. Sparks. A Mathematical Model for Calculating Electrical Conditions in Wire-Duct Electrostatic Precipitator Devices. J. Appl. Phys., Vol. 48, No. 6, June 1977.

3. Cooperman, P. Progress Report No. 46, Research Corporation Laboratory, (1952).

4. Peek, F., Jr. Dielectric Phenomena in High Voltage Engineering (University Microfilm International, Ann Arbor, Michigan, 1959), p. 73.

5. White, H. J. Industrial Electrostatic Precipitation (Addison-Wesley, Reading, Mass., 19), p. 98.

6. Penney, G. W., and R. E. Matick, Trans. AIEE 79, Part I, 91 (1960).

7. Loeb, L. B., Electrical Coronas Their Basic Physical Mechanisms (University of California Press, Berkeley, Ca. 1965), p. 46.

8. McDonald, J. R., S. M. Banks, and L. E. Sparks. Measurement of Effective Ion Mobilities in a Corona Discharge in Industrial Flue Gases. Symposium on the Transfer and Utilization of Particulate Control Technology: Volume 1, Electrostatic Precipitators. EPA-600/7-79-044a, U.S. Environmental Protection Agency, Research Triangle Park, North Carolina, February 1979.

9. S. Masuda, A. Mizuno, and K. Akutsu, Initiation Condition and Mode of Back Discharge for Extremely High Resistivity Powders. IEEE 1977 IAS Conference Record, Printcraft, Inc., Conneaut, Ohio.

10. S. Masuda and A. Mizuno, Flashover Measurements of Back Discharge. Journal of Electrostatics, 4, 215-231 (1978).

11. J. W. Baker and K. M. Sullivan, Reproducibility of Ash Resistivity Determinations. Joint Power Generation Conference, Long Beach, California, September 1977.

12. Work performed at Southern Research Institute under sponsorship of the U.S. Environmental Protection Agency on Contract No. 68-02-2114 (to be published).

13. F. M. Peek, Jr., Dielectric Phenonema In High Voltage Engineering, Third ed., McGraw-Hill, New York, 1929, pp. 43-53.

14. McDonald, J. R., R. B. Mosley, and L. E. Sparks. An Approach to Describing Electrical Characteristics of Precipitated Dust Layers. Submitted to the Journal of the Air Pollution Control Association in May, 1979 for review and consideration for publication.

APPENDIX

Electrical Solutions for the Approximate Model

An expression for the total potential which combines the separate contributions described in the text is shown below. The x and y components of the electric field are obtained by differentiating the potential expressions. After the functions have been matched at x = R we obtain

$$
\begin{aligned}
V(x,y) = {} & -\frac{2}{3}\left(\frac{2J}{b\varepsilon_0}\right)^{\frac{1}{2}}(S_x-R)^{3/2} + V_1 \ln\left[\frac{1-\cos(\pi R/2s_x)}{1+\cos(\pi R/2s_x)}\right] \\
& -a_0E_0 \Bigg\{ \left(\frac{\zeta-1}{2}\right) \ln\left(\frac{x^2+y^2}{R^2+y^2}\right) + (1+\delta(x^2+y^2-a_0{}^2))^{\frac{1}{2}} \\
& -(1+\delta(R^2+y^2-a_0{}^2))^{\frac{1}{2}} + \zeta \ln\left[\frac{\zeta+(1+\delta(R^2+y^2-a_0{}^2))^{\frac{1}{2}}}{\zeta+(1+\delta(x^2+y^2-a_0{}^2))^{\frac{1}{2}}}\right] \\
& -\left(\frac{\gamma-1}{4}\right)\left[\ln\left(\frac{x^2+y^2+4s_x(s_x-x)}{R^2+y^2+4s_x(s_x-R)}\right) + \ln\left(\frac{x^2+y^2+4s_x(s_x+x)}{R^2+y^2+4s_x(s_x+R)}\right)\right]\Bigg\} \\
& + V_1 \sum_{m=1}^{N} \Bigg\{ \ln\left[\frac{\cosh\pi(y-2ms_y)/2s_x - \cos(\pi x/2s_x)}{\cosh\pi(y-2ms_y)/2s_x + \cos(\pi x/2s_x)}\right] \\
& + \ln\left[\frac{\cosh\pi(y+2ms_y)/2s_x - \cos(\pi x/2s_x)}{\cosh\pi(y+2ms_y)/2s_x + \cos(\pi x/2s_x)}\right]\Bigg\} \\
& + V_{st} \sum_{m=-N}^{N} \ln\left[\frac{\cosh\pi(y-2ms_y)/2s_x - \cos(\pi x/2s_x)}{\cosh\pi(y-2ms_y)/2s_x + \cos(\pi x/2s_x)}\right]
\end{aligned}
\tag{A1}
$$

$$
\begin{aligned}
E_x(x,y) = {} & a_0E_0 \Bigg\{ \frac{x}{x^2+y^2}\left[(1+\delta(x^2+y^2-a_0{}^2))^{\frac{1}{2}} - 1\right] \\
& -\left(\frac{\gamma-1}{2}\right)\left[\frac{x-2s_x}{x^2+y^2+4s_x(s_x-x)} + \frac{x+2s_x}{x^2+y^2+4s_x(s_x+x)}\right]\Bigg\} \\
& - \frac{V_1\pi}{s_x}\,\mathrm{Sin}(\pi x/2s_x) \sum_{m=1}^{N} \Bigg\{ \frac{\cosh\pi(y-2ms_y)/2s_x}{\cosh^2\pi(y-2ms_y)/2s_x - \cos^2(\pi x/2s_x)} \\
& + \frac{\cosh\pi(y+2ms_y)/2s_x}{\cosh^2\pi(y+2ms_y)/2s_x - \cos^2(\pi x/2s_x)}\Bigg\} \\
& - \frac{V_{st}\pi}{s_x}\,\mathrm{Sin}(\pi x/2s_x) \sum_{m=-N}^{N} \Bigg\{ \frac{\cosh\pi(y-2ms_y)/2s_x}{\cosh^2\pi(y-2ms_y)/2s_x - \cos^2(\pi x/2s_x)}\Bigg\}
\end{aligned}
\tag{A2}
$$

$$
\begin{aligned}
E_y(x,y) = {} & a_0E_0 \Bigg\{ \left(\frac{y}{x^2+y^2}\right)\left[(1+\delta(x^2+y^2-a_0{}^2))^{\frac{1}{2}} - 1\right] \\
& - \left(\frac{y}{R^2+y}\right)\left[(1+\delta(R^2+y^2-a_0{}^2))^{\frac{1}{2}} - 1\right]
\end{aligned}
$$

$$- \left(\frac{\gamma-1}{2}\right) \Bigg[\frac{y}{x^2+y^2+4s_x(s_x-x)} + \frac{y}{x^2+y^2+4s_x(s_x+x)} - \frac{y}{R^2+y^2+4s_x(s_x-R)}$$

$$- \frac{y}{R^2+y^2+4s_x(s_x+R)} \Bigg] \Bigg\}$$

$$- \frac{V_1\pi}{s_x} \cos(\pi x/2s_x) \sum_{m=1}^{N} \Bigg\{ \frac{\mathrm{Sinh}\,\pi(y-2ms_y)/2s_x}{\cosh^2\pi(y-2ms_y)/2s_x - \cos^2(\pi x/2s_x)}$$

$$+ \frac{\mathrm{Sinh}\,\pi(y+2ms_y)/2s_x}{\cosh^2\pi(y+2ms_y)/2s_x - \cos^2(\pi x/2s_x)} \Bigg\}$$

$$- \frac{V_{st}\pi}{s_x} \cos(\pi x/2s_x) \sum_{m=-N}^{N} \Bigg\{ \frac{\mathrm{Sinh}\,\pi(y-2ms_y)/2s_x}{\cosh^2\pi(y-2ms_y)/2s_x - \cos^2(\pi x/2s_x)} \Bigg\} \quad \text{(A3)}$$

for x < R, and

$$V(x,y) = - \frac{2}{3} \left(\frac{2J}{b\epsilon_0}\right)^{1/2} \left[(s_x-R)^{3/2} - (x-R)^{3/2} \right]$$

$$+ (V_{st}+V_1) \sum_{m=-N}^{N} \ln \left[\frac{\cosh\pi(y-2ms_y)/2s_x - \cos(\pi x/2s_x)}{\cosh\pi(y-2ms_y)/2s_x + \cos(\pi x/2s_x)} \right] \quad \text{(A4)}$$

$$E_x(x,y) = - \left(\frac{2J}{b\epsilon_0}\right)^{1/2} (x-R)^{1/2}$$

$$- (V_{st}+V_1)\pi/s_x \,\mathrm{Sin}(\pi x/2s_x) \sum_{m=-N}^{N}$$

$$\left[\frac{\cosh\pi(y-2ms_y)\,2s_x}{\cosh^2\pi(y-2ms_y)/2s_x - \cos^2(\pi x/2s_x)} \right] \quad \text{(A5)}$$

$$E_y(x,y) = - (V_{st}+V_1)\pi/s_x \cos(\pi x/2s_x) \sum_{m=-N}^{N}$$

$$\left[\frac{\mathrm{Sinh}\,\pi(y-2ms_y)/2s_x}{\cosh^2\pi(y-2ms_y)/2s_x - \cos^2(\pi x/2s_x)} \right] \quad \text{(A6)}$$

for x > R, where

$$V_1 = \frac{a_0E_0(\gamma-1)s_x}{\pi R} \mathrm{Sin}(\pi R/2s_x) \Bigg\{ 1 - \frac{R}{2} \left[\frac{R-2s_x}{R^2+4s_x(s_x-R)} + \frac{R+2s_x}{R^2+4s_x(s_x+R)} \right] \Bigg\}, \quad \text{(A7)}$$

$\delta = 2Js_y/\pi\varepsilon_0 b a_0{}^2 E_0{}^2$,

$\zeta = (1 - \delta a_0{}^2)^{\frac{1}{2}}$,

$\gamma = (1 + \delta(R^2 - a_0{}^2))^{\frac{1}{2}}$,

E_0 = electric field at the wire,

a_0 = radius of the wire.

Because the potential on the plane $x = R$ must be constant, y^2 terms are empirically added to the integration constants of the cylindrically symmetric solutions. This would have little effect near the wire, but allows the boundary conditions to be met by a slight modification to the cylindrical solution. This solution not only yields a constant potential on the plane $x = R$, but also leads to x and y components of electric field which satisfy the necessary boundary conditions imposed on the solution by symmetry. Specifically, the x-component of electric field must vanish in the plane of the wires, while the y-component must vanish at the plates and at the two planes represented by dashed lines connecting the plane of the wires with the plates in Figure 1. For cases in which the radius (R) of the cylinder of space charge is larger than the half wire-to-wire spacing, adjacent cylinders of space charge will overlap. In this situation the effects of space charge would be overestimated. To correct for that difficulty in this simple model we reduce the contribution to the potential and electric field components from space charge associated with wires other than the central one by the fraction of the volume of the cylinder that does not extend beyond S_y. This fraction is given by

$$F = \begin{cases} 1 - \frac{2}{\pi}\left[\mathrm{ArcCos}(s_y/R) - \frac{s_y}{R^2}(R^2 - s_y{}^2)^{\frac{1}{2}}\right], & s_y < R \\ 1 & , s_y \geq R . \end{cases} \qquad \text{(A8)}$$

This factor would multiply V_1 in the space charge terms arising from wires other than the central one ($m = 0$). Surprisingly, this simplified approach to computing a correction factor yields rather good agreement between the approximate model and the numerically integrated solution.

LATERAL PROPAGATION OF BACK DISCHARGE

By:

Senichi Masuda

Department of Electrical Engineering
Faculty of Engineering, University of Tokyo
7-3-1, Hongo, Bunkyo-ku, Tokyo, Japan 113

Sadaji Obata

Ishikawajima Harima Heavy Industries Ltd.
Technical Research Center
3-2-16, Toyosu, Koto-ku, Tokyo, Japan 135

ABSTRACT

In a tri-electrode type precipitator having the discharge, third, and collecting electrodes, where the main voltage is applied between the third and collecting electrodes and a dc or pulse voltage is applied between the third and discharge electrodes for producing corona discharge, special precautions must be taken to avoid the lateral propagation of back discharge. The primary back discharge occuring in a resticted region on the collecting electrode facing to the discharge electrode tends to propagate in the lateral direction, once it takes the form of streamer-mode, finally to cover the whole surfaces of the collecting and third electrodes. The secondary back discharge resulted by this propagation becomes self-sustained if well developed, and does not disappear unless the main field strength is lowered below a certain critical level. The propagation initiates when the magnitude of the main field strength exceeds ca. 5 kV/cm in air at NTP, and it is extinguished at a slightly lower field strength. The use of pulse voltage for corona production decelerates the occurence of the propagation to a great extent. When high resistivity dusts causing back discharge are encountered, it is imperative to keep the main field strength below the extinguishing threshold of the propagation, in order to obtain the inherent advantage of the tri-electrode precipitator. The use of pulse voltage for corona production is also highly desirable. This lateral propagation occurs in any precipitators having a parallel plane electrode construction, too.

LATERAL PROPAGATION OF BACK DISCHARGE

1. INTRODUCTION

During the course of developmental efforts of the tri-electrode type precipitator as illustrated in Figure 1, where the main dc voltage is applied between the third and collecting electrodes for producing the collection field and the dc or pulse voltage is applied for producing a controlled corona discharge, a curious phenomenon was observed to occur when high resistivity dust causing back discharge was being collected. The collection performance as expected could be obtained only when the main field strength was kept below a certain critical level, beyond which a severe impairment of performance started to occur. In this case the surface glow of back discharge covered the whole surface of both collecting and third electrodes, not only the restricted region on the collecting electrode facing to the discharge electrode, but also the other regions where no ions from the discharge electrode were arriving. The back discharge, once occured in the region A facing to the discharge electrode because of its ionic current, propagated towards the remote regions where no primary ions were existing, because of the secondary ions emitted from the back discharge points. This phenomenon of lateral propagation of back discharge was already observed to occur in the author's experiments of electrostatic powder deposition using a parallel plate electrode system and tribo-charged resin powders (Masuda et. al. (1977)1)). In this paper are reported the results of investigations made by the authors in order to clarify this phenomenon in more details and to find out the condition to avoid this trouble.

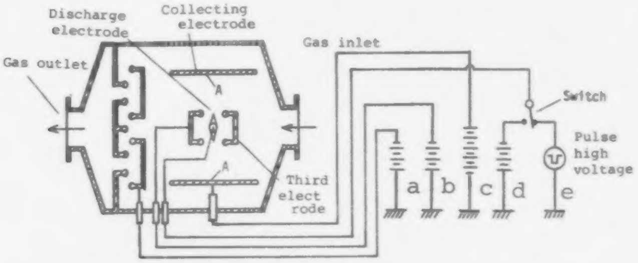

a,b,c,d: dc high voltage source
e: pulse high voltage source

Figure 1 Tri-electrode type precipitator.

2. METHOD OF EXPERIMENTS

Figure 2 illustrates the model tri-electrode system used in the present investigation, consisting of two parallel circular discs as the third and collecting electrodes and a needle located at the center of a small hole drilled at the center of the third electrode. The probe electrodes are attached to both the third and collecting electrodes for measuring current density distribution. Instead of dust samples, two kinds of towel paper samples are used: one with 1.2 mm thickness and 0.034 g/cm^3 volume density (low-density sample), and the other out of 5 original low density papers pressed to 1.2 mm thickness (high-density sample). The sample resistivity is changed in a wide range in air at NTP by changing the ambient air humidity within the humidity chamber in which the entire system is located. The inter-electrode field intensity between the third and collecting electrodes (main field intensity), $E_1 = V_B/D$, and the primary corona current from the needle are changed by changing the values of V_B and V_P. However, the primary corona current is not used as a parameter as it does not provide reproducible results, and the average field intensity between the third and needle electrodes, $E_2 = V_P/R$, is used instead. Between the third and needle electrodes is applied either a negative dc voltage or a negative pulse voltage. E_2 in the latter case represents the average field intensity in terms of pulse crest voltage.

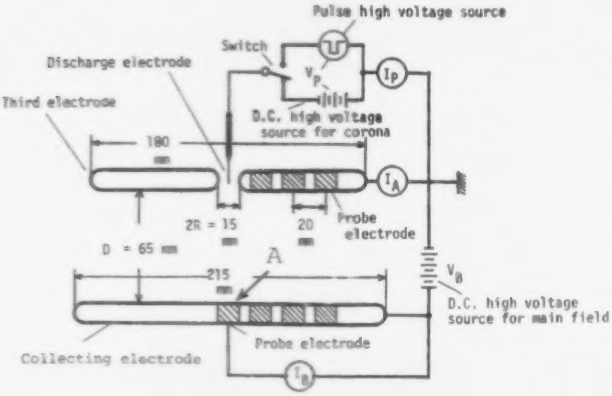

Figure 2 Test tri-electrode system

At first, the mode of the lateral propagation of back discharge is observed under different conditions using an image intensifier tube (EMI type 9912). Then, the initiation and extinguishing conditions of the secondary back discharge are measured. Finally, the current wave form of the secondary back discharge is observed.

3. RESULTS OF EXPERIMENTS

3.1 Mode of lateral propagation of back discharge

The primary back discharge, occured in the region A in Figure 2, can generally propagate in the lateral direction only when it takes the form of space-streamer-mode and the magnitudes of E_1 and E_2 exceed respectively their own threshold values, except a few cases to be described later. The development of the space-streamer-mode back discharge requires not only a sufficiently high main field intensity, E_1, but also enough quantity of corona current obtainable by raising E_2. Raising of E_1 at low E_2 only results in sparking without causing the primary back discharge itself, whereas raising of E_2 at low E_1 only causes the primary back discharge in a form of either surface-glow or very weak space-streamer so that no lateral propagation can take place. Except for the lower dust resistivity case at $\rho_d < 10^{11}$ ohm-cm, once the secondary back discharge occupied the whole inter-electrode region, it becomes self-sustaining and does not disappear unless the main field intensity, E_1, is lowered below a certain threshold, even if the primary back discharge is extinguished by lowering E_2. The propagation mode differs completely between the dc corona operation and pulse corona operation, so that it is described separately in the following.

a) DC corona operation. Figure 3 (a) - (d) are the photographs of the secondary back discharge occuring in the dc corona operation when only the collecting electrode is covered with the low-density sample. As shown in these pictures, the lateral propagation can occur even when the third electrode is kept clean. However, the secondary back discharge in this case always takes the form of space-streamer bridging across the third and collecting electrodes. It is evident that the negative ions to maintain the secondary back discharge in the outer region around A are being regenerated in the streamer channels. These ions are conveyed through the field-drift and diffusion processes towards the regions on the collecting electrode remote from the original back discharge spots.

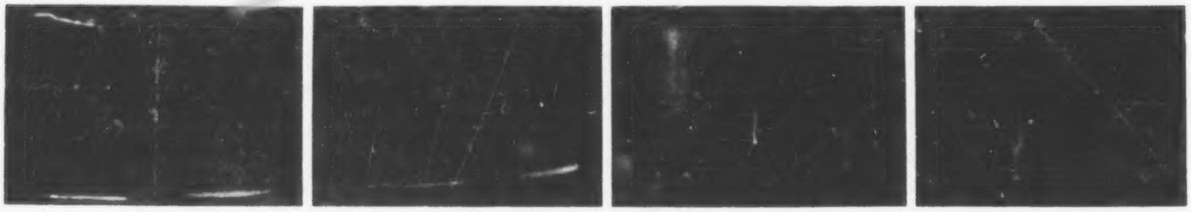

E_1 = 5.5 kV/cm
ρ_d = $1.1\text{x}10^{11}$ ohm-cm
(a)

E_1 = 5.1 kV/cm
ρ_d = $2.5\text{x}10^{12}$ ohm-cm
(b)

E_1 = 5.1 kV/cm
ρ_d = $1.4\text{x}10^{13}$ ohm-cm
(c)

E_1 = 5.4 kV/cm
ρ_d = $1.4\text{x}10^{14}$ ohm-cm
(d)

Figure 3 Secondary back discharge occured when only the collecting electrode is covered with a low-density sample layer.

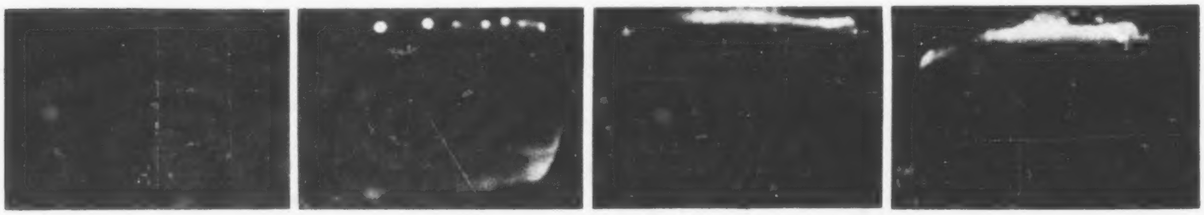

E_1 = 6.9 kV/cm
ρ_d = $1.1\text{x}10^{11}$ ohm-cm
(a)

E_1 = 5.2 kV/cm
ρ_d = $2.5\text{x}10^{12}$ ohm-cm
(b)

E_1 = 5.2 kV/cm
ρ = $1.4\text{x}10^{13}$ ohm-cm
(c)

E_1 = 5.2 kV/cm
ρ = $1.4\text{x}10^{14}$ ohm-cm
(d)

Figure 4 Secondary back discharge occured when both the collecting and third electrodes are covered with high-density sample layers.

In comparatively low resistivity region $\rho_d \simeq 10^{11}$ ohm-cm, below which no lateral propagation occurs, the secondary streamers are very weak, unstable, and move around rapidly in the inter-electrode spacing without covering its entire region (Figure 3 (a)). The secondary streamers in this stage are not self-sustaining. In the intermediate resistivity region at $\rho_d \simeq 10^{12}$ ohm-cm, the secondary streamers become well developed, self-sustaining, and can occupy the entire inter-electrode spacing (Figure 3 (b)). In the high resistivity region at $\rho_d \simeq 10^{13}$ ohm-cm, the leader channels begin to appear, stemming from the collecting electrode and splitting into many streamers at their upper ends (Figure 3 (c)). However, the appearance of the leaders seems to be colsely related to the increased breakdown strength of the sample which is raised at the same time by lowering the ambient air humidity to get high sample resistivity. In the very high resistivity range at $\rho_d \simeq 10^{14}$ ohm-cm, all the secondary streamers are originating from the leaders, as shown in Figure 3 (d), while the primary back discharge turns into surface-glow-mode. In the high resistivity range beyond 10^{13} ohm-cm, several curious phenomena are observed to occur. When the random sparking occurs repeatedly at very high value of E_1, the secondary streamers can start to appear without the aid of the primary streamers. Secondly, even after the secondary back discharge has been extinguished once by lowering E_1, it can be reignited when E_1 is raised again in due time.

When the low-density sample is replaced by the high-density sample in Figure 3, the mode of secondary back discharge as indicated by (a) - (d) occurs at the resistivity value one order of magnitude higher.

In case both the collecting and third electrodes are covered with the low-density samples, no appreciable change occurs in the secondary back discharge of each resistivity level. On the other hand, when the high-density samples are used instead to cover both electrodes, a drastic change appears as indicated by the photographs of Figure 4 (a) - (d). In the lower resistivity range at $\rho_d \simeq 10^{11}$ ohm-cm, the secondary back discharge appears only in a form of the scattered glow points primarily on the third electrode (Figure 4 (a)). Beyond 10^{12} ohm-cm the secondary streamers begin to appear and cover the entire electrode region. However, these streamers are always stemming from the collecting electrode, and do not bridge across the electrode gap (Figure 4 (b) and (c)). The back discharge on the third electrode remains in a form of surface-glow. In the very high resistivity range $\rho_d \simeq 10^{14}$ ohm-cm, the secondary streamers do completely disappear, and the back discharge in the surface-glow-mode covers both electrodes. In addition, in the high resistivity range beyond 10^{13} ohm-cm a new type of secondary back discharge appears on both electrodes at a fairly low value of E_1 at which the secondary streamers cannot occur. This is of the surface-glow-mode and extremely feeble so that it can be detected only with the aid of an image intensifier. Its current is also extremely small, so that it may be doubtful whether this back discharge will cause a detrimental effect on the collection performance.

b) Pulse corona operation. The pulse corona operation enables a large reduction in primary corona current without lowering the main field intensity, E_1 (Masuda et. al. (1976)[2](1977)[3](1978)[4]). This current-limiting characteristics hampers greatly the initiation of the primary back discharge itself and also its transition into the space-streamer which is the origin of the lateral propagation. This tendency is pronouced when both electrodes are covered with the high resistivity samples. The primary back discharge, once occured, usually remains in the surface-glow-mode and hardly turns into the space-streamer-mode to cause the lateral propagation unless the main field intensity, E_1, and the primary corona current are greatly increased. Here, the raising of the corona current can be made by either raising the pulse crest voltage, its repetition frequency f, or its duration time t_p.

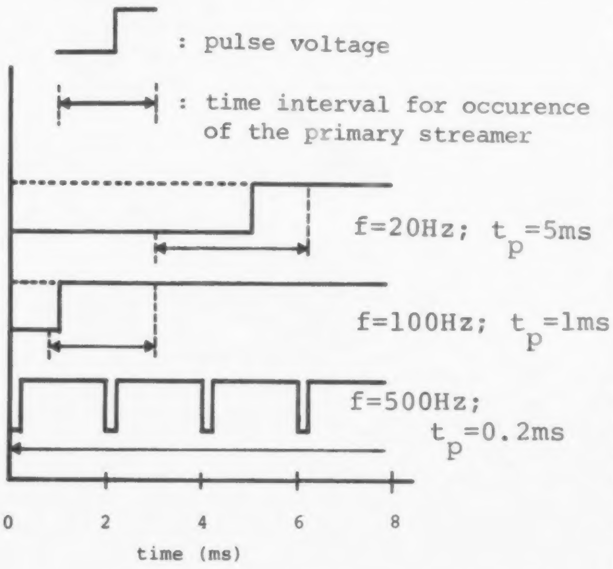

Figure 5 Delay of time interval for occurance of primary streamer.

In addition to the current-limiting effect as described above, the pulse corona operation has another large advantageous effect of hampering the lateral propagation, such that the primary streamers tend to occur in retard to the pulse voltage, as illustrated in Figure 5. The time interval in which the primary streamers occur becomes more and more retarded to the pulse duration interval with decreasing pulse duration time, t_p. As a result, the situation disappears that the primary streamers can be intensified enough to cause the lateral propagation by the strong space-charge field of oncoming ions which are supplied only in the pulse duration period. However, this effect becomes lost when the pulse repetition frequency f is excessively raised, because the time interval of the primary streamer occurance covers the entire time domain in this case, as indicated by the bottom curve in Figure 5.

Owing to these circumstances, the lateral propagation of back discharge is greatly decelerated when the pulse corona operation is used. However, this does not always exclude the possibility that the lateral propagation may be caused at very high values of E_1 and E_2 after enough time has elapsed during which ions accumulate on the sample surface in a sufficient amount. Actually the initiation threshold of the secondary back discharge in terms of E_1 does not change much from that in the dc corona operation. Moreover, once the lateral propagation has developed in the inter-electrode space, any difference is lost between the pulse and dc corona operations, because the secondary streamers, then, become self-sustained.

3.2 Initiation and extinguishing conditions of lateral propagation

a) Initiation condition. The initiation condition of the lateral propagation of back discharge does not differ much in all of the cases as described, and it is governed by the parameters E_1 and E_2. The curves in Figure 6 represent the typical instances of the initiation conditions for the dc and corona pulse operations. It can be clearly seen that the threshold value of the main field intensity, E_1, for the initiation of the lateral propagation, approximately 5 kV/cm, coincides well with the condition of streamer propagation in air at NTP.

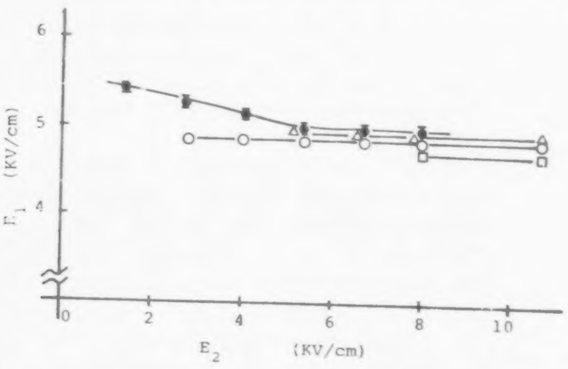

●: d.c. corona operation; only the counter electrode covered with a low-density samples; r_d= 1.4x10^{13}ohm-cm

△: pulse corona operation; both electrodes covered with high-density samples; r_d= 1.4x10^{13}ohm-cm

○: pulse corona operation: both electrodes covered with high-density samples; r_d= 1.4x10^{14}ohm-cm

□: pulse corona operation: both electrodes covered with high-density samples; r_d= 1.0x10^{15}ohm-cm

'igure 6 Initiation condition of secondary back discharge .

b) Extinguishing condition. There is no difference in the extinguishing condition of the secondary back discharge between the dc and pulse corona operations, and moreover, it is also independent of the magnitude of E_2. These are due to the self-sustaining effect of the secondary back discharge as described previously. The extinguishing condition is primarily governed by the main

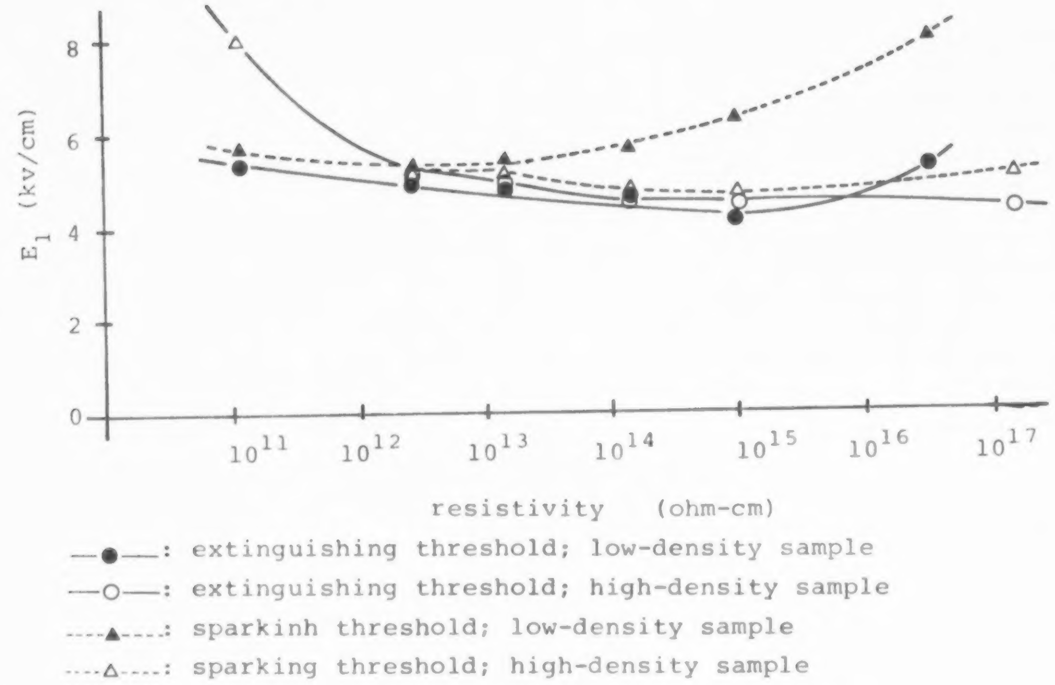

Figure 7 Extinguishing condition of secondary back discharge. (only the collecting electrode covered with a sample)

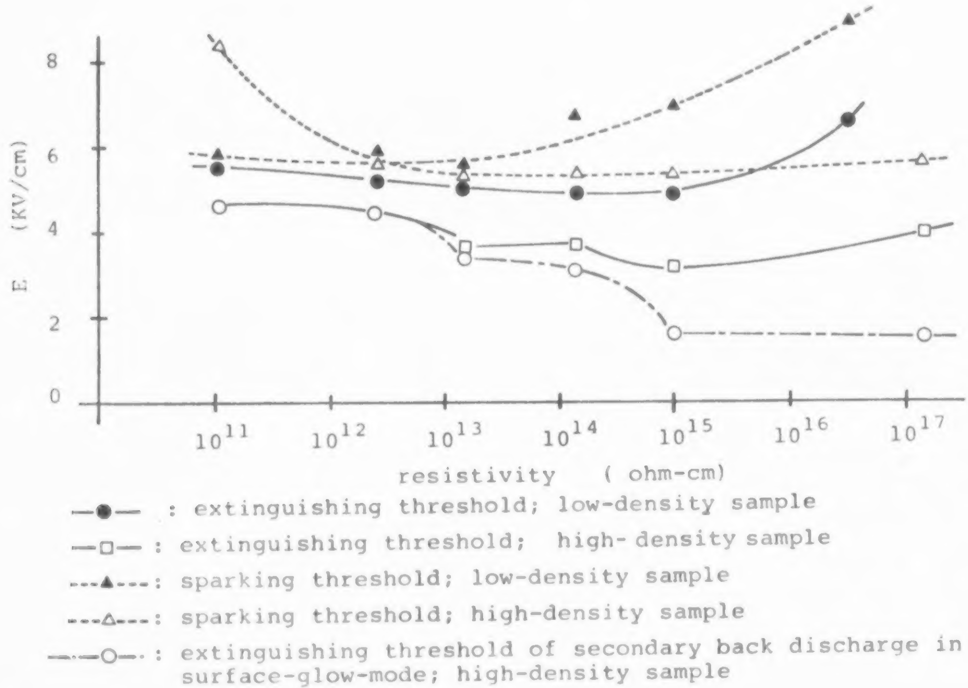

Figure 8 Extinguishing condition of secondary back discharge. (both the collecting and third electrodes covered with samples)

field intensity, E_1, and slightly by the sample resistivity, ρ_d, too. The solid curves in Figure 7 represent the extinguishing threshold of E_1 when only the collecting electrode is covered with the low- and high density samples, plotted against ρ_d. The solid curves in Figure 8 indicate the same threshold when both the collecting and third electrodes are covered with the low- and high-density samples. The dotted curves in Figures 7 and 8 represent the sparking threshold. The broken line in Figure 8 indicates the extinguishing condition of the very feeble secondary back discharge in the surface-glow-mode with negligibly small corona current, as described in the preceding section. It can be seen from Figures 7 and 8 that the extinguishing threshold of E_1 does not differ much in all of the cases, except a special case as described above. It lies in the range of 3.5 - 5 kV/cm and is always slightly lower than its initiation threshold under the same condition.

3.3 Current wave form

The current wave form of the secondary back discharge in the streamer-mode is essentially the same as that of the primary streamer back discharge which have been already reported (Masuda and Mizuno (1976/1977)[5]).

4. CONCLUSION

The experimental results thus far obtained provide the following conclusions:

1) The lateral propagation of back discharge starts to occur when the sample resistivity, ρ_d, exceeds the level of ca. 10^{11} ohm-cm, but it becomes dominant only when ρ_d exceeds ca. 10^{12} ohm-cm. It is resulted by the primary back discharge in the space-streamer-mode, and propagates mostly in a form of the secondary streamer. The secondary back discharge becomes self-sustaining once well developed, and it does not disappear unless the main field intensity, E_1, is lowered below a certain threshold level.

2) The magnitudes of the main field intensity, E_1, and primary corona current expressed in terms of E_2 play the most essential role in the initiation and extinguishing of the secondary back discharge. Their threshold values for the initiation and extinguishing do not differ much under different operating and dust resistivity conditions.

3) The threshold value of the main field intensity, E_1, for the initiation of the lateral propagation is about 5 kV/cm in air at NTP, which agrees well with the streamer propagation condition in atmospheric air. The threshold value of E_1 for the extinguishing of the secondary back discharge is always slightly lower than that for the initiation.

4) The lateral propagation of back discharge can be greatly decelerated by the use of the pulse corona operation with the suitable crest voltage, E_2, repetition frequency, f, and duration time, t_p. However, the possibility of the propagation to occur after a sufficiently long time for ion accumulation may not be excluded even in the pulse corona operation. This leads to the conclusion that the tri-electrode precipitator should be operated at the main field strength, E_1, below the extinguishing threshold as described above.

5) This extinguishing threshold of E_1, however, lies on a level (3.5 - 5 kV/cm in air at NTP) which is still sufficiently high for a satisfactory collection performance to be obtained.

The tri-electrode precipitator has its inherent large advantage to decrease freely the primary corona current, without lowering the magnitude of the main field intensity, down to the level at which no primary back discharge does occur. The use of the pulse corona operation makes this current-limiting action more easily, and it also makes the distribution of the primary corona current on the collecting electrode much more uniform, especially when the corona current is to be kept at a very low level. However, in order to exploit this advantage of avoiding back discharge, it is not sufficient to take precaution to avoid the primary back discharge only by lowering the primary corona current below a certain threshold level. Another additional precaution must be taken against the occurence of the secondary back discharge. In order to avoid this trouble under any circumstances, the tri-electrode precipitator should be operated at a main field intensity level below the extinguishing threshol as described.

Finally, it should be pointed out that the secondary back discharge of the similar character was obserbed, by the use of an image intensifier, to occur in the conventional twin-electrode precipitators collecting high resistivity dust at the frame-works supporting discharge electrodes. The secondary back discharge is also expected to occur in any type of collecting field comprizing the parallel plane electrode construction, such as the collection field of the two-stage type precipitator having a separate precharging section. The same precaution will be needed in such applications.

ACKNOWLEDGEMENTS

The author appreciates the assistance of his co-workers, Mr. Kensuke Akutsu and Mr. Yoshio Ogura, given to this research. The financial supports given by the Ministry of Education Japan and IHI Heavy Industries Ltd. are also appreciated.

REFERENCES

(1) Masuda, S., A. Mizuno and K. Akutsu. Initiation Condition and Mode of Back Discharge for Extremely High Resistivity Powders. Record of IEEE/IAS 1977 Annual Meeting. p. 867 (Los Angels, October 1977).

(2) Masuda, S., I. Doi, M. Aoyama and A. Shibuya. Bias-Controlled Pulse Charging System for Electrostatic Precipitators. Staub-Reinhaltung der Luft (Bonn). Vol. 36, p. 19 (1976)

(3) Masuda, S., I. Doi, I. Hattori and A. Shibuya. Utility Limit and Mode of Back Discharge in Bias-Controlled Pulse Charging System. Record of IEEE/Ias 1977 Annual Meeting. p. 875 (Los Angels, October 1977).

(4) Masuda, S. Novel Electrode Construction for Pulse Charging. Proc. of 1st EPA-Symposium on Transfer and Utilization of Particulate Control Technology. Vol. 1, p. 241 (Denver, July 1978).

(5) Masuda, S. and A. Mizuno. Light Measurement of Back Discharge. Journal of Electrostatics (Amsterdam). Vol. 2 (1976/1977), p. 375.

THEORETICAL MODELS OF BACK CORONA AND LABORATORY OBSERVATIONS

by

D.W. VanOsdell
P.A. Lawless

Research Triangle Institute
P.O. Box 12194
Research Triangle Park, N.C. 27709

and

L.E. Sparks

Industrial Environmental Research Laboratory
U.S. Environmental Protection Agency
Research Triangle Park, N.C. 27711

ABSTRACT

Several mechanisms for the generation of positive ions due to back corona were postulated. These mechanisms were then used in conjunction with an electrostatic precipitator model to produce calculated voltage-current (V-I) relationships for each back corona mechanism. Multiple values of the parameters of the back corona mechanism were used and the effect of space charge was investigated. It was found that near-vertical V-I relationships could be produced for most of the models and that the hysteresis present in actual data was possible with certain models. In particular, the model postulating that positive ions are generated in proportion to a threshold current density was found to be capable of giving a theoretical V-I relationship which exhibited the hysteresis and step structure of some experimental V-I relationships.

THEORETICAL MODELS OF BACK CORONA AND LABORATORY OBSERVATIONS

1.0 INTRODUCTION

The undesirable effects of back corona in electrostatic precipitators (ESPs) are well known. The emission of positive ions from the collection plate of an ESP achieving a bipolar ionic equilibrium reduces the net particle charge,[1,2] at a given current, and particle collection is degraded. The formation of the positive ion current leads to a rapid increase in total current as voltage is increased.[3,4] The increase can be so large as to give near-vertical or even negative slopes to the voltage-current (V-I) curves. This V-I characteristic is the most common indication of the presence of back corona, because direct detection of free ions of both polarities is very difficult. This paper postulates mathematical formulations for back corona, and, through an ESP model, relates these back corona mechanisms to calculated V-I curves. The implications for particle charging and collection are examined.

2.0 PRECIPITATOR MODEL

As back corona is difficult to observe directly, the back corona mechanisms were used as parameters in an ESP model to give calculated quantities which could be compared to actual measured conditions. The model used is based upon equations involving the local electric fields rather than the electric potentials. The reasons for this are the charges in electric fields are influenced only by the local conditions and that they are the natural coordinates for calculating particle charges and the forces on charged particles. It is fortuitous that the resulting equations are particularly simple and easy to solve. This ESP model will not be described further in this paper except to say that the numerical solution is relatively fast and that the solutions appear to fit actual ESP data quite well. Figure 1 presents V-I data taken on three identical sections of a pilot-scale precipitator. Comparisons with other experimental measurements[5] produce similar satisfactory agreements. The point is that this ESP model gives reasonable results and is suitable for comparison of back corona mechanisms.

3.0 BACK CORONA MECHANISMS

Although recent experimental work has begun to delineate the nature of back corona mechanisms[6,7] revealing streamer and glow models of propagation, the mechanisms of generating positive ions in the particulate layer are still uncertain. Electrical breakdown of the particles or the interstitial gases in the particle layer are postulated,[1,2] but detailed descriptions are lacking. The approach taken in this paper is to assume several simple model mechanisms for the generation of positive ions and to explore the consequences of each. All of these mechanisms are described in terms of a critical current density, since experimental evidence[7] indicates the sudden onset of back corona as the current density is increased. None of the mechanisms includes an effect due to local electric field because in standard electrostatic precipitators, the critical current density and the local electric field are jointly determined by the resistivity of the particle layer. All the proposed mechanisms are assumed to be local, with back corona onset in a given location having no direct effect on adjacent locations. Finally, all the mechanisms assume a continuous generation of ions, as opposed to the pulsing effects observed experimentally.[7] The five mechanisms chosen are described below.

I. Positive ions are generated in proportion to the amount that the total current density exceeds the critical current density. This can be written:

$$\rho_+ = \begin{cases} \beta(j_x - j_{th})/E_x b, & j_x > j_{th} \\ 0 & , j_x < j_{th}, \end{cases} \tag{1}$$

where ρ_+ is the positive free ion space charge density (C/m^3), β is an adjustable dimensionless parameter, E_x is the electric field strength (V/m), b is the carrier mobility (m^2/V-sec), and j_{th} is the threshold current density (A/m^2). The "x" direction is between the plate and wire. Since the generation of positive ions occurs in the dust layer near the plate, only the x-component of field is significant. For values of β near 1, this mechanism tends to keep the electric field at the dust layer constant by reducing the net space charge as the current density increases.

II. Positive ions are generated in proportion to the threshold current density, once the total current density exceeds the critical level:

$$\rho_+ = \begin{cases} \gamma\, j_{th}/E_x b, & j_x \geq j_{th} \\ 0 & , j_x < j_{th}, \end{cases} \tag{2}$$

where γ is an adjustable dimensionless parameter. This mechanism corresponds to a source-limited generation of ions. It can be seen to have a built-in hysteresis, because the presence of the positive ions increases the total current density by a fixed amount at the threshold.

III. Positive ions are generated in proportion to the total current density, once the total current density exceeds the critical level:

$$\rho_+ = \begin{cases} \delta j_x/E_x b & , j_x \geq j_{th} \\ 0 & , j_x < j_{th}, \end{cases} \tag{3}$$

where δ is an adjustable dimensionless parameter. This is similar to mechanism I for current densities far above the threshold, but should exhibit a hysteresis near the threshold current density.

IV. The positive ions are generated in proportion to the square of the total current density:

$$\rho_+ = \epsilon j_x^2 / j_{th} E_x b \, , \tag{4}$$

where ϵ is an adjustable dimensionless parameter. This mechanism could represent a source sensitive to heating effects. In this particular formulation, there is not a sharp onset threshold, but the quadratic increase in ρ_+ is sufficiently rapid to have the appearance of threshold. In practice, the increase of ρ_+ is so rapid that numeric instabilities occur unless a maximum limit is placed on ρ_+. This roughly corresponds to the physical situation in which the rate of heating is eventually balanced by losses to the surroundings. In this work, the positive ion current density at the plate was limited to 25 times j_{th}.

V. The positive ions are generated in proportion to the negative ion current density squared:

$$\rho_+ = \kappa j_-^2 / j_{th} E_x b \, , \tag{5}$$

where j_- is the x-component of the negative ion current density and κ is an adjustable dimensionless parameter. This mechanism describes a situation in which the positive ion current does not directly contribute to the heating effect, as would be the case if generation occurred at the surface of the layer.

In all the mechanisms except II, the adjustable parameter affects the ratio of the positive ion current to the negative ion current, and, in general, values can be found for which the ratio is nearly 1 over an extended range of currents. Mechanism II is different in that the adjustable parameter affects only the size of a step increase in positive ion density, and the positive and negative current densities will be equal at a single current only.

Consequences of Bipolar Particle Charging

In a unipolar ion field, a spherical conducting particle can be shown to obey the field charging equation:[1]

$$\frac{dq}{dt} = 3\pi r^2 j (1 - q/q_s)^2 , \tag{6}$$

where r is the particle radius, j is the current density (assumed to be uniform far from the particle), t is time, q is the charge on a particle C and q_s is the saturation charge on the particle, given by:

$$q_s = 12\pi r^2 \varepsilon_o E, \tag{7}$$

where E is the electric field magnitude far from the disturbing effects of the particle and ε_o is the free space permittivity (f/m). After a sufficiently long charging time, a particle essentially attains the saturation charge and stops charging. In the Stokes law regime, the drift velocity of the particle in the direction of the field is proportional to Eq_s, and therefore depends on the particle radius and the square of the electric field. At a given particle size, the velocity is proportional to E^2.

Where ions of opposite polarity impinge upon the particle, a charging equation of the following form results:

$$\frac{dq}{dt} = 3\pi r^2[j_-(1-q/q_s)^2 - j_+(1-q/q_s)^2], \tag{8}$$

where the sign convention chosen assumes that q_s is negative. The net charge q stops changing at an equilibrium value given by:

$$q_{max} = q_s[(\sqrt{j_-/j_+} - 1)/(\sqrt{j_-/j_+} + 1)] . \tag{9}$$

$$q_{max} \equiv q_s Q$$

The factor multiplying q_s we call Q for convenience. Q is less than 1 (even negative) for all non-zero values of j_+. Recalling that q_s does not depend on current density, the factor Q represents the degradation in particle charge that can be expected under bipolar charging conditions, and the particle drift velocity is proportional to the quantity E^2Q under bipolar charging conditions.

Effects of Particulate Space Charge

Since back corona effects are often observed in operating precipitators, it is worthwhile to calculate the additional effects attributable to the immobile particulate space charge. In general, particulate space charge has the effect of raising the entire voltage-current characteristic to higher voltages and increasing the electric field at the plate. A more subtle effect of the space charge is observed in the detailed calculations; it increases the current density at the plate directly opposite the corona wires and decreases it in the region between the wires for the same average current density. This effect modifies the onset of back corona under the five mechanisms from the condition of zero particulate space charge.

4.0 RESULTS OF THE CALCULATIONS WITH FIVE BACK CORONA MECHANISMS

The ESP calculations were made using the following fixed parameters:

temperature : 615°K
pressure : 0.86 atm
corona wire radius : 1.34 mm
wire-to-plate spacing: 11.43 cm
½wire-to-wire spacing: 11.43 cm
roughness factor : 0.8
mobility : $7.46\text{x}10^{-4}$ m^2/V-sec
j_{th} : $4.0\text{x}10^{-5}$ A/m^2
space charge : 0 or $-1\text{x}10^{-5}$ C/m^3

The choice of j_{th} is not critical. Too large a value means that unrealistically high current densities would be required to exceed the threshold while too small a value would obscure details as the threshold is crossed. The non-zero value of q is a substantial space charge density, but not an excessive one. The effects of the resistivity of the dust layer are not considered in the early work presented below.

The average current density was initially set to zero, and then incremented upward to a maximum value, with the corona wire voltage calculated at each step. The electrical conditions used as the starting values for a given step were the final solution values of the preceding step to mimic a real measurement of a voltage-current curve. After the maximum was reached, the current density was decremented to observe hysteresis effects, but many mechanisms showed no hysteresis effects at all. Some calculations could not be carried to completion because of numerical instabilities which were encountered, generally in cases with extreme back corona.

The voltage-current characteristics were calculated for wide ranges of the adjustable parameters for each mechanism. Particular attention was paid to achieving a near-vertical V-I characteristic and to checking for hysteresis effects, since these are observed characteristics in back corona situations.

Figures 2 through 6 present the voltage-current density curves calculated for the five mechanisms. In most instances, near-vertical curves could be obtained, and in some cases hysteresis was observed. Note that hysteresis was expected in mechanisms II and III (and was calculated), but it also appeared in mechanism IV in an unusual fashion. The hysteretic behavior of the current density at levels approaching the critical threshold does not correspond to physical reality for the following reasons. The electric field at the corona wire is held constant at the corona-start value; in the calculation it is the field required to sustain corona current in the absence of external influences, once it is initiated. But the presence of the positive ion back corona current is a significant influence which would allow the corona to be sustained at a lower value of the electric field. The result would be a fairly smooth decrease in voltage as the current decreases, whereas, in the present calculation, the calculated voltage "snaps" back to the starting voltage once the back corona current ceases. The hysteresis at current densities well above threshold should be little affected by this phenomenon.

The significance of the numerical instabilities which occurred for some values of adjustable parameters cannot be ascertained. The instabilities invariably occurred at high levels of positive ion current, where real physical instabilities might logically be expected due to the decreasing net ionic space charge. Nonetheless, it seems probable that the instabilities could be suppressed at least partially by careful choice of model parameters. It is worthwhile to note the stabilizing effect of a particulate space charge in all the mechanisms. Higher current densities were achieved without calculational instabilities when particulate space charge was included than when it was not.

The particulate space charge also tends to suppress the spread of back corona laterally between the wires. In Figures 3 and 4, the steps in the curves are due to the cell structure of the calculation, with each step corresponding to the formation of positive ions in one or two cells as the local current density exceeds the threshold. With q=0, the transitions occur in all the cells over a narrow range of total current densities. The lateral spread of back corona has been verified experimentally.[3,7]

Consequences of Back Corona

In the Deutsch-Andersen theory of precipitator collection,[1,2] the drift velocity of the charged particles appears as a multiplier in the argument of an exponential term in an expression for the collection efficiency, and is, therefore, especially significant. Recalling that the drift velocity is roughly proportional to E^2Q, we have plotted this quantity for the five mechanisms in Figures 7 through 11. The terms were evaluated at the plate, because collection occurs at the plate, and a simple linear average over all the cells was used.

The figures illustrate that the presence of back corona has a strong effect by whatever mechanism it occurs and regardless of the presence of a particulate space charge. (We note here that it would prove difficult to maintain an highly charged particulate in the presence of a bipolar charging field.) Two mechanisms are worthy of note: in mechanism II on the descending legs of the hysteresis curves, the E^2Q product average actually becomes negative; and in mechanism III, for $\gamma = 0.5$, the E^2Q product approaches zero rapidly as the current density increases. Both of these conditions are disastrous for particle collection. The other mechanisms, particularly in the presence of space charge, exhibit local E^2Q products which are zero or negative, but for which the overall average is positive. The use of a current density weighted average in these cases would depress the E^2Q value calculated even further.

In terms of operating strategy in a precipitator suffering back corona, the E^2Q product is generally a maximum at current densities which avoid initiating back corona, i.e. low current densities. Unfortunately, although E^2Q represents the drift velocity of a maximally charged particle, it does not describe the rate of charging which is a function of current density. If particle charging were accomplished in a prior section, the E^2Q product should then be maximized. If, on the other hand, charging and collection take place in the same section, operating at low current densities might not fully charge the particles in that section resulting in reduced collection efficiency.

The E^2Q curves also point out the enhanced drift velocity in the presence of a particulate space charge. Even though back corona degrades the E^2Q product, adding space charge can boost it to a significantly higher level.

5.0 COMPARISON WITH EXPERIMENTAL RESULTS

Laboratory measurements to challenge the validity of these mechanisms have not yet been performed, but two measurements in laboratory precipitators which exhibit back corona characteristics are presented here. The first is a voltage current curve measured on a pilot-scale precipitator[5] under controlled conditions after several hours operation collecting a high resistivity dust. The geometry factors were:

wire-to-plate:	11.4 cm
wire-to-wire :	3.8 cm
wire radius :	1.59×10^{-3} m (thickly covered with dust)
plate area :	3.0 m^2
temperature :	408°K

Such a configuration would be expected to have a corona starting voltage of about 45 kV under clean conditions and in excess of 30 kV with a roughness factor of 0.7. The actual V-I curve (Figure 12) was obtained on an X-Y recorder measuring the corona wire voltage and collector plate current as the voltage was slowly increased to a maximum and then decreased to zero. The particulate space charge was zero (no particulate feed).

The ascending leg of the curve exhibits both increases and decreases in the voltage as the current rises. More importantly, the X-Y recorder reveals small variations in voltages that would likely be missed in a point-to-point type of measurement. The descending leg of the curve is more regular but still has the small step-like character that the ascending leg has.

Of the five mechanisms, only mechanism II has the potential of such a pronounced hysteresis with step-like increases and decreases in voltage. Mechanism II is incomplete, however, in that it postulates only a single threshold. In order to produce a characteristic similar to Figure 12, multiple closely spaced thresholds would be required. Conceptually, there could be a spectrum of thresholds around the average value, or the actual current density along the length of the wire could vary due to minute physical differences, making the problem a three-dimensional one instead of the two-dimensional calculation used.

A composite voltage current characteristic based on mechanism II is presented in Figure 13. This composite can be thought of as a corona wire made up of five sections, the corona start voltage for each of the sections differing by 100 volts. This voltage offset corresponds to corona wire diameter variations of less than 1 percent per offset, which is reasonable for a dirty corona wire. The composite V-I curve shown in Figure 13 was generated from a sum of the V-I characteristics given in Figure 3.

Other mechanisms can produce V-I characteristics similar to the ascending leg of Figure 12 with proper choice of the threshold current density and the adjustable parameters, particularly mechanism IV. The difficulty is in giving physical meaning to the parameters which, in these calculations, are arbitrary. In mechanism II, the adjustable parameter controls only the size of the increase in current, and can potentially be related to the properties of the dust layer. It is the superposition of many small steps, near the same threshold, which can produce the steep increase in current, and it is the sum of the increases which leads to the hysteresis of the descending leg.

Masuda[6] has photographed back corona discharges in a point-plane apparatus. In a positive corona mode, isolated patches of back corona are observed in the dust layer, consistent with a composite mechanism II in which different regions have different thresholds.

The validity of back corona mechanisms can also be tested by examing the distribution of current across the plate. A current distribution under a dust layer as a function of horizontal position (Spencer[3]) is presented in Figure 14. The data indicate a much higher current density directly opposite the wire for dirty plates than for clean plates.

Current distribution for the five mechanisms without a resistive dust layer were calculated. With the exception of mechanism IV, there was not a strong tendency to concentrate current opposite the wire as in Spencer's[3] data. Mechanism IV did produce such a current distribution, but the significance of this was uncertain because of the effects of dust resistivity.

A resistive dust layer was then incorporated into the ESP model. The local voltage drop (across the dust layer within one cell) is given by the product of the local current density, dust resistivity, and layer thickness. Because the current density varies from cell to cell, the surface potential across the cells is variable, and calculable tangential electric fields exist at the surface of the dust layer. These fields are used as the boundary conditions for the electric field calculations in the ESP model. The system is iterated to achieve internal consistency. By itself, one might expect the presence of surface charges to tend to equalize the current distribution over the plate, the electric field realigning as the potential difference is reduced directly under the wire (due to the high negative surface charge). We further assume that when the dust breaks down, the voltage drop across the dust in a given cell remains constant at the breakdown value no matter how much current flows. This situation is analogous to the operation of gas breakdown devices (i.e. neon lamps).

Using these assumptions, we have obtained current distributions such as those presented in Figure 15. These behave qualitatively like the experimental curves, with the higher resistivity material showing a broader area in back corona at the point of initiation. The calculated V-I curves for these two cases are shown in Figure 16. These were obtained by using very small current density increments to pick out the step structure of the curves, and are not composite curves as in Figure 13. The calculated E^2Q curves are shown together in Figure 17.

6.0 CONCLUSIONS

A computer model has been developed which is capable of successfully simulating some aspects of back corona in electrostatic precipitators. Five simple mechanisms for the generation of back corona were examined. By comparing the calculated V-I curves with experimental curves, one particular mechanism was singled out for further study. Incorporation of the effects of dust layer resistivity and interstitial gas breakdown produced current distribution and V-I curves in good qualitative agreement with experimental measurements. The effect of back corona on particle collection was estimated for each mechanism, and the general trend observed is that collection is continuously degraded as back corona increases.

The computer model has proven to be a versatile calculation tool for diagnosing conditions inside a precipitator and will continue to be of value in further investigations.

7.0 ACKNOWLEDGMENT

This work was supported by EPA's Industrial Envrionmental Research Laboratory (Research Triangle Park, N.C.) under Grant No. R80-58-9701. J.H. Turner is the grant administrator.

8.0 REFERENCES

1. Oglesby, S. Jr. and G.B. Nichols. Electrostatic Precipitation. New York, Marcel Dekker, 1978.

2. White, H.J. Industrial Electrostatic Precipitation. Reading, Mass., Addison-Wesley, 1963.

3. Spencer, H.W. III. "Electrostatic Precipitators: Relationship Between Resistivity, Particle Size, and Sparkover." EPA-600/2-76-144 (1976). NTIS No. PB 257-130, May 1976.

4. White, H.J. J. Air Poll. Cont. Assn. 24, 314 (1974).

5. Penney, G.W. and R.E. Matick. Trans. Am. Inst. Elec. Engr. 1 79, 91, (1960).

6. Masuda, S. Inst. Phys. Conf. Ser. No. 27, Ch.3 (1975).

7. Masuda, S. and A. Miquno. Proc. 4th Intl. Clean Air Conf., Paper No. V-47, Tokyo, May 1977.

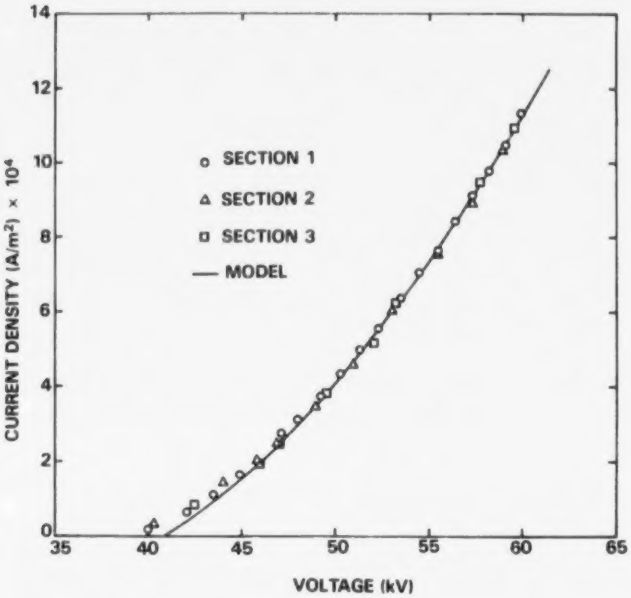

Figure 1. Agreement between a model calculation and an experimental VI curve.

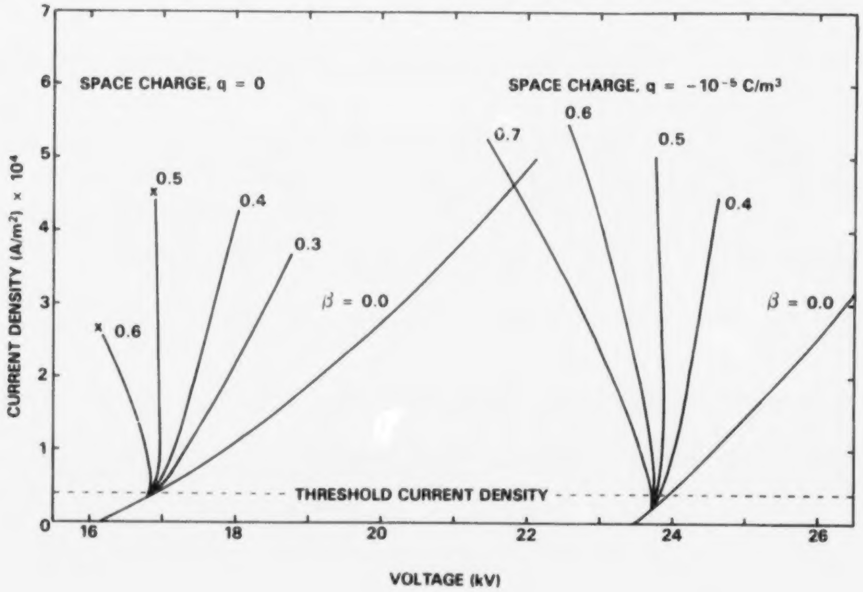

Figure 2. Voltage-current density curves for mechanism I.

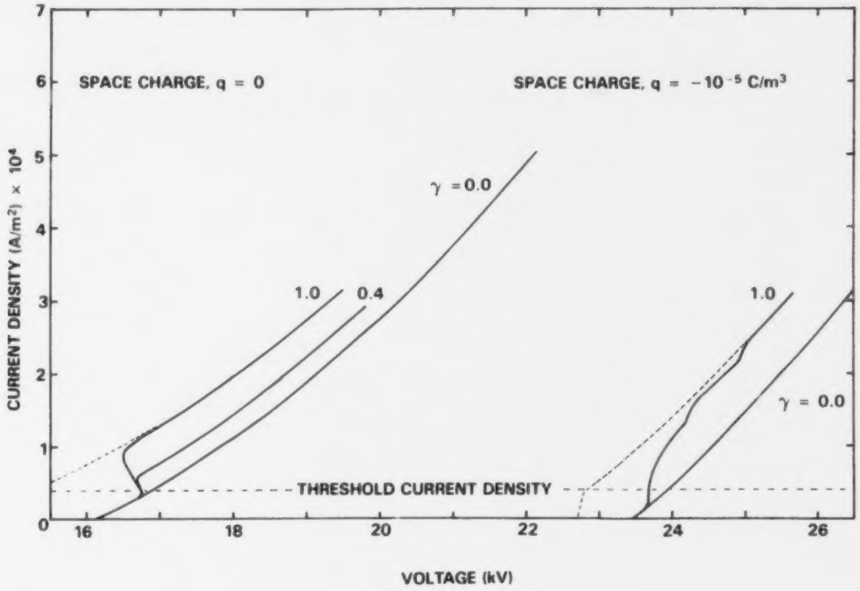

Figure 3. Voltage-current density curves for mechanism II. Hysteresis is indicated by dashed line.

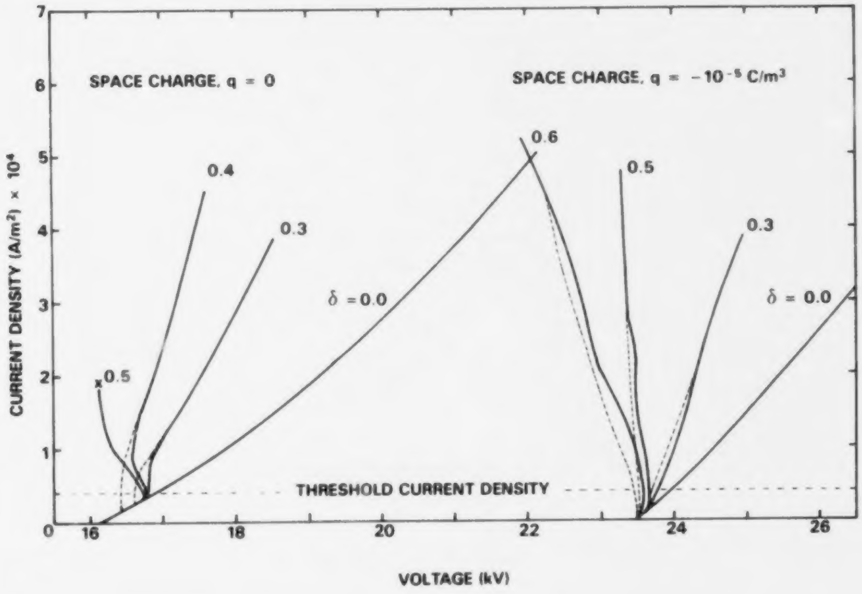

Figure 4. Voltage-current density curves for mechanism III. Hysteresis is indicated by dashed line.

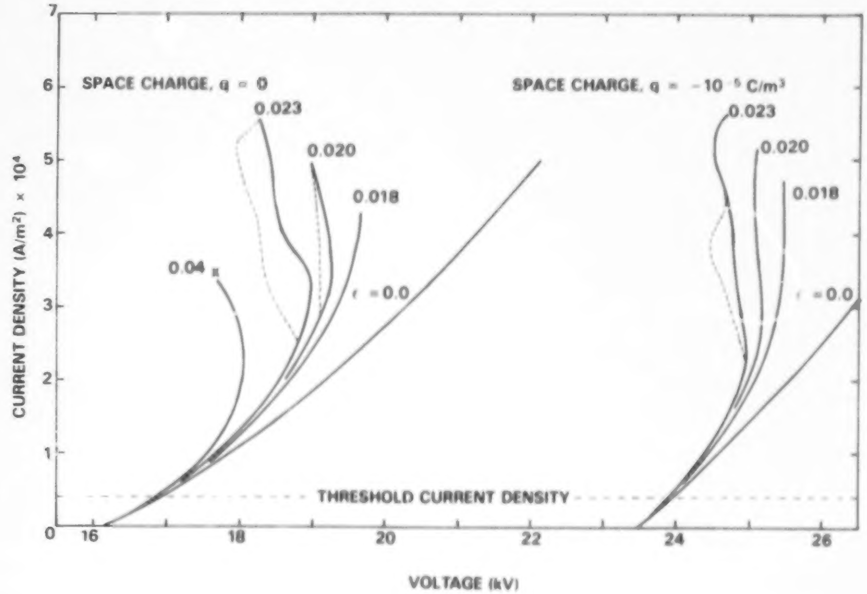

Figure 5. Voltage-current density curve for mechanism IV. Hysteresis is indicated by dashed line.

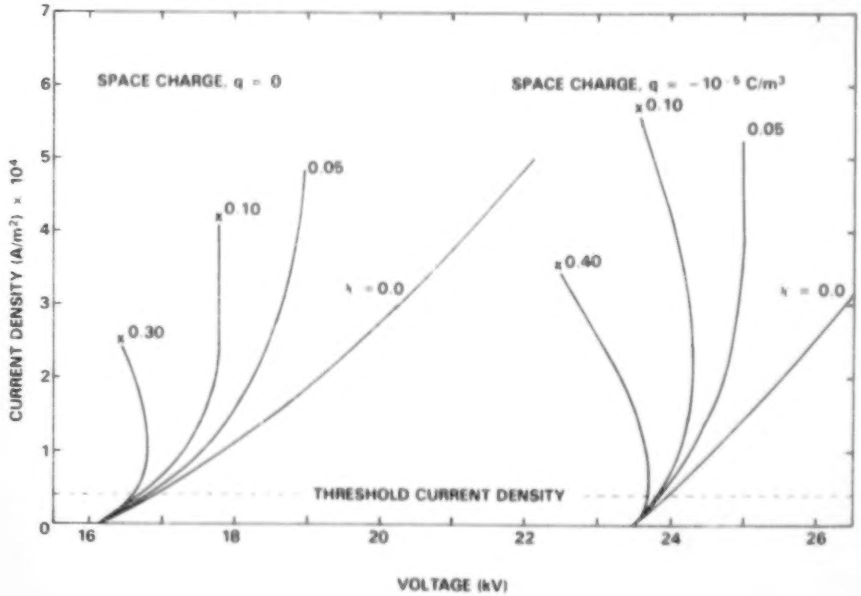

Figure 6. Voltage-current density curve for mechanism V.

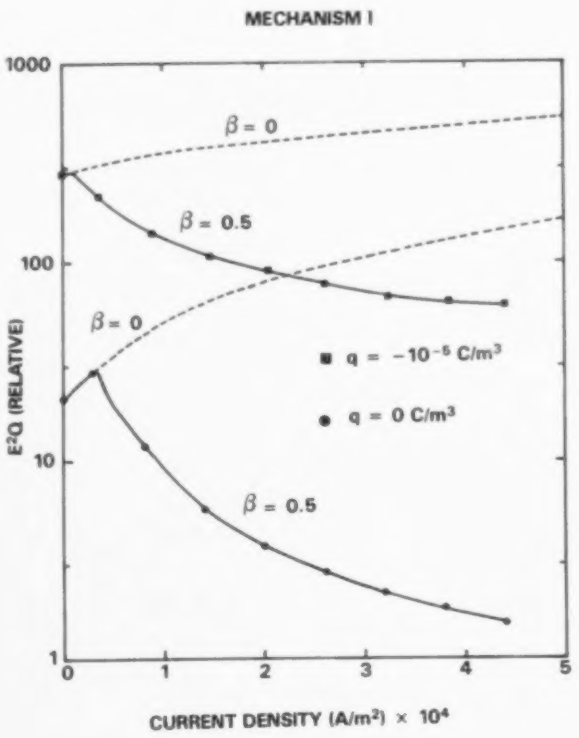

Figure 7. E^2Q as a function of current density for mechanism I.

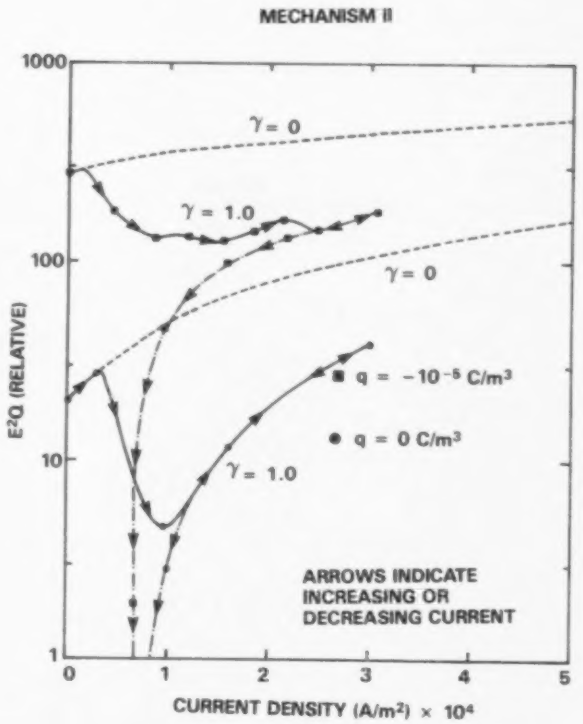

Figure 8. E^2Q as a function of current density for mechanism II.

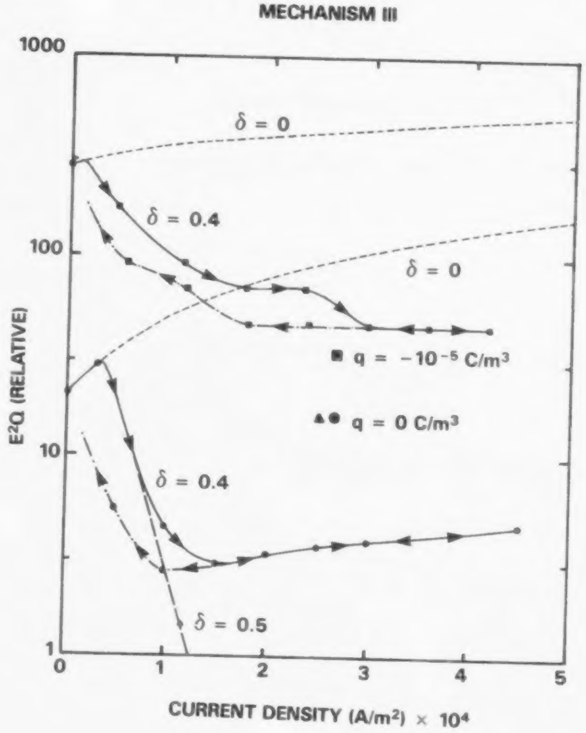

Figure 9. E^{2}Q as a function of current density for mechanism III.

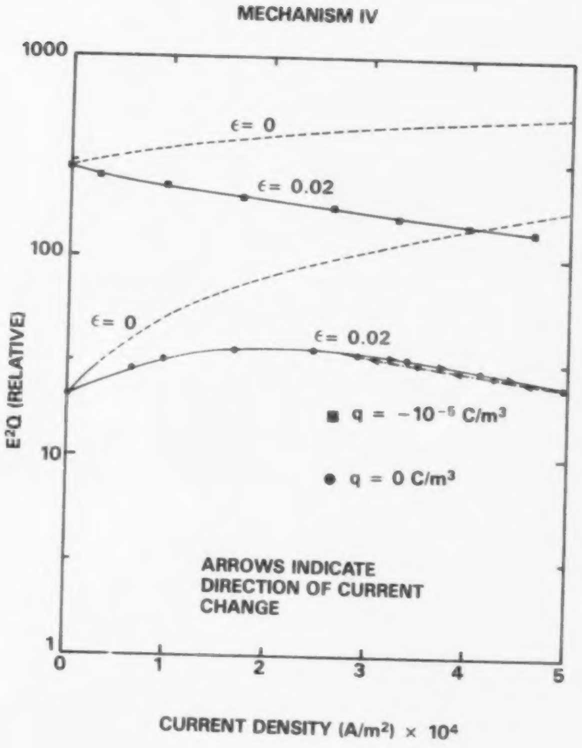

Figure 10. E^{2}Q as a function of current density for mechanism IV.

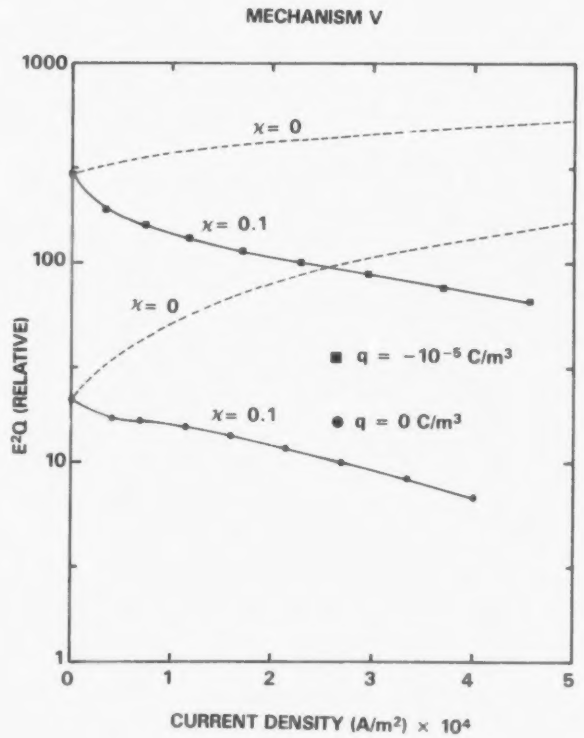

Figure 11. E^2Q as a function of current density for mechanism V.

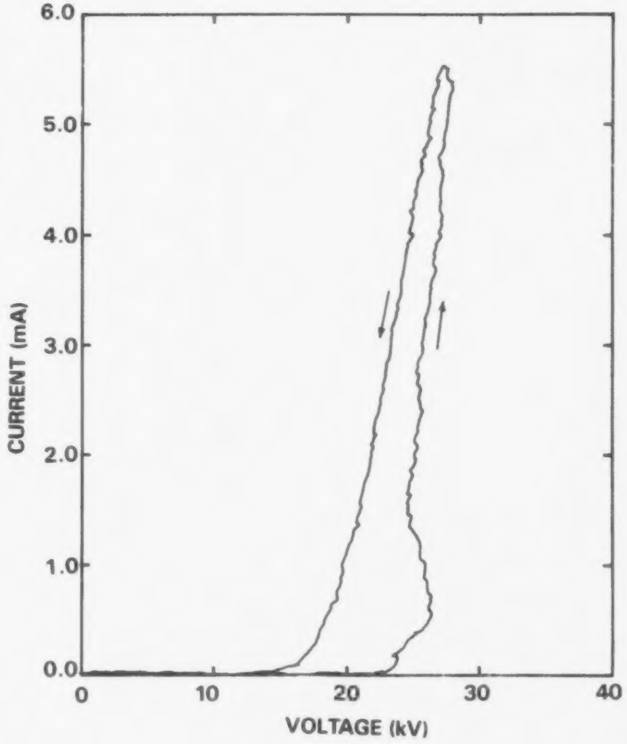

Figure 12. Voltage-current curve for an ESP section in back-corona.

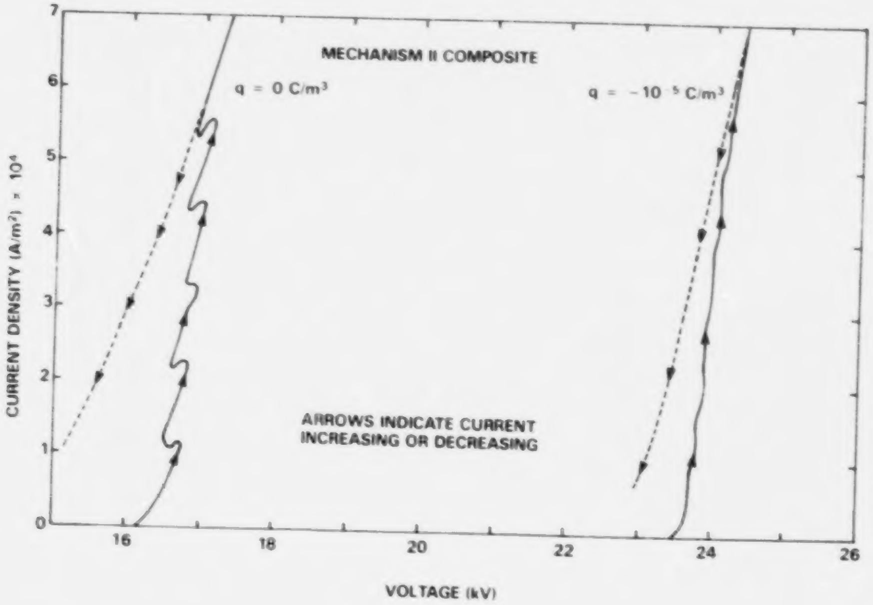

Figure 13. Voltage-current density curves with hysteresis for a composite mechanism II.

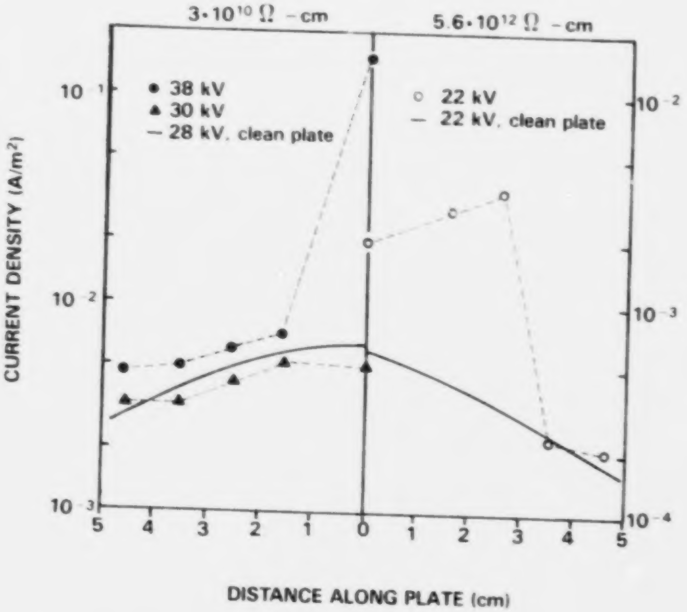

Figure 14. Current density distributions under a dust layer in a wire-plane geometry for two dust resistivities.

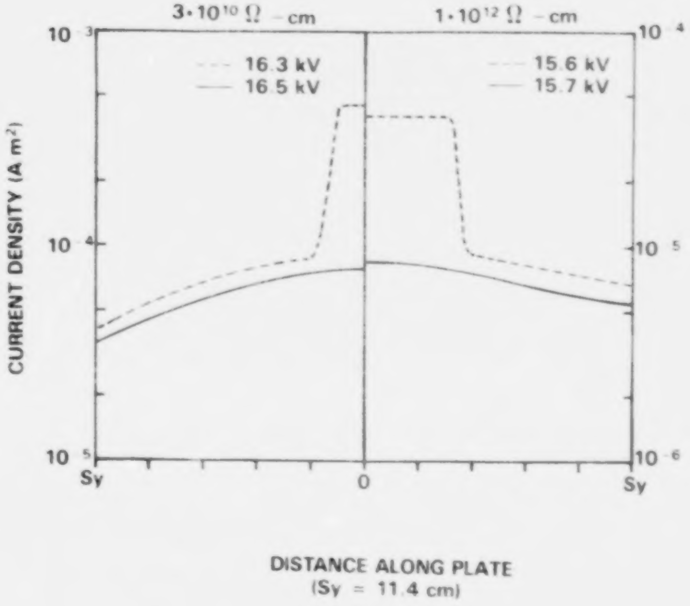

Figure 15. Calculated current density distributions with resistive dust layer incorporated in model (two resistivities). (j_{th} = 1.10^{-4} A/m^2, left; j_{th} = 1.10^{-5} A/m^2, right)

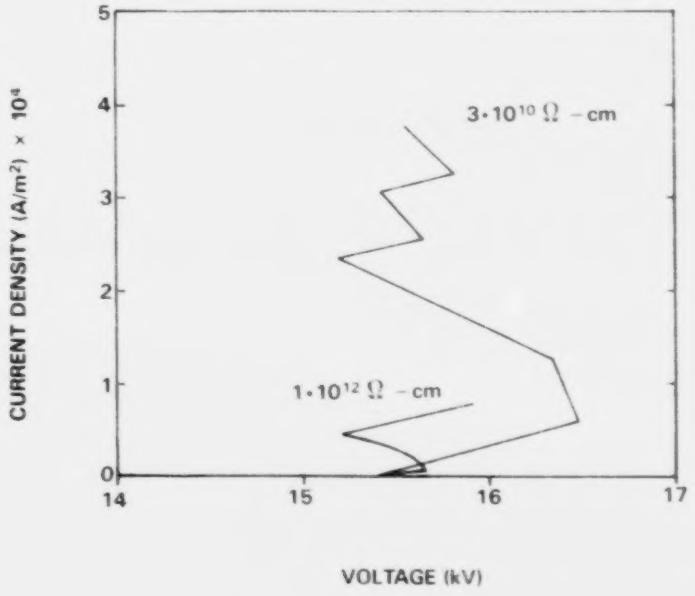

Figure 16. Calculated V-I curves for two resistive dusts.

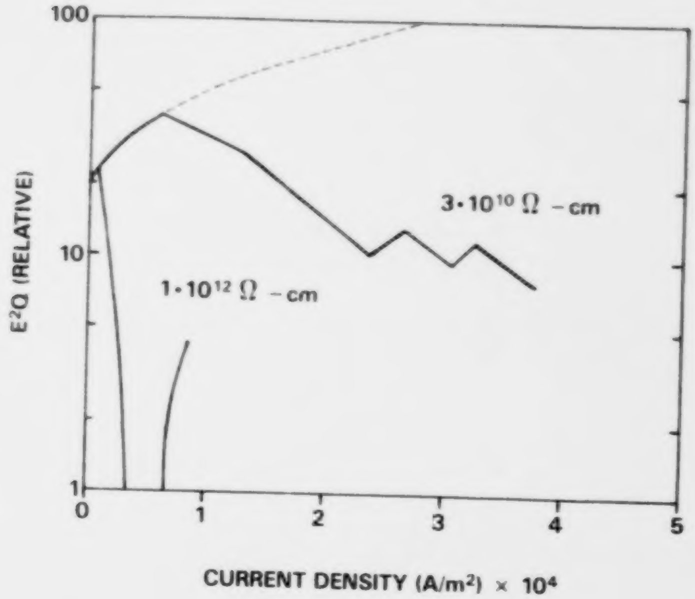

Figure 17. Calculated E^2Q as a function of current density for model incorporating resistive dust layer (two resistivities).

CHARGE MEASUREMENTS ON INDIVIDUAL PARTICLES EXITING LABORATORY PRECIPITATORS

Jack R. McDonald
Marlin H. Anderson
Ronald B. Mosley
Southern Research Institute
2000 Ninth Avenue South
Birmingham, Alabama 35205

and

Leslie E. Sparks
Industrial Environmental Research Laboratory
U.S. Environmental Protection Agency
Research Triangle Park, North Carolina 27711

ABSTRACT

The values of charge on individual particles exiting three different laboratory precipitators have been measured in an experimental apparatus which utilizes a Millikan cell. Measurements were obtained for dioctylphthalate (DOP) droplets and fly ash particles at temperatures from 23 to 343°C. At comparable voltages and currents for positive and negative corona, the data show that the ratio of the values of negative to positive charge for diameters in the range 1.2-2.6 µm increases from a value of approximately 1 to a value of approximately 2 as the temperature increases from 37 to 343°C. The predictions of a mathematical model of electrostatic precipitation which employs an ionic charging theory show good agreement with all the positive charging data but only show good agreement with the negative charging data at the lower temperatures. The data and model predictions are consistent with the postulation of free electron charging at elevated temperatures with negative corona.

INTRODUCTION

In the electrostatic precipitation process, particles suspended in a moving gas stream are charged as the gas is passed through a corona discharge. The particles are charged due to collisions with molecular ions and, possibly, free (unattached) electrons in the case of negative corona discharge. Since the force which drives a charged particle to a collection electrode is proportional to the charge on the particle, the mechanisms involved in the particle charging process and the attainable values of particle charge under various operating conditions are of fundamental importance with respect to understanding and utilizing the electrostatic precipitation process.

In the positive corona discharge, the electrons created in the avalanche process near the discharge electrode migrate to the discharge electrode leaving behind positive molecular ions which migrate into the interelectrode space toward the collection electrode. In this case, the interelectrode space, excluding the relatively small region near the discharge electrode where active gas breakdown occurs, consists of neutral gas molecules and positive molecular ions. Therefore, for the positive corona case, only positive ions may participate in the particle charging process.

In the negative corona discharge, the electrons created in the avalanche process near the discharge electrode migrate into the interelectrode space toward the collection electrode and attach in a probabilistic manner to neutral electronegative gas molecules to form negative ions. The positive ions formed in the avalanche process migrate to the discharge electrode. In this case, the interelectrode space, excluding the relatively small region near the discharge electrode where active gas breakdown occurs, consists of neutral gas molecules, negative molecular ions, and, possibly, free electrons. Therefore, there is the potential for both negative ions and free electrons to participate in the particle charging process.

Evidence and conjecture of the presence of free electron charging has been documented in the literature for laboratory charging experiments with small-scale charging devices at room temperature.[1,2] The mechanism by which free electrons charge particles could be quite different than that for ionic charging. Intuitively, the extent of free electron charging should depend on the electrode geometry (especially the spacing between the discharge and collection electrodes), applied voltage, gas temperature, and gas pressure. At the present, the mechanisms by which electrons would charge particles have not been described theoretically, and no experimental data are available that truly isolate electron charging from ionic charging. In applying fundamental principles to full-scale precipitators, effects due to free electrons are generally neglected.

The purposes of the work presented here were to develop a technique for measuring the charge and diameter of individual particles in an electrostatic precipitator and to make charge and diameter measurements in a typical full-scale, electrode geometry at various temperatures up to that which is typical in a hot-side precipitator. The values of charge and diameter of individual particles exiting three different laboratory precipitators have been measured with an experimental apparatus which utilizes a Millikan cell. Measurements were obtained for dioctylphthalate (DOP) droplets and redispered fly ash particles at temperatures from 23 to 343°C at various typical voltages and current densities.

It was anticipated that by making the above measurements some questions of importance could be answered. First, how well do existing ionic charging theories predict particle charge when applied to particles carried in a turbulent gas stream through a typical precipitator electrode geometry? The utilization of these theories is complicated due to the existence of a nonuniform electric field and current density and possible residence time phenomena due to the turbulent nature of the gas stream. Second, how do positive and negative corona compare in potential effectiveness for charging particles? Higher voltages and currents before sparkover may result with one type of corona discharge and may lead to significantly higher values of particle charge. The possibility of different charging mechanisms in the cases of positive and negative corona may result in significantly different values of particle charge under similar operating conditions. Third, do free electrons in the case of negative corona significantly enhance particle charging at higher temperatures (and/or reduced pressures)? Recent field data from a hot-side precipitator collecting fly ash indicate enhanced collection efficiencies for particles with diameters between 1.0 and 3.0 µm.[3] These collection efficiencies were predicted by using the measured operating voltages and current densities in conjunction with an ionic charging theory and were significantly lower than those measured. In this case, free electron charging may have been prominent in the electrostatic precipitation process.

MEASUREMENT TECHNIQUE AND APPARATUS

The technique utilized for simultaneously determining the charge and diameter of a particle is based on the downward and upward motion of a charged particle in an insulating gas under the influence of a uniform, reversible electric field. When the gravitational force and the force due to the electric field act on the charged particle in the same direction, then the charged particle will experience a net downward force given by

$$\begin{aligned} F_D = ma_D &= -qE - mg + F_d \\ &= -qE - (\rho_p - \rho_a)(\tfrac{4}{3}\pi a^3)\,g + (6\pi\eta a v_D)/(1 + A\ell/a), \qquad (1) \end{aligned}$$

where

F_D = net downward force (nt),
m = mass of the particle (kg),
a_D = downward acceleration (m/sec^2),
q = charge on the particle (C),
E = electric field (V/m),
g = acceleration due to gravity (m/sec^2),
F_d = drag force acting on the particle (nt),
ρ_p = density of the particle (kg/m^3),
ρ_a = density of the gaseous medium (kg/m^3),
a = particle radius (m),
η = viscosity of the gaseous medium (nt-sec/m^2),
v_D = downward velocity of the particle (m/sec),
$(1+A\ell/a)$ = Cunningham correction factor,
ℓ = molecular mean free path (m), and
$A = 1.257 + 0.400 \exp(-1.10\ a/\ell)$.

Similarly, the force acting on the charged particle due to the electric field can be made opposite to that of the gravitational force in such a manner that the charged particle will experience a net upward force given by

$$F_u = ma_u = qE - mg - F_d$$

$$= qE - (\rho_p - \rho_a)(\tfrac{4}{3}\pi a^3)\ g - (6\pi\eta a v_u)/(1 + A\ell/a), \qquad (2)$$

where

F_u = net upward force (nt),
a_u = upward acceleration (m/sec^2),
v_u = upward velocity of the particle (m/sec),
and all other symbols are as previously defined.

Assuming that the terminal velocity of the particle is reached instantaneously, then $a_u = a_D = 0$ and

$$v_D = S/t_D \qquad (3)$$

and

$$v_u = S/t_u\ , \qquad (4)$$

where

S = distance over which the particle moves (m),
t_D = time to fall the distance S (sec), and
t_u = time to rise the distance S (sec).

Adding equations (1) and (2) yields

$$-(\tfrac{8}{3}\pi a^3)(\rho_p - \rho_a)\quad g + [(6\pi\eta aS)/(1 + A\ell/a)]\ (\frac{1}{t_D} - \frac{1}{t_u}) = 0. \qquad (5)$$

Subtracting equations (1) and (2) yields

$$-\ 2\ qE + [(6\pi\eta aS)/(1 + A\ell/a)]\ (\frac{1}{t_D} + \frac{1}{t_u}) = 0. \qquad (6)$$

Equations (5) and (6) can be solved simultaneously to obtain expressions for a and q.

Equation (5) can be rewritten in the form

$$a^2 + (A\ell)a + \frac{9\eta S}{4(\rho_p - \rho_a)\ g}\ (\frac{1}{t_u} - \frac{1}{t_D}) = 0. \qquad (7)$$

Solving for a yields

$$a = \frac{-A\ell + \sqrt{A^2\ell^2 - \frac{9\eta S}{(\rho_p - \rho_a)g} \left(\frac{1}{t_u} - \frac{1}{t_D}\right)}}{2} . \tag{8}$$

Solving equation (6) for q yields

$$q = \frac{D}{V} \left[(3\pi\eta a S)/(1 + A\ell/a)\right] \left(\frac{1}{t_D} + \frac{1}{t_u}\right) , \tag{9}$$

where

$E = V/D$,
V = voltage applied across two parallel plates (V), and
D = spacing between the parallel plates (m).

A technique and apparatus have been developed for measuring the diameter and charge on individual particles which have been treated in an electrostatic precipitator. The technique consists of extracting a sample gas volume from the precipitator and directing part of this extracted sample into a modified Millikan measurement cell. A single particle can then be isolated, and its upward and downward motion under the influence of a uniform electric field can be utilized to determine its diameter and charge from equations (8) and (9).

A drawing of the measurement apparatus with its insertion into a precipitator is shown in Figure 1. The gas sample is extracted through 2-inch diameter tubing. The tubing can be made of teflon or metal as dictated by the temperature in the gas stream with equivalent results. This tubing contains two bends and is electrically grounded through a spiral wire which runs along the inner surface of the tubing. The tubing runs upward from the measurement cell and makes a right angle bend so that the tubing can enter a sampling port. The second bend in the tubing is made so that the tubing will be oriented opposite to the direction of the gas flow and so that the entrance to the tubing can be located inside the electrified regions although the port is located downstream from these regions. The tubing leading down to the measurement cell contains a butterfly valve which can be opened to allow a sample of gas to be drawn into the measurement cell and can be closed to prevent the sample from being drawn back into the precipitator which has negative pressure. The closed valve also prevents air flow disturbances during the measurements. Below this valve and below the measurement cell there is a connection to a pump. With the valve open, the pump is operated and particles are drawn into the measurement cell. When a sufficient number of particles are obtained in the measurement cell, the pump is turned off with simultaneous closing of the valve. Once the pump is turned off and the valve is closed, the particles very quickly cease to have any motion due to gas flow. At this point, only the gravitational field, viscous drag, and electric field which can be imposed across the parallel plates of the measurement cell have any influence on the motion of the particles.

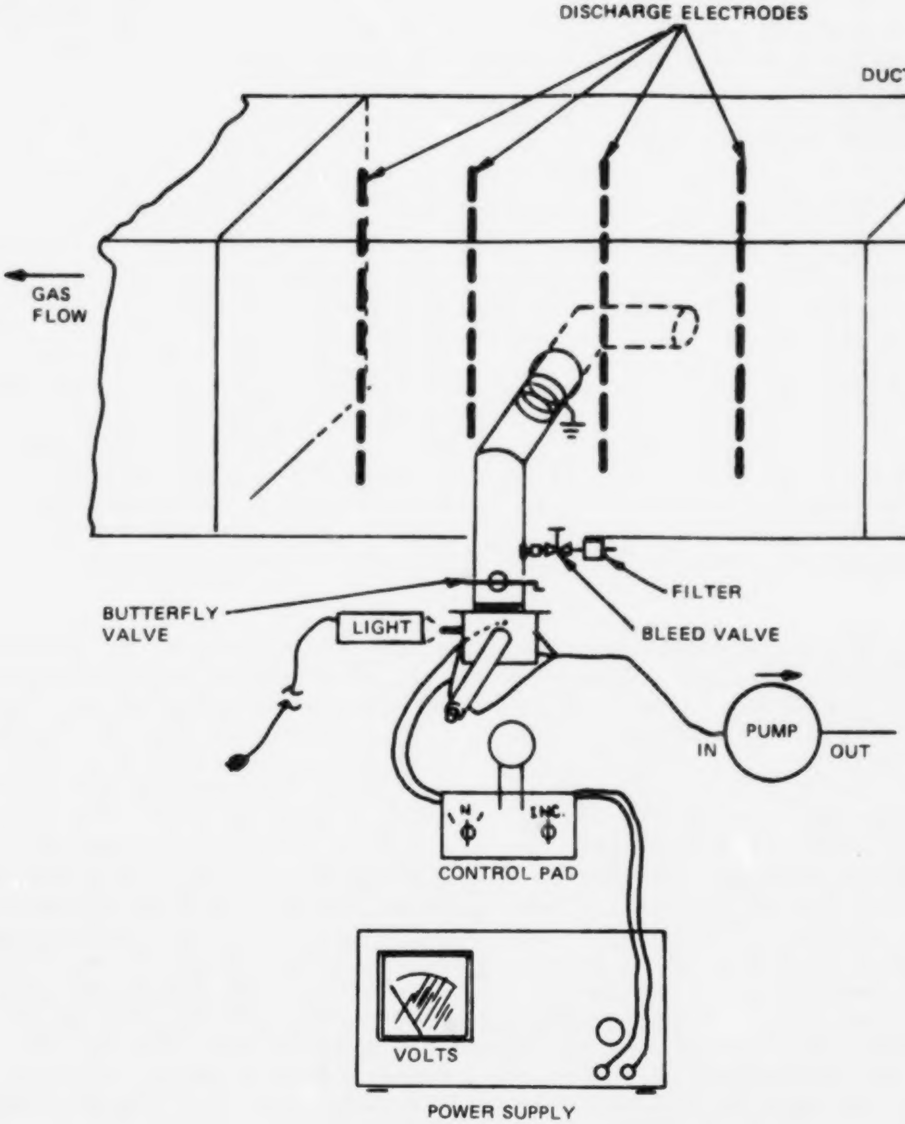

Figure 1. Experimental apparatus for measuring the diameter and charge of particles.

In those cases where the particle concentrations are too large for easy isolation of individual particles, the extracted gas sample can be diluted. Filtered, outside air can be mixed with the extracted sample by means of a bleed valve preceded by a filter.

The Millikan measurement cell is cylindrical in shape with a diameter of 3.8 cm and a plate spacing (or approximate height) of 0.5 cm. Gas enters the cell through a small hole in a conical depression in the top plate. The particles are illuminated by a high intensity microscope lamp and are viewed through a telescope attached to the measurement cell. The distance traveled by the particles is determined by a graticule which is mounted near the focal plane of the objective lens of the telescope. Measurement of the particle transit times was done with a stopwatch. Voltages on the order of 3 to 15 volts were applied across the plates to produce the electric fields necessary to generate the data presented in this paper. The temperature of the gas in the measurement cell was determined by means of a thermocouple.

In the system described here, particles with diameters down to approximately 0.4 μm can be observed. Measurements were concerned primarily with fine particles with diameters approximately between 0.6 μm and 3.0 μm since (1) they are the most difficult to collect in a precipitator, (2) their behavior in a precipitator is the most difficult to model, and (3) their escape into the atmosphere offers the greatest health hazard. Measurements on smaller particles can be readily obtained by allowing the larger particles to settle out. By waiting approximately 3 minutes after a new sample is introduced into the measurement cell, only particles of approximately 1.0 μm or less in diameter will remain in the field of view. Measurements on the larger particles can be readily made by choosing those particles which fall the fastest under the influence of gravity. The measurement system also has the capability of determining the magnitude and sign of the charge on a particle. Thus, the system has the potential to be used to analyze the effects on particle charge of back corona and rapping reentrainment. In addition, particles can be successfully extracted and analyzed from electrified regions at different locations in a precipitator.

EXPERIMENTAL PROGRAM, DATA, AND RESULTS

The first objective of the experimental program was to determine the capability of the technique and apparatus described earlier to make accurate measurements of the diameter and charge of particles treated in an electrostatic precipitator. In order to achieve this objective, measurements were performed under essentially idealized conditions in laboratory precipitator A. This precipitator has one gas passage, four electrical sections which are 0.76 m (2.5 ft) long, plates which are 38.1 cm (15 in.) high, a 25.4 cm (10 in.) plate-to-plate spacing, a 12.7 cm (5 in.) wire-to-wire spacing, and a 0.24 cm (0.094 in.) discharge electrode (wire) diameter. The normalized standard deviation of the gas velocity distribution and the gas sneakage per baffled electrical section were both measured to be less than 10%. For the experiments in laboratory precipitator A, low mass concentrations of dioctylphthalate (DOP) droplets were generated by an aerosol sprayer and were carried through the precipitator by air at ambient conditions. Since (1) the particles were spherical, (2) particle reentrainment could not exist, (3) back corona could not exist, and (4) gas sneakage was minimal, the results of the measurements could be interpreted with little ambiguity.

Measurements were made at precipitator operating conditions consisting of negative corona, an average applied voltage of 44.2 kV, an average current density of 21.5 nA/cm^2 (20.0 μA/ft^2), and a gas velocity of 1.5 m/sec (4.9 ft/sec). The data obtained at the precipitator outlet from the measurements on 486 individual particles are shown graphically in Figure 2 and are tabulated in Table 1. The data on each individual particle were obtained from the average values of three measurements each of the time required for the particle to travel downward a distance of 0.129 cm under the influence of an electric field and of the time required to travel the same distance upward. The bars on the average data points are one standard deviation and are not representative of the error in the measurement technique but, instead, they are more representative of the expected spread in charge on a particle with a given diameter due to the fact that different particles travel different paths through the precipitator and experience different charging electric field strengths and ion densities. Also, particle diameters in a narrow band have been grouped together with a diameter given by the midpoint of the band. The solid curve is a model[4] prediction of charge as a function of particle diameter at the outlet of the precipitator. The model employs an ionic charging theory.[5]

Table 1. MEASURED AND PREDICTED VALUES OF PARTICLE CHARGE AT THE OUTLET OF A LABORATORY PRECIPITATOR

Radius Size Range (10^{-6}m)	No. Part	Mean Charge (C)	Min Charge (C)	Max Charge (C)	Normalized Standard Deviation	Predicted Charge (C)
0.25-0.35	3	1.28×10^{-17}	4.20×10^{-18}	1.82×10^{-17}	0.481	1.61×10^{-17}
0.35-0.45	35	1.98×10^{-17}	5.22×10^{-18}	3.82×10^{-17}	0.270	2.62×10^{-17}
0.45-0.55	57	2.88×10^{-17}	1.96×10^{-17}	6.03×10^{-17}	0.265	3.81×10^{-17}
0.55-0.65	46	4.54×10^{-17}	2.76×10^{-17}	1.17×10^{-16}	0.346	5.16×10^{-17}
0.65-0.75	68	6.71×10^{-17}	3.74×10^{-17}	1.04×10^{-16}	0.234	6.75×10^{-17}
0.75-0.85	80	9.10×10^{-17}	4.16×10^{-17}	1.58×10^{-16}	0.271	8.49×10^{-17}
0.85-0.95	66	1.21×10^{-16}	6.41×10^{-17}	1.87×10^{-16}	0.280	1.05×10^{-16}
0.95-1.05	56	1.43×10^{-16}	6.08×10^{-17}	2.68×10^{-16}	0.330	1.26×10^{-16}
1.05-1.15	42	1.64×10^{-16}	8.09×10^{-17}	2.94×10^{-16}	0.306	1.48×10^{-16}
1.15-1.25	20	1.82×10^{-16}	1.16×10^{-16}	3.17×10^{-16}	0.289	1.75×10^{-16}
1.25-1.35	5	3.32×10^{-16}	2.39×10^{-16}	4.39×10^{-16}	0.237	2.02×10^{-16}
1.35-1.45	6	2.61×10^{-16}	1.48×10^{-16}	4.93×10^{-16}	0.438	2.31×10^{-16}
1.45-1.55	2	4.30×10^{-16}	3.95×10^{-16}	4.59×10^{-16}	0.748	2.61×10^{-16}

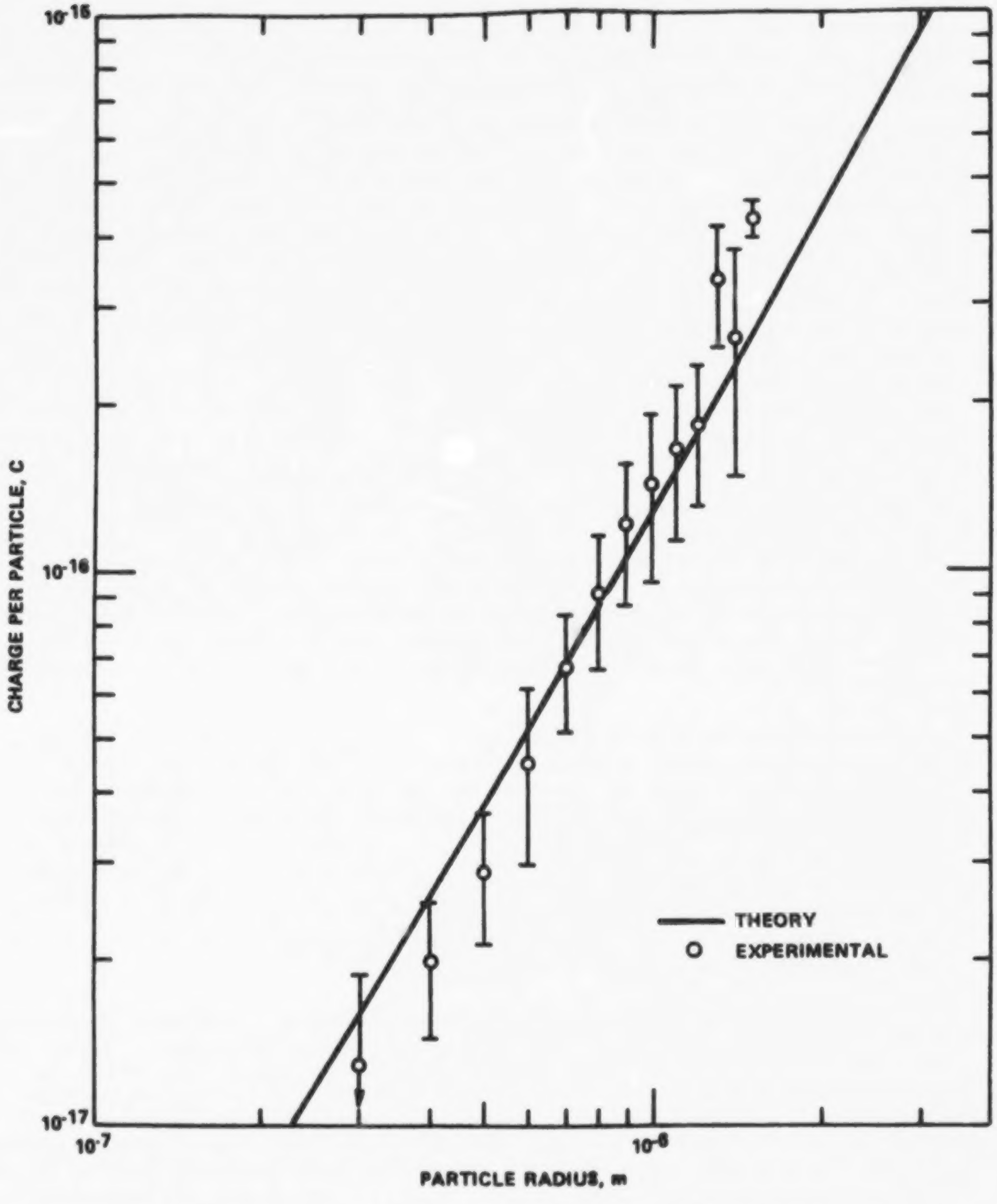

Figure 2. Theoretical and measured particle charge as a function of particle radius at the outlet of laboratory precipitator A at ambient temperature.

In a wire-plate geometry, the electric field does not vary significantly over a major portion of the interelectrode space and it varies rapidly only over a small high field region near the discharge electrode.[6] Thus, one would expect that the majority of the particles of a given diameter exiting the precipitator would have essentially the same charge but there would be a spread in charge lying in a range determined by the minimum and maximum values of the electric field. These expectations are evidenced in the data in that the normalized standard deviations are small. One might also expect that a certain percentage (possibly 5-10%) of the smaller particles (less than 1 μm in diameter) would pass through high electric field regions near the discharge electrodes and would acquire charges which are significantly higher than those predicted by the average electric field used in the model. Although values of the electric field in the high field region should be up to 8.5 times the average value of electric field used in the model, the ratios of measured charge to predicted charge did not exceed a value of 2.8. It was also observed that, while it was relatively easy to find particle charges significantly larger than that predicted by the model for diameters greater than approximately 1.5 μm, very few particles were found to have a significantly higher charge than predicted by the model for diameters less than approximately 1.5 μm. In fact, in the diameter range between 0.5 and 1.7 μm, only 1 particle out of 289 measured had a charge which was over a factor of 1.6 times the predicted charge. In addition many samples were observed in which the particles larger than 1.0 μm in diameter were allowed to settle out in order to determine if highly charged submicron particles were present. In all these samples, the remaining particles all moved with essentially the same velocity in an applied electric field. Thus, they all had approximately the same value of charge. Measurements made on gas samples taken from the middle of the inlet electrical section also produced the same results.

The limited data shown in Figure 2 and Table 1 indicate that the measurement technique is quite reliable and that the model predictions are in quite good agreement with the average measured value of particle charge. The higher theoretical predictions for particle diameters less than 0.6 μm are inherent in the approximate theory at the values of electric field which were utilized in the experiment. The use of an average electric field determined by dividing the applied voltage by the wire-to-plate spacing and of a particle residence time determined by dividing the precipitator length by the average gas velocity appears to be adequate for predicting particle charge. Also, an ionic charging theory appears to be adequate for describing the data.

The second objective of the experimental program was to make charge and diameter measurements in a typical full-scale, electrode geometry under both positive and negative corona at various temperatures up to that which is typical in a hot-side precipitator. In these experiments, the gas stream entering the precipitator was laboratory air containing low resistivity, redispersed fly ash particles. In principle, although sparkover may occur at a different applied voltage for positive corona than for negative corona in laboratory air at atmospheric pressure near sea level, the clean air, clean plate, voltage-current curves for the two cases should be nearly the same up to sparkover for typical full-scale plate spacings since the starting voltages and effective ion mobilities do not differ appreciably. Thus, for low mass loadings of low resistivity fly ash particles, comparisons of particle charging capabilities of positive and negative corona might be made where essentially the same applied voltages and currents are utilized in both cases. Any significant differences in particle charging capabilities under these conditions would indicate different charging mechanisms for the different types of corona.

At higher temperatures (and/or reduced pressures), the mean-free-paths of ions and electrons increase. Thus, in the case of negative corona, free electrons can penetrate further into the interelectrode space and possibly can have an increased effect on voltage-current characteristics and particle charging. Comparison of voltage-current characteristics and particle charging for both positive and negative corona at higher temperatures should provide further insight into the effect, if any, of free electrons. If significant penetration of free electrons occurs in the interelectrode space, this might be evidenced in a larger difference in positive and negative voltage-current characteristics than would be obtained if only ions carried the current. However, even if differences in voltage-current characteristics can not be firmly established, differences in particle charging capabilities may still exist.

The effect of temperature on particle charging was examined in laboratory precipitators B and C. Precipitator B has one gas passage, four electrical sections which are 91.4 cm (36 in.) long, plates which are 91.4 cm (36 in.) high, a 25.4 cm (10 in.) plate-to-plate spacing, a 22.9 cm (9 in.) wire-to-wire spacing, a 0.32 cm (0.125 in.) discharge electrode (wire) diameter. Precipitator C has one gas passage, four electrical sections which are 1.22 m (4 ft) long, plates which are 1.22 m (4 ft) high, a 25.4 cm (10 in.) plate-to-plate spacing, a 22.9 cm (9 in.) wire-to-wire spacing and a 0.32 cm (0.125 in.) discharge electrode (wire) diameter. Measurements at 38°C (100°F) were performed at the outlet of precipitator B, while measurements at 148°C (300°F), 232°C (450°F), and 343°C (650°F) were performed at the outlet of precipitator C.

Figures 3-5 show typical real time voltage-current traces obtained from precipitator C for clean air, wires, and plates at three different temperatures. All these curves were obtained sequentially over a relatively short time period. Under these conditions and with good electrode alignment, it can be seen that voltage-current curves which are nearly coincident are obtainable. Figures 6-8 show some typical average voltage-current curves obtained when the air stream contained fly ash particles and when the wires and plates were somewhat dirty. The data in Figure 6 represent an average over precipitator B. The data in Figures 7 and 8 were obtained from precipitator C with curves from all the electrical sections shown in Figure 7 and an average over the entire precipitator shown in Figure 8. All data with particles in the air stream obtained at 343°C (650°F) from precipitator C were acquired approximately 4 months prior to that at 148°C (300°F) and 232°C (450°F). During the later measurement period, the precipitator was not operating as well as before, and the voltage-current curves with particles for positive and negative corona were widely separated. Since the inlet mass loading was nominally on the order of 1.14 g/m^3 (0.5 gr/acf) and the particle size distribution was rather large, the effect of particles on the voltage-current curves could not be attributed entirely to a particulate space charge effect. The observed behavior of the voltage-current curves might have been due to deposits of a high resistivity ash on the wires and plates acquired during other experiments performed just prior to these measurements. In any event, it was often observed that the addition of particles

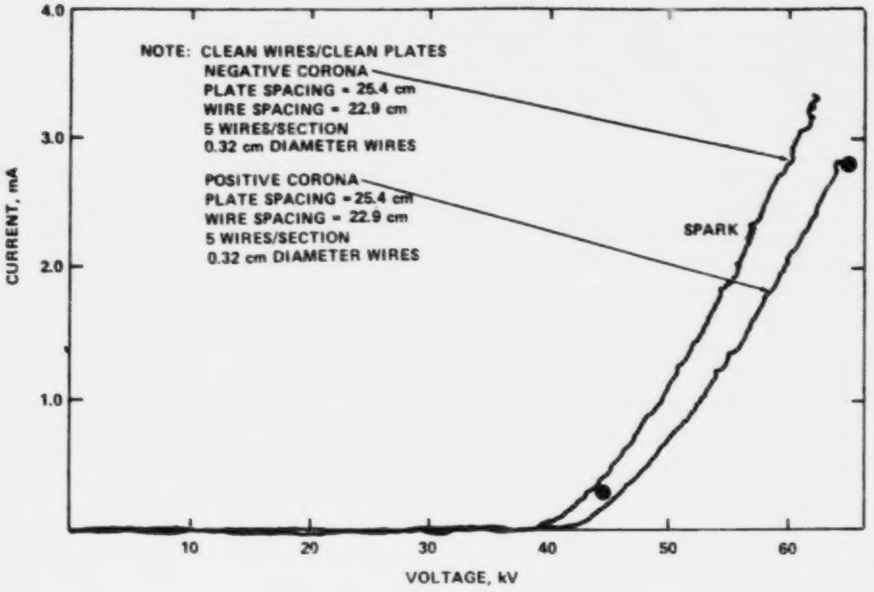

Figure 3. Clean air, wire, and plate voltage-current curves for precipitator C at ambient temperature.

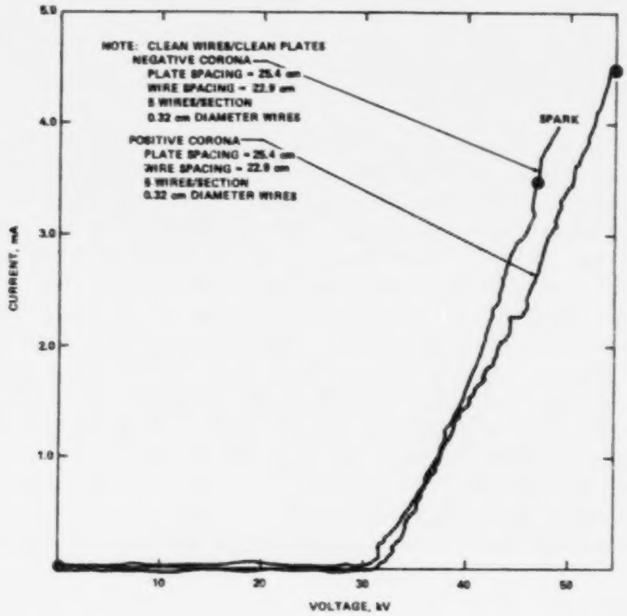

Figure 4. Clean air, wire, and plate voltage-current curves for precipitator C at 148°C (300°F).

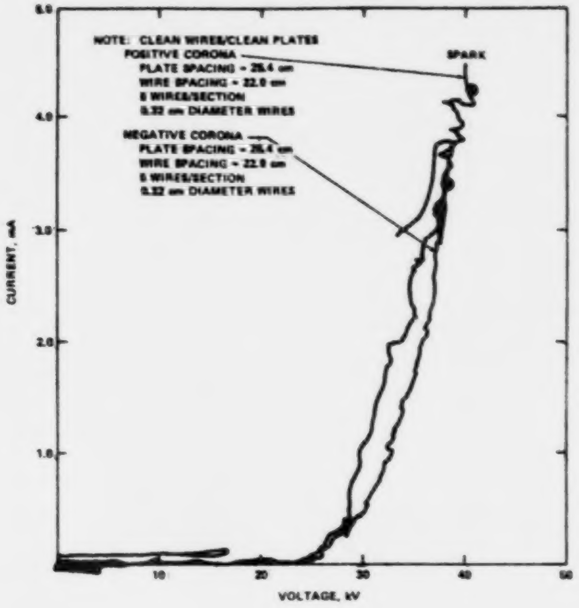

Figure 5. Clean air, wire, and plate voltage-current curves for precipitator C at 343°C (650°F).

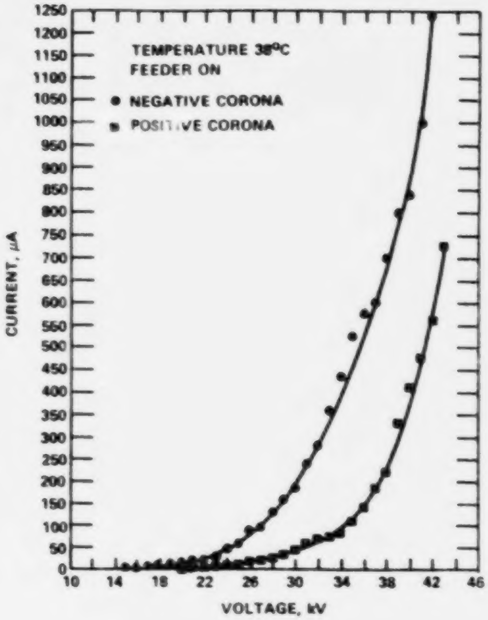

Figure 6. Average voltage-current curves with particles for precipitator B at 38°C (100°F).

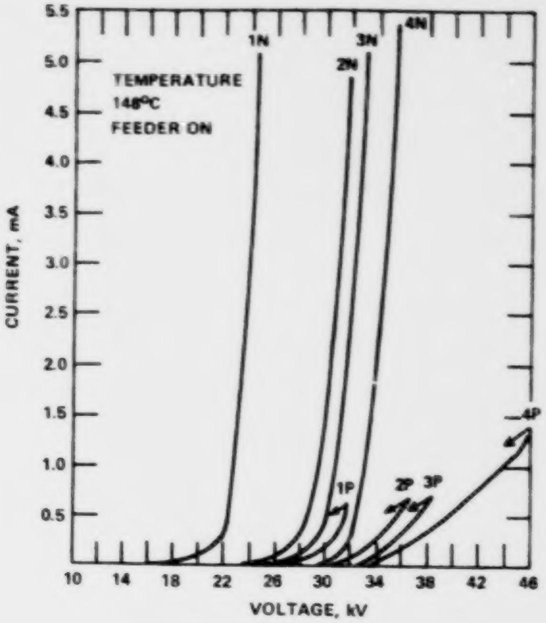

Figure 7. Voltage-current curves for the different electrical sections with particles for precipitator C at 148°C (300°F).

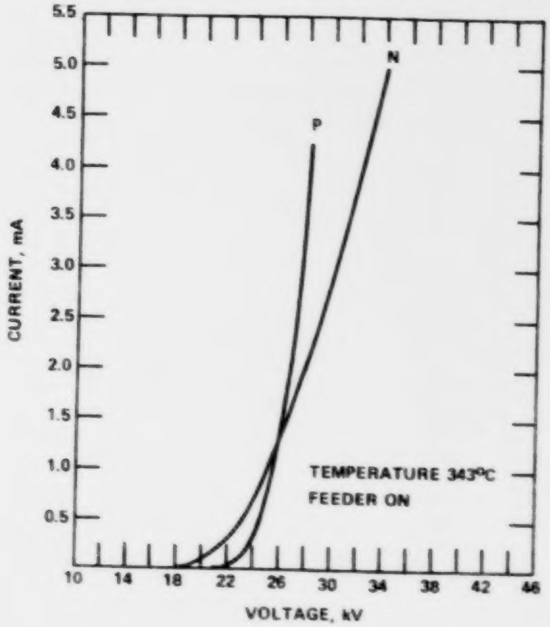

Figure 8. Average voltage-current curves with particles for precipitator C at 343°C (650°F).

caused the positive and negative voltage-current curves to separate to a larger extent than anticipated.

Figures 9-11 show particle diameter and charge measurements made at the outlet of precipitator B at 38°C (100°F) with an average gas velocity of approximately 1.5 m/sec (5.0 ft/sec). Model predictions for the different conditions are also shown for comparison with the data. The data in Figure 9 were obtained with a constant average current density of 15 nA/cm^2 (13.9 µA/ft^2) and average applied voltages for positive and negative corona of 38.0 kV and 34.5 kV, respectively. The data in Figure 10 were obtained with a constant average applied voltage of 35.0 kV and average current densities for positive and negative corona of 9 nA/cm^2 (8.4 µA/ft^2) and 15 nA/cm^2 (13.9 µA/ft^2), respectively. The data in Figure 11 were obtained for negative corona only at average applied voltages of 34.5 kV and 38.0 kV, corresponding to average current densities of 15 nA/cm^2 (13.9 µA/ft^2) and 36 nA/cm^2 (33.4 µA/ft^2), respectively. For all the data at 38°C (100°F), the theory and data show good agreement. Since the least amount of data was acquired for the smallest and largest diameter bands, the agreement with theory should be expected to be less for these particle diameters.

Figure 12 shows particle diameter and charge measurements made at the outlet of precipitator C at 148°C (300°F) with an average gas velocity of approximately 1.4 m/sec (4.5 ft/sec). The average applied voltage and current density for negative corona were 25.7 kV and 31.0 nA/cm^2 (28.8 µA/ft^2), respectively. The average applied voltage and current density for positive corona were 33.0 kV and 18.0 nA/cm^2 (16.7 µA/ft^2), respectively. During measurements with both positive and negative corona, it was difficult to maintain constant electrical operating conditions. Wide fluctuations in applied voltage and current occurred with intermittent sparking. Thus, these data are not useful for comparing positive and negative particle charging under comparable conditions. However, the data give an illustration of the capability of the measurement system to detect adverse charging conditions.

Figure 13 shows particle diameter and charge measurements made at the outlet of precipitator C at 232°C (450°F) with an average gas velocity of approximately 1.4 m/sec (4.5 ft/sec). The average applied voltage and current density for negative corona were 28.1 kV and 28.0 nA/cm^2 (26.0 µA/ft^2), respectively. The average applied voltage and current density for positive corona were 31.5 kV and 17 nA/cm^2 (15.8 µA/ft^2), respectively. After the measurements at 148°C (300°F), the wires and plates of the precipitator were cleaned by brushing. This resulted in more favorable and stable electrical operating conditions. For the operating conditions during the measurements, the theory predicts essentially the same charge versus diameter relationship for the positive and negative corona conditions. While the theory agrees well with the data obtained with positive corona for all particle diameters, it clearly underpredicts particle charge for diameters between approximately 1.4 µm and 2.4 µm. In this diameter range, the ratio of the average measured charge to the predicted charge ranges from 1.25 to 1.59, increasing with increasing diameter. These data indicate that negative corona is more effective than positive corona in charging particles with diameters between 1.4 µm and 2.4 µm at 232°C (450°F). Comparison of these data with the theoretical predictions and the information in Figures 2-5 suggests that the use of a completely ionic charging theory to describe negative particle charging at 232°C (450°F) is inadequate. Since the only major

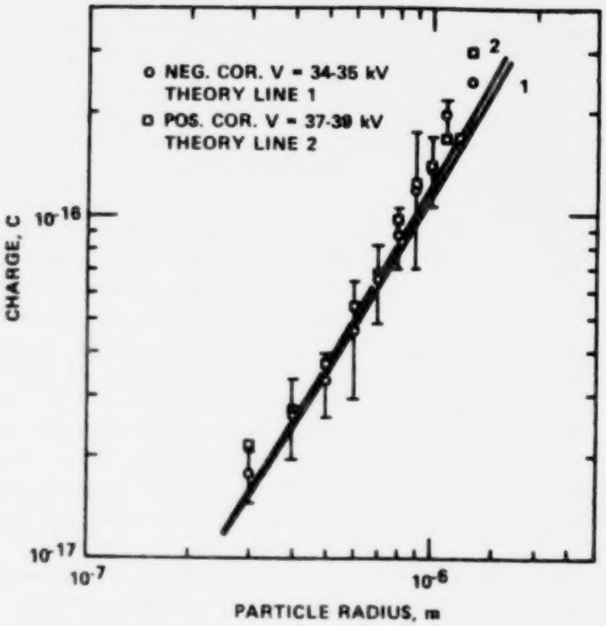

Figure 9. Measured positive and negative particle charge versus measured radius and comparison with theory at 38°C (100°F) and 15 nA/cm^2 (13.9 µA/ft^2).

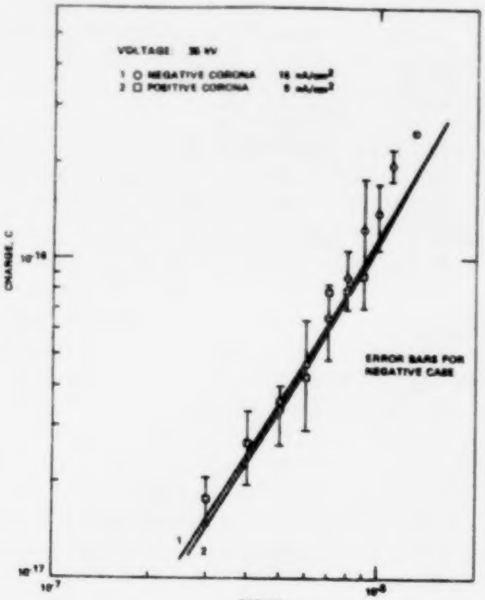

Figure 10. Measured positive and negative particle charge versus measured radius and comparison with theory at 38°C (100°F) and 35 kV.

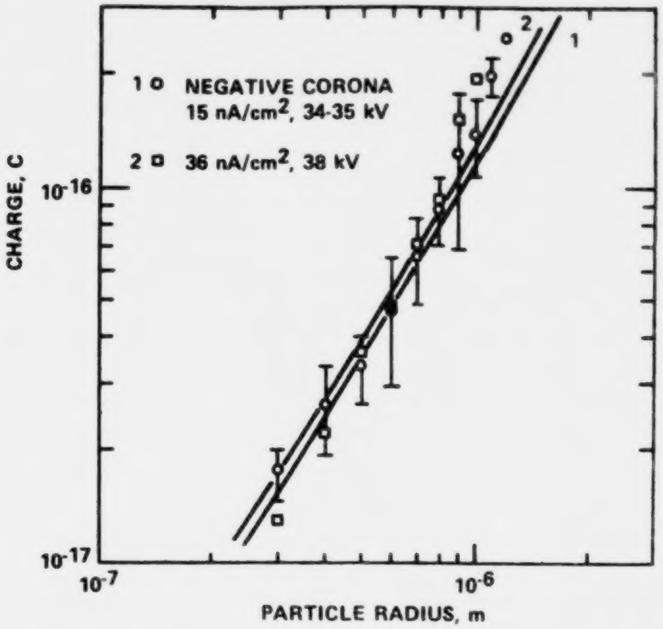

Figure 11. Measured negative particle charge versus measured radius and comparison with theory at 38°C (100°F) with 15 nA/cm^2 (13.9 μA/ft^2) and 36 nA/cm^2 (33.4 μA/ft^2).

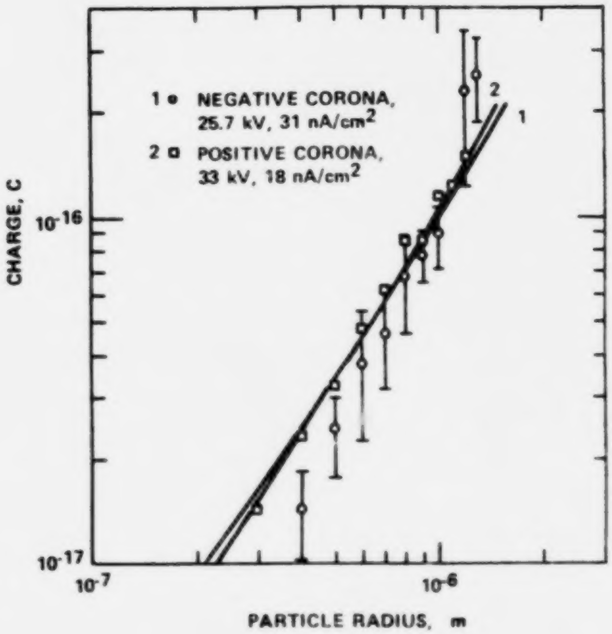

Figure 12. Measured positive and negative particle charge versus measured radius and comparison with theory at 148°C (300°F).

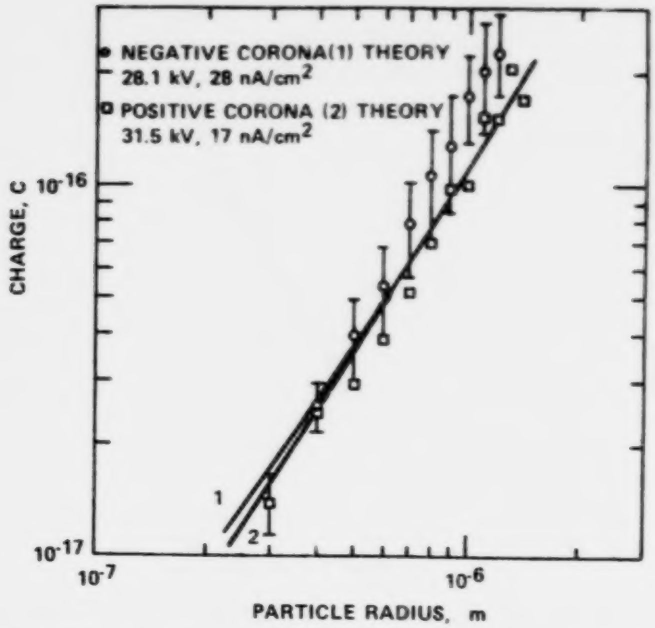

Figure 13. Measured positive and negative particle charge versus measured radius and comparison with theory at 232°C (450°F).

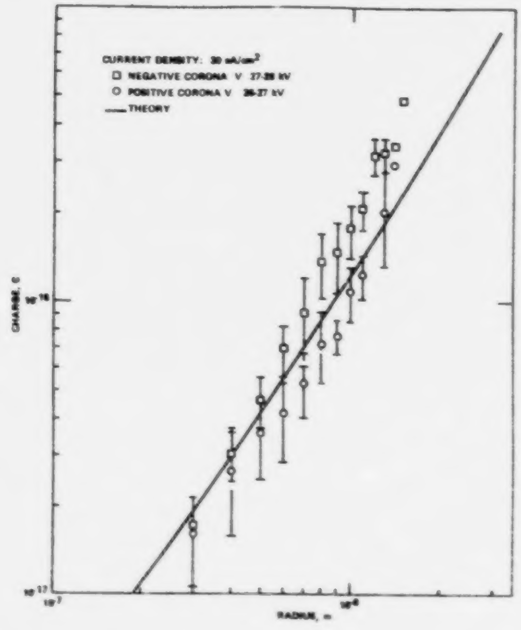

Figure 14. Measured positive and negative particle charge versus measured radius and comparison with theory at 343°C (650°F) and 30 nA/cm^2 (27.9 μA/ft^2).

physical difference between the positive and negative corona process is the free electron penetration into the interelectrode space in the negative corona case, the enhanced particle charge with negative corona at 232°C (450°F) might be due to increased free electron charging.

Figures 14-16 show particle diameter and charge measurements made at the outlet of precipitator C at 343°C (650°F) with an average gas velocity of approximately 1.4 m/sec (4.5 ft/sec). The precipitator had been cleaned thoroughly prior to these measurements. During the measurements, the electrical operating conditions were extremely stable. The data shown in Figure 14 were obtained for a current density of 30 nA/cm^2 (27.9 $\mu A/ft^2$) for both positive and negative corona with essentially the same average applied voltages of 26.5 kV and 27.5 kV, respectively. Similar to the results obtained at 232°C (450°F), the theory agrees well with the data for positive corona but clearly underpredicts particle charge obtained with negative corona for diameters between approximately 1.2 μm and 2.6 μm. In this diameter range, the ratio of the average measured charge to the predicted charge ranges from 1.27 to 1.94, generally increasing with increasing diameter. These data again suggest the possibility of free electrons participating in the charging process with negative corona.

Figures 15 and 16 contain data showing the effect of electrical conditions on particle charging with positive and negative corona at 343°C (650°F). Again, the theory agrees well with the data for positive corona but underpredicts particle charge obtained with negative corona for diameters between approximately 1.2 μm and 2.6 μm. The data show the same trend as the theory in that larger applied voltages and current densities result in higher values of particle charge. Also, the ability for negative corona to acquire a significantly higher voltage and current density prior to sparkover resulted in a further increase in particle charge as compared to the positive corona.

SUMMARY AND CONCLUSIONS

The apparatus and technique described for measuring particle diameter and charge are capable of providing reliable data on individual particles charged in an electrostatic precipitator. For temperatures up to 343°C (650°F), the measured values of charge acquired in positive corona by particles with diameters in the range between 0.6 μm and 3.0 μm are in good agreement with those predicted by an ionic charging theory. For temperatures less than 37°C (100°F), the measured values of charge acquired in negative corona by particles with diameters in the range between 0.6 μm and 3.0 μm are in good agreement with those predicted by an ionic charging theory. For temperatures of 232°C (450°F) and 343°C (650°F), the measured values of charge acquired in negative corona by particles with diameters between 1.2 μm and 2.6 μm are significantly higher than those measured for positive corona under similar conditions and those predicted from a completely ionic charging theory. These data indicate that the charging mechanisms for positive and negative corona differ as temperature increases. The enhanced values of particle charge for negative corona at elevated temperatures are consistent with the postulation of a free electron contribution in the particle charging mechanism. Thus, a general theory for particle charging in negative corona must contain ionic and electronic charging mechanisms whose relative contributions are temperature dependent. The data indicate that, even

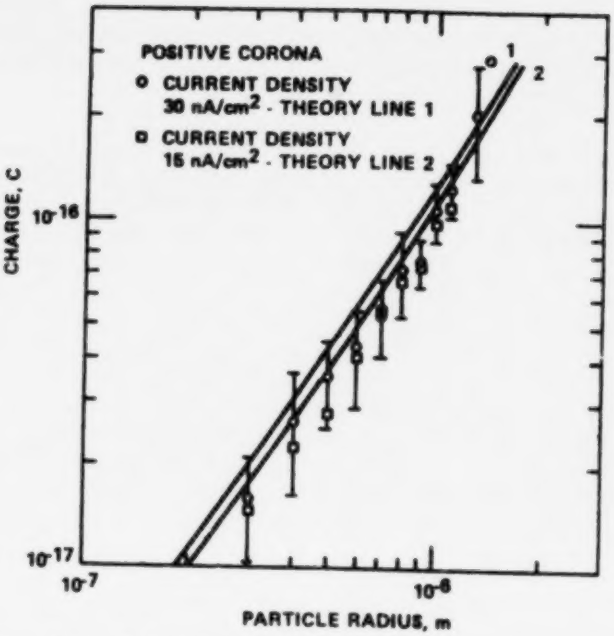

Figure 15. Measured positive particle charge versus measured radius and comparison with theory at 343°C (650°F) with 15 nA/cm^2 (13.9 μA/ft^2) and 30 nA/cm^2 (27.9 μA/ft^2).

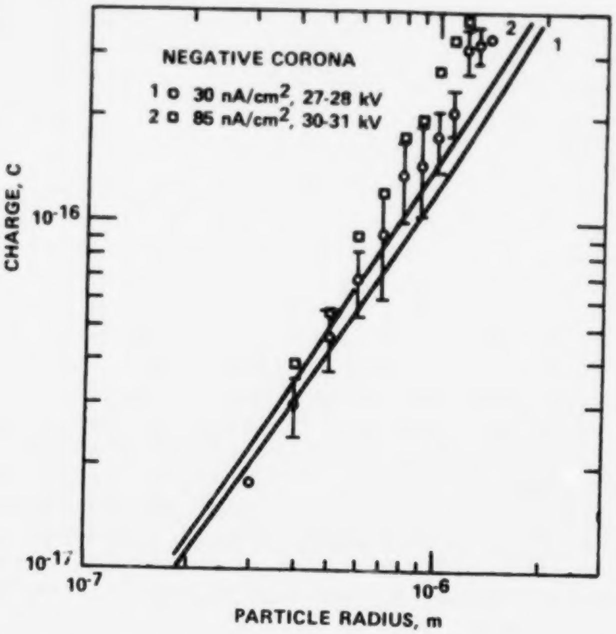

Figure 16. Measured negative particle charge versus measured radius and comparison with theory at 343°C (650°F) with 30 nA/cm^2 (27.9 μA/ft^2) and 85 nA/cm^2 (79.0 μA/ft^2).

in a full-scale precipitator utilizing negative corona, the effect of free electrons on the charging process can not be ignored for typical temperatures between 148°C (300°F) and 371°C (700°F).

ACKNOWLEDGMENTS

This work was supported by the Industrial Environmental Research Laboratory, U.S. Environmental Protection Agency, Research Triangle Park, North Carolina, under Contract No. 68-02-2610, Dr. Leslie E. Sparks, Project Officer.

REFERENCES

1. Penney, G. W., and R. D. Lynch. Measurements of Charge Imparted to Fine Particles by a Corona Discharge. AIEE, 76:294-299, July, 1957.

2. Pontius, D. H., L. G. Felix, J. R. McDonald, and W. B. Smith. Fine Particle Charging Development. EPA-600/2-77-173, NTIS No. PB 271-727/AS, U.S. Environmental Protection Agency, Research Triangle Park, North Carolina 1977.

3. Marchant, G. H., Jr. and J. P. Gooch. Performance and Economic Evaluation of a Hot-Side Electrostatic Precipitator. EPA-600/7-78-214, NTIS No. PB 292-648, U.S. Environmental Protection Agency, Research Triangle Park, North Carolina 1978.

4. McDonald, J. R. A Mathematical Model of Electrostatic Precipitation (Revision 1): Volume 1. Modeling and Programming. EPA-600/7-78-111a, NTIS No. PB 284-614, U.S. Environmental Protection Agency, Research Triangle Park, North Carolina 1978.

5. Smith, W. B., and J. R. McDonald. Development of a Theory for the Charging of Particles by Unipolar Ions. J. Aerosol Sci., 7:151-166, 1976.

6. McDonald, J. R., W. B. Smith, H. W. Spencer, and L. E. Sparks. A Mathematical Model for Calculating Electrical Conditions in Wire-Duct Electrostatic Precipitation Devices. J. Appl. Phys., 48(6):2231-2246, 1977.

OPTIMIZATION OF COLLECTION EFFICIENCY BY VARYING PLATE SPACING WITHIN AN ELECTROSTATIC PRECIPITATOR

E. J. Eschbach, Research Assistant

D. E. Stock, Associate Professor

Department of Mechanical Engineering
Washington State University
Pullman, Washington 99164

ABSTRACT

Use of the Deutsch equation as an evaluation tool of electrostatic precipitators has resulted in the restriction of precipitator design to a single plate spacing and has not enabled optimal use of the space charge arising from the presence of charged dust particles. Space charge is dependent on dust loading and plate spacing and also influences the electric field, hence the migration velocity and, therefore, collection efficiency. Thus a trade-off is indicated between plate spacing and collection efficiency as a function of dust loading. A first step examination of this trade-off indicates that varied spacing can be used in precipitators while maintaining high levels of efficiency and decreasing the required SCA by 15 to 25%.

OPTIMIZATION OF COLLECTION EFFICIENCY BY VARYING PLATE SPACING WITHIN AN ELECTROSTATIC PRECIPITATOR

INTRODUCTION

Electrostatic precipitators (ESP) can only remain competitive with other particulate control devices if their initial cost can be reduced while holding their performance, operating cost and maintenance cost at their present level[1]. Presently, most precipitator manufacturers use a standard plate spacing and size a precipitator based on a modified form of the Deutsch-Anderson equation. The effective migration velocity used in the Deutsch-Anderson equation is usually based on past experience and pilot plant testing with the standard plate spacing. This experience, however, cannot be used to evaluate the effect of using a different plate spacing in each stage of the precipitator. By restricting the design of an ESP to a single plate spacing, one is not utilizing the space charge arising from the charged dust particles to its optimum.

Recent experimental work has shown that wider than usual plate spacing results in increased efficiency [2] and not the decrease of efficiency as predicted by the Deutsch-Anderson equation and other models [3]. The potential of plate spacing as a design parameter cannot be evaluated appropriately by the use of the Deutsch-Anderson equation or by the use of existing data which applies only to a standard width precipitator. To examine the effect of plate spacing, one must analyze the fundamental processes governing precipitator performance.

Precipitator collection efficiency for a given physical geometry, gas flow field and particle size distribution depends on particle migration velocity, plate spacing and particle turbulent diffusivity. For constant plate spacing and particle diffusivity, increasing the migration velocity increases the collection efficiency and for constant migration velocity and particle diffusivity, increasing the plate spacing decreases collection efficiency. Therefore, if migration velocity can be increased as plate space is increased, it might be possible to hold collection efficiency constant and reduce the specific collection area, and therefore the initial cost of a precipitator. The influence of space charge on the electric field and the electric field's influence on migration velocity hold the key to understanding how the migration velocity varies with plate spacing.

The electric field at any point in the precipitator depends on the applied voltage, the plate spacing, and the space charge due to charged particles, ions and electrons. In this discussion we will hold the applied voltage divided by wire to plate spacing constant and neglect the influence of ions and electrons on the total space charge. Also, to make the discussion simpler, the wire and plate geometry will be modeled as a plate and plate precipitator with the particles charged to a saturation charge corresponding to the average applied electric field (applied voltage divided by wire to plate spacing). Using these assumptions, the electric field at any point in the precipitator depends on the applied electric field and the space charge due to the charged particles.

In the initial stage of the precipitator where the dust loading is still high, the particle space charge will have a considerable effect on the electric field, but in the last stages where most of the particles have been removed, the space charge will have very little effect on the electric field. The electric field near the collecting plate is, using our assumption, the applied electric field plus the integral of the space charge from the high voltage plate to the location of interest. This means for a stage with high dust loading, wide plate spacing will give a higher electric field near the collecting plate. And since migration velocity is directly related to electric field, a stage with high dust loading and wide spacing will have higher migration velocities than one with the same loading and narrower plate spacing. All this indicates that it might be possible to use wide plate spacing in the initial stage or stages without suffering a decrease in overall collection efficiency. Since wider plate spacing might result in a lower initial cost for the precipitator, the trade-off between plate spacing and collection efficiency as a function of stage loading needs to be investigated. As the first step toward determining this trade-off, a numerical scheme based on the assumption given above was developed and used to quantify the effect of plate spacing.

CALCULATION SCHEME

A calculation scheme was developed to determine how the collection efficiency varied with plate spacing as a function of dust loading. Since this was the first stage of our investigation, we wanted to include all major phenomena influencing collection efficiency without making the resulting calculations too involved numerically or too costly to perform. The goal of this set of calculations was to determine trends and not a detailed prediction.

The scheme is composed of three interconnected sections: migration velocity calculation, concentration calculation, and electric field calculation. Each section is described separately below as well as the scheme used to link the sections together.

Migration Velocity Calculation

The migration velocity is calculated assuming the velocity of the particle results from a balance of electrostatic and drag forces. The particle is assumed to be charged to saturation as set by the applied electric field E_c. Therefore the migration velocity is given by

$$w = \frac{\varepsilon_o E_c E_p d}{\mu}$$

where E_p = electric field at the particle location

E_c = applied electric field (applied voltage divided by plate to wire spacing

ε_o = permitivity of free space

μ = gas viscosity

For this investigation the applied electric field, E_c, was held constant at .4 MV/m.

Electric Field Calculation

Although relationships exist to calculate the electric field, current, and spare charge from first principles, a general numerical scheme has not yet been demonstrated. At this stage in our investigation, the electric field can be assumed to be that generated by a plate and plate precipitation with the space charge due only to the charged particles. The space charge due to ions and electrons will change the computed electric field slightly, but the results will have the same general trends. Neglecting gradients in electric field in the flow direction as compared to the transverse direction, the electric field is given by

$$E = E_c + \quad {}_y \frac{\rho}{\varepsilon_0} dy$$

where

y = transverse coordinate

E_c = applied electric field (applied voltage divided by plate spacing)

ρ = space charge due to the charged particles

ε_0 = permitivity of free space

Particle Concentration Calculation

Particle motion in a precipitator is the result of three transport processes: longitudinal motion of the gas, transverse motion due to the electric field, and particle turbulent diffusion. Assuming the particles follow the gas flow in the longitudinal direction and diffusion effects are only important in the transverse direction, the particle concentration at a point in the flow field is given by

$$V(\partial c/\partial y) + U(\partial c/\partial x) + W(\partial c/\partial y) - D(\partial^2 c/\partial y^2) = 0$$

where

c = particle concentration

U = longitudinal gas velocity

V = transverse gas velocity

W = migration velocity

D = particle turbulent diffusion coefficient

x = longitudinal coordinate

y = transverse coordinate

The boundary conditions at the collection plate and charging plate are

$D(\partial c/\partial y) = Wc$ at the charging plate

$\partial c/\partial y = 0$ at the collection plate assuming no re-entrainment

This set of equations has been used by others ±4, 51 to model ESP operation.

A turbulent particle diffusion coefficient must be specified before the equation can be solved. In general the diffusion would change with both longitudinal and transverse location in the precipitator. Since, at this stage of our analysis, interest is focused on trends in performance as a function of plate spacing, a constant diffusion coefficient of 0.0005 m^2/sec was used. Also the transverse velocity was assumed to be zero and the longitudinal velocity was taken as a constant at all locations.

Numerical Solution

The partial differential equation for particle concentration was converted to finite difference form using up-wind difference techniques for the longitudinal and migration velocity and central difference for the diffusion term. The resulting system of algebraic equations were solved by the Gauss-Seidel method.

The solution scheme is started by assuming the electric field at all locations in the precipitator is equal to the applied voltage divided by the wire to plate spacing. Using this electric field, the particle migration velocity at all locations is calculated and finally the particle concentration is determined by Gauss-Seidel iteration. Using the calculated concentrations, the electric field is determined including the effect of the space charge created by the charged particles. The migration velocity is then recalculated using the new electric field. The particle concentration equation is then solved again using the new estimate for particle migration velocity. This cycle is continued until no change is found in the calculated concentration between cycles. Typically, seven cycles are required for each particle size.

The dust entering a precipitator typically has a wide size distribution. This continuous distribution can be divided into a number of bands with each represented by a single particle size and a fraction of the total loading. Particle concentrations for each band would be calculated separately but the space charge used in the electric field calculation must include all particle sizes. In this work only one particle size was used since we were only interested in trends.

RESULTS

Calculations were first performed for three dust loadings and a range of wire to plate spacings. The results, shown in Figure 1, show that for a given plate spacing, increasing the dust loading increases the collection efficiency. The figure also shows the efficiency decreases with increasing plate spacing, but the decrease is very slight for the high loading case. We have not yet investigated the effect of gas velocity, ion space charge or turbulent particle diffusion on the relationship between efficiency and plate spacing. Under certain conditions it might be possible to increase the collection efficiency with increasing plate spacing. The results shown in Figure 1 are for the first stage at a precipitator with a seven foot plate length.

To show the effect of non-uniform plate spacing, three precipitator configurations were picked and the overall efficiency of each was determined. Tables 1, 2, and 3 give the geometry of each configuration and the calculated efficiency for each stage. Figure 2 shows the wider spacing decreased the collection efficiency slightly, but greatly reduced the specific collection area.

The results obtained in this initial investigation should only be taken as showing the trends to expect with wider plate spacing in the initial stages of a precipitator. The optimum configuration has not yet been determined. Additional work needs to be done to include the effect of ion space charge in the calculations.

ACKNOWLEDGEMENTS

This work was supported, in part, by Battelle Memorial Institute through their University Distribution Program.

REFERENCES

1. Stearns-Rogers Incorporated (Denver CO). Economic Evaluation of Fabric Filtration versus Electrostatic Precipitation for Ultrahigh Particulate Collection Efficiency. EPRI Final Report FP-775, Research Project 834-1.

2. Misaka, et al. Hitachi Plant Engineering and Construction Co.(Tokyo). Electric Field Strength and Collection Efficiency of Electrostatic Precipitators Having Wide Collecting Plate Pitches. CSIRO Conference on Electrostatic Precipitation, August 1978.

3. Eschbach, et al. The Influence of Plate Spacing on the Efficiency of an Electrostatic Precipitator. Washington State University. 1978 Annual Meeting PNWIS Air Pollution Control Association, November 1978.

4. Feldman, P.L., Kumar, K.S., Cooperman, G.P. Turbulant Diffusion in Electrostatic Precipitators. AIChE Symposium Series, Atmospheric Emissions and Energy Source Pollution73:165, 1977.

5. Soo, S.L. A Critical Review on Electrostatic Precipitators. AIChE Symposium Series, Air Pollution and Its Control. 68:126, 1972.

Table 1 GEOMETRY AND EFFICIENCY OF PRECIPITATOR A

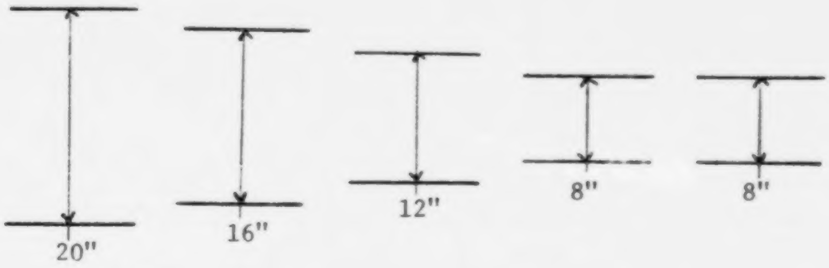

Stage	Wire to Plate	Dust Load In (kg/m^3)	Dust Load Out (kg/m^3)	Stage Efficiency
1	10" .2540m	$4.577(10^{-2})$	$2.155(10^{-3})$	95.29%
2	8" .2032m	$2.155(10^{-3})$	$8.221(10^{-4})$	61.85%
3	6" .1524m	$8.221(10^{-4})$	$3.642(10^{-4})$	55.70%
4	4" .1016m	$3.642(10^{-4})$	$1.319(10^{-4})$	63.79%
5	4" .1016m	$1.319(10^{-4})$	$5.111(10^{-5})$	61.26%

$$SCA = \frac{208\ ft^2}{1000\ ft^3/min}$$

Overall Efficiency, $\eta = 99.888\%$

Precipitator Parameters

plate length: 7 ft, 2.134m
gas velocity: 6 ft/s, 1.8288 m/s
gas viscosity: 2.80×10^{-5} kg/m·s
particle diameter: 1 micron
particulate density: 3000 kg/m^3
average electric field: .4MV/m

Table 2 GEOMETRY AND EFFICIENCY OF PRECIPITATOR B

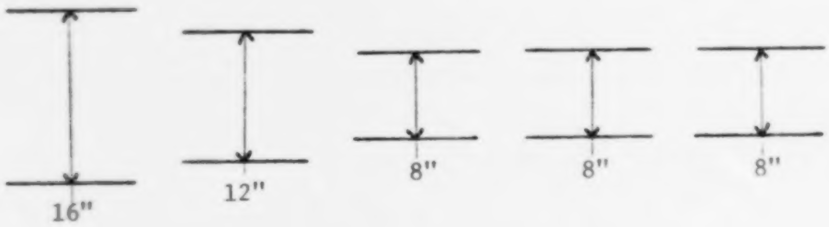

Stage	Wire to Plate	Dust Load In (kg/m^3)	Dust Load Out (kg/m^3)	Stage Efficiency
1	8" .2032m	$4.577(10^{-2})$	$2.005(10^{-3})$	95.29%
2	6" .1524m	$2.005(10^{-3})$	$6.778(10^{-4})$	66.20%
3	4" .1016m	$6.778(10^{-4})$	$2.257(10^{-4})$	66.69%
4	4" .1016m	$2.257(10^{-4})$	$8.503(10^{-5})$	62.33%
5	4" .1016m	$8.503(10^{-5})$	$3.342(10^{-5})$	60.70%

$$SCA = \frac{208 \text{ ft}^2}{1000 \text{ ft}^3/\text{min}}$$

Overall Efficiency, $\eta = 99.927\%$

Precipitator Parameters

plate length: 7 ft, 2.134m

gas velocity: 6 ft/s, 1.8288 m/s

gas viscosity: 2.80×10^{-5} kg/m·s

particle diameter: 1 micron

particulate density: 3000 kg/m^3

average electric field: .4MV/m

Table 3 GEOMETRY AND EFFICIENCY OF PRECIPITATOR C

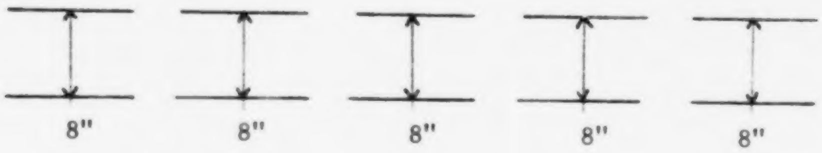

Stage	Wire to Plate	Dust Load In (kg/m^3)	Dust Load Out (kg/m^3)	Stage Efficiency
1	4" .1016m	$4.577(10^{-2})$	$1.419(10^{-3})$	96.90%
2	4" .1016m	$1.419(10^{-3})$	$3.985(10^{-4})$	71.92%
3	4" .1016m	$3.985(10^{-4})$	$1.429(10^{-4})$	64.13%
4	4" .1016m	$1.429(10^{-4})$	$5.517(10^{-5})$	61.39%
5	4" .1016m	$5.517(10^{-5})$	$2.189(10^{-5})$	60.70%

$$SCA = \frac{292\ ft^2}{1000\ ft^3/min}$$

Overall Efficiency, $\eta = 99.952\%$

Precipitator Parameters

plate length:	7 ft, 2.134m
gas velocity:	6 ft/s, 1.8288 m/s
gas viscosity:	2.80×10^{-5} kg/m·s
particle diameter:	1 micron
particulate density:	3000 kg/m^3
average electric field:	.4MV/m

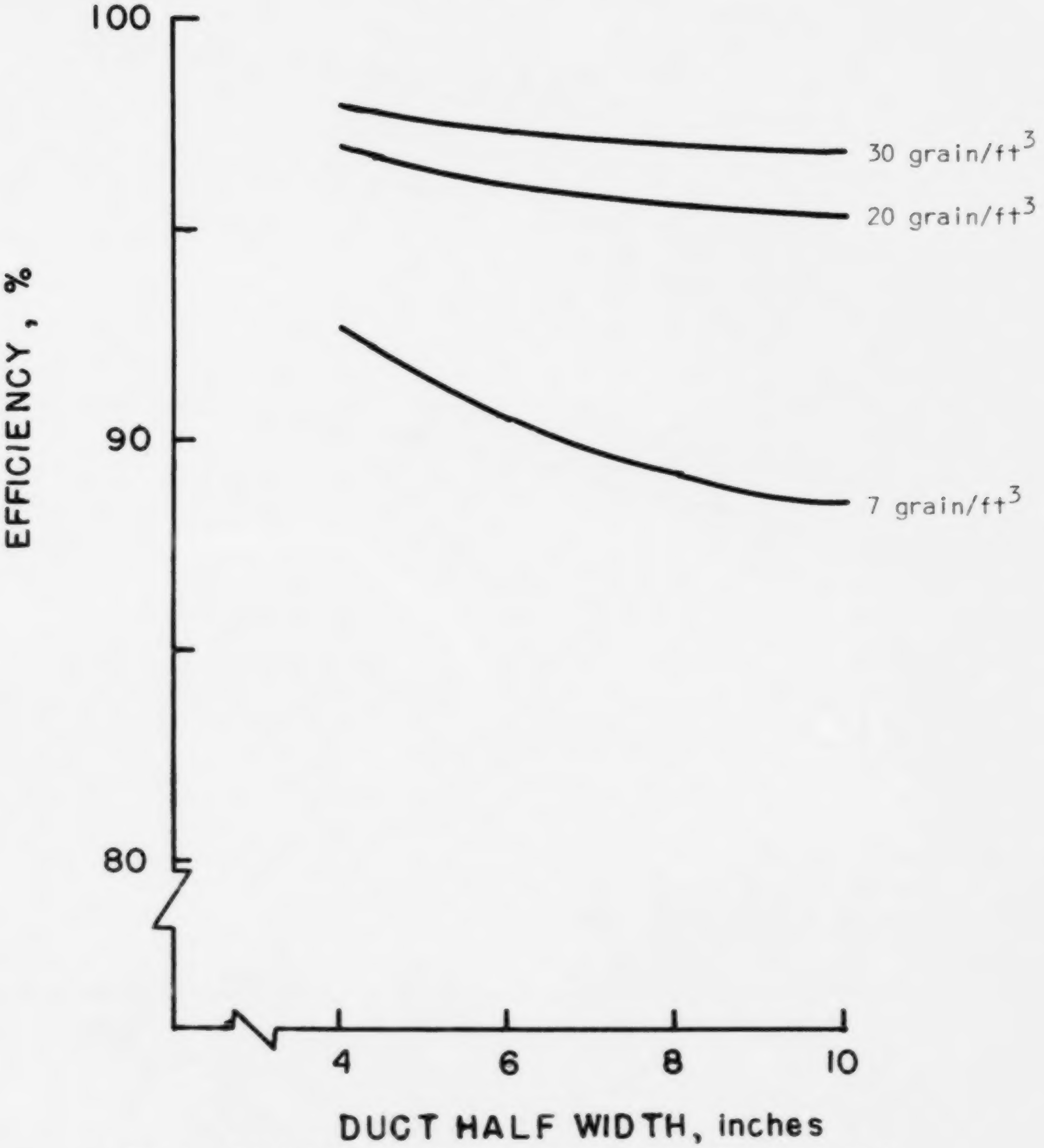

Fig.1 Efficiency variation with dust loading and duct half width in the first stage.

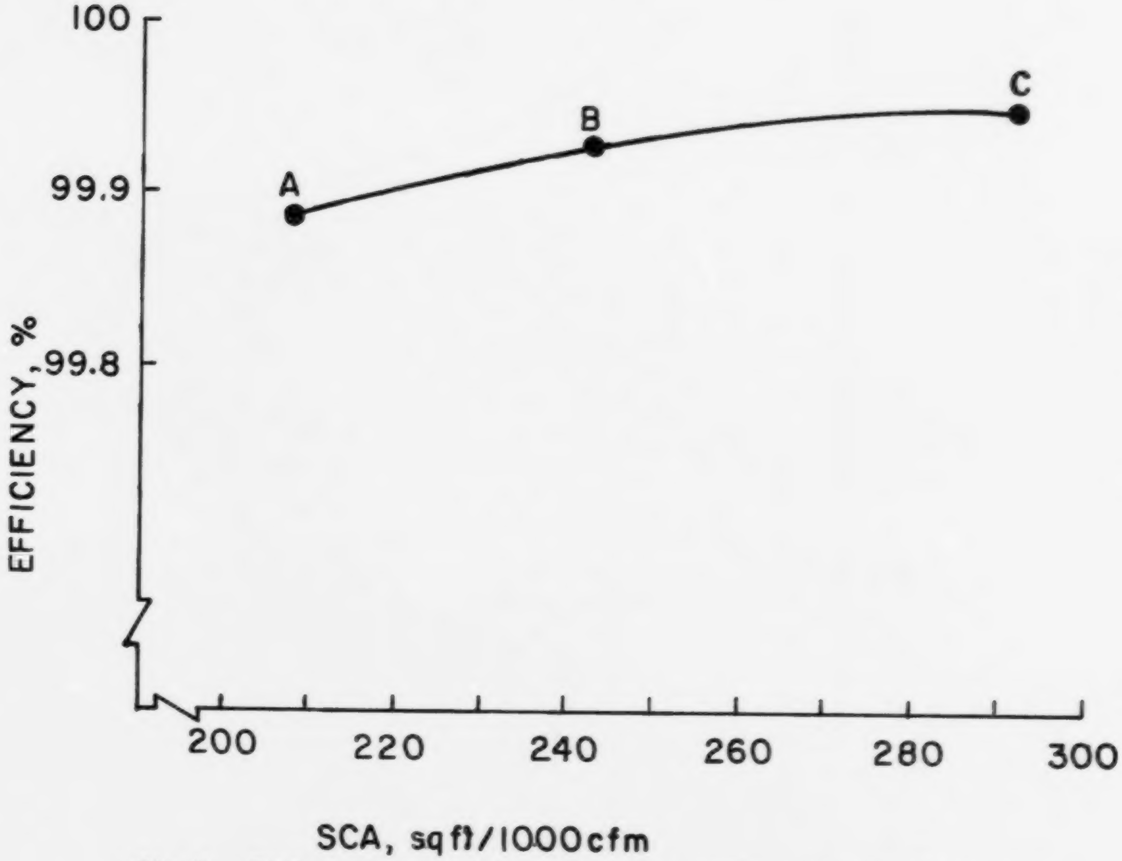

Fig.2 Efficiency and SCA of the precipitator configurations.

INTERACTION BETWEEN ELECTROSTATICS AND FLUID DYNAMICS IN ELECTROSTATIC PRECIPITATORS

By
Samuel Bernstein
and
Clayton T. Crowe

Paper to be Presented at the EPA
2nd Symposium on the Transfer and Utilization of
Particulate Control Technology

July 23 to 27, 1979

Denver, Colorado

INTERACTION BETWEEN ELECTROSTATICS AND FLUID DYNAMICS IN ELECTROSTATIC PRECIPITATORS

By

Samuel Bernstein, Flow Industries, Kent, Washington
Clayton T. Crowe, Washington State University, Pullman, Washington

ABSTRACT

Significant effort has been devoted by past researchers in electrostatic precipitators to electrostatics and particle chemistry. Relatively little, however, has been published on the effect of turbulent flow and its interaction with electrostatics and particle dynamics. This paper describes an experiment and a fundamental model which is focused on the coupled effects of the fluid dynamics and electrostatics.

A laboratory precipitator flow facility with a laser beam illumination was used to visualize smoke flow. Detailed photographs of flow patterns with and without electric field were recorded in a horizontal plane through the precipitator.

A theoretical model was used to numerically simulate the observed flow patterns in the experiment. In the model the flow was described by time-averaged mass and momentum equations with a two-equation turbulence model. The electric field was described by Maxwell electrostatic equation and the continuity of the current equation. The system of the coupled partial differential equations was solved by a finite difference scheme.

The interaction between fluid dynamics and electrostatics is shown to have a significant role in altering the flow in the precipitator. The practical implication is that the interaction will aid in particle migration in some regions, but it will increase reentrainment and reduce particle migration in others. Comparison between the results from the experiment and numerical computations shows good qualitative agreement between the two. Since both the electrostatic and the fluid dynamic flow fields depend on the electrode geometry, further investigation may lead to improved design of precipitators.

INTERACTION BETWEEN ELECTROSTATICS AND FLUID DYNAMICS IN ELECTROSTATIC PRECIPITATORS

1. Introduction

Electrostatic precipitators have been well suited to remove particulates from gas streams in applications requiring high collection efficiency of micron-size particles, large gas volumes, and low pressure losses. One common, and ever-increasing, application has been the removal of flyash particles from the exhaust gases of electric power plants fired by pulverized coal. In recent designs, however, precipitator size, and consequently its cost, have been increased considerably to meet strict performance criteria. This adverse economic trend provides the motivation for research to develop new precipitator technology. A better understanding of the fundamental process of electrostatic precipitators will provide guidance to reduce their size and cost while maintaining their high operating efficiency.

The subject of the investigation presented in this paper is one such fundamental mechanism in electrostatic precipitators; that is, the interaction between fluid dynamics and electrostatics. Although this interaction appears to be quite strong and a significant factor in precipitator performance, relatively little has been published on the subject to date. The discussion in the paper includes a brief outline of the state-of-the-art precipitator performance followed by a description of a laboratory experiment and a numerical simulation, both of which are focused on the coupling between fluid dynamics and electrostatics. Finally, some preliminary conclusions and recommendations for further work are presented.

2. Performance of Electrostatic Precipitator

The classically accepted operating principles of electrostatic precipitators are well documented in the literature (for example, see White (1963)[1], Robinson (1971)[2] and Oglesby and Nichols (1970)[3]). The common industrial precipitator consists of a row of wire electrodes suspended between vertical plate electrodes which constitute the duct for passage of the dust-containing gases. A high voltage applied between the wire and the plate electrodes generates a corona discharge and a flow of ions towards the duct walls. Some ions accumulate on the particles, imparting a net charge on them. The resulting charged particles are accelerated towards the duct walls by Coulomb forces and slowly migrate onto the plates. The accumulated dust particles on the plates are then dislodged into collecting hoppers by periodic rapping.

The above-simplified description of precipitator performance was the basis for Deutsch's classical analysis (see for example White (1963)[1]). The analysis resulted in the formulation of a one-dimensional equation which expresses the particulate collection efficiency as a function of the migration velocity, collecting electrode area, and the flue gas volume flow. Deutsch's analysis also assumes that turbulent mixing is strong enough to maintain a uniform dust concentration profile across the precipitator duct. It further assumes that the migration velocity is constant along the wall.

The migration velocity is predicted by equating the aerodynamic force and Coulomb force on the particle. However, the computation of particle migration velocity with Deutsch equation generally fails to yield a reliable prediction of collection efficiency. Consequently, precipitator designers use collection efficiency data and the Deutsch analysis to calculate an "effective" migration velocity for a precipitator design which then serves as an empirical factor for design of similar units. Numerous researchers (such as Robinson (1967)[4], McDonald (1978)[5], Inyushkin and Averbukh (1969)[6], and Friedlander (1959)[7] have developed modifications of the Deutsch efficiency equation by adjusting the migration velocity to account for such phenomena as turbulent flow effects, non-uniform electric fields and a distribution of particle sizes. Such an approach is, however, inadequate for either the evaluation of new precipitator designs or for the evaluation of existing precipitator designs for different operating conditions on which the migration velocity data is based. The use of the above approach can lead, and has led, to units which fall far below design specifications.

Another predictive model for collection efficiency has been proposed by Williams and Jackson (1962)[7] and Cooperman (1969)[8]. This model is based on solution of the field concentration equation for particle concentration in the precipitator.

The major limitations in past investigations have been the neglect or the use of overly simplified fluid dynamic models, the lack of description of the electrostatic field interaction with the fluid dynamic model via the ionic wind and the effect of the boundaries and electrodes on the electrohydrodynamic and particulate field. Consequently, these approaches require assumptions regarding particle transport laws and cannot adequately predict the performance of the precipitator. Of course, the complete treatment of precipitator performance requires the evaluation of numerous additional factors. These include (1) the effect of back corona discharge and particulate resistivity as influenced by gas chemistry and coal properties, (2) particle reentrainment from the collecting plates and from the hoppers both during rapping and normal operation, (3) plate vibration during rapping (4) electrode alignment, and (5) particle charging. It is suggested, however, that a proper description of the fluid dynamic flow field, the electrostatic field and their interaction is a necessary fundamental step for a meaningful evaluation of the device.

The following interactive phenomena including fluid dynamics, electrostatics and particle dynamics is hypothesized (see Figure 1): the fluid dynamic field is responsible for particle motion and is controlled primarily by the inlet conditions and duct geometry. In practical operation the flow field is turbulent, and particle transport will be influenced by the turbulence energy and characteristic length scales of the field.

The particles are charged by the discharge electrostatic field and are then subjected to the Coulomb force provided by the electrostatic field. At high electrostatic field intensity, the fluid dynamic flow field becomes ionized and develops a pressure gradient proportional to the ion charge density and the electric field intensity. This pressure gradient generates fluid flow referred to as ionic or electric wind.

In order to qualitatively examine the ineraction between the fluid dynamic flow field and the electrostatic flow field, both a laboratory experiment and a numerical simulation was conducted.

3. Experimental Investigation

3.1 Experimental Setup

The experimental investigation was conducted in a laboratory precipitator flow facility. The dimensions of the test section of the facility were 30 inches wide, 15 inches high and approximately 12 feet long. A bellmouth entry section with honeycomb flow straighteners preceded the test section. The gas flow through the facility was driven by a fan downstream of the test section. Gas flow rate was controlled by a damper and a variable ratio pulley which drove the fan. The facility was capable of generating flow rate in the range of 1 to 20 ft/sec. The gas flow in the test section was turbulent with uniform spatial distribution of its cross sectional area. All four sides of the test section were made of plexiglass with an iron frame. A smoke generator (Bernstein (1978)[9]) was used to generate fine smoke from petroleum based oil. In order to visualize one elevation in the precipitator flow facility, an Argon ion laser with beam intensity of 5 watts was dispersed into a thin sheet of light by means of a glass rod. The light scattered by the smoke particles at the beam elevation were then observed from above. In this illumination technique a two-dimensional view of one elevation was possible. The method is illustrated in Figure 2. The glass rod was positioned at several locations in the facility to obtain observation of fine details of the flow field. As illustrated in Figure 2 the flow field was observed through a TV monitor for safety.

Precipitator plate electrodes with normal flanges of approximately 1 inch width were placed in the facility with plate to plate spacing of 9 inches. The plates were mounted against the top and the bottom of the test section. Discharge wires with 0.109 inch diameters were placed at the center of the channel with approximate spacing of 8 inches. Two wires were placed between each two flagnes, the power supply used was capable of generating negative corona with a sparkover voltage of approximately 70 KV at ambient condition for the above plate arrangement.

3.2 Test Results

Qualitative observations of flow patterns were obtained over a range of flow velocities and electric field intensity. The observations were recorded in a video cassette recorder. The results reproduced here were photographed from a TV monitor screen. Figure 3 is a photograph of the flow pattern without the electric field. Although the electric field was not energized, one discharge wire may be seen in the photograph. The flow direction was from left to right and the glass rod can also be seen at the left portion of the picture. The average gas flow was 1.5 ft/sec and regions of high and low light intensity represent regions of high and low concentrations of smoke particles.

Figure 4 is a photograph of the smoke flow with average gas velocity of 1.5 ft/sec, field voltage of 39 KV and current of 1 milli A/m. Two circular shadow regions can be observed near each discharge wire. The flow between the discharge wire and the wall electrode is deflected towards the wall and does not have the same turbulent eddy structure as the fluid flow alone.

Finally, Figure 5 is a photograph of the instantaneous flow patterns with field voltage of approximately 50 Kv and current intensity of 0.8 milli A/m. In reviewing these results two comments should be emphasized. The first is that this preliminary qualitative description of the precipitator flow field is only an instantaneous view of the unsteady turbulent field. The second comment is that in numerous variations of gas flow velocity and electric field intensity it was not always possible to identify the flow patterns, especially when the video screening was stopped.

4. Numerical Simulation

4.1 Theoretical Model

The model used to describe the interaction between the fluid dynamics and electrostatics was described by Bernstein and Crowe (1978)[10]. A similar model for cylindrical geometry was used by Crowe and Stock (1974)[11] to predict the flow pattern in a wire-tube geometry. An outline of the former model, however, is included here since the referenced work may not be readily available in the U.S.

The flow field is described by a two-dimensional model similar to the illuminated plane as shown in Figure 2. The fluid dynamic model, originally developed at Imperial College (1973)[12] uses the time-averaged conservation equations of mass and momentum and a two-equation turbulence model. Such a model contains the usual drawback of a turbulence model; however, it does represent a state-of-the-art in turbulence modeling and it provides good flow predictions in flow fields not associated with precipitators. The electric field model includes Maxwell's electrostatic field equation and the continuity of current equation. The model contains a system of seven coupled non-linear partial differential equations as follows:

Fluid Dynamic Model

A. Continuity Equation:

$$\frac{\partial \rho u}{\partial x} + \frac{\partial \rho v}{\partial y} = 0 \qquad (1)$$

where u and v are the time-averaged velocity components in the stream-wise, x and lateral y directions respectively.

B. Momentum Equation: Using the Boussinesq approximation to relate the stress on the fluid to the rate of strain with turbulent flow, the momentum equation in the x-direction is given by

$$\frac{\partial}{\partial x}\left[\rho uu - \mu_{eff}\frac{\partial u}{\partial x}\right] + \frac{\partial}{\partial y}\left[\rho uv - \mu_{eff}\frac{\partial u}{\partial y}\right] = -\frac{\partial p}{\partial x} + \rho_{c_{ion}} E_x \qquad (2)$$

where μ_{eff} is the effective viscosity, p is the pressure, $\rho_{c_{ion}}$ is the ion charge density and E_x is the electric field intensity in the x-direction. The two terms on the left-hand side represent the momentum transport in the two coordinate directions by convection and diffusion. The terms on the right-hand side are the force due to pressure gradient and the body force due to motion of the ions caused by the electric fields (effect of the electric wind).

C. Y-Momentum Equation: The momentum equation in the y-direction can be written as

$$\frac{\partial}{\partial x}\left(\rho uv - \mu_{eff}\frac{\partial v}{\partial x}\right) + \frac{\partial}{\partial y}\left(\rho vv - \mu_{eff}\frac{\partial v}{\partial y}\right) = -\frac{\partial p}{\partial y} + \rho_{c_{ion}} E_y \qquad (3)$$

The terms are easily identified by referring to Equation 2.

D. Turbulence Kinetic Energy: The differential equation for turbulence kinetic energy as developed by Launder and Spalding[12] is

$$\frac{\partial}{\partial x}\left(\rho uk - \frac{\mu_{eff}}{\sigma_k}\frac{\partial k}{\partial x}\right) + \frac{\partial}{\partial y}\left(\rho vk - \frac{\mu_{eff}}{\sigma_k}\frac{\partial k}{\partial y}\right) = G - \rho\varepsilon \qquad (4)$$

where k is the turbulence energy, σ_k effective Prandtl number for turbulent energy transfer by diffusion (usually taken as unity) and ε is the dissipation rate. The two terms on the left-hand side represent turbulence energy transfer in the x and y directions by convection and diffusion. The term G is the generation term which is given by

$$G = \mu_{eff}\left\{2\left[\left(\frac{\partial u}{\partial y}\right)^2 + \left(\frac{\partial v}{\partial y}\right)^2\right] + \left[\frac{\partial u}{\partial y} + \frac{\partial v}{\partial x}\right]^2\right\} \qquad (5)$$

The turbulence energy equation as incorporated here does not include ion flow on turbulence energy generation or decay. Possible contribution of this effect is the subject of continuing research.

E. Turbulence Dissipation Rate: The differential equation for dissipation rate of turbulence energy as suggested by Launder and Spalding is

$$\frac{\partial}{\partial x}\left[\rho u\varepsilon + \frac{\mu_{eff}}{\sigma_\varepsilon}\frac{\partial\varepsilon}{\partial x}\right] + \frac{\partial}{\partial y}\left[\rho v\varepsilon - \frac{\mu_{eff}}{\sigma_\varepsilon}\frac{\partial\varepsilon}{\partial y}\right] \tag{6}$$

$$= \frac{C_1 \varepsilon G}{k} - \frac{C_2 \rho \varepsilon^2}{k}$$

where σ_ε is the effective Prandtl number for diffusion of energy dissipation. The C_1 and C_2 parameters are empirical constants which are assigned by comparing the predictions with experimental data in simple jet flow experiments unrelated to precipitators. As with turbulence energy, no attempt was made to account for particle or electric wind effects.

The remaining expression for "closure" of gas flow equations is the Prandtl-Kolmogorov equation for effective viscosity in terms of the turbulence kinetic energy and dissipation rate; namely,

$$\mu_{eff} = \mu + C_\mu \rho k^2/\varepsilon \tag{7}$$

where C_μ is another empirical constant assigned a value of 0.09.

Electrostatic Field Model:

The two dependent variables describing the electric field are the voltage and ion charge density. The electric field strength is by definition the negative gradient of the voltage. The two equations for the electric field are Maxwell's equation and the continuity of current flow.

A. Maxwell's Equation: The equation relating voltage and charge density is

$$\nabla^2 V = -\frac{1}{\varepsilon_1}\left[\rho_{c_{ions}} + \rho_{c_{particles}}\right] \tag{8}$$

where V is the voltage, ε_1 is the dielectric constant and ρ_c is the charge density. The charge of ions as well as the charge on the particles affect the electric potential.

It is a reasonable approximation, however, to regard the effect of charge density as a second-order effect and to use the voltage field obtained by the solution of Laplace equation. Cooperman (see Robinson (1971)[2]) obtained an analytic solution for the voltage distribution in a channel with wires spaced equidistant along the center of the channel as

$$V = V_o \frac{\sum_{m=-\infty}^{\infty} \ln \left[\frac{\cosh\left[\pi(x - mB)/A\right] - \cos(\pi v/A)}{\cosh\left[\pi(x - mB)/A\right] + \cos(\pi v/A)}\right]}{\sum_{m=-\infty}^{\infty} \ln\left[\frac{\cosh(\pi m B/A) - \cos(\pi r_o/A)}{\cosh(\pi m B/A) + \cos(\pi r_o/A)}\right]} \tag{9}$$

where A is the channel width, B is the distance between wires and r_o is the wire radius and V_o is the corona discharge voltage. The above series rapidly converge in several terms.

The electrostatic field intensity is obtained by taking the negative of the voltage gradient. The resulting expressions are

$$E_x = -k_1 \frac{2\pi}{A} \cos(y\pi/A) \sum_{m=-\infty}^{\infty} \frac{\sinh\left[\pi(x - mB)/A\right]}{\cosh^2\left[\pi(x - mB)/A\right] - \cos^2(y\pi/A)} \qquad (10)$$

$$E_y = -k_1 \frac{2\pi}{A} \sin(y\pi/A) \sum_{m=-\infty}^{\infty} \frac{\cosh\left[\pi(x - mB)/A\right]}{\cosh^2\left[\pi(x - mB)/A\right] - \cos^2(y\pi/A)} \qquad (11)$$

where k_1 is the corona voltage over the denominator for Equation (9). In the computation performed in this study for a single discharge electrode, the electric field solution was approximated using the method of images with an array of source-sink distribution.

B. Continuity of Current Flow - The continuity of current flow is expressed as

$$\nabla \cdot \vec{j} = 0 = \nabla \cdot (\rho_{c_{ions}} \; b\vec{E}). \qquad (12)$$

where $\vec{j}$ is the current flow vector, b is the ion mobility and $\vec{E}$ is the electric field intensity. The current flow due to particle motion is neglected, because the particle mobility is much smaller than ion mobility.

Using the same assumption pertaining to the second-order effect of charge on the voltage distribution, Cooperman (see Robinson (1971)^2) showed that the charge density may be assumed to be a constant in the channel and equal to

$$\rho_{c_{ion}} = \frac{\dot{j} \ln (d/r_o)}{2\pi \; b \; V_o} \qquad (13)$$

where d(m) is a function of duct width and wire spacing.

The solution of the electrohydrodynamic model was obtained by finite difference solution in a CDC 7600 computer. Typical run required 15 seconds of central processor for a flow field described by a grid of (22 x 22) elements.

4.2 Computed Examples

Four examples of computed flow fields are presented for comparison with the experimental data. These include (a) turbulent flow without electric fields, (b) turbulent flow with moderate intensity electric field generated by a single wire (c) turbulent flow with high intensity electric field generated by a single wire, and (d) turbulent flow with electric field generated by multiple wires. Although numerical values are used in this example, the results should be considered qualitative for the purpose of comparisons with experiments. No careful attempt was made to precisely match the geometry and operating conditions in both cases. The computed results are given in Figures 6, 8, 9, 10 for each case discussed above. Figure 7 includes the electric field distribution for the case of a single wire and multiple wires. This field calculation neglects the presence of the flanges on the collecting electrodes.

5. Discussion

The discussion is divided into two cases: the fluid dynamic flow field and the combined electrohydrodynamic field.

The experimental result of the fluid dynamic flow field, as shown in Figure 3, illustrates turbulent eddies with high and low smoke concentration of smoke particles. It is evident that turbulent diffusion is not sufficient to provide uniform particulate concentration as assumed by Deutsch's analysis. The numerical computations of the same case reveals a small recirculating bubble aft of the baffle and a short stagnation zone ahead of the downstream baffle. This predicted flow pattern was qualitatively confirmed in the experimental study. In the absence of strong ionic wind effect, significant reentrainment of particles from the wall electrode may develop due to scouring of the electrode by the flow.

Inspection of both experimental and computational results for the combined electrohydrodynamic field reveals a strong coupling in the flow. During the experiments, the flow field was found to be sensitive to the relative values of fluid velocity and electric field intensity. Qualitative agreement is observed between the computed flow field and the experiment. The observed agreement is particularly good between the computed cases of a single wire (Figures 8 and 9) and the photograph given in Figure 5. The preliminary computation with multiple wires, Figure 10, predicts multiple vortex flow near the walls. The results show horizontal flow patterns, although a vertical ionic flow as studied by Robinson (1976)[13] may also be present. The clover leaf flow pattern of two vortices near each wire, as hypothesized by Robinson, were not observed in either experiment or computation for the given electrode geometry and operating conditions. The preliminary nature of this investigation precludes any further evaluation regarding the conditions for existence of specific flow patterns with a given geometry and operating conditions, and these are the subject of continuing research.

6. Conclusions and Recommendations

The investigation reported here included a qualitative evaluation of the interaction between fluid dynamics and electrostatics in electrostatic precipitators. The evaluation was conducted by both an experimental effort and a numerical simulation in a horizontal plane through the precipitator. Several conclusions and recommendations can be drawn as follows:

(1) The interaction between fluid dynamics and electrostatics appears to be quite strong. Significant electric wind flow was observed experimentally and numerically at operating conditions of high electric voltages and currents. The voltage and current levels at which the electric wind was observed to significantly alter the flow field were lower for low average gas flow rates.

(2) Qualitative numerical simulation provided good agreement with observed flow patterns.

(3) The study documented both experimentally and numerically the existence of a strong electric wind in a horizontal plane. The experimental data indicate recirculating flow from the discharge wires to the collecting electrodes and back to the discharge wires. Such a flow pattern satisfies the continuity of flow requirement; however, a vertical flow due to the electric wind, as suggested by Robinson (1976)[13], can not be ruled out.

(4) The degree of interaction between the fluid dynamic flow field and the electrostatic field suggests that it may significantly affect the performance of the precipitator. The electric wind may increase the effective migration velocity at which particles are being transported to the collecting electrodes; however, the recirculating flow may contribute to reentrainment. In order to design an electrode geometry which would provide optimum performance, further investigation of the phenomena is necessary.

(5) Further evaluation is recommended to obtain quantitative data on the above interaction. Quantitative data should be used to verify the reliability of the numerical predictions which could then be used for cost-effective design work.

REFERENCES

1. White, H. J. (1963) "Industrial Electrostatic Precipitation" Addison-Wesley Publishing Co., Inc. Reading, Massachusetts.

2. Robinson, M. (1971) "Electrostatic Precipitation in Air Pollution Control" Part I. Ed. W. Strauss, John Wiley & Sons, Inc., New York.

3. Oglesby, S. Jr., and Nichols, G. B. (1970) "A Manual of Electrostatic Precipitator Technology, Part I: Fundamentals" Southern Research Institute, Birmingham, Alabama - Available through NTIS PB 196 381, Part II: Application, August.

4. Robinson, M. (1967) "A Modified Deutch Efficiency Equation for Electrostatic Precipitation" Atmospheric Environment, Pergamon Press, Vol. 1, pp. 193-204.

5. McDonald, J. R. (1978) "A Mathematical Model of Electrostatic Precipitation Vol. 1 Modeling and Programming" EPA-600/7-78 111a, June.

6. Inyushkin, N. V., Averbukh, Y. D. (1962) "Influence of Gas Flow Pressure Conditions on Dust Collection in an Electrical Field" Soviet J. of Non Ferrous Metals, pp. 35-38.

7. Friedlander, S. K. (1959) "Principles of Gas-Solid Separations in Dry Systems" Chemical Engineering Progress Symposium Series No. 25, Vol. 55, pp. 135-149.

8. Williams, J. C., Jackson, R. (1962) "The Motion of Solid Particles in an Electrostatic Precipitator" Proceedings Interactions Between Fluids and Particles, London, pp. 282-288, 3rd Congress of European Federation of Chemical Engineering.

9. Cooperman, P. (1969) "A New Theory of Precipitation Efficiency Central Electricity Research Laboratories" Leatherhead, G. B. Laboratory Note No. RL/L/N, 10/69, June.

10. Bernstein, S. and Crowe, C. T. (1978) "Fundamental Model of Fluid Dynamics Electrostatics and Particle Dynamics for Electrostatic Precipitators" CSIRO Conference on Electrostatic Precipitation, August 23, 24, Leura N.S.W.

11. Crowe, C. T. and Stock, D. E. (1974) "The Effect of Electrodynamic Secondary Flow on the Performance of Electrostatic Precipitator" Proceeding of the 1974 Heat Transfer and Fluid Mechanics Institute, Stanford University Press, pp. 234-265, June.

12. Gosman, A. D. and Pun, W. M. (1973) "Calculation of Recirculating Flows" Lecture Notes, Imperial College of Science and Technology.

13. Robinson, M. (1976) "Effects of the Corona Discharge on the Electric-Wind Convection and Eddy Diffusion in an Electrostatic Precipitator. Health and Safety Laboratory, Energy Research and Development Administration, New York, HASL-301, February.

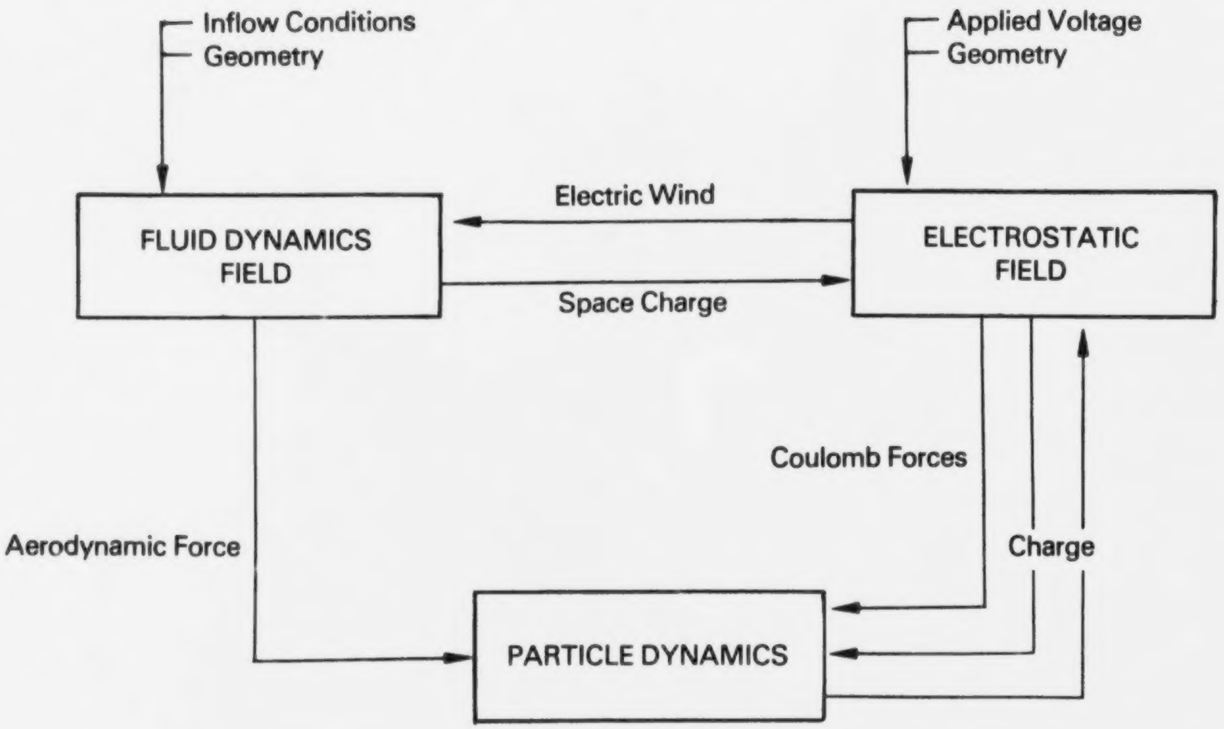

Figure 1. Interactive Phenomena in Electrostatic Precipitators.

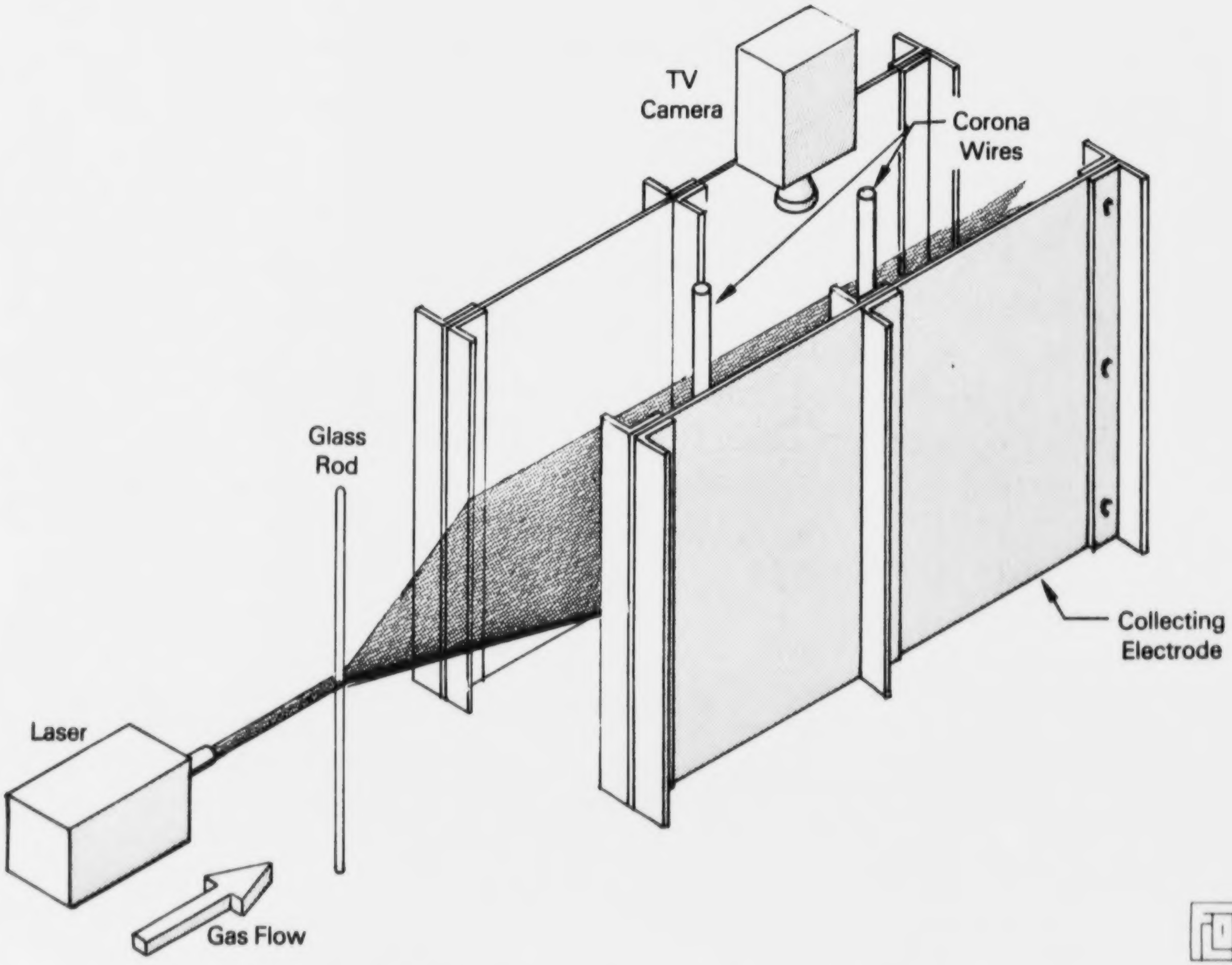

Figure 2. **Experimental Setup in Electrostatic Precipitator Flow Facility.**

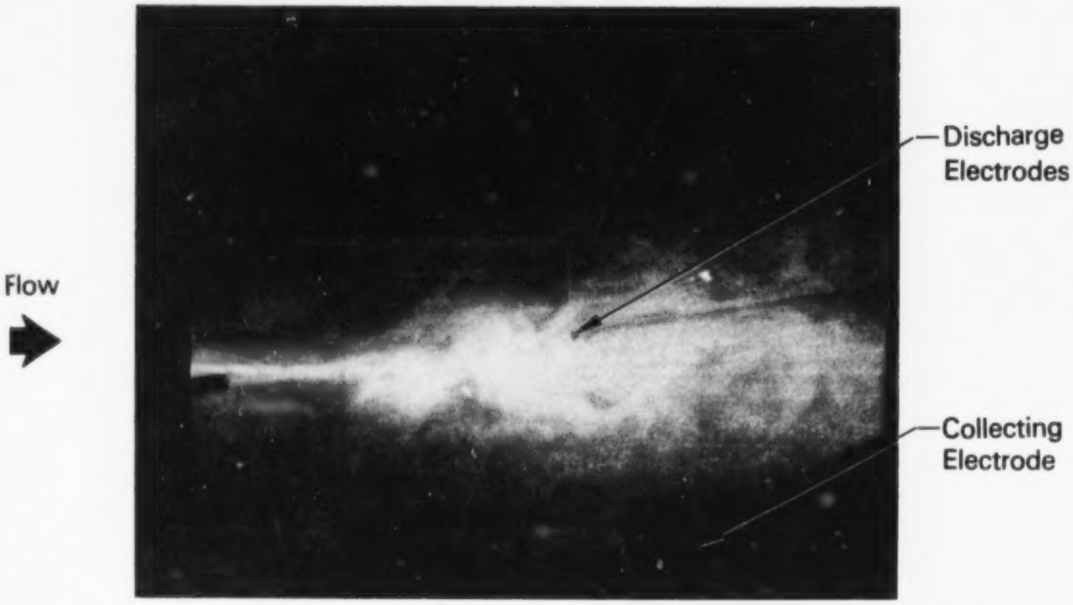

Figure 3. Visualization of Smoke Flow in Wire Plate Precipitator. (u_{ave} = 1.5 ft/sec Plate to Plate Spacing = 9 inches)

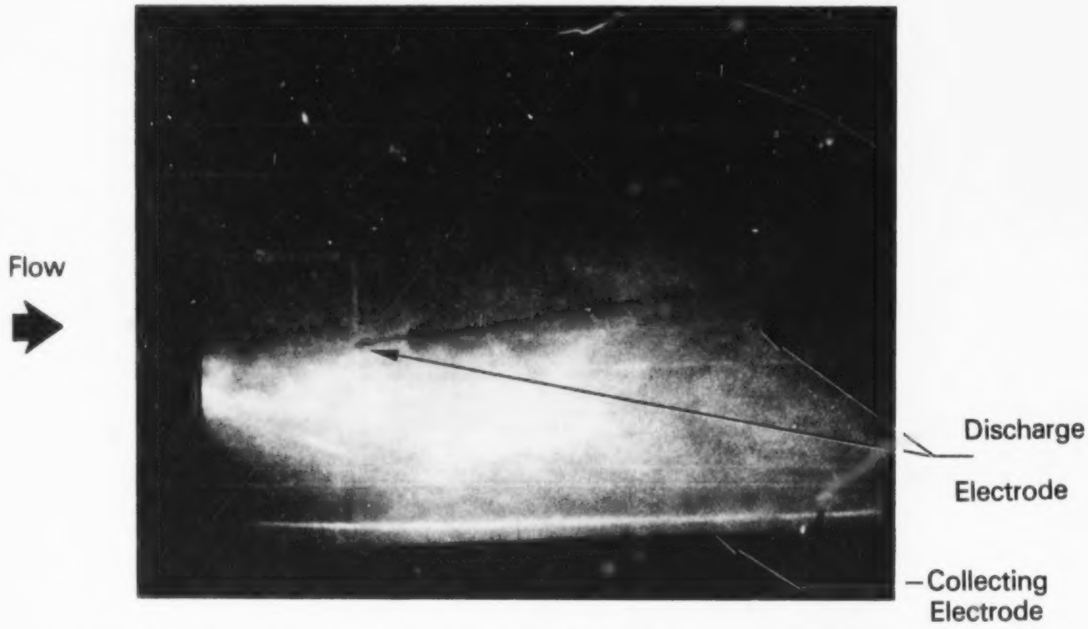

Figure 4. Visualization of Smoke Flow in Wire Plate Precipitator. (u_{ave} = 1.5 ft/sec, Plate to Plate Spacing = 9 inches, Electric Field Intensity = 39 KV and J = 0.5 Milli A/M)

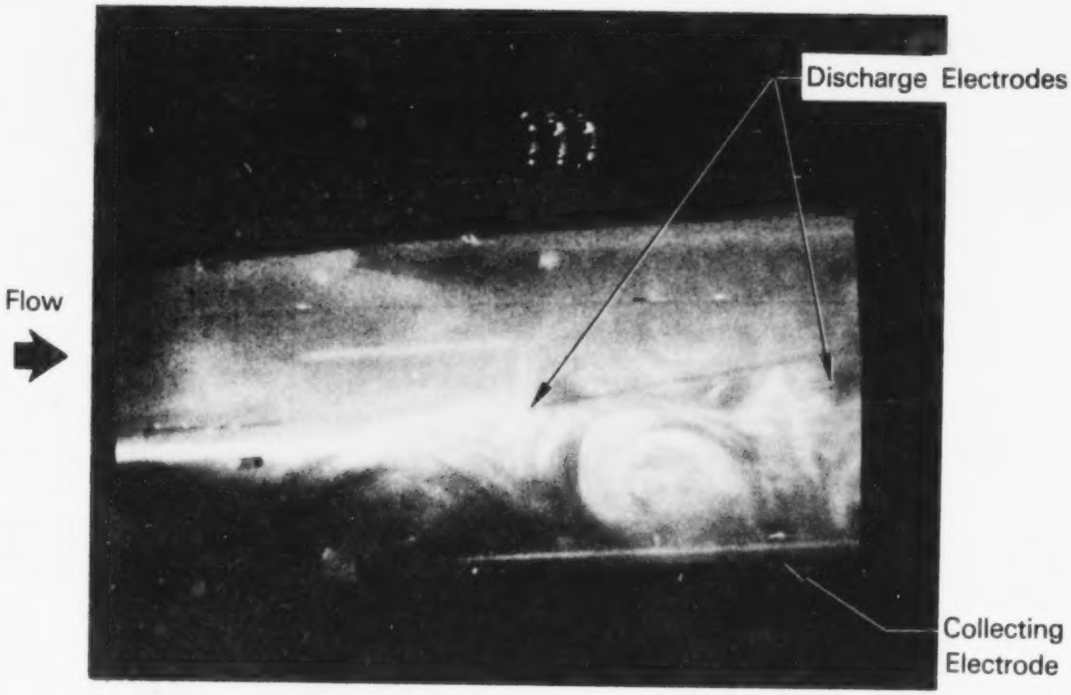

Figure 5. **Visualization of Smoke Flow in a Wire Plate Precipitator. (u_{ave} = 1.5 ft/sec, Plate to Plate Spacing = 9 inches, Electric Field Voltage = 50 KV and J = 0.8 Milli A/M)**

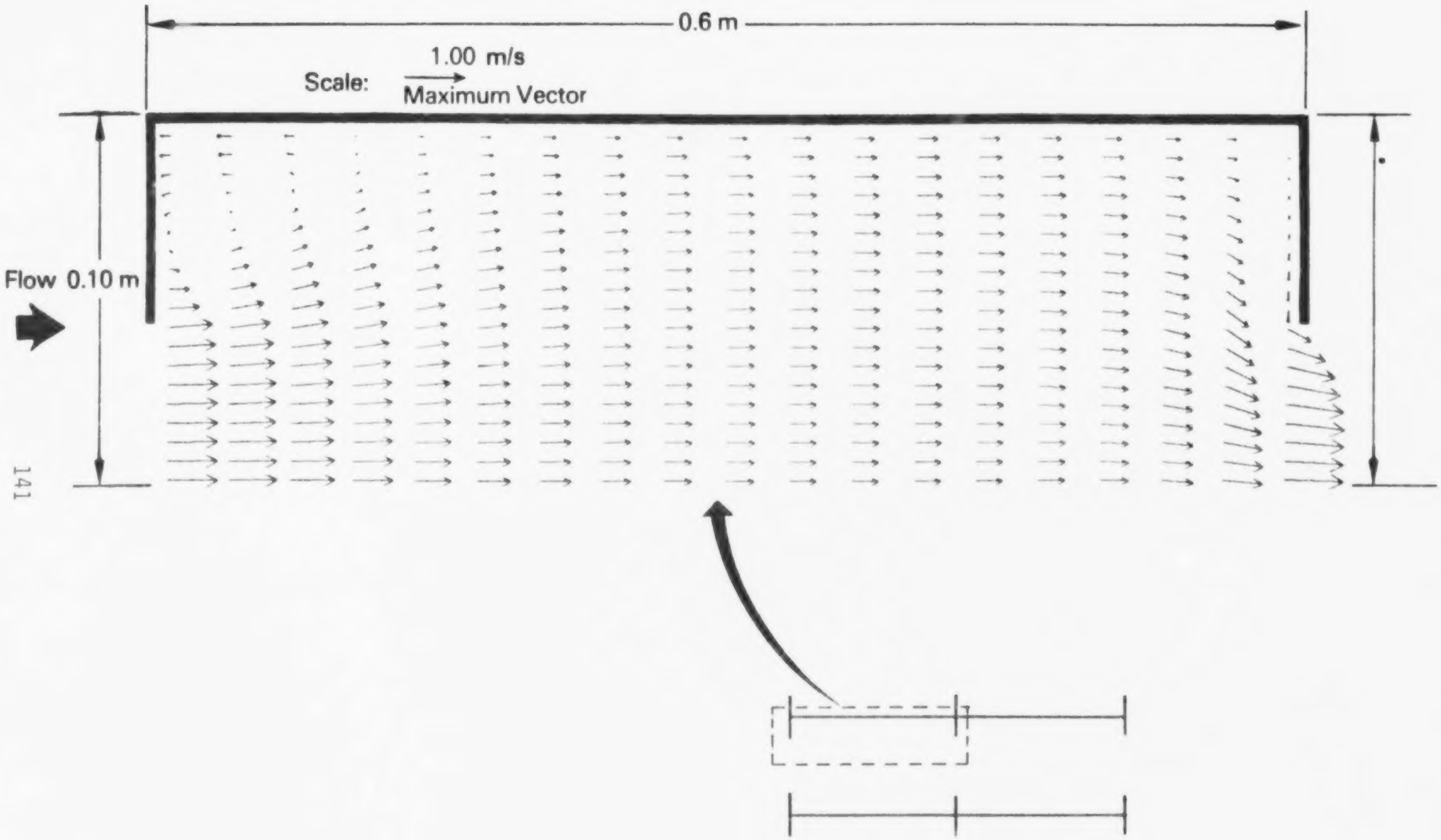

Figure 6. Computed Gas Flow Velocity Near Precipitator Electrode.

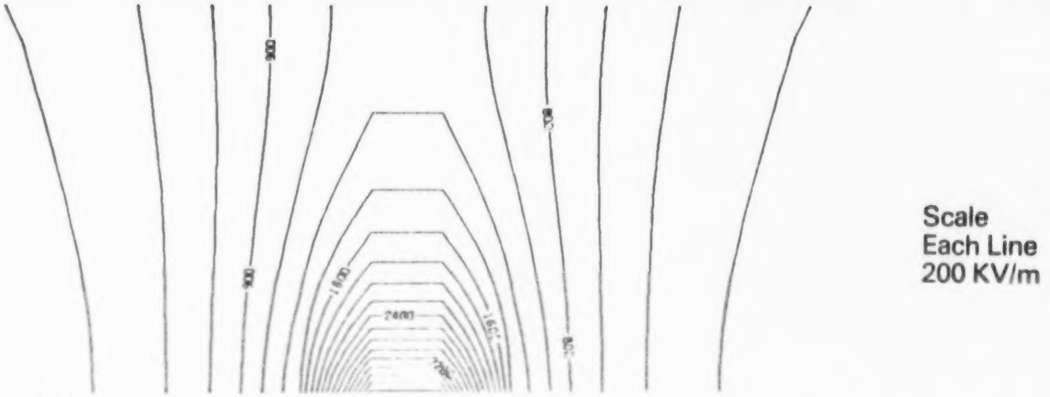

a. Single Discharge Wire.

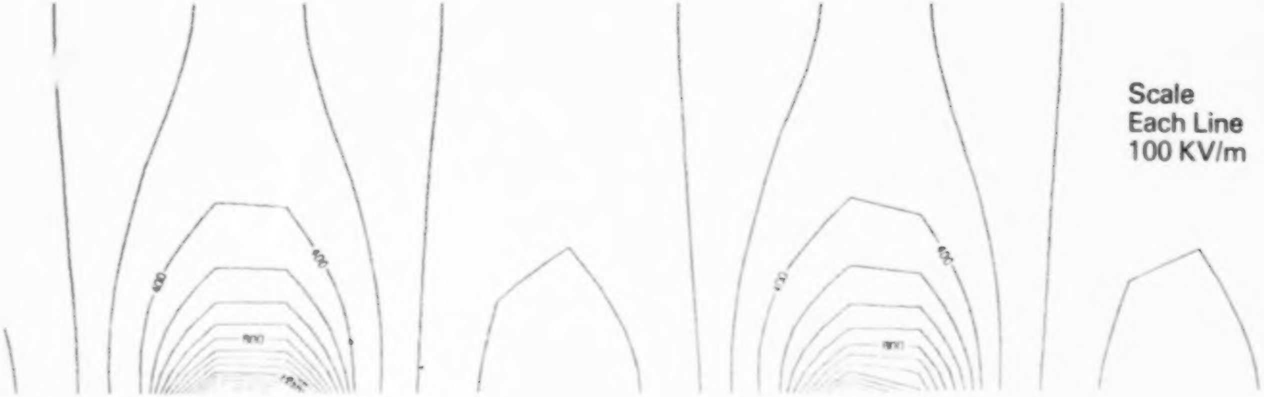

b. Multiple Discharge Wires.

Figure 7. Distribution of Electric Field Intensity in Wire Plate Precipitator.

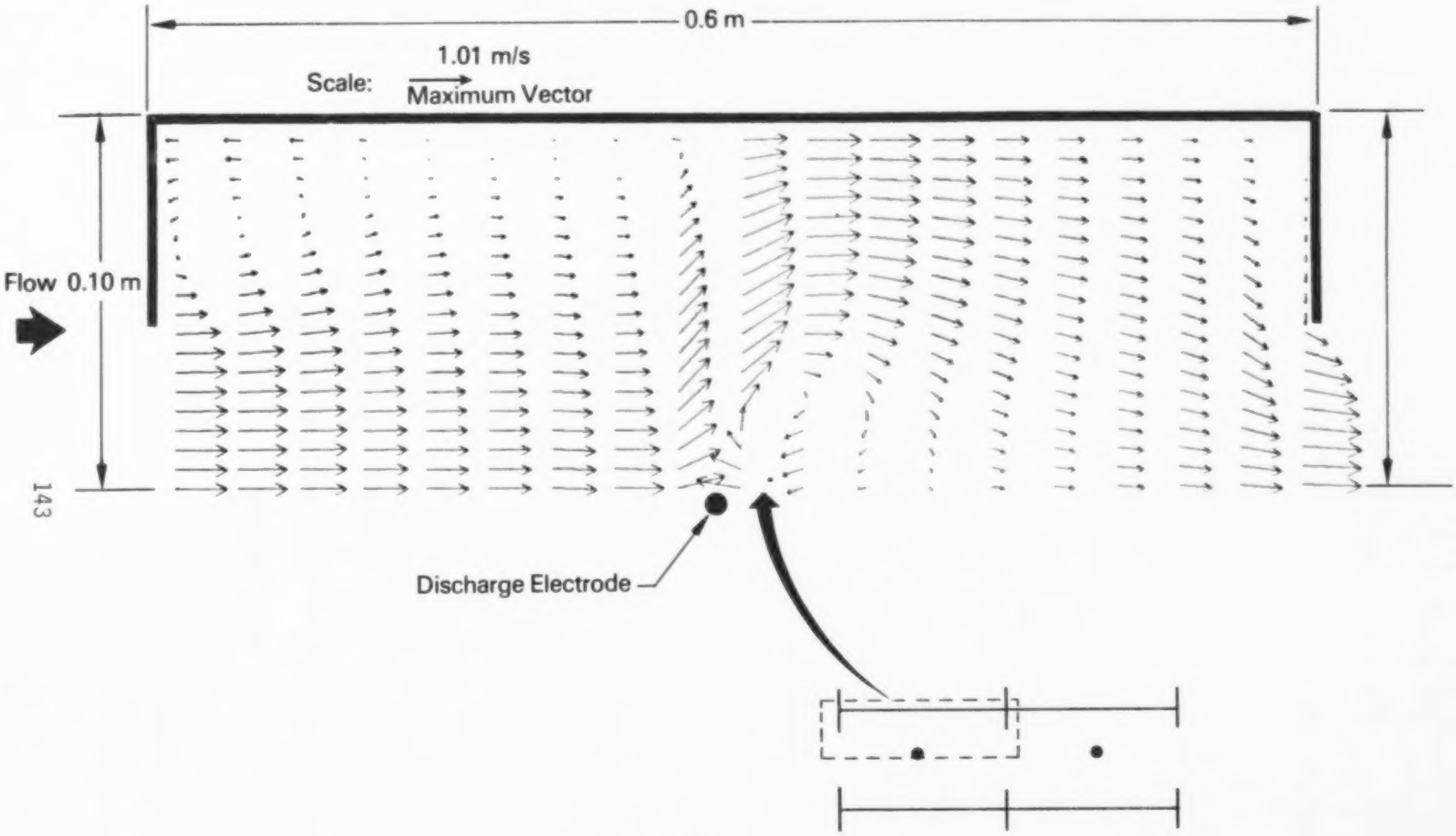

Figure 8. Computed Gas Flow Velocity in Electrostatic Precipitator with a Single Discharge Wire, Average Voltage of 70 KV and Ion Charge Density of 30 Micro C/m^2.

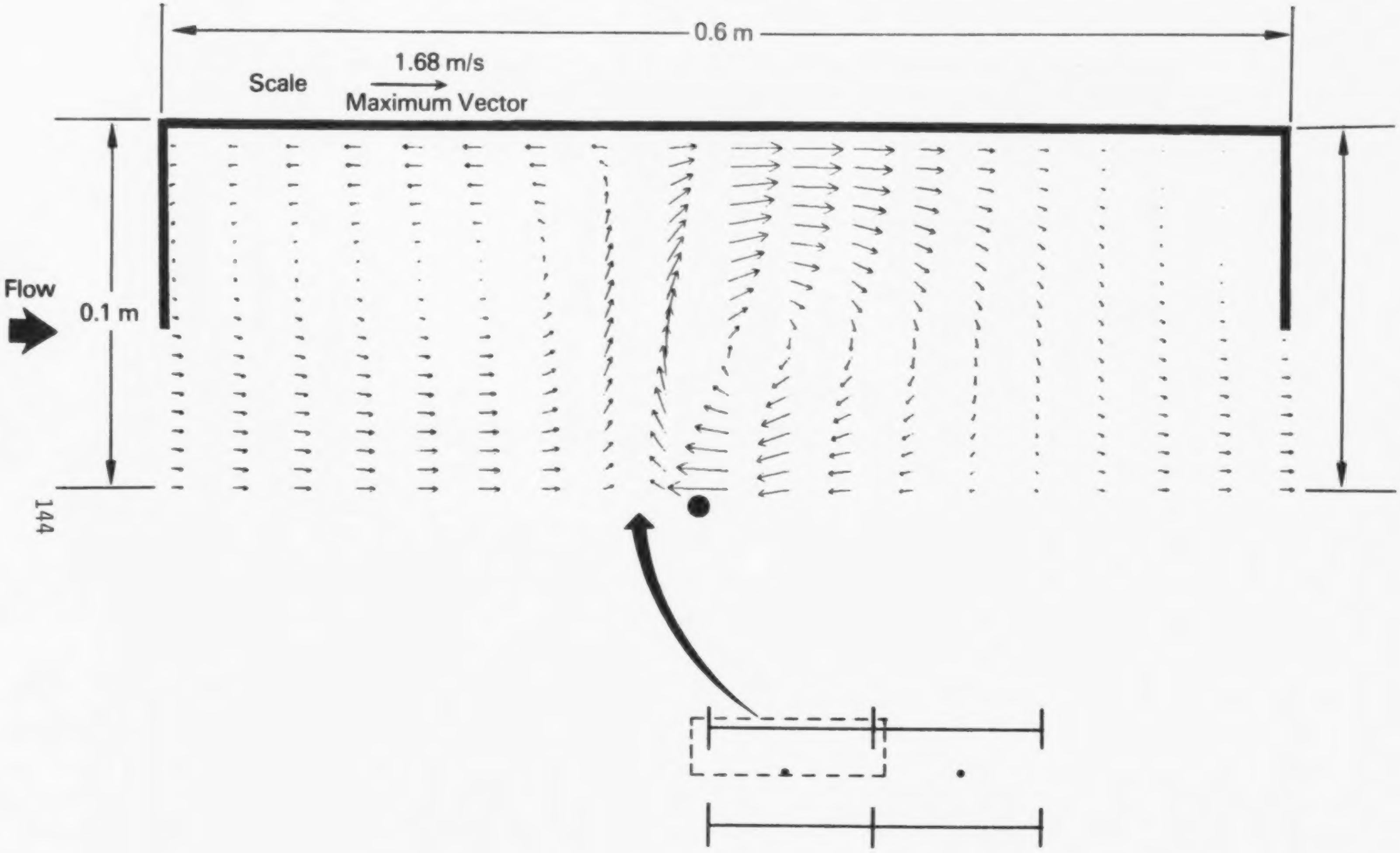

Figure 9. Computed Gas Flow Velocity in Electrostatic Precipitator with Single Discharge Wire, Average Voltage of 80 KV and Ion Charge Density of 45 Micro C/m^2.

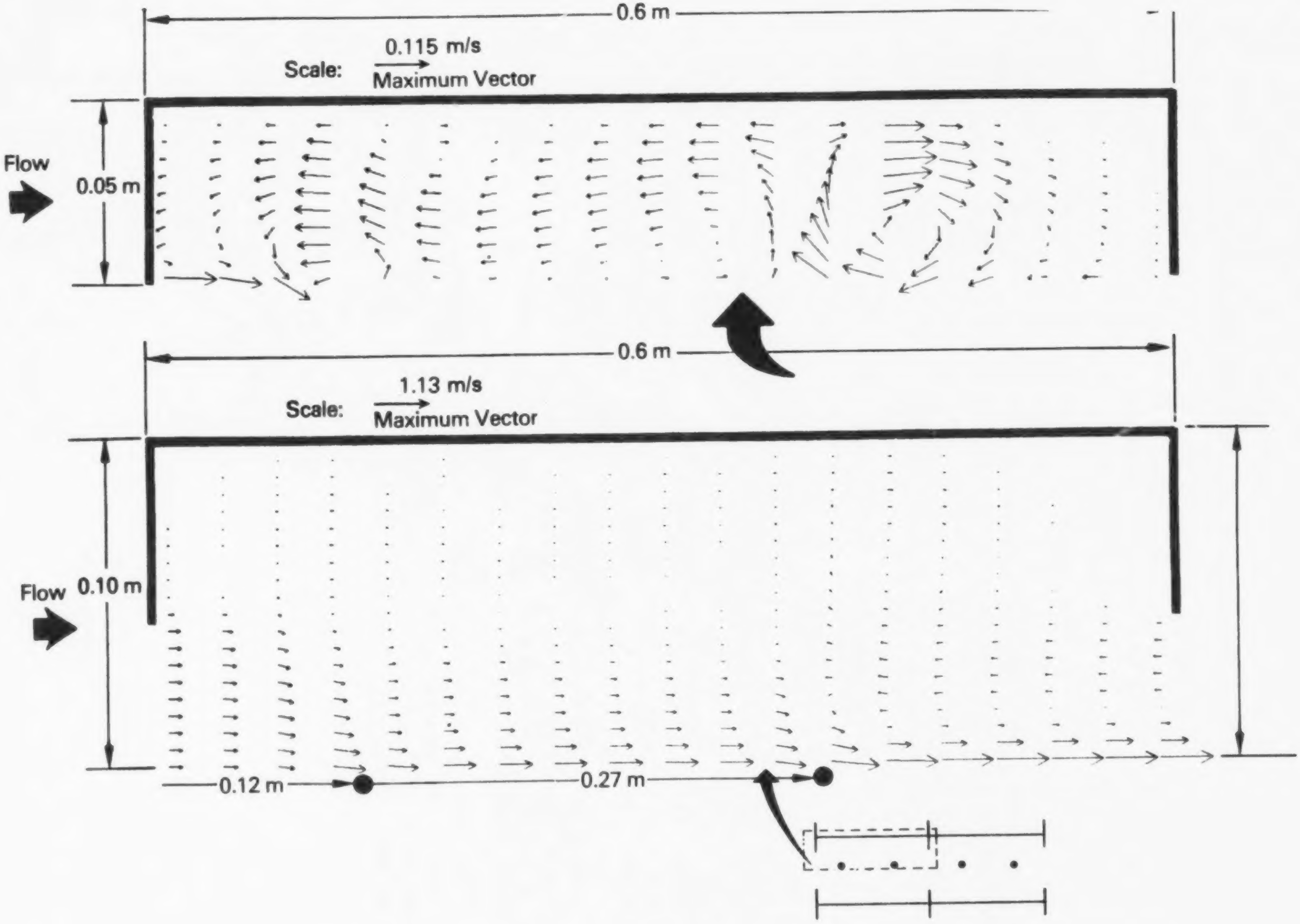

Figure 10. Computed Gas Flow Velocity in Electrostatic Precipitator with Multiple Discharge Wires and Average Voltage of 80 KV Ion Charge Density of 45 Micro C/m^3.

PARTICLE TRANSPORT IN ELECTROSTATIC PRECIPITATORS

G. Leonard, M. Mitchner and S. A. Self
High Temperature Gasdynamics Laboratory
Stanford University
Stanford, California 94305

We discuss the transport of particles in a precipitator due to the combined effects of mobility and eddy diffusion in the gas flow.

For an idealized model of a duct precipitator, the convective diffusion equation is solved analytically for the monodisperse particle concentration $n(x,z)$ as a sum of normal modes which can represent any entrance profile $n(x = 0,z)$. These modes decay exponentially in the flow direction, x, with the lowest (dominant) mode having the slowest decay and, therefore, controlling the efficiency in long ducts.

The dominant mode yields the fractional efficiency formula $\eta = 1\text{-}\exp\text{-}(w_E L/ud)F = 1\text{-}\exp\text{-}(w_E A/Q)F$, which reduces to the Deutsch result when $F = 1$. The multiplier F which is a function of $P_E = (w_E d/D)$, (a measure of the relative effects of migration velocity w_E and diffusivity D) is evaluated for different assumed boundary conditions. It appears that F values significantly greater than unity are possible, particularly for $P_E >> 1$.

Numerical solutions of the convective diffusion equation have also been computed for a uniform entrance profile $n(x = 0,z) = n_o$, which agree with the analytic results and show the entrance profile decaying to the self-similar dominant mode profile for $(w_E A/Q) \gtrsim 1$.

The implication of the results to precipitator performance and design are discussed. In particular, it is argued that the efficiency can be significantly higher than the Deutsch value, and that by improving gas flow quality to minimize turbulence, significant reductions of precipitator length could be achieved.

INTRODUCTION

In a precipitator the charged particles are transported to the collector walls by the combined influences of the Coulomb force due to the electric field and of particle interaction with the flowing gas.

Consider a uniform duct flow of velocity u in the x direction between parallel plates at $z = 0$, $z = d$ across which a uniform field E is maintained (Figure 1), and assume that monodisperse ash of radius a and charge q enters at $x = 0$. This is a good representation of the collection stage of a two-stage precipitator, and a fair representation of a single-stage precipitator if the plane $z = 0$ is taken as the center line of the duct where the high voltage wires are located. If the flow is perfectly laminar, and Brownian motion is neglected, the particles are convected in the x direction at velocity u and migrate in the z direction with velocity w_E given by

$$w_E = \frac{qEC}{6\pi a\mu} , \tag{1}$$

where μ is the viscosity and C is the Cunningham slip factor. Thus the particle trajectories are straight lines and all the entering particles would be collected within a distance $(u/w_E)d$. Also, if the particle concentration at the entrance were uniform, i.e., $n(0,z) = n_o$ say, then the profile is such that $n = n_o$ for $d > z > (w_E/u)x$ and $n = 0$ otherwise (see Figure 2).

If account were taken of Brownian motion with a diffusion coefficient

$$D_B = \frac{\kappa TC}{6\pi a\mu} , \tag{2}$$

where κ is Boltzmann's constant, one would expect a similar result, but with the sharp discontinuities in the concentration profiles rounded out. However for typical precipitator conditions, e.g., $T = 300$ K, $a = 1\ \mu m$, $\mu = 1.8 \times 10^{-5}$ Kg/m·s, we find $D_B \sim 10^{-11}\ m^2/s$, which is so small compared with the value of $w_E d \sim 10^{-2}\ m^2/s$, that the result is indistinguishable from that neglecting Brownian diffusion.

In all practical precipitators the flow is turbulent and the transport of particles is determined by the structure of the fluctuating flow. For flow in smooth-wall ducts the effect of turbulence is usually modeled in terms of an effective eddy diffusivity. This approach, while certainly not exact, often leads to surprisingly accurate representations of turbulent transport processes provided care is taken to avoid the generation of large eddies at the duct entrance.

In the Deutsch model, widely used in the design and evaluation of precipitators, it is assumed that turbulent diffusion and mixing is so dominant that the concentration profile is maintained uniform in the core flow, and the particles migrate across the boundary layer with the velocity w_E. A simple analysis[1] then leads to the following exponential decay of concentration in the flow direction:

$$n(x) = n(0) \exp - (\frac{w_E x}{ud}). \tag{3}$$

This leads to the Deutsch-Anderson efficiency formula

$$\eta = 1 - \frac{n(L)}{n(0)} = 1 - \exp(\frac{w_E L}{ud}) = 1 - \exp - (\frac{w_E A}{Q}), \tag{4}$$

where L is the duct length, A is the plate area and Q the volumetric gas throughput.

It should be noted that eq. (3) applies only to a single size class of particles having a given migration velocity w_E, so that eq. (4) refers to the fractional efficiency for a given size class. The overall mass efficiency must be obtained by appropriate integration over the prevailing distribution.

The Deutsch model has been widely used both in computer codes[2] for predicting performance and for characterizing the performance of precipitators in terms of an effective migration velocity determined from efficiency measurements and the use of eq. (4) assuming A and Q are known.

It is often stated in the literature that the effective migration velocity, so measured, is commonly found to be significantly lower than calculated from eq. (1), assuming that q and E are known either from theory or measurements. This leads to the viewpoint that the Deutch efficiency is the theoretical maximum value that precipitators are capable of attaining.

However, comparisons[3] of the measured fractional efficiencies on a number of power plant precipitators with computations from the SRI model[2] show that in the size range ~0.1 - 1 μm, where the efficiency minimum normally lies, the measured efficiencies (and migration velocities) are substantially higher than those computed. This is unexplained, and suggests a deficiency in the Deutsch model. Furthermore, the superior performance of precipitators with plate spacings significantly greater than the conventional value,[4] is also inexplicable on the basis of the Deutsch model.

The foregoing observations support the view that the Deutsch model is deficient and suggest that a more exact treatment of the precipitation process might lead not only to better performance predictions, but also to prescriptions for improving the efficiency above the Deutch value (or equivalently making smaller precipitators for the same efficiency).

A brief review of earlier treatments of the effect of turbulent diffusion on precipitation has been given by Robinson.[5]

MATHEMATICAL MODEL

We assume that for the model of Figure 1, the time-average gas velocity u is uniform but that there are turbulent fluctuations of gas velocity in the x and z directions. The particles are assumed to follow the instantaneous gas velocity, without slip, except for the steady, uniform migration velocity w_E relative to the gas in the z-direction.

Taking the time-average of the instantaneous continuity equation for the particles yields:

$$u \frac{\partial n}{\partial x} + w_E \frac{\partial n}{\partial z} + \frac{\partial \overline{n'u'_x}}{\partial x} + \frac{\partial \overline{n'u'_z}}{\partial z} = 0 \tag{5}$$

Here u'_x, u'_z are the fluctuating components of gas velocity in the x and z directions and n' is the fluctuating component of the particle concentration. The overbars represent time-averages of the associated products.

In eq. (5) the first two terms represent the divergences of the particle fluxes due to steady motion in the x and z directions, while the last two terms represent the divergences of the fluxes due to turbulent transport in these directions. We model the latter two terms in the conventional way, by introducing the concept of an eddy diffusivity D. Thus we put:

$$\overline{n'u'_x} = -D \frac{\partial n}{\partial x}; \quad \overline{n'u'_z} = -D \frac{\partial n}{\partial z}. \tag{6}$$

Assuming that D is isotropic and uniform, eqs. (5) and (6) can be combined to obtain the convective diffusion equation:

$$u \frac{\partial n}{\partial x} + w_E \frac{\partial n}{\partial z} - D \left(\frac{\partial^2 n}{\partial x^2} + \frac{\partial^2 n}{\partial z^2}\right) = 0. \tag{7}$$

The net particle velocity in the z direction due to both the electric force and turbulent diffusion, can then be written

$$w = w_E - \frac{D}{n} \frac{\partial n}{\partial z} . \tag{8}$$

Equation (7) is to be solved for $n(x,z)$ subject to boundary conditions to be specified at $z = 0$ and $z = d$, as well as an entrance profile $n(x = 0,z)$. Having solved for $n(x,z)$, then eq. (8) leads directly to $w(x,z)$, and hence to the net particle flux to the wall, nw.

To this point the problem is well posed and, subject to the assumptions stated, an exact mathematical representation of the idealized model. Also, in general, analytic solutions of eq. (7) are readily found by the standard technique of separation of the variables.

Examination of eq. (7) shows that the problem involves two dimensionless parameters, which may be taken as (w_E/u) and

$$P_E = \frac{w_E d}{D} . \tag{9}$$

The latter is a measure of the relative strengths of external force and diffusion on particle transport. The limit $P_E \to 0$ corresponds to the Deutsch hypothesis of infinitely rapid turbulent mixing. The dimensionless group P_E is commonly called the Peclet number. Here P_E is based on the electric migration velocity, and will be called the electric Peclet number.

Boundary Conditions

The principal problem in proceeding further relates to the specification of reasonable boundary conditions at the walls $z = 0$ and $z = d$, that are justifiable on the basis of the physics involved. For simplicity, we assume that re-entrainment due to bouncing, saltation or other effects is negligible, so that the collector wall(s) acts as a perfect sink. This would certainly be true for a wet wall precipitator.

Now the standard boundary condition for the diffusion equation at a boundary acting as a perfect sink, that is used in theories of molecular diffusion, ambipolar diffusion of charged particles in gas discharges, and neutron diffusion in reactors, is that the concentration is zero $(n = 0)$ at such a wall. In such cases, the diffusion coefficient is assumed constant up to the wall, or at least to within one mean free path of the wall. However, in the case of particle deposition in turbulent duct flows, the turbulent diffusivity falls to zero through the laminar sublayer, and if one assumes constant D up to the wall, with the boundary condition $n = 0$, then the calculated deposition rate due to turbulence alone is several orders of magnitude higher than that observed experimentally.[6-8] Effectively, the gas flow in the near-wall region acts as a barrier to particle diffusion.

In this circumstance there are two procedural choices. The first is to solve the convective diffusion equation with a non-constant $D(z)$ which models the effective diffusivity. This requires numerical solution. The second is to retain $D(z) = \text{constant}$ and use a modified boundary condition based on an analysis of the near-wall region. This second approach, which we follow here, has the advantage of allowing analytic solutions.

Thus we assume that $D = \text{constant}$ throughout the region up to a distance $z = (d - \varepsilon)$ where $\varepsilon << d$, and apply at this position a generalized boundary condition

$$c \frac{\partial n}{\partial z} + n = 0 \tag{10}$$

[redacted]

Here, c is a constant with dimensions of length which is determined by an analysis of the near wall region. Clearly, in the limit $c \rightarrow 0$, we recover the boundary condition $n = 0$, while in the limit $c >> d$ we obtain the boundary condition $n' \rightarrow 0$.

In the analysis which follows, we derive particular solutions for the two limiting cases $n = 0$ and $n' = 0$, and it is clear that all possible solutions fall between these two limits. The analysis of the near-wall region given in the appendix shows that for particle deposition from turbulent flows, the appropriate boundary condition lies close to the latter one, i.e. $n' = 0$.

The boundary condition to be applied at $z = 0$ is more straightforward. If $z = 0$ represents the central plane of a single stage wire-plate precipitator, symmetry requires that the z-directed flux at this point be zero, which, from eq. (8), yields

$$\frac{\partial n}{\partial z} - \frac{w_E}{D} n = 0 \qquad \text{at } z = 0 \,. \tag{11}$$

This condition will also be applicable to a two-stage precipitator with the plane $z = 0$ being the electrode which repels charged particles.

Analytic Solution

We assume that in eq. (7) $n(x,z)$ is separable in the form

$$n(x,z) = X(x)\, Z(z). \tag{12}$$

Substitution in (7) and division by XZ then yields

$$\left[u \frac{X'}{X} - D \frac{X''}{X}\right] + \left[w_E \frac{Z'}{Z} - D \frac{Z''}{Z}\right] = 0 \,. \tag{13}$$

Since the first term is a function of x only, and the second of z only, they must each be equal to a constant $\pm K$ (say), and we have

$$D \frac{d^2X}{dx^2} - u \frac{dX}{dx} - KX = 0 \,, \tag{14}$$

and

$$D \frac{d^2Z}{dz^2} - w_E \frac{dZ}{dz} + KZ = 0 \,, \tag{15}$$

where the separation constant K, which has dimensions of inverse time, is to be determined by the boundary conditions, i.e., it is an eigenvalue problem.

Equations (14) and (15) have solutions of the form

$$X = X_o \exp \alpha x \quad ; \quad \alpha = \frac{u}{2D}\left[1 \pm (1 + 4\frac{DK}{u^2})^{1/2}\right], \tag{16}$$

$$Z = Z_o \exp \beta z \quad ; \quad \beta = \frac{w_E}{2D}\left[1 \pm (1 - \frac{4DK}{w_E^2})^{1/2}\right] . \tag{17}$$

We seek solutions of (16) with α real, negative, corresponding to exponential decay in the flow direction. This requires

$$\frac{4DK}{u^2} > 0 \ , \quad \text{i.e., } K \text{ real positive} . \tag{18}$$

There are two roots for α, one positive, which we discard, and one negative, which we use.

Thus (16) yields for the x dependence

$$n(x) \propto \exp - \frac{u}{2D}\left[(1 + \frac{4DK}{u^2})^{1/2} - 1\right] x . \tag{19}$$

For the transverse dependence, we seek solutions of (17) with β complex, so as to yield solutions that can satisfy arbitrary boundary conditions at $z = 0,d$. Thus we require

$$\frac{4DK}{w_E^2} > 1 \ , \tag{20}$$

which is consistent with (19) and requires K real and $> w_E^2/4D$. Then we have two roots for β, and the z dependence has the form:

$$n(z) \propto \left\{\exp \frac{w_E z}{2D}\right\} \begin{matrix}\cos \\ \sin\end{matrix} \left\{\frac{w_E z}{2D}\left(\frac{4DK}{w_E^2} - 1\right)^{1/2} z\right\} . \tag{21}$$

The imposition of boundary conditions at $z = 0,d$, will yield a set of eigenvalues K_m and corresponding eigenfunctions which form a complete orthonormal set of modes. Any given entrance profile $n(x = 0,z)$ can be expanded in terms of this set, and each component mode will decay exponentially in the x direction, according to eq. (19) at different rates, so that the profile changes with x. For large x, the profile will tend to that of the fundamental mode, i.e., that having the smallest eigenvalue K_m, since it will decay most slowly. Defining

$$\theta_m \equiv \frac{w_E d}{2D}\left(\frac{4DK_m}{w_E^{\,2}} - 1\right)^{1/2} = \frac{P_E}{2}\left(\frac{4DK_m}{w_E^{\,2}} - 1\right)^{1/2} , \qquad (22)$$

and

$$F_m\left(\frac{w_E}{u}, P_E\right) \equiv \left(\frac{u}{w_E}\right)^2 \frac{P_E}{2}\left\{\left[1 + \left(\frac{w_E}{u}\right)^2\left[1 + \left(\frac{2\theta_m}{P_E}\right)^2\right]\right]^{1/2} - 1\right\} , \qquad (23)$$

the general solution to eq. (7) for $n(x,z)$ can be written:

$$n(x,z) = \sum_m \left\{\exp - \left(\frac{w_E x}{ud}\right) F_m\right\}\left\{\exp\left(\frac{P_E}{2}\,\frac{z}{d}\right)\right\}\left\{A_m \cos\left(\theta_m \frac{z}{d}\right) + B_m \sin\left(\theta_m \frac{z}{d}\right)\right\} . \qquad (24)$$

Here A_m, B_m are constants whose ratio is determined by the boundary conditions at $z = 0$, d, and whose magnitude is determined by the entrance condition $n(x = 0, z)$.

It will be recognized that the x-dependence in eq. (24) reduces to that of the Deutsch model, eq. (3), for $F_m = 1$. Thus our solution (24) generalizes the Deutsch result by representing n as a sum of modes with "Deutsch-like" exponential x-dependences, modified by the factors F_m which are functions of the two basic parameters (w_E/u) and $P_E = w_E d/D$. The exact forms of these factors, as well as the transverse profiles of the modes, depend on the boundary conditions at $z = 0,d$ through the eigenvalues θ_m.

Application of Boundary Conditions - Particular Solutions

In the following, we evaluate the general solution (24) for two particular cases. In each case we take the boundary condition at $z = 0$ as eq. (11). For the boundary condition at $z = d$, we take the two limiting cases $n = 0$, and $n' = 0$ corresponding respectively to taking $c = 0$ and $c \to \infty$ in eq. (10). These two cases bracket all intermediate boundary conditions corresponding to intermediate values of c (positive).

Application of the boundary condition at $z = 0$ leads to

$$A = \frac{P_E}{2}\,\theta B . \qquad (25)$$

Application of the first boundary condition $(n = 0)$ at $z = d$ yields

$$A = -B \tan \theta \cdot \tag{26}$$

Hence, from eqs. (25) and (26), the θ_m values are given by the roots of

$$\tan\theta = -\frac{2\theta}{P_E} . \tag{27}$$

Application of the second boundary condition $(n' = 0)$ at $z = d$ yields, in place of (26)

$$A \left[1 - \left(\frac{2\theta}{P_E}\right) \tan\theta\right] + B \left[\tan\theta + \left(\frac{2\theta}{P_E}\right)\right] = 0 . \tag{28}$$

From eqs. (25) and (28) we have θ_m given by the roots of

$$\tan\theta = \frac{-2 \left(\frac{2\theta}{P_E}\right)}{1 - \left(\frac{2\theta}{P_E}\right)^2} \tag{29}$$

instead of (27).

For either boundary condition, the transverse eigenmodes are of the form

$$n(z) = C_m \left\{\exp\left(\frac{P_E}{2} \frac{z}{d}\right)\right\} \left\{\left(\frac{2\theta}{P_E}\right)\cos\left(\theta_m \frac{z}{d}\right) + \sin\left(\theta_m \frac{z}{d}\right)\right\} , \tag{30}$$

where the C_m are constants determined by the entrance profile $n(x=0,z)$.

The nature of the roots θ_m of the alternative eqs. (27) and (29) is best seen by inspection of the graphical solutions shown schematically in Figures 3. In either case the root $\theta = 0$ is excluded.

Referring to Figure 3(a) for the first case $(n = 0)$, it is seen that the set of roots are bracketed by the inequalities

$$\pi/2 < \theta_1 < \pi ,$$

$$3\pi/2 < \theta_2 < 2\pi ,$$

$$(2m - 1)\frac{\pi}{2} < \theta_m < m\pi .$$

It may be noted that for $P_E \gg 1$, they tend to their lower limits. Also with increasing m, the roots tend to their lower limits. The first root θ_1 (for the dominant mode) is shown as a function of P_E in Figure 4.

Referring to Figure 3(b) for the second case $(n' = 0)$, it is seen that the situation is similar, but complicated by the pole in the right-hand side of eq. (29) at $\theta = (P_E/2)$. In general, if $(2p - 1)\pi/2 < (P_E/2) < (2p + 1)\pi/2$, the first p roots occur for $(2m - 1)\pi/2 < \theta_m < m\pi$, and higher roots $(m > p)$ occur for $(m - 1)\pi < \theta_m < (2m - 1)\pi/2$. The first root θ_1 (for the dominant mode) is shown as a function of P_E in Figure 4.

The Dominant Mode

The transverse concentration profiles $n(z)$ for the dominant mode calculated from eq. (30) are shown for the boundary condition $n = 0$, in Figure 5 for several values P_E. It is seen that when P_E is large there are relatively few particles in the inner region (where in eq. (30) the exponential factor dominates) and there is a pronounced peak in concentration close to the wall. From eq. (8) it is clear that the average particle velocity w is smaller than w_E inside the peak, and greater than w_E between the peak and the wall. As P_E decreases, the relative concentration at the center increases, the maximum is broader and moves towards the center. For small values of P_E the concentration approaches a monotonically decreasing function of z.

The transverse concentration profiles $n(z)$ for the dominant mode are shown for the boundary condition $n' = 0$ in Figure 6. In contrast to those discussed above, the profiles increase monotonically to a maximum at the wall. They show the same general dependence on P_E as the previous case and for small P_E approach the uniform profile assumed in the Deutch model. Note that $w < w_E$ everywhere except at the wall where $w = w_E$.

Of more engineering significance is the dependence of the axial concentration profile, since this determines precipitator efficiency. Of particular interest is the factor F_1, for the dominant mode, multiplying the exponent in the modified Deutch equation (24), and its functional dependence on the parameters (w_E/u) and P_E for the two cases.

From eq. (23) we have

$$F_1\left(\frac{w_E}{u}, P_E\right) \equiv \left(\frac{u}{w_E}\right)^2 \frac{P_E}{2} \left\{\left[1 + \left(\frac{w_E}{u}\right)^2 \left[1 + \left(\frac{2\theta_1}{P_E}\right)^2\right]\right]^{1/2} - 1\right\} . \qquad (31)$$

The functions $F_1(P_E)$ for the alternative boundary conditions are shown in Figure 7 for the case $(w_E/u) = 0.1$. For conditions of interest F_1 is a very weak function of (w_E/u).

In the laminar limit $P_E \to \infty$ both functions tend to infinity as $(P_E/4)$. For P_E decreasing from large values, down to at least $P_E \approx 10$, where $F_1 \approx 3$, both functions can be approximated by

$$F_1 \approx \frac{P_E}{4}\left[1 + \left(\frac{2\theta_1}{P_E}\right)^2\right]; \qquad (P_E \gg 1). \qquad (32)$$

For still smaller values of P_E (increasing diffusivity) the two functions diverge.

For the boundary condition $n = 0$, F_1 decreases to a minimum of $F_1 \approx 2.3$ at $P_E \approx 3$, and then increases again, eventually approaching the value

$$F_1 \to \pi^2/(4\ P_E) \qquad (33)$$

for

$$1 \gg P_E \gg (w_E/u)^2\ . \qquad (34)$$

Equation (33) leads to an efficiency

$$\eta_1 \to 1 - \exp-\left(\frac{\pi^2}{4}\ \frac{DL}{ud^2}\right), \qquad (35)$$

which does not involve w_E. In this limit, the boundary condition $n = 0$ predicts a (mechanical) efficiency which is very much larger than measured. For instance, putting $D = 150\nu = 2.2 \times 10^{-3}\ m^2/s$, a typical value of momentum diffusivity for fully developed duct flow in air at Reynolds numbers of interest[9], and with $d = 0.1$ m, $L/d = 50$, we find a mechanical efficiency of $\eta_1 \sim 75\%$, which is unrealistically high in the absence of electrical effects.

In contrast, for the boundary condition $n' = 0$, as P_E decreases, F_1 decreases monotonically to unity; specifically, for condition (34), we have

$$F_1 \to 1. \qquad (36)$$

This is the Deutsch limit corresponding to very large diffusivity which, with the boundary condition $n' = 0$ gives a uniform profile (see Figure 6 as P_E becomes small). In this limit, as $w_E \to 0$, the mechanical efficiency is predicted to be zero.

While, in practice, the mechanical efficiency is non-zero, it is very much smaller than given by eq. (35) for the boundary condition $n = 0$ and for precipitator applications the boundary condition $n' = 0$ is much closer to the correct one. Solutions for other boundary conditions, for intermediate values of c in eq. (10) will give results lying between those for the two limiting cases discussed above. In practice for precipitator calculations, we may use the results for the boundary condition $n' = 0$, being assured that it yields a (slightly) conservative value for F_1.

A most important result of the analysis of the dominant mode, given above, is that when account is taken of a finite particle diffusivity through the Peclet number $P_E = (w_E d/D)$, then the self-similar concentration profile which is established in ducts with $(L/d) >> 1$, has a minimum at the center and a maximum at the collector wall. Only in the limit $P_E \to 0$ (infinite diffusivity) does one recover the Deutsch result of a uniform profile. The larger is the Peclet number (the smaller the diffusivity), the steeper is the concentration profile. This is because migration in the electric field is causing particles to pile up near the collector and back diffusion has only a weak influence in counteracting this effect.

At the same time, the efficiency for the dominant mode is given by a Deutsch-like formula with a factor $F_1 (P_E)$ multiplying the exponent. The factor F_1 tends to unity in the Deutsch limit $P_E \to 0$ (infinite diffusivity) as it should. However, for non-zero P_E (finite diffusivity) the factor F_1 is greater than unity, and increasingly so as P_E becomes large (the laminar limit $P_E \to \infty$).

Physically, the reason for the increase of efficiency over the Deutsch value can be seen as follows. For the Deutsch model $n(z)$ is constant and equal to the mean value $\bar{n}$, while the migration velocity (from eq. (8)) everywhere equals w_E. Thus the flux to the walls is $\bar{n}\, w_E$. On the other hand, for non-zero P_E, when the concentration is higher at the wall than in the center, we have $n(d) > \bar{n}$. However, at the wall, with the boundary condition $n' = 0$, the migration velocity is still $w = w_E$, so that the flux to the wall is $n(d) w_E > \bar{n}\, w_E$. Thus for a given throughput of ash at a given duct location x, the piling up of ash near the wall with finite diffusivity causes a corresponding increase in precipitation rate, relative to the Deutsch model for infinite diffusivity.

Entrance Region Effects - Numerical Solutions

The analysis detailed above, in terms of a normal mode expansion is valuable in that the dominant mode gives the limiting efficiency for a precipitator of large (L/d) for any entrance profile. However, to find a complete solution for an arbitrary entrance profile $n(x = 0,z)$, this profile must be expanded in the complete set of normal modes and the total solution found by summing the contributions of all the modes. The higher modes decay more quickly than the dominant mode and, as a result, an arbitrary entrance profile will gradually be transformed into the self-similar profile of the dominant mode, as the flow progresses down the duct.

As an alternative to this analytic procedure, we have solved the two-dimensional convective diffusion equation numerically for the case of a uniform entrance profile

$$n(0,z) = n_o \text{ (constant)} \tag{37}$$

so as to investigate the entrance region effects.

In the analysis above, it was noted that F_1, and hence the dominant mode efficiency, is insensitive to the parameter (w_E/u) for typical conditions of interest. It can be shown that this is equivalent to saying that the axial transport of particles due to turbulent diffusion is negligible compared with that due to convection by the gas velocity u. Therefore, at this point we neglect the term in $(\partial^2 n/\partial x^2)$ in eq. (7), which removes the dependence on (w_E/u).

The resulting equation is solved subject to the boundary conditions eq. (10) (with $c \to \infty$, i.e. $n' = 0$), eq. (11) and the entrance profile eq. (37). The problem is solved numerically by a Crank-Nicholson finite difference scheme in the domain $(x = 0,L)$, $(z = 0,d)$. Once the solution for $n(x,z)$ is found, the penetration is evaluated from the formula

$$P = \int_0^d u\, n\,(L,z)\, dz \Big/ \int_0^d u\, n\,(0,z)\, dz\,, \tag{38}$$

and the efficiency is then given by

$$\eta(L) = 1 - P\,. \tag{39}$$

The problem has two independent dimensionless parameters, namely $P_E \equiv (w_E d/D)$ and

$$\frac{w_E L}{ud} = \frac{w_E A}{Q}\,. \tag{40}$$

The latter is the dimensionless precipitator length which appears as the exponent in the Deutsch-Anderson efficiency formula, eq. (4).

Figure 8 shows the computed efficiency as a function of $(w_E A/Q)$ for various values of P_E. On a logarithmic plot the Deutsch equation $(P_E \to 0)$ plots as a straight line through the origin. The solid lines for various finite values of P_E start off asymptotic to the Deutsch line (as they should because the profile is initially flat) and then bend up, becoming asymptotic to straight lines having a slope F_1 times the slope of the Deutsch line when the profile becomes that of the dominant mode. The laminar limit $(P_E \to \infty)$ is also shown and shows $\eta \to 100\%$ for a finite length $L = ud/w_E$. Also shown for reference, as broken lines through the origin, are the efficiencies for the same P_E values, which would apply if the entrance profile were that of the appropriate dominant mode.

It is clear from Figure 8 there is an effective entrance region where the profile develops from the flat entrance one to that of the dominant mode. The length of this entrance region increases with P_E; for instance for $P_E \approx 10$, it corresponds approximately to a normalized length $(w_E A/Q) \approx 1$, or about $L \approx 1$ m for typical conditions. Past this entrance region, additional lengths should yield the full efficiency enhancement due to the multiplier F_1 in the Deutsch exponent.

CONCLUSION

In evaluating the practical significance of the analytical and numerical results derived above, the most important question is what values of turbulent diffusivity D, and hence P_E can be expected in practice.

For the best case, assuming a smooth wall duct with well-engineered entrance conditions, so that there are no large-scale eddies and a low level of turbulence, and assuming that ion wind effects produce a negligible degradation of the flow quality, then we shall have a developing boundary layer flow in the front end of the duct which will evolve into a fully developed duct flow for large x/d. Thus we may take the value of eddy diffusivity established[8] for fully developed duct flow as a standard measure of D that might reasonably be expected to apply if care is taken to maintain good flow quality.

For fully developed pipe flow in the range of Reynolds numbers of interest, the eddy diffusivity[9] is of the order of 150 ν where $\nu \equiv \mu/\rho$ is the kinematic viscosity. For air at STP, $\nu \sim 1.5 \times 10^{-5}$ m^2/s, so that we should have $D \sim 2.25 \times 10^{-3}$ m^2/s. Then taking for typical precipitator conditions the duct half-width $d \approx 0.1$ m, and w_E in the range 0.1 - 0.2 m/s, we obtain P_E values in the range 5-10.

Reference to Figure 7 shows that for these conditions F_1 lies in the range 2-3. This is a very significant factor multiplying the exponent in the Deutsch efficiency formula. For a given precipitator the fractional penetration should be raised to the power F_1 relative to that given by the Deutsch value; alternatively, it should be possible to reduce the specific collector area by a factor F_1 and retain the same fractional efficiency as predicted by the Deutsch formula.

Reference to Figure 8 for the entrance region shows the penetration at $(w_E A/Q) \approx 1.5$ reduced by a factor ~3 for $P_E \sim 5$ and a factor ~6 for $P_E \sim 10$ relative to the Deutsch value. The effect is even more dramatic for larger values of $(w_E A/Q)$, corresponding to full-scale precipitators.

It may be noted that for particles of size greater than that corresponding to the efficiency minimum, field-charging theory yields a value of w_E which increases with size. Hence P_E increases with size and the increase of efficiency with size should be more rapid than indicated for a constant P_E (and F_1).

Apart from putting precipitator theory on a much more satisfactory theoretical basis, which takes the effect of particle diffusion into account in a physically satisfying manner, perhaps the most significant conclusion to be drawn from this work is that the gas flow quality, which has received little attention in the past, is a crucial factor in precipitator performance. Moreover, it is indicated that the Deutsch efficiency is not the theoretical maximum that can be expected, but that very much greater efficiencies and effective migration velocities should be possible if good flow quality can be engineered.

The fact that efficiencies and effective migration velocities no better than those predicted from the Deutsch model are often attained in practice indicates that either the flow quality is poor (due to large eddy mixing resulting from poor entrance conditions, the presence of baffles or possibly ion wind effects) or there are other unrecognized major effects degrading the performance. These include re-entrainment, back-discharge and sneakage, for example. The question of the efficacy of baffles on the collector plates seems particularly important. It is usually believed that such aerodynamic structures provide recirculation zones or regions behind the baffles which protect the precipitated layer from erosion by the main gas flow. However, there seems to be little concrete evidence for the efficacy of such baffles and it has been reported[10,11] that smooth wall precipitators can have efficiencies as high as structured ones. This is not unexpected, since such baffles will certainly introduce large eddies in the near-wall flow and produce a large increase in the effective turbulent diffusivity. Further investigation of this point is clearly indicated.

Finally, an interesting deduction from the theory is that in the regime $P_E >> 1$, where (from eq. (32)) $F_1 \approx (P_E/4)$, the efficiency reduces to

$$\eta \approx 1 - \exp - (\frac{w_E^2 L}{4uD}). \tag{41}$$

This shows that the efficiency is independent of duct width (2d), (other factors such as the electric field being equal), and is possibly the explanation of why wide-space precipitators[4] work as well as conventional ones, which is in conflict with the Deutsch model. It also shows that the exponent depends of the square of w_E rather than the first power, and is inversely proportional to D in this regime.

ACKNOWLEDGEMENT

This work was supported by the Electric Power Research Institute under contract number 533-1. The encouragement of Dr. O. J. Tassicker, Mr. D. Texeira, Mr. R. Hooper and Mr. P. Gelfan is gratefully recognized.

APPENDIX

To determine the appropriate boundary condition on the particle concentration n at the collector wall, we model the flow field as composed of two regions. The main region 1, where D is slowly varying occupies $0 \leq z \leq (d-\varepsilon)$; the near-wall region 2, where D decreases rapidly, occupies $(d-\varepsilon) < z < d$, where $\varepsilon << d$.

We solve the convective diffusion equation (7) in region 2 and require that both the particle concentration and particle flux match at the interface $z = (d-\varepsilon)$:

$$n_1 = n_2 \qquad \text{at } z = (d-\varepsilon) , \tag{A1}$$

$$w_E\, n_1 - D_1 \frac{\partial n_1}{\partial z} = w_E\, n_2 - D_2 \frac{\partial n_2}{\partial z} \,. \qquad \text{(A2)}$$

If we also require $D_1 = D_2$ at the interface, then eq. (A2) reduces to

$$\frac{\partial n_1}{\partial z} = \frac{\partial n_2}{\partial z} \quad \text{at } z = (d-\varepsilon) \,. \qquad \text{(A3)}$$

Before solving eq. (7) for region 2, we observe that the z-directed gradients are much larger than the x-directed ones, and that $u \to 0$, so we may approximate eq. (7) for region 2 as

$$w_E \frac{\partial n_2}{\partial z} - \frac{\partial}{\partial z} \left(D_2 \frac{\partial n_2}{\partial z}\right) = 0 \,. \qquad \text{(A4)}$$

Note that we have retained D_2 inside the gradient operator to allow for a varying D in region 2.

The boundary conditions on eq. (A4) are then

$$n_2 = 0 \quad \text{at} \quad z = d \,, \qquad \text{(A5)}$$

$$n_2 = n_1 \quad \text{at} \quad z = (d-\varepsilon) \,. \qquad \text{(A6)}$$

Note that because we model the z-dependence of D_2 near the wall, we can specify $n_2 = 0$ exactly at the surface.

Equation (A4) is readily solved, subject to (A5) and (A6). In terms of the wall coordinate $\xi \equiv (d-z)$ it yields

$$n_2 = n_1 \frac{\int_o^{\varepsilon} \exp \int_o^{\xi'} \frac{d\xi''}{f(\xi'')}\, d\xi'}{\int_o^{\varepsilon} \exp \int_o^{\xi'} \frac{d\xi''}{f(\xi'')}\, d\xi'} \,, \qquad \text{(A7)}$$

where

$$f(\xi) \equiv -\frac{D_2(\xi)}{w_E + \frac{\partial D_2}{\partial \xi}} \,. \qquad \text{(A8)}$$

Using eq. (A3) we find that

$$\frac{\partial n_1}{\partial z} + \frac{\exp \int_0^{\varepsilon} \frac{d\xi'}{f(\xi')}}{\int_0^{\varepsilon} \exp \int_0^{\xi'} \frac{d\xi''}{f(\xi'')} \, d\xi'} \, n_1 = 0 \,. \tag{A9}$$

Comparing this with the general boundary condition eq. (10), it is clear that we have obtained a prescription for evaluating the constant c:

$$c = \left[\frac{\exp \int_0^{\varepsilon} \frac{d\xi'}{f(\xi')}}{\int_0^{\varepsilon} \exp \int_0^{\xi'} \frac{d\xi''}{f(\xi'')} \, d\xi'} \right]^{-1} . \tag{A10}$$

If we assume that the diffusion coefficient decays linearly in region 2 from a value D_A at $\xi = \varepsilon$ to a value D_B at $\xi = 0$, eq. (A10) can be evaluated as

$$c = d \left(\frac{D_A}{w_E d} \right) \left(\frac{D_A}{D_B} \right)^{\left(\frac{\varepsilon}{d}\right)\left(\frac{w_E d}{D_A}\right)} \tag{A11}$$

Taking as typical values $(\varepsilon/d) \approx 0.1$, $(w_e d/D_A) \approx 10$ and $(D_A/D_B) \approx 10^3$ or larger, we find $c \approx 100\ d$.

We conclude from these arguments that c is large compared to d, and that a reasonable boundary condition for the main region 1 is

$$\frac{\partial n}{\partial z} = 0 \quad \text{at} \quad z = (d-\varepsilon) \approx d \,. \tag{A12}$$

This boundary condition for turbulent diffusion of particles is quite different from that for molecular diffusion and results from the rapid decrease in turbulent diffusivity in the near wall region. It is consistent with the Deutsch formulation and is consistent with the very low values of "mechanical" deposition of particles from turbulent flows. Of course, to obtain non-zero values of mechanical deposition rate in the absence of electrical effects ($w_E \to 0$) it is essential to allow for a large but finite value of c through a more detailed study of the dependence of D through the near-wall region. However, for precipitator applications the limit $c \to \infty$, corresponding to the boundary condition (A12) is adequate.

REFERENCES

1. White, H. J., Industrial Electrostatic Precipitators, Addison Wesley, 1963, Ch. 6.

2. McDonald, J. R., "A Mathematical Model of Electrostatic Precipitation, Vol. I., Modeling and Programming," EPA report 600/7-78-111a (June 1978).

3. Gooch, J. P. and McDonald, J. R., "Mathematical Modeling of Fine Particle Collection by Electrostatic Precipitation," Symposium on Particulate Control in Energy Processes, San Francisco, May 11-13 (1976).

4. Takimoto, K., "Wide Spacing E.P. is Available in Clearing Exhaust Gas from Industrial Sources," EPA Symposium on Transfer and Utilization of Particulate Control Technology, Denver, July 1978, Session A4.

5. Robinson, M., "Turbulence in Electrostatic Precipitators--A Review of the Research Literature," Minerals Processing, May 1968, pp. 13-17.

6. Friedlander, S. K., Smoke, Dust and Haze, Wiley, 1977, Ch. 3.

7. Beal, S. K., Nuc. Sci. and Engr., Vol. 40, p. 1 (1970).

8. Davies, C. N., Proc. Roy. Soc., Vol. 289, p. 235 (1966).

9. Kays, W. M., Convective Heat and Mass Transfer, McGraw-Hill, 1966, Ch. 9.

10. Dalmon, J. and Lowe, H. J., "Proc. Int. Symp. on Physics of Electrostatic Forces and Their Applications," Grenoble, France, 1961.

11. Lowe, H. J., "Reduction of Emissions of Pollutants," Phil. Trans. Roy. Soc. Lond. A 265, 301-307 (1969).

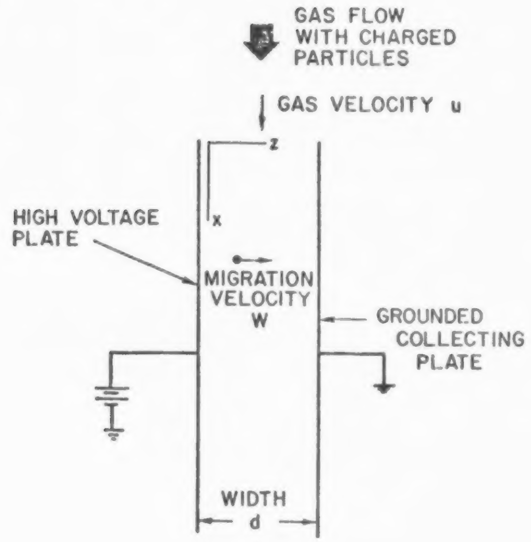

Figure 1. Physical representation of mathematical model for precipitation theory.

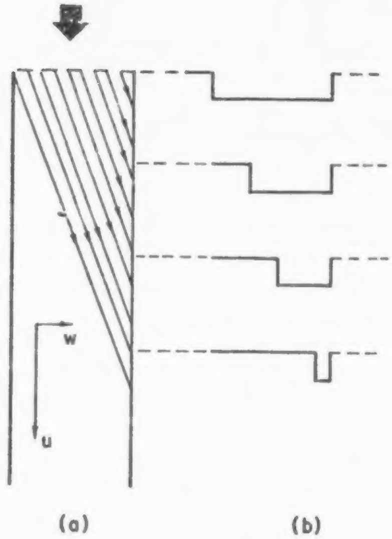

Figure 2. Laminar flow precipitator (a) particle trajectories (b) particle concentration profiles.

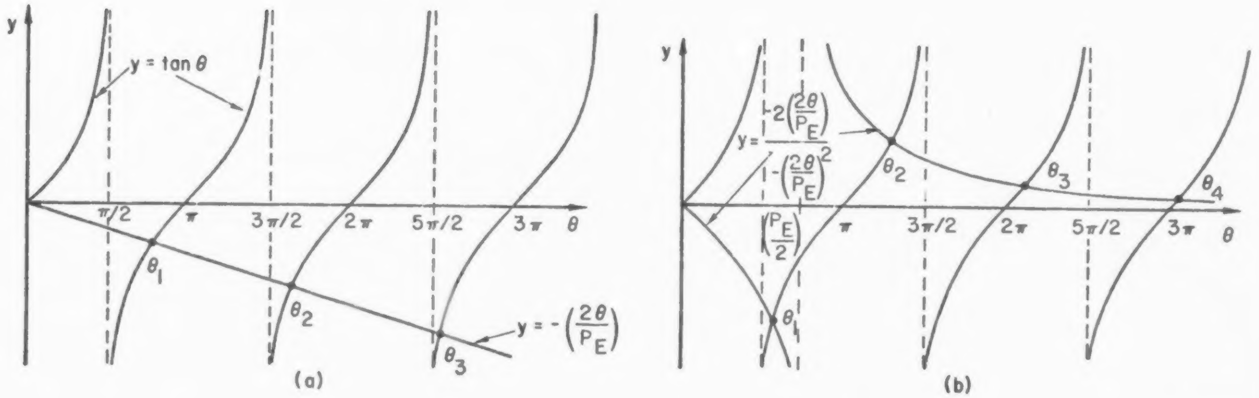

Figure 3. Graphical solution of (a) eq. 27 and (b) eq. 29.

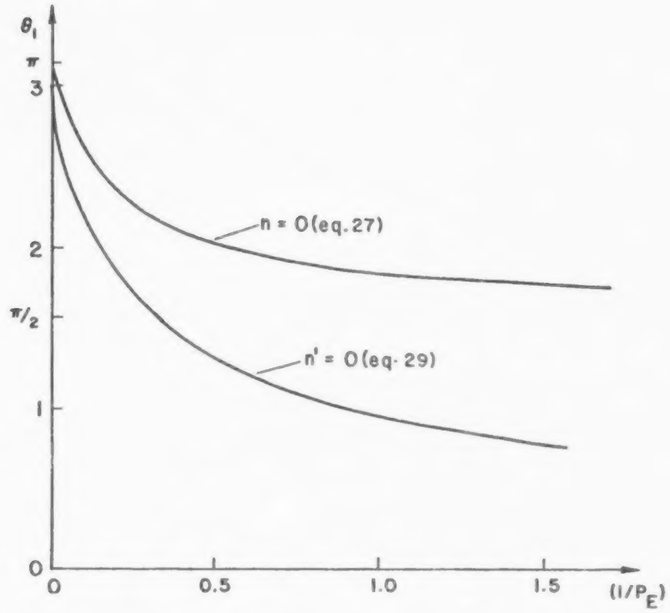

Figure 4. Solutions $\theta_1(P_E)$ of eqs. 27 and 29.

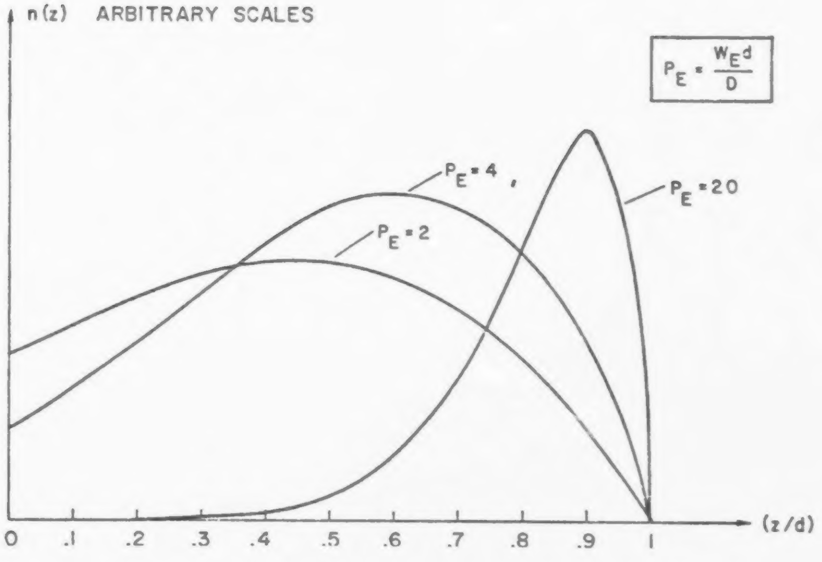

Figure 5. Concentration profiles $n(z)$ for boundary condition $n(d) = 0$ for various values of P_E.

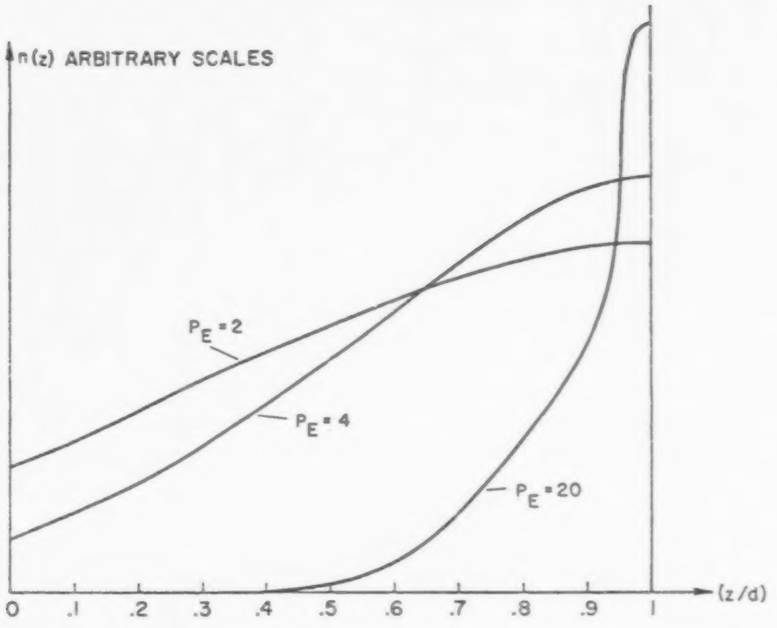

Figure 6. Concentration profiles $n(z)$ for boundary conditions $n'(d=0)$ for various values of P_E.

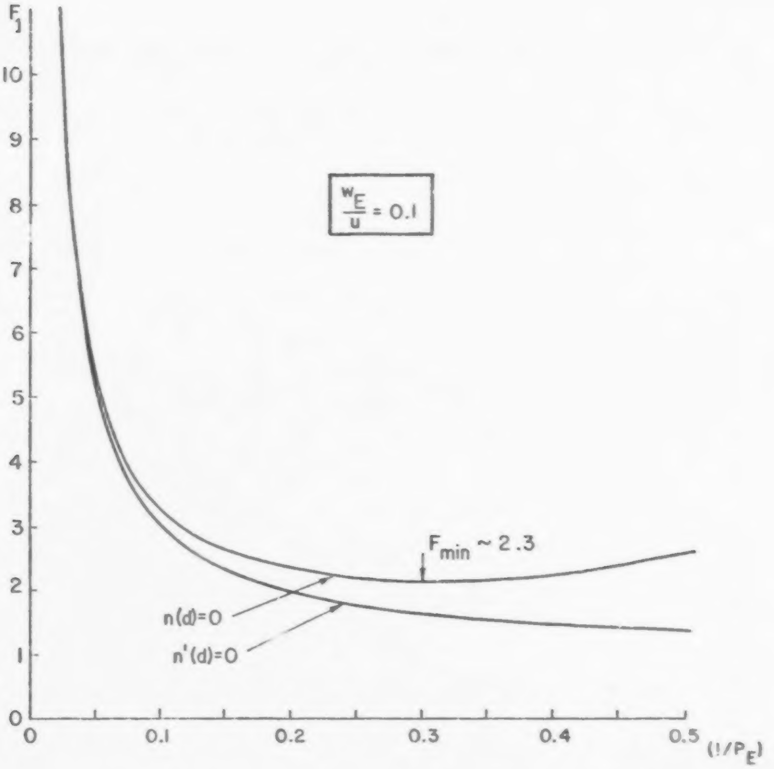

Figure 7. The factor $F_1(1/P_E)$ for the boundary conditions $n(d) = 0$ and $n'(d) = 0$.

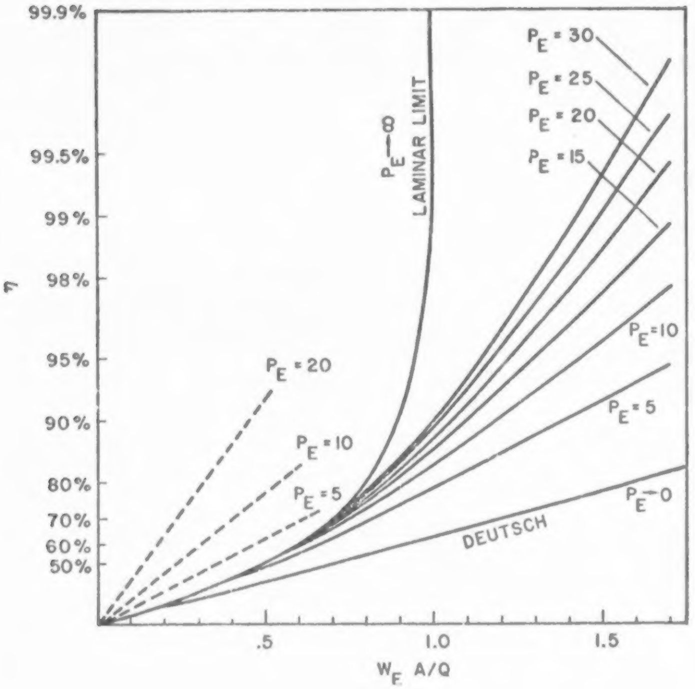

Figure 8. Precipitator efficiency for flat entrance profile taking into account entrance length effects.

THE "HUMAN ELEMENT" - A PROBLEM IN OPERATING PRECIPITATORS

By:
W.J. Buchanan
American Electric Power Service Corp.
Canton, Ohio 44701

ABSTRACT

We are constantly seeking ways to solve the various problems that make many electrostatic precipitators unsatisfactory, an effort which is urgently necessary, but I believe the technical problems are often easier to deal with than the all too common ones with the "human element" which can be quite complex and frustrating.

Although people, and the way they do their work, are (all too often) a problem throughout industry there are some "out-of-the-ordinary" elements that are of particular concern in operating precipitators, this paper examines what precipitators require and some ways to improve personnel participation.

THE "HUMAN ELEMENT" - A PROBLEM IN OPERATING PRECIPITATORS

INTRODUCTION

In the electric utility business, we have been operating boilers, turbines, generators, transmission lines and distribution equipment for decades with the realization that our success hinges upon reliability and efficiency. If this equipment breaks down, we will not be able to meet our obligations, and we will be in trouble. Any loss of efficiency means a financial setback, and that, too, can spell trouble.

About 10 years ago, it became necessary to get serious about reducing the discharge of ash into the air. Although electrostatic precipitators had been around for some seventy years, there were a few bugs to be worked out before these devices could achieve the reliability and efficiency levels they are capable of obtaining today.

One of the problems in operating precipitators has been the fact that, in general, people do not understand them. If we are to get the best performance from precipitators, we must determine why they have been so misunderstood, and discover how to correct that problem.

KNOW YOUR PRECIPITATOR

Historically, dust collectors have been mechanical devices used primarily to protect induced draft fans and to incidentally reduce stack emissions by what seemed, at the time, to be a large amount. They required a high maintenance effort, and substantial fan capacity.

Since passage of the Clean Air Act, the emphasis has been on reducing particulate emissions, and we have heightened our efforts with advances in precipitator technology. Today, the electrostatic precipitator is a very complex piece of equipment that can achieve efficiencies hardly envisioned a generation ago --- *if* it is properly designed and maintained.

Unless a precipitator is designed to make complete allowance for specific operating conditions and the ash to be collected, its performance usually will deteriorate relatively rapidly. Likewise, good internal electrical conditions must be consistently maintained, and gas flow must be well distributed.

A major cause for unsatisfactory precipitator performance is ash fouling of collecting and corona electrodes. Consistently acceptable performance requires adequate cleanliness --- a precipitator that will perform well when collecting "ideal" ash may fail miserably when subject to "problem" ash.

Proper care of anything or anybody starts with understanding, and precipitators are no exception. In evaluating a precipitator that is failing to meet requirements, it is essential to know its potential for doing the specific job assigned to it. This suggests the importance of appropriate design, of course, but also hints of the need for monitoring and record-keeping.

Long-term, continuous monitoring of these big, dirty boxes demands detailed documentation of their entire operation. Clues to conditions causing malfunction can be found by analyzing information that is dutifully kept. Among the needed details are such things as coal and ash analyses, gas temperatures, unit start-ups, and ambient conditions. It is important to observe the electrical performance to see if voltage, current, and sparking are normal. Stack emissions can say a lot about the health of a precipitator. Rapping losses can be discovered by making a "no-rap" test. All problems and component failures should be recorded in detail. Thorough internal inspections must be made when the precipitator is out of service.

The person who is keeping watch on precipitator performance must be able to distinguish between a process change and the deterioration of equipment. The most intriguing thing about precipitators is the complex interaction of a number of factors. Unfortunately, there are many among those who operate, maintain and manage plants where precipitators are used who are not equally intrigued. It seems that few of them really enjoy solving the mysteries of good precipitator operation --- perhaps it is easier to accept the first explanation for a malfunction that comes to mind than to think up the actual cause. This attitude leads to looking at the precipitators only when some very obvious condition makes it mandatory.

THE PEOPLE PROBLEM

Many individuals still have not accepted the idea that electrostatic precipitators are as important to the operation of a plant as the turbine or steam generator. They represent a major investment, and add significantly to operating costs. They were installed to reduce emissions, as required by law. Their reliable, efficient performance requires alert, intelligent attention. When a precipitator malfunctions, it is then too late to begin keeping records and become familiar with the operation of this equipment. At that point, it becomes a kind of panic situation where nobody knows what to do, and the person who must do something realizes that he should have taken a more active interest in the precipitator all along. I am not sure how many crises need to occur before people begin to follow consistent monitoring programs.

WHO'S RESPONSIBLE?

The general attitude of everyone in a power plant is influenced most by the manager. His personal manner and technical abilities will earn him respect, but unless he makes it clear that he wants the plant to be run efficiently and monitored closely, the typical employee at any level will do "only what he has to". The manager needs to emphasize the importance of the precipitator by assigning capable, experienced people to supervise it. Giving the responsibility to the least experienced worker says just the opposite.

From the manager to the individual physical employee, perhaps nothing gets work done better or more quickly than keen interest. It provides the incentive to think, and solve problems, much more so than money. (People do not become creative for material rewards.) It makes the clock move quickly.

Every employee in a plant needs to know that the manager really cares about what he (or she) is doing. And when an employee knows the boss is running the show, there will be greater accountability. A person in a managerial position cannot be expected to know every detail about a task he has delegated, but he needs to know the right questions to ask and how to tell when he is getting the right answers. Only then can he really know when something is slipping and what is being done to make corrections. Only then can he really show that he really cares about what his workers are doing.

Nearly everyone is interested in anything that makes a job easier, People may not relish taking a lot of seemingly useless readings, hunting for grounds and broken wires, and crawling around in dirt looking for answers to uncertain problems. But they may find that easier and more interesting if they are given clear explanations of what the electrical readings mean, told why wires break, and are helped to interpret the conditions that they find inside a malfunctioning precipitator. Most people, in other words, would like to do the right things --- if they only knew what they were and understood how to go about them.

LEADING THE WAY

It would help if there were uniform practices at all plants, but there are individual preferences on how to maintain precipitators and how to assign responsibilities. In some plants, an overall supervisor coordinates records, inspections, periodic maintenance, monitoring and trouble-shooting. In others, there is no one to tie it all together. When each department looks after a limited area --- with little concern for the "big picture" --- this makes it difficult to put all the pieces together and solve a problem. There needs to be better coordination of the operation, maintenance, and trouble-shooting aspects of precipitators if plants are ever going to really get "on top" of the situation.

Someone --- whether that is one of the plant people or some "outsider" --- will have to instruct all appropriate plant employees on what they need to know about precipitators. There should be written instructions and sessions on making inspections both in and out of service, on how to take electrical readings and other data, on how to look for grounds and their causes, and on how to record other useful information.

When several plants are involved within a company it is advantageous to set up a central coordinating office to monitor precipitator operation and maintenance. Improved communication --- even between only two competent individuals assigned to this work --- can accomplish a lot.

Likewise, central-office engineers can do many things to improve the quality of precipitator operation and maintenance, including the development of standardized reporting forms, assisting in personnel training, troubleshooting, interpreting operating data, and helping with routine inspections. When a system has several different make precipitators and a variety of operating conditions, the central-office people are in a position to have a much broader understanding which can be of particular advantage in a problem-solving situation.

Still another group exists whose members exert a significant influence on the health and well-being of precipitators: the manufacturers' field service engineers. Their job is to make pre-operational inspections to insure that assembly is correct, to set up controls for proper limits and action, to energize the transformer rectifiers and discharge system, to tune-up the entire installation under operating conditions --- and to instruct the user's people.

Many service engineers are able to do a reasonably good job of checking out the equipment initially and getting it in operation properly, but too many too often add to later confusion by misleading the operators and maintenance personnel with inaccurate or false ideas on fundamentals and problems.

Admittedly, precipitator manufacturers have had a monumental task in staffing their field positions. In a relatively short time, they have had to hire and train a great number of individuals. There is keen competition in the industry with high rates of turn-over. Performance problems, however, often are misinterpreted by inexperienced field engineers who are unable to effect proper corrections or communicate effectively with competent technical back-up people in their home offices. More should be done to assure the technical competence of this important group.

CONCLUSION

Electrostatic precipitators can make significant contributions toward a cleaner environment, and are here to stay. But their reliability and efficiency depends in large measure on proper design and adequate maintenance. Indifference among those who operate and maintain precipitators must give way to interest. Management can and should cultivate a better attitude among those involved in this challenging aspect of electricity generation by providing both leadership and encouragement by example.

ELECTROSTATIC PRECIPITATORS - ELECTRICAL PROBLEMS AND SOLUTIONS

By:
Ronald K. Raymond
Pennsylvania Power & Light Company
Allentown, Pennsylvania 18101

Efficient collection of flyash by an Electrostatic Precipitator is very sensitive to electrical operation. Most problems that occur in an Electrostatic Precipitator quickly cause changes in the normal operating electrical readings. Broken wires, poor mechanical clearances, and inadequate rapping are examples of these problems. Any one of these problems will cause the electrical readings (hence the precipitation efficiency) to degrade.

This paper tells about recent experience gained at Pennsylvania Power & Light Co. in analyzing and correcting electrical problems associated with T-R control circuits, electrical sectionalization, support insulator failure, wire failure, and T-R set metering. These topics cover the common areas of electrical operation in an Electrostatic Precipitator.

ELECTROSTATIC PRECIPITATORS - ELECTRICAL PROBLEMS AND SOLUTIONS

INTRODUCTION

About 4 years ago PP&L established a team of engineers to study various factors affecting flyash electrostatic precipitator performance. Among the various factors studied were:

1. Fuel characteristics
2. Flue gas conditioning
3. Rapping systems
4. High voltage control systems
5. Electrical sectionalizing
6. Mechanical design features

In order to study the effects of these various factors on electrostatic precipitator performance they were altered in a controlled manner and the change in precipitator performance recorded. While particulate emission testing was occassionally used for performance evaluation, most of the time the opacity monitor data was used for judging a performance change.

This study program has resulted in PP&L undertaking a program to modify some of its electrostatic precipitators to improve their collection ability. This paper deals with the electrical portions of this investigation.

HIGH VOLTAGE CONTROL SYSTEMS

PP&L has, throughout its system, weighted wire design electrostatic precipitators supplied by a number of different vendors. All of these units have wire failures to one degree or another. Two factors are primarily responsible for the amount of wire failures. They are the high voltage control system and the design of the wire emitting frame system.

A typical control system is shown in Figure 1. It has three components, the control element, the control logic, and the TR set. The primary function of this system is to keep the high voltage as high as possible while preventing excessive sparking and power arcing. Primarily, two devices are used for the control element. They are the saturable core reactor and the silicon control rectifier (thyristor).

The saturable core reactor is basically an inductor whose core material may be saturated magnetically by passing a DC current through a control winding. When the core is unsaturated, the coil has a high voltage drop across it. When it is saturated, it has a small voltage drop across it. This device limits the peak as well as the RMS voltage applied to the TR set.

The silicon control rectifier (thyristor) is a solid state switch. It conducts with very little voltage drop when turned on and presents an open circuit when it is off. As such, this device will not limit the peak current to a TR set, it will only control the RMS value. To get around this effect, thyristors are used with a series inductance. This inductor reduces the amplitude of current peaks and tends to broaden the current wave shape.

Typical current wave shapes for a saturable core reactor are shown in Figure 2 and 4. A thyristor wave shape is shown in Figure 3.

The control logic circuit senses the operation of the TR set and attempts to adjust the primary voltage for stable maximum kV operation. As Figure 1 shows, the logic can control using one or more signals obtained from various points in the system. Some control manufacturers claim higher spark sensing ability on the secondary side of the TR set then the primary. In practice, at PP&L, no appreciable difference in sensitivity was observed between control systems of each design.

Two types of operation were observed on PP&L operating control systems. They are the "spark rate" and the "spark sensing" types of operation. The first type integrates sparking as it occurred in the precipitator. This signal is compared to a set point value and the TR primary voltage is adjusted to keep the spark rate constant. The second system of control increases TR-set primary voltage until a spark occurs or a maximum value for primary current has been reached. After a spark occurs, the primary voltage is removed for several cycles of AC voltage. As the precipitator recovers from the spark, the primary voltage returns to a value equal to or slightly less than the value it had before the spark occurred.

The spark rate (first type) control had to be constantly adjusted in order to prevent wire failures. The second type of control logic was much more effective in controlling the TR set automatically with little or no wire failures. To see the effect of the two logic systems on precipitator operation, two units at PP&L's Martins Creek plant were chosen. The control logic on Unit 1 and Unit 2 was monitored for one month. Then the logic on Unit 1 was changed from the "spark rate" type to the "spark sensing" type. The readings were again recorded for one month. Averages for primary voltage and current were calculated for each unit before and after the change. This data is presented in Table 1.

Since both units burn essentially the same type of coal, any change in operating conditions due to fuel changes would be indicated by a change in the Unit 2 average before and after modification. Table 1 shows there was a slight change in the readings due to fuel changes. However, a very significant change was observed in the readings for the unit whose control logic was replaced. Even though the readings were higher, there were no wire failures due to high voltage arcing. It should be noted that the wires in these units were in poor mechanical condition and that since these tests they have been replaced. Also, the control systems installed for these tests have been permanently installed on Unit 1 and 2 at Martins Creek.

The third element in the control system is the TR set. Other than failure due to improper operating conditions, no difficulties have been experienced.

ELECTRICAL SECTIONALIZING

The Martins Creek Unit 1 electrostatic precipitator was tested to determine the effects of various electrical sections on Unit operation. This precipitator has five electrical sections connected in series in the direction of gas flow. Test procedures were designed to obtain electrical information on various electrical sections and their importance in the precipitator dust collection process. The effects of additional TR sets as well as their position in the precipitator were studied. Electrical sections were deenergized to simulate various SCA's. This was done in an effort to apply the results to other units as well as the Martins Creek Unit 2.

Initial testing at Martins Creek on the Unit 1 precipitator consisted of taking one section of the Unit out of service. This was done using a systematic procedure--one section at a time from outlet to inlet--one side of the precipitator at a time. Voltage, current, and opacity readings were recorded. Figure 5 shows the layout of the Unit 1 precipitator. The systematic procedure used, referred to as a double response test, was done by removing sections in an orderly way such as E_A, D_A, C_A, B_A, A_A, then E_B, D_B, C_B, B_B, A_B. Note, at any time only one section was out of service. Any changes in precipitator operation were attributed to loss of the deenergized section.

The data recorded during the sectionalizing study had several limitations in accuracy and validity. Several limitations apply to the voltage, current and opacity data.

The current and volt meters on the precipitator electrode control panel stuck at various points in their measurement range. This made exact readings difficult. The meters had to be tapped gently to obtain a true value. Also, the meters used to record voltage and current values are average reading meters, calibrated for RMS sine wave response. Voltage and current wave shapes at the output of the silicon control rectifiers are not sine wave. To determine true RMS values for these readings, a shape factor must be applied. It is virtually impossible to calculate this factor because it is different for different operating points on the TR set. Therefore, the readings obtained show relative increases or decreases - not absolute levels.

Secondary meter readings, kV and mA, are related to the primary voltage and current. Tests on units equipped with primary and secondary metering show that the relationship between primary and secondary is not linear. It appears that no constant factor, such as transformer turns ratio, can be used to relate the primary to secondary. Thus, in a control cabinet that does not have secondary metering, such as the outlet cabinet on the Martins Creek Unit 1 precipitator, it is impossible to calculate one. Qualitatively, it may be stated that as primary values increase, so do secondary.

The opacity monitor shows that opacity changes occur when a section of precipitator is being energized. Rapping spikes and a shift upward in base line values indicate a section has been deenergized. Opacity data indicates very rapidly a change caused by a section being removed from service. This data, while useful for changes in any particular short term test, should not be used for long-term comparisons. Factors such as particle size distribution and boiler operation (excess air to name one important parameter) can affect the opacity without changing particulate emissions. The monitors presently installed on the test unit exhibit a long-term stability problem. Stack zero checks during different outages indicate a random drift.

An example of the opacity data obtained during a typical test is shown on table 4. The outlet fields, D and E, had three electrical buses connected to them during this trial, see Figure 6. The other sections were in groups of two. When either D or E was removed from service, more area was de-energized than from the others. This fact, as well as the fact that each of them was an outlet, made their effect on opacity more severe than the other sections.

Other effects were noted in opacity data. When an outlet field was de-energized, rapping spikes were more prevalent then when the other fields were de-energized. In almost all tests there was a general decline of opacity during the tests. Probably, this was due to air sweeping which occurs during the de-energized test periods.

During testing of the Unit 1 precipitator there was an increase of the voltage and current readings from initial to final values. Subsequent tests showed that the increase was due to its electrode controls. They lacked the ability to keep power levels at optimum values. Table 2 shows the results before and after installation of new control logic. This table shows that the controls were responsible for this change in base line data. Note the absence of the base line shift in the data taken with the new control logic installed. As the double response tests progressed, the sum of individual currents was larger than the current with both were connected (i.e., $A_A + A_B$ was greater than A_{A+B} - see figure 5). This result was observed after the new control logic was installed. Therefore, the control was eliminated as a possible cause for the effect. Table 3 shows these results. In all but one case the amount of this increase was about 20 percent or higher with little or no sparking.

This increase indicates that increase in current input could be expected from additional electrical sectionalizing. This idea is not new. It has been expressed by Harry J. White in his book "Industrial Electrostatic Precipitation". Opacity measurements made during these tests show opacity spikes are more pronounced when all outlet fields are removed from service. A conclusion made from these two results is that improved precipitator performance can be obtained by increasing outlet sectionalizing.

If present precipitator configuration consists of two sections electrically tied together and energized by one TR set, then better performance can be expected if the sections are electrically separated and each energized by its own TR set. The most significant change from this type of sectionalizing will occur when an outlet field is separated.

These results are used in one of PP&L's upgrading plans. As part of this plan, additional TR sets are being added to the outlet fields.

GENERAL COMMENTS

As previously stated, secondary readings for TR set are difficult to calculate from the primary current and voltage readings. An observation made during the test program was that TR sets equipped with secondary kV and mA meters were more useful in determining precipitator operation than those without these meters. PP&L is installing secondary meters on most of its precipitator installations.

Another area of frequent difficulty is the emitting frame support insulator compartments. These compartments protrude above the roof of the precipitator. Because of this they provide a potential cold spot. Acid mist and flyash can collect on the support insulators. This can cause electrical tracking on the insulators. A heating system is usually installed on the ventilation system that feeds this compartment. This heating system is being made larger to improve reliability and capacity. Also, PP&L is studying insulation methods for these compartments.

One final area of difficulty is alignment of the high voltage emitting frame. PP&L has added stabilization insulators in the bottom of the emitting frame to help hold it in alignment. This alignment frame and the wire to plate spacing has been carefully checked and adjusted to the design criteria.

CONCLUSIONS

The results presented in this paper have been used to formulate part of a particulate compliance program at PP&L. Some existing precipitators are being modified to improve their performance. Others need additional polution control equipment. Modification of existing equipment has included replacing the high voltage control systems, adding T-R sets, and improving the emitting frame stability and alignment. As a monitor, secondary metering has been added to evaluate performance and the condition of the percipitator during operation.

These modifications were made on a pulverized coal fired boiler. Their relative effectiveness on other types of installations has not been investigated. As an example, it may be said -- in a general sense -- that at installation where heavy sparking occurs the "spark sensing" control will generally work better then the "spark rate" control. However if the precipitator does not spark heavily than the control system is not very important.

These modifications and additions will not change a precipitators performance from bad to perfect. However, these changes will improve performance to some degree and assure the existing precipitator is operating at its maximum capability.

RKR #378:5

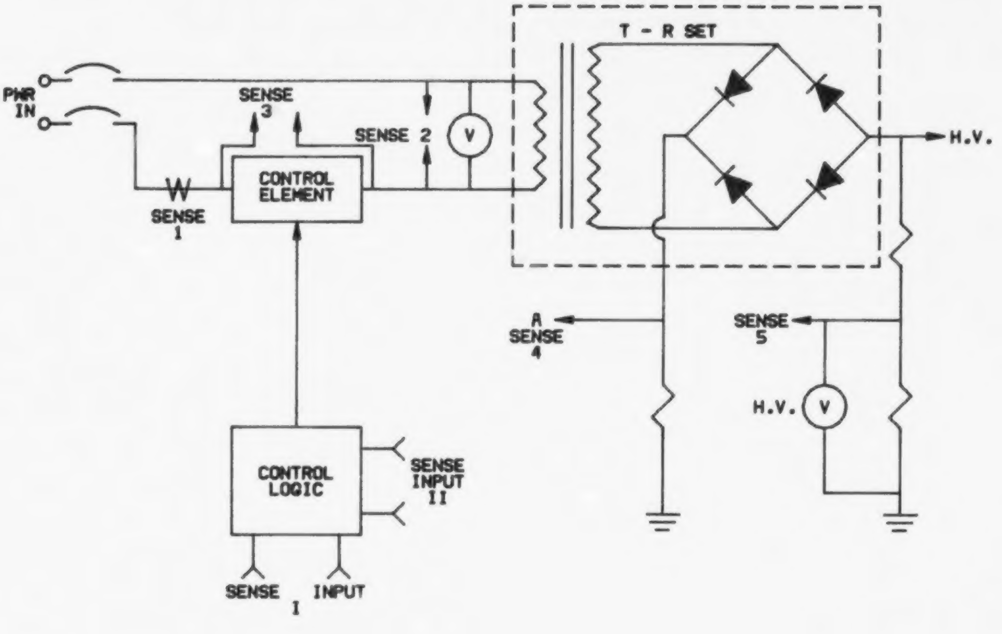

CONVENTIONAL HIGH VOLTAGE
ELECTRODE CONTROL SYSTEM

FIG. 1

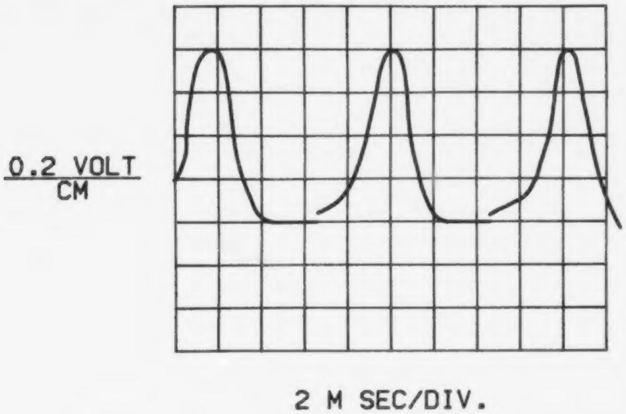

SATURABLE CORE REACTOR
TR SECONDARY CURRENT WAVE SHAPE
(3a - 4a)
FIG. 2

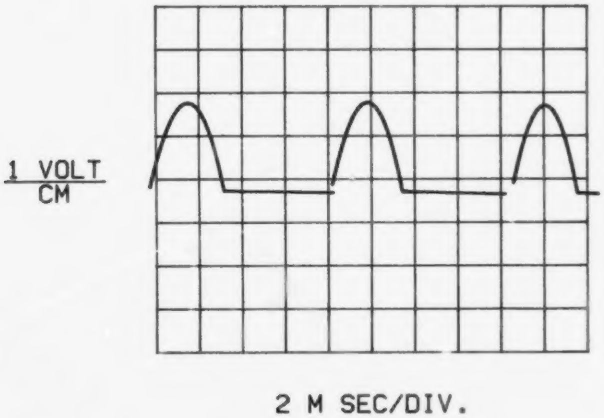

SILICON CONTROL RECTIFIER
(THRISTOR)
TR SECONDARY CURRENT WAVE SHAPE
(5d - 6d)
FIG. 3

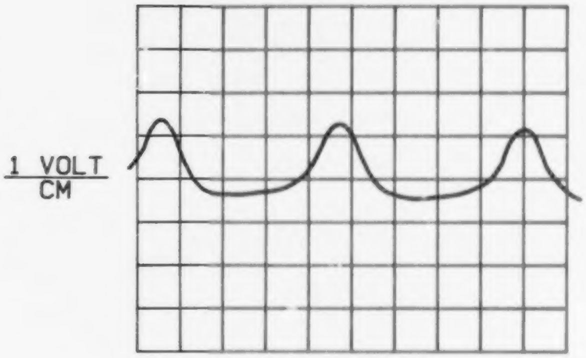

2 M SEC/DIV.

SATURABLE CORE REACTOR
TR SECONDARY CURRENT WAVE SHAPE
(3d - 4d)
FIG. 4

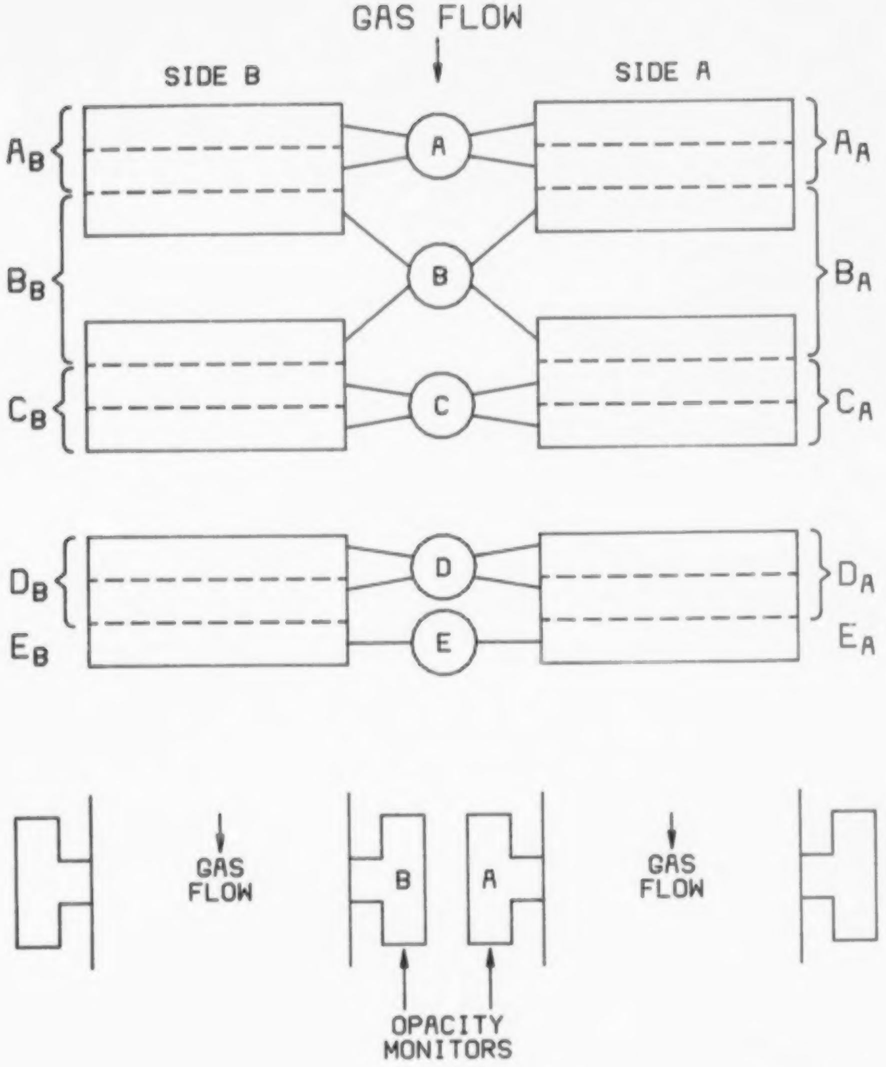

MARTIN'S CREEK SES
UNIT #1 PRECIPITATOR

FIGURE 5

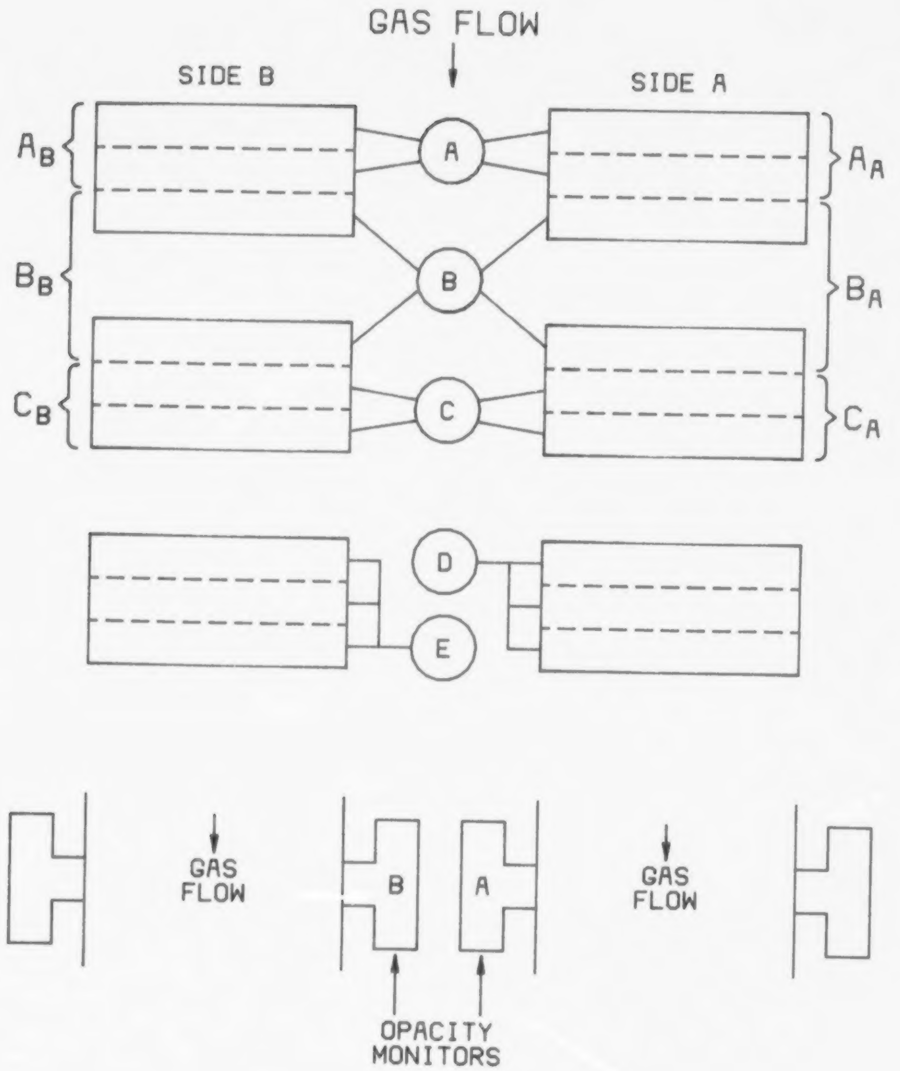

MARTIN'S CREEK SES
UNIT #1 PRECIPITATOR

FIGURE 6

EFFECTS OF CONTROL MODIFICATIONS

		PRIMARY VOLTAGE (VOLTS)			PRIMARY CURRENT (AMPS)		
	TR SET	BEFORE	AFTER	%	BEFORE	AFTER	%
UNIT I	A	175	191	9%	54	63	16.7%
	B	201	240	19.4%	53	82	54.7%
	C	186	234	25.8%	53	84	58.5%
	D	193	259	34.2%	61	110	80.0%
UNIT II	A	187	189	1.1%	44	36	1*.2%
	B	183	194	6.0%	38	53	39.5%
	C	177	186	5.1%	46	50	8.7%
	D	202	219	8.4%	60	63	5.0%

TABLE 1

"E" TR SET DID NOT CHANGE ON EITHER UNIT.

BASE LINE SHIFT

		START		FINISH	
	SECTION	VOLTAGE	CURRENT	VOLTAGE	CURRENT
TRIAL I	A	190	55	220	75
	B	220	50	240	70
	C	240	88	260	110
	D	200	69	265	109
	E	370	85	385	100
TRIAL II	B	240	65	250	72
	C	240	85	265	104
	D	230	87	250	100
	E	380	90	375	80
TRIAL III	A	200	65	290	145
	B	230	65	260	100
	C	250	100	280	130
	D	255	105	290	138
	E	370	130	360	130
NEW CONTROL LOGIC	A	190	55	190	55
	B	230	60	230	60
	C	240	66	235	65
	D	295	135	290	125
	E	360	90	370	85

TABLE 2

PRIMARY CURRENT (I_p) & PRIMARY VOLTAGE (V_p)

DATE	SECTION	BASE			THE LISTED SECTION ON A SIDE OUT		THE LISTED SECTION ON B SIDE OUT		SUM OF SECTION CURRENTS A SIDE PLUS B SIDE
		V_p	I_p	V_p	I_p	V_p	I_p	I_p	% OF BASE
11/25/76	A	175	50	175	25	180	38	63	126
	B	200	42	200	39	195	32	71	169
	C	180	40	160	30	200	39	69	172
	D	210	62	200	54	230	64	118	190
	E	355	70	330	35	350	20	55	78
12/8/76	A	200	70	200	60	225	70	130	185
	B	230	80	240	70	270	85	155	194
	C	210	76	200	55	230	76	131	172
	D	200	84	250	80	220	85	165	196
	E	370	110	340	45	360	70	115	105
1/6/76	A	172	48	200	48	200	47	95	198
	B	200	41	190	38	225	41	79	193
	C	180	39	205	38	200	38	76	195
	D	170	37	190	35	190	40	75	203
	E	380	80	375	40	360	40	80	100
NEW CONTROL 6/18/76	A	190	55	170	20	190	45	65	118
	B	230	60	210	21	215	46	67	111
	C	240	66	200	32	220	50	82	124
	D	295	135	235	54	275	105	159	117
	E	360	90	370	50	365	58	108	120

TABLE 3

OPACITY CHANGES

SECTION	A SIDE OUT OPACITY A	A SIDE OUT OPACITY B	B SIDE OUT OPACITY A	B SIDE OUT OPACITY B
A	20%	6%	10%	10%
B	20%	7%	10%	10%
C	24%	8%	10%	10%
D	55%	--	16%	--
E	--	17%	--	60%

BASE LINE OPACITY -	START	FINISH
A	14%	10%
B	9%	6%

DECREASE IN OPACITY FROM START TO FINISH

TABLE 4

ELECTRODE CLEANING SYSTEMS:
OPTIMIZING RAPPING ENERGY AND RAPPING CONTROL

Author: Michael Neundorfer
Wm. Neundorfer Co., Inc.
Cleveland, Ohio 44124

ELECTRODE CLEANING SYSTEMS:

OPTIMIZING RAPPING ENERGY AND RAPPING CONTROL

Methods for improving Electrostatic Precipitator performance by increasing electrode excitation level during rapping, and by optimizing rapping control, are presented in this paper. Design modifications can reduce mechanical impedence to vibration transmission during rapping. These same modifications can eliminate areas of high stress concentration where fatigue failure often occurs. Rapping system control parameters are presented as they relate to variations in field collection and shedding rates. Anti-coincident rapping control for plate rappers minimizes peak opacity levels during rapping if sufficient "rest times" between raps can be maintained. When anti-coincidence must be sacrificed due to insufficient rest times on large installations, suggestions for anti-coincident rapping by section are presented. Methods for optimizing field rapping repeat rates using available opacity, ash pull, and precipitator power information are discussed.

Michael Neundorfer
Wm. Neundorfer Co., Inc.

ELECTRODE CLEANING SYSTEMS: OPTIMIZING RAPPING ENERGY AND RAPPING CONTROL

INTRODUCTION:

Traditionally, the functions of dry type industrial electrostatic precipitators have been described as follows:

1) To charge the dust particles
2) To separate the charged particles from the gas stream by attraction to grounded collecting electrodes
3) To transfer the separated particles from the collecting electrodes to external containment with minimal loss

In addition to these three functions, a fourth function, dust agglomeration, will be discussed in this paper. Dust agglomeration is critical for effective precipitator performance since, without agglomeration, nearly all of the dust removed from the collecting electrodes would remix with the gasses and be carried downstream. (Plato, 1969)[1]. Even with agglomeration, transfer losses (rapping reentrainment) account for up to 70% of total precipitator emissions (Gooch, Marchant, 1978)[2]

This paper addresses the relationships between electrode cleaning and precipitator functions and offers suggestions for physical and operational changes in electrode cleaning which will improve precipitator efficiency.

CHARGING, SEPARATION AND FOULED ELECTRODES

Electrostatic precipitators operate best with clean electrodes. This is especially true with dust resistivities exceed 10^{10} ohm-cm. Dust build up on collecting plates degrades precipitator performance in three ways:

1) Given a constant average corona voltage level, corona current density decreases as the thickness and/or resistivity of the dust on the plates is increased. As corona current density is reduced, corona power is reduced. The rate of collection can be related to corona power as follows:

   $w = k_1 \, Pc/A$

   w = rate of collection
   K_1 = constant
   Pc = Corona Power
   A = Collecting surface area

   Therefore, a reduction in corona power reduces the rate of collection which reduces the probability of capture which, in turn, reduces overall collection efficienty. In extreme cases, improved rapping has increased corona current by more than 6 times. (Neundorfer)[3].

2) As dust layer thickness and/or resistivity is increased, sparkover voltage is reduced. As sparkover voltage declines, the precipitator must be operated at a lower voltage to avoid excessive sparking. This means a reduction in corona power and, therefore, a reduction in overall collection efficiency. The reduction of sparkover voltage results from localized electrical breakdown of the dust layer. All corona current must pass through the resistive dust layer to ground. The resulting voltage drop across the dust can reach 20KV and follows ohms law:

$V_{dL} = j\varrho l$

V_{dL} = Voltage drop across resistive dust
j = average corona current density
ϱ = dust resistivity
l = dust layer thickness

Sparkover originates at points on the plates where electrostatic resistance values are lowest. These points of low resistance are thin spots or discontinuities in the dust layer.

3) Back discharge neutralizes negative ions and charged dust particles. Back corona discharge on the exposed surface of the collecting electrode dust layer can produce positive ions. These ions are attracted to and migrate towards the discharge electrode and interfere with normal particle charging and migration.

These three factors indicate that from an electrical standpoint, it is desirable to maintain the dust layer on collecting electrodes as thin and as uniform as possible. Build-up on the discharge electrodes of low resistivity dust will increase the effective electrode diameter and therefore increase the corona starting voltage. High resistivity deposits on wires will decrease the corona current at a given voltage. Discharge electrodes should always be kept clean.

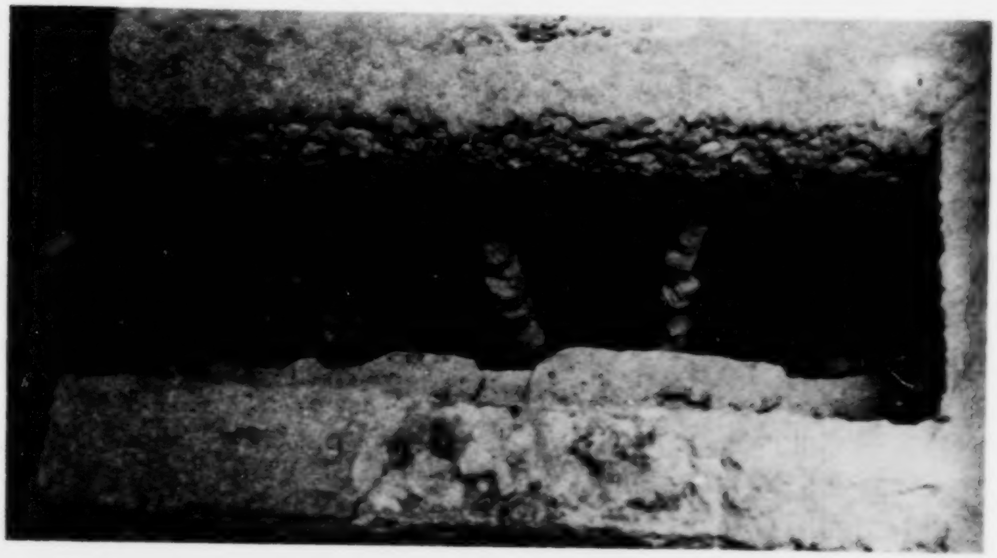

Figure 1. Fouled discharge electrodes: Flyash application with SO_3 conditioning.

Fouled discharge electrodes: Cement kiln: High resistivity dust.

TRANSFER, REENTRAINMENT AND AGGLOMERATION

Transfer of the collected dust from the electrodes to the hoppers is initiated by rapping. Rapping is the direct or indirect mechanical excitation of electrodes. If rapping is effective in shearing the dust from the plates, the dust will either: 1) reattach itself to the electrode, 2) fall into the hopper or 3) reentrain in the gas stream for downstream re-separation or discharge through the stack.

Reentrainment is the recapture of collected dust by the gasses. It occurs after dust has been attached to electrodes or to other structures, such as walls and ceilings. Dust also can be reentrained after it has entered the hoppers. Two conditions are required for reentrainment: (1) a disturbance which dislodges the dust and (2) gas velocity sufficient to carry the dislodged dust.

The most obvious disturbance which dislodges dust is rapping which accounts for the majority of reentrainment. Sparking can also dislodge dust from electrodes as can high gas velocity and the sheer weight of a dust layer.

Studies have found that the percentage of emissions due to rapping reentrainment increases with increasing particle size. This may be explained, in part, by the fact that smaller particles agglomerate into larger ones from inlet to outlet of the precipitator (Spencer, 1976)[4] In these studies, emissions due to rapping losses of particles less than 0.3 um were not significant while rapping losses of particles 2.0 um and larger accounted for up to 90% of those particles emitted (Gooch, Marchant, 1978).[5] The total contribution to precipitator emissions of rapping losses has been measured in a range between 18% and 90% (Gooch, Marchant (1978), Spencer (1976),[6] (Nichols, et. al. (1975).[8] These findings demonstrate the potential for overall efficiency improvement which is possible by reducing rapping losses.

As agglomeration of particles into larger particles or "chunks" is increased, the influence of the gas flow on the dust agglomerates is decreased resulting in a higher probability that rapped dust will be removed to external containment. Agglomeration can be enhanced through proper rapping control, process changes, and gas conditioning.

DUST ADHESION AND TENSILE STRENGTH

In order to understand the amount and type of work required to dislodge dust from collecting electrodes (plates), the conditions affecting dust layer tensile strength and adhesion must be examined. These conditions are: particle dielectric and work function properties, dust deposit density, particle size, gas humidity, interelectrode current density and field strength. (Tassicker, 1975) .

Electrical forces of adhesion due to field strength and current density compact the dust layer and hold the dust to the plates. Electrical adhesion forces increase proportionally as the current density increases. Electrical adhesion forces also increase with increasing dust resistivity. If electrical adhesion forces were the main component of dust adhesion, very light rapping, with momentary "power off" in the field being rapped, would remove high resistivity dust. However, since electrical adhesion forces generally are not the main component of dust adhesion, success with "power off" rapping is limited. When it is successful, long periods of continuous rapping with "power off" are required to make measurable improvement in cleanliness.

Although electrical forces of adhesion tend to compact the dust layer and hold it against the plates, contact potential adhesion holds the dust layer together. Although the total particle surface charge equals zero, surface charge (work function) may vary in value around the particle surface. As particles are collected, they are aligned by the field forces and surface potential differences from particle to particle cause coloumb force adhesion. The contact adhesion forces are significant for particle sizes less than 3.0 μm (Penney, 1975).[10] In general, fine particles have much higher adhesive characteristics than larger particles.

While the precipitator field force contributes to the alignment of particles for contact potential adhesion, other influences, such as rapping and disturbances of the dust layer by newly deposited dust, rearrange particle positions in the layer. The rearrangement causes higher layer density and stronger electrostatic and mechanical adhesion. This is supported by the observation that dust which remains after the first rap has higher tensile and shear strengths than newly collected dust (Spencer, 1976).[11]

The relationship between dust layer tensile strength and layer density has not been developed. However, the relationship between dust layer mass/unit area of plate and rapping effectiveness is well established (Gooch, Marchant, 1978)[12], (Spencer, 1976)[13], (Sproull, 1965)[14]. With voltage applied, Plato found that 90% removal was possible with dust mass/unit area of 0.25g/cm^2 while removal efficiency with dust mass/unit of .07g/cm^2 was only 30% (Sproull, 1965).[15] Plato also found that at values up to about 0.1g/cm^2 the dust formed a cloud during rapping. When the dust mass/unit area exceeded 0.1g/cm^2 it caked when rapped. (Sproull, 1965)[16] Therefore, rapping higher mass/unit area dust layers caused less reentrainment.

If rappers are effective, and if precipitator inlet conditions are constant, plate dust layer mass/unit area at any point along the gas flow can be approximately expressed as "time between raps". This is true until the dust layer begins to degrade the processes of charging and separation.

THE MECHANICS OF PLATE RAPPING

Rapping effectiveness for a given dust condition is related to plate acceleration. Plate acceleration refers mainly to acceleration of the surfaces of the plates rather than to the whole plate or group of plates as a unit. Most of the acceleration is plate surface distortion resulting from the disturbing force of rapping. Peak acceleration normal to the plate surface is primary in dislodging dust; however, simultaneous shear acceleration contributes to cleaning (Spencer, 1976),[17] (Sproull, 1972).[18] In comparing shearing acceleration with normal acceleration, Sproull found that it took twice as much shearing acceleration as normal acceleration to shear a given quantity of dust (Sproull, 1965).[19]

When plates are rapped the dust shears from itself rather than from the plate surface leaving a residual layer of dust. In order for dust to break away from this residual layer in large chunks, some sliding must take place. For sliding to occur the static coefficient of friction must be overcome; the lower value kinetic coefficient of friction resists sliding. As sliding speed increases, the value of the kinetic coefficient of friction becomes smaller.

Peak plate acceleration resulting from rapping can be measured by attaching low mass piezoelectric accelerometers to different points on the plates. Measurements taken by single axis transducers measuring normal acceleration can be most consistently related to rapping efficiences. Sustained minimal peak normal accelerations on the plates of 10-60 g's (0 to peak) will generate good dust shearing. If single impact or low frequency cleaning is employed, higher peak acceleration can be required for adequate cleaning.

DESIGN PARAMETERS AFFECTING EXCITATION

For a given rapper disturbing force, mean peak acceleration of the plate is affected by the following conditions: plate size, shape and rigidity; the number of plates per rapper; the method of plate suspension; and the location and method of transmitting rapping force from the rapper to the plate. The presence of a dust layer on the plates during rapping will reduce plate acceleration.

As plate designs become longer and wider, it becomes more difficult to attain uniform excitation of the plates. The difficulties of rapping larger plates has been overcome to a degree by rapping fewer plates with a rapper. The area of plate per rapper is a good indicator of potential rapper effectiveness. Most recent weighted wire installations range from 74.3m^2 (800 ft^2) to nearly 465m^2 (5000 ft^2) of plate per rapper. European designs are more conservative with from less than 27.9m^2 (300 ft^2) to about 83.6m^2 (900 ft^2) per rapper.

Minor field modifications to plate suspension members and rapper anvil beams can more than double minimum peak plate accelerations. In some cases, relocation of the rapper with respect to plate beam suspension points has tripled minimum peak acceleration. The use of a common plate frame support/rapper shaft reduces rapper effectiveness significantly. (Neundorfer)[20].

Transmitting rapping energy from the rapper or point of impact into the plates requires mechanical linkage. When this linkage is loose, substantial energy is lost and destructive wear and fatigue can occur. Tapered interference fits at joints in the linkage can eliminate these problems.

TYPES OF RAPPERS

There are two basic types of rappers: (1) single impact rappers and (2) frequency rappers. Single impact rappers set up natural frequency vibration which is maintained entirely by elastic forces in the structure. Frequency rappers impart a periodic disturbing force which results in steady state forced vibrations.

Single impact designs include mechanical drop hammers, magnetic impulse, and pneumatic single impulse rappers. When plate free vibration is generated by single impact types, the frequency depends only on the plate/rapper system's physical configuration and the initial loading. The only adjustment available on single impact type rappers is the variation of impact level of the initial loading. Some magnetic impact rappers impact more than once per rapping cycle. The frequency of these rappers (less than 10 cps) is too low to initiate forced vibration in the plates. Therefore, they are classified with single impact rappers.

Frequency rappers include electric vibrators, eccentric pneumatic vibrators (not widely used), and pneumatic frequency impactors. Frequency rappers operate at frequencies between 25 and about 90 cps. In a rapper reentrainment study at Bull Run, plate acceleration in three axes was measured. Acceleration was highest in the normal axis with frequency rapping. Using single impact rappers, normal acceleration was lowest. (Nichols et. al., 1975).[21]

Electric vibrators operate by drawing an anvil against a stop at a given frequency with variable force. The displacement and anvil mass are small relative to other rapper types. Therefore, electric vibrators are seldom used for difficult dusts.

Pneumatic frequency impactors work like a jackhammer. A piston weighing between 1526g (3½ lbs.) and 5230g (12 lbs.) is pneumatically reciprocated in a cylinder with a relatively long stroke. The piston impacts at the lower end of the stroke and is air-cushioned at the top. Frequency and amplitude are varied by changing air pressure. Pneumatic frequency impactors simultaneously generate both natural frequency and forced vibrations in the electrodes. Pneumatic frequency impactors are widely used for salt cake and other difficult dust. Recently, these rappers have been used to upgrade fly-ash rapping where high resistivity dusts and/or gas conditioning exist.

At the point of highest peak acceleration (near rapper),the main influence to plate acceleration is the free vibration caused by each impact. At the points farthest from the rapper, transient motion in the first few cycles is gone and a lower energy natural frequency is sustained.

DISCHARGE ELECTRODE RAPPING

Discharge electrode rapping is accomplished with both single impact and frequency rappers. There is little published regarding wire rapping effectiveness. This is probably because: (1) discharge electrode rapping contributes little to reentrainment emissions and (2) charging and separation degradation due to discharge electrode fouling is less obvious than degradation due to plate fouling. Some installations of hot-side fly-ash precipitators have experienced very difficult wire dust build-up problems. These have been solved by tightening wire rapper transmission assemblies and using frequency impact rappers with relatively high energy, short duration (less than 0.4 sec) bursts. This approach produces a high level of wire excitation for a short period of time. The high level of excitation assures that all wires on the frame vibrate. The short duration minimizes chances for wire mechanical failure.

Discharge electrode frames are supported with a minimum number of steel pipes or bars in tension. These members are supported by ceramic or porcelain insulators on the top of the precipitator shell. The insulators are in compression. The best rapping results are achieved when rapper rods are positioned on the wire support frames independent of the support members. Double tapered ceramic shafts with tapered steel connectors and a tapered rapper attachment guarantee tight shaft couplings, minimal mechanical impedence to energy transmission from the rapper to the frame, and the best resistance to electrical tracking available. This system will function at well above the highest precipitator operating temperatures.

Original wire rapper insulating shaft. Bolted line-post insulator. Note misalignment at anvil.

Replacement of original shafting with threaded/socket coupler and double-tapered ceramic shaft.

Wire rapper shafts using 2 double tapered ceramic shafts each for electrical isolation.

DISCHARGE ELECTRODE RAPPER INDUCED MECHANICAL FAILURE

Discharge electrode failure is the most frequent and/or severe precipitator maintenance problem. The cause of discharge electrode failure is most often arcing; corrosion is second in causing failure; and mechanical failure is the least frequent cause of discharge electrode failure. (Engelbrecht, 1976).[22]

It is important to be able to differentiate between failure caused by arcing, corrosion and fatigue. It is also important to record wire failures by wire location, type of failure, and point of failure along the wire. With this information, patterns relating to discharge electrode failures can be observed.

Most mechanical failures of wires can be traced to over-rapping. Many wire rapper vibrating systems operate for several seconds per cycle. If the dust has not broken from the electrode within one second, it generally will not be sheared by that level of excitation. Long periods of continuous wire rapping can cause wire breakage.

Wire frame support insulator and rapper insulating shaft breakage are probably more common than entirely mechanically induced wire breakage. When the coupling at the ends of the insulating shafts become loose, misalignment and chatter cause measurable rapping energy loss and can cause insulating shaft breakage. The solution to this problem is to periodically tighten couplings or replace bolted and spring loaded coupled shafts with double-tapered ceramic shafts.

Wire frame support insulators are often broken by surface contamination and subsequent tracking. When rapping causes support insulator failure, it is the result of uneven distribution of the frame weight on the insulator, or, more commonly, inadequate clearance where the rapper shaft penetrates the insulator cap causing rapping energy to transmit through the insulator. Rapping through the wire frame support shaft can also cause support insulator breakage.

Inadequate or uneven tensioning of the wire will reduce rapping effectiveness and cause excessive wear at suspension points. This wear problem in the wire support frame at the wire button can be caused by spit arcing as the wire bounces and rotates with respect to the frame.

Seals at points where rapping shafts penetrate precipitator shells and penthouse roofs should be gas and water tight. However, they must not significantly dampen rapping energy or transfer it to the shell. Packing glands are not acceptable since they absorb too much rapping energy. Steel guide pipes with less than 1/8" radial clearance can corrode and bind the rapping shaft. Leaky seals will allow corrosion of the guide pipe and shaft. This leakage can cause contamination of discharge electrode insulating shafts by water, gas, condensables, and dust, leading to electrical tracking from lower conducting assemblies to the precipitator shell.

To summarize, when the following conditions are met, maximum discharge electrode rapping will result:

1) Shaft connection tight from the rapper to the frame (preferably all tapered).
2) Rapper shafting well aligned and not binding.
3) Wires adequately and evenly tensioned.
4) Rapper shafting independent of frame supports.
5) Rapper shafting located on the frame for best action.
6) Short bursts (0.5 sec or less) of frequency impact rapping at an intensity and repeat rate required to maintain clean wires.

MECHANICAL FAILURES OF COLLECTING ELECTRODES

Collecting system mechanical failure occurs in the form of stress cracks, stress fracture, broken bolts and broken welds. These fractures occur at points of high stress concentration such as rapper shaft attachment to the anvil beam, plate attachment to the anvil beam, and rapper shaft connections. The reduction of stress concentration at these points of failure can often be accomplished with relatively minor field modifications.

The highest stress concentration in most plate rapping systems is at the base of the rapper shaft. At this point the total rapping energy is transmitted through as little as 20.6 cm^2 (3.2 = in^2) of area and 40.6 cm^2 (6.3 inches) of weld. Since the lower end of the shaft and the anvil beam are not mated, machined surfaces, the actual area of energy transmission is much less than 20 cm^2 (3.2 in^2) and will be concentrated in the weld. Welded gussets from rapper shaft to beam can distribute rapping imposed stresses.

The best method of eliminating shaft/anvil beam failure is to install a cast steel tapered socket on the beam and use a tapered rapper shaft. The cast steel socket receives rapping energy through an interference fit tapered connection with the shaft and delivers this energy over an area 6 to 8 times higher than a butt-end connection. Weld length is increased 3 to 4 times. This approach reduces stress concentration at the shaft base and in the anvil beam since the rapper loading is transferred to the beam over a broader area. Tapered rapper shaft connections of 5 cm (2 in) to 7.6 cm (3in) of coupling length length guarantee shaft alignment, and minimize stress concentration through high contact area. The important result of this stress reducing design is that over stressing is less likely to occur.

Fatigue failure results when metals are subjected to high stress levels for repeated loadings. If any component is loaded repeatedly with stresses above its fatigue limit, it will fail after a number of cycles. The number of cycles before failure depends on the stress level. If rapping induced stress levels in all components of the plate assembly are below the fatigue limit for the materials of construction, fatigue failure will not occur regardless of the number of cycles. S-N curves indicate that if fatigue has not occurred by about 10^6 cycles, the system has not been stressed above the fatigue limit. In the case of the frequency type vibrators and rappers, 10^6 cycles will occur in 5 to 6 hours of continuous rapping.

If stress failure has occurred at some point in the collecting plate system, the proper fix is not necessarily the obvious one of reducing rapping intensity. Effective rapping energy (measured as plate acceleration) will often be increased by reducing stress concentrations at failure points.

In one case, replacement of the shaft butt weld with a tapered base socket increased energy transmission and reduced stress levels (Neundorfer, 1977).[23] Vertical zero to peak acceleration of over 1000 g's were measured on one precipitator 22.8 cm (9 in) from the rapper shaft termination on the anvil beam. On the same plate system, there was no measurable normal excitation at the bottom of the plate. The anvil beams were stiffened, the plates to anvil beam connection improved, and tapered sockets and rapper attachments were installed. These improvements increased the normal acceleration at the bottom of the plates to about 15 g's (0 to peak). This improvement included bolting a tapered base to the existing single impact rappers but no rapper change. When tapered mount pneumatic frequency rappers were installed, the vertical anvil beam acceleration 22.8 cm (9 in) from the shaft was reduced from more than 1000 g's in the original case to less than 300 g's and the normal acceleration at the bottom of the plate averaged 28 g's (Neundorfer, 1976)[24].

See scope traces below:

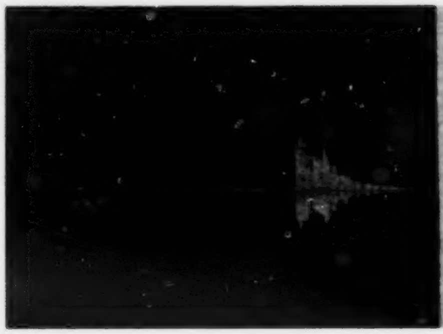

Vertical acceleration at anvil beam: magnetic impulse rapper. 1000 g's (0-peak) 20 ms/DIV 10v/DIV.

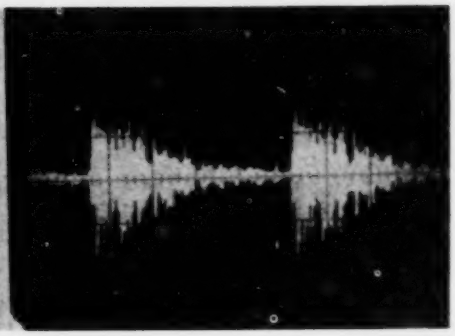

Vertical acceleration at same point on anvil beam: pneumatic frequency rapper.
293 g's (0-peak)
5 ms/DIV. 2v/DIV.
operating pressure 45 psi

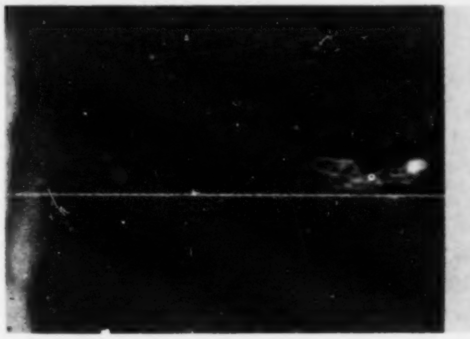

Normal acceleration at bottom of plate: magnetic impulse rapper. 0.0 g's (0-peak)
10ms/DIV .02V/DIV

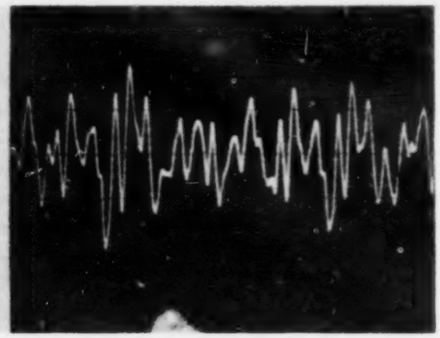

Normal acceleration at bottom of plate: pneumatic frequency rapper. 28 g's (0 - peak)
5 ms/DIV .2V/DIV
Operating pressure 35 psi

The improved plate and wire cleaning raised the corona current from a maximum of 150 ma with the original non-tapered, non-reinforced system to current limit (600 ma) with the improvements. Outlet grain loading was measurably reduced as would be expected.

IMPROVEMENT OF RAPPING MECHANISMS

Effective rapping energy cannot be transmitted through air. High area, tight connections between the rapper, rapper shaft, rapper shaft anvil beam, and anvil beam to plate will maximize the effect of available rapping energy. In one installation, the acceleration (0-peak) normal to the plate at the bottom of a top rapped plate was increased by 45% by applying a 1-1/2" long weld between the plate and its support beam at the top of the plate. This weld increased contact area.

Areas of high stress concentration in rapping systems can result in mechanical failure, but also cause high impedence to the transmission of rapping energy. Designing these areas out of the system using tapered connections and broad based anvil sockets solves a two-pronged problem.

A stress analysis of a plate or wire assembly would be very costly, if it were possible. The use of low mass accelerometers to measure accelerations at various points on both the electrode frames and electrodes generates information useful in design modifications to existing systems which will enhance rapping effectiveness.

RAPPING CONTROL

Precipitator rapper control plays a crucial part in attaining high precipitator efficiencies and low stack opacity. Thirty years ago continuous rapping of precipitator electrodes was introduced. This improvement was the beginning of an operational refinement with high potential for reducing precipitator emission. Rapping reentrainment losses, which can account for up to 90% of all precipitator emissions, can be reduced by as much as 85% through optimization of rapper control (Sproull, 1972).[25]

The following general principles of precipitator operation apply to most installations:

1) Plate rapping effectiveness increases with increased mass/unit area of dust (reentrainment is reduced).
2) Mass/unit area of dust can be expressed as a "time between raps" for any point in the precipitator along the gas flow as long as dust build-up does not affect charging and separation and as long as rapping is effective when it occurs.
3) This time between raps is inversely related to distance from the inlet of the precipitator for a given dust mass/unit area.
4) Plate response to a given rapping disturbance is reduced as dust build-up increases.
5) Simultaneous plate rapping increases the magnitude of instantaneous rapping loss. This may not necessarily increase overall emissions, but can increase the level of opacity.
6) Minimum rapper "on times" which result in good cleaning should be used.

Precipitator collecting electrode rapper control is normally designed so that rapping fields correspond to electrical fields. Each rapping field repeat time (the time it takes for a given rapper in that field to repeat after it has rapped) should be adjustable independent of the other field repeat times. The reason for independent field repeat time control is that in a multifield precipitator the mass build-up rate of dust from inlet to outlet field can vary by one to two orders of magnitude. Since rapping effectiveness is related to mass/unit area of dust on the electrodes, the field rapping repeat rate must be separately adjustable from inlet to outlet.

Unfortunately, field repeat rates cannot be set strictly according to field build-up rates. One reason is that migration velocity increases with particle size. Therefore, the precipitator is also a classifier, collecting larger particles in the inlet fields, and finer particles in the outlet fields. This classification affects dust tensile strength, agglomeration, and adhesion, and, therefore, affects the relationship between mass/unit area and repeat time. The extent of particle classification is reduced to some degree by the fact that larger particles are reentrained in much higher percentages than smaller particles; this results in passage of some of the larger particles from inlet fields to outlet fields through rapping reentrainment in the inlet fields.

Field repeat rates must be established for each installation. In most installations, processes, fuels and precipitator operating conditions may require the development of several sets of field rapping rates. Automatic field repeat feedback systems are being investigated but feedback parameters available are indirect and delayed. This lack of isolated direct feedback makes automatic repeat rate control a difficult problem.

Most precipitators are set up with much too frequent field repeat times. In almost every case, when field repeat times are studied in relationship to opacity and overall efficiency, repeat rates are found to be too frequent. In studies by Gooch, Spencer, Sproull, Nichols and Schwartz,[20] field repeat rates were changed from minutes to hours with very positive results.

In addition to field repeat rate control, plate rapper control should include anticoincidence. This feature allows only one plate rapper to operate within a time block. This time block should be greater than or equal to the time it takes for a rapping disturbance to clear the precipitator outlet. Anticoincidence rapping minimizes the magnitude of opacity spikes resulting from rapping disturbance.

Anticoincidence rapping can be applied to multiple precipitators sharing a common stack. Rapping only one plate rapper per stack at a time is helpful in meeting opacity regulations.

On some large precipitators and multiple precipitator installations, the number of plate rappers per stack may be as high as 700. In these cases, it is impossible to maintain a sufficient time block between raps, proper field repeat times, and total anticoincidence. When this condition exists, total anticoincidence is sacrificed in favor of anticoincidence in as many outlet fields as possible while maintaining a sufficient time between raps and field repeat times. Anticoincidence in outlet fields will have the greatest effect on minimizing rapping opacity spike magnitude. Opacity increases during rapping can last for more than 6 seconds; therefore, the time block per rapper is set at more than 8 seconds.

RAPPER CONTROL DESIGN

Rapper controls should offer field repeat rate adjustment, rapper on time adjustment, (or intensity or both) and rapper rest time adjustment for each field. Anticoincidence should be available. Totally solid state digital systems are desirable since they can offer broad program flexibility, with relatively few components. Time values are set with labeled switches with linear resolution.

Digital solid state rapper controls are very reliable if properly designed. Electrical line noise should be filtered and relays should be photoisolated. Rapper energization indicators and rapper failure indication are desirable features.

METHODS OF TUNING RAPPER SYSTEMS

Optimizing precipitator rapping with normally available feedback information requires documentation, patience, and some degree of imagination. The feedback information is obtained from:

1) Transmissometers (optical density)
2) Automatic voltage control console readings
3) Hopper evacuation system vacuum charts or other indications of relative amounts of dust discharged from each hopper.
4) Visual observation of electrodes being rapped during precipitator operation. (This can be done in some cases using access covers with pyrex viewing windows and high intensity lights).
5) Plate fouling observed during internal inspections with the precipitator shut down.
6) Recording of outlet grain loading and particle size distribution (this is generally not available).

Transmissometers, which measure optical density of flue gas, can be used to determine the degree of rapping reentrainment and the duration of the disturbance after the rap. Optical density relates linearly to dust concentration for a given type of dust. The relationship between optical density and dust concentration is available or can be developed for specific dusts.

Optical density increases resulting from rapping of the outlet fields and one or two fields directly upstream of the outlet fields, can be used directly to evaluate rapper intensity and field repeat times. Inlet field rapping disturbance often blends into the background opacity level. Therefore, inlet field repeat times and rapping intensity are adjusted to reduce opacity background levels.

Console readings are closely monitored during rapping optimization. Precipitator power should be maintained as high as possible between raps. A decrease in precipitator power due to electrode fouling will also be observed as an increase in optical density. When this occurs field repeat rates and/or rapper intensity in the field(s) affected should be increased.

If information can be developed indicating the amount of dust being collected from each field, rapping can be adjusted so that actual field collection efficiencies approach theoretical values.

Actual viewing of the electrodes during rapping while the precipitator is operating will reveal the amount of agglomeration of the dust and the size of dust chunks broken away by rapping. Corona quench resulting from high dust concentration during rapping may also be observed.

Precipitator inspections during outages will reveal the thickness and smoothness of the dust build up on electrodes. Direct manual rapping of electrodes or wash down during an outage and its effect on operation after start-up can demonstrate whether improved on-line electrode cleaning will improve performance. Highly irregular dust build up on the plates and back corona craters indicate special problems associated with high resistivity ash.

If outlet grain loadings and particle size distribution can be taken reliabily and continously during a rapping system "tune-up" the information derived will most directly help to establish an optimum rapping program.

REFERENCES:

1. Plato, H. Rapping of Collecting Plates in Electrostatic Precipitators. Staub-Reinhalt Luft (in English) 29: 22-30 (1969)

2. Gooch, J.P., G. H. Marchant, Jr. Electrostatic Precipitator Rapping Reentrainment and Computer Model Studies. Prepared for EPRI by SRI. EPRI FP-792. 3: (1978)

3. UN Published work done by Wm. Neundorfer & Co., Inc. Two Eastern Utilities (1976)

4. Spencer, H.W. III. Rapping Reentrainment in a nearly full Scale Pilot Electrostatic Precipitator. Prepared for U.S. EPA by S.R.I. EPA-600/ 2-76-140: 76 (1976)

5. Gooch and Marchant, op. cit.

6. Ibid

7. Spencer, op. cit.

8. Nichols, G.B. S.W. Spencer, and J.D. McLain. Rapping Reentrainment Study, S.R.I. November (1975)

9. Tassicker, O.J. Some Aspects of Electrostatic Precipitator Research in Australia. Symposium on Electrostatic Precipitors for Control of Particles. P.B. 240440:101-129 (1975)

10. Penney. G.W. Adhesive Behavior of Dust in Electrostatic Precipitation. Symposium on Electrostatic Precipitators For The Control of Fine Particles EPA-650/2-75-016: 65 (1975)

11. Spencer, op. cit.

12. Gooch and Marchant, op. cit.

13. Spencer, op. cit.

14. Sproull, W.T. Fundamentals of Electrode Rapping in Industrial Electrical Precipitators. J.A.P.C.A. 15/2: 50-55 (1965)

15. Ibid

16. Ibid

17. Spencer, op. cit.

18. Sproull, W.T. Minimizing Rapping Loss in Precipitators at 2000 Megawatt Coal Fired Power Station J.A.P.C.A. 22/3: 181-186 (1972)

19. Ibid

20. Unpublished work done by Wm. Neundorfer & Co., Inc. for a midwestern utility. (1977)

21. Nichols et al, op. cit.

22. Englebrecht, H.L. Electrostatic Precipitator Inspection and Maintenance. Plant Engineering pp 193-196 April (1976)

23. Neundorfer, 1977, op. cit.

24. Neundorfer, 1976, op. cit.

25. Sproull, 1972, op. cit.

26. White, H.J. Industrial Electrostatic Precipitation. Addison-Wesley Publishing Co., Inc. 1963.

27. Schwartz, L.B. Effect of Rapping Frequency on the Efficiency of an Electrostatic Precipitator at a Municipal Inunerator. Proceedings of the Fourth Annual Environmental Engineering and Science Conference Mar. 3-4, 1974, U. of Louisville.

COMPOSITION OF PARTICULATES
SOME EFFECTS ON PRECIPITATOR OPERATION

By:

Jack D. Roehr
Wahlco, Inc.
Santa Ana, California 92704

Precipitator operators and designers often review spectrographic analyses when attempting to resolve problems with installations or designing future installations. These analyses can be misleading. Those responsible for operation and design must have a knowledge of the compounds of the elements that can make up the particulate under study as well as the process that produced these compounds and the operating conditions existing at the point of particulate formation. Several of the most common elements and compounds are discussed with a review of their effects on precipitator operation.

COMPOSITION OF PARTICULATES
SOME EFFECTS ON PRECIPITATOR OPERATION

When this planet Earth was formed it was made up of various and sundry elements. These elements - whether they be carbon, copper, zinc, calcium, or whatever - were subsequently discovered by man and he set about finding ways and means of extracting these elements for his use. It was soon learned that in no two places on the surface of the Earth were these elements found in the same abundance or in the same ratios or in the same mixtures making up compounds of the elements.

Because of these differences and also because of technological advances and/or the findings of a multitude of inventions, we have almost as many different methods of processing ores to extract the wanted elements or of making use of some compounds such as the burning of coal as there are individual industrial plants on this Earth.

This is the root of the problem when we are concerned with the operation of an electrostatic precipitator being used or to be used to clean the gas evolved from one of these processes. In any case we are concerned with the capture of particulates made up of compounds of various elements when we very seldom, if ever, know what the compounds are.

For purposes of expediency as well as economy, chemical analyses of particulate are usually obtained by means of a spectrograph. In some instances no analyses will be made on the dust or particulate from an installation unless the vendor is in trouble. If the equipment meets performance guarantees, that point is proven and the test people pack up their gear and leave. Nothing beyond that is learned. For particulate analyses, each element reported in a spectrographic analysis is usually stated as the oxide of the element, i.e., iron is reported as Fe_2O_3 and calcium as CaO when, in fact, the elements could be in the form of a sulfide or a sulfate or some other compound.

It is these results that are fed into computers over the world in attempts to derive an equation for calculating the drift velocity or effective migration velocity in the Deutsch equation. Although several of these have been published, the authors usually admit that each has its limitations and drawbacks. As an indication of the problems that can be had please refer to Table 1. Here are the coal and ash analyses from a pulverized coal-fired boiler and precipitator system.[1] In this case there were two parallel precipitators. The ash analyses for each was, for all practical purposes, identical. One precipitator exceeded the design performance while the other failed by a wide margin. In fact on the basis of the tested performance the precipitator would have had to be doubled in size to meet design conditions, even more if you are a believer in the square root rule or double power function version of the Deutsch equation.

They subsequently learned that due to some unknown factor in the boiler system the SO_3 content in the gas to precipitator 1B was about 30 ppm and the SO_3 in the gas to the other unit was about 1 or 2 ppm. After conditioning the gas with SO_3 the performance of the precipitator exceeded the design by a considerable amount.

The purpose of this discussion is not to reveal the latest in black magic on how to arrive at proper precipitator size or prognostication on the anticipated performance of an existing or planned installation. Rather it is to discuss operating problems that can be experienced when certain elements or compounds are present in the particulates or gases to be cleaned with a precipitator. Also, we are not restricting this to a single application such as a pulverized coal-fired boiler.

ALUMINUM

This is found in such applications as coal-fired boilers, cement kilns, fluid catalytic cracking units and in the primary aluminum industry. Generally it is in the form of aluminates and silico-aluminates of high electrical resistivity.

For successful precipitator operation the gas must be conditioned to attain surface conductivity. Water vapor is most commonly used, either by water evaporation in conditioning chambers or as a natural consequence in the process such as in a wet process cement kiln; ammonia, in addition to water vapor, has been found to be a good conditioner especially for precipitators on fluid catalytic cracking units, and sulfur trioxide is the preferred agent for fly ash. Certain alumina containing clays can be particularly troublesome. For example, a precipitator on a coal-fired boiler in Alabama gave operating difficulties when they were burning coal from a particular mine. There was very little difference in the spectrographic analyses of the ash. However, it was learned that in the coal ash from the one mine that gave the trouble the aluminum and silica in a portion of the ash were present as an especially fine kaolin clay dust. This fraction of the ash resisted all attempts to be rapped from the collecting plates leaving a thin film of very high resistivity dust.

ARSENIC

This is only mentioned here for those in the non-ferrous metallurgical industry that are concerned with a furnacing operation with a charge containing arsenic. Arsenic will be readily volatilized off in the furnace as the oxide and will condense out of the gas as the temperature decreases. Gas cleaning is usually done in two stages, the first over 500°F to get the bulk of the dust and pass the volatile arsenic oxides and the second below 270°F to catch the condensed oxides. The gas must be shock cooled so that the arsenic will be condensed out ahead of a cold precipitator. Any arsenic that condenses out in the precipitator can give real trouble, the most common of which is the growth of needle-like crystals on the discharge electrode with decreased electrical clearance and low voltage operation. In the temperature range of 350-450°F the condensing arsenic compounds seem "plastic" and sticky resulting in sure problems in the precipitator. Very low operating temperature can also be troublesome as acid dew point is reached with the SO_3 formed in the furnacing operation.

CALCIUM

This is usually found in the dust to the precipitator, depending on the process involved, as calcium oxide, calcium carbonate or calcium sulfate. Any of these can be detrimental to precipitator operation as they have an inherent high electrical resistivity. The first "hot" precipitator in the industry, on a cement kiln in 1912, had high voltage support insulators made up from a stack of marble slabs (a form of limestone).

When calcium compounds are the predominate constituent in the dust to be collected you must follow the resistivity curves in your precipitator operation and have either high moisture content or very low or very high operating temperature. For example - resistivity problems on iron ore sintering machines can be directly related to the lime content of the charge. High lime, self-fluxing plus sinter mixes are the worst in this regard.

Calcium sulfate can form in a lime-gas reaction in the system. If permitted to form while the dust is in the precipitator it will result in a very hard dust cake on both the discharge electrodes and collecting plates. Where the flues are long or large enough to permit formation of the sulfate either in the process or in the flue system ahead of the precipitator, the resultant dust will be essentially free-flowing after it is collected.

IRON

If this is in the form of the dry oxide the electric resistivity will be high and suitable precautions must be taken to have operating temperatures on either side of the peak of the curve and sufficient moisture must be present for conditioning, particularly on the high temperature end of the scale.

Precipitators have been used for collecting the fumes from the oxygen blown steel-making facilities, both for building ventilation and for vessel discharge gases. The fume is essentially iron oxide and can readily be collected at ambient conditions for the first case and with the use of water evaporation conditioning for the second case.

Furnacing operations that have sulfur in the charge such as with a pyrite roaster will result in a dust that will consist of a high percentage of iron sulfates. The iron oxide in the gas serves as a catalyst for the formation of SO_3 which then reacts with the oxides to form the sulfate. Iron sulfate itself is not a difficult dust to precipitate and handle if it is in that form as it enters the precipitator.

If sufficient time has not elapsed between the roasting operation and the precipitator so that the formation of the sulfate occurs after the dust is collected, it will invariably result in build-up on the discharge electrodes and collecting plates of hard clumps that can be of rock-like consistency, impossible for the rappers to remove.

No two cases are ever alike and solutions are difficult to find. The process is time and temperature dependent. For example, a large clump or nodule taken from a discharge electrode can be analyzed for iron sulfate. You will find that the stratum that was closest to the discharge electrode will be very high in sulfate - say 25% - with correspondingly less sulfate content as you approach the outer boundary of the clump or the "newest" portion. Also, as the sulfate content increases, so does the hardness.

The best solution to this sulfating problem is to change the operating temperature. The reason for this is not clearly understood. An increase in operating temperature from 700°F to 900°F has corrected a situation, while in others going to 1100° was required. In still other cases a lower temperature has been the answer.

LEAD AND ZINC

These two have been lumped together for the purpose of this discussion because the end results, as far as precipitator operation is concerned, are so similar.

Most precipitator applications are on the gases from sintering machines or roasting operations. The differences in operations and conditions are as numerous as there are plants in operation. No two are alike.

Sinter machine practice with older techniques gave fumes of very high resistivity and made external flue gas conditioning a necessity. A general rule of thumb was to evaporate sufficient water to result in a relative humidity of 60%. Consolidated Mining Company, Trail, B.C., used to condition the gas to achieve a moisture content of 1% in the dust. The precipitator worked satisfactorily at this condition. Less moisture than that resulted in spontaneous combustion of the dust in the hoppers and more than that resulted in a sticky dust that could not be rapped from the collecting plates.

In the earlier days when the multiple hearth furnace was common in roasting zinc concentrates, precipitator operation on these gases was no real problem. This was because of the relatively low roasting temperatures with sufficient time to permit the formation of zinc sulfate. With the advent of more modern roasting machinery such as fluid bed reactors it was a different situation. Here there is a very high temperature and a very short residence time within the roaster, and the dust to the precipitator is a real fume made up of condensed zinc oxide which had volatilized as zinc in the furnace and then oxidized to create a sub-micron particle most difficult to collect in a precipitator.

This dust not only has high resistivity but it is very light, not unlike feathers. Some plants have had to resort to closed damper-power off rapping to achieve successful operation. Others have abandoned the precipitator entirely and have resorted to high temperature fabric filters.

Most copper smelters have had to increase the dust collection efficiency of their plants because of air pollution restrictions. Since they return the precipitator catch to the system, because of the high copper content, they are, if they have appreciable zinc or lead content in their concentrate charge, adding to the zinc or lead content of the dust. This is a vicious cycle since the only way to get rid of these "impurities" is via the stack or by discarding the dust. If they don't discard the dust the zinc or lead content continues to increase and with it a degradation of precipitator performance. A typical example of this is a copper smelter in Canada, where the recirculating dust has resulted in very high concentrations of lead and zinc from their converter gas. Lead content varies from 18 to 40% and zinc content varies from 6 to 20%, dependent on the stage of the blow for the various converters. In situ resistivity measurements showed that the resistivity was a function of zinc content varying from 10^{10} at 8% to over 10^{12} at 20% at the operating temperature of 500 - 600°F.

In a study to determine what could be done to upgrade precipitator performance a pilot precipitator was installed. The only thing that would reduce opacity at the stack was a combination of moisture and SO_3 injection. The addition of about 3% by volume water vapor and 50 ppm SO_3 reduced opacity to, essentially, zero.

MAGNESIUM

High magnesium content dusts are most commonly found in plants that extract the element from brines or sea water and precipitators are used on the magnesium hydroxide calciners. Precipitation is ordinarily easy due to high water content of the gases, although rapping can be difficult due to the light, fluffy nature of the collected material. One exception is in plants that do not have a fresh water wash for the precipitate and wind up with a high chloride content which is volatilized off in the kiln resulting in a very fine fume making precipitation more difficult.

MOLYDENUM

For this element we find precipitators on moly-sulfide roasters. After difficulties with the earliest installation it was established that success hinges on the temperature of operation. Above 700°F the dust is sticky and plastic, soon resulting in a wall-to-wall mess. Although the SO_2 content of the roaster is not very high, the SO_3 formation is quite high resulting in a very high dew point of approximately 400°F below which temperature corrosion is a real problem. These factors limit the successful operating temperature to a fairly narrow band. However, it can and has been done.

PHOSPHOROUS

This element is included here as a matter of interest since it has been pegged as one of the culprits in the failure of a precipitator to perform on a coal-fired boiler not too far from Denver.

Precipitators have been used for elemental phosphorous furnaces for years. This is one of the worst if not the worst duties for a precipitator due to rapid and extreme temperature variations. However, these precipitators are not really for the purpose of collecting phosphorous as the temperature is high enough that all phosphorous, theoretically, is in the vapor state and the precipitator is to collect the particulate, mostly silica, before the phosphorous is condensed out down the line in the process.

It has been reported by the operators at the above mentioned utility that 1 - 4% P_2O_5 in the ash resulted in impairment of precipitator operation. This could be the result of vaporization of the phosphorous in the boiler with subsequent condensation into one of several forms that can be very sticky and build up on discharge electrodes.

A plant in Idaho has a precipitator on a phosphorous rock calcining kiln and with very good success. The dust has a P_2O_5 content of about 15%. The dust is very fine making a venturi scrubber, which they tested before purchasing a precipitator, out of the question because of the very high pressure drop requirement. Their furnacing operation is only in the range of 1600°F and this may be the reason for the difference in the resultant dust in comparison to the coal-fired boiler operation.

POTASSIUM AND SODIUM

These two are also lumped into the same discussion. They are both in the alkali group of metals and both have comparable results concerning precipitator operation. Either can do the following, they can act as conditioners to enhance precipitator performance or they can be the chief cause of impaired precipitator performance. The real key to this is in the process that caused the dust in the first place.

Sodium content of the ash has been an indication of the failure or success of precipitators on coal-fired boilers being fired with low sulfur coal, with the trend being better operation with higher sodium content. As examples we have Utah Power & Light's Huntington and Naughton stations. At Huntington when they had 5 - 6% sodium in the ash their precipitators operated in the high 99%+ range with drift velocity in the neighborhood of 8 cm/sec. At Naughton where the sodium was down in the 1% or lower range the precipitator on one boiler operated in the 3 - 4 cm/sec. range and they had to use SO_3 flue gas conditioning to achieve satisfactory precipitator performance.

Sodium has also been used with varying degrees of success as an additive. This certainly is not new. Thirty-five years ago a saturated solution of salt water was added to the gas from a dry process dolomite kiln. This permitted them to operate their precipitators at 550°F with good performance. Without the salt addition they had to operate at 700°F for good performance.

Salt has been added to the furnace charge in various non-ferrous metallurgical operations. This was not for the purpose of enhancing precipitator performance but to aid in volatilizing elements such as cadmium or lead. A secondary result was an aid in precipitator performance. It is believed that the chloride compounds formed had an affinity for water vapor and this lowered the resistivity. The sodium may have had a bearing also.

In some applications, particularly cement kilns, the potassium and sodium actually downgrade the precipitator performance. The precipitator will actually be selective in that the cement making constituents, i.e., CaO, Al_2O_3, Fe_2O_3, MgO and SiO_2 will be precipitated out in the first fields and the K_2O and Na_2O will be caught in subsequent fields with the highest potassium and sodium content being in the stack effluent. This is due to the method by which the soda and potash fumes are made. The kiln temperature in the burning zone is high enough to volatilize off the alkali. In fact this is what they want - to get the alkali out of the clinker. This alkali subsequently condenses out as a fine fume and downgrades precipitator performance, because of the fine particle size. On cooling, they may go through a plastic condition in the 600 - 650°F range and should this occur in the precipitator you are in trouble from build-up. You must get the temperature down to at least 550°F and this should be accomplished by water evaporation.

With kilns that practice insufflation, i.e., kiln feed charged via the burners, the situation is aggravated because of the extreme temperature where all the alkalies will be driven off as a vapor.

In cement plants that have gypsum in the feed or are firing with high sulfur oil sulfates of both potassium and sodium can be formed. These must be cooled so that condensation occurs in the flues well ahead of the precipitator.

SULFUR

This element can mean success or failure with a precipitator on a process. If in the elemental form, as caught in the precipitator, it means trouble. (This is very rare but it has happened in special cases.) It melts at about 300°F and is a solid a few degrees below that temperature, and a super-viscous liquid a few degrees above. It has a high resistivity. It can quickly plug up a precipitator and/or result in build-up and short circuiting.

When oxidized to SO_3 it can condition the gas and dust so as to greatly enhance precipitator performance.

If the SO_3 goes to the formation of sulfate compounds it can result in build-up problems as discussed above.

GENERAL

There are other elements or their compounds that precipitator operators or designers will be confronted with. However, the above discussion should cover the most prevalent.

CONCLUSION

When designing precipitators for a new plant or when attempting to determine the reasons for the poor performance of an existing installation an analysis of the particulate will give you only a partial answer. You must consider the environment at the place in the process where the particulate is being formed, as well as subsequent to this point in the process, so that you will have a better understanding of the exact chemical and physical nature of the particulate under consideration at the time it enters the precipitator.

TABLE 1

COAL ANALYSES

Hydrogen	3.4%
Carbon	51.0
Water	15.0
Sulfur	1.6
Ash	21.6

ASH ANALYSES

	Unit A	Unit B
SiO_2	48.9%	49.6%
Al_2O_3	25.1	26.1
Fe_2O_3	8.6	8.2
CaO	4.8	4.4
MgO	1.3	1.4
TiO_2	0.7	0.7
K_2O	5.4	5.6
P_2O_5	-	-
$NaOH$	2.6	2.4
SO_3	1.1	1.4

PRECIPITATOR EFFICIENCY

	Unit A	Unit B
Design	98.5%	98.5%
Test	89.9	98.9
Test w/SO_3	99.2	-

Literature Cited:

1. Busby and Darby (May, 1963) Journal of The Institute of Fuel

INCREASING PRECIPITATOR RELIABIILTY BY PROPER LOGGING AND INTERPRETATION OF OPERATIONAL PARAMETERS - AN OPERATOR'S GUIDE

By:

Peter P. Bibbo - Product Manager, Precipitators
Peter Aa - Product Analyst
Research-Cottrell, Inc.
Utility Division
Somerville, New Jersey 08876

Maintaining efficient and reliable electrostatic precipitator operation is dependent to a large extent on the operator's knowledge of the precipitation process and on the type, amounts and use of operational data and records. Analysis of properly recorded information can heighten the operator's knowledge of precipitator behavior and, through his actions, precipitator performance and reliability can be enhanced.

This paper discusses the type of data needed for an operator's evaluation of precipitator performance, where and how to obtain this data, and how to interpret the collected data.

The procedures contained in this paper are the recommendations of a manufacturer's field service personnel, who have had extensive experience in working with and training operators in the proper operation and care of precipitators. With the more intimate knowledge and experience that only comes with daily plant level responsibility for precipitator performance, it is expected that operators who read this paper will tailor the detailed recommendations to better suit their own situation.

INCREASING PRECIPITATOR RELIABILITY BY PROPER LOGGING AND INTERPRETATION OF OPERATIONAL PARAMETERS - AN OPERATOR'S GUIDE

BASIS OF PRECIPITATOR PERFORMANCE

Since this paper deals with the collection and interpretation of operational data which could be useful in maintaining optimum precipitator performance, a review of the fundamental operating parameters which control precipitator performance is an appropriate starting point.

Simply stated, the operating conditions at the inlet of the precipitator plus the operating conditions inside the precipitator determine exactly what conditions result at the outlet of the precipitator. In spite of this simple cause and effect relationship, different theories and opinions abound which attempt to explain the precise relationships among the many parameters that control precipitator behavior. Fortunately for the operator, the parameters to which he can measure and adjust are not complex, and can be effectively controlled to maintain precipitator performance at the maximum possible levels.

Operating conditions at the inlet of the precipitator are completely dependent upon the fuel being fired, and by the boiler design and its operation. If a gas conditioning system is installed, these inlet conditions may be altered somewhat. The inlet conditions important to the operator are shown in Table 1. The conditions inside the precipitator are mainly a function of the precipitator design. To the extent that the manufacturer has followed good design practices and provided the means for adjustment, this is where the operator has the greatest control over the precipitator performance level. Important precipitator conditions are shown on Table II.

MAINTAINING EFFICIENCY AND RELIABILITY

The availability performance of electrostatic precipitators is typically among the best for any mechanical equipment in a power plant. Availabilities over 90 percent are not uncommon.

However, the progress of environmental legislation in this country indicates that availability levels at or above 90 percent will have to become the ordinary rule rather than a proud exception. It has been and still is the position of Research-Cottrell that the key to maintaining reliable precipitator performance is through a working preventive maintenance program, regardless of individual precipitator design features or manufacturer's claimed reliability.

The data logging and interpretations recommended in this paper augment any precipitator preventive maintenance program. In fact, some of the recommended data logging activities are identical to preventive maintenance steps outlined by Research-Cottrell in earlier literature. An example of recommended preventive maintenance steps for precipitators is shown in Table III.

DATA TO BE RECORDED FOR INLET CONDITIONS

Since the precipitator operator typically has little control over boiler operation, there may be a natural reluctance toward obtaining useful boiler data at the appropriate times. However, at all times, practically all the conditions that the precipitator must treat are being produced by the boiler. Speaking from our own experience, we can say that there have been many cases where proper boiler data collection has revealed causes for fluctuations in precipitator performance, and operational changes were made to favor precipitator performance, without detriment to the performance of the boiler.

Table IV lists the data source documents that can be used to obtain all the essential data indicated in Table I for precipitator inlet conditions.

Boiler Data

Frequently, we find that too much boiler data is recorded when its only purpose is to support analysis of precipitator behavior.

Figure 1 shows a recommended boiler data sheet. The heading should be completely filled out each time a new sheet is used. Too often, this detail is overlooked, causing considerable confusion. This commentary pertains to all data sheets. Data taken on separate days should not be entered on the same sheet. Information on boiler operation should be recorded at least once per day, at representative load conditions.

Coal Analysis

Many different report formats are used, but they all contain essentially the same information. Common deficiencies in these reports are failure to report the exact dates the samples were taken and the coal source identification. To accurately identify the coal, the mine name, seam, and geographical location must be logged. To be most meaningful and accurate, the analyses should at least be reported "as received" (A.R.).

Ash Analyses

Similarly, ash mineral analysis report formats vary widely although they generally contain the same information. Dates and coal source should also be logged, and since ash composition is influenced by the combustion process, a notation should be made indicating whether the sample was fly ash or coal ash. Coal ash is the residue obtained by completely combusting a coal sample in a laboratory. Fly ash should be considered as a sample obtained downstream of the boiler economizer section. Ten minerals plus LOI (loss on ignition, which is not the same as carbon content) are the constituents that are always of interest to precipitator performance.

Many plants perform composite coal proximate analyses once per week. The operator should obtain a copy of these and any other coal and ash analytical results that are available, and keep them in the precipitator file.

Precipitator Performance Test Results

Although this data source is normally obtained only once per year at most, it is the only source that contains the most comprehensive set of related data useful in evaluating precipitator performance, and usually it is the only document that contains information the operator cannot readily obtain himself, such as actual dust concentration, particle size distribution, ash resistivity, and so on. Gas flow uniformity is usually measured only once and may not be measured at all. Since uniformity is determined mostly by the geometry of the actual installation (and to a much lesser extent operating conditions such as boiler load), and cannot be easily adjusted, it is of little interest to the operator.

DATA TO BE RECORDED FOR PRECIPITATOR INTERNAL CONDITIONS

A properly designed precipitator should be capable of efficiently treating all the conditions delivered to its inlet by the boiler. Therefore, the operator should find the greatest control he has over performance and reliability will be by the actions he takes on the precipitator.

The important operating variables that lead to maximum precipitator performance and reliability aren't many, but it is not possible for an operator to recall the essential information without a systematic procedure of data logging. Table V lists the data source documents that can be used to record all the data necessary to understand and maintain maximum precipitator performance and reliability.

Electrical Energization Data

The entire precipitation process depends fundamentally on the quality of electrical energization, and power readings are sensitive to changes in coal quality and boiler operation. For these reasons, power data should be taken frequently. A form used by Research-Cottrell for recording these readings is shown in Figure 2, but any format which requires the same information would be useful.

Voltage-Current Curves

Again, speaking from practical experience, it is difficult to imagine any data that is as useful as voltage-current curves in understanding precipitator behavior, yet they seem to be used infrequently at the plant level. While more time-consuming to obtain than electrical readings, voltage-current data need not be taken as frequently as power data, and curves do not have to be generated for every T/R set for the data to be useful. The data can be recorded on the form shown in Figure 3, but it is best interpreted when plotted on a curve, as shown in Figure 4.

Energization data should be taken at least once per day, or at any time when a major change in boiler operation occurs. Voltage-current curves should be recorded at least once on all T/R sets to reflect normal operating conditions for each major coal source fired in the boiler. Thereafter, voltage-current curves need only be taken for a fraction of the T/R sets to serve as a check. Plants may wish to record these electrical data more frequently, but experience will probably show it is not necessary.

Electrode Cleaning Equipment Data

Next to energization data, information on electrode cleaning system operation is of most use to the operator. Electrode cleaning system data important to precipitator operation appears in Table VI.

Few operators log the operation of electrode cleaning equipment. Yet this system's operation has a large effect on the efficiency and reliability of the precipitator.

Since electrode cleaning system operation is infrequently changed, it is not necessary to record this data on a frequent basis. However, any changes that are made to the operation should be logged, the reason for the change noted, and the effect on precipitator operation recorded.

Ash Removal System Operation

The most prevalent cause of poor precipitator availability is electrical section grounds caused by full hopper conditions. An ash removal system operation log can be an important aid in analyzing and understanding precipitator reliability. Dates and times of all full hopper conditions or suspected full hopper conditions should be entered in the log.

Since the actual ash pulling cycle is frequently controlled automatically on a demand basis, it should only be necessary to record dates and time of all full hopper conditions or suspected full hopper conditions. To identify dust maldistribution in the precipitator, the operator may wish to record the time required to pull each hopper.

Internal Component Inspection Data

The internal condition of the precipitator is a major controlling factor in precipitator operation and reliability. During any outage of sufficient length, a precipitator internal inspection should be performed. Major items to be inspected during an internal inspection are listed in Table VII.

Research-Cottrell has developed an internal inspection log, shown in Figure 5 that simplifies the logging of internal conditions. During an internal inspection the inspector simply codes his findings on the log, and converts the codes into a verbal inspection report after the inspection is complete. Additional items can be added to the code as necessary.

Complete inspections and reports should be made with each annual outage and on any other occasion when time permits. Internal inspections are particularly important during unscheduled outages if localized poor electrical performance has occurred.

Replacement Parts Log

The recording of part descriptions, failure dates and replacement dates will show whether component failures are on a reoccurring or random basis. There are many components that have a direct effect on associated components, and without replacement records the direct cause of component failure may never be detected.

HOW TO INTERPRET THE DATA

In order to maintain optimum precipitator performance, we believe the operator must first know what the design or expected precipitator performance level is. He should then be able to compare this to the present performance level, and finally investigate and correct the apparent cause for malperformance if it exists. Thus, we also believe the operator should have a basic understanding of what precipitator performance depends upon. This paper does not pretent to present all the knowledge of precipitation theory in a few pages of print, for that would result in a gross oversimplification. However, by at least recognizing some of the more important aspects of precipitator behavior, the operator will be able to do his job better.

Precipitation Fundamentals

Precipitator performance level is totally dependent on three general quantities: the amount of energized bus sections, the total gas volume passing through the precipitator, and the sum of all other system parameters such as ash composition, particle size distribution, precipitator voltage and current levels, and all the other inlet and internal conditions. The baseline is the level of performance that results when all these conditions are considered "normal".

Deviation from expected performance cannot be detected unless the baseline performance is known. Since the baseline in reality will be a broad line, information that the operator records that is indicative of "normal" performance level will contribute to the definition of baseline performance.

Likewise, recorded information that is not indicative of "normal" performance gives the operator insight as to what factors may be adversely affecting precipitator performance. It is convenient to divide the data into two categories: operational factors and physical factors.

Operational Factors

Boiler data, coal and ash analyses, electrical readings and voltage-current curves, rapper operation, and ash removal system data are all examples of operational factors. All operational factors are related to one another in some way, and they all make a contribution to precipitator performance.

For example, gas volume, one of the three precipitation fundamentals, can be estimated from simple boiler data. A better estimate of gas volume can be obtained by a coal analysis. Comparison of the estimated gas volume with "normal" gas volume can indicate a cause for deviation in precipitator performance.

Likewise, comparison of electrical readings can supply insight into precipitator behavior. For instance, changes in voltage levels can indicate changes in coal or ash properties, internal dust build-up, gas temperature excursions, and so on.

The relationships among all the operational factors can become complex. Figure 6 is a simplified guide to understanding some of the most important relationships that normally exist. This guide will not satisfactorily answer every question that can arise, but it should help the operator avoid misconceptions and assist him in defining potential problems.

Physical Factors

Precipitator performance and reliability can be affected by actual or imminent equipment faults which are completely independent of the operational factors. These can also be complex. Figure 7 is a fault tree (1) for typical precipitator hardware. The operator can use this tree to quickly ascertain real or potential equipment failures that can cause deviations from "normal" performance.

CONCLUSIONS

Logging important precipitator operating and physical conditions will give the operator useful insight into the factors that contribute to changes in precipitator performance levels. A written record of the cause and effect relationships that have occurred in the past, along with a fundamental knowledge of precipitator behavior, will aid the operator in identifying and correcting potential failure causes in the future. Hopefully, the information and guidelines presented in this paper will be helpful in enhancing precipitator performance and reliability by making the operator more effective in what he does. In this latter regard, we make three final comments

First, we recommend that all pertinent data collected on precipitators be maintained separately from records for other plant equipment. Also data should be filed by date. This is to ensure that information is readily available for analysis and cross-checks without the need to collate various files or sub-files.

Second, wherever possible, a single person or group at the plant level should be made responsible and held accountable for proper record keeping and for precipitator performance and reliability. The reason for this is that the precipitation process depends upon the interaction of process and equipment variables that are best understood and controlled by those with hands-on experience.

Finally, operators should recognize that the procedures and recommendations contained in this paper can readily be incorporated into a preventive maintenance program; that the information is useful in identifying real problem areas that require corrective maintenance; and that the sum total of all the corrective and preventive maintenance actions the operator performs will ultimately lead to optimum precipitator performance and reliability.

---

(1) The Fault Tree shown in Figure 7 is a partial tree. A complete tree can be obtained by writing to the authors.

Table 1. FUNDAMENTAL ESP OPERATION CONDITIONS

PRECIPITATOR INLET
GAS VOLUME, VELOCITY & UNIFORMITY
GAS TEMPERATURE
GAS HUMIDITY
TYPE AND RANK OF FUEL FIRED
DUST CONCENTRATION
DUST SIZE DISTRIBUTION, RESISTIVITY, AND OTHER PROPERTIES
CARBON CARRYOVER & OTHER BOILER OPERATING CONDITIONS

Table 2. FUNDAMENTAL ESP OPERATING CONDITIONS

PRECIPITATOR INTERNAL
ENERGIZATION & SECTIONALIZATION
INTER-ELECTRODE ALIGNMENT
DISCHARGE & COLLECTING ELECTRODE RAPPING & CLEANLINESS
GAS FLOW DISTRIBUTION
AMBIENT AIR INLEAKAGE
HOPPER ASH LEVEL

Table 3. PM CHECKLIST FOR A TYPICAL FLYASH PRECIPITATOR

DAILY

- TAKE AND RECORD ELECTRICAL READINGS AND TRANSMISSOMETER DATA
- CHECK OPERATION OF HOPPERS AND ASH REMOVAL SYSTEM
- EXAMINE CONTROL ROOM VENTILATION SYSTEM
- INVESTIGATE CAUSE OF ABNORMAL ARCING IN TR ENCLOSURES AND BUS DUCT

WEEKLY

- CHECK RAPPER AND VIBRATOR OPERATION
- CHECK AND CLEAN AIR FILTERS
- INSPECT CONTROL SET INTERIORS

MONTHLY

- CHECK OPERATION OF STANDBY TOP HOUSING PRESSURIZING FAN AND THERMOSTAT
- CHECK OPERATION OF HOPPER HEATERS
- CHECK HOPPER LEVEL ALARM OPERATION

QUARTERLY

- CHECK AND CLEAN RAPPER AND VIBRATOR SWITCH CONTACTS
- CHECK TRANSMISSOMETER CALIBRATION

SEMIANNUAL

- CLEAN AND LUBRICATE ACCESS DOOR DOG BOLTS AND HINGES
- CLEAN AND LUBRICATE INTERLOCK COVERS
- CLEAN AND LUBRICATE TEST CONNECTIONS
- CHECK EXTERIOR FOR VISUAL SIGNS OF DETERIORATION, AND ABNORMAL VIBRATION, NOISE, LEAKS

Table 3. PM CHECKLIST FOR A TYPICAL FLYASH PRECIPITATOR (CONT'D)

ANNUAL

- CONDUCT INTERNAL INSPECTION
- CLEAN TOP HOUSING OR INSULATOR COMPARTMENT AND ALL ELECTRICAL INSULATING SURFACES
- EXAMINE AND CLEAN ALL CONTACTORS AND INSPECT TIGHTNESS OF ALL ELECTRICAL CONNECTIONS
- CLEAN AND INSPECT ALL GASKETED CONNECTIONS
- CHECK AND ADJUST OPERATION OF SWITCHGEAR
- CHECK AND TIGHTEN RAPPER INSULATOR CONNECTIONS

SITUATIONAL

- RECORD AIR LOAD AND GAS LOAD READINGS DURING AND AFTER EACH OUTAGE
- CLEAN AND CHECK INTERIOR OF CONTROL SETS DURING EACH OUTAGE OF MORE THAN 72 HOURS
- CLEAN ALL INTERNAL BUSHINGS DURING OUTAGES OF MORE THAN 5 DAYS
- INSPECT CONDITION OF ALL GROUNDING DEVICES DURING EACH OUTAGE OVER 72 HOURS
- CLEAR ALL SHORTS DURING EACH OUTAGE
- CHECK ALL ALARMS, INTERLOCKS AND ALL OTHER SAFETY DEVICES DURING EACH OUTAGE

Table 4. DATA SOURCE DOCUMENTS FOR PRECIPITATOR INLET CONDITIONS

BOILER DATA SHEET

COAL ANALYSIS - PROXIMATE (A.R.)
ULTIMATE (A.R.)

ASH MINERAL ANALYSIS

PRECIPITATOR PERFORMANCE TEST REPORTS

MANUFACTURER'S GAS FLOW DISTRIBUTION TEST RESULTS

Table 5. DATA SOURCE DOCUMENTS FOR PRECIPITATOR INTERNAL CONDITIONS

- ELECTRICAL ENERGIZATION READINGS
- VOLTAGE - CURRENT CURVES & WAVEFORM DATA
- RAPPER OPERATION DATA
- ASH REMOVAL SYSTEM OPERATION
- INTERNAL INSPECTION REPORTS
- REPLACEMENT PART LOG

Table 6. ELECTRODE CLEANING SYSTEM DATA

TIMING CYCLE OF CLEANING SYSTEM

INTENSITY OF CLEANING DEVICES

SEQUENCE OF CLEANING DEVICES

Table 7. MAJOR INTERNAL INSPECTION ITEMS

AMOUNT OF PARTICULATE BUILDUP ON COLLECTING AND DISCHARGE ELECTRODE SURFACES

ALIGNMENT BETWEEN COLLECTING ELECTRODES

BROKEN OR SEVERELY WORN DISCHARGE ELECTRODES

WARPED OR BOWED COLLECTING ELECTRODES

MISSING DISCHARGE ELECTRODES

CLINKER FORMATION

CLEANLINESS OF SUPPORT AND ISOLATION INSULATORS AND SIGNS OF TRACKING

EXTREMELY CLEAN OR DIRTY AREAS VS. NORMAL AREAS

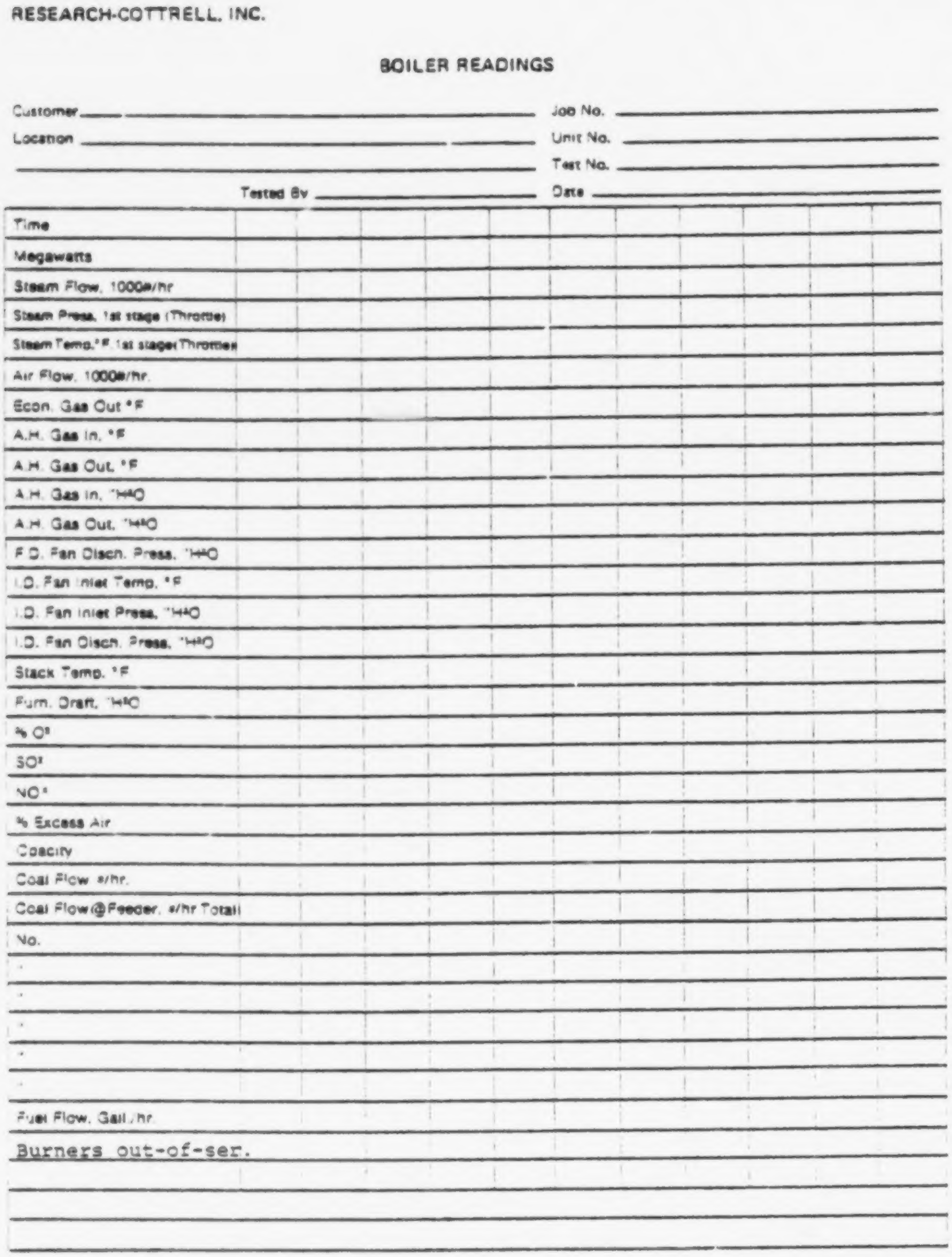

RESEARCH-COTTRELL, INC.

BOILER READINGS

Customer ____________________ Job No. ____________________

Location ____________________ Unit No. ____________________

____________________ Test No. ____________________

Tested By ____________________ Date ____________________

Time											
Megawatts											
Steam Flow, 1000#/hr											
Steam Press. 1st stage (Throttle)											
Steam Temp. °F 1st stage (Throttle)											
Air Flow, 1000#/hr.											
Econ. Gas Out °F											
A.H. Gas In, °F											
A.H. Gas Out, °F											
A.H. Gas In, "H_2O											
A.H. Gas Out, "H_2O											
F.D. Fan Disch. Press. "H_2O											
I.D. Fan Inlet Temp. °F											
I.D. Fan Inlet Press. "H_2O											
I.D. Fan Disch. Press. "H_2O											
Stack Temp. °F											
Furn. Draft, "H_2O											
% O_2											
SO_2											
NO_x											
% Excess Air											
Opacity											
Coal Flow #/hr.											
Coal Flow@Feeder, #/hr Total											
No.											
.											
.											
.											
.											
.											
Fuel Flow, Gal./hr.											
Burners out-of-ser.											

Figure 1. Boiler readings

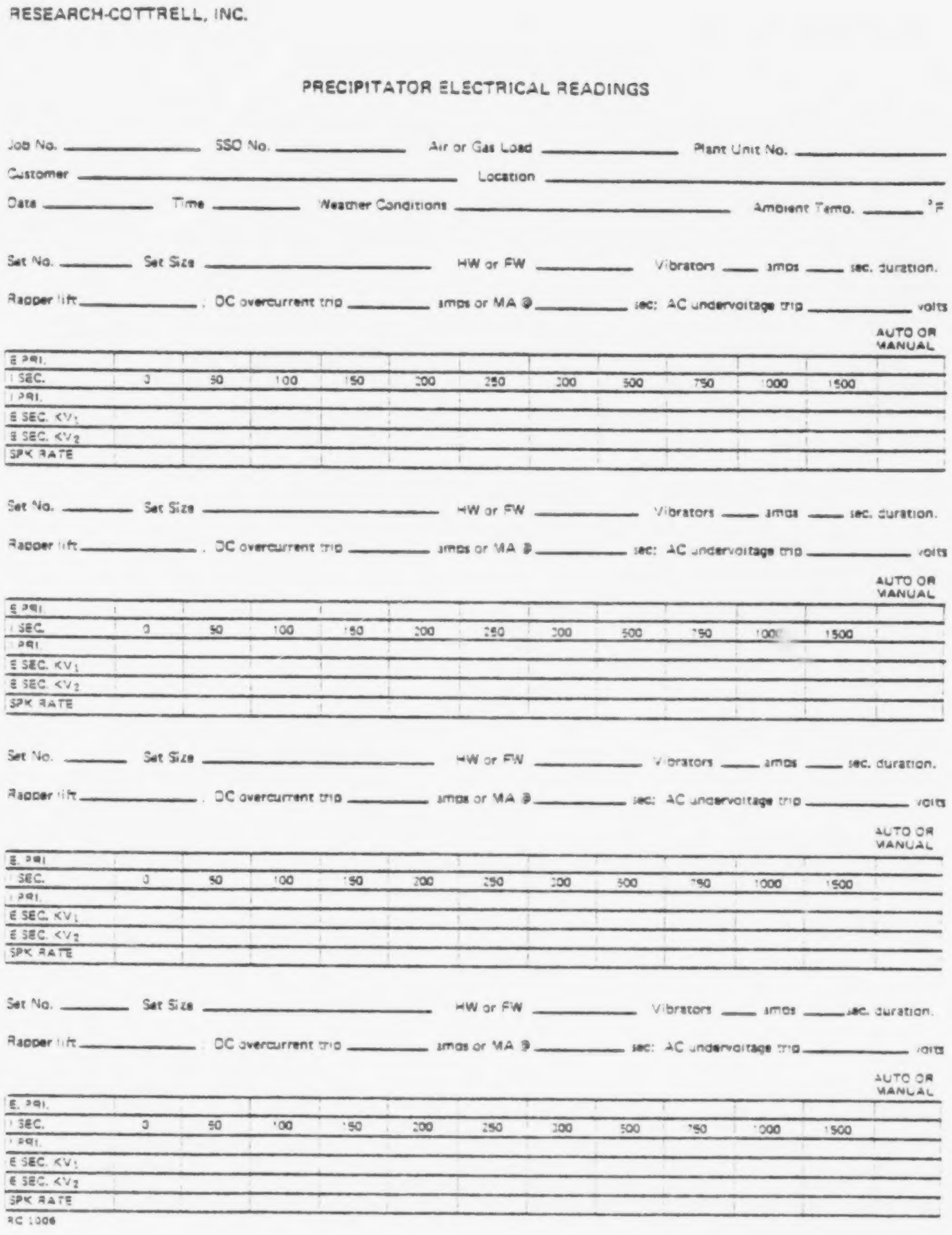

RESEARCH-COTTRELL, INC.

PRECIPITATOR ELECTRICAL READINGS

Job No. ________ SSO No. ________ Air or Gas Load ________ Plant Unit No. ________

Customer ________ Location ________

Date ________ Time ________ Weather Conditions ________ Ambient Temp. ________ °F

Set No. ________ Set Size ________ HW or FW ________ Vibrators ____ amps ____ sec. duration.

Rapper lift ________ ; DC overcurrent trip ________ amps or MA @ ________ sec; AC undervoltage trip ________ volts

												AUTO OR MANUAL
E PRI.												
I SEC.	0	50	100	150	200	250	300	500	750	1000	1500	
I PRI.												
E SEC. KV$_1$												
E SEC. KV$_2$												
SPK RATE												

Set No. ________ Set Size ________ HW or FW ________ Vibrators ____ amps ____ sec. duration.

Rapper lift ________ ; DC overcurrent trip ________ amps or MA @ ________ sec; AC undervoltage trip ________ volts

												AUTO OR MANUAL
E PRI.												
I SEC.	0	50	100	150	200	250	300	500	750	1000	1500	
I PRI.												
E SEC. KV$_1$												
E SEC. KV$_2$												
SPK RATE												

Set No. ________ Set Size ________ HW or FW ________ Vibrators ____ amps ____ sec. duration.

Rapper lift ________ ; DC overcurrent trip ________ amps or MA @ ________ sec; AC undervoltage trip ________ volts

												AUTO OR MANUAL
E. PRI.												
I SEC.	0	50	100	150	200	250	300	500	750	1000	1500	
I PRI.												
E SEC. KV$_1$												
E SEC. KV$_2$												
SPK RATE												

Set No. ________ Set Size ________ HW or FW ________ Vibrators ____ amps ____ sec. duration.

Rapper lift ________ ; DC overcurrent trip ________ amps or MA @ ________ sec; AC undervoltage trip ________ volts

												AUTO OR MANUAL
E. PRI.												
I SEC.	0	50	100	150	200	250	300	500	750	1000	1500	
I PRI.												
E SEC. KV$_1$												
E SEC. KV$_2$												
SPK RATE												

RC 1006

Figure 2. Precipitator electrical readings

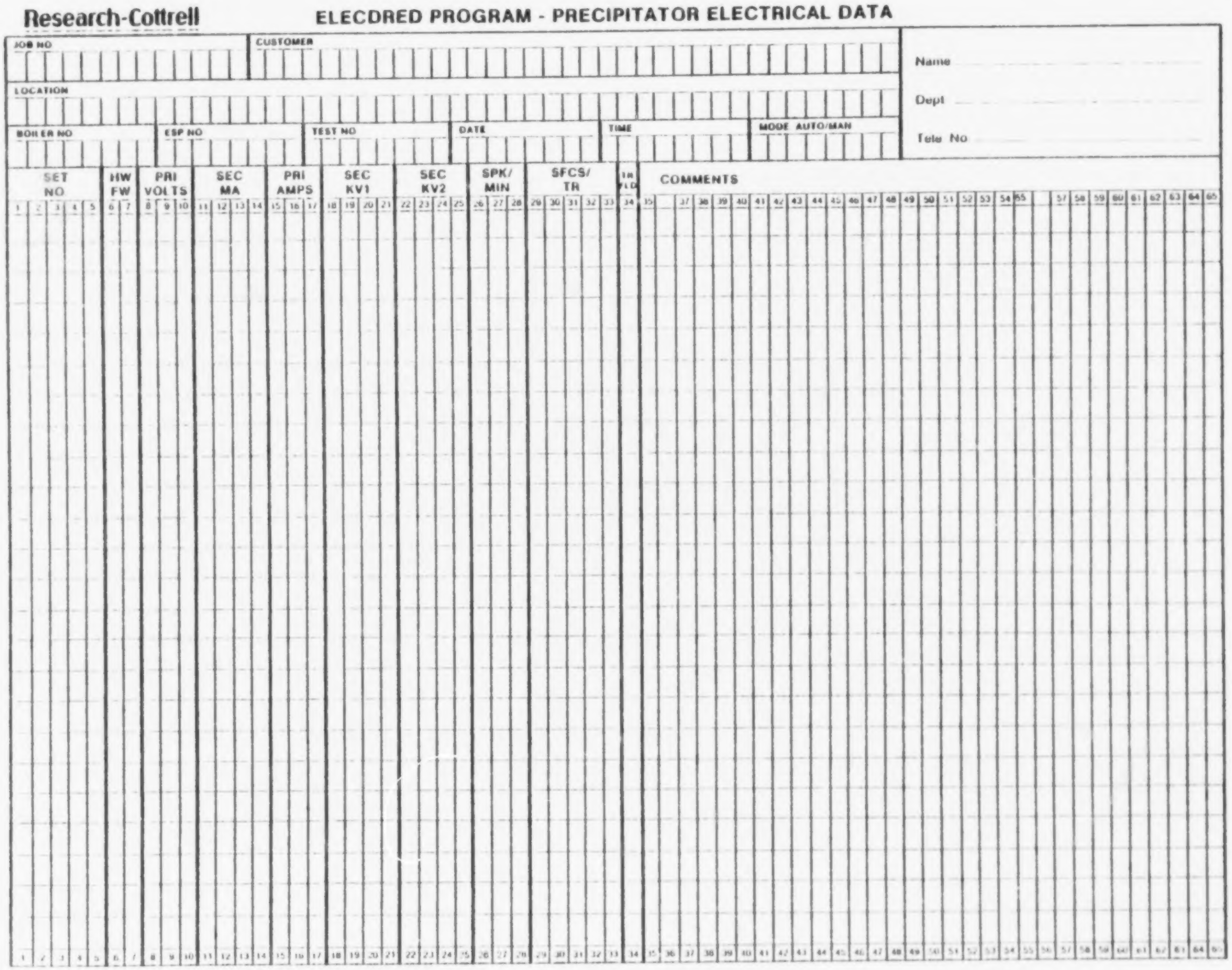

Research-Cottrell

ELECDRED PROGRAM - PRECIPITATOR ELECTRICAL DATA

JOB NO

CUSTOMER

LOCATION

BOILER NO

ESP NO

TEST NO

DATE

TIME

MODE AUTO/MAN

Name

Dept

Tele No

SET NO	HW FW	PRI VOLTS	SEC MA	PRI AMPS	SEC KV1	SEC KV2	SPK/ MIN	SFCS/ TR	TR FLD	COMMENTS
1 2 3 4 5	6 7	8 9 10	11 12 13 14	15 16 17	18 19 20 21	22 23 24 25	26 27 28	29 30 31 32 33	34	35 37 38 39 40 41 42 43 44 45 46 47 48 49 50 51 52 53 54 55 57 58 59 60 61 62 63 64 65

Figure 3. Precipitator electrical data

JOB NO. ____________

TR NO. ____________

DATE ____________

☐ HW

☐ FW

TIME ____________

GAS TEMP ____________ °F

OPACITIES.

BASE ____________ %

SPIKES ____________ %

RAPPING_____ MIN_____FT-LB

VOLTAGE - CURRENT CHARACTERISTICS

READ ☐ LEFT ☐ RIGHT

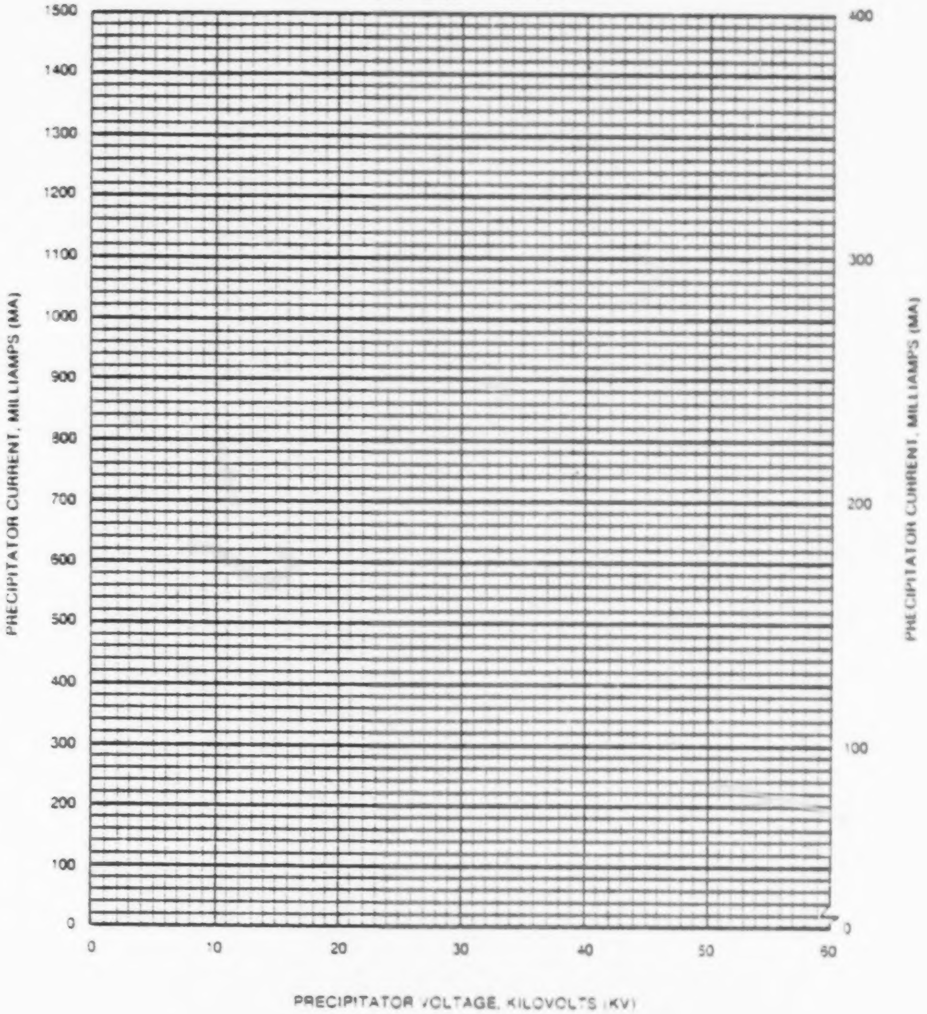

Figure 4. Voltage-current characteristics

PRECIPITATOR INSPECTION LOG

PLANT NAME ____________________

PRECIPITATOR # ____________________

DATE ____________________

INSPECTED BY ____________________

LOCATION OF INSPECTION ____________________

REASON FOR INSPECTION

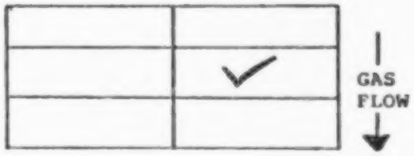

PRECIPITATOR LAYOUT REFERENCE

INSPECTION CODE

1 KINKED DISCHARGE ELECTRODE
2 WARPED DISCHARGE ELECTRODE FRAME
3 BROKEN DISCHARGE ELECTRODE FRAME
4 BROKEN DISCHARGE ELECTRODE
5 BOWED COLLECTING ELECTRODE
6 HEAVY DUST BUILD-UP
7 HEAVY CORROSION
8 RAPPER ALIGNMENT OFF-CENTER
9 IMPROPER COLLECTING ELECTRODE SPACING
10 IMPROPER DISCHARGE ELECTRODE TO COLLECTING ELECTRODE SPACING

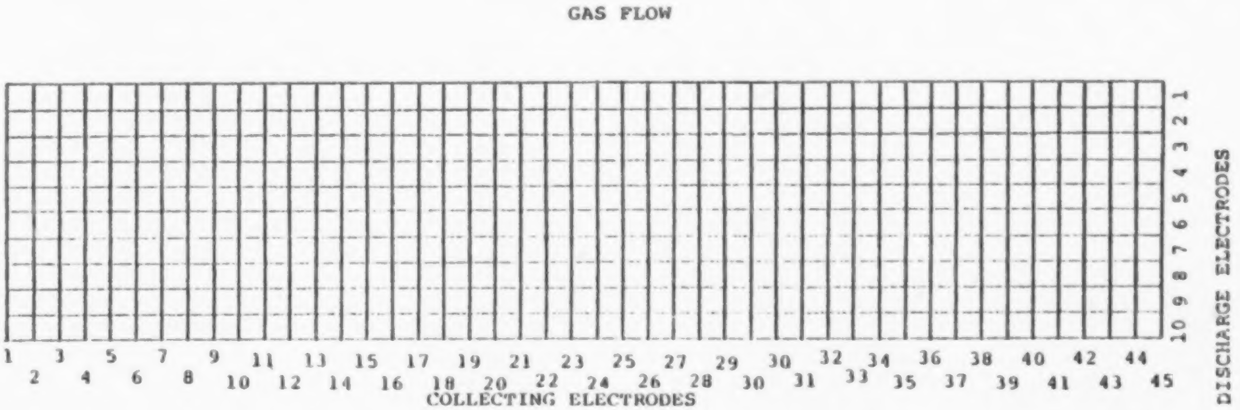

Figure 5. Precipitator inspection log

PARAMETER CHANGE-CAUSE	SOURCE DOCUMENTS	CHANGES - NOTES	EFFECT - CHANGED PARAMETERS																
			GAS VOLUME	GAS TEMPERATURE	GAS HUMIDITY	TYPE OF FUEL	DUST CONCENTRATION	DUST RESISTIVITY	DUST PARTICLE SIZE	CARBON CARRYOVER	ENERG. - VOLTAGE	ENERG. - CURRENT	PLATE CLEANLINESS	D.E. CLEANLINESS	FLOW DISTRIBUTION	AIR INLEAKAGE	HOPPER ASH	SPARK RATE	PERFORMANCE - OPACITY
-INLET CONDITIONS-																			
Gas Volume	Boiler Data Coal Analysis	+ Increase - Higher Velocity - Decrease - Less Total Ash		N	N	N	N	N	N	N	N	N	- +	- +	N	+ -	+ -	+ -	- +
Gas Temperature	Boiler Data	+ Increase - Decrease	+ -		- +	N	- +	+ -	N	N	- +	+ -	N	N	N	+ -	N	+ -	(N)
Gas Humidity	Boiler Data Coal Analysis Test Report	+ Increase - Decrease	+ -	- +		N	I	- +	N	N	+ -	- +	- +	- +	N	I	+ -	+ -	E
Type of Fuel	Coal Analysis Ash Analysis	+ Better Rank - Poorer Rank	E	E	E		- +	- +	+ -	N	- (N) +	+ (N) -	+ -	+ -	N	N	N	- +	+ -
Dust Concentration	Coal Analysis Boiler Data	+ Increase - Decrease	N	N	N	N		N	N	N	+ -	- +	- +	- +	N	N	+ -	+ -	- +
Dust Resistivity	Ash Analysis Test Report	+ Increase - Decrease	N	N	N	N	N		N	N	+ -	- +	- +	- +	N	N	N	+ -	- +
Dust Particle Size	Coal Analysis Test Report	+ Larger Size - Smaller Size	N	N	N	N	N	N		N	- +	+ -	+ -	+ -	N	N	I	- +	+ -
Carbon Carryover	Ash Analysis	+ Increase - Decrease	N	N	N	N	+ -	- +	+ -		- +	+ -	+ -	+ -	N	N	+ -	E	- +
-INTERNAL CONDITIONS-																			
Energization - Voltage	Electrical Data V-I Curves	+ Increase - Decrease	N	N	N	N	N	N	N	N		E	E	E	N	N	E	+ -	(E)
Energization - Current	Electrical Data V-I Curves	+ Increase - Decrease	N	N	N	N	N	N	N	N	E		E	E	N	N	E	- +	(E)
Collecting Plate Cleanliness	Rapper Log V-I Curves	+ Cleaner - Dirtier	N	N	N	N	N	N	N	N	- +	+ -		N	N	N	N	- +	+ -
Discharge Electrode Cleanliness	Electrical Data Rapper Log	+ Cleaner - Dirtier	N	N	N	N	N	N	N	N	- +	+ -	N		N	N	N	- +	+ -
Flow Distribution	Test Report	+ More Uniform - Less Uniform	N	N	N	N	N	N	N	N	N	N	N	N		N	N	+ -	- +
Air Inleakage	Boiler Data	+ More Leakage - Less Leakage	+ -	- +	I	N	N	I	N	N	+ -	- +	N	N	- +		N	+ -	- +
Hopper Ash Level	Electrical Readings Hopper Log	+ High Level Potential - Low Level	N	N	N	N	N	N	N	N	- +	+ -	N	N	N	N		+ -	- +
Spark Rate	Electrical Data	+ Increase - Decrease	N	N	N	N	N	N	N	N	- +	- +	+ -	+ -	N	N	N		- +

Assumptions & Key:

1. At typical full load
2. Cold side ESP
3. Changes are from "normal"
4. Symbols: Opacity: + = Increase
   - = Decrease
   N : No Direct Effect
   I : Insignificant Effect
   E : Either improves or degrades
   ( ) : May occur

Figure 6 - Operational factors

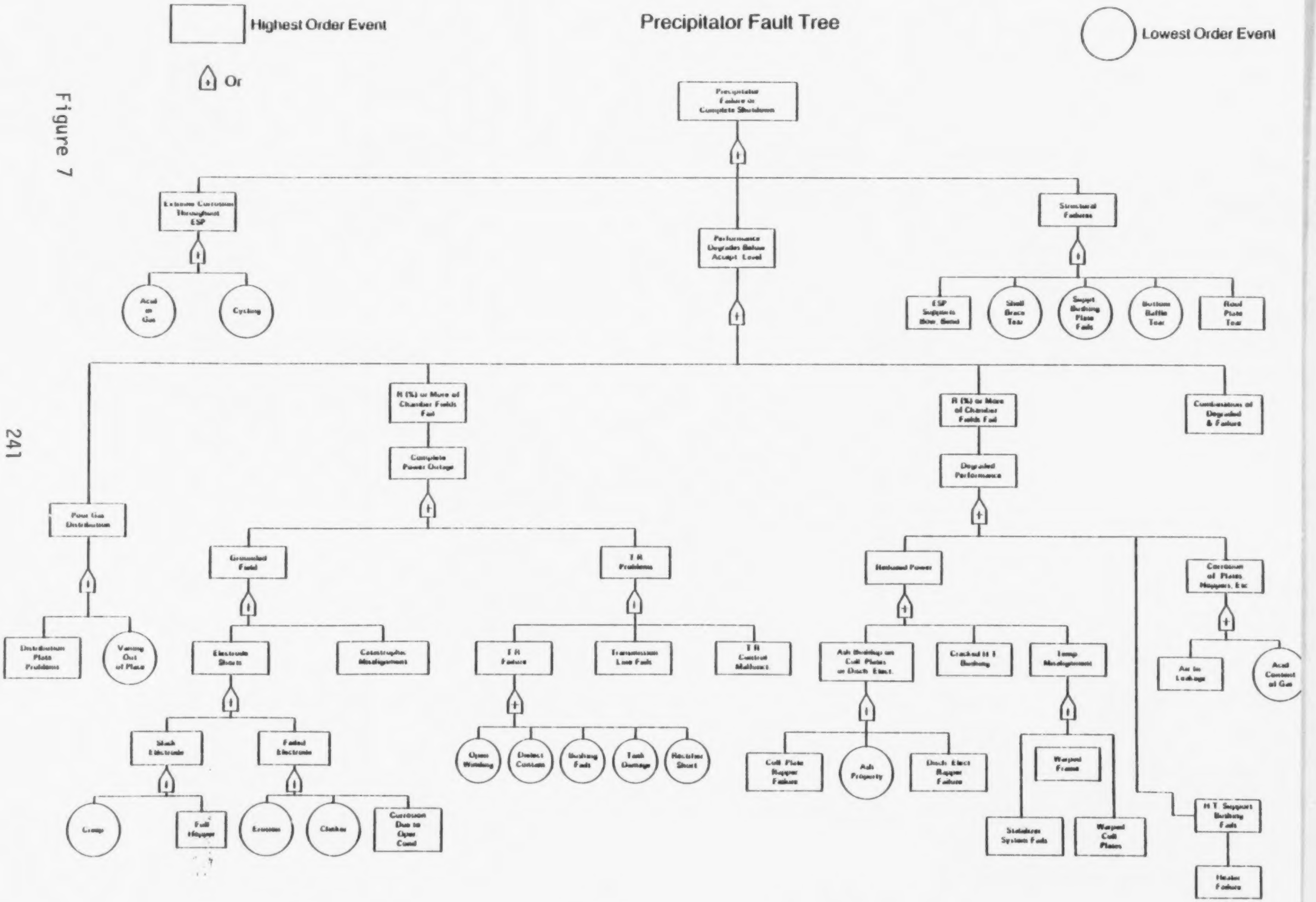
Highest Order Event
Precipitator Fault Tree
Lowest Order Event
Or
Precipitator Failure or Complete Shutdown
Extreme Corrosion Throughout ESP
Acid in Gas
Cycling
Performance Degrades Below Accept. Level
Structural Failures
ESP Supports Bow, Bend
Shell Brace Tear
Suppt Bushing Plate Fails
Bottom Baffle Tear
Roof Plate Tear
Poor Gas Distribution
R (%) or More of Chamber Fields Fail
Complete Power Outage
R (%) or More of Chamber Fields Fail
Degraded Performance
Combination of Degraded & Failure
Distribution Plate Problems
Vanes Out of Place
Grounded Field
Electrode Shorts
Catastrophic Misalignment
Slack Electrode
Failed Electrode
Creep
Full Hopper
Erosion
Clinker
Corrosion Due to Oper Cond
T R Problems
T R Failure
Transmission Line Fails
T R Control Malfunct.
Open Winding
Dielect Contam
Bushing Fails
Tank Damage
Rectifier Short
Reduced Power
Ash Buildup on Coll Plates or Disch Elect.
Cracked H T Bushing
Temp Misalignment
Coll Plate Rapper Failure
Ash Property
Disch Elect Rapper Failure
Warped Frame
Stabilizer System Fails
Warped Coll Plates
Corrosion of Plates Hoppers, Etc
Air In Leakage
Acid Content of Gas
H T Support Bushing Fails
Heater Failure

Figure 7

[redacted]

ELECTROSTATIC PRECIPITATORS START-UP, LOW LOAD, CYCLING AND MAINTENANCE CONSIDERATIONS

By:

F. A. Wybenga and R. J. Batyko
Babcock & Wilcox Company
Fossil Power Generation Division
Barberton, Ohio 44203

ABSTRACT

Particulate control devices for large fossil fired steam generators, now predominantly coal fired, are being designed for increasingly higher efficiencies to meet current and proposed new regulations. Heavy emphasis is placed on minimizing occurrences when emission limits are exceeded during all phases of operation or for reasons of malfunction of the control device.

These requirements make it desirable, if not necessary, to energize electrostatic precipitators during the early stages of boiler start-up. This also calls for planned, regular maintenance.

This paper discusses precipitator design and operating considerations that will allow energization during initial coal firing of precipitator equipment. With start-up and shut-down becoming of even greater importance on boiler units designed for cycling service, the paper also addresses items to be considered in design of precipitators, precipitator accessory equipment and the total boiler system to facilitate cycling operation and extended low load operation.

ELECTROSTATIC PRECIPITATORS
START-UP, LOW LOAD, CYCLING
AND MAINTENANCE CONSIDERATIONS

INTRODUCTION

With increasingly stringent limits being placed on particulate emissions from fossil fired steam generating equipment, and the need for reporting instances when emissions exceed established limits, additional emphasis has to be placed on maintaining clear stacks over the full range of operating conditions. In this paper, we will be discussing electrostatic precipitators as applied to coal fired utility boilers, particularly what is being done and what can be done to allow precipitators to perform reliably over a full range of operating conditions. In addition to the normal start-ups, these operating conditions may include, either initially or in the future, frequent start-ups and shut-downs for load cycling and extended low load operation. All will likely result in low flue gas temperatures in back-end particulate control systems, considered undesirable for obvious reasons.

There are limits to what can be done to particulate control devices, whether precipitators or bag filterhouses, to make them suitable for low gas temperature operating conditions. For this reason, more emphasis has to be given to the "back-end" equipment in a power plant when the total boiler system is planned and designed. If precipitators are expected to handle whatever is produced by the power production process, poor performance may be expected if there are equipment incompatibilities. Poor performance and resulting dirty stacks are no longer acceptable. Consequently, the particulate control devices as well as all other pollution control equipment have to be given equal consideration in the total plant design.

The pollution control problems facing the utility industry are numerous and complex. Considering the varied needs of the utility companies, the variety in available fuels, local environmental regulations and economic restrictions, the solutions will be different for each installation. In this paper, we do not claim to solve these problems but is is our intent to frankly state what precipitators can do, based on our experience, and also address what they cannot be expected to do. For the latter case, we will be giving some food for thought to the users, their consulting engineers, and the equipment suppliers so that, together, solutions can be found and incorporated in the total plant system.

While it may appear from some of our statements that we are taking the total industry to task for past omissions, this is not the case. What has been done in the past was done for good reasons, and in general, the objectives strived for were achieved. We now find ourselves in different situations and in a different environment which may call for a different approach from that followed in the past.

BOILER "BACK-END" SYSTEM DESIGN PRACTICES

Before we discuss electrostatic precipitators and their operation, it may be well to review normal design practice for the boiler "back-end" system i.e., all equipment located downstream of the boiler economizer. Refer to Figure 1.

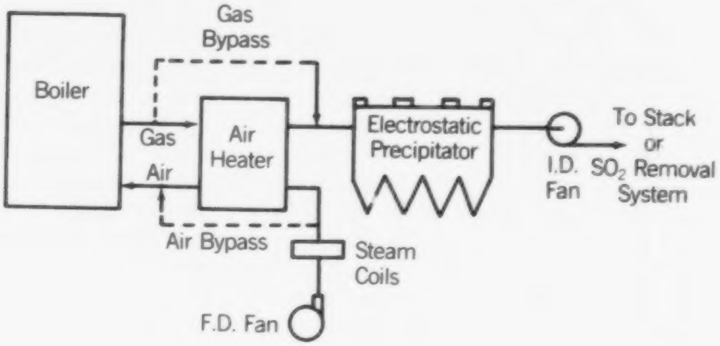

Figure 1 Boiler "back-end" system.

Exit Gas Temperature

When preparing utility boiler specifications, it is customary for the owner/user or his Consulting Engineer to select and specify the air heater exit gas temperature at full load operating conditions. This value is selected on the basis of the fuels to be burned and overall economics. With rapidly rising fuel costs and 40°F gas temperature being roughly equal to 1% in boiler efficiency, the lowest possible exit gas temperature is of course preferred. Typically, exit gas temperatures are in the 260°-300°F range for coal fired units.

Air Heaters

Air heaters are selected and sized by the boiler manufacturer to produce the specified exit gas temperature and the air outlet temperatures required for the fuel preparation and burning equipment. With air heater size established, a review is made of air heater material requirements and corresponding minimum cold end average temperatures. For regenerative air heaters with corrosion resistant low-alloy steel in the cold end elements, minimum average metal temperature recommendations are shown in Figure 2. The minimum temperature limits are a function of the flue gas acid dewpoint, hence the increase as sulfur content in the fuel increases. By maintaining these minimum temperature limits, air heater corrosion can be kept to a minimum.

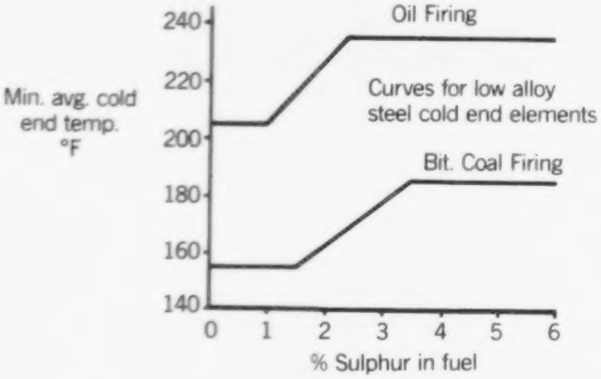

Figure 2 Air heater minimum average cold end temperature guide.

Air Heater Cold End Temperature Control

Controlling cold end average temperatures over a normal range of boiler loads requires either an air by-pass or auxiliary heating at the air heater air inlet. Typically, either steam, hot water, or glycol heaters are installed at the air heater air inlet for this purpose. They are sized to handle not only a load range but also the anticipated range of ambient air temperatures.

Electrostatic Precipitators

Precipitators are normally purchased for full load operating conditions. This is certainly the correct approach if collection efficiency under normal operating conditions, at or near full load, is the main consideration. However, as new units are added to the system, the older installations are now frequently called on for cycling duty or, if not suitable for cycling service, kept at extremely low loads for extended periods. It can be expected that units purchased today for base loading will at some time in the future also be used in cycling service.

In a recent survey of the utility industry conducted by Babcock & Wilcox Company, we asked what operating and maintenance problems had been experienced on boiler back-end equipment used for cycling or low loads. All those respondents who had any appreciable experience with this type of operation reported problems that can be broadly described as "dew point" problems. These include problems with air heater pluggage and corrosion, precipitator fouling with resulting poor performance, ash handling system pluggage and corrosion of flue expansion joints and stacks. Most respondents expressed the opinion that the solution to these problems is to maintain gas temperatures above the acid dewpoint under all operating conditions. Steam coils were the most frequently offered suggestion, followed by air heater gas or air by-pass systems or even an economizer by-pass. Better materials, suitable for below dewpoint operation, were suggested by 20% of the respondents.

The results of this survey reinforce our opinion that start-up, cycling, and low load operation, as they affect precipitators and other back-end equipment, should be given full consideration when new systems are designed and equipment is selected. For units not initially slated for this type of service, economics may well dictate that those units be designed with limited initial flexibility. Even so, major equipment, not readily modified, should be selected with the future in mind.

START-UP OPERATIONS

For precipitators, the preferred solution to minimizing dewpoint and moisture problems has traditionally been to delay energizing the precipitator until gas temperatures are above 200°F. Even though the equipment still has to pass through the dewpoint transition, delayed energization will minimize the deposition of potentially wet and sticky materials. Unfortunately, federal and/or local regulations may no longer permit this mode of operation if it results in particulate emissions above allowable limits. This then points to the desirability of energizing electrostatic precipitators as soon as coal firing is begun. We see no reason why this cannot be done with properly designed equipment.

Pre-Start-up

In preparation for precipitator energization upon first coal firing, our experience indicates that certain pre-start-up procedures should be followed. For any given installation, precipitator operating instructions manuals should be consulted for specific recommendations.

Prior to boiler start-up, preferably eight hours or longer, all rapping systems on the precipitator should be placed in operation. Also, all heating systems on the hoppers and insulators, if provided, should be energized. This will allow hoppers and insulators to heat up and stay dry through subsequent start-up operation. Seal or purge air fans, if provided, should also be started early.

Hopper ash removal systems should be ready to operate and preferably in service to remove all accumulated ash.

Boiler Purge

Regardless of all other considerations, we consider it of utmost importance that the precipitator power supplies be kept de-energized whenever explosive mixtures may be present within the boiler system setting. While documented cases of precipitator gas side explosions are rare, sparking from any source, whether fuel ignitors or precipitators, should not be allowed during any boiler purging operation or whenever the boiler master fuel trip prevents firing. We, therefore, recommend that all precipitator power supplies be interlocked with the master fuel trip and firing permissive.

Initial Firing

Typical utility practice is to use oil or gas ignitors or start-up burners for the initial firing of the boiler. As long as these fuels are burned exclusively and good combustion conditions are maintained, there should be no need for precipitators to be energized for stack appearance reasons. It would, therefore, be our recommendation to keep precipitators de-energized while maintaining good combustion with the auxiliary fuel, both for stack appearance reasons and protection against air heater deposits and the possibility of fires.

Coal Firing

Exactly when coal firing can be initiated will be a function of the individual boiler unit, its burner design, coal characteristics, and the ability to obtain adequate combustion air temperatures to sustain good combustion, with or without auxiliary fuel support. Cost and availability of auxiliary fuel and load carrying capacity on auxiliary gas or oil will also have to be considered. Assuming that coal firing will begin at or near unit synchronization and that precipitators are to be energized at this time, gas temperatures will still be quite low at the air heater outlet as shown in Figure 3 for a typical coal fired unit. The curve shows exit gas temperature rise above entering air temperature.

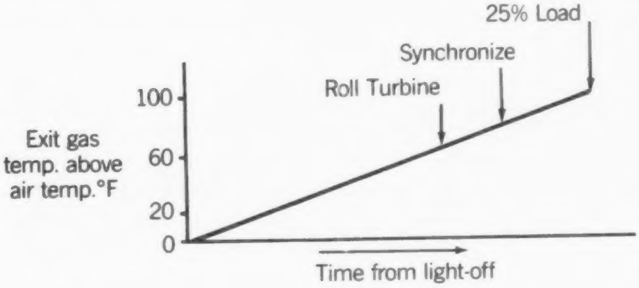

Figure 3 Exit gas temperature rise above air inlet temperature during initial operation.

Exit gas temperature being directly related to air heater air inlet temperature then points to the desirability of having high air preheating capability, preferably steam or water coils. There are other means of accelerating the air heater gas outlet temperature rise such as air or gas by-passing or even completely stopping the air heater rotation. All of these will also have the undesirable effect of drastically reducing combustion air temperatures. Air heater gas by-passing will also reduce air heater cold end temperatures. Inlet coils are, therefore, the preferred solution.

Figure 3 also points out the desirability of shortening the boiler warm-up phase and, once synchronized, raising unit load as quickly as possible. This will minimize the length of time during which the precipitator has to be exposed to low gas temperatures.

With generally lower acid dewpoints with coal firing as compared to oil firing, and the inherent neutralizing effect of coal ash, anything that can be done to minimize the auxiliary oil firing percentage will also be helpful to the precipitator.

Precipitator Design Considerations

Continuing on the assumption that the precipitator will be energized upon initial coal firing, the design has to be capable of handling this operation. It has been our experience that properly designed precipitator equipment can readily handle this situation. Essential design features are discussed below.

Hopper and Insulator Heating Systems. An adequate heating system on all ash hoppers is a must for early start-up capability. Preheated hoppers will minimize flue gas condensation problems in the critical lower portion of the hoppers and assist with ash removal.

A heating system on all electrical insulators exposed to flue gas and fly-ash is equally important. This heating could either be direct or in conjunction with the seal/purge air system used on insulator components. Insulators should preferably be kept dry and clean, although dry ash or dust deposits, except with extremely low resistivity dust, will probably not cause any problems.

Insulator Materials, Location, and Arrangement. When possible, electrical insulators should be kept out of the dirty gas stream. The most troublesome arrangement is to have flue gas on one side or surface with colder ambient conditions on the other side. Condensation and resulting damp deposits are now most likely to occur, unless adequate heating is provided on the colder side.

Support insulator systems frequently used on the B&W precipitator consist of the primary support insulators completely outside the gas stream as shown in Figure 4. Even with this arrangement, a sealing (shroud) insulator is required around the hanger rod. By externally heating the shroud insulator, deflecting flue gas away from the insulator and introducing some purge air, this insulator can be kept clean and dry.

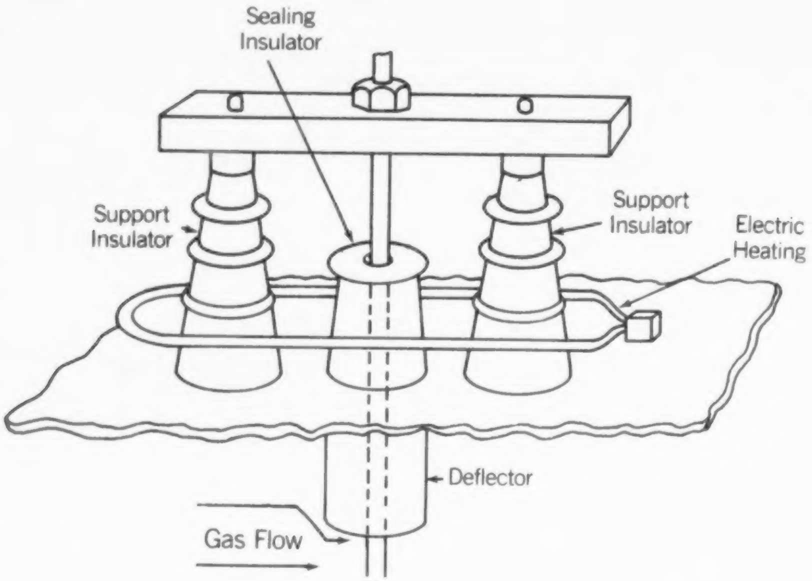

Figure 4 Support insulator arrangement.

Concerning insulator materials, we are of the opinion that only the best available materials should be specified. This is undoubtedly alumina. Besides having excellent dielectric properties, it is extremely strong and can better withstand temperature variations and even tracking and its potential damaging effects.

Rapping Intensity. Of primary importance to precipitator operation at low gas temperatures is heavy rapping. Most European design precipitators have rapping systems that were developed for difficult to remove, high resistivity, ash. This also makes them better suited to also remove caked on deposits collected during low temperature operation.

Our experience indicates that heavy rapping can adequately remove start-up deposits. While actual removal may not take place until the deposits have dried, subsequent precipitator operation and performance are not significantly affected. Depending on the frequency of start-ups, time required at low temperatures and sulfur content of the fuel, there is still the possibility that hardened, difficult to remove deposits could accumulate to the point where optimum performance can no longer be maintained. Water washing may then have to be used to restore performance. We have not had occasion to recommend water washing on any of our utility precipitator installations but are familiar with a German installation that water washes periodically. This unit typically has 20 start-up cycles yearly and maintains precipitators energized throughout start-up.

Heavy rapping impact on collecting plates is as much a function of rapper design as it is of collecting plate support and attachment. Transverse acceleration (perpendicular to the plate surface) is most effective in removing deposits. A rigid means of attachment for each plate will cause most of the available rapping force to translate into a transverse cleaning component. On designs where individual plates are loosely supported, much of the available rapping force will go into swinging the entire curtain. The resulting decrease in transverse acceleration values has been demonstrated in tests on collecting curtains. As shown in Figure 5, impact values decreased 40% when plate fixation bolts were loosened.

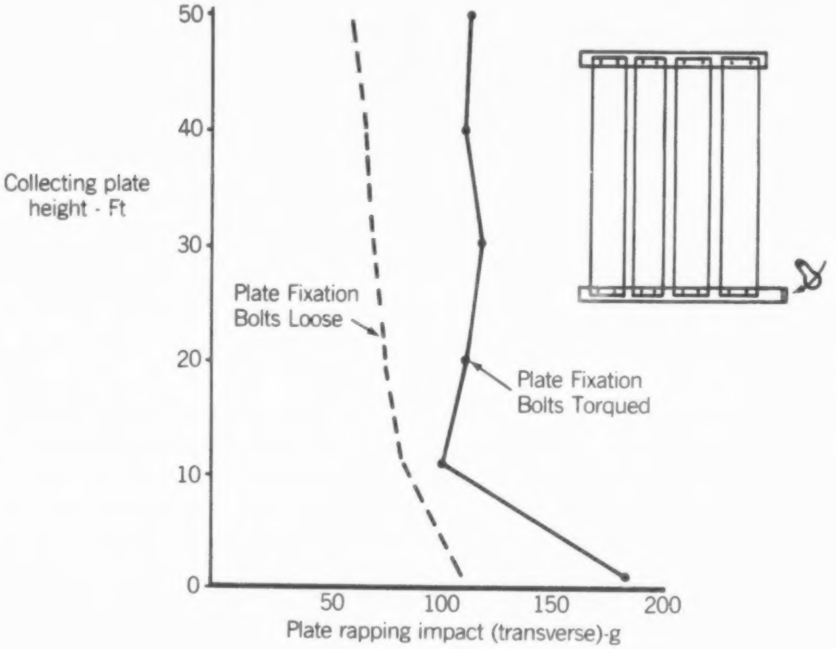

Figure 5 Effect of plate fixation on rapping impact.

While transverse acceleration values are of primary importance, the acceleration component within the plane of the plate (parallel) can also be very beneficial if plates are rolled with shear planes and ridges to facilitate removal of deposits.

The overall importance of adequate rapping impact on collecting surfaces is now generally recognized and specifications frequently call for minimum accelerations of 50g to 100g. Not always specified is the direction in which it is to be measured, transverse or parallel to the surface. How meaningful actual reported impact data is to the user is an unresolved question. For example, it has been demonstrated that a lower weight accelerometer will give higher readings, all other conditions being the same. This is an area where some industry standards would be helpful so that test results using different procedures and instrumentation can be quantified and comparisons made.

High impact, low amplitude rapping has given excellent cleaning results on our units now in service. Falling hammer type rapping systems and rigidly fixed collecting plates can combine to give these results. Regardless of how specified, the important consideration has to be the ability of the rapping system to keep collecting plates and electrodes clean, especially for start-up operations.

For discharge electrodes, rapping impact may not be as important as on plates, nevertheless, it should be adequate to keep electrodes reasonably clean for optimum power input. Rigid discharge frames with tightly strung electrodes and individual falling hammer type rappers have excellent cleaning characteristics. Sharp edge, sheared discharge strips will also facilitate cleaning.

Precipitator Operating Procedures

One possible option available to the operator to minimize harmful effects from start-up operations on the precipitator is to isolate certain chambers or casings, if adequate dampers have been provided. This type of operation will expose only selected portions of the precipitator to start-up conditions.

Another approach commonly used is to allow gas to pass through the entire precipitator while energizing only a single field. The initial field to be energized should be the last field since it will collect the least amount of ash during normal operation and any remaining ineffectiveness due to start-up deposits will have a minimum effect on subsequent operation.

On the other hand, there are some who believe that the leading field should be the first one energized, since subsequent operation with coarser ash will help to scour off remaining start-up deposits. Whichever approach is followed, partial energization can be beneficial. It does, however, require more operator involvement especially if remote start-up capability or added automation has not been provided.

Summarizing, we firmly hold to the opinion that routine boiler start-ups can be accomplished with precipitators in operation whenever coal is fired. This is based on proven capability and experience with properly designed equipment.

LOW LOAD OPERATION

As covered in the earlier section of this paper dealing with back-end system design practices, if there is a need for extended low load operation, the total system has to be specified and designed accordingly. Current practice calls for predicting boiler performance down to 25% of full load. This does not necessarily insure, however, that exit gas temperatures are high enough for satisfactory precipitator performance down to these low loads.

Figure 6 shows a plot of gas and air temperatures for a typical coal fired unit over a wide load range. Steam coils are provided for air heater cold end average temperature control. For this example, the coils would be in operation whenever inlet temperature is decreased below 80 degrees F and/or unit load drops from full load in order to maintain an average cold end temperature of 180 degrees F, typical for 3% sulfur coal.

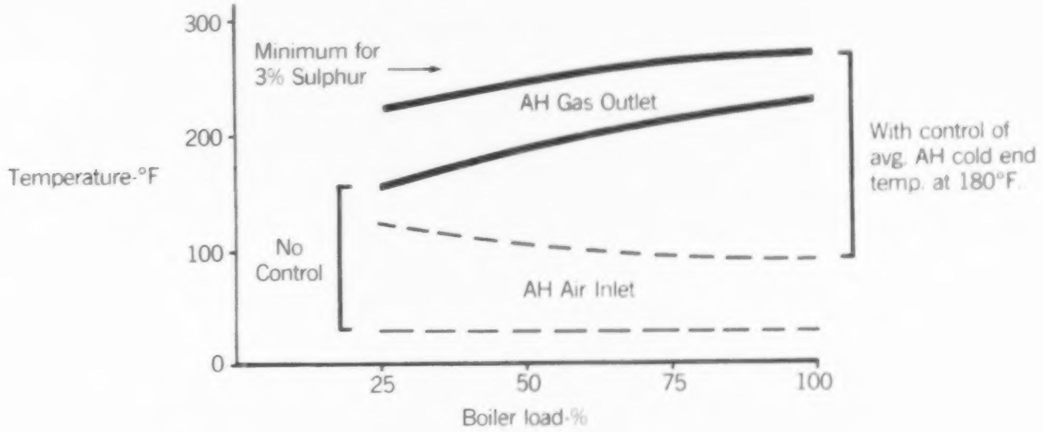

Figure 6 Exit gas temperature vs. load.

Much has been written on acid dewpoint as related to fuel sulfur content and at what temperatures moisture and corrosion become troublesome. With 3% sulfur coal, a reasonable minimum gas temperature is on the order of 250°F. Referring back to Figure 5, this temperature level for our typical unit is reached at 50% load with steam coils in service. Operating for extended periods at even lower loads can now lead to severe fouling problems, corrosion, and ash handling problems.

System Design Solutions

The most obvious solution is to provide additional inlet coil air preheating capacity which will in turn increase exit gas temperature. Gas temperatures have to be increased if the back-end equipment is expected to operate successfully at these low loads.

Precipitator Design Solutions

Design features such as hopper and insulator heating systems and high rapping intensity as found necessary for early start-up capability are equally needed on units expected to operate at low loads. Even so, these will not allow operation below the dewpoint for extended periods.

With operating temperatures approaching dewpoint, the main concern now becomes corrosion. Metal surfaces exposed to gas on one side and air on the outside are likely to operate considerably below gas temperature and condensation will occur. While this may not be detrimental to operation, it can be extremely damaging over the long term. Possible solutions are given below:

Corrosion Resistant Materials. Low alloy steels have proven improved resistance to acid dewpoint attack. Using these materials for the precipitator shell and hoppers can be of definite advantage. We question the value of using similar materials for precipitator internals, if this choice is made on the basis of extended low load operation only. If gas temperatures are kept high enough to keep the ash dry, as it should be, then corrosion of precipitator internals should be no problem either.

Insulation. Thermal insulation on back-end equipment is normally kept to a minimum since heat losses no longer affect system efficiency. If low load operation at marginal temperatures is being considered, insulation thicknesses should probably be specified at 3 or 4 inches, double layer preferably, rather than the 1 or 2 inches now normally used to provide personnel protection. There should be an emphasis on good workmanship, thermal barriers and no voids around penetrations thereby eliminating cold spots on all casing surfaces.

CYCLING OPERATION

By cycling operation, we refer to frequent nightly and weekly start-up and shut-down. As applied to boiler equipment, a cycling unit would typically be designed for 200 full start-up and shut-down cycles over the life of the unit, five nightly cycles per week with boiler pressure decaying down to 500 psig and one weekend cycle per week with boiler pressure decaying down to 100 psig. For 30 years of plant life, this could add up to 9,560 cycles.

The normal start-ups, 200 or over the 30 year life time or 7 per year, can be handled with properly designed equipment as already described. To handle potentially six start-ups per week, even though they are hot restarts, is more of a problem. There are few coal fired units operating in this manner and operating experience is limited. To be sure, "dewpoint" problems could be severe unless system design is carefully considered.

Precipitator Design Considerations

Design features as required for early start-up or low load operation should be incorporated for cycling service. Also to be included are corrosion resistant collecting plates and discharge electrodes primarily for out of service corrosion reasons.

Whereas seal air/purge air fans for insulator compartments are normally not required on negative pressure units, such fans should be called for on cycling units. During outage periods with induced draft fans shut down, flyash will drift into insulator compartments and eventually fill them. A continuous flow, even though small, of heated air is needed to keep these areas purged.

System Design Considerations

Isolation. One definite requirement for cycling equipment subject to frequent hot restarts is a need to maintain residual heat. Good thermal insulation and tight isolation dampers at system inlet and outlet would be important.

Gas Temperature Control. Controlling exit gas temperatures at reasonable levels for all operating conditions should be investigated. Later vintage cycling boilers are now frequently sold with turbine steam by-pass systems. Although these systems as designed result in minimum quantities of available excess steam, some steam should be made available to supply a large air heater steam coil.

Hot Side Precipitators. The other item that should be given further consideration is the use of hot side precipitators for cycling duty. Normal pressure decay in a cycling boiler is such that temperatures in the vicinity of the economizer may still be above $300^{\circ}F$ even for a 32 hour weekend shutdown. This could well make the choice of hot side precipitators attractive, but not for reasons of collectability of ash as was promoted several years ago. The undesirable aspects of hot side precipitators such as higher gas volumes and system temperature loss would have to be weighed against the advantage of having the precipitator located in a more favorable gas temperature zone.

MAINTENANCE

How well equipment operates is highly dependent upon the amount of maintenance performed, especially preventive maintenance. With precipitators not a part of the main process of generating power, past industry practice has been to provide only a minimal amount of maintenance. With the current legislative environment and the absolute necessity of meeting EPA emission limits or paying fines or reducing boiler load, the need for maintaining this equipment in good operating condition is a must.

Qualified and trained personnel should be assigned to inspect the electrostatic precipitator and also be given the responsibility to schedule and oversee required repair work and a preventive maintenance program. External inspections of the precipitator should be carried out on a routine basis with internal inspections whenever the unit is out of service. The precipitator vendor normally supplies operating and maintenance instructions. Using these instructions and with the vendors' help, an inspection and preventive maintenance schedule should be developed. If the schedule is followed and adequate maintenance performed, cases of malfunctioning equipment causing excessive emissions can be kept to an absolute minimum.

For personnel training, many utilities now have vidio tape equipment and many vendors have the ability to provide both operating and maintenance training tapes. B&W can provide such training tapes for our precipitators. With the normal turnover in operator and maintenance personnel, vidio tapes can be of tremendous value in bringing new people quickly up to date on maintenance requirements.

Another important consideration is keeping good records of both operating and maintenance data. Daily recording of current and voltage characteristics on power supplies should be obtained and tracked. This will detect changes in operating conditions and can point to specific areas to be inspected during subsequent outages.

CONCLUSION

Long term reliability of electrostatic precipitators and continued good performance over a wide range of operating conditions are now a matter of necessity. Precipitators have to be selected with design features and accessory equipment to allow operation at less than ideal operating conditions. On installations being designed for cycling service or extended low load operation, it is essential that full consideration be given to the design and operation of back-end equipment.

Once decisions have been made on what special features are needed in the equipment to be selected, these should be carefully specified to potential vendors so all will be bidding to the same needs. The air pollution control industry is an extremely competitive business with many qualified bidders. Few vendors are willing to incorporate more expensive options, whether they be better materials, added features or systems, to provide additional long term reliability unless such options are either specified or will be given favorable evaluation. The situation in the boiler industry is no different. If, for example, during the planning stages for a new plant, it is deemed necessary to maintain a high exit gas temperature over the load range, this will have to be specified to the boiler vendors. A mere statement in equipment specifications requiring that the "equipment shall be suitable for a wide range of loads with any fuel(s) specified" will most likely not produce the desired end result.

Once purchased and installed, electrostatic precipitators have to be given equal consideration in the total plant maintenance effort. Precipitators are now a vital part of the total system and have to be treated accordingly.

ELECTROSTATIC PRECIPITATOR EMISSION AND OPACITY PERFORMANCE CONTROL THRU RAPPER STRATEGY

By:

William T. Langan
Jon H. Oscarson
Envirotech Corporation
Buell Emission Control Division
Lebanon, Pennsylvania 17042

Scott Hassett
Utah Power and Light Corporation
Salt Lake City, Utah 84110

ABSTRACT

The opacity and emission performance of two "identical" cold-side precipitators at a power plant utilizing a Western coal source was investigated through an extensive test program. The test program included establishment of outlet emission versus opacity correlations for the two "identical" units, correlation of rapper strategy (frequency and amplitude) with opacity, and correlation of power-off rapping strategy with opacity.

Analysis of the test program data demonstrates that the opacity-emission correlations from the two "identical" units can be significantly different. The potential reasons for the differences between the two units are identified and examined in light of the test program data.

Strong correlation of opacity with rapping strategy was developed from the test program. Results demonstrate that an automatic power-off rapping technique can significantly enhance precipitator performance on ash from Western coal.

ELECTROSTATIC PRECIPITATOR EMISSION AND OPACITY PERFORMANCE CONTROL THRU RAPPER STRATEGY

INTRODUCTION

The Utah Power and Light Corporation has two "identical" cold-side electrostatic precipitators at the Huntington Station in Huntington, Utah. Utah Power and Light Corporation required these electrostatic precipitators to be designed to a higher performance level than the then existing EPA regulatory of 0.1 $lb/10^6$ BTU. Utah Power and Light Corporation demanded this higher than required performance to ensure that the scenic Utah surroundings would not be degraded by pollutants. To meet this goal, Buell/Envirotech designed the precipitator units to achieve a 99.5% collection efficiency, which corresponds to an emission rate of 0.05 $lb/10^6$ BTU.

Each of the precipitator units was designed to collect fly ash resulting from the firing of the same low sulfur coal.

The coal is mined from the Hiawatha seam of Deer Creek mine in Emery County, Utah.

Not only are the station's two precipitators duplicate units, but the other equipment in the system from the boiler to the precipitator is also identical. Utah Power and Light Corporation ordered duplicate equipment to ensure that the second system would achieve the same high level of performance/operation as the initial system.

The Unit #1 electrostatic precipitator was started up in June, 1977, and the Unit #2 electrostatic precipitator (see Figure #1) was started up in August, 1974. The precipitator efficiency has been measured at 99.6%.

PROGRAM DESCRIPTION

The present program was initiated to determine the opacity resulting from normal operation of the system and to assess the influence of the collection system rapping strategy upon the opacity.

To obtain these data, performance tests were conducted on one-half (chamber) of each precipitator. The opacity measurement was obtained by a portable Lear Siegler instrument installed in the outlet ductwork. The emissions were obtained by use of EPA-17 test method at a test port located slightly upstream of the opacity measurement.

The emission-opacity relationship is a complex function of many factors. These factors include particle size distribution, moisture content of flue gas, and representative light path of measurement. Correlation of these factors has resulted in the following opacity relationship (Reference 1).

$$\ln (I/I_o) = \frac{-Lw}{KP}$$

Where w is outlet grain loading
I/Io is light transmittance
L is light path length
P is average particle density
K is extinction coefficient, a function of the particle size for a given refractive index.

For this study, an emission-opacity correlation was experimentally determined for each unit. There are several approaches that may be practically employed to obtain such a relationship. These approaches include: reduction of the precipitator's effective specific collection area by de-energizing various electrical sections, variation of the precipitator's effective specific collection areas by variations of the boiler load, and alteration of the collecting system rapping strategy.

Of these possible approaches, the alteration of collecting system rapping strategy was employed to obtain emission-opacity correlation for each unit.

This approach was appropriate for the Huntington Station since the fly ash exhibited adhesive characteristics. This characteristic principally resulted from the level of sodium in the fly ash. With modification of the collecting plate rapper system strategy, additional fly ash is allowed to accumulate on the collecting plates.

This results in a reduction of the effective collection field applied voltage caused by the voltage drop through the dust layer (Reference 2). This phenomenon is illustrated in Figure #2. The practical implementation of this method indicated that the change of one steady state level fly ash layer to another was achieved within one day after changing the particular rapping approach. This is illustrated in Figure #3 which presents the opacity level versus time for two different rapping approaches. The opacity corresponding to each particular rapping strategy was measured for one week before changing to a different rapping strategy.

During the emission-opacity correlation tests, coal samples, boiler conditions, fly ash samples and opacity measurements were all monitored. Two measurements were taken for each of four different collecting system rapper conditions for both the Unit #1 and the Unit #2 precipitator.

EMISSION-OPACITY CORRELATION

The results of the emission-opacity correlation tests for Huntington #1 are presented in Figure #4. The measured opacity values shown in this figure correspond to the outlet duct location, rather than the stack, since only one-half of the precipitator was tested. If the unit were performing identically in both chambers, the stack opacity would be roughly 1.7 times the duct opacity, and the stack emissions would be twice the duct emissions.

Because the opacity meter was calibrated on clean outside air, the data have been fitted with a special case of the method of least squares that requires the curve to pass through the origin. The resulting correlation (Figure #4) is a good fit through the data with little scatter.

The mean coal and ash analyses for the samples taken during the Huntington #1 emission-opacity tests are shown in Table I. These data indicate that there were no major variations in the coal or ash properties during the test series. The particle size distribution and the resistivity-temperature dependence of representative fly ash sample obtained during the test program are presented in Tables II and III, respectively. The results of the laboratory bulk electrical resistivity measurements demonstrate that range of resistivities are within acceptable values for effective precipitator performance.

The results of the emission-opacity correlation tests for Huntington #2 are presented in Figure #5. The curve fitting approach utilized was the same technique employed for Huntington #1. However, the resulting correlation is not the same quality of that for Unit #1, since most of the emissions and opacities are quite low. The mean coal and ash analysis for the emission-opacity correlation tests for Huntington #2 are presented in Table IV. Examination of these data indicate there were no major changes in either coal or fly ash characteristics during the test program. The measured particle size distribution for Huntington #2 is given in Table V, along with the loss on ignition and specific gravity values. The measured electrical resistivity from a representative fly ash sample for Huntington #2 is shown in Table VI.

Comparison of resulting emission-opacity correlations from Unit #1 and Unit #2 show a large difference between the two units. Examination of the differences between the coal and fly ash samples for Unit #1 (Table I) and Unit #2 (Table IV) does not reveal any characteristic difference that would adequately explain the differences between the units.

A comparison of particle size distributions between the two units (Figure #6) indicate that Unit #2 exhibits significantly higher particle sizes than Unit #1. These particular size distribution measurements were taken at the inlet of the precipitator in an attempt to resolve the difference in emission-opacity correlation that apparently exists between the two units. The fact that Unit #2 has a higher particle size than Unit #1 qualitatively explains the fact that Unit #2 has a lower opacity than Unit #1 for a given emission level. Particle size influence upon the opacity is larger than one would estimate. This anomaly may result from an insufficient number of data measurements at higher opacity values for Unit #2.

Examination of the hardware at the two "identical units" revealed that mill differences developed between the two units due to operational conditions. This situation explains the different particle size distribution between the two units.

EMISSION-POWER RESULTS

The correlation of emissions versus precipitator power was derived from the present test program. The data and correlation for the emission-corona power for Huntington #1 and #2 are presented in Figures #7 and #8, respectively. These data show an asymptotic approach to limiting emission as power is increased. This indicates that, although power may be added, it is not useful in terms of enhanced collection efficiency. That is, the increase in power (through current, not increased voltage) does not effectively improve precipitator performance.

This was verified through modeling of the precipitator performance through use of the Southern Research Institute Mathematical Model (Reference 3). Analysis confirmed that increased corona power delivered through increased current, not voltage, may not significantly enhance precipitator collection efficiency.

RAPPING STRATEGY

Since the resulting emissions were found to be a function of the rapping approach, the technique of power-off rapping was applied to assess the potential performance enhancement for a given rapper intensity level.

The technique of power-off rapping is to de-energize an electrical section and rap the collecting plates. This approach has the potential advantage of enhanced fly ash removal from the plates, since the electrical pinning force is removed during the rapping sequence and minimum fly ash is collected on the plates since the applied collection field is removed. This approach is only attractive with highly sectionalized electrostatic precipitators.

The power-off rapping technique was applied to Unit #1. Comparison of the emissions indicate the power-off rapping technique obtains the same opacity with rapper levels that are only 60% of those required for power-on rapping. Test results from the power-off rapping technique are presented in Figure #9.

SUMMARY

The opacity-emission correlation from two "identical" cold-side electrostatic precipitators operating on ash from low-sulfur Western coal were found to exhibit significant differences. The particle size distribution difference between the units was found to contribute to the opacity-emission differences. This was found to result from mill difference between the two units. Additionally, correlation was found to be sensitive to the opacity levels upon which the correlation was derived.

The emission-corona power correlation demonstrates asymptotic emission limit with increasing power. Data demonstrates power levels may be achieved after which additional power will not significantly enhance precipitator performance.

The technique of automatic power-off rapping has indicated significant enhancement of precipitator performance on low-sulfur coal. Rapping intensity, using the power-off rapper technique, can be only 60% of the normal rapping level to achieve equivalent performance.

TABLE I

COAL AND ASH ANALYSES FOR EMISSION-OPACITY CORRELATIONS AT HUNTINGTON NO. 1

	Mean	Standard Deviation
Moisture	2.50	0.10
Ash	13.57	0.50
Sulfur	0.51	0.02
SiO_2	60.48	0.88
Al_2O_3	18.66	0.51
TiO_2	0.81	0.11
Fe_2O_3	3.31	0.13
CaO	5.23	0.68
MgO	1.33	0.23
Na_2O	2.50	0.18
K_2O	1.34	0.08
P_2O_5	0.24	0.02
SO_3	4.33	0.16
Base/Acid	0.18	0.01
Silica/Alumina	3.24	0.10

TABLE II

UTAH POWER AND LIGHT COMPANY, HUNTINGTON #1
SUMMARY OF PARTICLE SIZE DISTRIBUTION,
LOSS ON IGNITION AND SPECIFIC GRAVITY

Hopper Sample	Test #4	Test #5	Test #6	Test #7	Test #8
+149 μ	0.43%	0.34%	0.36%	0.26%	0.45%
+ 45 μ	6.1	4.6	4.9	8.8	8.3
+ 40 μ	7.1	5.2	5.6	9.9	9.4
+ 35 μ	8.2	6.2	6.2	11.1	10.6
+ 30 μ	9.8	7.6	7.3	13.0	12.2
+ 25 μ	11.8	9.0	8.8	15.5	14.7
+ 20 μ	15.8	11.7	11.7	19.0	18.8
+ 15 μ	21.8	17.0	17.2	25.5	25.0
+ 10 μ	37.0	29.9	31.0	40.2	40.0
+ 5 μ	58.5	50.0	50.1	57.2	62.2
- 5 μ	41.5	50.0	49.9	42.8	37.8
Specific Gravity	2.2076	2.3679	2.1952	2.1285	2.1277
Loss on Ignition	1.56%	1.74%	1.72%	1.38%	1.45%

TABLE III

UTAH POWER AND LIGHT COMPANY, HUNTINGTON #1
SUMMARY OF BULK ELECTRICAL RESISTIVITY

Temperature (^oF)	280	300	340
Test #4			
Resistivity (OHM-CM)	9.00×10^9	6.79×10^9	3.35×10^9
Breakdown Voltage (VOLTS/CM)	1.70×10^4	1.30×10^4	1.40×10^4
Moisture (%)	6.12	6.10	6.10
Test #5			
Resistivity (OHM-CM)	1.00×10^{10}	7.50×10^9	6.08×10^9
Breakdown Voltage (VOLTS/CM)	1.50×10^4	1.60×10^4	1.40×10^4
Moisture (%)	6.16	6.13	5.91
Test #6			
Resistivity (OHM-CM)	9.58×10^9	6.18×10^9	3.29×10^9
Breakdown Voltage (VOLTS/CM)	1.50×10^4	1.60×10^4	1.30×10^4
Moisture (%)	6.21	6.26	6.08
Test #7			
Resistivity (OHM-CM)	1.48×10^{10}	8.45×10^9	6.57×10^9
Breakdown Voltage (VOLTS/CM)	1.70×10^4	1.60×10^4	1.50×10^4
Moisture (%)	6.08	6.22	5.90
Test #8			
Resistivity (OHM-CM)	1.46×10^{10}	8.77×10^9	4.92×10^9
Breakdown Voltage (VOLTS/CM)	1.50×10^4	1.80×10^4	1.60×10^9
Moisture (%)	6.10	6.22	6.12

TABLE IV

COAL AND ASH ANALYSES FOR EMISSION-OPACITY CORRELATIONS AT HUNTINGTON NO. 2

	Mean	Standard Deviation
Moisture	1.59	0.11
Ash	11.86	1.10
Sulfur	0.49	0.02
SiO_2	59.03	2.07
Al_2O_3	19.55	0.39
TiO_2	1.08	0.13
Fe_2O_3	3.62	0.08
CaO	6.86	0.73
MgO	1.62	0.73
Na_2O	2.98	0.29
K_2O	1.19	0.14
P_2O_5	0.30	0.03
SO_3	4.75	0.54
Base/Acid	0.21	0.02
Silica/Alumina	3.02	0.10

TABLE V

UTAH POWER AND LIGHT COMPANY, HUNTINGTON #2 SUMMARY OF MICRO PARTICLE DISTRIBUTION, SPECIFIC GRAVITY AND LOSS ON IGNITION

Inlet Thimble Sample

Test #	1	2	3	4	5	6	7	8
+149 μ	2.89%	2.92%	3.63%	3.31%	3.83%	3.52%	5.86%	2.49%
+ 45 μ	34.2	32.1	34.3	33.5	33.2	31.9	50.2	35.5
+ 40 μ	36.8	34.1	36.2	35.8	35.0	33.9	52.5	37.9
+ 35 μ	40.0	37.0	38.5	38.2	37.0	36.5	55.0	40.5
+ 30 μ	43.5	40.2	41.6	41.5	40.0	39.5	58.0	44.0
+ 25 μ	48.0	44.5	45.5	44.8	43.9	43.0	61.5	47.5
+ 20 μ	53.8	50.0	50.1	49.0	48.8	47.0	65.5	53.5
+ 15 μ	61.0	56.2	56.5	55.9	55.0	53.5	70.5	59.5
+ 10 μ	70.5	67.5	66.5	65.9	65.5	63.5	78.0	68.8
+ 5 μ	83.7	79.0	77.2	77.2	76.5	79.5	86.4	78.8
- 5 μ	16.3	21.0	22.8	22.8	23.5	20.5	13.6	21.2
*	2.1704	2.1595	2.1708	2.1109	2.2566	2.0864	2.1865	2.1346
**	2.18%	2.34%	2.70%	2.84%	3.09%	2.90%	2.40%	2.45%

*Specific Gravity
**Loss on Ignition

TABLE VI

UTAH POWER AND LIGHT COMPANY, HUNTINGTON #2
SUMMARY OF BULK ELECTRICAL RESISTIVITY

Temperature (°F)	250	280	310
Test #1			
Resistivity (OHM-CM)	5.32×10^9	5.06×10^9	2.12×10^9
Breakdown Voltage (VOLTS/CM)	1.30×10^4	1.20×10^4	1.20×10^4
Moisture (%)	6.92	7.02	6.64
Test #2			
Resistivity (OHM-CM)	5.84×10^9	5.82×10^9	5.15×10^9
Breakdown Voltage (VOLTS/CM)	1.40×10^4	1.30×10^4	1.30×10^4
Moisture (%)	7.06	6.78	6.56
Test #3			
Resistivity (OHM-CM)	8.04×10^9	6.37×10^9	5.87×10^9
Breakdown Voltage (VOLTS/CM)	1.40×10^4	1.20×10^4	1.20×10^4
Moisture (%)	7.06	6.94	6.58
Test #4			
Resistivity (OHM-CM)	7.93×10^9	5.72×10^9	5.32×10^9
Breakdown Voltage (VOLTS/CM)	1.40×10^4	1.20×10^4	1.20×10^4
Moisture (%)	7.04	6.92	6.64
Test #5			
Resistivity (OHM-CM)	7.52 x 109	6.47×10^9	4.70×10^9
Breakdown Voltage (VOLTS/CM)	1.10×10^4	1.20×10^4	1.20×10^4
Moisture (%)	6.80	6.90	7.10

TABLE VI (CONT'D)

UTAH POWER AND LIGHT COMPANY, HUNTINGTON #2
SUMMARY OF BULK ELECTRICAL RESISTIVITY

Temperature (^oF)	250	280	310
Test #6			
Resistivity (OHM-CM)	1.11×10^{10}	7.54×10^{9}	5.94×10^{9}
Breakdown Voltage (VOLTS/CM)	1.20×10^{4}	1.40×10^{4}	1.40×10^{4}
Moisture (%)	6.86	6.92	7.27
Test #7			
Resistivity (OHM-CM)	1.49×10^{10}	5.97×10^{9}	5.32×10^{9}
Breakdown Voltage (VOLTS/CM)	1.20×10^{4}	1.20×10^{4}	1.10×10^{4}
Moisture (%)	6.84	6.99	6.86
Test #8			
Resistivity (OHM-CM)	9.85×10^{9}	9.16×10^{9}	5.67×10^{9}
Breakdown Voltage (VOLTS/CM)	1.40×10^{4}	1.40×10^{4}	1.40×10^{4}
Moisture (%)	6.74	7.24	7.08

References

1. Ensor, D. S. and Pilat, M. J. Calculation of Smoke Plume Opacity from Particulate Air Pollutant Properties. APCA Journal, Volume 21, No. 8, August 1971.

2. White, H. J. Industrial Electrostatic Precipitation. Addison-Wesley, Reading, Massachusetts, 1963.

3. McDonald, J. R. A Mathematical Model of Electrostatic Precipitation: Revision 1, Volume I, Modeling and Programming. EPA-600/7-78-111a, U. S. Environmental Protection Agency, Research Triangle Park, North Carolina, June, 1978.

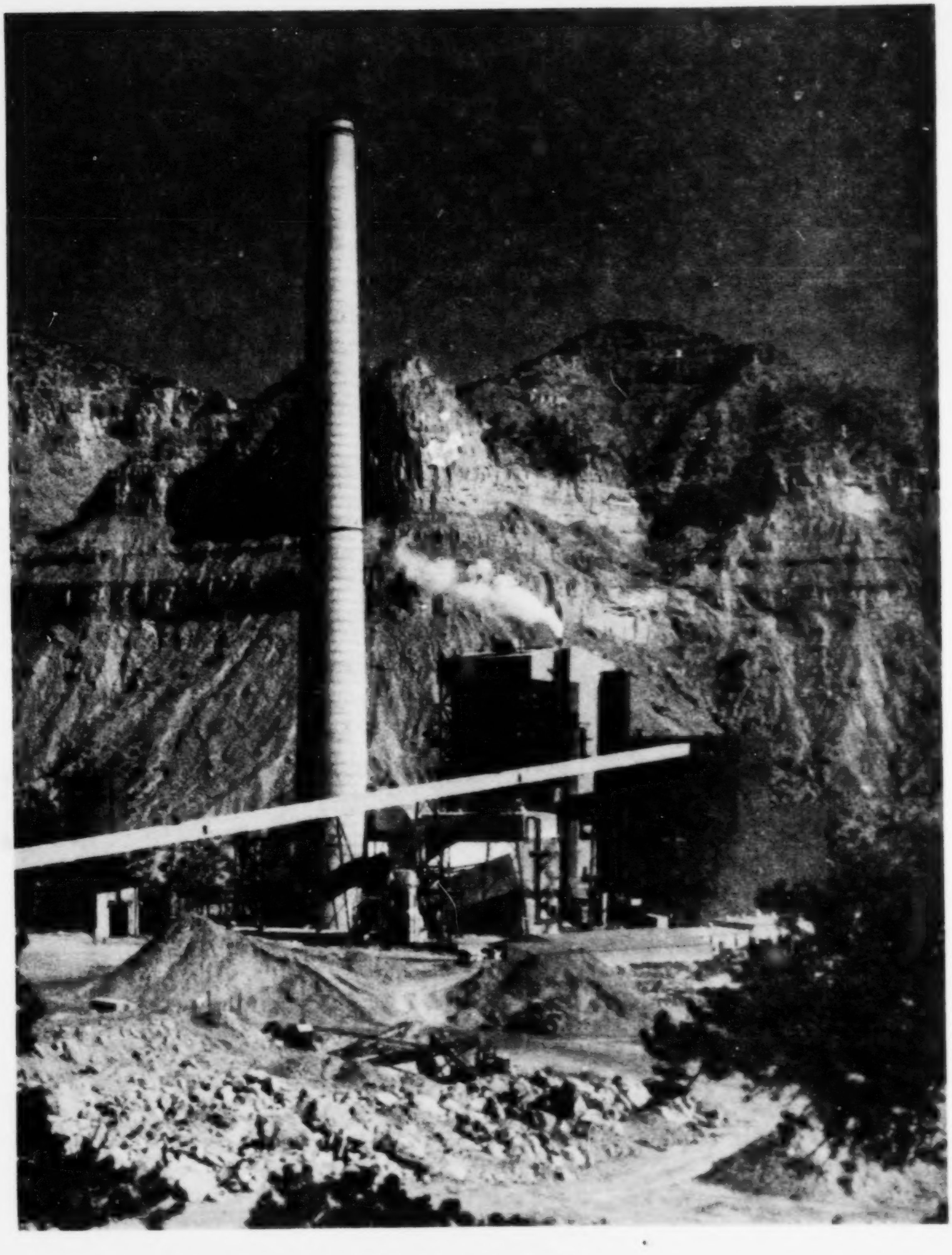

Figure 1. Huntington Station Unit #2 on-line

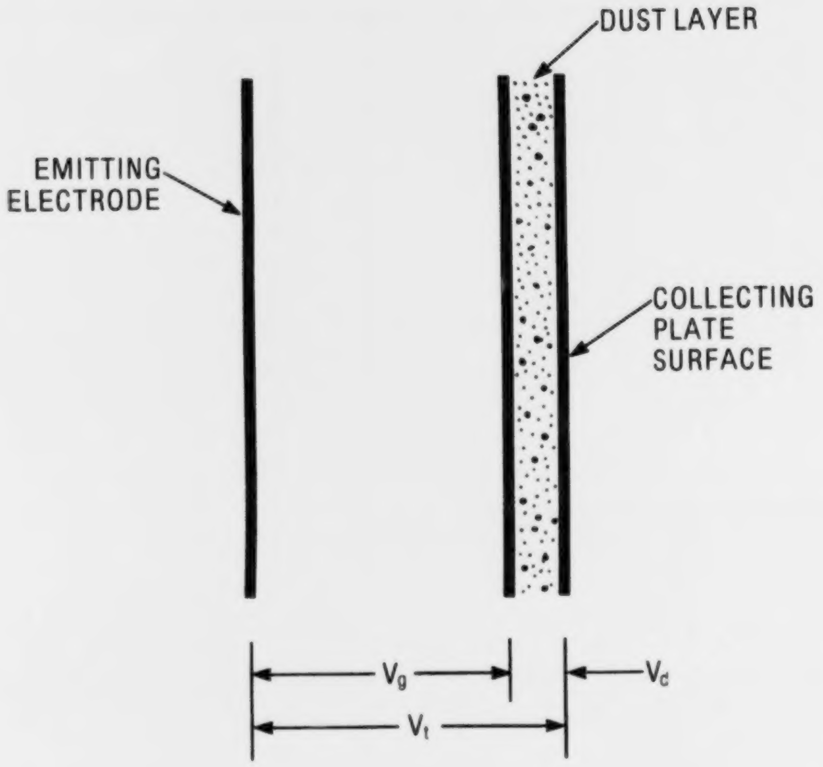

$$
\begin{aligned}
V_t &= V_g + V_d \\
&= V_g + RJd
\end{aligned}
$$

where V_t is total voltage drop
V_g is effective voltage drop across the gap
V_d is voltage drop across dust layer
R is resistivity of dust layer
d is dust layer tickness
J is current density

Fig. 2 — SCHEMATIC REPRESENTATION OF VOLTAGE DROP THROUGH DUST LAYER.

STRATEGY NO. 1

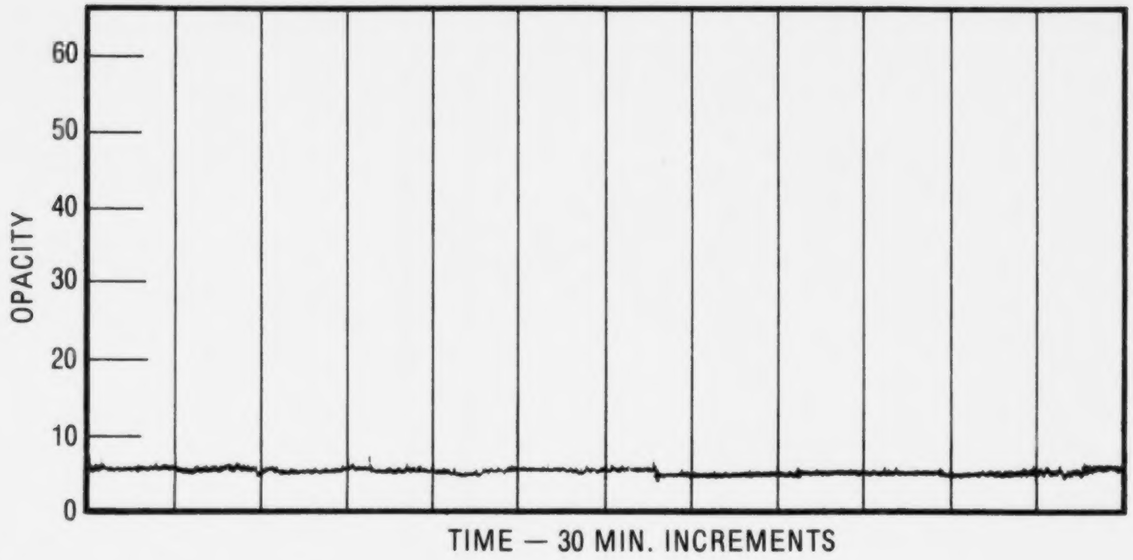

STRATEGY NO. 2

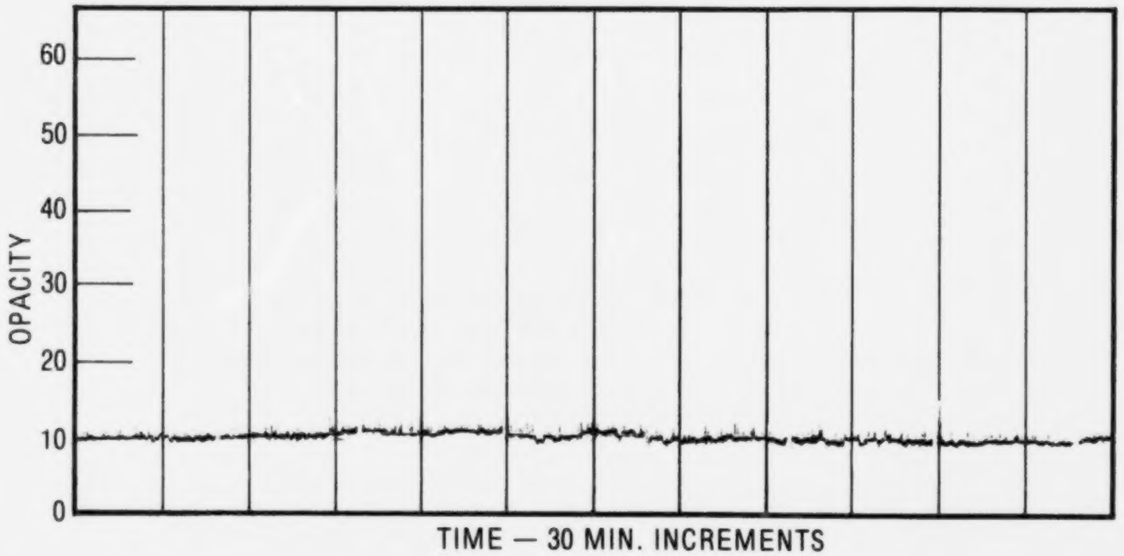

Fig. 3 REPRESENTATIVE OPACITY FOR DIFFERENT RAPPER STRATEGIES

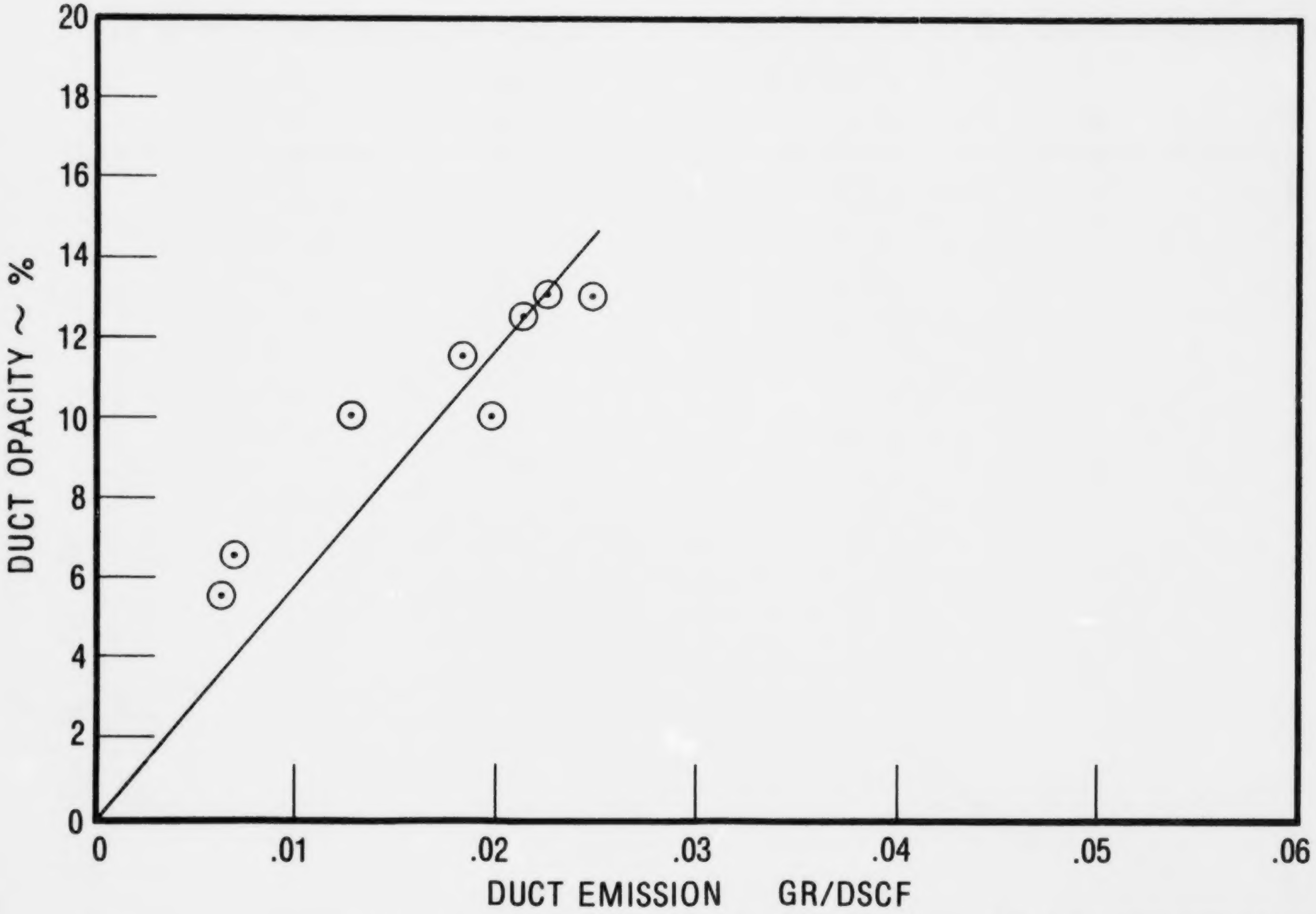

Fig. 4 — HUNTINGTON NO. 1 — OPACITY VS. OUTLET CONCENTRATION

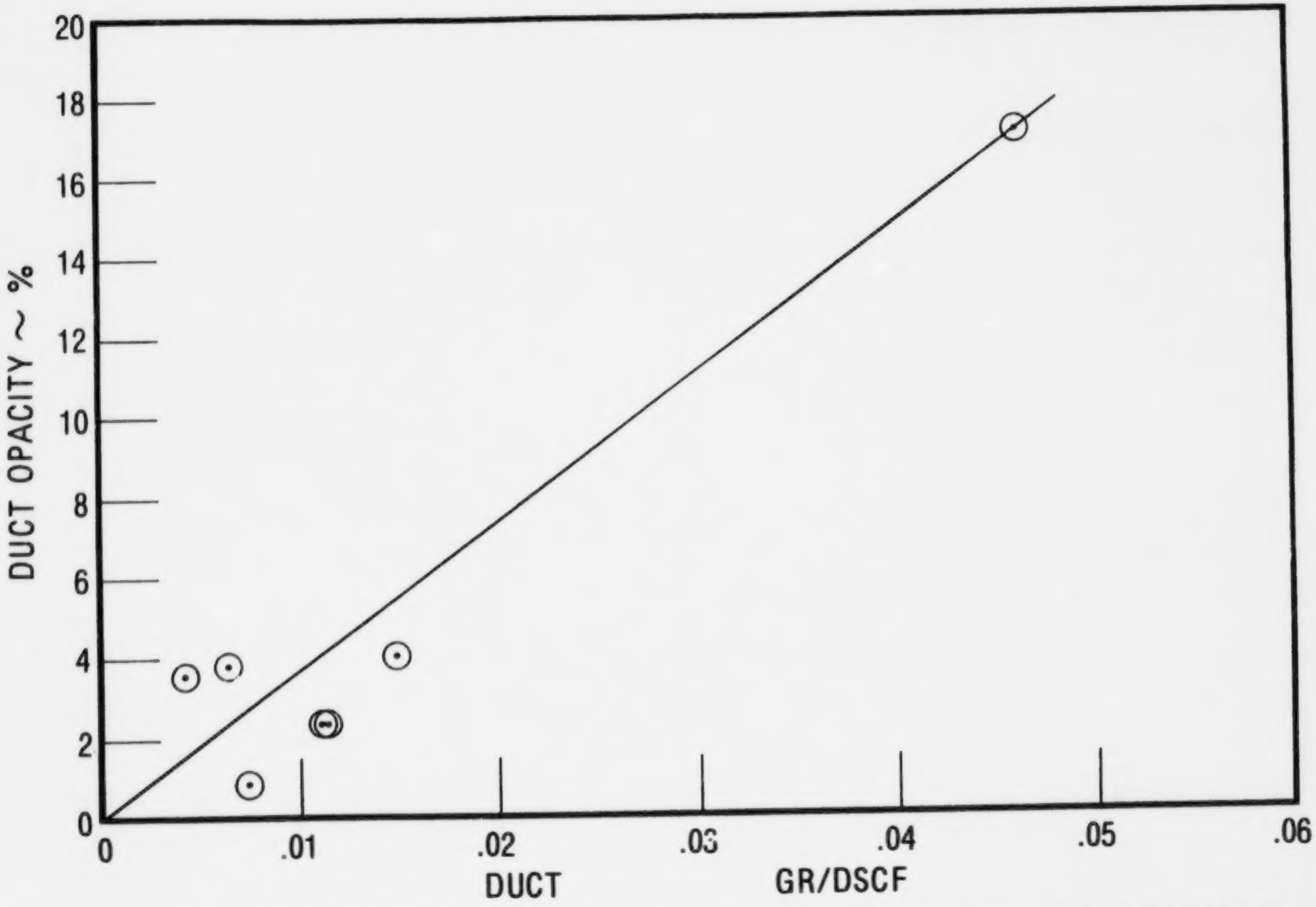

Fig. 5 — HUNTINGTON NO. 2 — OPACITY VS. OUTLET CONCENTRATION

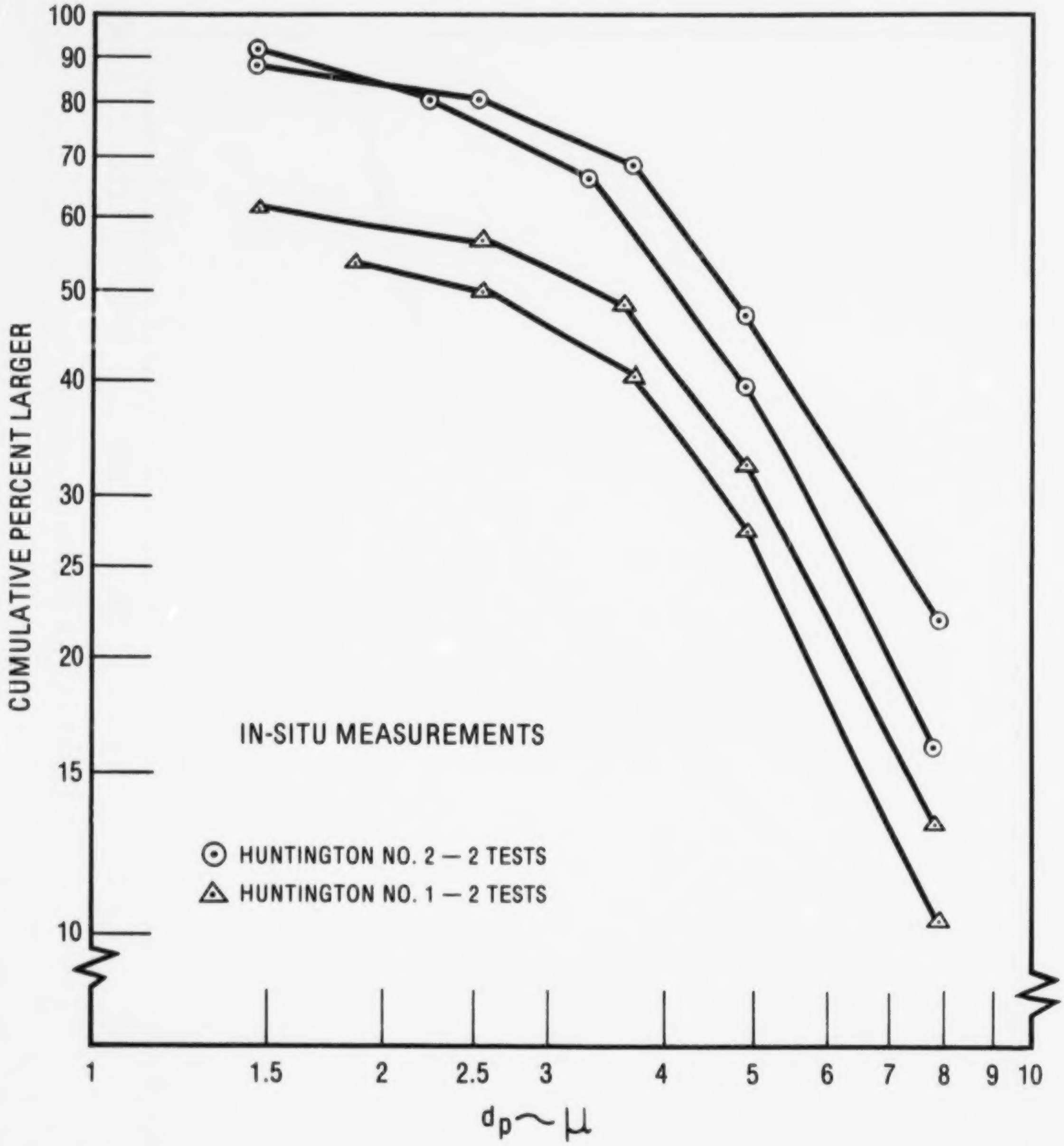

Fig. 6 — PARTICLE SIZES

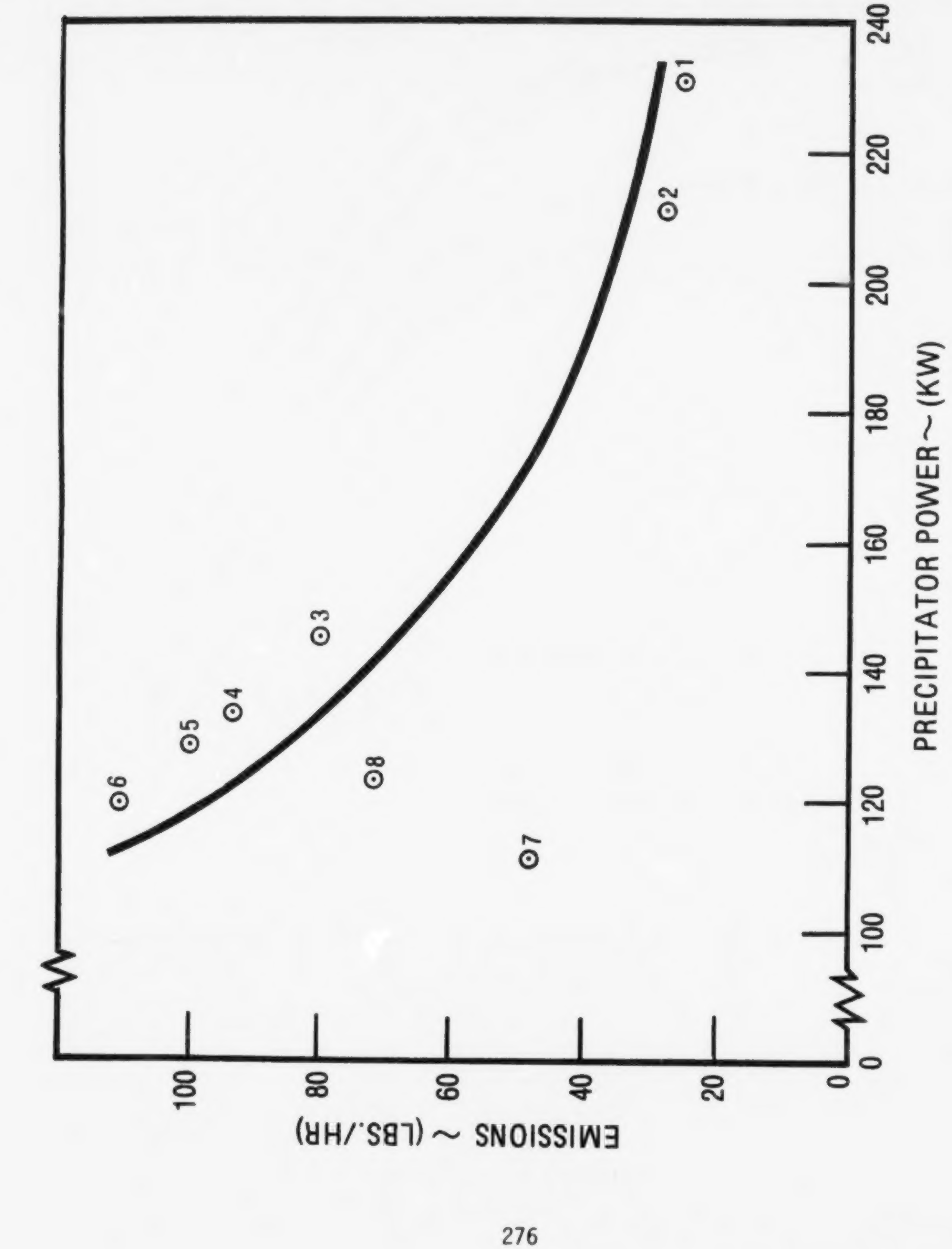

Fig. 7 — HUNTINGTON NO. 1 — EMISSIONS VS. POWER

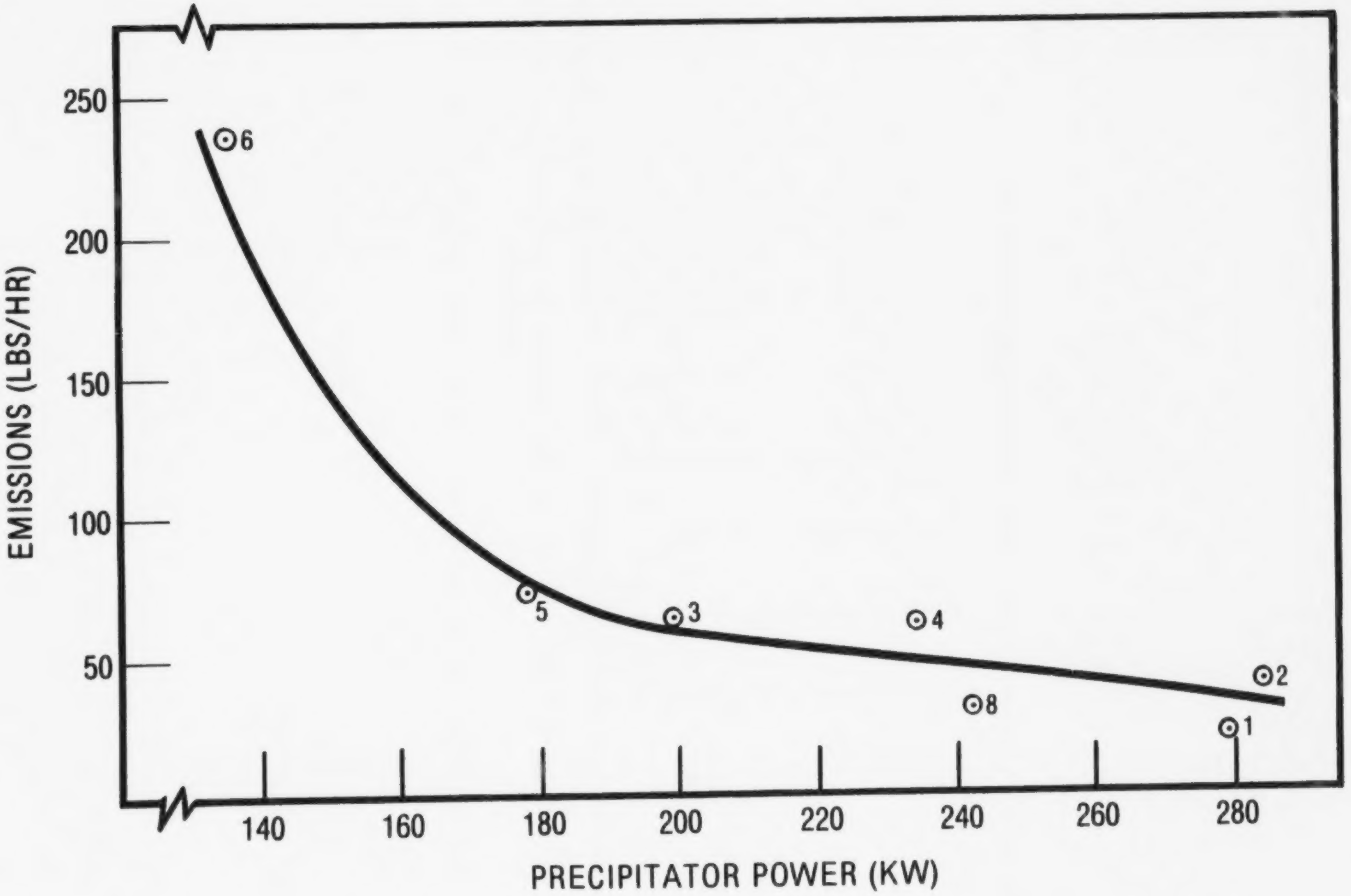

Fig. 8 — HUNTINGTON NO. 2 — EMISSIONS VS. POWER

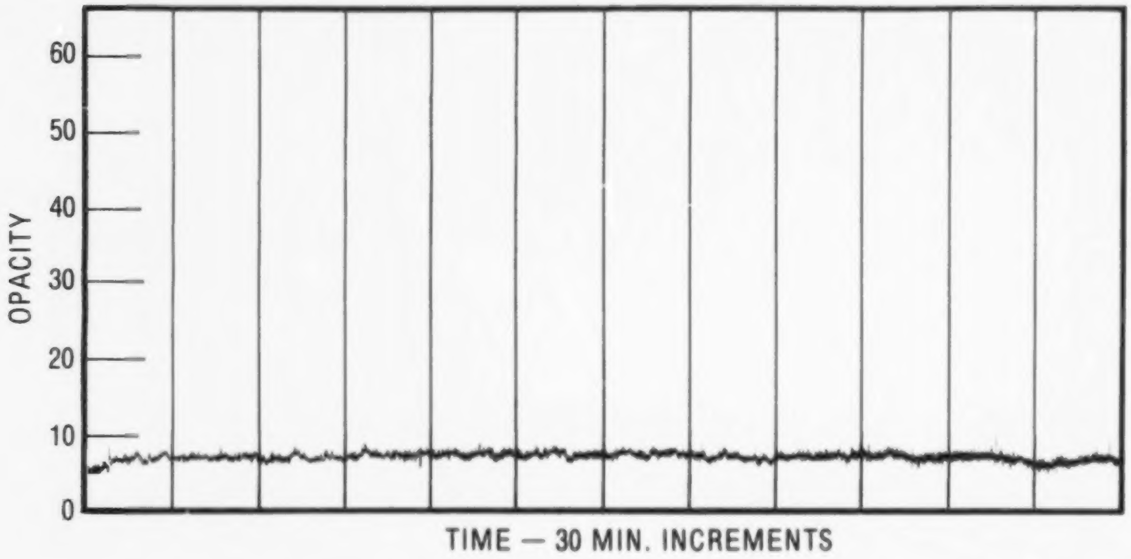

Fig. 9 REPRESENTATIVE OPACITY FOR POWER-OFF RAPPING

RAPPING SYSTEMS FOR COLLECTING SURFACES IN AN ELECTROSTATIC PRECIPITATOR

By:

Heinz L. Engelbrecht
Air Pollution Control Division
Wheelabrator-Frye Inc.
Pittsburgh, Pennsylvania

ABSTRACT

Dust build-ups on adjacent surfaces is often an unwanted effect in industrial processes handling pulverized materials. In the case of electrostatic precipitation, build-up of dust on the collecting surface is the purpose of the process. Removal of these build-ups is sometimes difficult, but necessary to maintain the continuity of the process. Dry-process methods for dust removal include rapping by impact.

It is the intent of this paper to provide information on the general subject of dust removal from plates, on rapping systems used in electrostatic precipitators, and on measurements and order of magnitude of rapping forces.

Rapping acceleration test results obtained in the Laboratory are expanded to cover full-scale collecting surface plates.

Effects of plate design, plate height and length, method of support, rapping, hammer weight and lift are analyzed.

INTRODUCTION

Handling of pulverized materials is common to many industries and processes; a few examples may be manufacturing of cement, processing of foods, and separation and recovery of materials. Sometimes, these materials cause build-ups on adjacent surfaces as an unwanted effect, but in the case of an electrostatic precipitator, build-up of dust on the collecting surface plates is the explicit intent.

The electrostatic precipitation process includes the phases of particle charging, precipitation and removal. All of these phases are affected by the residual layer of particles on either the collecting surface plates or the discharge wires. Thus, periodical removal of these build-ups is necessary to maintain the continuity of the precipitation process. The removal of the precipitated dust requires consideration of the precipitation process and prevention of reentrainment.

Reentrainment of particles occurs constantly in an electrostatic precipitator. All particles entering the electrical field are charged, but not all charged particles are precipitated. Of those which are, a certain number is reentrained by saltation, by erosion, by electrical wind, and/or electrical arcing. More reentrainment occurs during dust removal. Additional reentrainment of particles can originate in the hopper area caused by hopper boil-up. All reentrainment will add to the fraction of particles which escape the electrical field without ever being precipitated. This total makes up the outlet dust residual of the precipitator.

A quantitative analysis of the various fractions of the outlet dust residual has not been attempted, but it has been shown that rapping reentrainment is the major contributor to the outlet residual.

Therefore, the removal process is important for the continuity of the precipitation process, requiring a carefully selected equilibrium between cleaning of the collecting surface plates and prevention of particle reentrainment.

Dry-process methods for removal of dust from collecting surface plates depend on mechanical devices using impact forces generated by single impact hammers or multiple impact vibrators. It is the intent of this paper to describe a rapping system, which uses rotating, single-impact hammers to achieve dust removal from the collecting surface plates.

COLLECTING SURFACE PLATES

Collecting surface plates consist of thin metal plates (16 to 20 Ga.) spaced evenly at centerline distances of 8 to 20 in. to form gas passages, in which the discharge or emitting electrodes are centered. Curtains with a height of up to 50 ft. and a length of up to 12 ft. in direction of gas flow can be made out of single stiffened sheets or individual roll-formed strips 18 to 24 in. wide.

Basic requirements on the design of a collecting surface are: rigidity, light weight, quiescent zones and good vibrational characteristics. These are met by a roll-formed strip, which includes three pockets and means to interlock with adjacent strips to form a continuous curtain (Figure 1).

The curtain is supported at the top by two hangers per strip and connected at the bottom by means of a continuous bar and anvil assembly (Figure 2).

RAPPING SYSTEM

Rappers are of the impulse or vibrator-type; one producing a single impact, the second, a continuous vibration of a certain duration. The impulse type rapping system described in this paper uses a slowly rotating shaft, mounted cross-wise to the gas flow inside of the precipitator, with hammers attached in a staggered fashion around its periphery. Each hammer is in line with a rapper bar, which connects the lower ends of a number of collecting surface strips making up one collecting surface curtain (Figure 3). As this shaft, which is normally located at the outlet end of each electrical field, rotates, one hammer after the other reaches a vertical position with the hammer head standing up. At this point, the force of gravity takes over, and the hammer head rotates approximately 180 degrees around a pin in its attachment and hits the anvil at the end of the rapper bar. This impact is introduced into the collecting surface curtain and produces definite plate movements and acceleration in two axis, normal to the plate and in direction of the impact, of which the acceleration normal to the plate is of greater importance in the removal process of the particles.

MEASUREMENTS OF PLATE ACCELERATIONS

Plate accelerations provide data for comparisons of various plate designs, sizes, and rapping systems. Accelerations normal to the surface of the plate are measured in multiples of g, with one g = 32.2 ft/sec^2. These are measured at selected points using an electro-mechanical pick-up system, with a piezo-electric effect to visualize and/or measure the acceleration of the collecting surface curtain. The voltage is proportional to the acceleration of the object.

The electrical signal from the pick-up is amplified in a voltage amplifier and fed to an impulse-type sound level indicator which allows the display of the effective values (RMS) or the maximum values by using a holding circuitry.

The measurements of the plate accelerations are made at a suitable number of test points on the collecting surface curtain. The number of test points (horizontally and vertically) has to be determined in such a manner as to give sufficient data to evaluate the expected acceleration pattern. The rapping impact is produced with a standard rapping hammer by manually releasing the hammer from the upper lift point. The average acceleration values are calculated for each collecting surface strip and also for each elevation and plotted graphically. As a lower limit for suitable removal of the accumulated dust layer, a minimum acceleration of 100g is considered acceptable for most electrostatic precipitator applications.

Up to six individual measuring points are used in each collecting surface strip in each test elevation (Figure 4). Normally, testing is done in three different elevations: top, center, and bottom. The number of strips to be tested depends on the total number of strips in the collecting surface curtain. Three to five measurements are taken at each of the designated test points, and the following average test results calculated for each of the test points:

a) arithmetic average of the test points in one location

b) arithmetic average of the test averages in one of the tested elevations of one strip. This average is used for the acceleration profile.

c) arithmetic average of the acceleration in one collecting surface strip

d) total arithmetic average of the rapping acceleration in one collecting surface curtain

This total average represents a mean rapping acceleration for a specific collecting surface curtain and can further be used to calculate a rapping profile based on percentages of the mean rapping acceleration. An example for test results obtained at the test points of the collecting surface plate shown in Figure 4 is given in Table 1; graphical presentations of the acceleration profile are made for absolute values of g, and for percentages of the mean rapping acceleration at each test elevation (Figure 5).

INFLUENCES ON RAPPING INTENSITY

Influences on the rapping intensity in an electrostatic precipitator, not necessarily in sequence of their importance, are:

- Plate design
- Curtain length
- Curtain height
- Plate connection to rapper bar
- Plate support
- Location of impact point
- Hammer weight
- Hammer lift

Tests have been performed with various plate designs, methods of connecting plates to rapper bars, curtain heights and lengths, and hammer weights. The lift of the hammer was always taken at approximately 180°, which represents the maximum lift inherent with this rapper design.

PLATE DESIGN

Basic tests were conducted using a so-called C-type collecting surface plate. Comparative tests showed that a CS-type plate has a higher level of rapping intensity than the C-type. For example, the absolute acceleration for the C-type plate was 188g in the far corner diagonally opposite the point of impact, whereas the CS-type showed 400g at the same location (Figure 6).

In addition, the acceleration of the far points represented 51% of the average acceleration of the C-type and 78% of the average acceleration of the CS-type plate. This shows a lower dampening effect of the CS-type curtain. (Figure 7).

CURTAIN LENGTH

As it can be expected, there is a definite influence of the curtain length in the acceleration of the collecting surface plates. Comparing curtains with 4.5, 7.5, and 12 ft. length, the maximum accelerations at the point of impact are 1076 to 1160g, reduced to 560, to 400g respectively at the far points (Figure 8). These tests were performed using a standard CS-type collecting surface curtain with a field height of 20 ft. The mean accelerations in g are 747g, 575g, and 513g respectively. Local accelerations expressed in percent of the mean accelerations are shown on Figure 9. The acceleration profile remains almost constant for the first 4.5 ft. from the point of impact regardless of total curtain length.

CURTAIN HEIGHT

Tests with a curtain height of 50 ft. revealed a substantial acceleration at the point of impact, which rapidly decreased to approximately mid-height and then remained almost constant for the upper half of the collecting surface curtain. The acceleration profile in g and the percentage of the average acceleration are shown in Figure 10.

METHOD OF PLATE SUPPORT

The only method of plate support further investigated in this respect was characterized by a loose connection between plate and support beam. All other methods using a rigid connection were ruled out because of their inherent inability to provide for graduated expansion of the collecting surface curtain during start-up and the dampening effect of the rigid connection on the acceleration of the upper third of the collecting surface curtain.

METHOD OF CONNECTING PLATE TO RAPPER BAR

Comparative tests between a system using a "rigid" connection between the plate and the rapper bar and one using a "loose" connection (Figure 11) revealed that the rigid connection will achieve a higher average acceleration (412g compared to 101g), and also provide for a higher acceleration in the upper far corner (296g compared to 89g).

LOCATION OF IMPACT POINT

Locating the rapper hammer impact point normal to the surface of the collecting plate results in a considerable lower average plate acceleration, as well as a drastically reduced acceleration in the upper far corner (Figure 12). Therefore, the hammer impact point is always parallel to the axis of the plate.

Locating the rapper bar at approximately the mid-point of the collecting surface curtain and maintaining the direction of the hammer impact, the local acceleration at the point of impact is extremely high (Figure 13), but the distribution of the plate acceleration is rather non-uniform. Therefore, besides design considerations, such as accessibility, etc., it is best to maintain the point of impact at the bottom of the collecting surface curtain.

HAMMER WEIGHT

A comparison of the rapping accelerations obtained with two different hammer weights is shown on Figure 14. The average accelerations follow the ratio of the hammer weights, i.e., 1.58 to 1.00

HAMMER LIFT

It is inherent in this design that the hammer lift approximates 180 degrees, therefore, no tests at other lift angles were made, although it can be expected that the average acceleration is also a linear function of the hammer lift.

AVERAGE PLATE ACCELERATION

An analysis of the results of numerous rapping tests revealed a mathematical relationship between the average rapping acceleration of a collecting surface curtain and the curtain dimensions and the hammer weight.

This relationship can be described as follows:

$$\bar{b} = K W H^{-d} (2.08 L)^{-c}$$

with $\bar{b}$ = average rapping acceleration (g)
W = hammer weight (kg)
L = curtain length (m)
H = curtain height (m)
c, d, K = constants

INFLUENCES ON PRECIPITATOR EFFICIENCY

Periodical removal of the precipitated dust from the collecting surface plates is necessary to maintain the continuity of the precipitation process. The preferred method of dust removal in dry-process precipitators is by plate acceleration using a suitable rapping system. The rapping hammer impact on the collecting surface curtain can be varied by freqency and intensity.

The influence of rapping frequency on the performance of the electrostatic precipitator is not an easily predictable parameter, but depends on process variables, such as particle shape and size, electrical field and specific dust resistivity (all of which vary with the location in the precipitator), and general variables, such as gas velocity, gas temperature, collecting surface plate design, field height, and field length. Thus, rapping frequency becomes one of the parameters to be established during precipitator start-up or fine-tuning.

The influence of rapping intensity is used to counteract electrical, mechanical and chemical forces opposing the removal of the precipitated dust, and is, thus, more germane to the source of the dust; i.e., the process itself. Requirements for rapping intensity are more predictable and can be handled by design of the hammer; i.e., weight of the hammer head and/or length of the hammer handle (shaft).

Rapping intensity expressed as mean rapping acceleration can be calculated. For a typical CS-type collecting surface plate with the following data:

Length:	2.4m	K = 197
Height:	6.0m	c = .387
Hammerweight:	6.2 Kg	d = .227

the average plate acceleration calculates to 436g (see Table 1, Figures 4 and 5). The results of a series of calculations of average rapping intensities for various field lengths; i.e., various number of strips in comparison with measured average rapping accelerations is shown on Figure 15.

Rapping frequency is controlled by adjustable electric timers, which can be set to provide either or two typical modes of operation: rapping of one single curtain followed by a short pause or rapping of several or all curtains followed by a long pause. In either mode, an individual plate will be rapped approximately the same number of times during a long time span.

Two dust samples (fine and coarse particulates) were investigated in a pilot precipitator and the penetration noted as a function of the rapping cycle. In the case of the sample consisting of fine dust, an optimum performance; i.e., a minimum of penetration was observed at a rapping cycle of 160 minutes, whereas in the case of the coarse dust sample, the optimum was observed at a rapping cycle of 110 minutes. The penetration levels with continuous rapping were 40 and 10 percent respectively (Figure 16).

Rapping optimization tests at an electrostatic precipitator serving a municipal incinerator were made, resulting in a change from a stack opacity reading characterized by heavy spiking every 10 minutes (rapping cycle 7/8 minutes on and 9-1/8 minutes off) to an opacity reading under 10 percent with practically no spikes (calibration spikes show every 4 hours). The latter was taken with a rapping cycle of 1 minute on and 20 minutes off (Figure 17).

SUMMARY

Rapping systems for collecting surface curtains in electrostatic precipitators have long been considered mechanical devices designed for ease of installation, reliability of operation, and low cost. The recent emphasis on high collecting efficiencies, even for fine dust particles, requires a new look at the design and operation of these systems. Fine tuning of the rapping systems in multi-field electrostatic precipitators will strive to prevent rapping losses, which could make up for 60 to 80 percent of the outlet residual. Here, the work on the outlet field is of prime importance. Real time instrumentation, such as opacity meters and oscilloscopes, have to be used to gain immediate results from changes made during the fine tuning process. Needless to say that this is an ongoing continuous process and any changes in the operation of the source of the gas can result in changed operating conditions for the precipitator and, thus, in a need for adjustments of the rapping system.

ACKNOWLEDGEMENT

Information and data for this paper were provided by LURGI Umwelt und Chemotechnik GmbH, Frankfurt, Germany.

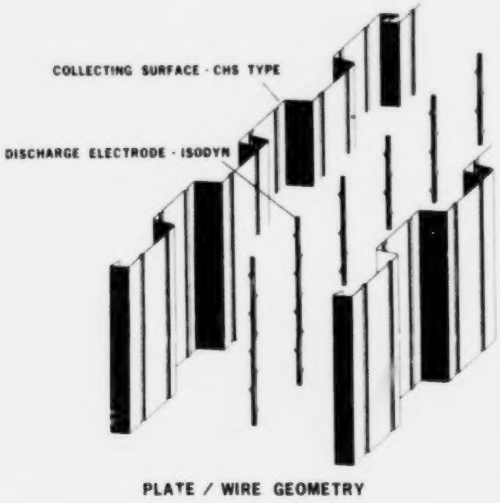

FIGURE 1

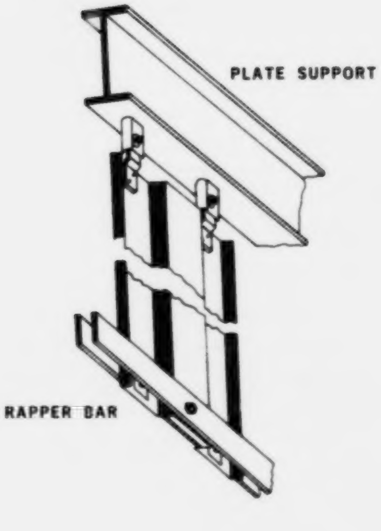

FIGURE 2

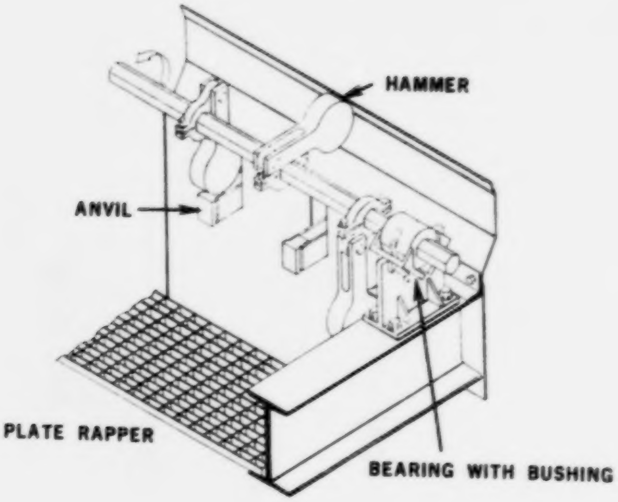

FIGURE 3

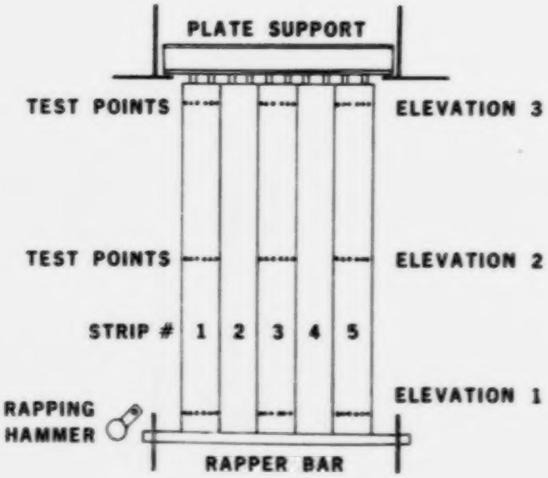

FIGURE 4

TABLE 1: ACCELERATION MEASUREMENTS
(ALL VALUES IN MULTIPLES OF (g)

STRIP	STRIP 1						STRIP 3						STRIP 6					
POINT	1	2	3	4	5	6	1	2	3	4	5	6	1	2	3	4	5	6
ELEVATION 3 *	410	470	430	260	650	450	290	260	330	150	370	210	250	200	230	130	240	180
	445						270						205					
ELEVATION 2 *	450	450	440	310	560	430	320	310	330	220	310	240	270	220	230	135	310	220
	440						290						230					
ELEVATION 1 *	1280	1220	1240	780	1960	950	480	460	750	390	740	280	320	310	400	220	770	320
	1240						515						380					
STRIP AVERAGE	710						360						275					
TOTAL AVERAGE	448																	

* ARITHMETIC AVERAGE OF THREE TESTS

TABLE 1

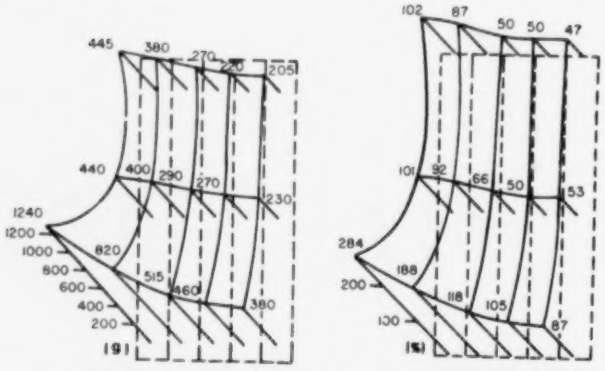

RAPPING ACCELERATIONS IN (g)

RAPPING ACCELERATIONS IN % OF AVERAGE (b AVG. = 437 g)

RAPPING ACCELERATIONS FOR TEST COLLECTING SURFACE

FIGURE 5

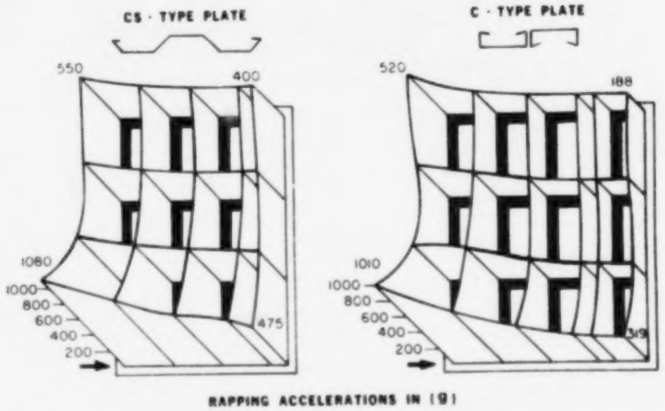

COMPARISON BETWEEN CS · TYPE AND C · TYPE
COLLECTING SURFACE PLATE

FIGURE 6

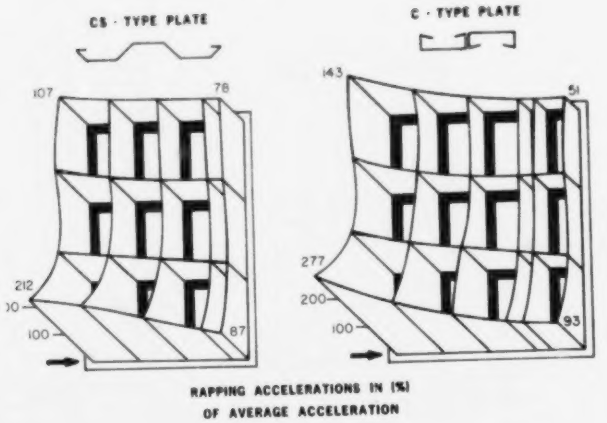

COMPARISON BETWEEN CS · TYPE AND C · TYPE
COLLECTING SURFACE PLATE

FIGURE 7

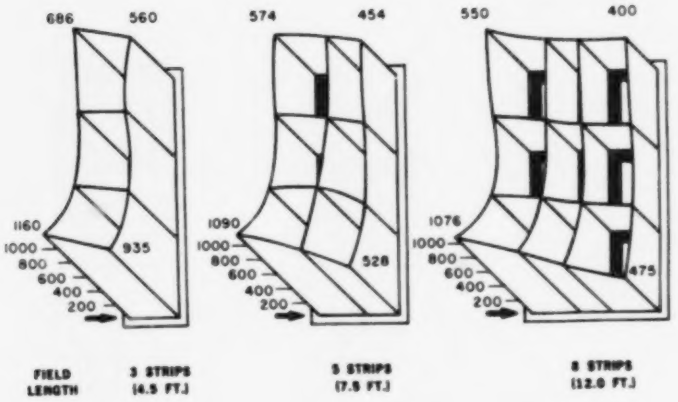

COMPARISON OF RAPPING ACCELERATIONS OF VARIOUS FIELD LENGTHS IN (g)

FIGURE 8

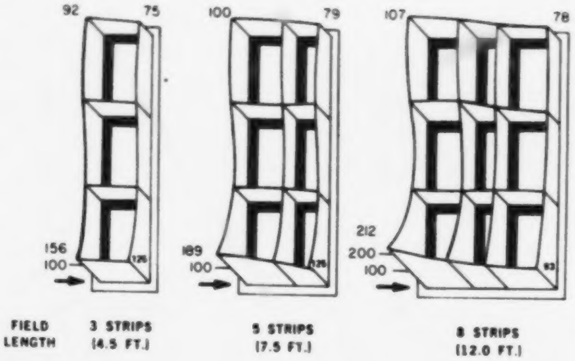

COMPARISON OF RAPPING ACCELERATIONS OF VARIOUS FIELD LENGTHS IN (%)

FIGURE 9

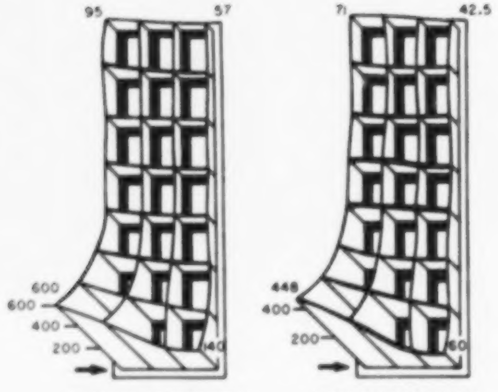

RAPPING ACCELERATION IN (g)

RAPPING ACCELERATION IN (%) OF AVERAGE

RAPPING ACCELERATIONS OF 50 FT. / 12 STRIP
C - TYPE COLLECTING SURFACE PLATE

FIGURE 10

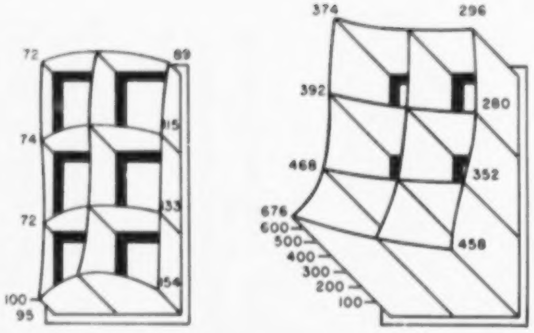

"LOOSE" CONNECTION

"RIGID" CONNECTION

BETWEEN COLLECTING SURFACE
PLATES AND RAPPER BARS

RAPPING ACCELERATIONS

FIGURE 11

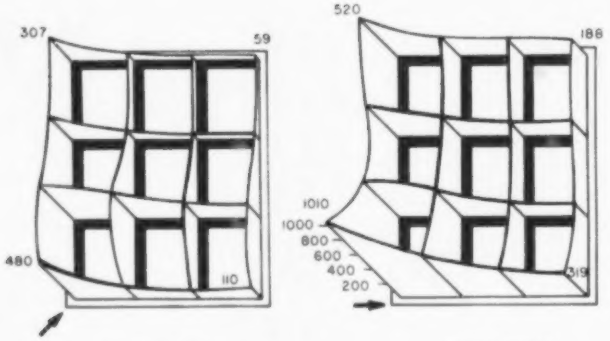

RAPPING IMPACT NORMAL TO THE SURFACE OF THE PLATE

RAPPING IMPACT PARALLEL TO THE SURFACE OF THE PLATE

RAPPING ACCELERATIONS IN (g)

FIGURE 12

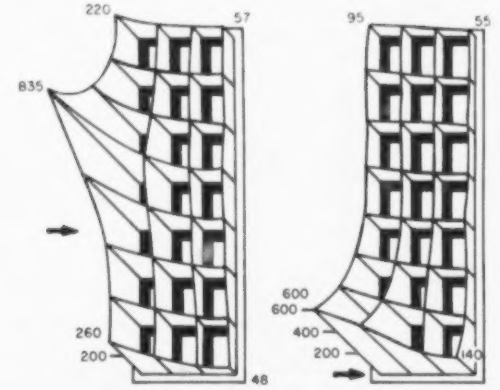

RAPPING IMPACT NEAR THE CENTER OF THE PLATE

RAPPING IMPACT AT THE BOTTOM OF THE PLATE

RAPPING ACCELERATIONS IN (g)

FIGURE 13

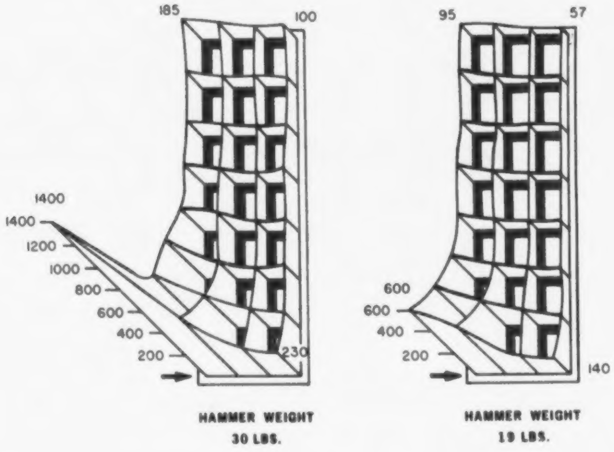

RAPPING ACCELERATIONS IN (g)

FIGURE 14

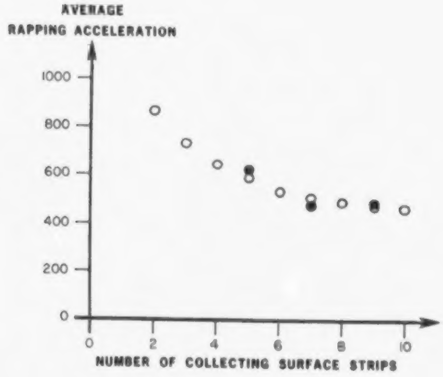

COMPARISON BETWEEN CALCULATED
AND
TESTED RAPPING ACCELERATIONS

FIGURE 15

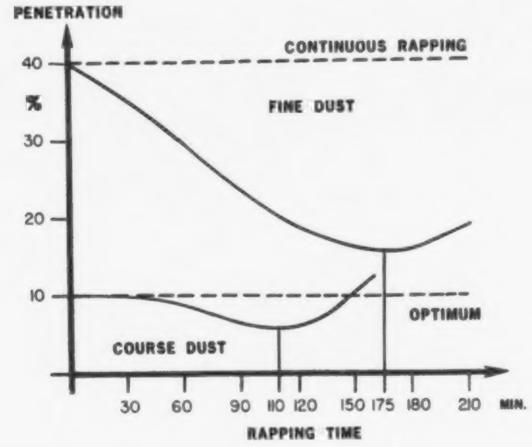

RAPPING OPTIMIZATION

FIGURE 16

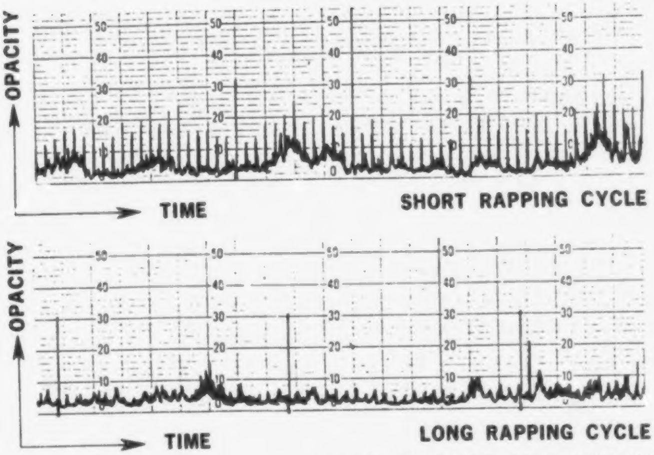

RAPPING CYCLE AND OPACITY

FIGURE 17

LOW POWER PRECIPITATION

A Logical Solution To Collection Problems Experienced With High Resistivity Particulate.

By:

John H. Umberger
36 Main Street
Holmdel, N.J. 07733

Cold-side precipitation offers capital and energy savings over hot-side collection of high resistivity particulate. The major limitations of cold-side collection are premature back corona and tenacious particulate accumulations on collecting surfaces and discharge electrodes.

Consistent with theory, reduction in corona current does much to alleviate these limitations. This report describes field-proven methods to accurately identify back corona, adjust power supply for maximum precipitation, and to adjust rapping to minimize accumulations and reentrainment.

Although the presentation is geared for operators and manufacturers representatives, it contains useful feedback for Research and Development personnel.

LOW POWER PRECIPITATION

I. INTRODUCTION

Typically Precipitators are tuned to a spark-limited equilibrium. This report describes another equilibrium to tune to, one which better satisfies all conditions required for efficient, reliable collection of moderately high resistivity particulate. It discusses energization and rapping tuning methods whereby conventional cold-side wire-plate precipitators can be tuned to obtain reliable omega's in the range of 9.0 cm/second, when collecting particulate with in situ resistivity in the 10^{11} ohm-cm range. These tuning methods were developed in the field on cold-side ESP's collecting fly-ash from the firing of low sulfur, low sodium oxide southeastern coals. Abbreviated versions of these methods were applied on ESP's collecting fly-ash from western low-sulfur coals with enough success to merit further work with this system on all cold-side high resistivity applications. Success of any tuning method was determined with the help of the optical transmissometer. All units tuned employed single impact drop-hammer rappers which could impact with energies of up to 16 ft-lb. Area of collecting surface was no more than 5400 square feet per rapper. Specific collection area (SCA) for the precipitators tuned ranged from 0.55 sec/cm to 0.72 sec/cm. (275 to 360 ft^2/1000 ACFM).

II. TUNING THE ELECTRICS

A. Background

Electrical power is used to charge the particulate and then assist in its motion towards the collecting surface. The electric field provides the force for charging the particles and the current density supplies the charge carrying ions and electrons. The electric field forces these charges onto the particles. Current flowing in the precipitator not only supplies charge, it also generates a force which holds the particulate to the collecting surface. As resistivity increases this holding force also increases for a given current density. Both collecting surface buildup tenacity and positive corona discharge increase with increasing current density. Therefore, it seems reasonable to reduce operating current to solve both problems.

B. Back Corona Detection

The first step in correct tuning is to locate the energization point at which back corona starts. The method is simple and reliable, and is accomplished by monitoring the raw precipitator voltage wave form. The equipment needed to detect back corona is a single trace oscilloscope of at least one megaohm input impedance, a voltage divider with a dividing ratio selected to assure a balance between safety and S/N ratio, sufficient RG59u coaxial cable to transfer the voltage waveform from the power supply to the power supply control, a functional secondary averaging current meter, and a reliable control element with sufficient stability to limit secondary current at any point between corona onset and sparking. No averaging or integrating elements are allowed between the power supply and the oscilloscope in the KV monitoring circuit. However, the "averaging" corona current meter supplied with the vendors controls is sufficient for obtaining characteristic curves. Back corona detection is also possible using the peak corona current obtained from a second trace on the oscilloscope, but the shape of the characteristic curve is different.

After installing or modifying all circuit elements as shown in Figure 1a the transformer-rectifier (T/R) being measured should be energized and adjusted to an operating point below sparking. The waveform viewed on the oscilloscope should appear the same as shown in Figure 1b. If not, a check should be made on all wiring for errors or damaged elements.

Attenuate the T/R to just above the threshold of corona, that is the point where secondary current just begins to flow in the precipitator. To detect back corona slowly increase the current, noting the deformation of the waveform. During any half cycle the voltage rises to a peak value (KV_p) and the decays to a minimum value (KV_m). Watch the relationship of KV_m and the average precipitator current (ma). As you slowly increase the current you will note a value of current at which KV_m stops increasing, where $dKV_m/dI=0$. This is the point of the onset of back corona. If you run the current at higher levels, for instance on the outlet field only, you can get as much as a 12% increase in opacity without sparking. Figure 2 shows the graphical location of back corona.

KV minimum can take any position along a continuous line within the shaded area after the $dKV_m/dI=0$ point. Once in a while, opacity will not deteriorate at current levels above the $dKV_m/dI=0$ point. One fact always holds! Precipitator performance will not be any better than it is at this point!!!

For in situ resistivity of 10^{10} to 10^{11} ohm-cm the back corona glow can barely be seen at this point. For very high resistivity (10^{12} to 10^{13} ohm-cm) particulate the back corona glow is obvious.

C. Half-Wave and Full-Wave Energization

Figure 2 also compares the characteristic curves of both half-wave (H-W) and full-wave (F-W) energization for equivalent precipitation conditions.

The differences are:

1) For equal average current the average KV is roughly the same.

2) The average current at which back corona occurs in full-wave energization is roughly twice the average current at which back corona occurs in half-wave.

FIGURE 1

HIGH VOLTAGE MONITORING

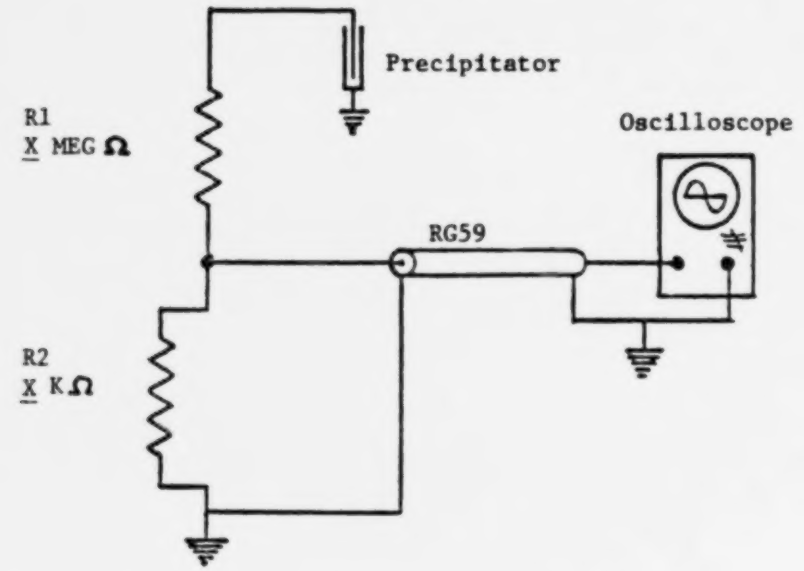

a) Monitoring Circuit

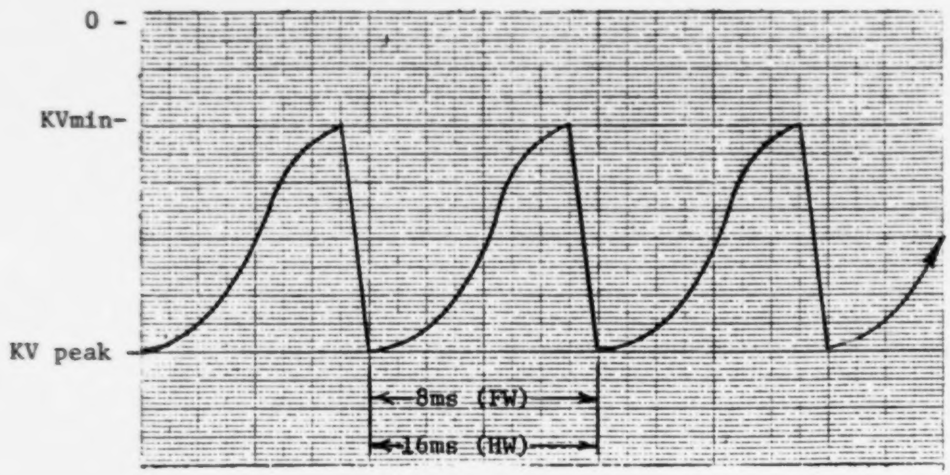

b) Typical Voltage Waveform

FIGURE 2

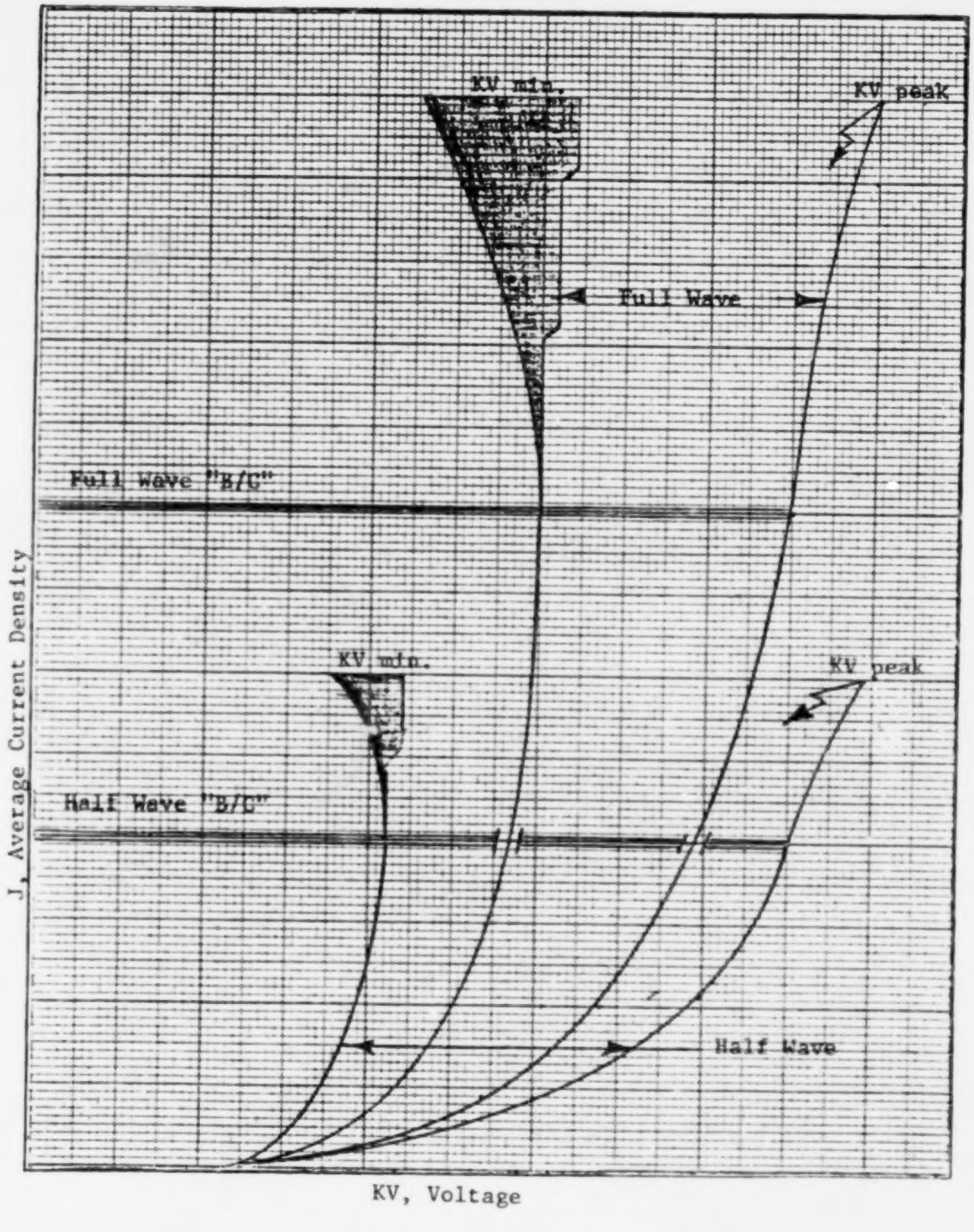

Figure 2 : Characteristic V-I Curve showing Back Corona (B/C)

3) The peak voltage at back corona onset is roughly the same for both F-W and H-W energization.

4) The percentage increase in average corona current from the point of back corona to the initial point of sparking can be as great as:
   a) 100 to 200% for F-W
   b) 10 to 20% for H-W

The more effective the rapping, the greater this percentage increase can be.

5) KV_m is much lower and KV_p is much higher at the same average current for H-W.

All these observations are explainable and consistent with theory.

Most workers in this field agree that back corona occurs when a critical field strength (Eds) is reached. This field strength equals ρ times a critical current density (j_{ds}). To avoid back corona we can move the mountain to Mohammed -- that is, use gas conditioning to lower particulate resistivity -- or we can bring Mohammed to the mountain -- that is, lower precipitator current to lower the electric field in the dust layer. I chose the latter and successfully expanded the useful range and reliability of every cold-side precipitator on which I lowered the current density to the onset of back corona point.

I find H-W energization superior to F-W for three reasons:

1) 1/3 to 1/4 the power consumption of F-W at back corona (B/C) point

2) Slightly lower opacity than F-W at B/C point

3) Longer term stability of tuned-in performance

There are two other advantages to the low power strategy which alone justify the small effort required to detect back corona and to keep transmissometers running. The first is obvious, the virtual elimination of wire discharge electrode failure. Keep in mind that the precipitator is now operating well below the threshold of sparking, and sparking is the major cause of D.E. failure. Corrosion another cause of failure, is generally not a problem for low sulfur coals. The qualifier "virtual" is used because hoppers can still be overfilled and even at low power levels it is possible that a D.E. can be burnt in two. This cause of failure can be avoided by a reliable undervoltage trip. I recommend that undervoltage be sensed on the secondary of the T/R unit.

I have also discovered that particulate accumulations on the discharge electrodes are frequently caused by back corona. During numerous internal inspections of collecting surface buildups, I got used to seeing wire buildups ranging from 5mm total diameter (2.77 mm wire diameter + buildup) to 20 mm total diameter. Generally the population and size of accumulations increased from inlet to outlet of any given chamber. After retuning the same precipitators to the threshold of back corona the internals were re-inspected to monitor collecting surface buildups. During these inspections I found that the same wires were metal clean. I concluded that this type of wire buildup was the collection of positively charged particulate from back corona sites on the collecting surfaces.

To review, the electrical tuning methods are simple:

1) Identify back corona by method specified and reduce secondary current to this point by current limit.

2) Energize precipitator in double half-wave mode to get maximum ratio of KV_p/I_{ave}.

For low power collection or 10^{11} ohm-cm particulate and half-wave energization you will find $KV_m \approx 21$, $KV_p \approx 40$ to 50, and $j_{ave} \approx 6$ na/cm^2 (5 ma/1000 ft^2). You will also find that total power consumption will be 5 to 10% the power consumed when the precipitator operates in a FW spark limited mode. Thus, the label low power precipitation.

III. TUNING COLLECTING SURFACE RAPPING

Poor electrical stability and excessive re-entrainment are largely due to improperly applied collecting surface rapping. Deterioration of precipitator performance due to ineffective rapping is most critical when collecting high resistivity particulate.

Owen Tassicker (1972)[1] did a great deal of study on the mechanics of collecting surface rapping and, like the earlier researchers Ruckelschausen (1957)[2] and Sproull (1965)[3], concluded that normal to the collection surface accelerations are the predominant means of particulate removal. After much study within and outside of the precipitation field he derived his formulation for the tensile strength (P) of a particulate layer on a collecting surface in the influence of an electric field.

(Equation 2)

$$P = A_1/d^2 + A_2/d^2 + 10^5 \frac{\varepsilon_o}{2} J^2 (\varepsilon_\ell^2 \rho_\ell^2 - \rho_g^2)$$

P = Dust layer tensile strength (gm/cm^2)

A_1 = Van der Waal constant

A_2 = Capillary constant

d = Particle diameter (cm)

ε_o = Permittivity of free space (F/m)

J = Current density (A/cm^2)

ρ_ℓ = Layer resistivity (ohm-cm)

ρ_g = Gas resistivity (ohm-cm)

ε_ℓ = Relative permittivity of dust layer (solids and voids) (no units)

Figure 2.1 a & b (taken from Tassicker) gives a reasonable illustration of the electrical parameters involved.

This is primarily a D.C. equation, since the mode of energization I promote has greater A.C. components, capacitances of the circuit in Figure 2.1 could have relevant components which may alter the validity of the equation. The relevance of the electrical term of this equation has been observed by many rapping researchers and in ways can be drawn from field experience. Tassicker presented a table which I reproduce here.

TABLE 1

	Case 1 (low)	Case 2 (med)	Case 3 (high)
E_g (KV/CM)	5	5	5
ε_ℓ	4	4	4
J ($\mu a/cm^2$)	0.05	0.05	0.05
ρ_g (ohm-cm)	10^{11}	10^{11}	10^{11}
ρ_ℓ (ohm-cm)	10^{9}	5×10^{10}	5×10^{11}
P (gm wt/cm^2)	-0.011	0	$+1.1$
	(-repulsive)		(+attractive)

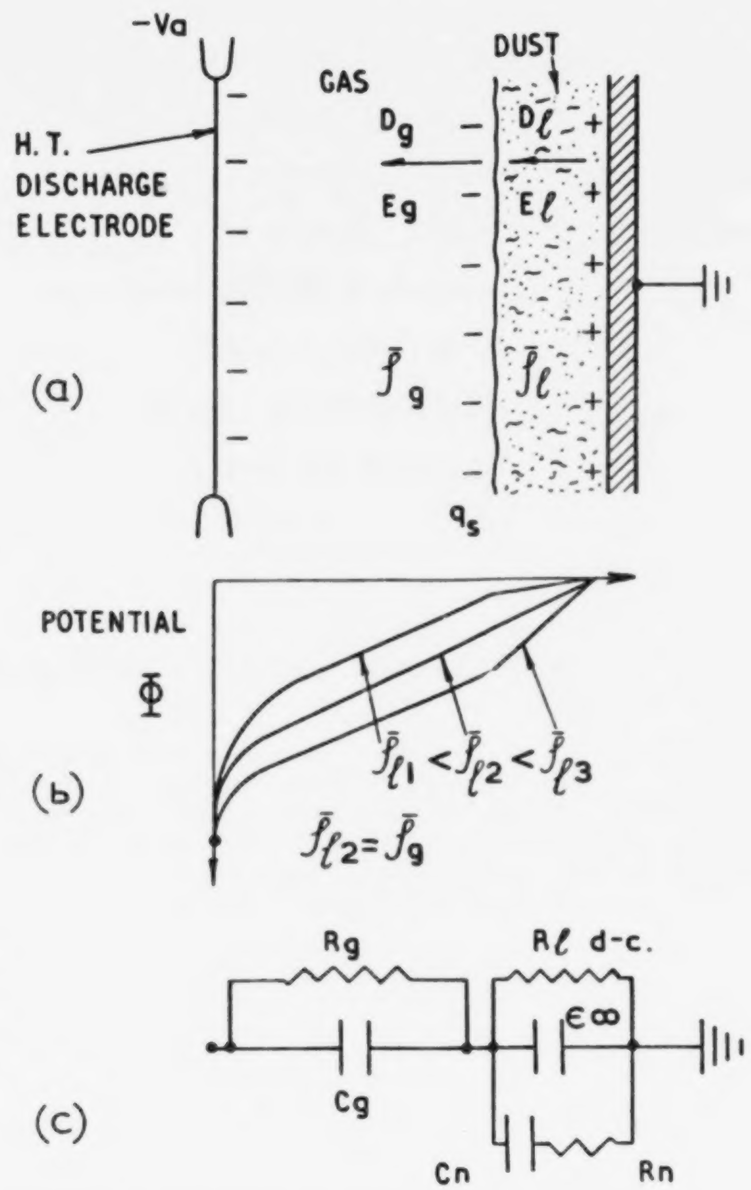

FIG. 2.1 ELECTRIC FIELDS AT THE DUST/GAS INTERFACE

(a) At the dust interface there are changes in electric field due to surface charges and also to differing resistivities.

(b) The electric field $\nabla\Phi$ is the same in the two phases only for equal resistivities.

(c) Nominal equivalent circuit showing that resistivities determine d.c. gradients while capacitances determine a.c. gradient.

(From Tassicker, 1972, p. 45)

Table 1 helps explain the rapping problems experienced with both high resistivity and low resistivity. We know that we can rap low 10^{10} ohm-cm particulates without too much trouble. Usually we do not have many problems with heavy accumulations unless the precipitator serves cycling duty. In this case, the capillary term in equation 2 probably takes prominence.

Generally, we can effectively dislodge 10^{10} ohm-cm particulate with a light to medium impact. This light rap provides enough force to overcome the Van der Waals and capillary forces. For simplicity's sake we will assume that these components of particulate layer strength are unaffected by changes in resistivity and electrical conditions.

The last term of Equation 2 provides the justification for reducing current densities to the low levels suggested. The electrical component of tensile strength increases with the square of the electrical field in the dust. From Figure 2 it is evident that as current density increases the electrical component of particle tensile strength grows larger at an increasing rate. If we double the current density, we will more than double the electrical component of the tensile strength. When running in a spark limited mode, current densities typically varied between 20 and 50 na/cm^2. After correct electrical and rapping tuning techniques were developed, the same precipitators were operative (artificially current limited) at approximately 5 na/cm^2. In effect the electrical component of the fly-ash strength had been reduced considerably. It seemed logical to reduce current density and now that it has given positive results, it seems even more logical.

The mechanical aspects of rapping and dust strength should also be considered. As the earlier researchers noted, a residual layer remains on the collecting surface after a rap. Ruckelshausen defined this residual as basic layer. Rapping efficiency, as defined by Sproull, is the percentage of the particulate layer removed by a single blow or total layer thickness minus basic layer thickness, all divided by total layer thickness. Sproull found that rapping efficiency increased with an increase in layer thickness. Or, for a given rapping efficiency, the thicker the buildup the lighter the rap needed to dislodge it.

The conventional American design precipitator has the disadvantage of having a relatively unresponsive collecting surface structure. Generally, too many collecting surfaces are cleaned by one rapper. Also, it is probable that too much rapping energy is absorbed by the collecting surface supports of the top-rapped precipitator. As particulate resistivity gets higher the demands on the rapping system become greater, and the marginal abilities of the top-rapped precipitator become obvious. The precipitators on which the low power techniques were developed could be considered worse than average in rapping responsiveness. Yet, the methods to be prescribed are quite effective.

With Sproull's findings in mind, it seems logical that for any given collecting system there would exist a thickness of particulate accumulation for which the rapping accelerations available could clean with a reasonable efficiency. To assure reasonable rapping efficiencies, the lower the acceleration available, the thicker the accumulation would have to be. Taking complete advantage of Sproull's findings requires that collecting surfaces should be rapped only when a certain minimum particulate layer thickness is reached, and not before. Since each successive collecting fields in a precipitator collect particulate at slower rates (in thickness or mass per unit time), rapping should be less frequent at outlet ward fields relative to inlet ward fields. To find the relative layer growth rates the Deutsch equation can be used. Consider the following example:

A precipitator having an SCA of 0.8 sec/cm (400 ft^2/ 1000 ACFM) is designed to collect high resistivity particulate (ρ = 5x10^{11} ohm-cm) with an efficiency of 99.5%. The inlet dust concentration is 5.72x10^{-6} gm/cc (2.5 gr/ACF). The precipitator has four equal collecting fields in the direction of gas flow. Particulate density is 1.1 gm/cm^3 (70#/ft3).

Using the Deutsch equation, we get an ω of 6.7 cm/second. Each of the four fields should collect 73.4% of the fly-ash they receive. Allowing for fly-ash concentration and density we get the following growth rates: first field, 0.675 mm/hr; second field, 0.179 mm/hr; third field, 0.048 mm/hr; last field, 0.013 mm/hr.

If we use a constant thickness system we would choose rapping periods for any precipitator field in direct proportion to its particulate growth rate. In this example, the period for one rap for each collecting surface would be; (inlet) τ, 3.78 τ, 14.1 τ, 52.0 τ (outlet). We now know the ratio of buildup rates and all rapping should be timed in accordance.

The next task is to ascertain the absolute timing. This is a tricky business. Incorrect rapping adjustments may take three days to four weeks to deteriorate performance on a 300 to 500 SCA precipitator, and as long as five months on a 1000 SCA precipitator. The best known way to find τ would be to monitor inlet field opacity. τ should be set to the longest time possible before opacity deteriorates. Remember, the thicker the ash deposit, the easier it is to dislodge. Transmissometer monitoring at the outlet of the precipitator is not really suitable for direct determination of τ because effective ω for each collection field will vary from position to position and in time during the performance degeneration period.

Experience shows that once rapping is timed as recommended, precipitator sensitivity to particulate source transient behavior is drastically reduced. Reasonable success has been realized using τ in the range of 0.75 to 1.50 hours. For the 400 SCA precipitator rapping times would be:

Field 1 (inlet) each rapper is fired once every 0.7 to 1.5 hours
Field 2 each rapper is fired once every 2.8 to 5.6 hours
Field 3 each rapper is fired once every 10.4 to 20.8 hours
Field 4 (outlet) each rapper is fired once every 38.5 to 76.9 hours

To many these intervals man seem too long, but keep in mind that these timings allow only 0.5 to 1.0 mm average accumulation of particulate on the collection surfaces for this particular precipitator.

If current densities are constant from inlet to outlet and the constant thickness system is applied to rapping timing, there is no logical reason to say the intensity of rapping should not be the same throughout the precipitator. However, in practice, field representatives and operators generally reduce rapping intensity at the outlet of a precipitator in an effort to reduce rapping puffs. From my experience this is a bad practice. The effort to reduce short-term emissions results not only in higher long-term emissions due to ineffective collecting surface cleaning, but can actually aggravate the problem the reduction was applied to eliminate.

Figure 4 says it best:

FIGURE 4

Comparison of Outlet Field Rapping Puffs

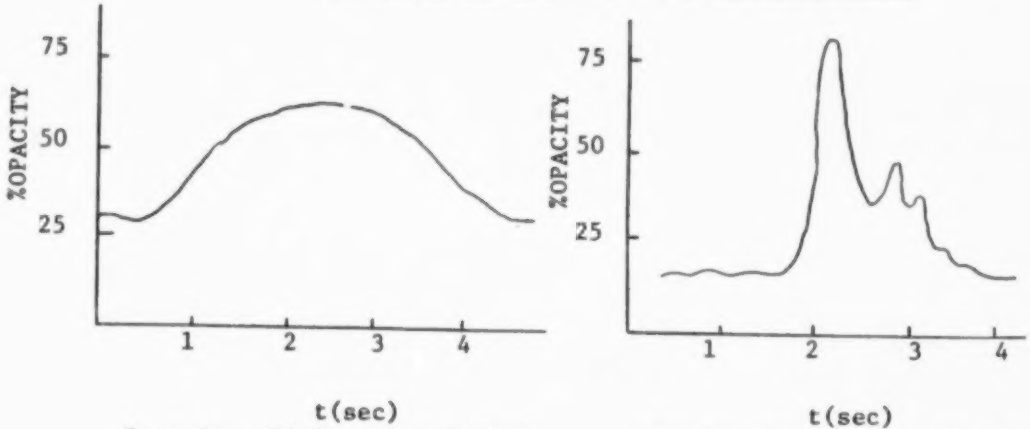

Case A: Light rap = 4 ft-lb
(everywhere) τ = 0.033 hr.

Case B: Heavy rap = 16 ft-lb
(outlet) τ = 8 hr.

Figure 4 demonstrates some differences between very light-frequent rapping and very heavy-infrequent rapping. Although the peak opacity is higher for heavy rapping the total emissions may be less. The secondary puffs for Case "B" are believed to be due to hopper boilup. This does not happen for Case "A", implying that little or no particulate is going into the hopper, but instead totally re-entering the gas stream.

Considering the conditions, one could conclude that the light-frequent rapping dislodges the fine and/or most recent accumulations from the collecting surface before they have a chance to agglomerate. These observations reinforce the recent findings of Nichols (June 1978)[4].

When the low power strategy is applied to solve collecting surface cleaning problems, other advantages will be realized. The major one is: when operating at low current densities, the electric field strength in the gas zone stays the same or increases with increases in particulate layer thickness on the collecting surfaces. In comparison, the typical high current density approach encourages a degradation of electric field strength in the gas interface as particulate layer thickness increases. This fact alone would discourage the use of a slow rapping system. One would have to clean collecting surfaces at accumulation thicknesses approaching the diameter of the particles themselves, a virtual impossibility.

One concern, not mentioned before, is the need for uniform current distribution at the collecting surface. Figure 5 taken from Tassicker (1972)[5] shows the increase in J uniformity with decrease in average current. The analogy between the correlation of Figure 5 and precipitators tuned to low power should be made with caution since the dust layer and space charge in an actual precipitator will alter the analogy. Both dust layer and space charge will increase the ratio of peak KV to average current. This would suggest greater uniformity for low power tuning than is shown in Dr. Tassicker's data since actual current densities are one to two orders of magnitude less. In addition the mere presense of the dust layer will alter current density uniformity although it is not obvious which way. However, the pattern of back corona craters found on collecting surfaces does tend to agree with Dr. Tassicker's profiles of a two wire system. The craters exist only on the collecting surfaces directly across from the discharge electrodes, and on the edges of collecting surface gas flow baffles.

Figure 6a compares stack opacity for a precipitator tuned in a conventional manner (F-W, Jave = 30 na/cm^2, KV_p = 62 KV; τ = 0.033 hours everywhere; outlet rapping energy = 4 ft-lb.) To the same precipitator tuned to low power criteria (H-W, j_{ave} = 5 to 10 na/cm^2; KV_p = 40 KV; τ = 8 hours on outlet; rapping energy anywhere = 16 ft-lb.).

Figure 6b compares long-term performance of the same precipitator operating in F-W spark limited mode to one operating in the prescribed low power method. This plot helps to explain why low power tuning is

FIGURE 5

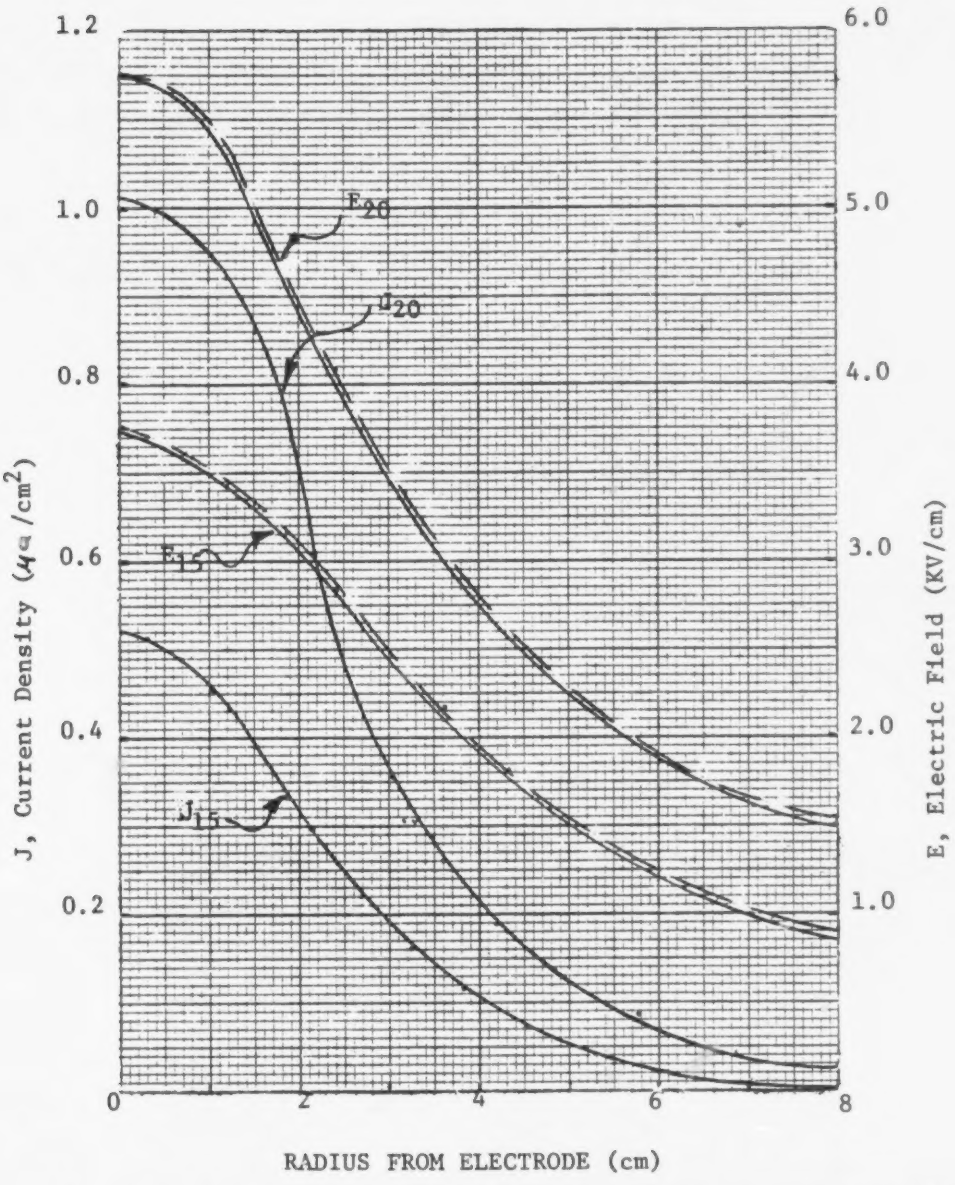

Figure 5: Comparison of Electric Field and current density distribution along the anode for 15 and 20 KV applied voltages. (afterTassicker, 1972 [5])

FIGURE 6

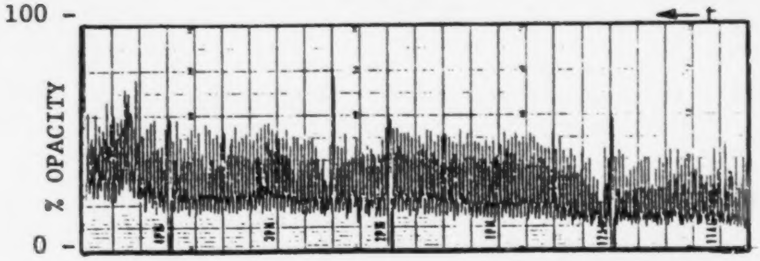

Spark Limited: $j = 40\ \mathrm{na/cm^3}$, $\tau = 0.033$ hr.

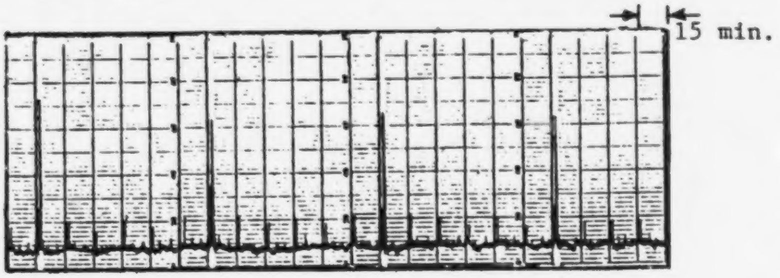

Low Power: $j = 8\ \mathrm{na/cm^3}$, $\tau \approx 8.0$ hr.

a) Stabilized: Comparing Spark Limited, light and frequent Rapping-to-Low Power, Heavy and infrequent rapping. (See Text)

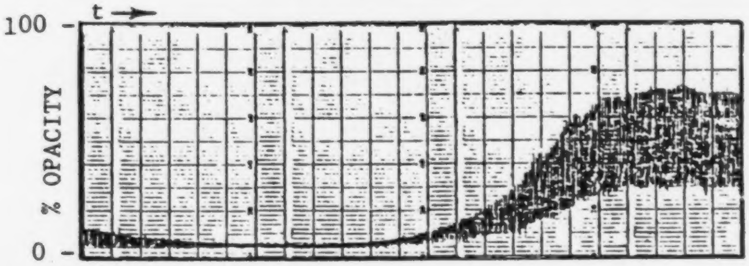

Spark Limited

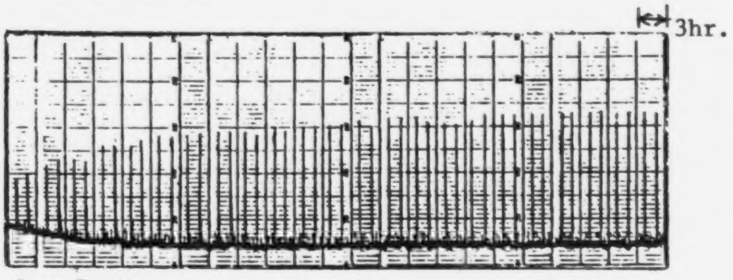

Low Power

b) From Metal Clean Startup: (See Text)

not obvious. The vendor start-up engineer sees much better performance on a metal clean ESP with high powered full-wave energization than with low powered half-wave energization. At start-up, high powered energization may give opacities of 2 to 6% (possible efficiency of 99.8+%) where low power would give opacities of 10 to 20% (possible efficiency of 99.0 to 99.5).

As particulate accumulates on collecting surfaces the electrical equilibrium changes. For spark limited precipitation the combination of back corona and excessive voltage drop across the dust layer degenerate precipitator performance to unacceptable levels, that is, opacities in the 30 to 60% range (efficiency ranging from 85 to 98.5%). The rate of deterioration depends on particulate resistivity (the higher the ρ the faster the deterioration), the precipitator SCA (the larger the precipitator, the slower the deterioration), and the effectiveness of collecting surface geometry and responsiveness (ratio of acceleration/energy input), collecting system suspension, and as suggested here, electrical input.

For low power precipitation the accumulation of particulate actually improves the behavior of the precipitator. When started-up, stack opacity will be greater. As particulate accumulates on the collecting surface and equilibrium is reached, performance will improve slightly. The initial relatively poor low power performance is still much better than the level of deterioration which spark limited operation will yield.

After proper application of the recommended low power techniques, it will become obvious that average current density of 5 - 10 na/cm^2 and peak KV's of 40 to 50 can be more than sufficient to obtain overall omega's greater than 9 cm/sec for 10^{11} ohm-cm particulate. It will become obvious that increases in corona current can cause more harm than good.

The methods and philosophies prescribed here are not without limitation. High 10^{11} ohm-cm and higher resistivities could require precipitators which can support KV_p/jave, at least one order of magnitude higher (strangly enough this ratio comes out in the units of resistivity, ohm-cm; for $\rho = 10^{11}$ ohm-cm , KV_p/jave = 10^{12} for $\rho = 10^{12}$ ohm-cm, Ep/jave = 10^{13}, etc.) and rapping accelerations one order of magnitude higher (if minimum sufficient normal acceleration for 10^{11} ohm-cm particulate is 20 g's for 10^{12} ohm-cm you may need 200 g's minimum normal acceleration).

Like most precipitators, the low power precipitator is sensitive to cycling. The only solution that is possible with present technology is a massive (100 g's or greater) power-off rap before the gas temperature drops below 230°F. But, if you forget to do it once when coming-off line, while collecting high resistivity particulate, there are only two cures 1) thorough, and I mean metal clean, water-wash or 2) a three to five day constant firing of high sulfur coal to condition the baked-on particulate.

The rapping adjustments are also simple: 1) Rap any collecting field once and only when the particulate layer thickness reaches a predetermined minimum thickness. Precipitators of different manufacture will have different critical minimum thickness. Determining the best timing for the best performance will take weeks, not minutes or hours. 2) Rap the surface with energies high enough to get sharp spikes on your transmissometer readout. Rap all fields with equal energy. I prefer the drop weight rapper to any other rapper. Although the results are preliminary, I have found that the vibrator-type of rapper tends to stimulate basic layer growth and generate undesirable electrical instabilities.

IV. CLOSING REMARKS

The methods described will give positive results. The closer one adheres to these methods, the more sucessful these results will be. If one chooses to diverge from any of the recommended adjustments, I advise that only one adjustment be changed at a time. The success or failure of any change (power or rapping) can only be reasonably judged after completion of at least two weeks of operation.

In closing power strongly affects rapping and rapping strongly affects power.

REFERENCES

1) Tassicker, Owen, "Aspects of Forces on Charged Particles in Electrostatic Precipitators, "Doctoral Thesis, University of New South Wales, July 1972, p.p. 3742, 4594 (available in EPRI reprint).

2) Ruckelshausen, Kurt, "Removal of Powdered Deposits from Technically Smooth Metal Surfaces," Doctoral Dissertation, Technischen Hochschule, Stuttgart, No. DK Giese-Druk, Kg Offenbach/M, 1957.

3) Sproull, Wayne T., "Fundamentals of Electrode Rapping in Industrial Precipitators, "Journal of the Air Pollution Control Association, Feb. 1965, No. 2, p.p. 50-55.

4) Nichols, Grady B., "Rapping Reentrainment in a Near Full Scale Pilot Electrostatic Precipitator,"Southern Research Institute for the Environmental Protection Agency, EPA-600/7-78-112, June 1978, p. 3.

5) Tassicker, Owen, Ibid., 1972 - p.p. 156-157.

HIGH INTENSITY IONIZER TECHNOLOGY APPLIED TO RETROFIT ELECTROSTATIC PRECIPITATORS

By

C. M. Chang and A. I. Rimensberger

UNION CARBIDE CORPORATION
Linde Division
Tonawanda, New York 14150

ABSTRACT

This paper presents the results of a study concerning the application of High Intensity Ionization technology to a flyash electrostatic precipitator.

Described in detail are the adopted method of performing functional design for ionizer-precipitator systems, selected results of ionizer-precipitator flow model tests, and the proposed physical retrofit. Also presented is the projected performance of the ionizer-precipitator system, derived from an empirical model which takes into account the phenomena of space charge and gas velocity distribution.

HIGH INTENSITY IONIZER TECHNOLOGY APPLIED TO RETROFIT ELECTROSTATIC PRECIPITATORS

INTRODUCTION

The High Intensity Ionizer (HII) is a novel device capable of charging particulates contained in flue gases to levels significantly higher than what can be achieved in conventional electrostatic precipitator (ESP) systems, Schwab, et al (1976)[1] and Tassicker and Schwab (1977)[2]. By using the High Intensity Ionizer as a pre-charger, greater overall migration velocities result in the precipitators. Of particular value is the use of HII to enhance the ESP's collection efficiency for fine particulates, i.e. particles with diameter less than three microns, which determine the opacity of the process gas leaving the system.

This paper presents the results of a study concerning the application of High Intensity Ionizer technology to a flyash electrostatic precipitator. It includes detailed description of the proposed physical retrofit, results of flow model tests, and the projected performance of the precipitator retrofitted by High Intensity Ionizers.

DESCRIPTION OF BASE ELECTROSTATIC PRECIPITATOR

Figure 1 shows the arrangement of the base electrostatic precipitator to be retrofitted by High Intensity Ionizers. It has 80 parallel ducts. There are three mechanical fields and five electrical sections in the gas flow direction. The base conditions of this precipitator, as shown in Table 1, are derived from data provided by the customer. The upgrade requirement is such that the emission rate should not exceed 60.2 $g/10^9$ J (0.14 lb/mm BTU) which corresponds to 0.11 grams/m^3 (0.048 grains/ACF) at the maximum load of 150 MW.

FUNCTIONAL DESIGN OF IONIZER-PRECIPITATOR SYSTEMS

In predicting the performance of an electrostatic precipitator retrofitted by High Intensity Ionizers, use has been made of the following resources:

A. All available HII-ESP pilot test data, including those conducted at TVA John Sevier steam plant, Huang, et al, (1978)[3], which have been systematically correlated.

B. Results of an in-house computer study on three-dimensional space-charge distribution in HII-ESP systems, as affected by the design of the transition zone between HII and ESP, as well as the prevalent space charge density therein.

C. Results of an empirical correlation for optimal HII placement in an ionizer-precipitator system.

D. EPA-SRI Computer Program, McDonald (1978)[4], for electrostatic precipitators, modified to use for ionizer-precipitator systems.

E. Comments of Union Carbide consultants with recognized expertise in precipitation technology.

The empirical correlation of optimal HII placement in an ionizer-precipitator system takes into account the fact that as the single HII array is moved downstream from the inlet of a precipitator with a fixed overall length, the collection area of the precipitator section downstream of HII becomes smaller, resulting in having a smaller specific collection area of the precipitator being augmented by the enhanced charging capabilities of the HII array. Furthermore, the total charge imparted to the entrained particulates by the HII array decreases due to the reduced concentration and smaller mean particle size of the particulates processed by the HII array, as the HII array is moved downstream. On the other hand, ionizer performance is improved as the grain loading of the gas entering the HII array decreases. This allows the HII to operate more closely to its maximum design capabilities in terms of achievable corona power density and specific corona current. The space-charge density in the transition zone between the HII array and the downstream precipitator also decreases, so that the chances of discharge and arcing, which tend to neutralize the high charge produced by HII, are significantly reduced. An additional effect favoring a downstream location is that the HII is applying all its charging potential to smaller particles which are typically more difficult to collect. Thus, factors affecting the optimization of ionizer-precipitator systems include the collection efficiency of the base electrostatic precipitator without HII, inlet grain loading, particle resistivity, prevailing ambient pressure, purge air flow as a fraction of total gas flow, and any change in precipitator flow distribution due to the installation of HII.

Figure 2 shows that the maximum performance of a typical HII-ESP system is to be obtained by placing HII between fields and at about eleven feet downstream from the leading edge of the first collecting field of the precipitator.

The EPA-SRI computer program for ESP performance simulation, McDonald (1978)[4], developed by Southern Research Institute, was modified to allow electrostatic charge to exceed the saturation level permitted by the local electrical field. Charge density level achieved at a given location within the precipitator is carefully investigated to monitor the amount of particle charge added by HII. A preliminary empirical correlation of electrostatic charge produced by HII was developed based on limited experimental data available to date. Additional work is required to develop a more complete understanding of HII charging capability. The maximum charge density permissible in a given transition zone design was assessed.

In order to make space for the installation of the HII array, three feet of collecting plate length of the base electrostatic precipitator must be removed. Our results show that by placing the HII array at a location 12 feet downstream from the leading edge of the first collecting field of the base precipitator, a system performance of 99.36% could be expected.

As shown in Figure 3, the mass loading decreases rapidly in the region downstream from the High Intensity Ionizer whereas the charge density increases first before it decreases rapidly thereafter.

Figure 4 illustrates the dependency of the predicted system performance on the standard deviation of velocity distribution. The fractional collection efficiency of the HII-ESP system computed by the modified EPA-SRI program is illustrated in Figure 5.

FLOW MODEL STUDY

The objective of this experimental program was to determine the gas flow distribution downstream of HII, which results from a change in the position of the inlet turning vanes and the installation of discharge electrode system, HII array, and a velocity distribution device downstream of HII. The mechanical arrangement of a 1/10 scale flow model tester is shown in Figure 6. The laboratory assembly of this unit is shown in Figure 7. Figure 8 illustrates the schematic diagram of the velocity profile recording circuitry.

The hot wire anemometer used is the Data Matrix Model 800-LV with a Model U-18 probe. An automatic traverse device was developed to produce predetermined vertical and horizontal motions of the hot wire anemometer, whose signal is sequenced and timed by the data logger. A teletype records on tape typically 520 to 1040 data points per test, which are fed into a data processor where the standard deviation of flow distribution is computed. A Calcom plotter is also connected to produce three-dimensional velocity distribution plots. Figure 9 illustrates the modification of turning vanes implemented during the test series. Sample results of the flow model tests are included in Table 2. Figure 10 illustrates a typical chart recorder plot of the velocity distribution downstream of HII, whereas Figure 11 depicts a three-dimensional velocity distribution plot.

MECHANICAL SYSTEM DESIGN

The HII system, as shown in Figure 12, consists of a purged bulkhead resting on support beams, with an array of installed HII throats and a high voltage discharge system. Each throat consists of a bellmouth, diffuser, purge rings and an exit cone (see Figure 13). A supply of clean, heated gas is required to purge the rings in the HII throats, in order to effectively prevent back corona therein. The discharge electrode system consists of a mast and electrode assembly which is suspended from the precipitator roof, supported by insulators and stabilized at the bottom. A velocity distribution device is located downstream of the bulkhead. A commercially available high voltage power supply and control system is used.

To install the HII system in an existing electrostatic precipitator presents two fundamental design challenges, namely, physically locating the HII and determining a source and system for the purge gas supply. The present design was for a side-loaded precipitator with HII located downstream of the inlet and between the fields. Figure 14 presents the proposed arrangement. To provide space for the HII system in this existing precipitator, three feet of collecting plate length from the second field had to be removed and use was made of the internal catwalk space between the fields. In a side-loaded precipitator, temporary reinforcement of the side walls and roof will be required before cutting an opening for the installation of the bulkhead. The bulkhead assembly could then be slid into the precipitator on its support beams. The discharge electrode system and distribution device could also be installed from the same location (see Figure 15). High voltage power supply for the HII, e.g. transformer/rectifiers, is located on the roof of the precipitator. In some cases, a relocation of the transformer/rectifier sets for the existing precipitator may be required to prevent interference. Insulator housings and the high voltage feed to the discharge electrode system are located on the precipitator roof.

Reliable operation of the HII system requires a continuous purging of the HII anodes and a source of heat to temper the purge gas, as required. Several potential sources of heat are available in most applications: blow-off steam, air coming off the preheater, electric heaters, waste heat, e.g. boiler-house air, or clean flue gas. Since an ample supply of boiler-house air was available, the arrangement as shown in Figures 16 and 17 was selected. This arrangement of the purge gas system consists of: spool piece with filters, inlet nozzle into the bulkhead, duct work, fan, heat exchanger and electric heater as a back-up system.

Based on a comprehensive evaluation of many design options, the design described above represents the most efficient and economical choice available for this site-specific application.

SUMMARY AND CONCLUSIONS

In defining the performance of a flyash electrostatic precipitator retrofitted by an HII, the following program steps have been taken:

A. Assess performance of the base electrostatic precipitator, White (1963)[5].

B. Define upgrade requirements.

C. Define flow velocity distribution in HII-ESP by scaled model tests.

D. Define the most economical design choice and perform mechanical system design.

E. Predict the performance of ESP retrofitted by HII.

These steps have been carried out in a systematic manner. As a result of this study, we have proposed to retrofit a flyash electrostatic precipitator by installing an HII array at a location 12 feet downstream from the leading edge of the first collecting field of the precipitator, removing three feet of collecting plate length from the second field, and installing a suitable velocity distribution device downstream of HII. Based on the flow model test results and available HII-ESP pilot test data, the performance predicted for this HII-ESP system is well above the level required to meet the emission rate of 60.2 g/10^9 J (0.14 lb/mm BTU).

ACKNOWLEDGEMENTS

The authors wish to acknowledge the able assistance of Dr. Roger Brown, in performing the computation using the EPA-SRI Computer Program for electrostatic precipitators; Mr. W. C. Fong, in supervising and implementing the flow model tests; Dr. Ravi Bansal, in designing the flow model test data processing system; Mr. A. B. Stewart, in designing and constructing the automatic traverse device used for the flow model tests; and Mr. E. L. Tytka, in instrumentation and data reduction.

We also appreciate many useful discussions with Dr. Harry J. White, Scientific Consultant, Carmel, California.

REFERENCES

[1] Schwab, J., et al. Development Program for an Ionizer-Precipitator Fine Particle Dust Collection System as Applied to Coal=Fired Utility Steam Generators. Final Report EPRI FP-291, Volume I & II, October 1976.

[2] Tassicker, O.J. and Schwab, J. High Intensity Ionizer for Improved ESP Performance EPRI Journal, 56-61, June/July 1977.

[3] Huang, C. M., et al. Pilot Evaluation of High-Intensity Ionizer for Improving Electrostatic Precipitator Efficiency. Paper #73B, AIChE 85th National Meeting, Philadelphia, Pa. June 4 - 8, 1978.

[4] McDonald, J. R. A Mathematical Model of Electrostatic Precipitation. Volumes I & II, EPA-600/7-78-111b. June 1978.

[5] White, H. J. Industrial Electrostatic Precipitation Addison-Wesley. 1963.

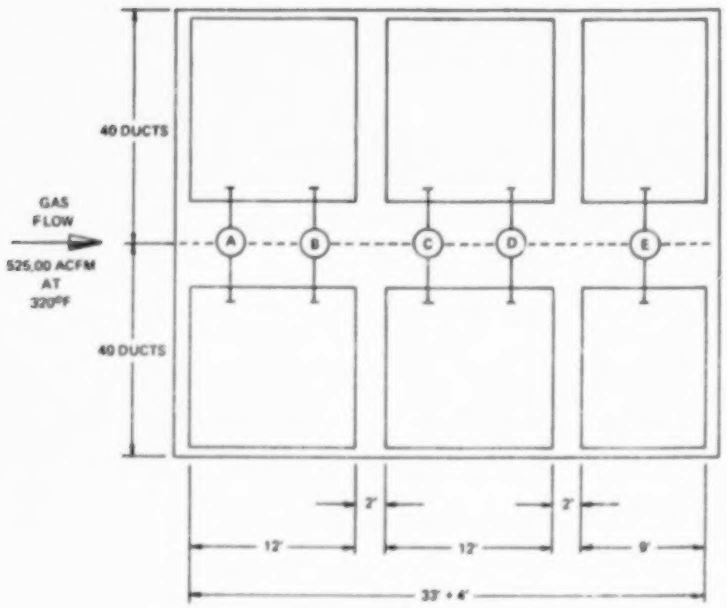

Figure 1. Arrangement of base ESP.

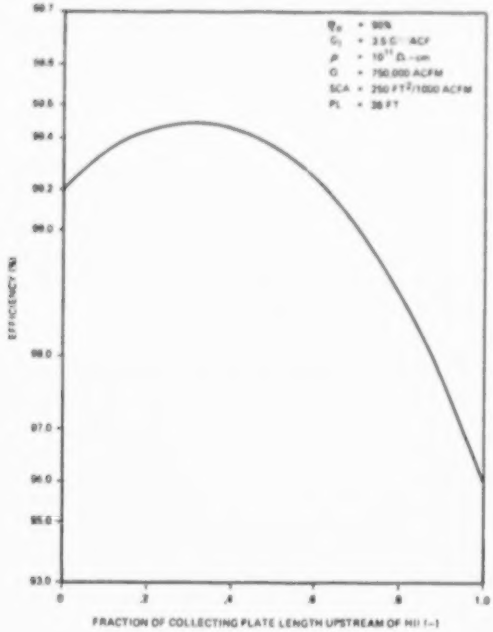

Figure 2. Sample results of performance prediction for an HII-ESP system.

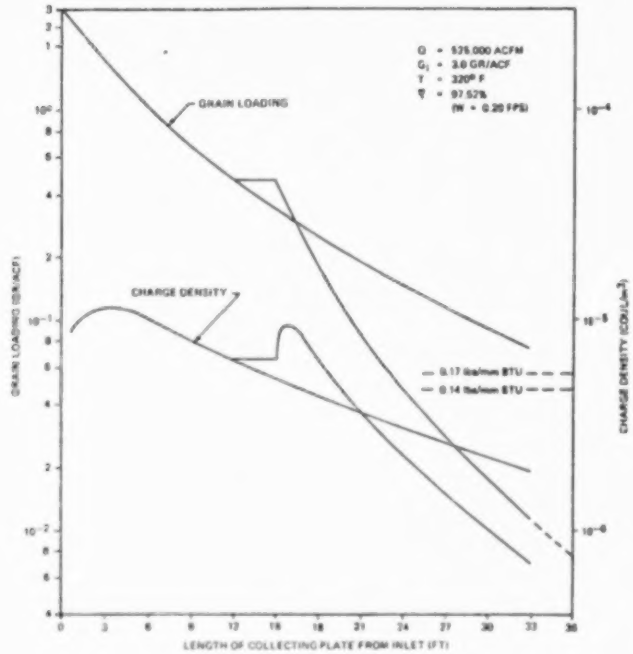

Figure 3. Sample results of performance prediction for an HII-ESP system.

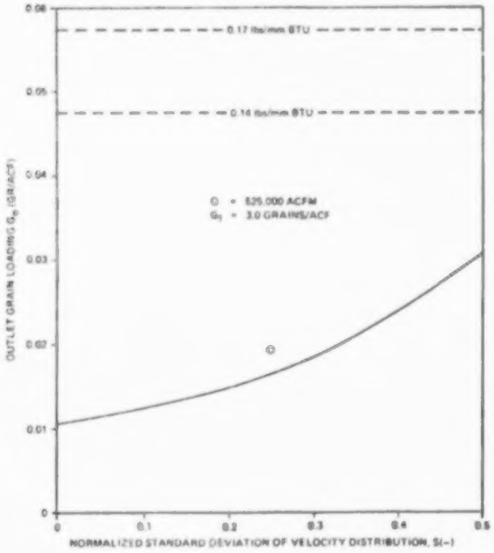

Figure 4. Summary of predicted HII-ESP performance results.

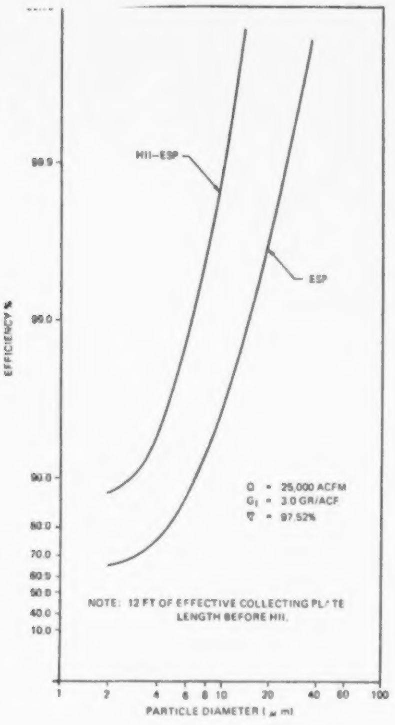

Figure 5. Fractional collectional efficiency of HII-ESP system.

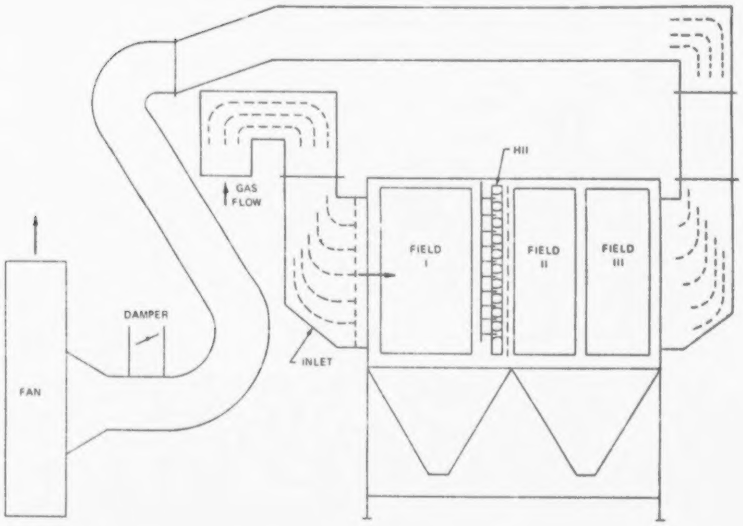

Figure 6. Schematic diagram of flow model tester.

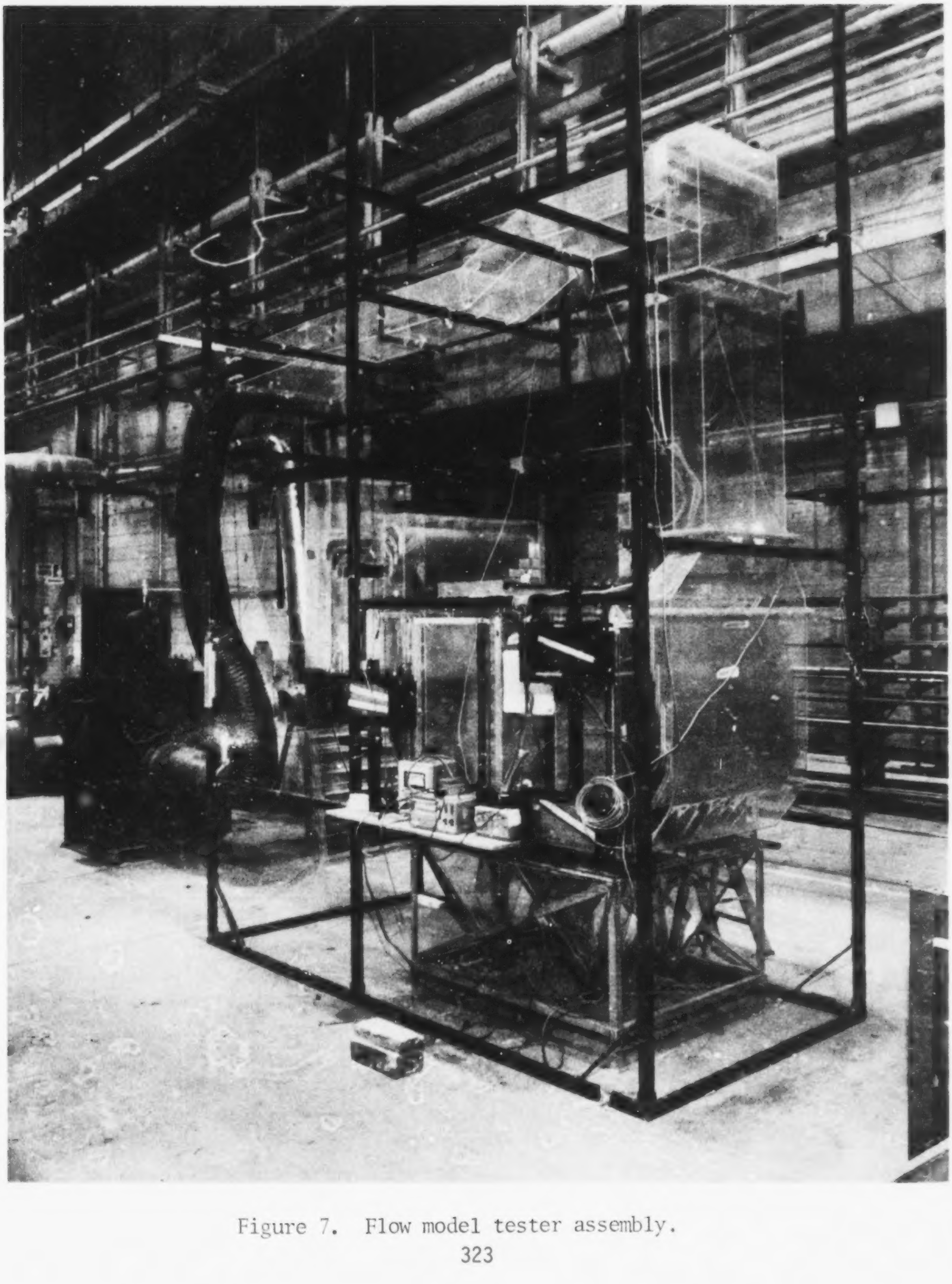

Figure 7. Flow model tester assembly.

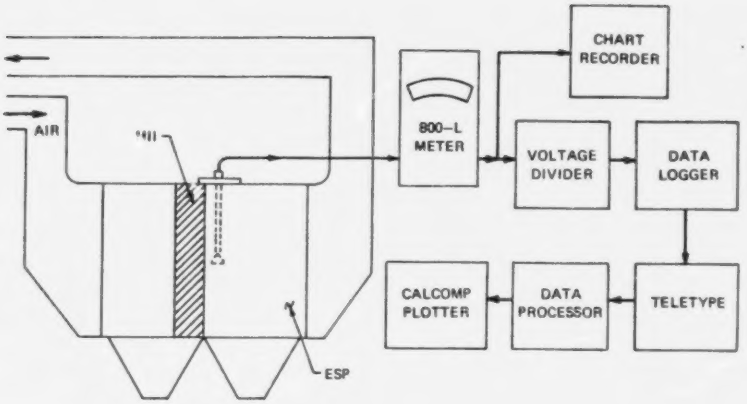

Figure 8. Schematic diagram of HII-ESP flow model velocity profile recording circuit.

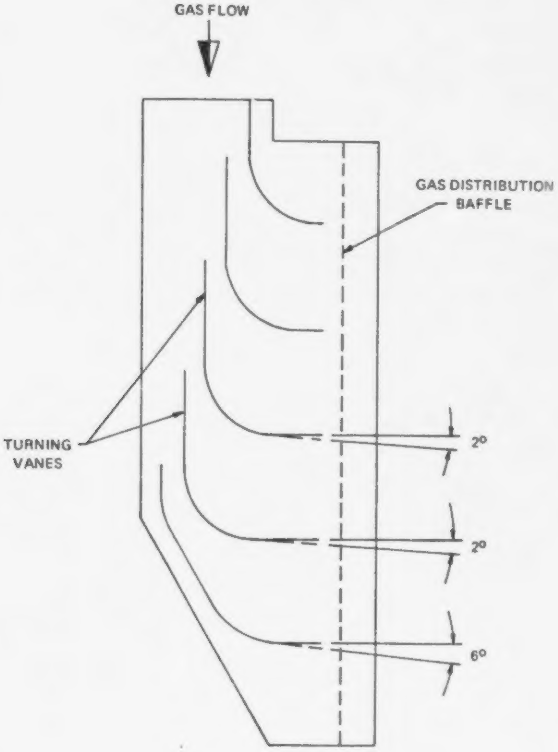

Figure 9. Modification of turning vanes.

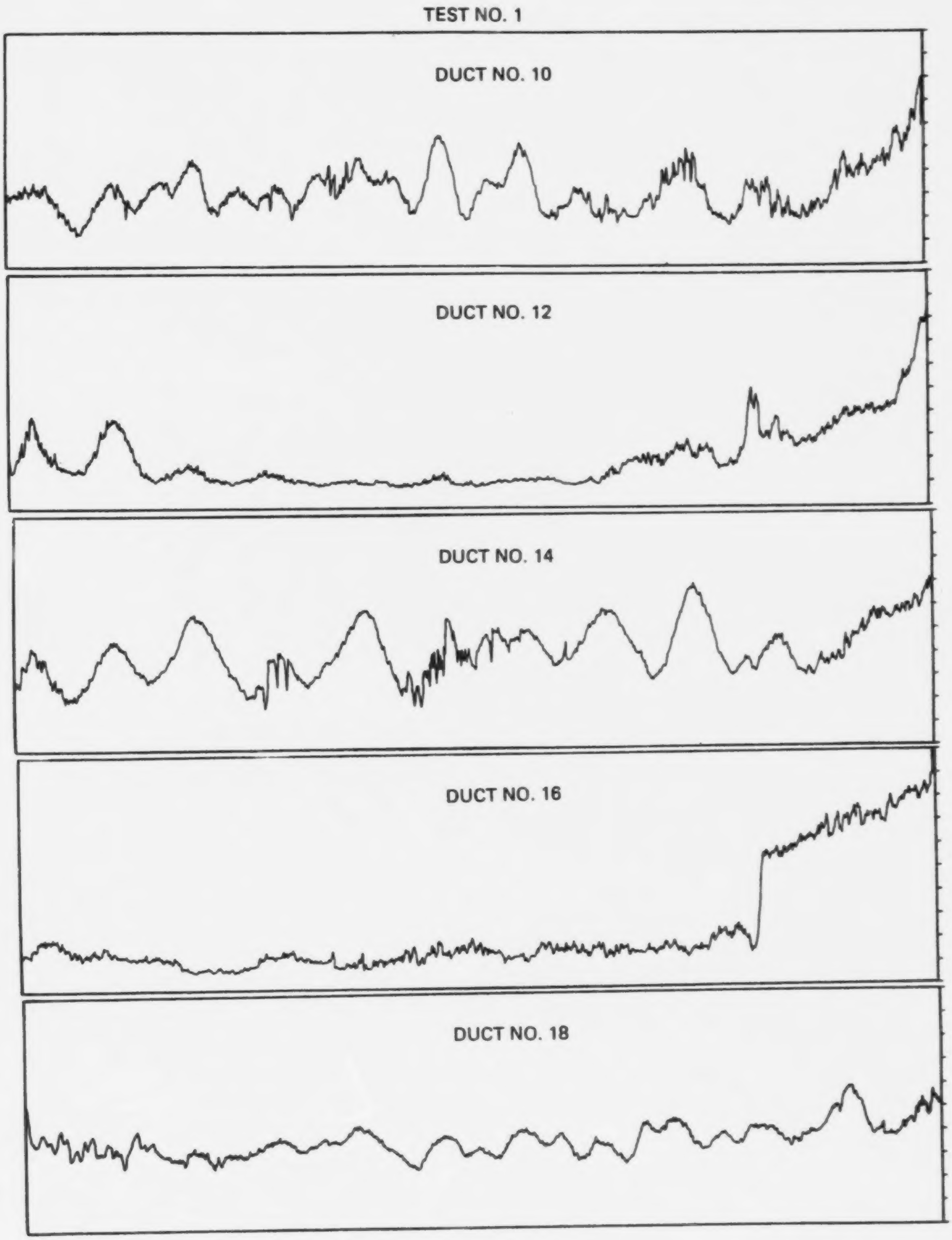

Figure 10. Velocity distribution.

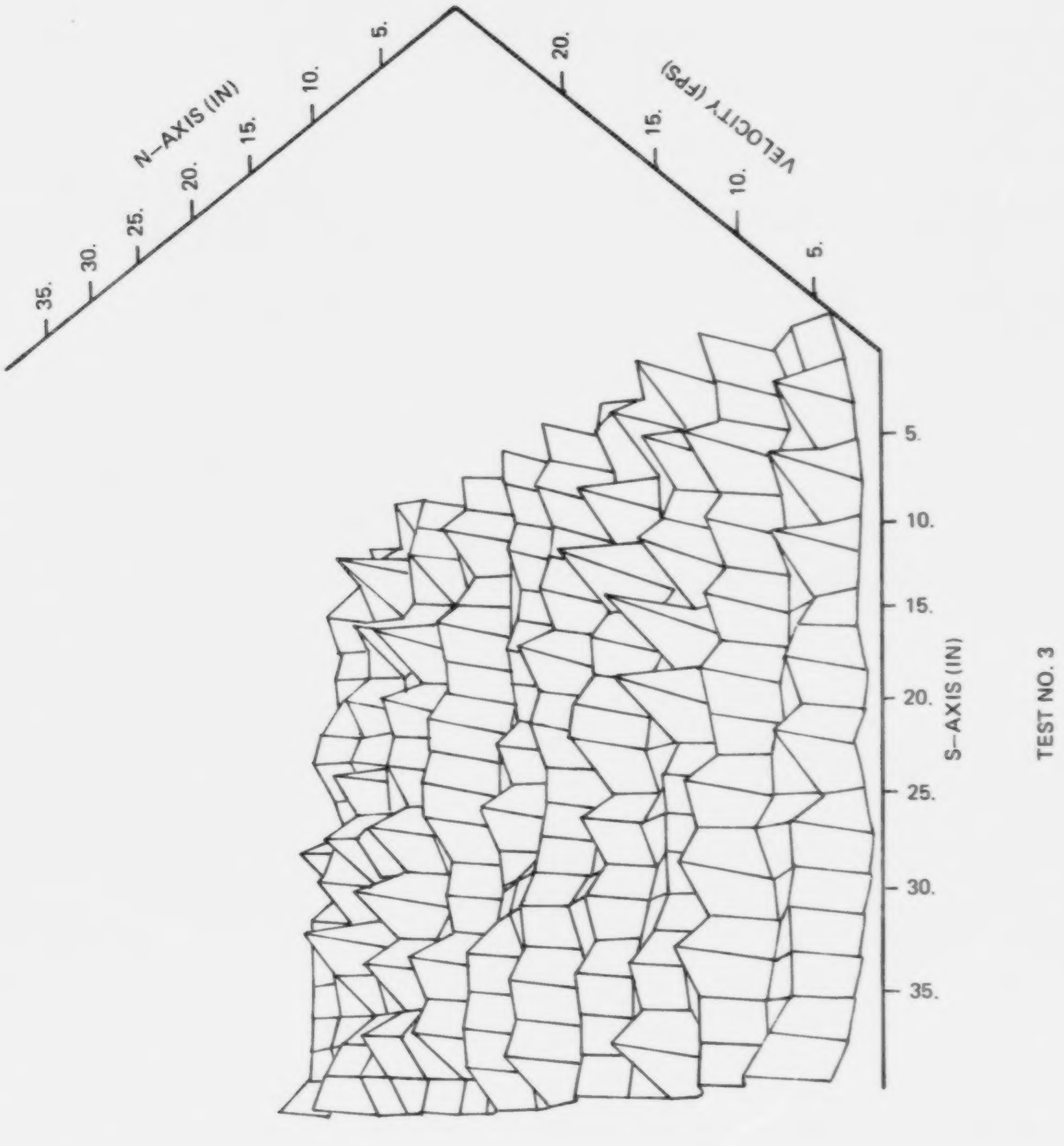

Figure 11. Velocity distribution plot.

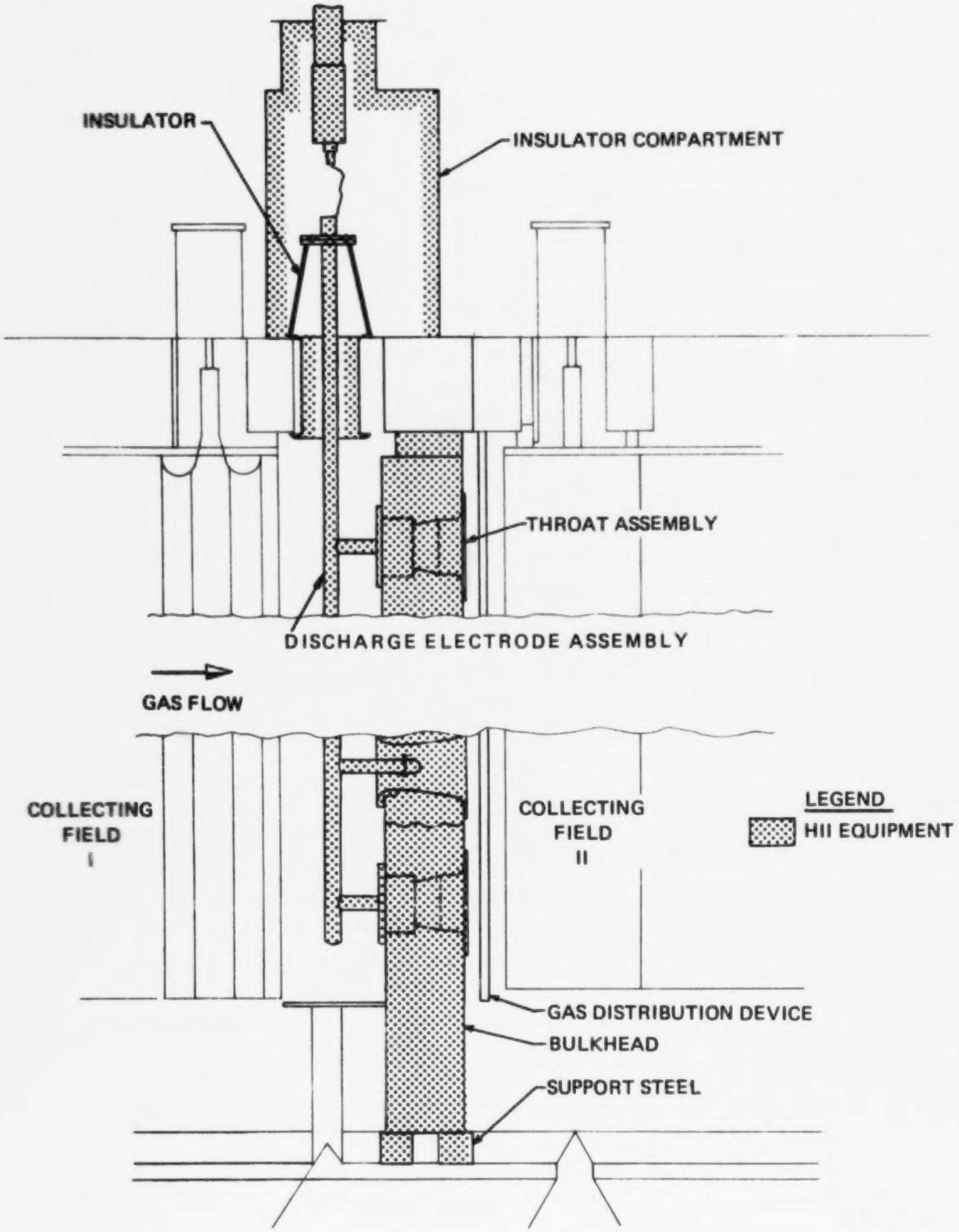

Figure 12. High intensity ionizer system.

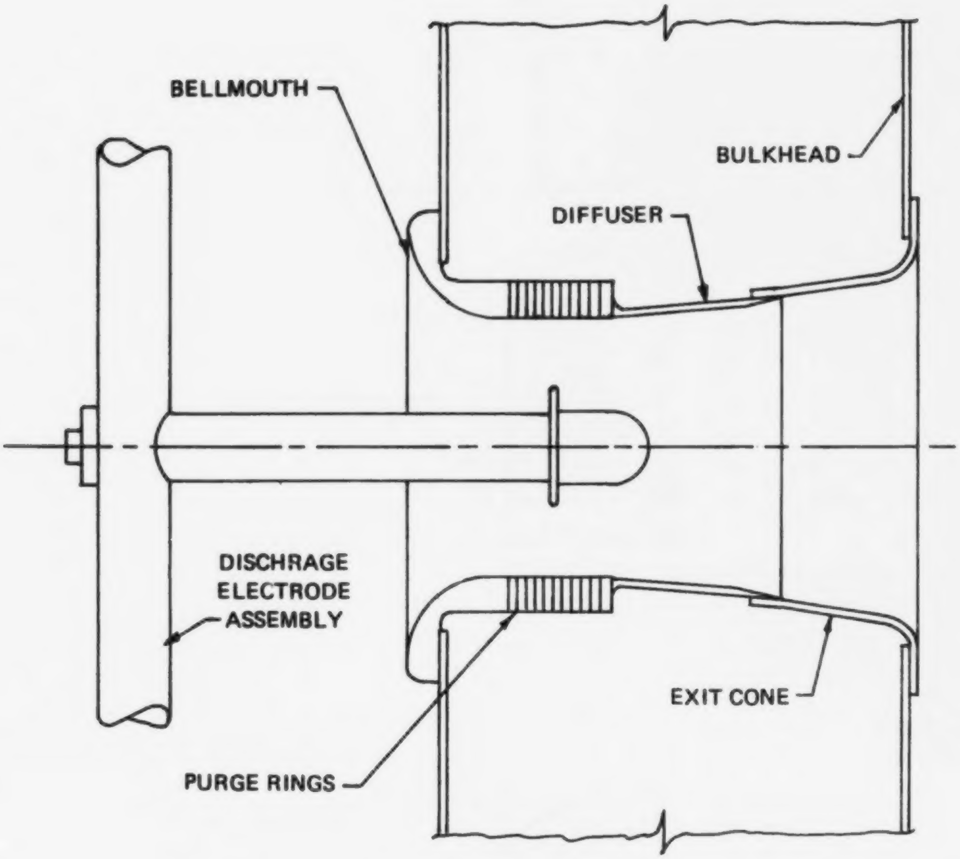

Figure 13. Throat assembly.

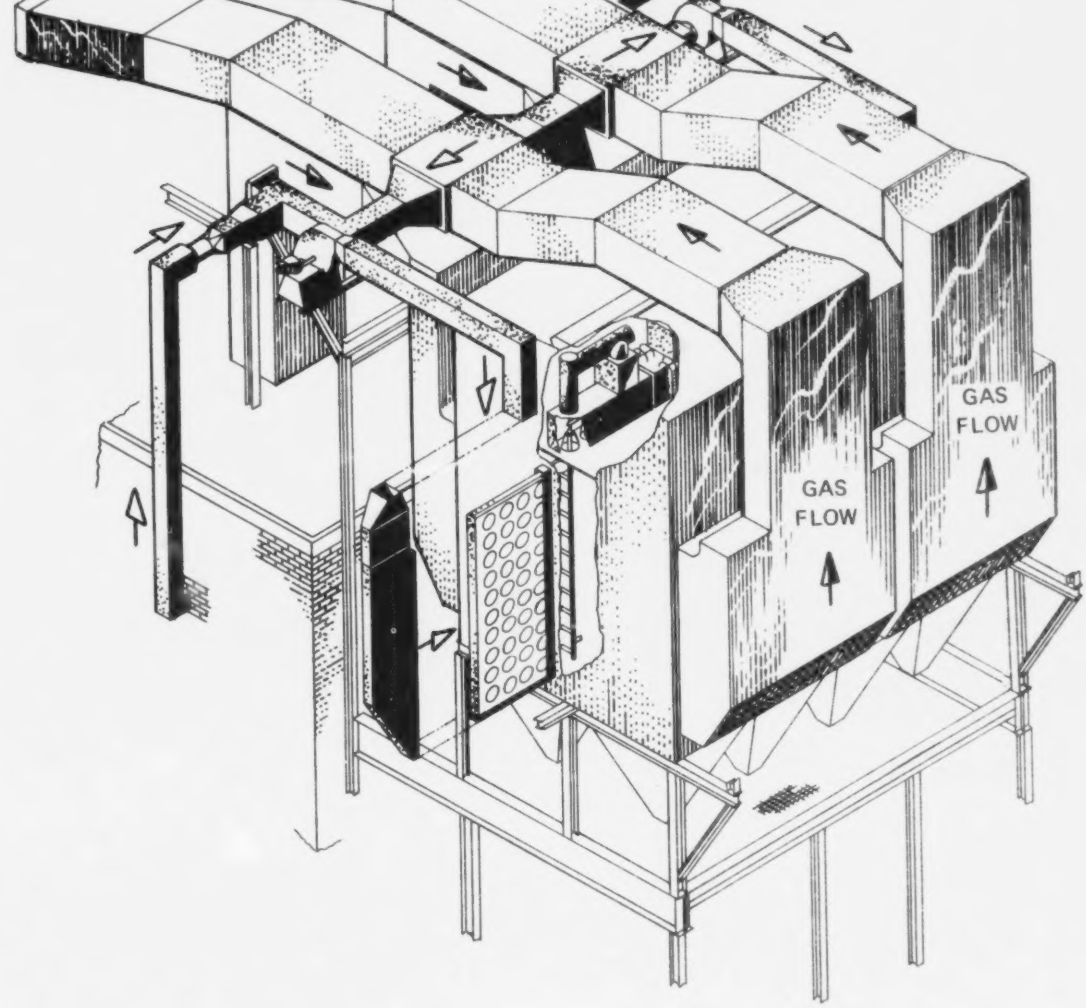

Figure 14. High intensity ionizer system.

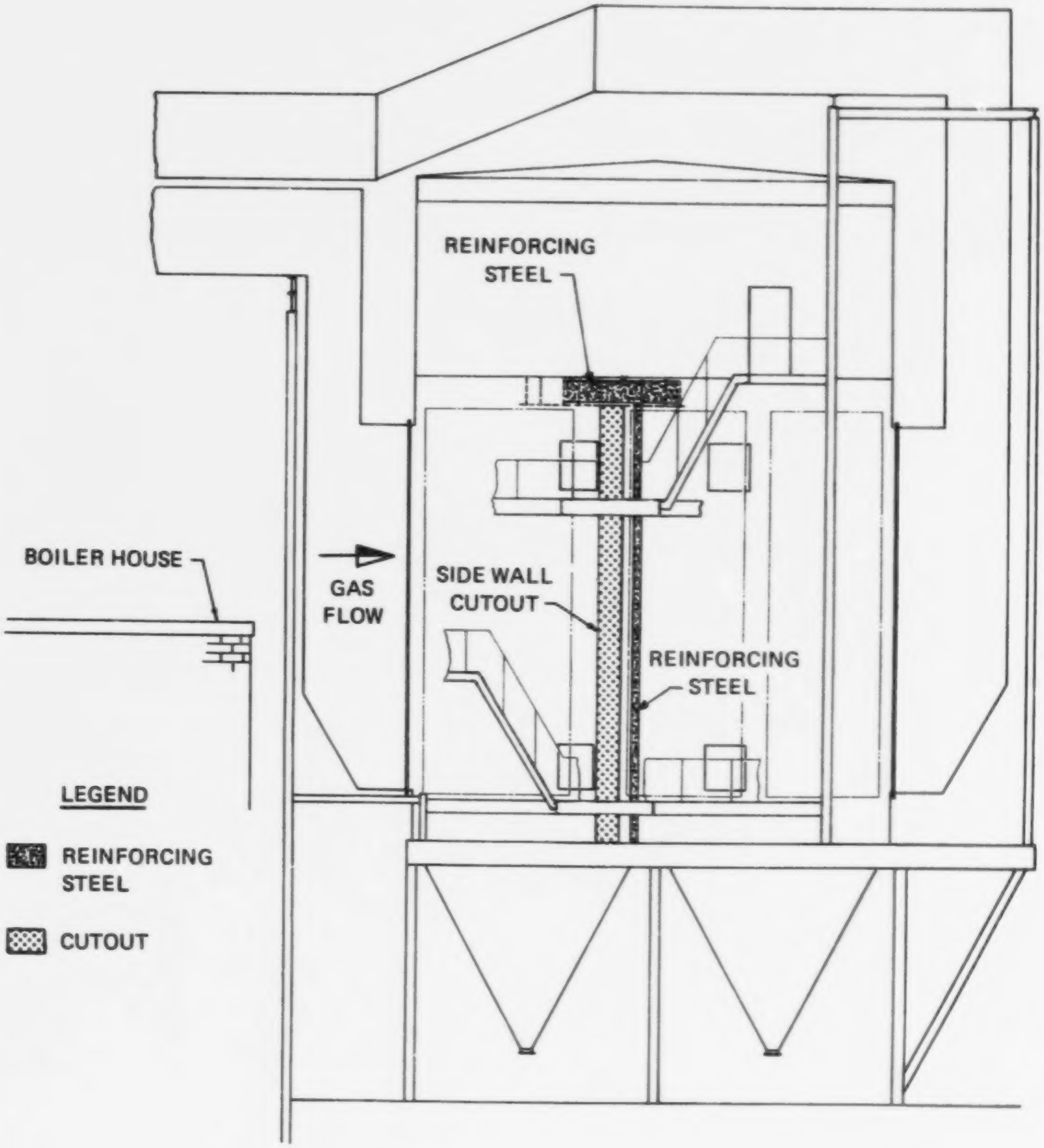

Figure 15. Construction alterations.

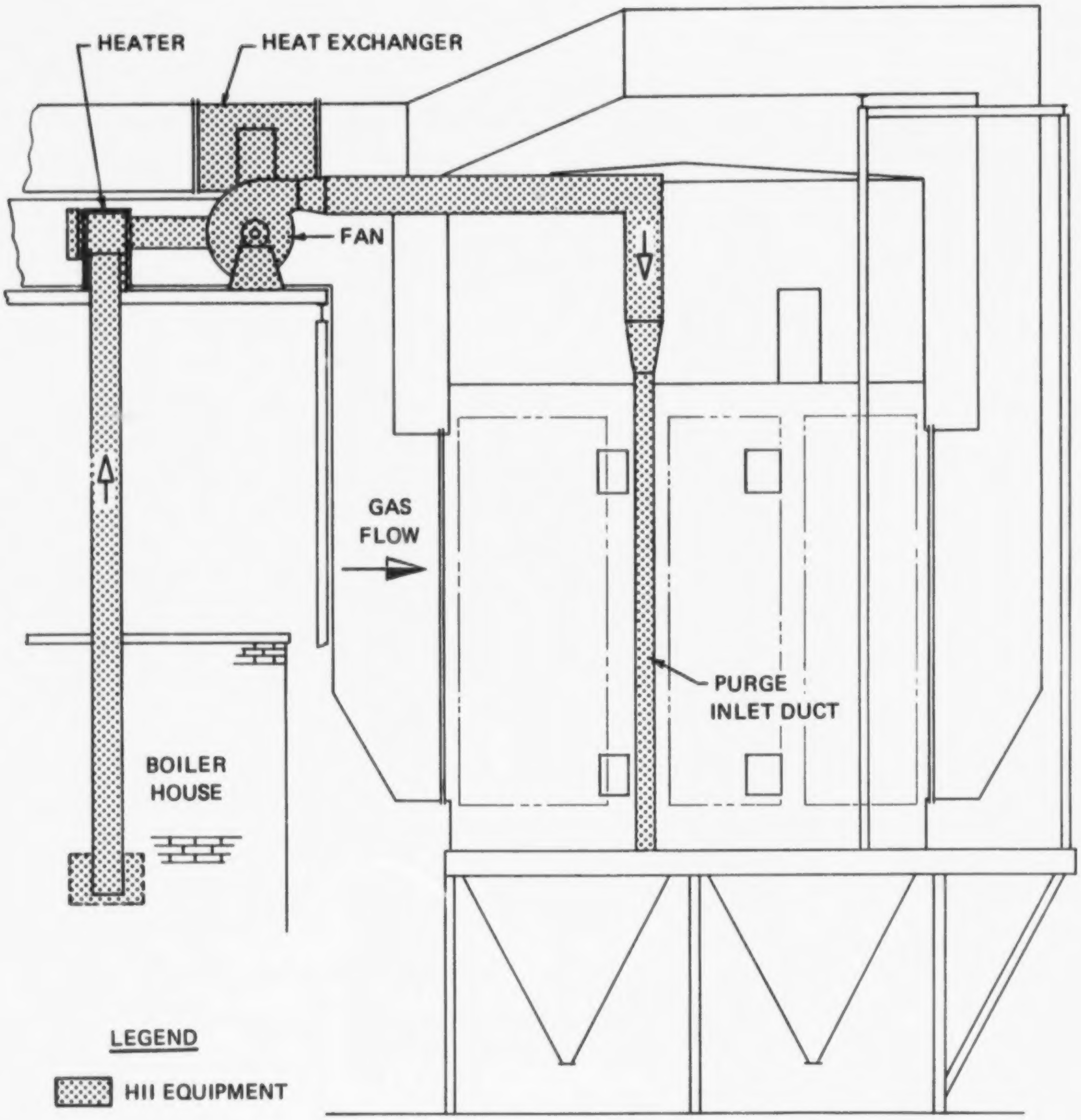

Figure 16. High intensity ionizer system arrangement (elevation).

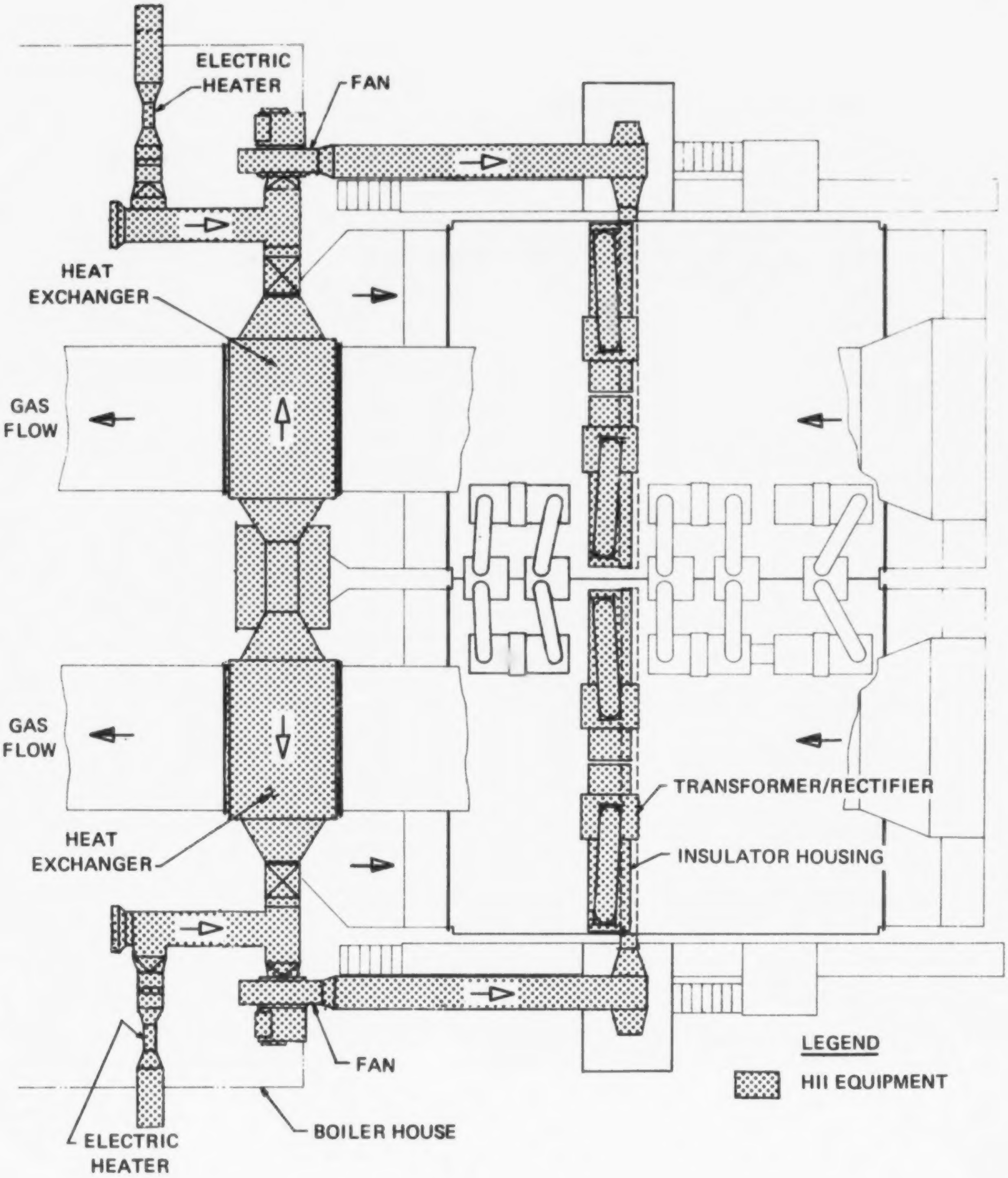

Figure 17. High intensity ionizer system arrangement (plan view).

TABLE 1. DESIGN BASIS FOR HII RETROFIT

LOAD = 150 MW

FLOW RATE = 525,000 ACFM

TEMPERATURE = 320° F

INLET GRAIN LOADING = 3.0 GR/ACF (4.32 GR/SCF)

MIGRATION VELOCITY ≥ 0.21 FT/SEC

COLLECTION EFFICIENCY = 97.52% (PRESENT ESP)

OUTLET GRAIN LOADING = 0.0672 GR/ACF (PRESENT ESP)

RESISTIVITY ≅ 10^{11} Ω − cm

MASS MEAN DIAMETER = 24 μ m

PARTICLE SIZE
STANDARD DEVIATION = 2.4

SULFUR CONTENT = 1.1 TO 1.3%

ASH CONTENT = 14.88%

MOISTURE = 7.52%

HEATING VALUE = 11,625 BTU/LB

TABLE 2. SAMPLE RESULTS OF FLOW MODEL TESTS

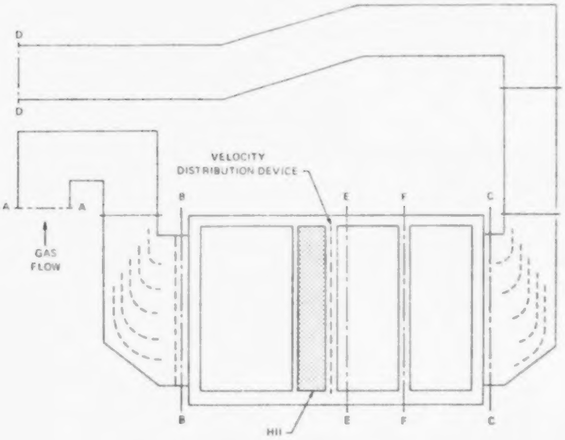

RUN NO	1	2	3
VELOCITY DISTRIBUTION DEVICE NO	1	1	2
HOT WIRE PROBE POSITION	E	F	E
FACE VELOCITY (FT/SEC)	4.54	4.39	5.52
ΔP_{AD} ("H_2O)	3	2.40	3.90
ΔP_{AB} ("H_2O)	1.12	0.9	1.44
ΔP_{HII} + DISTRIBUTION DEVICE ("H_2O)	0.42	0.35	0.64
ΔP_{CD} ("H_2O)	1.6	1.1	1.80
S (−)	0.62	0.45	0.447

BOXER-CHARGER - A NOVEL CHARGING DEVICE

FOR

HIGH RESISTIVITY DUSTS

By:

Senichi Masuda and Hajime Nakatani
Department of Electrical Engineering
Faculty of Engineering, University of Tokyo
7-3-1, Hongo, Bunkyo-ku, Tokyo, Japan

Akira Mizuno

Ishikawajima Harima Heavy Industries Ltd.
Technical Research Center
3-2-16, Toyosu, Koto-ku, Tokyo, Japan 135

ABSTRACT

A novel charging device has been developed for effective precharging of high resistivity dusts to be collected in electrostatic precipitators, bag-filters or other electrostatically augmented dust collectors. Charging is performed by mono-polar ions in an ac field by bombardment from both sides of dust particles, so that this device is called "BOXER-CHARGER". The charging current density is one order of magnitude higher than that in the conventional dc corona current, so that its charging speed is very high, allowing its installation inside the inlet-duct where gas speed is higher than 10 m/s. The device consists of parallel electrode assembies facing each other, between which an ac main voltage is applied. They are excited alternately by high frequency voltage sources at the negative period of the main frequency to produce a planer plasma ion source which supplies negative ions to the inter-electrode space. The charge accumulated on the dust deposit on the electrode assemply is completely eliminated by this plasma in each exciting period, so that no back discharge occurs even at the resistivity beyond 10^{15} ohm-cm. The characteristics and performance of this charger are decribed with its application data in a model precipitator in laboratory.

BOXER-CHARGER - A NOVEL CHARGING DEVICE FOR HIGH RESISTIVITY DUSTS

1. INTRODUCTION

The development of high performance pre-chargers capable of charging dust particles, especially with high resistivity, to a theoretical limit in a short time has become a matter of increased concern. Such pre-chargers can be used not only for retrofit purposes, but also in combination with the advanced precipitator systems, such as the pulse charging type precipitator. They can be also used in all of the electrically augmented dust collectors. The High Intensity Charger developed by Air Pollution Systems Inc. and being tested in the EPRI Test Facilities in Alapahoe Power Station represents one of such developmental efforts. Another effort is being made by the Southern Research Institute to develop the tri-electrode type charger having a grid electrode near the collecting electrode.

The authors and his co-workers have developed another novel type of charging device called "BOXER-CHARGER" in which charging is made by bombardment of unipolar ions in an ac field. This device consists of the parallel planar electrode assemblies facing each other, between which an ac main voltage is applied to produce an ac charging field. In synchronization to this voltage is applied a high frequency exciting voltage to each one of the electrode assemblies alternately to produce a plasma on its surface when it becomes negative in polarity. The plasma emits negative ions to the charging space, so that dust particles coming into this space are bombarded by the negative ions from both sides alternately. The charging current density by these negative ions is ca. one order of magnitude higher than that obtainable in the conventional dc corona charging. As a result its charging speed is very high, allowing its installation inside an inlet-duct of a collector. The charged dust particles undergo an oscillatory motion, so that they are mostly fed out of this charger without being collected on the electrode assemblies. The dust deposits occuring on the electrode assemblies in a small amount do not cause back discharge, because the charge accumulation due to oncoming ions is quickly neutralized by the plasma to appear in the next exciting period. This results in a large advantage of back discharge free operation in this device even at a very high dust resistivity beyond 10^{15} ohm-cm.

In this paper are described the basic construction and charging characteristics of the BOXER-CHARGER with its application data in a model precipitator in the author's laboratory.

2. PRINCIPLE AND CONSTRUCTION

Figure 1 illustrates the basic construction of the BOXER-CHARGER which is the modification of its prototype (Masuda (1978)[1]) made applicable in the dusty gas at elevated temperatures. In Figure 1 (a), three planar electrode assemblies are arranged parallel to each other in the gas flow direction. Each assembly consists of a number of parallel discharge electrodes as illustrated in Figure 2, connected every two units to form two groups which are insulated from each other. When a dc or ac exciting voltage is applied between the two groups of the discharge electrodes, corona discharge occurs to form a planar plasma ion source along the electrode assembly. The main ac voltage of a sinusoidal or square wave form at a low frequency of 50 - 500 Hz is applied between the adjacent electrode assemblies (A) - (B) and (B) - (A')to produce the uniform ac charging fields therebetween. When an electrode assembly takes a predetermined polarity, negative in this case, its is supplied with the exciting voltage, which is a high frequency ac voltage at 1.5 - 20 kHz in this case, to produce the planar plasma ion source over this assembly. Thus, the electrode assemblies (A), (B) and (A') are alternately excited as shown in Figure 1 (b) during the negative half period of the main voltage. In the next positive half period, the excitation is interrupted so that no positive ions are supplied to the charging spaces. The excitation has to be stopped slightly ahead of the polarity change to allow the extinction of residual plasma capable of providing positive ions, so that the exciting period Tc is made shorter than the half period of the main voltage. The negative ions are extracted by the main field from the planar ion sources to travel across the charging spaces in the alternating directions, and bombard the dust particles coming into the charging spaces from both sides alternately to impart them negative charge. The residual ions arrive at the opposite electrode assemblies to be absorbed there. If, however, the opposite assemblies are contaminated by high resistivity dust, the oncoming ions are accumulated on the surface of the dust deposit to raise its surface potential. But this accumulated charge is effectively eliminated in the next half period by the plasmas to appear on the opposite electrode assemblies now in the exciting cycle. Hence, under the proper design of current density, J, and exciting period, Tc, the maximum surface potential of the dust deposit can be kept below its breakdown threshold, so that no back discharge takes place. In case the elimination action is insufficient in the excitation period, an additional excitation for elimination has to be made for a period Te, as shown in Figure 1 (b), at which the main voltage must be kept zero to avoid the emission of positive ions. The possibility of this back discharge free operation represents one of the largest advantagesinherent to the BOXER-CHARGER. The second advantage is the uniformity of charging field in space which contributes to the well defined theoretical charge to be imparted to dust particles. The third advantage is that the particles, even if highly charged, undergo only an oscillatory motion without being collected onto the electrodes as in the case of dc corona charging, so that they can be supplied at the charger outlet with little loss. The forth advantage is that, owing to the bi-directional charging, the particles having an extremely high resistivity can be much better charged than in the case of the uni-directional charging by dc corona (Masuda and Washizu (1979)^2).

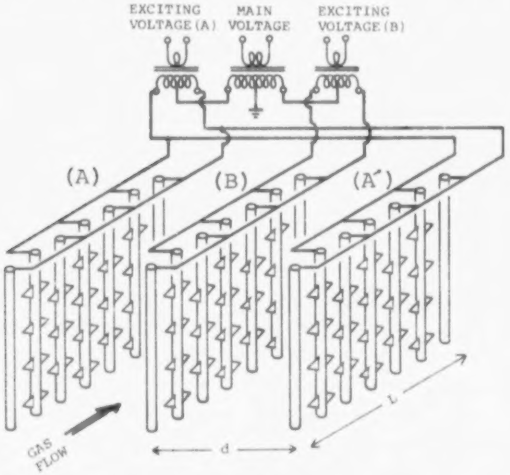

(a) Electrode Assemblies.

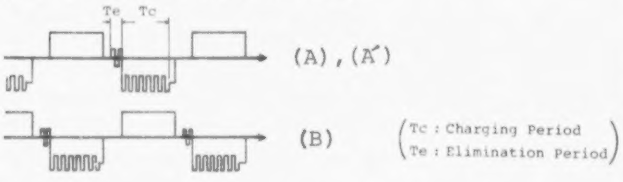

(b) Voltage Applied to (A), (A') and (B).

Figure 1 Construction of BOXER CHARGER.

The fifth advantage is the high field intensity beyond 10 kV/cm obtainable in air at NTP under medium or low dust resistivity condition, which provides a high saturation charge to the dust particles. Finally, the sixth advantage is a very high ionic current density, J, more than one order of magnitude higher than that obtainable in dc corona charging, which results in a very high charging speed as to allow its installation in the inside of an inlet duct of a precipitator or other dust collector. Figure 2 illustrates the different constructions of the electrode assemblies tested in the present research. (a) represents the prototype electrode assembly consisting of two series of strip electrodes attached on both surfaces of an insulator plate in zigzag relationship. The exciting voltage is applied between the two series to cause silent glow corona on the periferies of each strip electrode. The insulator plate serves as a holder of the strip discharge electrodes and avoides the occurence of sparking which can cause ignition of flammable gas or powders. This represents a large advantage in its applications in electrostatic painting or powder coating, although its ion emissibity is rather poor. (b) represents an assymmetrical construction consisting of strip discharge electrodes and non-corona rod electrodes arranged alternately. This construction allows the use of a dc bias voltage to be inserted in series to the exciting voltage, which hampers the occurence of corona in the non-exciting period. As a result, the applicable main field intensity can be raised, so that the saturation charge to be imparted to dust particles can be increased. On the other hand, its charge elimination ability is rather poor, so that it cannot be used in the high resistivity dusts. (c) represents the construction having the largest teeth length, which provides the highest ion emisibity but lowest applicable main field strength. Hence, its maximum saturation charge is rather limited, whereas its charge elimination ability is very high so that it is suitable in high resistivity dusts. (e) represents the construction having the smallest teeth length which provides a high saturation charge and poor charge elimination ability, so that it is suitable to medium or low resistivity dusts. (d) is the intermediate construction having the chopped teeth, which can be used in a wide dust resistivity range. The detailed characteristics of these electrode assemblies are to be described later.

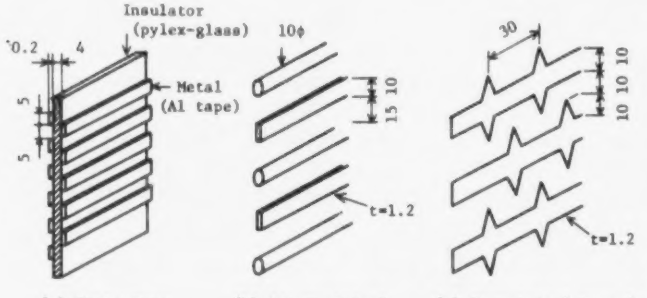

(a) Proto-type **(b) Assymmetrical type** **(c) Symmetrical type I**

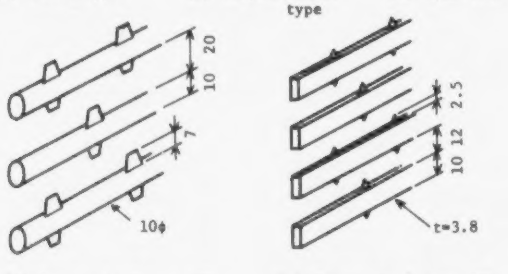

(d) Symmetrical type II **(e) Symmetrical type III**

Figure 2 Construction of electrode assemblies.

3. THEORETICAL CHARACTERISTICS

The performance of BOXER-CHARGER has to be considered from two different aspects; one from its charging ability in terms of the maximum charge and charging speed, the other from its charge elimination ability to avoid back discharge.

3.1 Charging characteristics

When a square wave main voltage is used, the quantity of charge imparted to a spherical particle by BOXER-CHARGER can be expressed by Pauthenier's equation (Pauthenier and Moreau-Hanot (1932)3):

$$Q = Q_\infty \cdot t/(t + \tau) \qquad (1)$$

$$Q_\infty = 12\pi\varepsilon_o\varepsilon_s a^2 E/(\varepsilon_s + 2) \quad \text{(saturation charge)} \qquad (2)$$

$$\tau = 4\varepsilon_o E/J \quad \text{(charging time constant)} \qquad (3)$$

where t = effective charging time, ε_o = dielectric constant of vacumm; ε_s = specific dielectric constant of particle, E = charging field intensity, a = particle radius, and J = charging current density. The maximum charge to be imparted to a particle is governed by both Q_∞ and τ, which in turn are determined by the maximum values of E and J possible to realize in a BOXER-CHARGER.

3.1.1 Saturation charge. The magnitude of saturation charge, Q_∞, is limited by the highest value of field intensity applicable to the charging space, E_{max}. When the field intensity E exceeds a certain threshold, corona discharge starts to occur from the electrode assemblies not subjecting to the excitation voltage, so that the bi-polar charging begins to prevail. This corona starting threshold of E at the electrode assemblies provides the magnitude of E_{max}. This threshold value, $E_{st\ max}$, is measured for the electrode assemblies (a) - (e) in Figure 2 using an apparatus as shown in Figure 3. The results obtained are tabulated in Table 1. The effect of teeth length as described in the preceding section is clearly indicated. The effect of the bias voltage, V_b, is also tested in the assymmetrical configuration (b) in Figure 2 where the saw teeth electrode (c) is used instead of the strip electrode. When $V_b = 0$, the magnitude of $E_{st\ max}$ is 10 kV/cm, which can be raised to 13 kV/cm at $V_b = 8$ kV. This increase is resulted by the dc bias voltage inserted in series to the exciting voltage to lower the concentration of field at the teeth edges. It should be noted that these values of $E_{st.max}$ measured in the dc tests does not immediately provide the magnitude of E_{max} in the BOXER-CHARGER expressed in terms of average field intensity, $E_{max} = V_{max}/d$. In BOXER-CHARGER the field intensity at the electrode assemblies at rest (without excitation) becomes maximum owing to the space-charge field, so that the magnitude of E_{max} as above is always more or less smaller than that of $E_{st.max}$. In the ideal case when the space-charge limited current is prevailing, Equation (5) to be decribed later provides $E_{max} = (2/3)\,E_{st\ max}$.

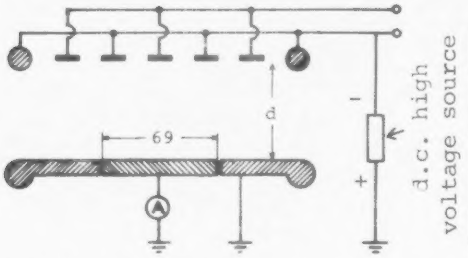

Figure 3 Arrangement for dc tests.

Table 1 CORONA THRESHOLD FIELD INTENSITY

electrode assembly	electrode spacing: d	$E_{st\ max}$ (T=15°C)	$E_{st\ max}$ (T=150°C)
(a)	30 mm	>15 kV/cm	15 kV/cm
(b)	30 mm	11 kV/cm	10 kV/cm
(c)	60 mm	≃10 kV/cm	6.5kV/cm
(d)	60 mm	>10 kV/cm	≃10 kV/cm
(e)	30 mm	14 kV/cm	12 kV/cm

3.1.2 Charging time constant. Since the magnitude of E must be kept as high as possible to raise the saturation charge, Q_∞, the only possible way to lower the charging time constant, τ, to increase the charging speed is to raise the charging current density, J, up to its maximum value, J_{max}, obtainable at $E = E_{max}$. J_{max} is limited by either of the two factors. When the planar ion source can produce a sufficiently high plasma density to provide mono-polar ion emission more than needed for the space-charge limited current density, J_{sp}, the magnitude of J will be limited by the value of J_{sp} at $E = E_{max}$, i.e. $J_{sp\ max}$. Otherweise, depletion occurs at the ion source, so that J_{max} is limited by the ion emitting ability of the source at $E = E_{max}$ and becomes lower than $J_{sp\ max}$. The duty factor of the corona excitation, DF, is also another factor.

We derive the general expression of the charging current density, J, at first. The potential U, local field intensity E and charging current density J_{sp} inside the charging space under the space-charge limited condition can be derived by solving the Poisson's equation and Ohm's law, considering the corresponding boundary conditions. The solutions are:

$$U = V_o\ (1 - x/d)^{3/2} \tag{4}$$

$$E = -\ (3/2)\ E_o\ (1 - x/d)^{1/2} \tag{5}$$

$$J_{sp} = (9/8)\ \varepsilon_o\mu\ E_o^{\,2}/d \tag{6}$$

where V_o = main voltage, E_o = average field intensity, x = distance from the electrode assembly at rest, and d = gap between the two adjacent electrode assemblies. The charging current density can be expressed in terms of J_{sp} as follows:

$$J = K \cdot DF \cdot J_{sp} \tag{7}$$

$$= K \cdot DF \cdot (9/8)\varepsilon_o\mu\ E_o^{\,2}/d \tag{8}$$

where K = coefficient of ion emission ability ≤ 1.

In order to examine the validity of the relationship as described by Equations (7) and (8), experiments are made using the apparatus shown in Figure 3, the the exciting voltage applied. The magnitude of J is affected by E_o, the exciting voltage, V_{ex}, its frequency, f_{ex}, gas composition and its temperature, T, and electrode geometry. The measurements are made in air at normal pressure and different temperatures.

Figure 4 represents the effect of V_{ex} on J in the electrode assembly (c) measured at DF = 1 and a frequency f_{ex} = 20 kHz with different values of E_o. J rises linearly with V_{ex} until sparking occurs between the two adjacent discharge electrodes, and no saturation occurs. This indicates that even this type of the electrode assembly having the highest ion emission ability does not provide a sufficient ion density so as to produce the space-charge limited current.

Figure 5 indicates the effect of E_o on J in the electrode assembly (c) measured at DF = 1 and V_{ex} just below the sparking threshold with the different values of f_{ex}. The dotted curve (1) represents the space-charge limited current, and the curve (5) the same characteristics in the assembly (a). It can be seen that the electrode assembly (c) can produce a quite satisfactory curr-

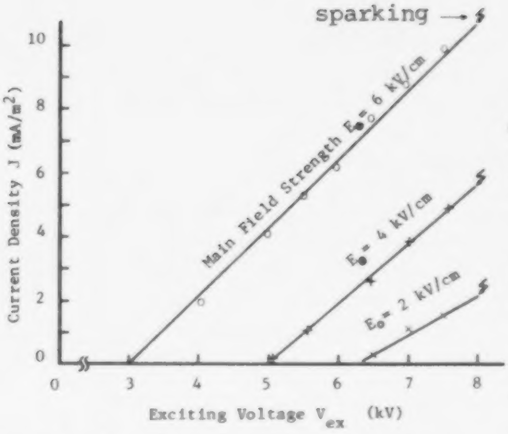

Figure 4 Effect of V_{ex} on J at dc-tests.((c); d=5.5cm; DF=1; f_{ex}= 20kHz; air at T=20°C)

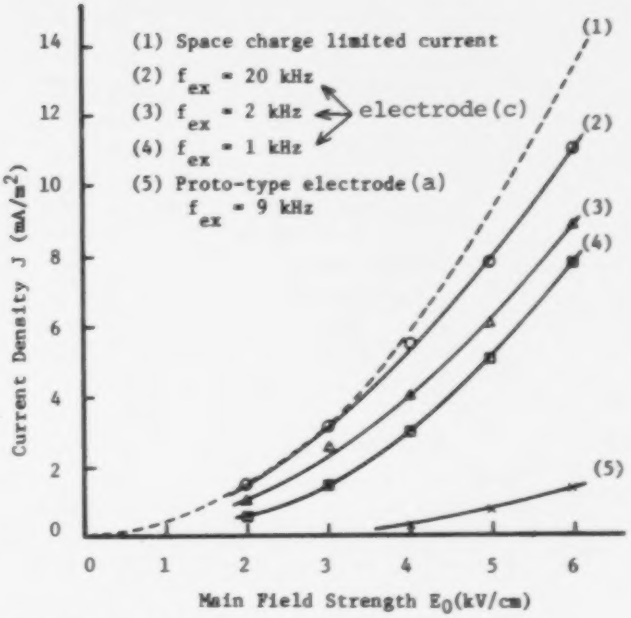

Figure 5 Effect of E_o on J at dc-tests. ((a) and (c); d=5.5cm; DF=1; V_{ex} just below the sparking threshold; air at T=20°C)

ent density J = 0.76 J_{sp} at E_o = 6 kV/cm with f_{ex}= 20kHz and J = 0.57 J_{sp} at the same field intensity even with the lowest frequency f_{ex}=1 kHz. Whereas the assembly (a) having an insulator plate produces a much lower current density J = 0.10 J_{sp} at the same field intensity with f_{ex} = 9 kHz. J rises proportionally with the square of E_o, and the effect of f_{ex} is not substantial, allowing the use of a low exciting frequency, such as f_{ex} = 1 kHz.

The validity of Equations (7) and (8) are further tested by plotting (Jxd) against E_o at d = 35 and 60 mm and f_{ex} = 1.5 and 20 kHz, using the assembly (c). The results obtained are shown in Figure 6, which indicates the rise of (Jxd) to be approximately proportional to E_o^2, as expected from Equation (8). The magnitude of J are further measured with changing the duty factor in the range of DF = 0.1 - 1.0. The exciting voltage is periodically interrupted for this purpose. It is confirmed that J changes proportionally with DF.

From the foregoing test results, it seems pertinent to express J by Equations (7) and (8), taking K as a constant representing the ion emission ability of each electrode assembly. The values of K for each assembly measured under different conditions are given in Table 2.

Table 2 EMISSION ABILITY K

electrode	f_{ex}=20 kHz	f_{ex}=1.5 kHz
(a)	0.1 - 0.2	-
(b)	0.8 - 1.0	-
(c)	0.8 - 1.0	0.6 - 0.65
(d)	0.8 - 0.9	0.6
(e)	0.8 - 1.0	-

Finally, the effect of T on J is measured. The results obtained are shown in Figure 7. Since the ion mobility, μ, is proportional to the absolute temperature, J is expected to rise proportionally with the temperature (see Equation (8)). The measured results agree approximately with this assumption.

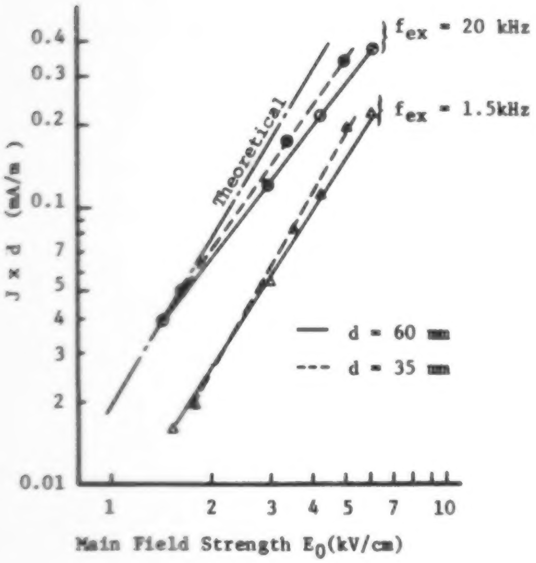

Figure 6 (J x d) vs. E_o.
((c); V_{ex} just below 8kV; air; 20°C)

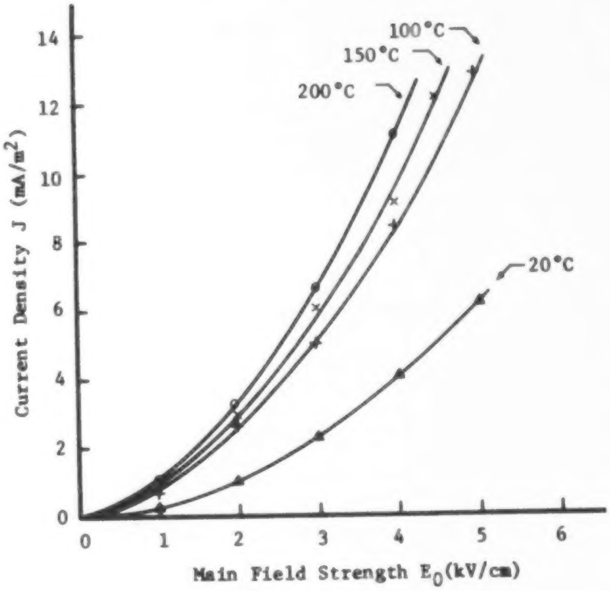

Figure 7 Effect of Temperature on J
((c); V_{ex} just below spark voltage; d=5.5 cm; f_{ex}=2 kHz; DF=1; air).

3.2 Charge elimination characteristics and conditions for avoiding back corona.

The charge elimination characteristics is largely dependent on the geometry of the electrode assembly, as previously described. But, it also depends on the exciting frequency, f_{ex}. The use of a low frequency results in a better charge elimination effect, because a longer time is available for the ions of opposite polarity to arrive at the surface charge accumulated on the deposit through Coulombic transport and diffusion. On the other hand, the ac corona, appearing in a form of point glow at high frequency (20 kHz), tends to turn into streamer corona which causes the reduction in sparking threshold of the exciting voltage, V_{ex}. This, however, does not produce much disadvantage in relation to J, as indicated in Figure 5.

The back discharge can be avoided when either of the following conditions are fulfiled:

(i) Charging period ends before the breakdown of the deposit layer on the opposite electrode assembly at rest occurs, and all the accumulated charge on the layer is completely discharged by the succeeding elimination period:

$$E_d = (1/\varepsilon_s\ \varepsilon_c)\cdot J\cdot T_c\cdot S \leqq E_{ds} \tag{9}$$

where E_d = field strength in the desposit, T_c = charging period, S = space factor of the electrode assembly, and E_{ds} = breakdown field strength of the deposit. T_c = (1/2f) when DF = 1, where f = frequency of main voltage. The magnitude of charge elimination period is (T_e + T_c) (see Figure 1 (b)), and it becomes (1/2f) when DF = 1 and no additional elimination is made.

(ii) Ions from the excited electrode assembly cannot arrive at the opposite electrode assembly at rest within a period when the main voltage appears in its half cycle, T_a:

$$\int_0^{t_a} \mu E(t) \cdot dt \leqq d \qquad (10)$$

When the main voltage is a square wave with no additional elimination period to be made at zero voltage, Equation (10) becomes:

$$\mu E \cdot (1/2f) \leqq d \qquad (11)$$

4. CHARGING PERFORMANCE

The charging performance of BOXER-CHARGER is tested using a steel ball and calcium carbonate powders.

4.1 Charging performance test using a steel ball.

A steel ball with 3.0 mm in diameter is hung by a nylon thread (diameter: 100 μm) into the charging space of a BOXER-CHARGER for a sufficiently long time, and its saturation charge is measured with a Faraday-cage. Tests are made on the effects of the charging polarity, electrode geometry, charging field intensity, charging position, and the additional charge elimination action.

4.1.1 Maximum saturation charge. At first the comparison is made of the charging performance between the positive and negative charging polarities, using the electrode assemblies (c). The polarity can be easily altered by reversing the phase of excitation. Figure 8 shows the results obtained. The theoretical saturation charge according to Equation (1) is also depicted. At positive charging, the saturation charge, Q_∞, rises with the main field intensity, E_o, approximately along the theoretical line up to E_o = 5 kV/cm, at which, however, it drops very sharply. This is because the streamers develop from the teeths of the positive discharge electrodes being excited into the charging space to produce bi-polar ions along their channels and decrease the saturation charge. At negative charging, on the other hand, Q_∞ rises proportionally with E_o along the theoretical line up to a much higher level limited by sparking of the main field, because the development of streamers are greately hampered in this case. The main voltage frequency used is f = 50 Hz with DF = 1.

Figure 9 shows the comparison of the charging performance between the electrode assemblies (c) and (e). The magnitudes of Q_∞ in (c) and (e) do not differ from each other and agree very well with the theoretical line up to their sparking thresholds. The sparking threshold of E_o, which represents the maximum applicable main field intensity, E_{max} (average values as described), is much higher in (e) than in (c) in accordance with the difference in $E_{st\ max}$ given in Table 1. The magnitude of E_{max} and the ration ($E_{st\ max}/E_{max}$) are given in Table 3 for each electrode assembly together its calculated value of charging time constant, τ, at E_{max}. It can be seen that this ratio is not much different from its theoretical value (3/2) described above. This enables the estimation of E_{max} and, thus, Q_∞, from the value of $E_{st\ max}$ measured from the dc-test.

Table 3 COMPARISON OF Emax BETWEEN (c) and (e)

electrode	curve	Emax	Est max/Emax	τ
(c)	(i)	6.5kV/cm	1.4	3.5 ms
(e)	(ii)	8 kV/cm	1.75	4.5 ms

4.1.2 Augmentation of charge elimination. In the case when the surface of

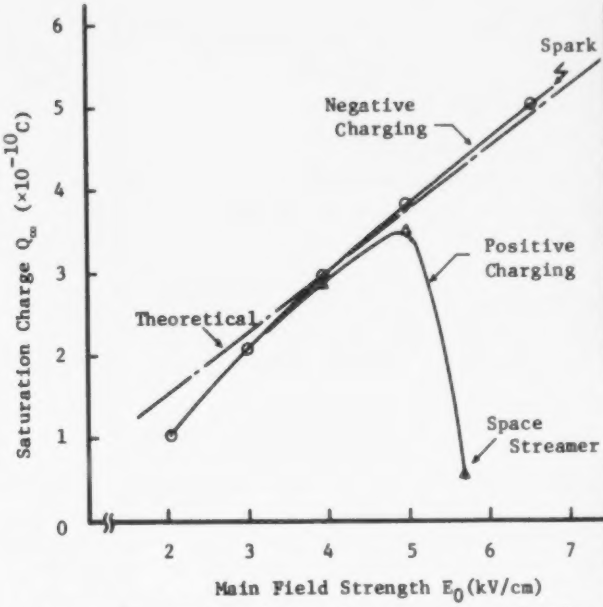

Figure 8 Saturation charge of a steel ball in the positive and negative charging plotted against E_o.((c); d=83mm; DF=1; f_{ex}=20kHz; f=50Hz; 2a=3mm; 20°C)

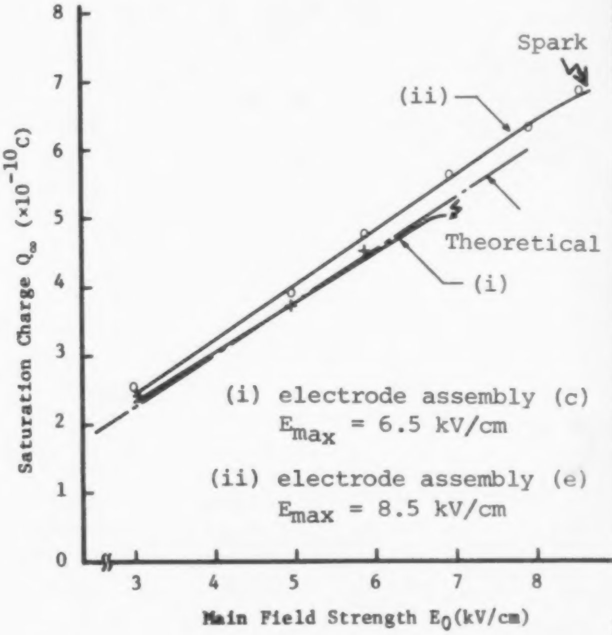

Figure 9 Saturation charge of a steel ball in electrode assemblies (c) and (e). (negative charging; DF=1; f_{ex}=20 kHz; f=50Hz; d=65mm; air at 20°C).

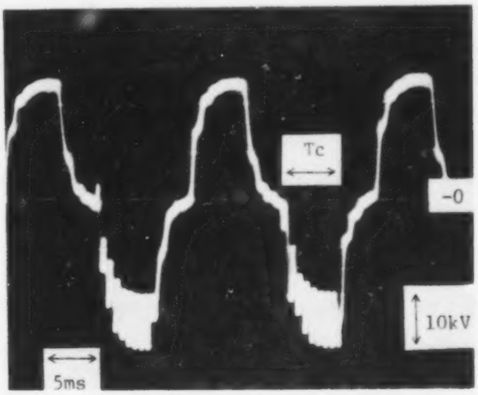

(a) wave form # 1 (T_c=5ms; T_e=0)

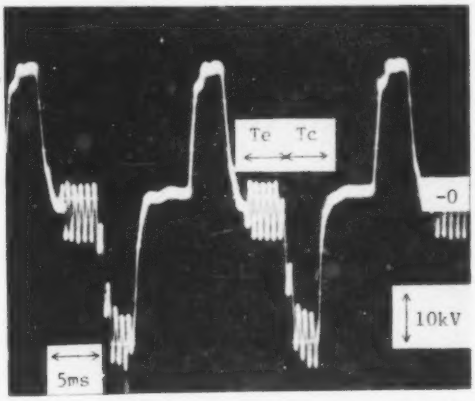

(b) wave form # 2 (T_c=4ms; T_e=4ms)

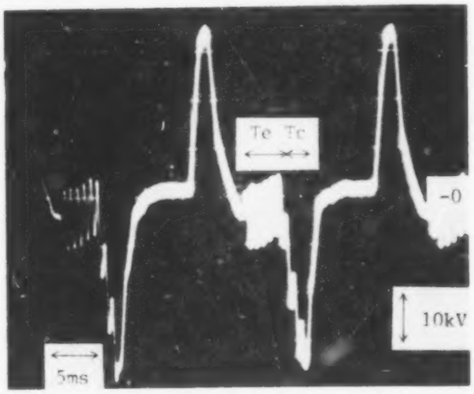

(c) wave form # 3 (T_c=2ms; T_e=4ms)

Figure 10 Wave form of main voltage used for augmentation of charge elimination ability (frequency of main voltage f = 50 Hz).

the electrode assemblis are covered with extremely high resistive layers, the charge elimination ability of BOXER-CHARGE at its ordinary operation mode with DF = 1 becomes insufficient so as to cause back discharge. In order to overcome this difficulty, the following methods of augmenting charge elimination can be used:

(a) A part of the half period of the main voltage is made zero, and an additional excitation for charge elimination is made for a period T_e during this zero voltage interval under zero main field condition (additional eliminat-ion method).

(b) The excitation for charging is limited to a part of the interval when the charging main voltage appears (reduced exciting period method). This method is equivalent to the use of a higher main voltage frequency. The exciting period in this case is denoted as T_c.

These methods are illustrated in Figure 1 (b) and Figure 10 (a) - (c).

Tests are made on these augmentation methods by measuring Q_∞ of the steel ball under an extremely high resistivity condition where the polyethylene sheets with resistivity beyond 10^{15} ohm-cm and many pinholes (diameter = 0.3 mm; spacing = 5 mm) are attached on all of the discharge electrodes of the electrode assemblies (d) facing to each other. T_e is varied from zero to 4 ms whereas T_c from 2 to 5 ms. The results obtained are compared with the blanc case with clean electrodes.

The solid curves in Figure 11 show the results obtained using the main voltages of the wave form # 1 - # 3 in Figure 10, measured at different position in the charging space with f_{ex} = 1.5 and 20 kHz. The data for the clean electrodes are also indicated by the dotted curves. It can be seen that Q_∞ rises in the vicinity of the electrodes when no additional elimination is made (T_e = 0), possibly due to the space charge field. Whereas, when the additional elimination is made with T_e = 4 ms, Q_∞ at the center region is appreciably lowered and it drops in the near electrode region. This tendency becomes more pronounced when the lower frequency f = 1.5 kHz is used. These phenomena seems to be caused by the plasma produced in the additional elimination period, T_e. The positive ions from the plasma will be extracted by the oppositely charged suspended particle to reduce its saturation charge, Q_∞. The charge reduction will be more effective in the near electrode region, and when a lower frequency f = 1.5 kHz is used.

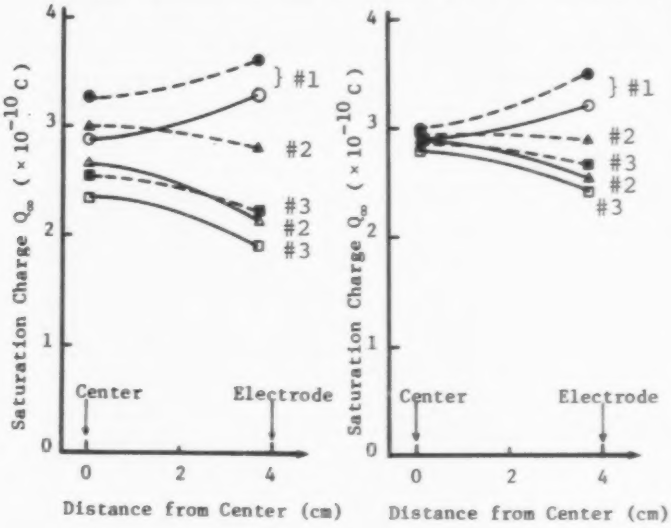

(a) f_{ex} = 1.5 kHz　(b) f_{ex} = 20 kHz

Solid curve: Covered Electrode

Dotted curve: Clean Electrode

Figure 11 Effect of charging position on Q_∞ (E_o=3.8kV/cm; steel ball; 2a=3mm; air at 20°C)

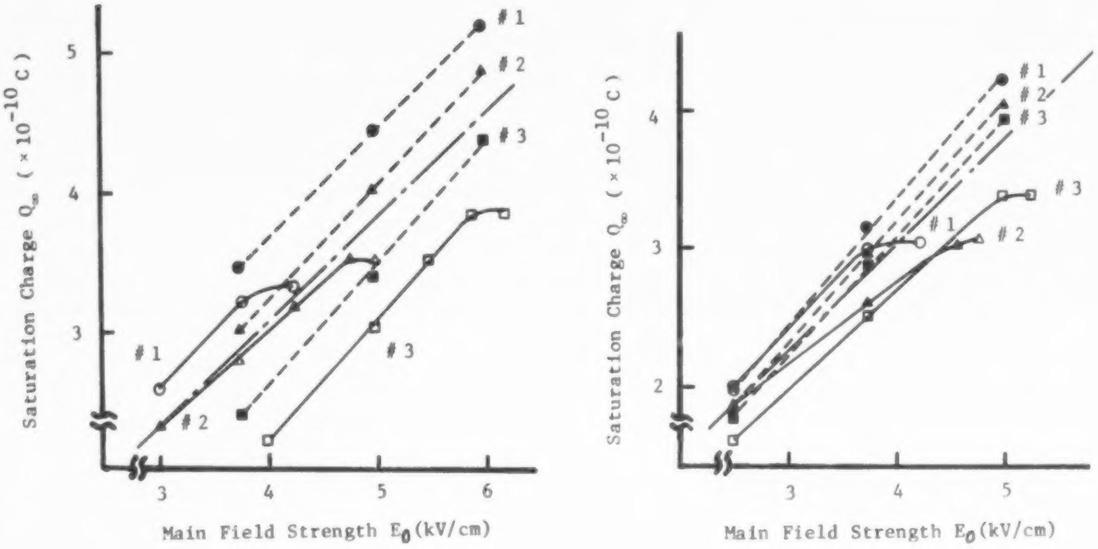

(a) f_{ex} = 1.5 kHz

(b) f_{ex} = 20 kHz

Figure 12 Effect of augumented charge elimination for avoiding back discharge (d = 80 mm; air at 20 °C; main voltage frequency = 50 Hz).

The visual observation of the coronas shows that they take a form of diffused streamers bridging across the neighbouring discharge electrodes at the lower frequency f_{ex}=1.5 kHz, whereas they remain to be the stable spot-like glows at a higher frequency f_{ex} = 20 kHz. It is evident that the diffused streamers can provide the positive ions more effectively to cause the lowering in Q_∞. It should be added that a severe back discharge starts to occur at E_0 = 3 kV/cm when the ordinary wave form with DF = 1 is used.

Figure 12 indicates the effect of the methods of augmenting charge elimination using the wave forms # 1 - # 3 in Figure 10 in avoiding back discharge. The wave form # 1 represents the case where only the exciting period is reduced from 10 ms (f = 50 Hz) to T_c = 5 ms. T_c is further reduced in # 2 and # 3 to 4 and 2 ms respectively, whereas the additional elimination is made at T_e = 4 ms in these wave forms. The magnitude of Q_∞ is measured at f_{ex} = 1.5 and 20 kHz under the covered and clean electrode conditions at different positions in the charging space, and its average values are plotted against E_0. Again the solid curves represent the results obtained with the covered electrodes, and the dotted curves those with the clean electrodes. The theoretical line is also depicted. It can be seen that the maximum value of Q_∞ can be greately raised by using the wave forms # 1 - # 3 which increase the back discharge starting threshold of E_0 from 3 kV in the ordinary wave form with DF = 1 up to 4, 4.7 and 6 kV respectively. The solid curves rise parallel to and near the theoretical line, and they begin to saturate at the threshold field intensities as described above. If compared at the same magnitude of E_0, # 1 with the least augmentation provides the highest Q_∞. But, the largest value of the maximum Q_∞ can be obtained by # 3 with the highest augmentation. The dotted curves for the clean electrodes are also parallel to the theoretical line, and no saturation appears in the tested range of E_o. The wave form # 1 provides the highest value of Q_∞, whereas # 3 the lowest value, probably due to the balance between the effects of different charging time T_c and eliminating time T_e. Q_∞ lies above its theoretical value except for the case using # 3 in (a). This phenomenon is also attributable to the effect of space-charge which produces in every half cycle of the main voltage the field intensity higher than its average value E_o at any local point in the charging space. The comparison between the figures (a) and (b) leads to the conclusion that the use of a lower exciting frequency f_{ex} = 1.5 kHz, much more preferable in all the respects, is acceptable because the magnitude of the maximum Q_∞ obtainable at this frequency is almost the same as that obtainable at a much higher frequency f_{ex} = 20 kHz, so far as a suitable augmentation measure be taken in charge elimination. However, it should be noted that the use of any augmentation method as previosly described causes inevitably the rise of charging time constant, which requires the increased length of BOXER-CHARGER.

4.2 Charging performance Tests using powder samples.

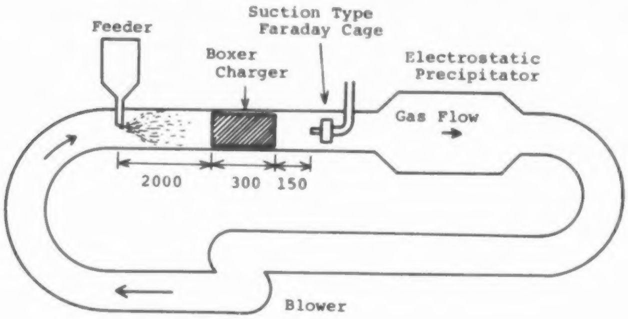

Figure 13 Race track system for powder charging tests (f_{ex}=1.5kHz; f=50Hz; d=120 mm; L=300 mm; v_g=0-16 m/s; T=20-200°C; air; calcium carbonate powder sample)

The charging performance of a BOXER-CHARGER for powder samples is tested in a race track system as shown in Figure 13 under the ordinary and back discharge conditions. Calcium carbonate powders are used for this purpose, as they provide an ordinary resistivity $\rho_d = 9 \times 10^9$ ohm-cm at 20 °C to cause no back discharge and an extremely high resistivity $\rho_d = 8 \times 10^{13}$ ohm-cm at 150 °C to cause a very severe back discharge. A BOXER-CHARGER of general purpose type (d) with the dimensions d = 120 mm and L = 300 mm is located inside of the inlet-duct. The frequencies of the exciting and main voltages are fixed at f_{ex} = 1.5 kHz and f = 50 Hz throughout these tests. The gas flow rate can be raised up to 3,000 m^3/h which produces the gas velocities v_g = 16 m/s at the inlet duct and v_g = 2 m/s in the precipitating zone. The powder sample is fed with a constant feeder at the upstream of the BOXER-CHARGER into the duct at a constant feeding rate to provide the mass loading of C_i = 0.2 - 1.0 g/Nm^3. No special means is taken to improve the dispersion of the powder into gas stream. The powder passes through the BOXER-CHARGER to be charged, and arrives at the precipitating zone where it is collected by a precipitator of tri-electrode type. The specific charge (charge-to-mass-ratio) of powders is measured at the downstream of the charger with a suction type Faraday-cage. The gas temperature can be raised by electric heater elements up to 200 °C. Ambient air is used throughout these tests. The particle size of the powder sample is fairly large, ranging from 5 to 50 μm with ca. 25 μm in average diameter. This produces a rather low magnitude of the powder specific charge, as it is inversely proportional to particle size.

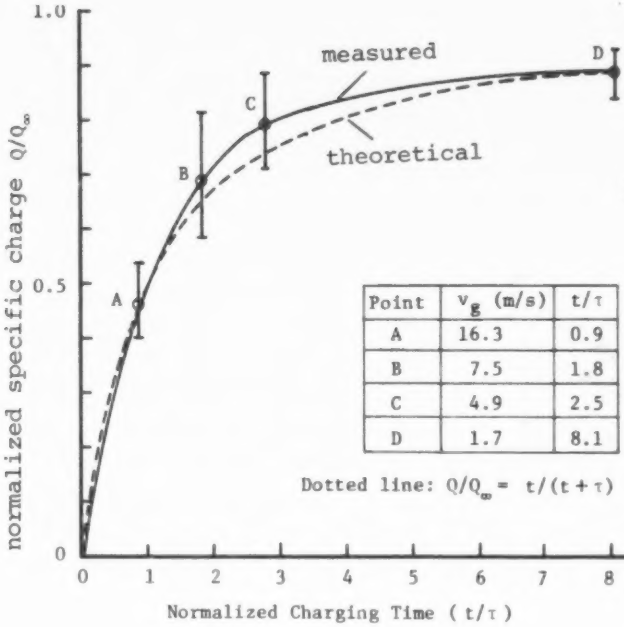

Point	v_g (m/s)	t/τ
A	16.3	0.9
B	7.5	1.8
C	4.9	2.5
D	1.7	8.1

Figure 14 Normalized specific charge of powder as a function of normalized charging time ((d); #1; d=120mm; E_O=5kV; τ=21ms; f_{ex}=1.5kHz; f=50Hz; calcium carbonate powder; $\rho_d=9\times10^9$ohm-cm; air at 20°C).

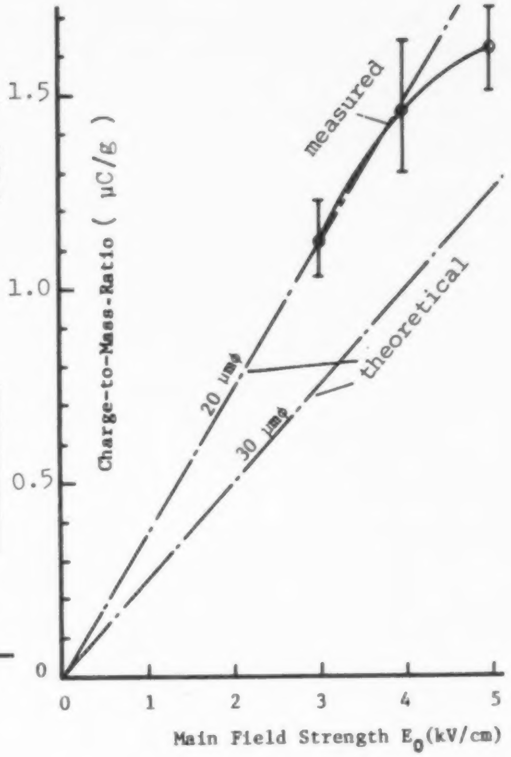

Figure 15 Specific charge of powder at room temperature ((d); #1; d=120mm; f_{ex}=1.5kHz; f=50Hz; calcium carbonate; $\rho_d=9\times10^9$ohm-cm; air at 20 °C).

4.2.1 Tests at room temperature. The wave form # 1 is used throughout these tests. At first, the dependence of powder specific charge on the charging time, t, is examined, by changing the duct air velocity, v_g. In this case, t = L/v_g. The operating condition of the BOXER-CHARGER is kept constant, so that its charging time constant, calculated from Equation (8) and Table 2, becomes constant at τ = 21 ms (see Figure 14). The measured values of the specific charge are normalized by its value at v_g = 1.7 m/s, which corresponds to t/τ = 8.1 to produce 89 % of the its saturation value if Equation (1) holds in this case. Then, these normalized values are plotted against the charging time normalized by the charging time constant τ = 21 ms.in Figure 14. The point D in the figure represents the reference value used for normalization. The dotted curve represents the theoretical curve according to Equation (1). A very good agreement between the two curves provide a support to the time increase in powder specific charge to follow the theoretical relation (1). Thus, the specific charge is expected to arrive approximately at its saturation value at t = 3 τ.

Then, the powder specific charge Q/M measured at a very low gas velocity v_g = 1.7 m/s (t/τ = 8.1 at E_o = 5 kV/cm) and different E_o is plotted against E_o in Figure 15. The measured values are expected to represent approximately the saturation values, and agree very well with the theoretical curve for 20 µm particle size. The theoretical curve for 30 μm particles is also depicted. As the average particle size of the powder sample used is ca. 25 μm, the results in Figure 15 lead to the conclusion that the BOXER-CHARGER can provide the theoretical saturation charge according to Equation (2), so far as no back discharge occurs.

4.2.2 Tests at 150 °C. The specific charge of the powder samples is further measured at 150 °C at which its resistivity becomes as high as $\rho_d = 8 \times 10^{13}$ ohm-cm to cause a severe back discharge in the ordinary dc corona The three wave forms # 1, # 2 and # 3 in Figure 10 are used in this case as the augmenting means of charge elimination. The measurements are made again at $v_g = 1.7$ m/s using $f_{ex} = 1.5$ kHz and f = 50 Hz. The results obtained are plotted in Figure 16. The normalized charging time, t/τ, lies in the range of 3 - 8 as shown in Table 4, so that the measured specific charges approximately represent their saturation values before back discharge begins to take place.

Table 4 NORMALIZED CHARGING TIME

wave form	E_o (kV/cm)			
	3	4	5	6
# 1	6	(8)	(11)	(13)
# 2	5	7	(8)	(10)
# 3	(2.5)	3.3	4	5

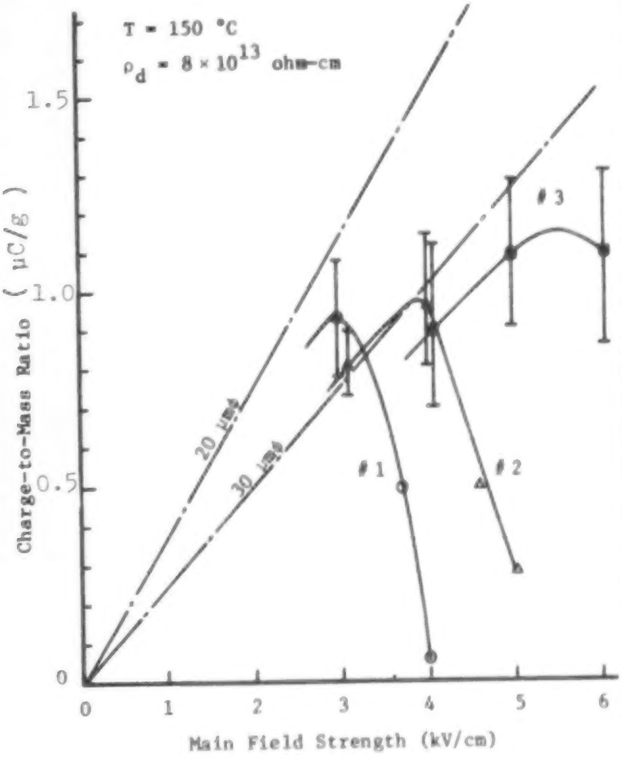

Figure 16 Specific charge of calcium carbonate powder at 150 °C ((d); d=120 mm; f_{ex}=1.5kHz; f=50Hz; $\rho_d = 8 \times 10^{13}$ohm-cm; air)

It can be seen that the specific charges rise at first proportionally with E_o in all of the wave forms. They arrive at their respective peaks, and then drop sharply because of back discharge initiation. Their values in the normal regions are slightly lower than the theoretically expected values. The wave form # 3 having the highest augmentation provides the highest peak value of the specific charge and the highest threshold of E_o for back discharge initiation. It should, however, be noted that the wave form # 1 with the lowest augmentation can provide a fairly high peak value of the specific charge, only 17 % lower than that given by # 3, although the threshold value of E_o for back discharge occurence is substantially lowered in # 1 wave form. It is concluded from Figure 16 that the BOXER-CHARGER can provide approximately the theoretical specific charge even to the extremely high resistivity powders up to a certain threshold field intensity of E_o in the range of 3 - 6 kV/cm if the appropriate augmenting wave form for charge elimination be used. The corresponding maximum specific charge for the present coarse particles with 25 μm average diameter is ca. 1 μC/g . In case of much amaller particle size, this magnitude is expected to rise in the inversely proportional relationship with its size.

5. PRECIPITATION TEST

Preliminary tests are made to examine the effect of the BOXER-CHARGER to enhance the collection performance of a precipitator located at its downstream using the race track system shown in Figure 13. Four units of a tri-electrode precipitator are connected in series as a collecting section, as shown in Figure 17. A dc high voltage of 27 kV is applied to the third electrodes, and a variable voltage is applied between the third and discharge electrodes to provide different current densities, J_{EP}, in the collecting electrodes. Tests are made at a room temperature T = 30 °C with the gas velocities v_g = 7.5 m/s in the BOXER-CHARGER section and v_g = 1 m/s in the precipitator section. The dimensions of the BOXER-CHARGER and its operating conditions are the same as in the preceding section. Calcium carbonate powders are used as the test sample which does not cause back discharge under the present room temperature. The magnitude of E_o in BOXER-CHARGER is kept fairly low at $E_o \leqq 4$ kV/cm. The mass concentration of dust at the outlet of the collecting section, C_o (mg/Nm^3), is measured with a continuous dust monitor "KONITEST" based on tribo-electrification. The mass concentration of dust at the inlet, C_i, is kept at 2 g/Nm^3. The KONITEST is calibrated with a glass filter for the uncharged calcium cabonate powders used in the present tests. It shows the blanc emission level C_i = 890 mg/Nm^3 when both the BOXER-CHARGER and the collecting section are separated from the voltage sources. Since mechanical collection also occurs in the collecting section, this blanc emission level is used as the reference emission level to indicate only the electrical effects, and the mass penetration of dust, C_o (mg/Nm^3), under different operating conditions is expressed in a percent ratio as 100 (C_o/890).

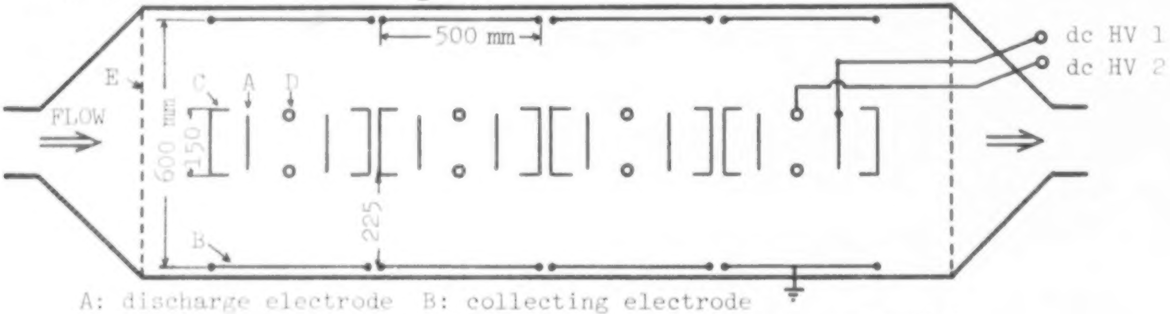

A: discharge electrode B: collecting electrode
C: third electrode D: shielding electrode E: perforated plate

Figure 17 Tri-electrode precipitators used as a collecting section in the race track system.

Figure 18 shows the results obtained at different values of E_o for different precipitator current densities J_{EP}. The penetration lowers with increasing E_o, and its reduction becomes 30 - 50 % of the initial penetration for each value of J_{EP} at E_o = 4 kV/cm. The results at E_o = 4 kV/cm are replotted against J_{EP} in Figure 19, which clearly shows a substantial decrease in penetration caused by the BOXER-CHARGER at each precipitator current level. The collection efficiencies shown in Figures 18 and 19 are not the overall efficiencies, but those resulted by the electrical effects based on the reference emission level as described above, i.e. (1 - penetration). It should be noted that

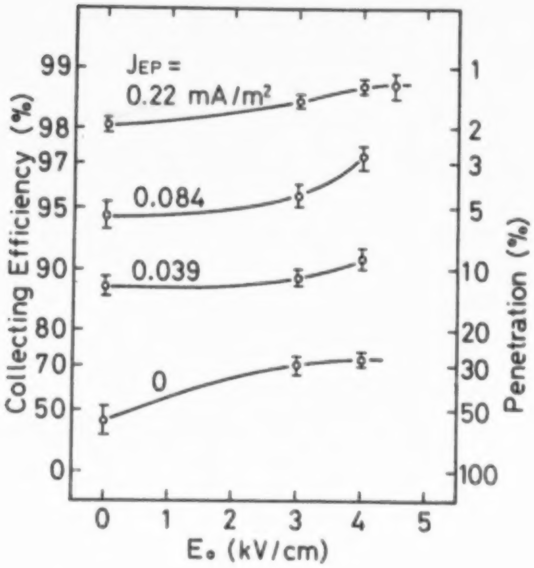

Figure 18 Dust penetration vs. E_o. (air at 30 °C)

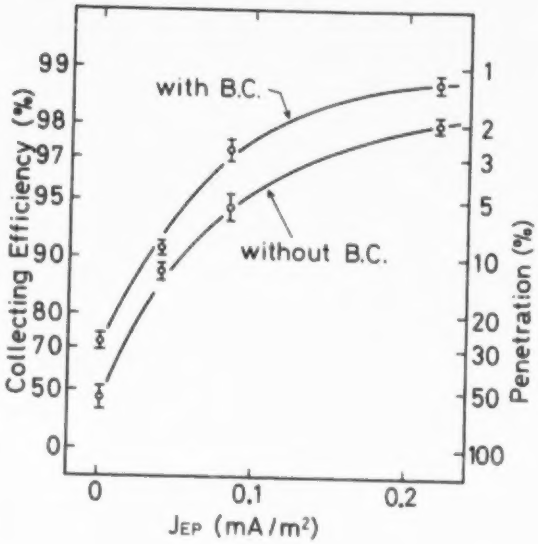

Figure 19 Dust penetration vs. J_{EP}. (E_o = 4 kV/cm; air at 30°C)

"KONITEST" monitor produces an error reading for the already charged particles because of its principle, and that this error in this case is expected to be an over reading. This means that the penetration decrease in the charged conditions may be higher than that indicated in Figures 18 and 19. This rough measuring means is used primarily for the purpose of quick examination at the present stage of tests, and the more exact measurements are being undertaken.

It can be concluded from the present tests that the BOXER-CHARGER evidently enhances the collection performance of the succeeding precipitation section.

6. CONCLUSION

The performance of BOXER-CHARGER as a precharging means is tested in detail, and the following conclusions are derived:

(1) BOXER-CHARGER has a sufficiently high charging performance to be used as a precharger of an electrostatic precipitator. The magnitude of the average operating field intensity in its charging space can be made as high as 8 kV/cm in air at room temperature and normal pressure. Its operating current density amounts to 60 - 90 % of the space-charge limited current in a parallel plane system, which is one order of magnitude higher than the current density obtainable in the ordinary dc corona system. As a result, its charging time constant becomes very low at ca. 5 ms. This produces a high charging speed so as to enable the use of the BOXER-CHARGER inside the inlet duct of a precipitator.

(2) BOXER-CHARGER can provide a sufficiently large quantity of charge even to the extremely high resistivity powders with more than 10^{13} ohm-cm resistivity, without causing back discharge. It can be operated at the main

field strength of 6 kV/cm at 150 °C, even when its electrodes are completely covered with the very high resistivity powder deposit with 8×10^{13} ohm-cm resistivity. Back discharge is avoided automatically by the inherent charging mechanism of BOXER-CHARGER , such that the plasmas produced on the electrode assemblies for charging purpose eliminate at the same time the charge accumulated on the high resistivity deposit covering the electrodes in each charging cycle.

(3) This charge elimination ability can be augmented easily by the use of an additional excitation of the electrode assemblies at zero main field and the reduced excitation period.

(4) The use of a low exciting frequency $f_{ex} = 1.5$ kHz and a low main voltage frequency $f = 50$ Hz is acceptable, which enables a large cost reduction in the power pack of BOXER-CHARGER.

(5) The use of a BOXER-CHARGER enhances the collection performance of a precipitator installed at its downstream.

(6) BOXER-CHARGER can be installed not only inside the inlet duct of a precipitator, but also within its casing in front of each collecting field, because its length in the gas flow direction can be made very small when the gas velocity is very low in the range of 1 m/s.

From these inherent advantages of BOXER-CHARGER, it is expected that it can be used also for the retrofit purpose of an existing precipitator or other kind of dust collector to increase its overall collection performance.

ACKNOWLEDGEMENTS

The authors are indebted to their co-workers, Mr. K. Akutsu and Mr. M. Washizu for their great help and valuable discussions.

REFERENCES

1. Masuda, S., M. Washizu, A. Mizuno and K. Akutsu. BOXER-CHARGER - A Novel Charging Device for High Resistivity Powders. Record of IEEE/IAS 1978 Annual Meeting (Tronto, Canada), p. 16 (October, 1978).
2. Masuda, S. and M. Washizu. Ionic Charging of A Very High Resistivity Spherical Particle. Jounal of Electrostatics, 6 (1979) p. 51.
3. Pauthenier, M.M. and M. Moreau-Hanot. La Charge des Particules Spherique dans un Champ Ionise. J. Pysique Radium, 3 (1932) p. 590.

PRECIPITATOR ENERGIZATION UTILIZING AN ENERGY CONSERVING PULSE GENERATOR

H. Hoegh Petersen
F.L. Smidth & Co.
77, Vigerslev Allé, DK-2500 Valby
Copenhagen, Denmark

Preben Lausen
High Voltage Laboratory, Building 329
Technical University of Denmark
100, Lundtoftevej, DK-2800 Lyngby
Copenhagen, Denmark

ABSTRACT

The performance of a conventional two-electrode type precipitator collecting high resistivity dust can be improved by pulse energization. Pulses of a suitable duration and repetition rate superimposed on the DC voltage permit higher peak-voltage without sparkover, improve particle charging and current distribution, and allow independent regulation of the precipitator voltage and current. A considerable quantity of energy, however, is required for each pulse to charge the precipitator to the pulse voltage level. For high pulse voltages only a minor part of this energy is necessary for the discharge current in the precipitator. For reasons of economy, the recovery of the energy stored in the precipitator capacitance during each pulse is therefore extremely important for pulse energization of large precipitators. An energy conserving pulse generator with pulse transformer, a pulse initiating switch element, and a feed-back diode for the energy recovery is described. The design and the instrumentation of a pilot precipitator specially developed for the comparison of different kinds of precipitator energization are outlined. The ability of the applied pulse energization system for controlling the corona discharge current independently of the precipitator voltage is demonstrated. Further, results from field tests showing the performance of the system under operating conditions are presented.

PRECIPITATOR ENERGIZATION UTILIZING AN ENERGY CONSERVING PULSE GENERATOR

INTRODUCTION

Pulse energization for improvement of the performance of a precipitator was first investigated by H.J. White about 30 years ago. It has since been further examined by a number of investigators in U.S.A., Europe, Australia, and Japan.

The advantages claimed for pulse energization in comparison with conventional DC-energization are:

- Higher peak voltage without excessive sparking, and therefore improved particle charging in accordance with the classical theory for particle charging.
- More effective extinguishing of sparks and better suppression of insipient back corona.
- By variation of the pulse repetition frequency and pulse amplitude the discharge current can be controlled independently of precipitator voltage. This allows reduction of the discharge current to the back corona threshold limit for a high resistivity dust without reducing the precipitator voltage.
- With short duration pulses the corona discharge takes place well above the corona onset level for constant DC voltage and is suppressed during the remaining part of the pulse by space charges. This results in a more uniformly distributed corona discharge along the discharge electrode.
- Corona discharges from short duration pulses are less influenced by variations in gas and dust conditions. This improves the internal current distribution of a separately energized field.
- Corona discharges are obtainable from surfaces with larger diameter curvatures. This permits the use of large diameter discharge wires, or rigid type discharge electrodes with comparatively short and blunt tips, reducing the risk of discharge electrode failures.
- Permits a higher power input and thereby improves precipitator performance.
- Increases particle migration velocity, particularly for high resistivity dusts, permitting reduction of the collection area for new installations or improvement of the efficiency of existing installations without increase of the collection area.

Utilization of pulse energization on a commercial scale, however, has not been realized until now, mainly because of problems connected with energy requirements and pulse generator design. A pulse energization system solving these problems is described here. Further, results from investigations carried out to evaluate the practical value of the system are presented.

PULSE ENERGIZATION PRINCIPLES

Two-Electrode Systems

In the pulse energization development work carried out by White and Hall around 1950 a high-power pulse generator, supplying high-voltage pulses in the order of 100 microseconds' duration to a conventional two-electrode system precipitator through a hold-off diode, was used.[1] The electric energy stored in the capacitance of the precipitator at the crest value of the pulse maintained the corona current during the period between the pulses. The pulse voltage therefore had a fast rise and a slow decay and somewhat resembled a sawtooth wave shape in form. The development work was brought to full scale field test with a prototype pulse generator. The lack of reliable high-power switch elements, however, then prevented commercial development.

The later advent of high-power electronic switch elements created renewed interest in pulse energization. The Environmental Protection Agency in 1969 thus sponsored a pulse energization development and field test program.[2] However, only the first phase of this program, which was based on the earlier work of White and Hall, was completed.

One of the problems in pulse energization is the amount of energy required for repetitive charging of a precipitator to a high pulse voltage level. An interesting solution of this problem has been described by Milde[3]. High voltage pulses of sufficiently short duration to charge only a small portion of the precipitator at any given instant of time are superimposed on an operating DC voltage. The very narrow pulses propagate as travelling waves along series-connected discharge wires or discharge wire systems, sequentially charging these. Hereby is obtained an energy saving in comparison with pulse energization systems where the total precipitator capacitance is charged simultaneously and the stored energy is dissipated between pulses either in the precipitator [4], or in a pulse forming network [5]. In the energy conserving principle described here, the saving is obtained by returning the energy stored in the precipitator to the pulse generator.

Three-Electrode-Systems

Lüthi[6] introduced a pulse system with an auxiliary electrode in the vicinity of the discharge electrode. With this third electrode it was possible to create a uniform field with a high sparkover level between third electrode and collection electrode, and therefore high charging and collecting field strengths in the main field. The corona-creating pulse field was produced between the discharge electrode and the third electrode making the corona discharge almost independent of the main field. The corona current could be regulated by the pulse voltage as well as by the pulse repetition frequency. With this system Lüthi obtained independent regulation of the current density and the charging and collecting field strengths in laboratory precipitator experiments, achieving more favourable electrical precipitator energization with high resistivity dusts. Pulse widths from 1 to 50 μs were used, and the high ion concentration in these short duration corona discharge pulses was shown to cause sufficient expansion of the ion cloud to ensure a reasonably good current distribution on the collection electrode in spite of the uniform main field. According to Lüthi, the capacity of the high resistivity dust layer on the collection electrode smoothed the pulse current flow through the dust layer sufficiently to avoid back ionization.

Masuda et al.[7] improved the three-electrode system by introducing a DC bias-voltage between the discharge electrode and the third electrode. The bias-voltage maintains the potential of the discharge electrode in the pulseless period at a level ensuring that no corona discharge occurs between pulses, also with the gap between discharge electrode and third electrode increased to a practical level of 10 cm. The bias-voltage also enables the use of half or full wave AC-voltage. Large scale installations using this latter mode of energization are today in operation in Japan.[8]

To improve the distribution of the current density in the dust layer on the collection electrode in the three-electrode system Penney and Gelfand[9] have proposed a special third electrode design in combination with a lowering of the potential of the third electrode during the corona pulse.

GENERAL PRINCIPLE

The system described here is used with conventional two-electrode type precipitators. Short duration high voltage pulses are repetitively superimposed on an operating DC voltage, refer Figure 1. The pulse duration is within the range 50 - 200 µs, and pulse repetition frequencies from 25 to 400 pulses per second are used.

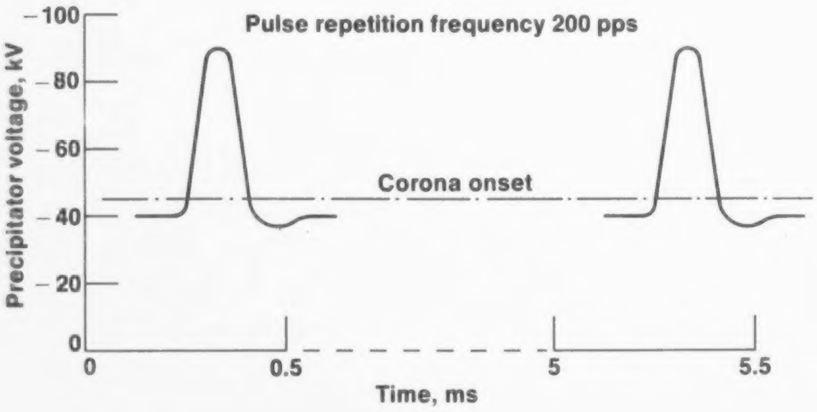

Figure 1. Voltage wave form for pulse energization.

It is characteristic of the operation of the system that the DC voltage is maintained slightly below the corona onset voltage. The object is to extinguish the corona discharge completely after each pulse. This allows full control of the discharge current by means of the pulse repetition frequency as demonstrated later.

Further, the extinction of the corona discharge after each pulse combined with suitably long intervals between the pulses allows the DC field to remove the ion space charge from the interelectrode spacing, before the next pulse is applied, permitting high pulse peak voltages without sparking.

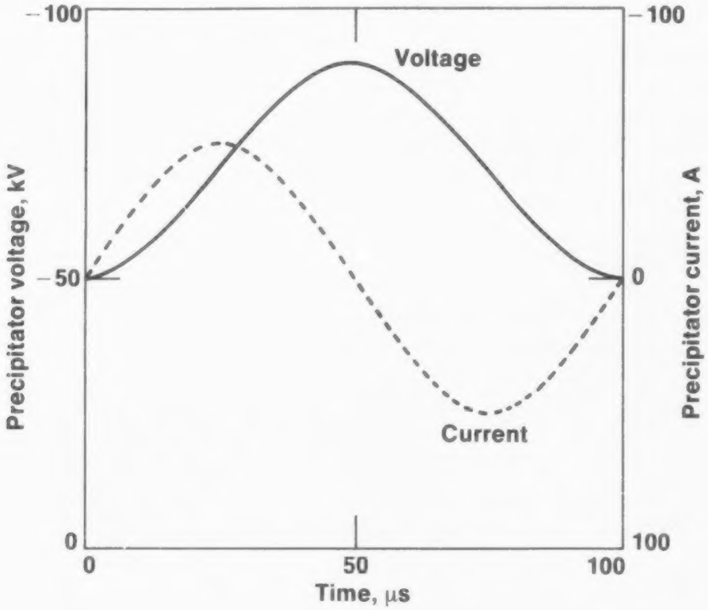

Figure 2. Ideal wave forms of precipitator current and voltage.

Figure 2 idealized shows the precipitator pulse current and voltage. During the first half of the pulse time a negative current flows from the later described pulse generator to the precipitator, charging the precipitator capacitance from the operating DC voltage level to the pulse voltage peak level. For high pulse voltages only a minor part of this charge is emitted as corona discharge during the pulse in order to maintain a collection plate current density of 0.1 - 0.2 mA/m^2. The remaining, and major part of the charge is returned to the generator as a reversed current flow during the second half of the pulse time, thus bringing the precipitator voltage back to the operating DC voltage level.

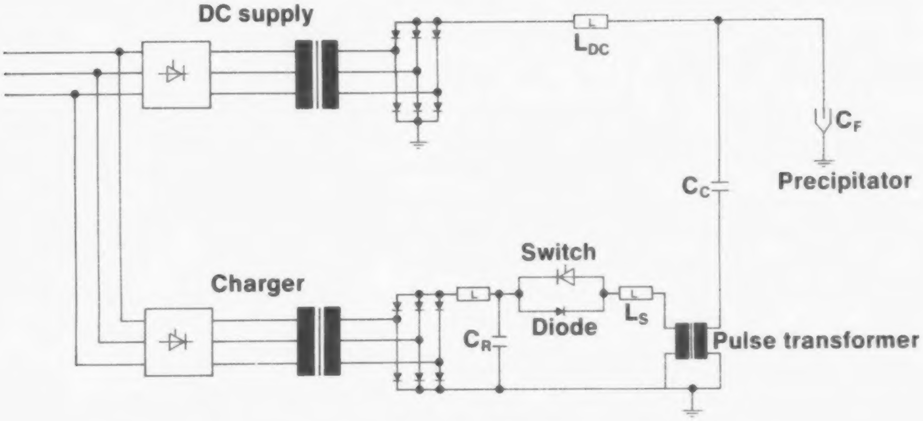

Figure 3. Energy conserving pulse generator principle.

A basis diagram of the energy conserving pulse generator system[10,11] is shown in Figure 3. The DC operating voltage is maintained by a DC supply with a blocking inductor L_{DC} preventing the pulse voltage from entering the supply. A coupling capacitor C_C blocks the DC operating voltage from the pulse transformer. The pulse circuit includes a charger supplying a storage capacitor C_R, a thyristor switch, a feed-back diode, and a series inductance L_S. The storage capacitor C_R, the series inductance L_S together with the pulse transformer leakage inductance, the coupling capacitor C_C, and the precipitator capacitance C_F forms a series oscillatory circuit.

The storage capacitor C_R is charged to a controlled DC level by the charger. The thyristor switch is turned on, and the precipitator represented by the capacitance C_F is charged to the maximum pulse voltage level by the first half-period of the oscillatory current. Because of the series oscillation, the energy supplied to C_F is returned to C_R through the feed-back diode by the current in the second half-period. During this interval, the thyristor switch is turned off and the current in the pulse circuit is blocked until the next ignition of the thyristor switch. The energy is stored in C_R during the interval between the pulses and is used for the next pulse.

Typically, an industrial precipitator has a capacitance of 40 - 50 pF per square meter collection area. Charging of this capacitance to a high pulse voltage level a large number of times per second without energy recovery would require a considerable quantity of energy. Depending on pulse voltage level and pulse repetition frequency, the charging energy might amount to several times the energy absorbed by the precipitator as useful corona discharge energy. For reasons of economy, recovery of the charging energy is consequently extremely advantageous in connection with pulse energization of large precipitators.

CURRENT-VOLTAGE RELATIONSHIP

The electrical parameters, as described by the corona current density at the collection electrode surface and the precipitator voltage, determine the precipitator performance.

For conventional DC energization, the relationship between the parameters mentioned above is usually presented as a current-voltage curve, showing average value of current density versus average value of precipitator voltage.

For pulse energization the current-voltage curves can be presented as average value of current density versus peak value of superimposed pulse voltage U_P for various pulse repetition frequencies. For such a set of curves, the operating DC voltage level U_{DC} and the pulse width are fixed. Figure 4 shows an example of such current-voltage curves obtained with a special pulse discharge electrode.

These current-voltage curves have been obtained under operation conditions with hot dustladen gas and with the DC voltage level set slightly below the corona onset voltage.

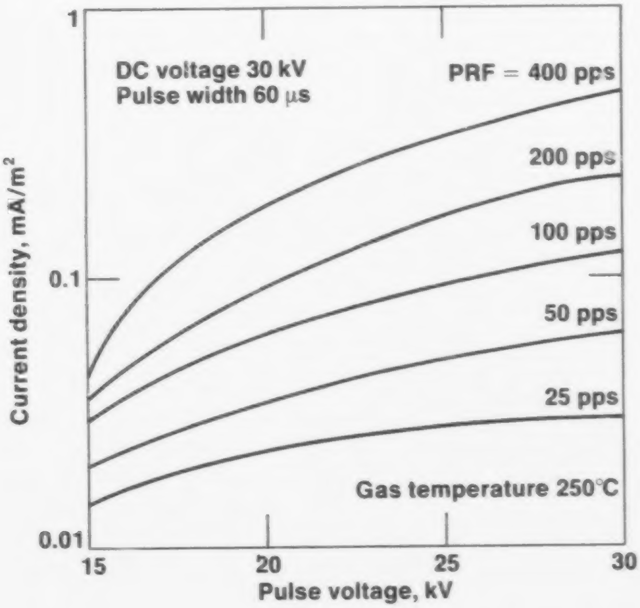

Figure 4. Current density versus pulse voltage with pulse repetition frequency PRF as parameter.

Alternatively, the same set of current-voltage curves can be presented as current density versus pulse repetition frequency for various pulse voltages as shown in Figure 5.

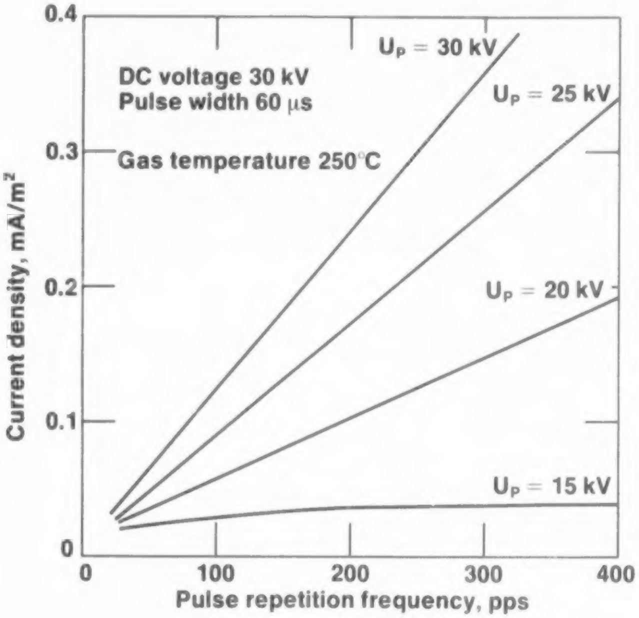

Figure 5. Current density versus pulse repetition frequency with pulse voltage U_P as parameter.

The curves show that, within wide limits, the precipitator current can be regulated independently of the precipitator voltage by variation of the pulse repetition frequency. A practical consequence of this is that it becomes possible to adjust the current to the limit for back ionization without reducing the precipitator voltage. This means more favourable electrical energization for high resistivity dusts than obtainable with conventional DC-energization, where the current cannot be regulated independently of the precipitator voltage.

DISCHARGE ELECTRODES FOR PULSE ENERGIZATION

Discharge electrodes for pulse energization must primarily have a geometry which, in combination with the collection electrodes used, will ensure suitable current-voltage curves for this particular mode of energization.

Further, the electrode geometry must produce a sufficiently high collecting field strength close to the surface of the collection electrode with the operating DC voltage maintained just below the corona onset voltage. Finally, the electrode geometry must ensure that the collecting field close to as well as the current distribution on the surface of the collection electrode are reasonably uniform.

These pulse discharge electrode requirements favour the use of rigid type electrodes with comparatively short and blunt tips. Further, such designs reduce the risk of discharge electrode failure and deterioration.

DOUBLE PIPE TEST PRECIPITATOR

A mobile, double pipe test precipitator in which the operation conditions of two parallel pipe precipitators can be kept identical during slipstream testing has been used for studying the differences between DC and pulse energization as well as the effect on precipitator performance of the different pulse energization parameters.

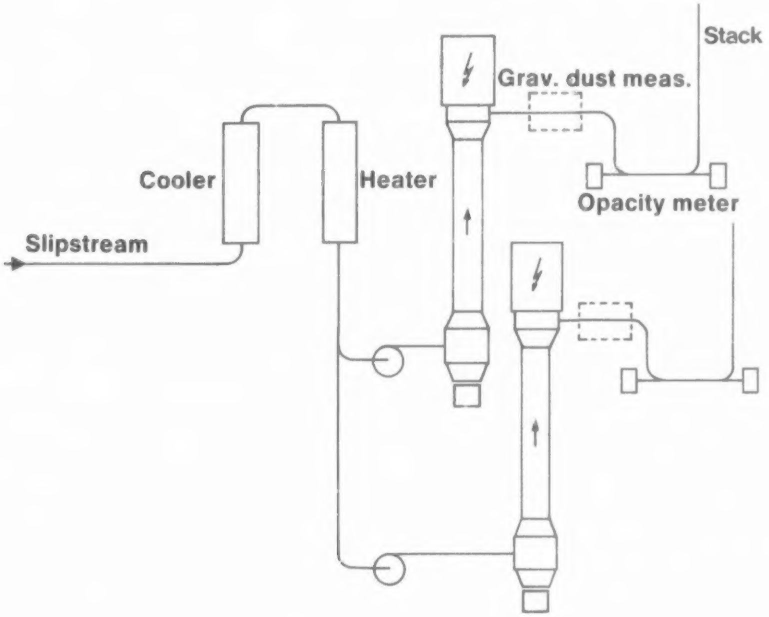

Figure 6. Schematic diagram of double pipe test precipitator.

Figure 6 shows a schematic diagram of the double pipe test precipitator. The gas slipstream from the main gas duct is fed through a conditioner and a heater to obtain the desired values of humidity and temperature. A carefully designed, adjustable splitter together with two independently controlled fans ensures an equal division of dust and gas between the two parallel precipitators. The temperature of the two precipitators is independently controlled by heating elements on the pipes.

The diameter of the precipitators is 250 mm and their effective length is 3.5 m. The main design criteria have been a collection efficiency at DC operation of about 99 %, a gas velocity of 0.5 - 2 m/s, an inlet dust concentration of maximum 50 g/Nm^3, and an operating temperature of maximum 400 °C.

The test precipitator has controls for the operation parameters and equipment for measurements of mechanical and electrical characteristics.[11] The collection efficiency is determined gravimetrically by measurement of the outlet dust concentration together with weighing of the dust collected in the hoppers. Opacity meters are inserted in the tubes leading from the precipitators to the stacks.

For measurement of the precipitator voltage a voltage divider is used, designed for a peak voltage of 120 kV and a frequency range from DC to 20 MHz. The current to the discharge electrode is measured at high potential by means of a shunt and a battery operated oscilloscope. The shunt is placed directly at the discharge electrode in the hot gas in order to eliminate the effect of leakage resistances and stray capacitances, refer the cross section of the pipe precipitator shown in Figure 7.

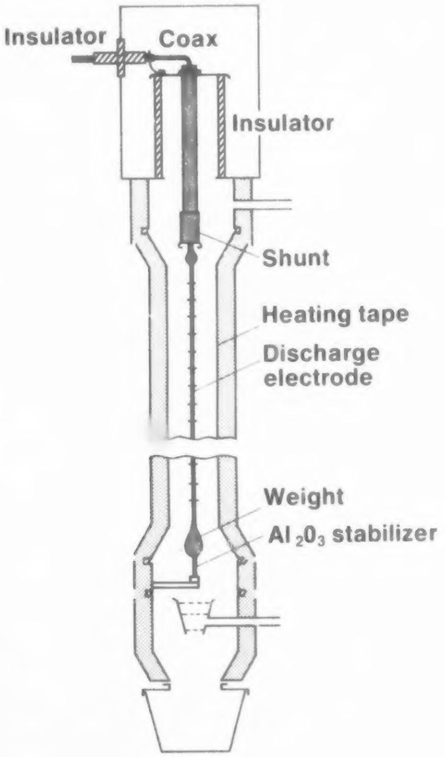

Figure 7. Cross section of pipe precipitator.

Further, the current flowing to the collection electrode part of the pipe precipitator can be measured separately at low potential. Also possible currents from the rod supporting the lower end of the discharge electrode, from the insulator housing, and from the hopper can be measured separately.

The total installation, including the high voltage power supplies and the control and measuring equipment, is placed in a 30 feet standard container for easy transport.

PILOT PRECIPITATOR FIELD TESTS

For a period of about one year and a half, the double pipe test precipitator was installed at a lime burning rotary kiln. The precipitator here dedusted a slipstream with a gas volume of about twice 200 m^3/h, taken from the 350 °C hot exit gases from the 290 t/24 h lime kiln.

The fuel used was a mixture of coal and oil, typically 60 % and 40 %, respectively, related to calorific values.

Typical pilot precipitator gas temperature was about 250 °C in order to obtain a high resistivity level, water content about 15 % moisture by volume, and dust concentration 25 - 40 g/Nm^3. Particle size median was 17 μm, and dust resistivity was 10^{11} - 10^{13} ohm·cm at 250 °C, refer Figures 8 and 9 showing dust particle size distribution and dust resistivity, respectively.

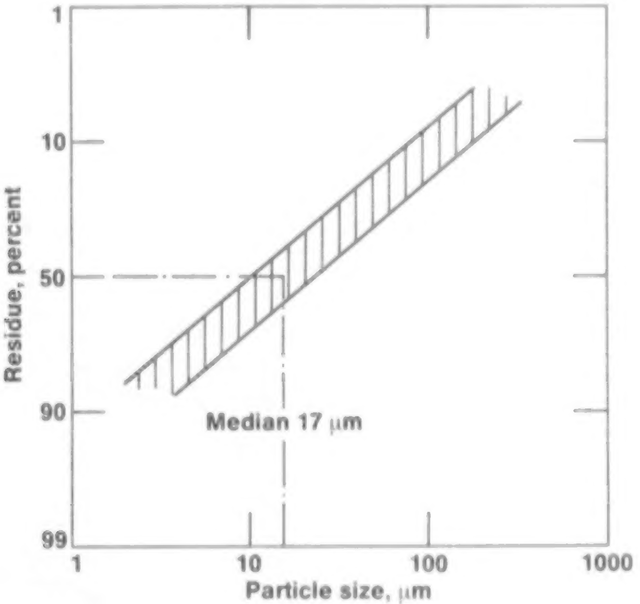

Figure 8. Particle size distribution of dust from lime kiln.

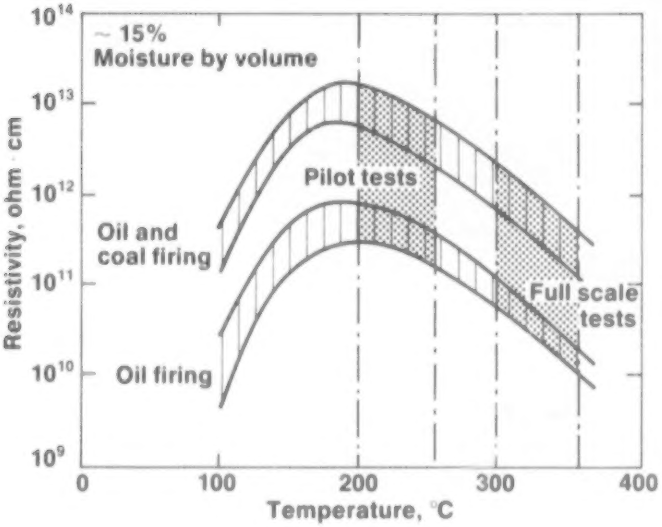

Figure 9. Resistivity of dust from lime kiln.

For the pulse energization tests the DC voltage level was usually set just below the corona onset in order to avoid corona discharge between pulses. DC corona discharges between pulses resulted in poor current control and deterioration of precipitator performance.

A great number of comparison tests were performed with various pulse energization parameters and with conventional DC operation as reference. The discharge electrode used in the DC reference precipitator was a 3 mm diameter wire. The comparison tests were performed simultaneously and with the same corona discharge current density (typically 0.1 mA/m^2 or 0.2 mA/m^2) in the two pipes. It was generally not possible to produce sparkovers in the precipitators with these current densities.

The precipitator efficiency and the w_k migration velocity were determined from measurements of the inlet and outlet dust concentrations and the gas volume flow rate. The w_k concept is useful, since the necessary precipitator volume is inversely proportional to w_k.

An improvement factor was defined as the ratio between the w_k values for pulse and for DC energization found for the same corona discharge current. As seen from the following table, the improvement factor was strongly dependent on the degree of back ionization as judged from resistivity measurements and the corresponding current-voltage curve for DC energization.

OPERATION CONDITION	w_k IMPROVEMENT FACTOR
Without back ionization ~ 10^{11} ohm•cm	1.2
Moderate back ionization ~ 10^{12} ohm•cm	1.6
Severe back ionization ~ 10^{13} ohm•cm	> 2

PILOT PRECIPITATOR LABORATORY TESTS

During another period of about one year, the double pipe test precipitator was used in a laboratory set-up comprising a gas burner, a dust feeder, and a steam generator. The dust used was from the earlier mentioned lime kiln, with particle size distribution and resistivity as shown in Figures 8 and 9.

The purpose of the laboratory experiments was to examine thoroughly the influence on the precipitator performance of pulse voltage level, DC voltage level, pulse repetition frequency, and pulse width, etc. The tests revealed that the pulse height is the most important factor influencing the dust loss. This is illustrated in Figure 10, which shows the relationship between collection efficiency and precipitator peak voltage for constant DC voltage and for various current densities.

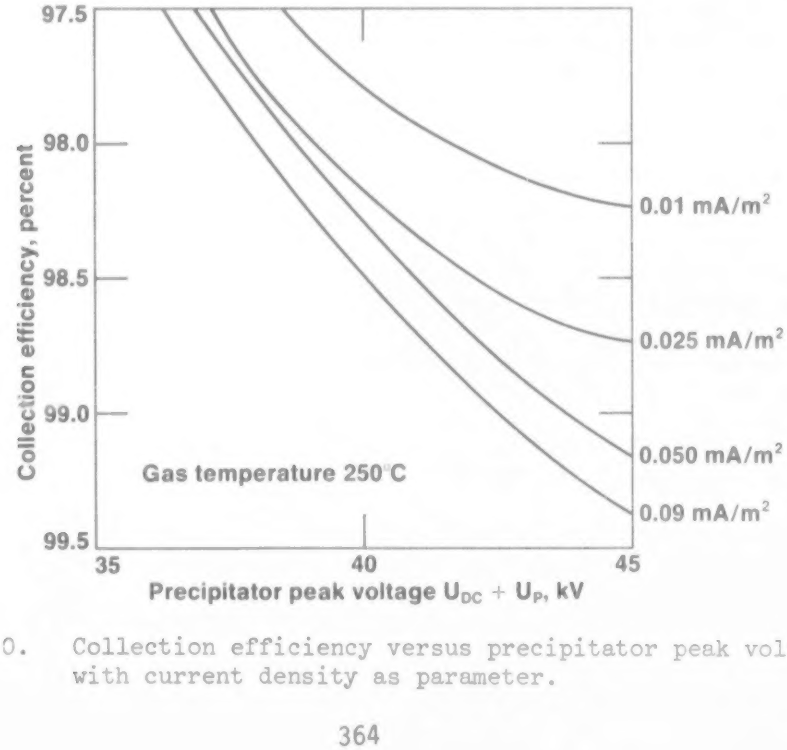

Figure 10. Collection efficiency versus precipitator peak voltage with current density as parameter.

The laboratory experiments further confirmed that the precipitator performance is less influenced by high resistivity dust with pulse energization than with DC energization. Increasing the dust resistivity to a high level by stopping the steam injection reduced the w_k value for the DC energized precipitator by a factor of about 3, while the w_k value for the pulse energized precipitator was only slightly reduced.

FULL SCALE TESTS

Full scale tests have been carried out for about one year on a precipitator dedusting the earlier mentioned lime kiln. The total collection area of the precipitator is about 1400 m^2, the duct width is 250 mm, and the discharge electrodes are of the conventional 2.7 mm diameter helical type. The gas velocity is about 0.6 m/s, giving a treatment time of 6 seconds.

The gas temperature in the precipitator is about 350 ^{o}C, the water content about 15 % by volume, and the dust load about 50 g/Nm^3. The dust resistivity varies from about 10^{10} to 10^{12} ohm•cm at 350 ^{o}C depending on raw materials and kiln operation, refer Figure 9.

The precipitator can be energized from either a pulse generator or a conventional DC power supply (single phase, full-wave raw rectified DC).

The sparking rate with this DC energization is in the order of 60 sparks per minute at an operating voltage of about 30 kV. With the pulse energization, the sparking rate is drastically reduced to a value of about one spark every 3 minutes for a sum of operating DC voltage and pulse voltage of about 60 kV. The installed pulse generator which was originally designed for a smaller precipitator cannot give sufficient pulse voltage to operate the precipitator at higher sparking rate where better use might be made of the possibilities of the pulse energization principle.

The full scale tests performed under these conditions have given w_k improvement factors of 1.3 - 1.4 thus confirming the w_k improvement tendencies found with the double pipe test precipitator.

A prototype of an automatic control, specially designed for pulse energization has been in operation at the above mentioned installation for about four months.

The automatic control equipment regulates the DC voltage level, pulse height, and pulse repetition frequency on the basis of criteria related to suppression of corona discharges between the pulses, the sparking rate, and the current density, respectively.

Further, the automatic control includes fast precipitator voltage recovery after sparkover, as necessary in order to fully utilize the pulse energization at high sparking rate. This is illustrated in Figure 11, which shows precipitator voltage recovery after sparkover. It is noticed that the operating DC voltage as well as the pulse voltage is recovered after approximately 20 ms.

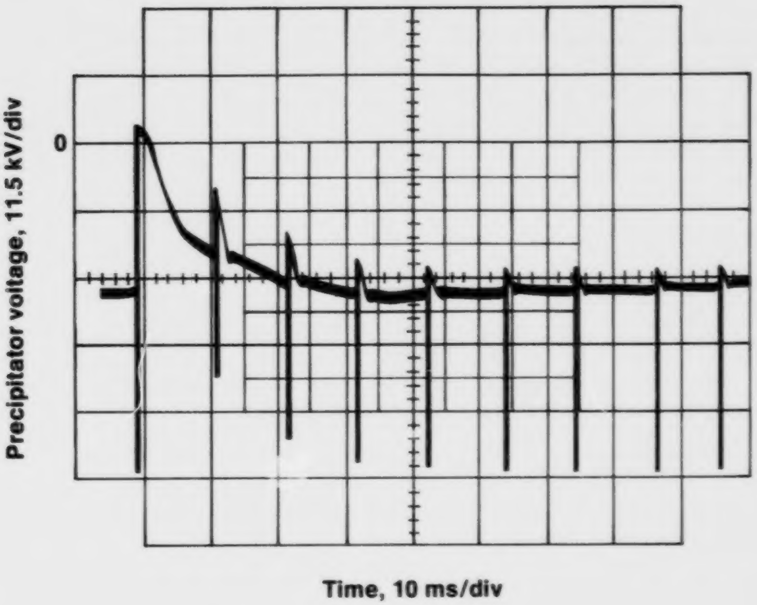

Figure 11. Precipitator voltage recovery after sparkover.

At present, experiments are being performed with the purpose of refining the control criteria and the control equipment. Further, endurance tests to check the reliability of the equipment are being carried out.

CONCLUSION

Short duration high voltage pulses are superimposed on an operating DC voltage by means of a pulse generator capable of conserving a predominant part of the energy stored in the precipitator capacitance at the crest of the pulse voltage, and not used by the corona discharge. The energy conservation is especially advantageous with high pulse voltages, high pulse repetition frequencies, and large precipitators. A pulse generator, based on pulse transformer and thyristor technology available to-day, has been developed, and has been in operation for about one year at a full scale precipitator installation. Further, a mobile double pipe test precipitator with equipment for measurements of mechanical and electrical characteristics has been built in order to study the differences between DC and pulse energization. The pilot precipitator tests, as well as full scale tests, have shown that by maintaining the DC operating voltage just below the limit for corona discharges between pulses it is possible to control the discharge current by means of the pulse repetition frequency, and it is further possible to operate at high precipitator peak voltages with a low sparkover rate. Regulation of the precipitator current independent of the precipitator voltage means more favourable electrical energization than obtainable with conventional DC operation, particularly for applications with high resistivity dusts.

Determination of precipitator efficiency and migration velocity w_k, performed on the double pipe test precipitator as well as on the full scale precipitator, shows substantial w_k improvements as compared to conventional DC energization for high resistivity dusts.

The w_k improvement factors show that the pulse energization system can be used successfully to improve the performance of existing precipitator installations having conventional discharge electrodes and operating with high resistivity dusts.

The test results further show that considerable reduction of the total collection area is obtainable for new high resistivity application precipitators utilizing specially designed pulse discharge electrodes.

Finally, the current control capabilities of this pulse energization system make it well suited for energization of the collection stage of a two-stage precipitator where effective control of a small discharge current for limitation of reentrainment is desirable.

For all these applications the energy conserving pulse generator system will be advantageous, particularly for large precipitators.

REFERENCES

1. White, H.J. A Pulse Method for Supplying High-Voltage Power for Electrostatic Precipitation. Trans. AIEE, Nov., 1952. p. 326-329.

2. Belco Pollution Control Corporation. Technical Description of the Belco Pulsed Power Supply. Environmental Protection Agency Contract CPA 22-69-143. 18 March, 1970.

3. Milde, H.I. Reduced Power Input for Improved Electrostatic Precipitation Systems. US Patent 4,133,649. Jan. 9, 1979.

4. Feldman, P.L. and H.I. Milde. Pulsed Energization for Enhanced Electrostatic Precipitation in High-Resistivity Applications. Symposium on the Transfer and Utilization of Particulate Control Technology. Denver, Colorado. July, 1978. Conference Records Vol. 1, p. 253-274.

5. Fuchs, H. Electronic Dust Separator System. US Patent 3,981,695. Sept. 21, 1976.

6. Lüthi, J.E. Grundlagen zur elektrostatischen Abscheidung von hochohmigen Stäuben. Diss. Nr. 3924. ETHZ, Zürich. 1967.

7. Masuda, S., I. Doi, M. Aoyama, and A. Shibuya. Bias-Controlled Pulse Charging System for Electrostatic Precipitator. Staub-Reinhalt. Luft 36. No. 1, January 1976. p. 19-26.

8. Masuda, S. Novel Electrode Construction for Pulse Charging. Symposium on the Transfer and Utilization of Particulate Control Technology. Denver, Colorado. July 1978. Conference Records Vol. 1, p. 241-251.

9. Penney, G.W. and P.C. Gelfand. The Trielectrode Electrostatic Precipitator for Collecting High Resistivity Dust. J. Air Poll. Control Assoc. 28, No. 1. January 1978. p.53-55.

10. Kide, L. Electrostatic Precipitator Arrangements. US Patent 4,052,177. Oct. 4, 1977.

11. Lausen, P., H. Henriksen, and H. Hoegh Petersen. Energy conserving Pulse Energization of Precipitators. To be presented at IEEE/IAS 1979 Annual Meeting, Cleveland, Ohio. October 1-4, 1979.

PRECHARGER COLLECTION SYSTEM - DESIGN FROM THE LABORATORY THROUGH FIELD DEMONSTRATION

Morey A. Nunn
Lodge-Cottrell-Dresser
Houston, Texas 77002

Duane H. Pontius
Southern Research Institute
Birmingham, Alabama 35205

J. H. Abbott and L. E. Sparks
Industrial Environmental Research Laboratory
U.S. Environmental Protection Agency
Research Triangle Park, North Carolina 27711

Abstract

Southern Research Institute with the support of the EPA has developed a two-stage precipitator which has shown encouraging results in the laboratory. The two-stage ESP consists of a precharger for the first stage and a conventional ESP operating at low current densities. Lodge-Cottrell's assistance was enlisted to design and supply a 1060 m^3/min precharger collector system. The design was to be based on the functional parameters arrived at from the laboratory tests. In addition to the basic requirements, the system was designed utilizing features that could be readily incorporated in systems treating gas volumes of commercial size.

PRECHARGER COLLECTION SYSTEM - DESIGN FROM THE LABORATORY THROUGH FIELD DEMONSTRATION

INTRODUCTION

Southern Research Institute, with the support of the Particulate Technology Branch, Industrial Environmental Research Laboratory, Research Triangle Park, U.S. Environmental Protection Agency, has been investigating a two-stage approach to a solution of the problem of precipitating high resistivity particulate materials. In a two-stage ESP, particle charging occurs principally in the first stage or precharger. Particle collection occurs in the second stage, or collector, which would be designed to operate at a relatively low current density and high electric field strength. Thus it is in the precharger that back-corona poses the greatest difficulty.

The precharger design for suppression of back-corona is based on a simple wire-plate electrode geometry, with the addition of perforated screen electrodes parallel to the plates, as illustrated in Figure 1 (Patent Pending - U.S. Serial No. 882,673, March 3, 1978). A high voltage applied to the corona wire will bring about corona conduction. In general, part of the current will go to the plate and part to the screen, depending on the relative potentials at each. If the plate is grounded the screen is set at a potential having the same polarity as that of the corona wire; ions moving toward the plate will tend to be repelled away from the screen. If the magnitude of the potential at the screen is great enough, the screen current may go to zero, while a considerable corona current passes through the openings in the screen proceeding from the corona wire to the plate.[1]

After successful confirmation of the theory in the laboratory, the Southern Research Institute decided to solicit the assistance of a precipitator manufacturer to design, fabricate, and erect a pilot precharger and precipitator. Lodge-Cottrell was awarded the contract for this work in October 1978.

DESIGN OBJECTIVES

The conventional design philosophy was modified in response to two general considerations. First, the unusual nature of the precharger requires special treatment due to the clearances associated with two nested, high voltage electrode systems, and second, provisions for adjustments and modifications are desirable because of the developmental aspects of the program. An inflexible design would allow no room for correcting nonoptimum parameters. In addition to the basic requirements, the system was to be designed utilizing features that could be readily incorporated in systems treating gas volumes encountered in commercial operation. For example, the use of insulating spacers between the screen and plate electrodes in the original prototype were found to be impractical, and the techniques used for electrical isolation of the three separate electrode systems were not readily adaptable to scaling up. A second generation device designed by the cooperative efforts of Southern Research Institute and Lodge-Cottrell incorporated a more rugged design philosophy along with many of the electrical suspension features planned for the pilot demonstration unit. This device performed at least as well as the original prototype, thus confirming the overall design strategy.

DESIGN CONCEPTS

Design of the pilot pr-charger began by utilizing design concepts evolved from Lodge-Cottrell's precipitators. Examples of this include:

1) "Lead thru" insulators with the support insulators located on the roof out of the flue gas.
2) Supports for the collectors, screens, and discharge electrodes isolated from the casing with springs.
3) Methods for guiding and adjusting the alignment to obtain the initial electrical clearances and maintain them.

The first problem encountered when reviewing the required equipment was available space. The earlier 28 m^3/min units had not required the support system necessary for the larger unit. The necessity of maintaining electrical clearances and the provisions for erecting the unit grew in complexity.

This led to the choice of stacking the discharge and screen electrode support frames, separated by insulators. A final arrangement of the hardware inside the unit, which maintained the necessary electrical clearances and could be erected efficiently, was developed after extensive layout work (Reference Figure 2). The arrangement drawings were reviewed with the personnel involved in constructing the smaller unit and it was decided to provide additional adjustments.

The next design problem was in maintaining electrical clearances between the screen and the collector plate. The collectors are a nominal 2.16 m in width and 3.12 m in height. The height to width ratio was of concern and a rib was added to the plate section to increase its rigidity. The screen to plate clearance was increased by 6.4 cm because of fabrication and erection tolerances.

The rappers used with the precharger are electromagnetic vibrators. They were chosen because of the ease with which the intensity can be varied. The main concern was effective rapping of the screen. It is difficult to transmit vibration through the cross section of the screen and it was important to keep the screen as clean as possible without reentrainment of the dust. Spring diameters and heights were selected on the basis of availability, so that the spring rate could be easily changed.

As with any type of electrostatic precipitator, good gas distribution and elimination of gas sneakage is important. A 1/2-scale model of the precipitator and precharger was built and gas surveys were performed (Figure 3). Baffles were added to confine the flue gases within the treatment areas and gas distribution devices were installed in the nozzle to obtain even distribution at the inlet of the precharger.

CURRENT STATUS - CONCLUSION

The precharger concept has been tested with regard to electrical characterization, particle charging effectiveness, and its effect on the collection efficiency of a two-stage system with various electrode configurations in the downstream collector stage. These tests have been carried out on laboratory pilot scale systems, both at Southern Research Institute and at the U.S. Environmental Protection Agency's Industrial Environmental Research Laboratory, Research Triangle Park. The devices used in these tests were designed to handle nominally 42 m^3/min, and redispersed fly ash was used under controlled temperature conditions where the resistivity was maintained in the range of 10^{11} - $5x10^{12}$ohm cm. Some of the results of the tests were reported in another paper presented at this conference. For tests under actual flue gas conditions, another 42-84 m^3/min unit has been fabricated for use in the field at a coal-burning power plant that produces a high resistivity fly ash. The small pilot scale field evaluation is scheduled to take place later this summer.

The pilot testing program carried out thus far has provided valuable information concerning both the feasibility of the concept and the nature of the problem areas to be considered in the design of the larger pilot demonstration unit.

A site has been selected for installing and testing the large pilot demonstration unit. The principal requirement of the test site was that the fly ash resistivity be high enough to represent a significant challenge for the device - on the order of 10^{11} - 10^{12}ohm cm. The design work is approximately 90% completed at this time, and the fabrication phase will begin within the next several months.

The ultimate goal of this program is to demonstrate that the precharger concept under development can perform under realistic field conditions, and to determine to what extent benefits may accrue from this new technology in the form of improved precipitator collection efficiency and/or reduced cost of pollution control equipment. If proven feasible, the precharger could be useful, not only as part of new, integrated two-stage ESP system, but also because of its small size along the direction of gas flow, as a retrofit to existing precipitators where dust resistivity is significant problem.

Reference

Pontius, D. H., and L. E. Sparks. A novel Device for Charging High Resistivity Dust. APCA Journal, Vol. 28, No. 7, July, 1978.

TOWARDS A MICROSCOPIC THEORY OF ELECTROSTATIC PRECIPITATION

BY

C.G. Noll, T. Yamamoto
United McGill Corporation
Groveport, Ohio 43125

ABSTRACT

The statistical mechanics of particles at the surface of a dust deposit are presented as a step towards a microscopic theory of electrostatic precipitation. The paper consists of three major divisions: (I) Field induced entrainment, (II) Particle condensation at the surface, and (III) Hydrodynamic limits on precipitation.

In Part I, the entrainment of dust from surfaces by electrostatic forces was considered as a simple Markov process. A choice of x^{-1} for the dependence of the adhesive potential (van der Waals particle attraction) led to an exponential emission rate in the Kramers-Chandrasekhar approximation. This result suggested a simple experimental procedure for determining the adhesive properties of the dust. In addition it was found that both thermal Brownian and particle-deposit collisions contribute to the entrainment.

In Part II, the precipitation problem was discussed in terms of a two-dimensional Ising model. The Markovian assumption demanded that the efficiency of the EP geometry be divided into a product of factors depending on particle migration and condensation in the two-dimensional surface. From this perspective a new collection criteria was established and the importance of particle collisions was emphasized.

Finally, in Part III the role of bulk fluid flows in particle condensation and migration was addressed. The superficial gas flow and secondary flow were found to introduce anisotropy into the Ising lattice and also to enhance the mean particle energy at the surface. The Navier Stokes Equation was numerically integrated for the case of a wire-plate type corona. Plots of the stream function and gas velocity profile were presented and these suggested the existance of a lower limit on the shear stress that acts on surface particles.

TOWARDS A MICROSCOPIC THEORY OF ELECTROSTATIC PRECIPITATION

INTRODUCTION

A property common to all electrodeposition is the growth of a deposit. Hence, whether we are concerned with solid or liquid deposition, a theory of the growth process is extremely desireable.

The complexity of the usual problem, makes it necessary to formulate models that attempt to describe the growth process at different levels. Macroscopic models are in abundance and these can be used to predict the number of particles or thickness of a deposit at time t. Several representative models are listed in the References. (Cooperman (1977)[1], Gothard (1977)[2], Robinson (1967)[3]) Should an adequate model of this type be formulated, it then becomes necessary to construct models which deal with the physical and chemical properties of the particulate that might be responsible for generating the observed collection. Models of this type might be called microscopic.

Most of the work on electrostatic deposition has been primarily concerned with the development of deterministic models of the macroscopic type. The emphasis has been directed towards particle transport in the gas stream and such parameters as "effective migration velocity" and diffusion coefficient have been introduced. In this approach a functional equation (differential or integral equation, etc.) for the number of particles in the layer at time t, say n(t), is derived on the basis of some postulated mechanism. (The postulated mechanism may or may not reflect the internal processes responsible for changes in layer thickness). This deterministic equation, together with boundary conditions, is then solved to obtain n(t). The operable results are expressed as an efficiency. The major problem with such treatments is that they are deterministic. One obtains the result that the dust layer thickness at a given time t will always be the same if the initial conditions are not changed. Since macroscopic models do not take into consideration the large number of random or chance factors that can influence the growth of the deposit, a multitude of empirical constants must be introduced.

It is the contention of the authors that an approach to the microscopic model must be made through an understanding of the statistical mechanics and the surface physics of the particles at the dust layer/gas stream interface.

The combined process of particulate deposition and adhesion is known to be aided by an electric field (Penney and Klingler (1962)[4]). However, adhesively bound particles are also known to be entrained from a surface by an electric field (Zimon (1969)[5]). Thus, a knowledge of the steady state behavior of the deposit, conditioned by these competing mechanisms, is crucial to the formulation of the microscopic model.

Part I of this paper considers the entrainment problem as a simple Markov process; that is, the two particle mechanics at the interface are deterministic between impulse events and, consequently, the second order (phase space) transition probability density satisfies the Smoluchowski - Chapman - Kolmogorov equation. This first order approach leads to diffusion equations for gross particle transport and a local exponential (Deutsch-Anderson) type collection equation. However, such a model is inadequate, since the real problem must include both deposition and entrainment. The combined process requires the deposition to be described by at least a third order Markov process. The present simplified case, though, gives needed insight into the entrainment problem.

A model-surface/particle - binding potential is proposed, which contains both adhesive and electrostatic terms. The subject particle localization is then discussed in terms of the Kramers-Chandrasekhar solution of the generalized Fokker-Planck equation. Such a model suggests an analogy between electrostatic precipitation and chemical kinetics. The model is also consistant with trends in coagulation theory (Ruckenstein (1978)[6]).

In Part II the precipitation problem is discussed in terms of a two - dimensional Ising model. The Markovian assumption demands that the efficiency of an EP geometry be divided into a product of factors depending on particle migration and condensation in the two-dimensional surface. From this perspective a new collection criterion is established and the importance of particle collisions is emphasized.

Finally, Part III summarizes some work done by one of the authors on the electrohydrodynamics of electrostatic precipitators. This material is included to link the surface transport phenomena to bulk fluid flows. The superficial gas flow and secondary flow introduce anisotropy into the Ising lattice and also enhance the mean particle energies at the surface.

The purpose of the electrohydrodynamic study was to experimentally and theoretically investigate not only the induced secondary flow but also the interaction of the secondary flow with the primary flow. Numerical solutions for the electric field strength with a space change density distribution were obtained through an extension of Leutert and Bohlen's (1972)[7] numerical methods. The principle objectives of the theoretical study were (1) To calculate the secondary flow velocity distribution for the single wire and the two wire configurations by integrating the Navier Stokes equation for the case of two-dimensional incompressible flow, and (2) To calculate the flow interactions with the primary flow for the single wire and the two wire configurations, for various magnitudes of flow.

The uniqueness of the present work lies in the division of various particle surface interactions into low frequency effects, which determine the binding potential and particle migration, and stochastic accelerations, which statistically determine entrainment. From this perspective the fundamental concern lies in the adhesion of dust to the surface.

PART I. DUST ENTRAINMENT

Statement of Problem

When an external field is applied to a moderately conductive ($\sigma > 10^{-8}$ Ω^{-1} m^{-1}) dust layer, particles in the surface of the layer experience a competition between adhesive and electrostatic forces. This competition can lead to an entrainment of the dust.

The particle-dust layer interaction $\phi(\vec{r},t)$ consists of adhesive and external electrostatic terms. A differential equation, subject to this potential, can be defined to describe the motion of the particle.

$$\frac{d\vec{u}}{dt} = -\beta\vec{u} + \vec{A}(t) + \vec{K}(\vec{r},t) \qquad (1)$$

In (1) the quantities $\vec{r}$ and $\vec{u}$ are independent random variables which describe the position and velocity of the particle in phase space, $\vec{K}(\vec{r},t)$ is the gradient of the potential, and $\vec{A}(t)$ is the driving term. The relaxation time β^{-1} is included to account for viscous energy losses: $\beta^{-1} = \rho d^2/18\eta$ where η is the viscosity of the medium and (ρ,d) is the (bulk density, diameter) of the dust.

For the problem to be tractable two additional assumptions must be made: (1) It must be assumed that the particle exhibits Brownian motion, subject to binding in the layer. Such an assumption is plausible since the gas stream and surface of the dust layer are in thermal equilibrium. However, in the case where particles collide with the surface and other disturbances exist, the spectral density must be shown to be constant and frequency independent within the response range of the particle layer system. (2) It must be assumed that the potential $\phi(\vec{r},t)$, which binds the particle, remains continuous during the time interval in which the Brownian motion process is to be described. This assumption demands that the impacting particles do not adhere at the site of interest. In the ensemble sense, this restriction is not crucial, because the adherence of impacting particles leads to new or replacement sites. However, a removal of this restriction would require the deposition/entrainment process to be described as a third order Markov process.

Under the present assumptions, the solution of (1) can be written as a second order conditional probability density $W(\vec{r},\vec{u},t|\vec{r}_o,\vec{u}_o,t_o)$, a quantity which obeys the generalized Liouville (Fokker-Planck) Equation.

$$\frac{\partial W}{\partial t} + \vec{u}\cdot \mathrm{grad}_{\vec{r}} W + \vec{K}\cdot \mathrm{grad}_{\vec{u}} W = \beta\, \mathrm{div}_{\vec{u}}(W\vec{u}) + D\nabla^2_{\vec{u}} W \qquad (2)$$

where D is determined by the spectral density of the source, $\psi_s(\nu) = 2D$.

An approximate, quasi-steady state solution to (2) was obtained by Kramers for the case of atomic scale particle emission past a barrier of height $\phi(x_C)$ (Kramers (1940)[8], Chandrasekhar (1943)[9]). In terms of an emission rate, his efforts gave

$$\Gamma_{em} \cong \frac{1}{2\pi}\frac{\omega_A}{\omega_c}\left\{\left[\left(\frac{\beta}{2}\right)^2+\omega_c^2\right]^{1/2}-\frac{\beta}{2}\right\} \exp\left[-\frac{\beta}{D}\phi(x_c)\right] \tag{3}$$

where $\omega_A^2 = \left.\frac{\partial^2\phi}{\partial x^2}\right|_{x=x_A}$, $\omega_c^2 = \left.\frac{\partial^2\phi}{\partial x^2}\right|_{x=x_c}$, and $\phi(x_A) = 0$.

Although Kramers' interest was directed towards problems of chemical kinetics, a generalization of the thermal spectrum to include other driving components and a generalization of the analysis to macroscopic particles are trivial. The important point is this: The emission of initially bound particles depends solely on properties of the binding potential and its modification by an external field. Since the adhesive potential is short range, the potential need only be modeled within the diffusion boundary layer thickness δ. This is the interaction force boundary layer approximation employed in coagulation theory.[6]

Application to van der Waals Binding

The adhesive component of the potential $\phi(\vec{r},t)$ can be modeled (crudely, but adequately (Zimon (1969)[10])) by a macroscopic van der Waals attractive term and by a macroscopic Born type repulsive term. In the present case it is assumed that the minimum in the adhesive well is located at x_A and that x_A and ω_A are not appreciably affected by an external field. Thus, for $x_A<x<\delta$ the following potential can be written:

$$m\phi(x) = \frac{A}{12}d\left(\frac{1}{x_A}-\frac{1}{x}\right) - qEx \tag{4}$$

where the Born repulsive term has been ignored and A is an effective Hamacker constant ($A \sim 10^{-19}$ J). The particle's charge in the presence of an external static field E is determined by the Maxwell relation (Cho (1964)[11]).

$$q = \frac{\pi^2}{24}(4\pi\epsilon E d^2) \tag{5}$$

where ϵ is the permitivity of the surrounding medium. For the potential defined by (4) and (5):

$$x_c = \sqrt{\frac{Ad}{12qE}} \tag{6a}$$

$$\omega_c = 24\sqrt{3}\,\frac{A}{\rho\pi d^2}\left(\frac{qE}{Ad}\right)^{3/2} \tag{6b}$$

and

$$m\phi(x_c) = \frac{A}{12}\,\frac{d}{x_A} - \sqrt{\frac{qEAd}{3}} \tag{6c}$$

Equations (5) and (6) indicate that the barrier height $\phi(x_C)$ decreases linearly with increasing field and that $\omega_C \sim E^3$.

Thermally Induced Entrainment. If $\omega_C >> \beta/2$ and only thermal Brownian forces drive the particles, then (3) reduces to

$$\Gamma'_{em} \cong \frac{1}{2\pi}\,\omega_A\, e^{-\frac{Ad}{12x_A kT}} \cdot e^{\frac{\pi}{3} d\sqrt{\frac{\pi\epsilon Ad}{2}}}\,\frac{E}{kT} \tag{7}$$

Thus, at constant temperature the particle emission rate increases exponentially with increases in field and at constant field the particle emission rate increases with increasing temperature. Field criteria for the application of (7) are estabished from the assumption on ω_C and the fact that the potential well is not to be saturated by the external field, $m\phi(x_C)<0$.

$$\left[\frac{\rho^2 . d}{72\pi^3\mu\epsilon}\left(\frac{Ad}{\pi\epsilon}\right)^{1/2}\right]^{1/3} \ll E \ll \frac{1}{x_A}\left(\frac{\pi}{2}\,\frac{A}{\epsilon d}\right)^{1/2} \tag{8}$$

These criteria are met for most dusts encountered in electrostatic deposition problems.

Particle Induced Entrainment (Sticking and Scattering Events Ignored). Collision incidents at the surface of the deposit obey Poisson statistics, that is, if an ensemble of intervals of duration T is averaged and if the average number of collisions per second at a site is λ, then the probability of k events at the site in the internal T is given by the Poisson distribution:

$$P_k = e^{-\lambda T} \cdot \frac{(\lambda T)^k}{k!} \tag{9}$$

Not all collisions need to be direct "hits" since the close contacts of the bound particles transfer energy to the site of interest. The spectral density for a collision-type source is written

$$\psi(\nu) = \lim_{T\to\infty} \frac{1}{T} \sum_k P_k |f_k(\nu)|^2 \cong \frac{2\lambda\xi}{m}\left(\frac{\sin \tau\nu}{\tau\nu}\right)^2 \tag{10}$$

where $f_k(v)$ is the Fourier transform of the pulse train. The approximate result in (10) was determined for Poisson distributed rectangular pulses with duration τ and kinetic energy ξ. The bound particles respond only to spectral components near ω_A, and thus, the primary concern is directed towards processes for which $\tau<2\pi\omega_A^{-1}$. Such processes require direct impact of particle and surface; this is shown as follows.

In analogy with (4) the potential's action on the incident particle must be

$$m\phi(x) = \frac{A}{12} d\left(\frac{1}{x_A} - \frac{1}{x}\right) + \alpha(x) qEx \tag{11}$$

where $\alpha(x)$ is the fraction of the Maxwell charge carried by the incident particle ($-1<\alpha(x)<1$). In the absence of microdischarge processes (Berger (1971)[12]) a potential barrier does not exist. Consequently, the incident particle's kinetic energy exceeds that for the bound particle, $\tau<2\pi\omega_A^{-1}$, and

$$D \cong \frac{\beta kT}{m} + \frac{\lambda\xi}{m} \tag{12}$$

Particle Induced Entrainment (Microdischarge Processes) When microdischarge processes occur, the incident particles encounter a potential barrier as defined by (4). The position at which $\alpha(x)=0$ is critical to particle-deposit collision, since the kinetic energy of the particle at this point must be sufficient to permit the particle to subsequently surmount the barrier (4). In this case $\tau>2\pi\omega_A^{-1}$ and one must retreat all the way back to (1).

Incidently, it is not sufficient to assume that dust resistivity is the determining factor in entrainment. The important parameter is the incident particle's kinetic energy and the distance the particle lies from the potential barrier when charge reversal occurs. Again, the adhesive potential will determine the deposition.

PART II. PARTICLE CONDENSATION

The Assumption of a 2-D Canonical Ensemble

At the basis of the generalized Liouville (Fokker-Planck) Equation is the assumption that the surface of the layer can be described by a canonical ensemble. The Boltzmann factor in the particle emission rate (3) is just a consequence of this assumption. If the assumption of a canonical ensemble is valid, a whole host of mathematical and physical techniques can be applied to the precipitation process. It is therefore an imperative that we consider the particle-site lattice in greater detail.

Suppose that the sites have equivalent statistical geometry (identical spherical particles) and that they form a surface of thickness equal to the interaction range x_C. The mean kinetic energy of particles in this ensemble is determined by (1) the thermal energy of the bulk (kT), (2) the kinetic energy of the incident particles, and (3) the energy supplied by structural vibration and rapping. The steady-state (or mean) energy of the surface is then defined as $\bar{E}$. Of course, the layer may grow or deplete but the surface will remain quasi-static in energy. Note the limitation imposed by the simple Markovian approximation.

The energy of each site may change with time but should take on a distinct set of values. The discrete set of levels may be made arbitrarily large, and thus, their number inconsequential so long as $\bar{E}$ is maintained . If the allowed states are numbered $1, \cdots, r$, then the number of distinct ways of configuring a particles such that a_1 of them are in state r=1, a_2 are in state r=2, etc, is given by

$$\Gamma = \frac{a!}{\prod_r a_r!}$$

or

$$\ln \Gamma = \ln a! - \sum_r \ln a_r \tag{13}$$

Since the surface contains many paricles and many states, Stirling's approximation may be applied and

$$\ln \Gamma \cong a \ln a - \sum_r a_r \ln a_r \tag{14}$$

The extremum of this quantity, subject to the constraints on particle number and mean energy, may be determined by the method of Lagrange multipliers.

$$\sum_r (\ln a_r + \alpha' + \beta' E_r) \delta a_r = 0 \tag{15}$$

where E_r is the energy of the rth site and (α', β') are the Lagrange multipliers. With a proper choice of (α', β'), all the δa_r become independent, and thus,

$$a = e^{-\alpha'} e^{-\beta' E_r} \tag{15}$$

where $e^{-\alpha'} = a(\sum_r e^{-\beta' E_r})^{-1}$ by normalization. The parameter β' is determined by the constraint on the energy.

$$\frac{\sum e^{-\beta' E_r} E_r}{\sum e^{-\beta' E_r}} = \bar{E} \tag{17}$$

The result is just the canonical ensemble. However, for the lattice sites to be described by a canonical ensemble, there must be a communication of statistical information between sites. This communication is accomplished through the long range adhesive potential, $\phi_{ad} \sim r^{-1}$. It is thus proposed that the surface of the layer behaves as canonical ensemble, raised to a temperature

$$\Theta = T + \lambda \xi / \beta k \tag{18}$$

Note that the relaxation rate β is included to account for energy transfer from the surface - only thermal and collision related energy processes are included in (18).

A dilute particle fluid model, subjected to other energy sources besides thermal, is quite familiar in physics. In particular, much progress has been made in understanding the NMR spin-lattice relaxation process in solids by employing a spin-temperature hypothesis (Goldman (1970)[13]). Since the Larmor frequencies for the electron and nuclear systems differ by many orders of magnitude, rf radiation can be used to separately alter the nuclear and electron "temperatures". The particle case, though, has reduced dimensionality and expected condensation. (Note that the hyperfine interaction $\phi \sim r^{-3}$).

The central concern for precipitation lies in an analogy between site occupancy and the long range order of two-state magnetic systems. Deposition is then defined in terms of the long range order or correlation between sites. The interaction parameter which determines occupancy is the well depth $m\phi(x_C)$ and the range of the interaction is x_C.

The 2-D Ising Model Approximation

In 1952 Lee and Yang[14] sought to describe gas condensation in terms of the Ising model, a model developed to explain magnetic phase transitions. The present phase transition has two characteristics which make the two-dimensional Ising model an attractive choice: (1) The lattice, unto which condensation occurs, is static and (2) The condensation problem is purely two dimensional. The only "easy" two-dimensional problem is the Onsager (square, equivalent site) lattice with constant anisotropy (McCoy and Wu (1973)^{15}). In this case the long range order or occupancy correlation is written:

$$<\sigma_{0,0}\sigma_{N,N}> = \left[1 - \left(\sinh\frac{m\phi_{\parallel}}{k\Theta}\sinh\frac{m\phi_{\perp}}{k\Theta}\right)^{-2}\right]^{1/4} \qquad (19)$$

where $m\phi_{\parallel}$ and $m\phi_{\perp}$ are the trapping energies along and transverse to the gas flow.

The collection efficiency in terms of (13) is simply

$$\eta_s = <\sigma_{0,0}\sigma_{N,N}>^{1/2} \qquad (20)$$

Consequently, the overall efficiency of an EP, which collects monodisperse particles, must be the product of η_s and an efficiency dependent on particle migration

$$\eta = \eta_m \eta_s \qquad (21)$$

The quanity $\eta_m \sim (1-\exp(-t/\tau))$ where t is the residence time for the dust in the EP and $\tau = H/bE$. In the expression for τ, H is the spacing between collection electrodes and b is the particle mobility. We have ignored both neutralizing collisions in the gas stream (density correction) and secondary flow processes.

Equation (19) is significant, because it introduces a critical temperature determined by the following relation

$$\sinh\frac{m\phi_{\parallel}}{k\Theta_c}\sinh\frac{m\phi_{\perp}}{k\Theta_c} = 1 \qquad (22)$$

Above this effective temperature, dust collection cannot occur.

PART III. FLUID TRANSPORT IN THE EHD FIELD

The efficiency product (15) was written to suggest a statistical independence of gas stream transport and surface condensation. This assumption is consistant with the simple Markovian approximation, and thus, it is sufficient to demonstrate the strength of the interaction and then to include the coupling phenomenologically as a change in the adhesive potential for surface particles.

Recently, T. Yamamoto succeeded in numerically intregrating the Navier Stokes Equation in the presence of a uniform gas flow normal to a wire-duct corona geometry. The calculations were extensive, so only an outline and example results will be presented here. The details will be published elsewhere.

Under normal EP flow conditions, the external body force due to the space charge and field strength is not affected by the secondary flow, since the ion velocity is approximately two orders of magnitude greater than the secondary flow velocity. Consequently, the flow problem is simplified by a separation of the problem into a solution of Poisson's equation followed by a solution of the Navier Stokes equations, modified by body force terms due to the electric field.

The Poisson and continuity equations were solved simultaneously, subject to experimentally determined boundary conditions on the electrode potentials and current density. A finite difference procedure was chosen along with the successive-over-relaxation method (SOR) to assure faster convergence. The equations were solved self-consistantly. When the calculated and measured current densities at the collection surface became matched, the space charge density became determined.

Next, the two-dimensional Navier Stokes equation, suitably modified by the body force terms due to the electric field, was transformed into a vorticity equation and then solved along with the Poisson equation for the stream function. Although the calculation scheme permitted a specification of the incident flow conditions, a uniform initial flow was assumed. This permitted a reflection symmetry about the plane of the wire. Also, a condition of non-slip was demanded at the wall.

The vorticity equation was solved using finite difference approximations with special attention given to the non-linear convection terms. Numerically induced oscillations were experienced, when using the central difference approximation for cases of high current density and low kinematic viscosity. In the explicit finite difference approach to the vorticity equation, stability was obtained by using the up-wind difference method in the convection terms.

The computational cost of the solution depended strongly on the efficiency of solving the problem in the finite difference form. Because of this, the Fast Direct Solution (FDS) method was employed for solving the Poisson equation for the stream function. A detailed algorithm for the FDS is described by Nakamura (1977)[16].

The steady state velocity field and stream function were calculated for the one and two wire in duct geometries. In the two wire case, the dependences of these fields on gas flow is exhibited in Figures. 1-3, along with the appropriate initial conditions. At zero gas flow the results are in qualitative agreement with the circulation reported by Yabe, Mori, and Hijikata (1978)[17], except that the center for circulation (in their non-symmetrical geometry) was located above the corona wire. Note that the relative importance of corona induced secondary flows decreases with gas speed. It was noted, however, that the circulation increased with current density. Under the illustrated conditions, the maximum current density was near 3.5 mA/m^2.

The calculations have shown that for gas speeds greater than 1.5 m/s, secondary flow effects need not be considered as a contributor to entrainment. However, at lower gas speeds, the secondary flow introduces a limit on the minimum shear stress experienced by the surface particles. Such a limit only exists in single-stage type electrostatic precipitators.

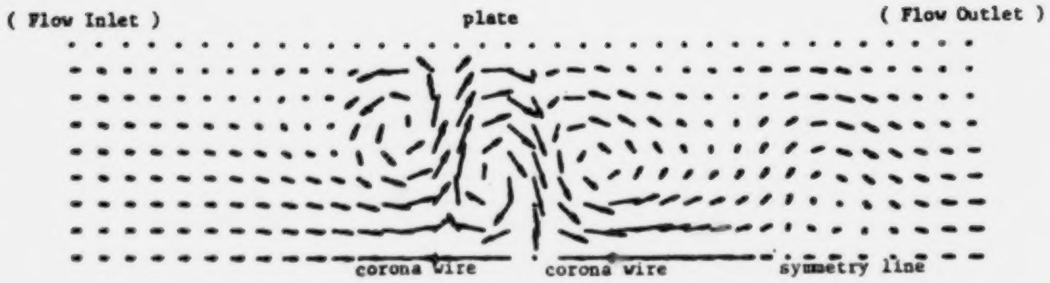

$U_0 = 0.5$ ft/sec, $V_0 = 15.0$ kV, $N_{EHD} = 10.57$

Velocity Vectors of Flow Interaction with the Primary Flow for the Two Wire Geometry

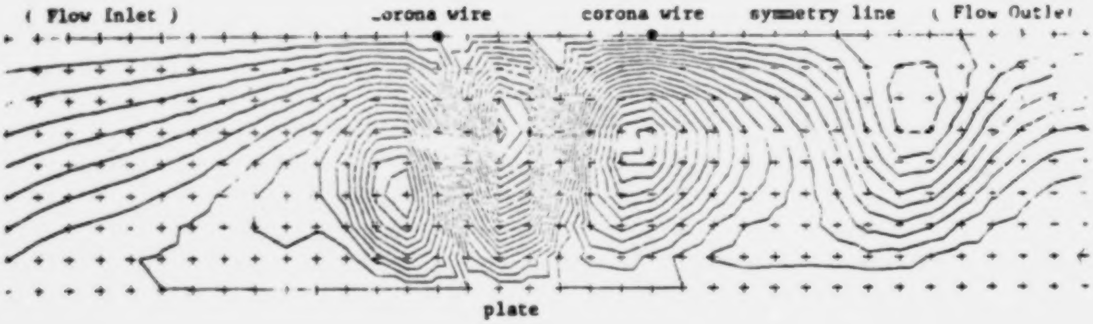

$U_0 = 0.5$ ft/sec, $V_0 = 15.0$ kV

Streamline of Flow Interaction with the Primary Flow for the Two Wire Geometry

Figure 1.

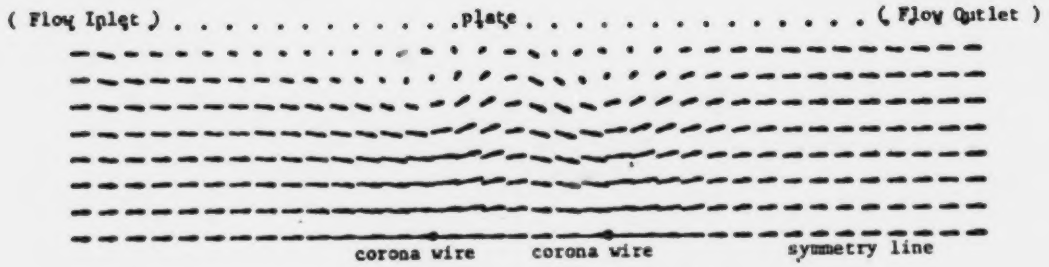

$U_o = 2.0$ ft/sec, $V_o = 15.0$ kV, $N_{EHD} = 2.65$

Velocity Vectors of Flow Interaction with the Primary Flow for the Two Wire Geometry

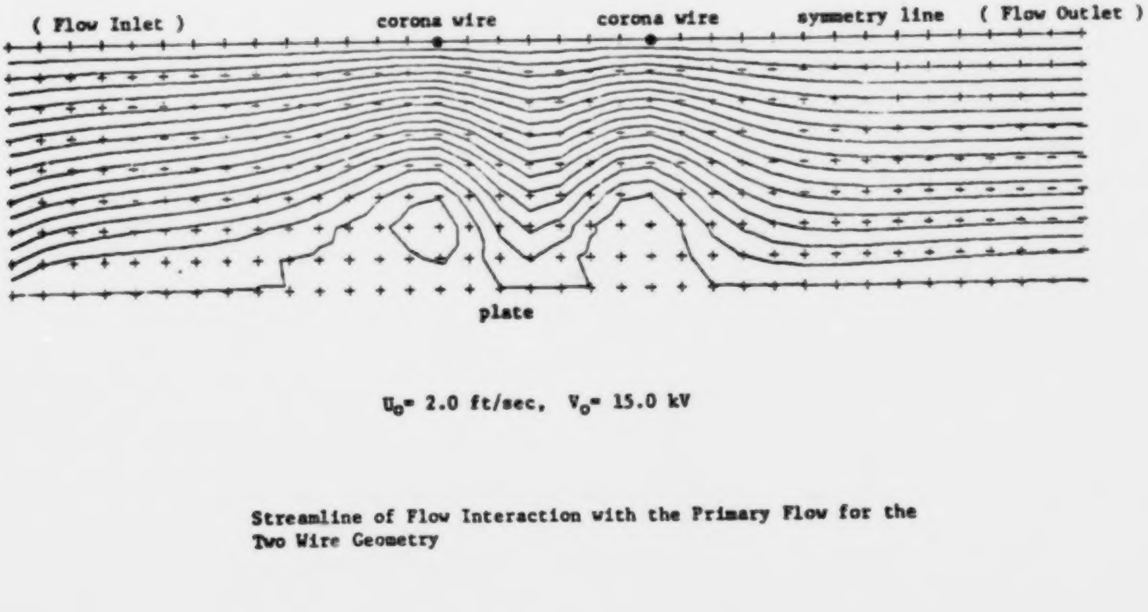

$U_o = 2.0$ ft/sec, $V_o = 15.0$ kV

Streamline of Flow Interaction with the Primary Flow for the Two Wire Geometry

Figure 2.

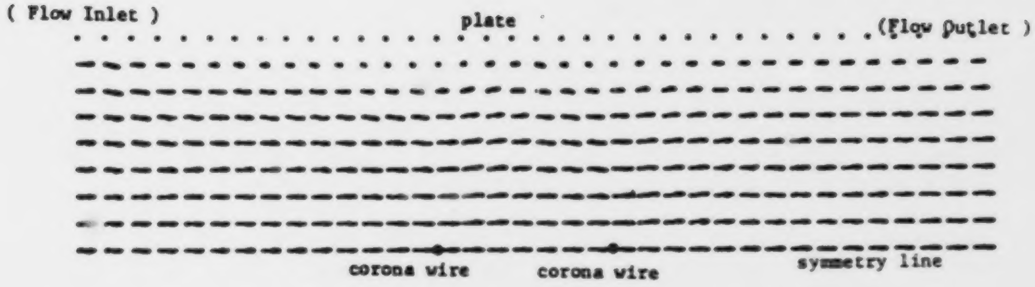

$U_o = 4.0$ ft/sec, $V_o = 15.0$ kV, $N_{EHD} = 1.32$

Velocity Vectors of Flow Interaction with the Primary Flow for the Two Wire Geometry

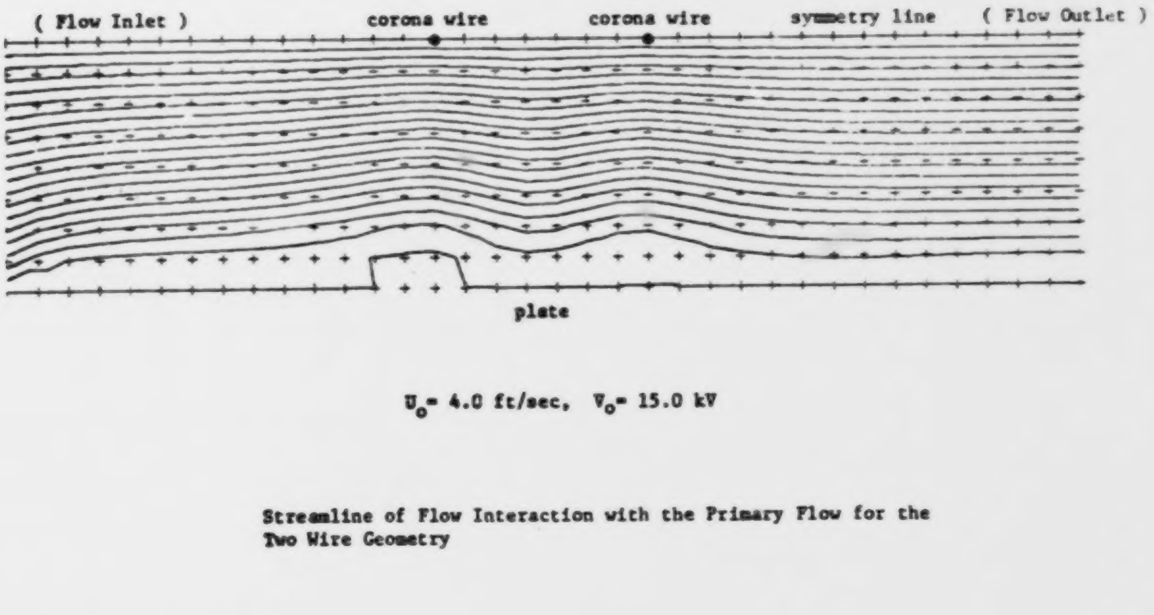

$U_o = 4.0$ ft/sec, $V_o = 15.0$ kV

Streamline of Flow Interaction with the Primary Flow for the Two Wire Geometry

Figure 3.

CONCLUSIONS

Dust collection in an electrostatic precipitator is not assured by particle charging and subsequent migration. The particle must adhere or "condense" onto the surface lattice.

In the present paper we have recognized that the assumption of dust collection as a simple Markov process permits the isolation of surface "condensation" from particle transport. This observation allowed a factorization of the efficiency equation into a part dealing with particle transport and a part representing surface phenomena.

The mathematical structure for describing the surface effects is greatly simplified by separating the two-body particle interaction into stochastic forces(molecular impacts, particle impacts, bulk lattice vibrations, structural vibrations, rapping impulses, etc.) and quasi-steady forces (adhesive, electrostatic, EHD shear stress, gravitational, etc.).

With these assumptions the surface of the layer can be described as a two dimensional lattice fluid with collection occuring below an effective temperature-determined by the ratio of the stochastic energy to the quasi-steady binding energy. Thus, any effect such as back corona or secondary flow induced particle transport will increase the effective temperature of the surface and inhibit condensation.

Condensation is closely related to entrainment. The electrostatic entrainment of dust depends on the spectral response, range, and depth of the adhesive potential. Both thermal sources and particle deposit collisions contribute spectral components in the range appropriate to entrainment. Under the assumptions of the present theory, the Kramers-Chandrasekhar model can be adapted to describe entrainment. Then, if a "macroscopic" v.d. Waals adhesive binding is assumed, the emission rate increases exponentially with the applied field. In this case laboratory studies should provide microscopic information on the adhesive vector (x_A, ω_A, A). Also, the analysis revealed the importance of incident particle kinetic energy in determining the collection of low resistiviy dusts.

The model was developed under the physical limitations of equal-sized, isotropic spheres, near a 2-D square lattice. Of course, this is a gross approximation. However, the simple model has revealed most of the qualitative effects usually left to parameters or supplementary conditions. Refinements of the model to include coupling effects and some experimental investigations to confirm it are in progress.

REFERENCES

1. Cooperman, P. Efficiency Theory and Practice in Electrostatic Precipitation. Proc 4th Int Clean Air Cong (Tokyo) 46:835-8, May 1977.

2. Gothard, N. An Approach to Calculate the Collection Efficiencies of Electrostatic Precipitators. Staub Reinhalt Luft 37:14-6, January 1977.

3. Robinson, M. A Modified Deutsch Efficiency Equation for Electrostatic Precipitation. Atm Environ 1:193-204, May 1967.

4. Penney, G.W. and E.H. Klingler. Contact Potentials and the Adhesion of Dust. Trans AIEE 81:200-4, July 1962.

5. Zimon, A.D. Adhesion of Dust and Powder. New York, Plenum Press, 1969. pp 347-66.

6. Ruckenstein, E. Reversible Rate of Adsorption or Coagulation of Brownian Particles - Effect of Shape of the Interaction Potential. J Coll Int Sci 66:531-43, October 1978.

7. Leutert, G. and B. Bohlen. The Spatial Trend of Electric Field Strength and Space Charge Density in Plate-Type Electrostatic Precipitators. Staub Reinhalt Luft 32:27-33, July 1972.

8. Kramers, H.A. Brownian Motion in a Fields of Force and the Diffusion Model of Chemical Reactions. Physica 7:284-304, April 1940.

9. Chandrasekhar, S. Stochastic Problems in Physics and Astronomy. Rev Mod Phys 15:1-89, January 1943.

10. Zimon, A.D. op. cit. pp.22-34.

11. Cho, A.Y.H. Contact Charging in Intense Electric Fields. J Appl Phys 35:2561-4, September 1964.

12. Berger, S.K. Reduction of Breakdown Voltage in Uniform and Coaxial Fields in Atmospheric Air through Moving Conducting Spheres. In: IEE Conf Pub 118:380-4, 1974.

13. Goldman, M. Spin Temperature and Nuclear Magnetic Resonance in Solids. Oxford, The Clarendon Press, 1970.

14. Lee, T.D. and C.N. Yang. Statistical Theory of Equations of State and Phase Transitions. II. Lattice Gas and Ising Model. Phys Rev 87:410-9, August 1952. (See Also, H.N.V. Temperley, The Mayer Theory of Condensation Tested Against a Simple Model of the Imperfect Gas. Proc Phys Soc (London) LXVII:233-8, March 1953.)

15. McCoy, B.M. and T.T. Wu. The Two-Dimensional Ising Model. Cambridge, The Harvard University Press, 1973. pp 216-48.

16. Nakamura, S. Computational Methods in Engineering and Science with Applications to Fluid Dynamics and Nuclear Systems. New York, Wiley-Interscience, 1977. pp.193-8, 418-23.

17. Yabe, A., Y. Mori, and K. Hijikata. Heat Transfer Augmentation around a Downward-Facing Flat Plate by Non-Uniform Electric Fields. In: Heat Transfer Annual Meeting (Toronto). pp.171-6, June 1978.

ION CURRENT DENSITIES PRODUCED BY ENERGETIC ELECTRONS IN ELECTROSTATIC PRECIPITATOR GEOMETRIES*

By:

W. C. Finney, L. C. Thanh, and R. H. Davis
Department of Physics, The Florida State University
Tallahassee, Florida 32306

ABSTRACT

A new laboratory test system for electron beam ionization in electrostatic precipitator geometries has been constructed to measure ion current densities as a function of voltage differences for clean (bare) plate conditions. The new system incorporates improved electrodes which withstand a driving voltage of ±55 kV, a factor of 5 increase over the previous test system. A 3 MeV Van de Graaff accelerator produced ionizing electron beams of 1.2 and 2 MeV and currents of 10.5 and 21 μA in place of corona wire ionization. Current densities of up to 130 mA/m^2 were measured before breakdown between the plates, and no current saturation was observed. A comparison of I-V curves and sparkover voltages for various beam energies, currents, and collimation are discussed and the need for measurements with good beam geometry is reviewed.

ION CURRENT DENSITIES PRODUCED BY ENERGETIC ELECTRONS IN ELECTROSTATIC PRECIPITATOR GEOMETRIES*

INTRODUCTION

Experiments using electron beam ionization instead of corona wire ionization in electrostatic precipitators were introduced in an earlier paper (Davis and Finney, 1978)[1]. In these earlier experiments, ion current densities were measured which were 65 times larger than those which could be obtained in a duct-type electrostatic precipitator with corona ionization (White, 1963)[2]. Since particulate charging and collection in electrostatic precipitators depend on the ion current density within the interelectrode space, electron beam ionization is being appraised as a replacement for corona wire ionization.

In this paper, a new laboratory scale electrostatic precipitator test system incorporating improved electrodes and higher operating voltages was used to extend the earlier measurements which were limited by the available power supplies. Current versus voltage curves for several electron beam energies, beam currents, and beam profiles were measured, and increased ion current densities were noted in all cases. No saturation of ion current density was observed and the reasons for this will be discussed.

The earlier paper (Davis and Finney, 1978)[1] presented data using a poor geometry beam configuration in which the electron beam was not scanned or trimmed by collimators to form a narrow corridor of ionization but instead formed a plasma in and beyond the ionization zone. In a second set of measurements, a collimator was used to confine the beam and restrict its spreading. The present work incorporates uncollimated and collimated beam profiles and these are discussed in conjunction with good geometry experiments which are planned to further investigate electron beam precipitation.

EXPERIMENTAL APPARATUS

The objective of this work was to study the effects of beam energy, current, and profile on the ion current characteristics of the laboratory precipitator. A schematic diagram of the test system is shown in Figure 1.

The laboratory scale electrostatic precipitator constructed for these experiments was composed of an upper and a lower set of 3 parallel plates separated by a distance of 10 cm. The plates are ½ inch thick aluminum, and the plate margins were rounded and polished to a smooth finish to reduce edge effects on the field distribution of the system. The collecting area was 400 cm^2 for plates b, b', d, and d' and 200 cm^2 for plates c and c'. The outside plates served as guard electrodes while the current flow through the inner two plates (c and c') was measured. Two DC power supplies capable of delivering 130 kV (optional polarity) and 28 mA were connected to the electrodes so that the upper set was positive (anode) and the lower set was negative (cathode), both with respect to ground.

The electron beam was delivered between the electrodes by the 3 MeV Van de Graaff electron accelerator at the Florida State University (Davis, 1976)[3],

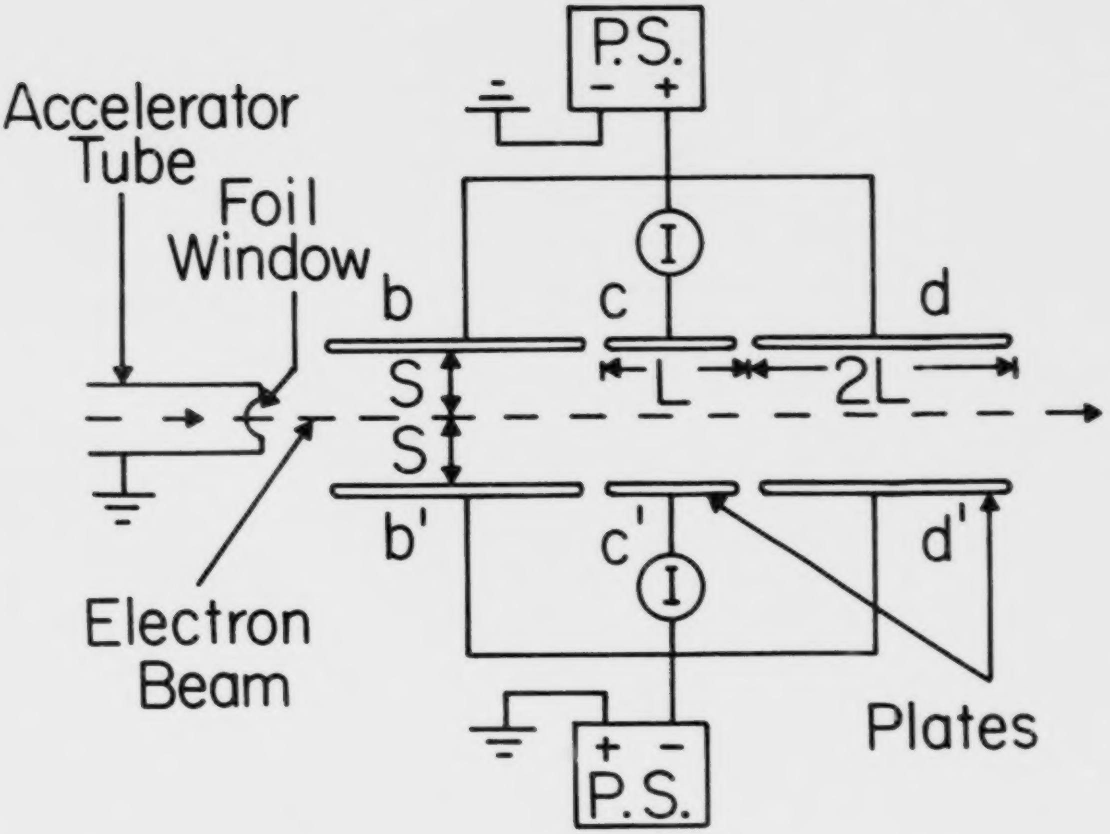

Figure 1. Schematic diagram of the experimental apparatus. The electron beam is delivered between the upper and lower sets of plates. S = 5 cm, L = 10 cm.

which was operated to produce beam energies of 1 MeV and 2 MeV and initial beam currents of 10.5 μA and 21 μA. The distance from the foil window to the center of plates c, c' was 55 cm. To determine the effect of electron beam collimation on the ion current characteristics of the system, a ±0.1 radian honeycomb collimator was mounted on the end of the accelerator tube downstream of the foil window.

RESULTS

Current-to-voltage characteristics for two beam energies, two initial beam currents, and with and without the collimator are shown in Figure 2. Only the anode current (c) is plotted against voltage because the anode and cathode currents were equal in magnitude. For all six experimental conditions plotted, the I-V curves approximate straight lines, indicating an ohmic relationship between current and voltage. No tapering off of current at the highest voltage readings occurs, therefore no saturation in ion current density is observed for the experimental conditions reported here.

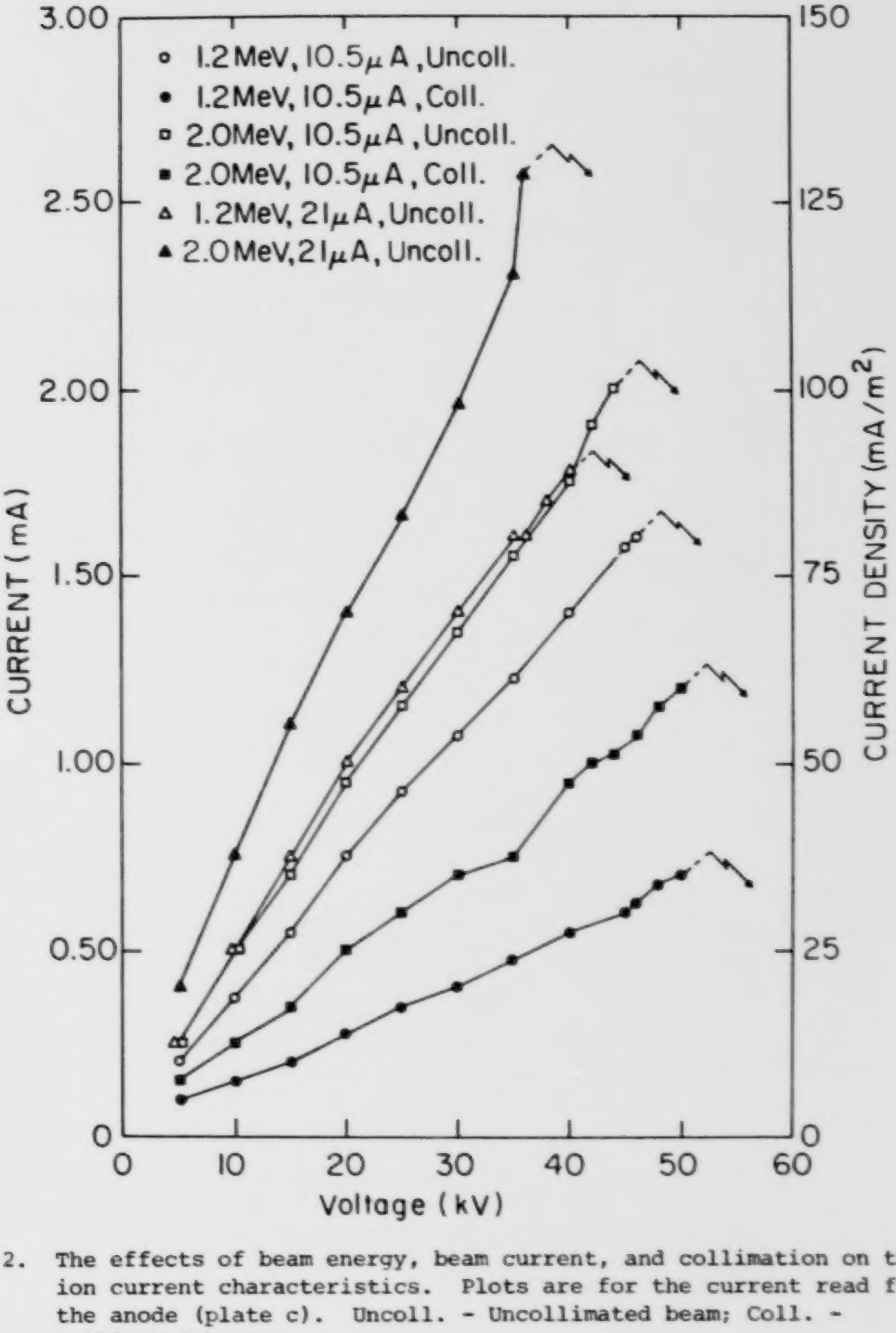

Figure 2. The effects of beam energy, beam current, and collimation on the ion current characteristics. Plots are for the current read from the anode (plate c). Uncoll. - Uncollimated beam; Coll. - Collimated beam.

Table 1. Sparkover Voltages and Maximum Ion Current Density for Various Beam Conditions

	Sparkover Voltage (kV)			Maximum Ion Current Density (mA/m^2)		
	10.5 μA		21.0 μA	10.5 μA		21.0 μA
Energy	Uncoll.[a]	Coll.[b]	Uncoll.[a]	Uncoll.[a]	Coll.[b]	Uncoll.[a]
No Beam	55	--	--	0	--	--
1.2 MeV	48	52	40	80	35	89
2.0 MeV	46	52	ca. 40	100	60	130

[a] Uncollimated
[b] Collimated

Large ion current densities were obtained in each case as shown in Table 1. For 1.2 MeV beam energy, 10.5 μA beam current, and uncollimated beam, an ion current density of 80 mA/m^2 was obtained, six times the ion current density of 13 mA/m^2 found in earlier experiments under similar beam conditions (Davis and Finney, 1978)[1]. The highest ion current density found was 130 mA/m^2 for 2.0 MeV energy, 21.0 μA current, and uncollimated beam.

Several general results are illustrated in Figure 2 for the values of beam energy, beam current, and collimation conditions studied here. As beam energy increased from 1.2 to 2.0 MeV, ion current density increased by ~25% and 75% for uncollimated and collimated beam, respectively. A doubling in beam current from 10.5 to 21 μA caused an ion current density increase of 33% and 50% for 1.2 and 2.0 MeV energies, respectively. Finally, the uncollimated beam produced ion current densities of 150% and 100% greater than the collimated beam for 1.2 and 2.0 MeV beam energies, respectively.

As seen in Figure 2, the current versus voltage curves for each experiment were extended until sparkover occurred. Sparking usually occurred between the lateral edges of plates c and c'. Further control of edge effects may be important in preventing premature sparkover. A comparison of sparkover values for various experimental conditions is summarized in Table 1. For specific conditions, beam energy had little effect on sparkover voltage (a 2 kV or less difference between 1.2 and 2.0 MeV). Doubling the beam current from 10.5 to 21.0 μA causes sparkover voltage to decrease by 6-8 kV. A slight (4 kV) increase in sparkover voltage is noted with collimated versus uncollimated beam.

DISCUSSION

Ion Current Characteristics

The relationship between the ion current and the applied voltage is approximately ohmic for voltages up to sparkover value. This suggests that most of the space between plates c and c' is occupied by a virtually grounded plasma generated by the ionizing collision of the electron beam and air molecules. The driving field is limited by the breakdown field strength, which is, in turn, determined by the presence of a copious supply of ions and the effective plasma-to-plate distance. Therefore, saturated extraction of ions is not expected, and, as shown in Figure 2, no current saturation occurs in any of the I-V plates. Higher driving voltages not limited by sparkover or lower ionization production rates are required to reach the saturation point.

The linear relationship between current and voltage in the electron beam test system is in contrast to the quadratic ($I \alpha V^2$) (White, 1963)[2] relationship prevailing in corona wire ionization systems. This difference may represent an advantage of the electron beam precipitator over its corona wire counterpart.

Ion current densities which are much higher than previously obtained have been produced in these experiments. Using electron beam ionization with the electrode system shown in Figure 1, the ion current density is 100 mA/m^2 at 2.0 MeV energy, 10.5 µA current, uncollimated beam, and ±44 kV applied voltage. For a similar plate geometry, conventional electrostatic precipitators have a maximum ion current density of about 0.2 mA/m^2 (White, 1963)[2] which is space charge limited. Therefore, the laboratory electron beam precipitator yields an ion current density that is ~500 times greater than a conventional corona precipitator, and to date it is limited only by sparkover, which is in turn determined by beam geometry, plate spacing, and edge effects.

As shown previously, ion current density increased as beam energy and beam current increased which is expected because with greater beam energy or current more ionization takes place and a larger extraction of charge occurs. The uncollimated beam produced larger ion current densities because the collimator reduces the actual beam current delivered to the interelectrode space while providing a better beam geometry with less beam spreading. Even so, the ionization yield was not exhausted prior to sparkover.

In these poor geometry experiments, the spreading of the plasma column generated by the electron beam reduces the effective distance between plates c, c', and the grounded plasma. It has been estimated (Davis and Finney, 1978)[1] that for a beam energy of 1 MeV and a beam current of 10.5 µA that the penetration of the electric field adjacent to each electrode is 2.5 cm at a current density of 13 mA/m^2 and an electrode voltage +10 kV (anode) and -10 kV (cathode). The sparkover between parallel plates at this distance (5.0 cm) is ~137 kV (Meek and Craggs, 1978)[4]. A higher driving voltage would be required to reach current saturation. The sparkover voltage is further reduced by field distortion caused by the edges of the electrodes. Collimation

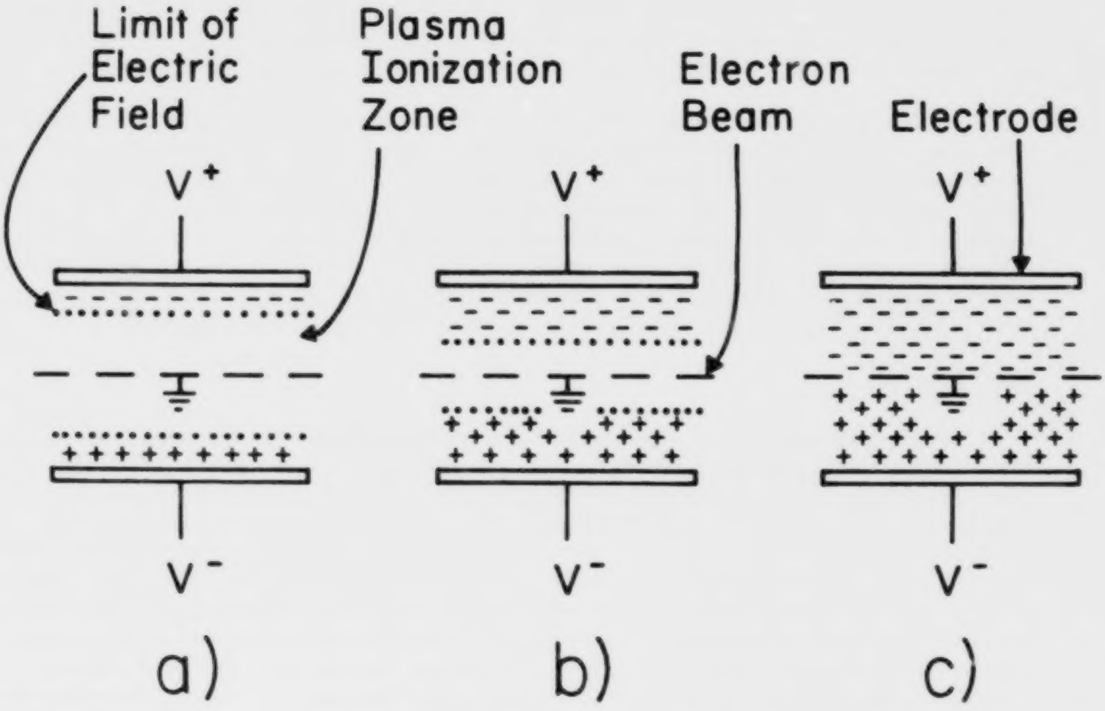

Figure 3. Diagram of three different electron beam geometries. A poor geometry beam configuration with a wide ionization zone is shown in part a). The collimated geometry used in the present experiments with a more restricted plasma is shown in part b). Good geometry with a very narrow ionization zone is shown in part c).

of the beam confines the plasma column to a smaller cross-sectional area, thus increasing the plasma-to-electrode distance and the effective interelectrode gap. Consequently, this results in a slight increase in sparkover voltage as shown in Table 1.

Poor vs. Good Geometry Beam Configurations

To simulate the small radius ionization cylinder of a corona wire, an electron beam should be prevented from spreading and instead retained within a narrow region centered between the electrodes. As pointed out earlier, the spreading of the plasma column is probably the major cause of early sparkover because the effective gap distance from electrode to plasma is reduced. This poor geometry beam configuration is diagrammed in Figure 3a, and shows the limited reach of the electric field and the expanded ionization zone and reduced effective gap.

A honeycomb collimator which passes electrons within ±1/10 radian of the beam direction was used to trim the edges of the beam and the result was less scattering, a wider electrode-to-plasma gap, and an increased sparkover voltage (Figure 3b). The beam current is reduced because the surface area of the collimator tubes presents an obstacle and eliminates the fraction of the beam which is not projected straight through the honeycomb.

Although the honeycomb collimator does improve beam geometry, further refinement is projected by reducing the surface area of the collimator in the beam path while further reducing scatter. A good geometry beam configuration, shown in Figure 3c, would restrict the ionization zone to a column with small cross-sectional area, allowing more complete charge extraction and raising sparkover voltage to a level at which ion current density saturation may be found. Collimation of the beam just prior to its entry into the electric field may serve to further define the ionization zone.

CONCLUSIONS

Earlier experiments using electron beam ionization in electrostatic precipitators were extended using a new laboratory scale test system and larger power supplies. An approximately ohmic relationship between ion current and plate voltage suggests the formation of a large grounded plasma region between the electrodes. Large current densities, as high as 500 times that of conventional precipitators, have been observed with no saturation. Variations in ion current densities with beam energy, current, and collimation are due to the intensity of beam ionization in the interelectrode space. Sparkover voltage is probably determined by beam geometry which controls the plasma-to-electrode gap distance and the width of the ionization zone. Measurements with good geometry are required to observe saturation and investigate the interplay between ionization zone restriction and sparkover. Future work (Thanh _et_ _al_., in preparation)[5] will include the use of a medium which simulates fly ash and will address the phenomenon of back corona and its effect on sparkover.

*Supported in part by Department of Energy Contract No. Et-78-S-01-3199.

REFERENCES

[1] Davis, R. H. and W. C. Finney. Ionization by Electron Beams for Use in Electrostatic Precipitators. Energy Research. 2:19-27, 1978.

[2] White, H. J. Industrial Electrostatic Precipitation. Reading, Mass., Addison-Wesley, 1963.

[3] Davis, R. H. Ion Source and Accelerator Applications to Electrostatic Precipitators. In: Conference Record 76CH1122-1-1A, IEEE Industrial Applications Society. Chicago, 1976. p. 328.

[4] Meek, J. M. and J. D. Craggs. Electrical Breakdown in Gases. John Wiley and Sons, 1978. p. 608.

[5] Thanh, L. C., W. C. Finney, and R. H. Davis. The Effects of Back Corona Discharge on Ion Current Density in Electron Beam Precipitators. submitted for publication.

EXPERIMENTAL STUDIES
IN THE ELECTROSTATIC PRECIPITATION
OF HIGH-RESISTIVITY PARTICULATE

BY:

John C. Modla
Robert H. Leiby
Thomas W. Lugar
Kris E. Wolpert

Buell Emission Control Division
Envirotech Corporation
Lebanon, PA 17042

ABSTRACT

A pulsed charging system is described that eliminates reverse ionization in electrostatic precipitation. The motivating concept is a purely electrical approach. The fundamental characteristic of this method is the relaxation time of the precipitated particulate. Laboratory studies indicate that this powering concept could increase precipitator performance on high-resistivity particulate by more than two orders of magnitude. Pilot results are also presented.

EXPERIMENTAL STUDIES
IN THE ELECTROSTATIC PRECIPITATION
OF HIGH-RESISTIVITY PARTICULATE

INTRODUCTION

Electrostatic precipitation is the removal of suspended particulate from a gas stream by the application of an electric field. This method of pollution control appears simple on a microscopic level, but in reality the phenomenon of electrostatic precipitation on a microscopic level is a very complex process. The fundamental processes of electrostatic precipitation consist of corona generation, particulate charging, and particulate collection. Corona generation is the formation of a self-sustained electrical discharge between a high-voltage electrode (usually at a negative potential) and a grounded or passive electrode. Negative ions are formed by the attachment of electrons to electronegative gases and are accelerated by means of an electric field. The ions become attached to the suspended particulate within the gas stream by a combination of direct collisional and diffusional processes. The unipolar charged particulate is attracted to the passive electrode for subsequent removal. The role of the corona generation is twofold. The first is to charge the particulate. Secondly, together with the static electric field, the unipolar space charge density also aids in the process of particulate collection.

PRECIPITATOR LIMITATIONS

The surface and bulk electrical resistivity of the particulate is a crucial variable that limits the performance of an electrostatic precipitator. It is a well-established fact that for materials with a resistivity in the range of 10^{10}-10^{13} ohm cm the phenomenon of reverse or back ionization occurs, thus reducing the effectiveness of the precipitator. Reverse ionization,[1] as associated with electrostatic precipitation, is categorized as an abnormal electrical discharge emanating from the dust-electrode interface. The light signal from the electrical discharge consists of two light waves: a primary light wave that rises very rapidly in time and a secondary light wave that rises more slowly. The former proceeds into space while the latter proceeds along the precipitated dust layer surface. When a sufficiently high voltage pulse is applied at low pressure, reverse ionization is triggered by free electrons. As the pressure is increased, the triggering mechanism is due to negative ions.

CRITERIA FOR REVERSE IONIZATION

Reverse ionization is a phenomenon whereby the gas molecules among the porous precipitated dust layer are electrically overstressed to such an extent that the gas molecules become ionized. Positive ions are formed which, in some cases, produce a local surface disruption within the dust layer. The positive ions are accelerated toward the emitting electrode, thus neutralizing the negative space charge density. A simple analysis of the occurrence of reverse ionization is given by the following equation:

$$E = J\rho'$$

where

E: electric field strength; volt/m

J: current density, amp/m^2

ρ': resistivity, ohm m

As can be seen from the above equation, a large electric field strength can be obtained for modest current densities through the precipitated dust layer, provided the resistivity of the particulate is large.

The occurrence of reverse ionization generally causes a reduction in the breakdown voltage of the gas thus leading to a spark, a substantial increase in the precipitator current, and unsteadiness in the current-voltage characteristic curve (hysteresis). The immediate effects of reverse ionization as far as pollution control is concerned are a reduction in the charging and precipitating electric fields, a substantial increase in particulate reentrainment from the collecting plates, and an increase in emitting wire vibrations.

METHOD OF CONTROL

A common method of minimizing the process of reverse ionization is to condition either the gas-entrained particulate, the flue gas, or both. The conditioning process is achieved by the addition of chemical additives to the main gas stream. There are two schools[2] of thought which attribute the reduction in reverse ionization to the increase in surface and bulk conductivity of the particulate or to a modification in the electrical characteristics of the flue gas itself (i.e., the formation of ion clusters, which leads to lower ion mobilities).

Another method[3] of minimizing reverse ionization is to revert to the concept of "wide space" precipitators. The concept of wide spacing refers to the separation between emitting electrodes and collecting electrodes. The likelihood of the occurrence of a disruptive spark due to reverse ionization is reduced with larger spacings.

Very recent studies[4] on the minimization of reverse ionization have concentrated on the control of the current density through the precipitated dust layer. This method of control can be accomplished by electrical means. The idea behind this control strategy is based on the electrical properties of the flue gas and particulate. The criteria[5] for the initiation of reverse ionization are based on steady state conditions and the continuity of the electric field and current density across a boundary. The crucial parameters that determine the occurrence of reverse ionization are the relaxation time of the flue gas compared to the relaxation time of the precipitated particulate dust layer. The relaxation time is defined as the product of the permittivity of the media in question and the resistivity of the same media. The initiation of ionization will occur when the relaxation time of the dust layer exceeds the relaxation time of the flue gas. These criteria imply that reverse ionization will occur because the conductivity of the flue gas is larger than the conductivity of the dust layer. This observation suggests a way to minimize reverse ionization by correlating the electric field due to the ionic space charge density to the relaxation time of the precipitated dust layer.

RELAXATION TIME APPROACH

The Tri-Electrode Precipitator[6] is a device which minimizes the occurrence of reverse ionization. The concept is based on the relaxation time of the precipitated dust layer. A derivation of this relaxation time approach is given below:

Consider the continuity equation:

$$\nabla \cdot J = -\frac{\partial \rho}{\partial t}; \quad \rho: \text{ space charge density}$$

But $J = \frac{E}{\rho'}$

Assume that the resistivity of the dust layer is uniform (no spatial variation)

$$\nabla \cdot (E/\rho') = \nabla(1/\rho') \cdot E + \rho/\varepsilon\rho' = \partial\rho/\partial t$$

$$\rho(t) = \rho_0 e^{-t/\tau}; \quad \tau = \rho'\varepsilon$$

where ρ_0 is the space charge density at time $t = 0$, and ε is the permittivity of the particulate.

The above equation describes how the space charge density decays with time. This equation is analogous to the decay of a typical capacitor-resistor circuit. To minimize the occurrence of reverse ionization, the space charge density must be allowed to relax to a level below the breakdown strength of the flue gas.

ARCHITECTURE OF THE TRI-ELECTRODE PRECIPITATOR

The basic architecture of the Tri-Electrode Precipitator, as compared to a conventional precipitator, is the additon of a third non-ionizing electrode. The purpose of the non-ionizing electrode is to further enhance the performance of the precipitator by producing a strong long-range static electric field. The device employs two separate pulsating power supplies for the ionizing and non-ionizing electrodes. The two sets of electrodes are operated with variable DC reference voltages with superimposed high voltage pulses. The pulse forming network is a resonant charging scheme which is discussed by Glaso and Lebacqz.[7] By connecting many thyristors in series with the proper voltage grading circuits, the desired voltage rating can be achieved. This leads to a highly reliable solid-state switch[8], as compared to using relays or vacuum tubes. The power supply has the capability of varying the pulse amplitude, pulse duration, pulse frequency, and rise and fall times of the pulses.

MODE OF OPERATION

The mode of operation is to pulse the corona emitting electrode at a rate which correlates with the relaxation time of the precipitated dust layer. The duration of the pulse (pulse width) and the amplitude of the pulsed voltage (more specifically, the peak electric field) determines the quantity and rate of negative ion production (i.e., the ionic space charge density). This, in turn, determines the degree of charge acquired by the particulate. The pulsed voltage that creates the corona current can have a pulse width of one to four milliseconds. Since the pulse duration is short, the applied voltage to the emitting electrodes can be larger than the charging voltage of a conventional precipitator. These short corona pulses have been found to be effective in charging the particulate.

The frequency of the pulsed corona voltage depends on the resistivity of the particulate. As an example, for particulate with a resistivity of 10^{11} ohm cm and a relative dielectric constant of 2, the relaxation time is 180 milliseconds. This means that the space charge density requires 180 milliseconds to decay to 37% or ε^{-1} of its initial value. This implies that if the electric field associated with the initial space charge density is near the threshold value for reverse ionization, the corona emitting electrode should be pulsed at a rate not exceeding 30 Hertz. Too long a period between pulses results in a low electric field through the dust layer (poor collection), while too short a period between pulses permits so little decay in the ionic space charge density that the dust layer cannot accept the full pulse current (reverse ionization).

With the emitting electrode at a low potential (i.e., below the corona emitting potential), the unipolar charged particulate migrates towards the collecting electrode. This process of particulate collection is categorized as space charge precipitation. This technique of pollution control also has a characteristic relaxation time which is quite long. Thus, to aid in the particle collection, a non-corona emitting electrode is pulsed with a high voltage whenever the emitting electrode is at a voltage below corona generation.

In essence, the Tri-Electrode Precipitator is basically a two-stage precipitator itself. The pulsed corona emitting electrode charges the particulate, while the non-corona emitting electrode aids in the collection process. The pulsing scheme controls the flow of current through the precipitated dust layer, so the occurrence of reverse ionization is minimized.

LABORATORY TEST

Laboratory tests were conducted under the supervision of Professor GaylordPenney at Carnegie Mellon University for the Buell Division of Envirotech Corporation. A sketch of the test apparatus is shown in Figure 1. The passive electrodes are three-foot-square aluminum sheets mounted four inches apart. The spacing from wire to ground is two inches, with three inches between wires. The third electrodes (non-emitting) are tubes that are mounted midway between the wires. The system is operated in a closed-loop fashion. A calibrated orifice is used to meter the air flow. Compressed air is supplied to a fluidized-bed dust feeder which, in turn, supplies the test dust. Leaving the feeder, the entrained particulate passes through a small-diameter, high-efficiency cyclone to remove agglomerates. The temperature of the air is adjusted to give the desired resistivity as measured by a resistivity cup located in the outlet chamber of the precipitator. The system is seasoned before actual efficiency measurements are taken.

A schematic of the pulsing scheme for resistivity in the range of 10^{11} ohm cm is shown in Figure 2. The pulse width of the corona emitting electrode is two milliseconds, with a millisecond on the rise and fall time.

A comparison of the performance of the Tri-Electrode Precipitator and a typical Research Cottrell precipitator over the resistivity range of 10^{11} to 10^{13} ohm cm is shown in Figure 3. To normalize comparison, the efficiencies for the two-electrode precipitator were taken with the non-emitting electrodes present and removed. The measurements indicate that the pulsed system of operation is far superior.

Scale-up studies with the Tri-Electrode Precipitator, based on scale factors obtained from the Deutsch-Anderson equation, are shown in Figures 4 and 5. The scale factor is two on the wire-to-plate spacing with additional plate area. Also shown in the same figures are results obtained for a conventional precipitator by the removal of the third electrode and the pulsed power supply. Operating under identical conditions, the Tri-Electrode Precipitator is roughly two orders of magnitude more efficient on the high resistivity materials.

PILOT STUDIES

A pilot unit has been constructed in a 45-foot-long, 13.5-foot-high, drop frame - tandem axle trailer. The primary elements of the pilot unit are listed in Table I. The geometrical arrangement of the three-electrode system is shown in Figure 6.

An initial series of tests has been completed at a utility located on the east coast. A chemical analysis of the fly ash is given in Table II. Laboratory measurements of the fly ash resistivity using planar electrodes varies from 2×10^{11} ohm cm to 5×10^{11} ohm cm within a temperature range of 232°F to 268°F. Figure 7 shows the experimental results of the efficiency as a function of the gas velocity for both the Tri-Electrode and conventional precipitator design. Note that the conventional design is powered with a DC voltage. The migration velocity, ω, can be obtained from the efficiency measurements via the Deutsch-Anderson equation. Figure 8 displays the relationship between ω and gas velocity. Initial conjecture as to the reason for this phenomenon may be related to the role of ionic wind, i.e. electrical relaxation time, in precipitation.

Further tests are planned to quantify the effect of the rise time of the pulsed voltage. The effect of a positive pulsed scheme is also under investigation.

REFERENCES

1. Masuda, S., "Research on Electrostatic Precipitation - 1975", Dept. of Electrical Engineering, University of Toyko.
2. Loeb, L.B., "Fundamental Processes of Electrical Discharge in Gases", 1939, John Wiley & Sons, Inc.
3. Private communication with personnel from Sumitomo Metal Mining Co., Ltd.
4. Penney, G.W., Gelfand, P.C., "The Tri-Electrode Precipitator for Collecting High Resistivity Dust", APCA Journal, Vol. 28, No. 1, Jan. 1978.
5. Cooperman, P., "Back Corona and Relaxation Time", IEEE Transactions on Industry and Applications, Vol. 1A-12, No. 1, Jan. 1976.
6. U.S. Patent 3,915,672.
7. Glaso, G.N., Lebacqz, J.V., "Pulse Generators", McGraw Hill, Vol. 5, MIT Radiation Laboratory Series, 1948.
8. Shoup, J.F., Mason, C.A., "A High Voltage Thyristor Valve for Precipitator Applications", future paper in Electronics Journal.

TABLE I

TRI-ELECTRODE PILOT PRECIPITATOR

DESIGN PARAMETERS

Number of Fields	1
Depth of Field	9 ft.
Plate Height	6 ft.
Total Plate Area	600 ft.
Gas Passages	6
Gas Volume	7100 ACFM
SCA	84.5
Plate Spacing	9"
Emitting Electrode	Rigid Frame Rods
Total Emitter Length	430 ft.
Tube Electrode	Standard Pipe
Dust Removal	Vibrators
Hopper	Continuous Discharge System, Drag and Screw Conveyer

TABLE II

CHEMICAL ANALYSIS OF FLY ASH

Parameter	Percent
SiO_2	55.91
Fe_2O_3	7.80
Al_2O_3	25.71
CaO	3.80
MgO	1.60
K_2O	3.13
Na_2O	0.43
P_2O_5	0.31
TiO_2	1.19
Li_2O	0.04

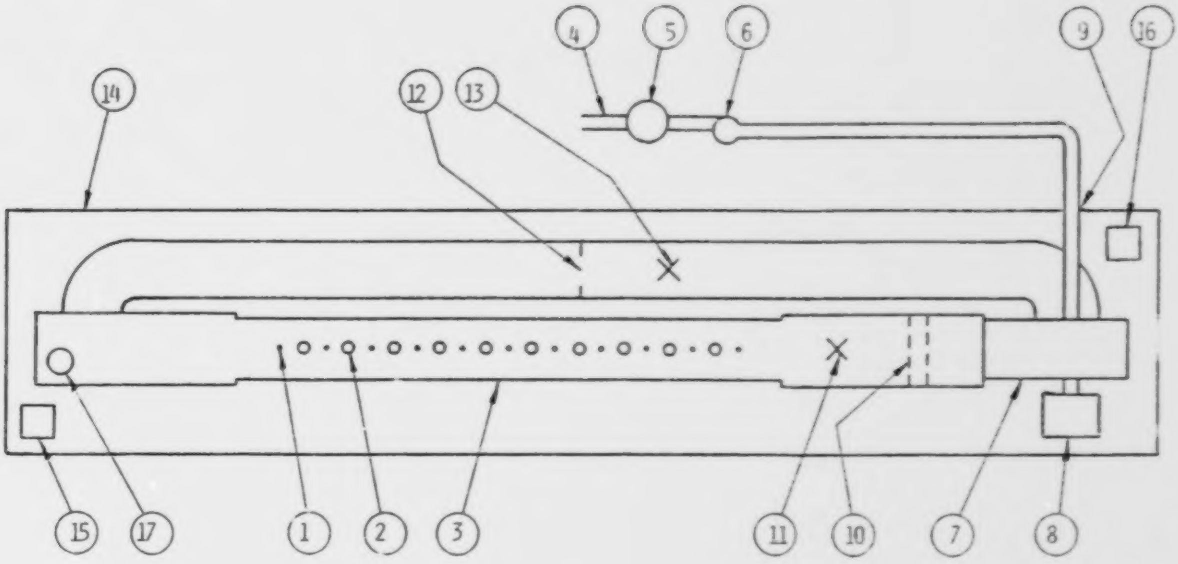

1. Corona Wires
2. Tubular Third Electrode
3. Grounded Dust Collecting Electrode
4. Compressed Air Inlet
5. Fluidized Bed Dust Feeder
6. Cyclone Dust Collector
7. Fan
8. Motor
9. Dust Delivery Pipe
10. Distribution
11. Inlet Sampling Point
12. Orifice
13. Outlet Sampling Point
14. Enclosure
15. Heater And Fan
16. Heater And Fan
17. Resistivity Test Cup

Fig. 1. Tri-Electrode Precipitator test model

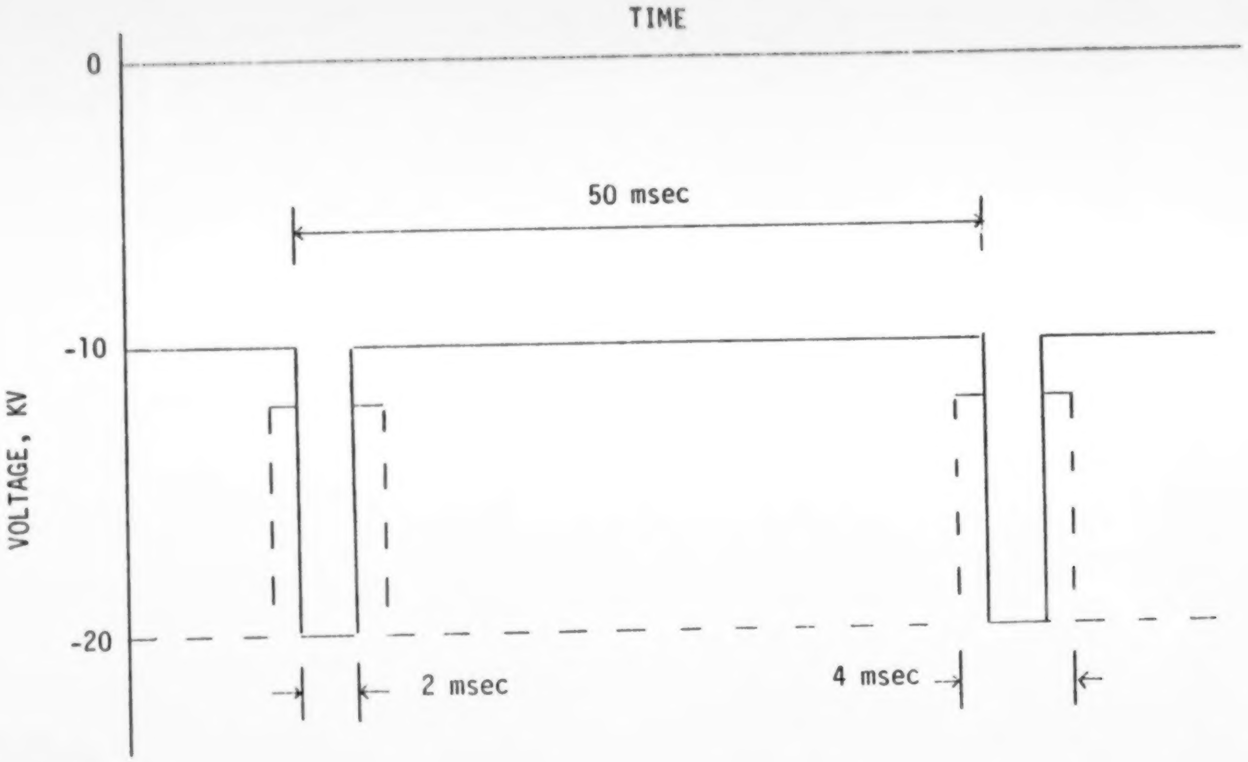

Fig. 2. Typical static and dynamic potential for resistivity of 5×10^{11} ohm-cm

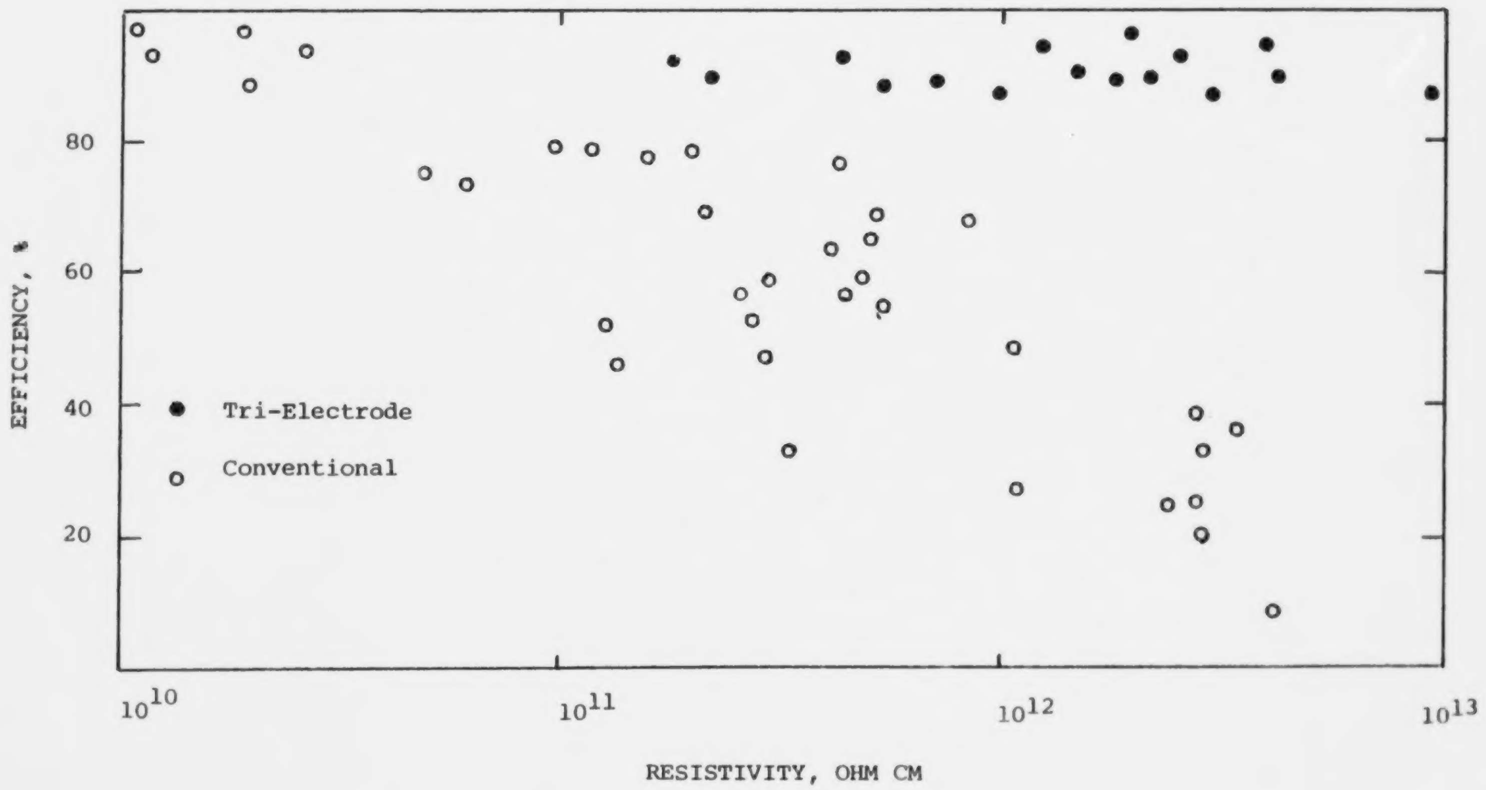

Fig. 3A. Efficiency comparison of laboratory Tri-Electrode Precipitator with conventional precipitator

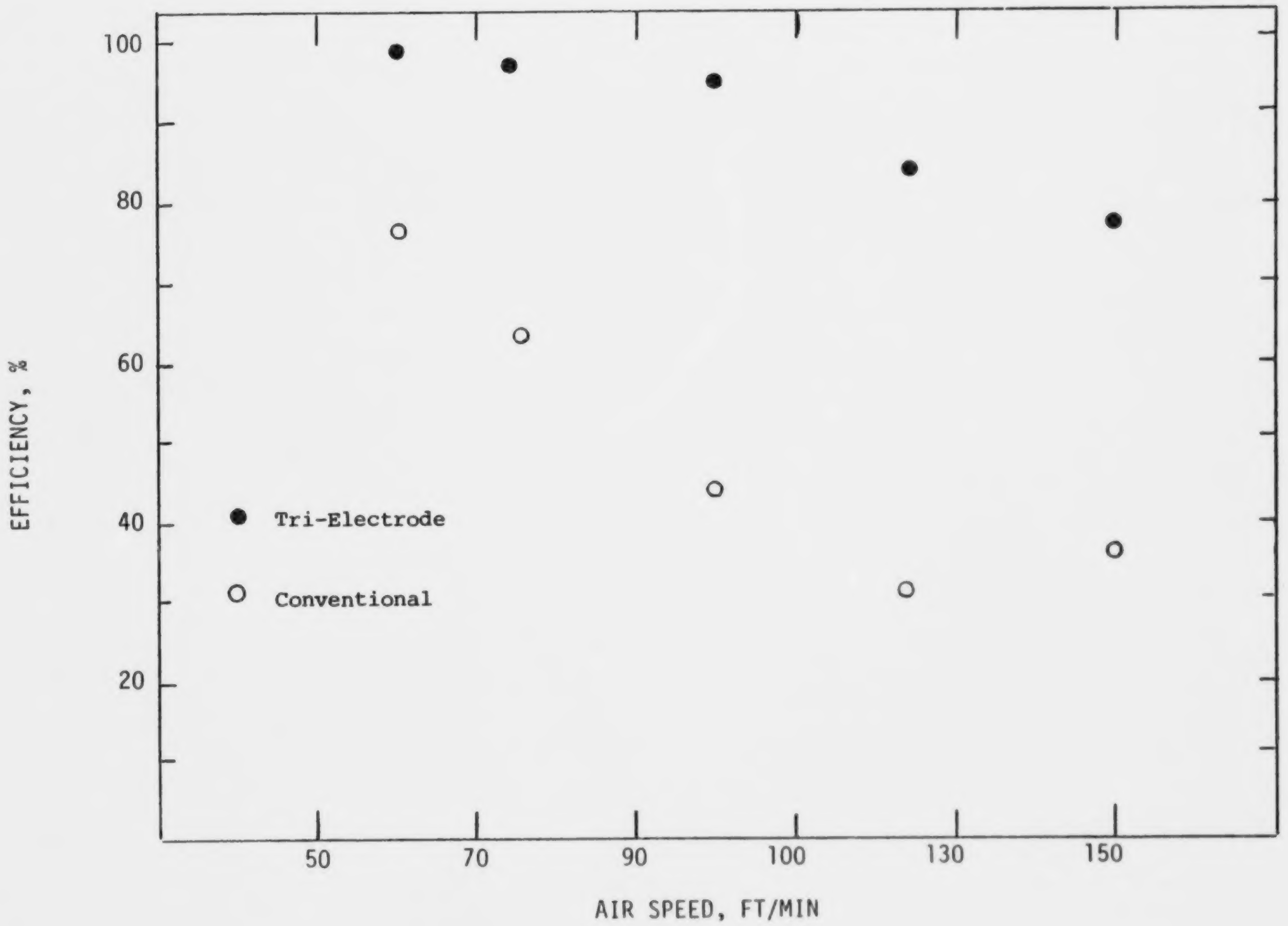

Fig. 3B. Precipitator performance as a function of air speed

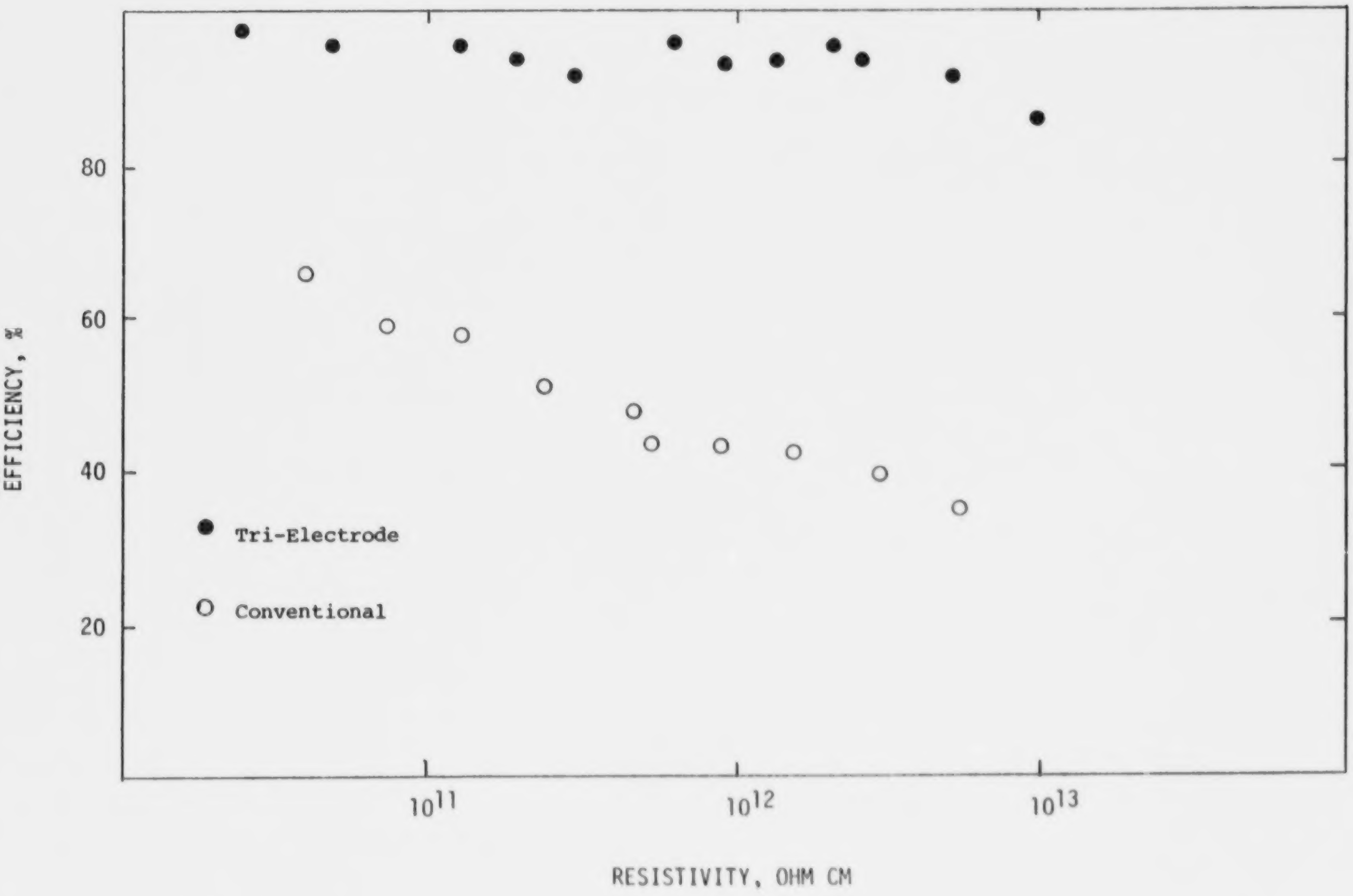

Fig. 4. Laboratory full scale Tri-Electrode-conventional precipitator tests

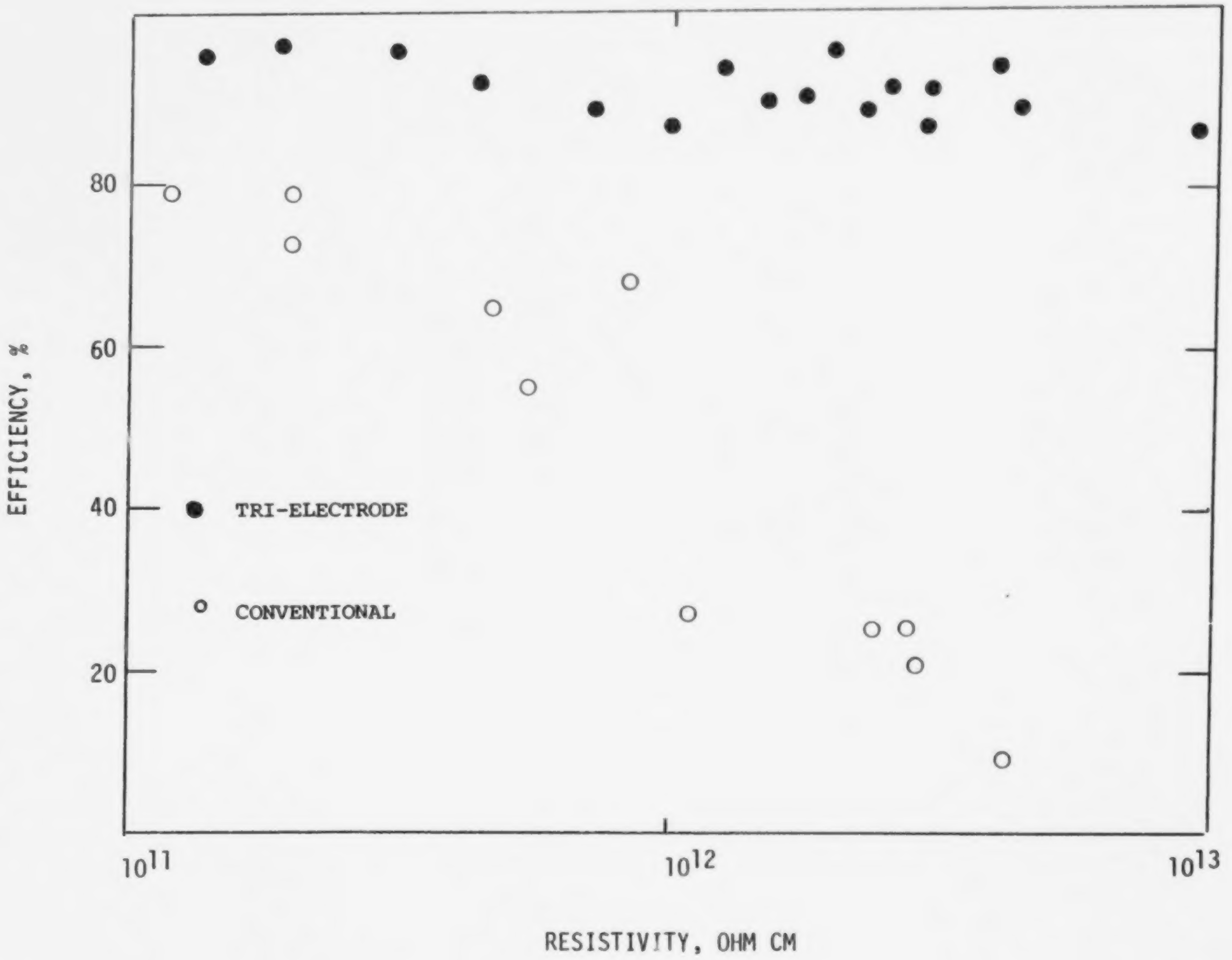

Fig. 5. Efficiency comparison with tubes present

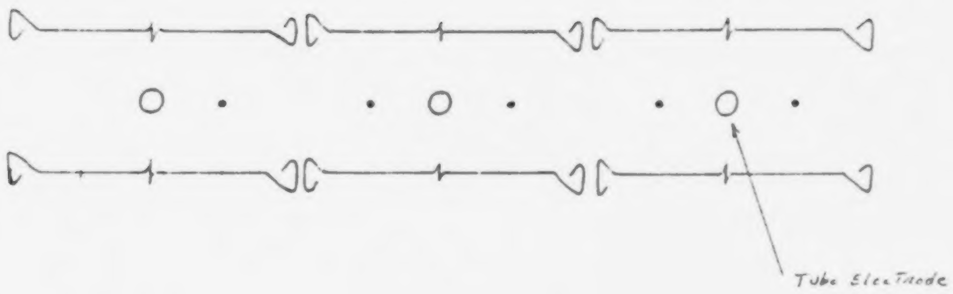

Fig. 6. Pilot Tri-Electrode
Precipitator gas passage

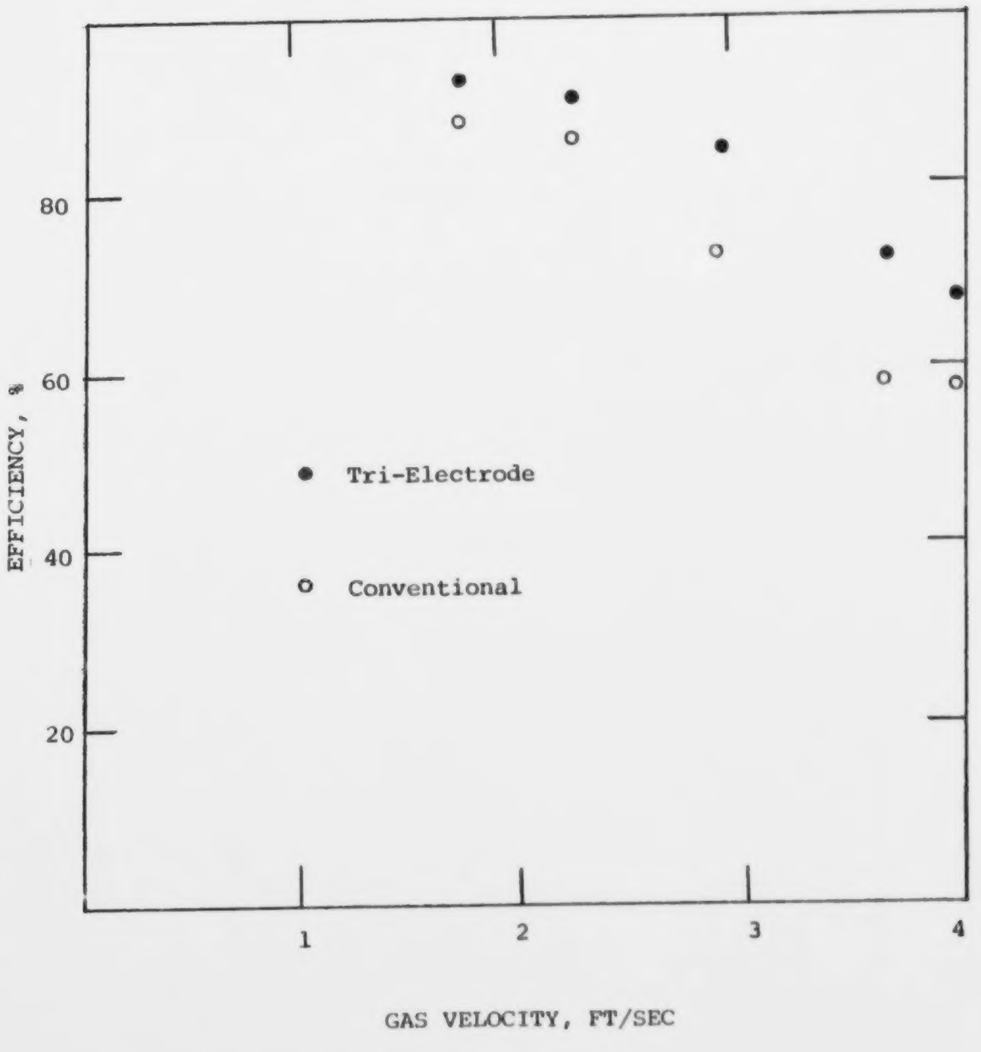

Fig. 7. Pilot study of Tri-Electrode Precipitator

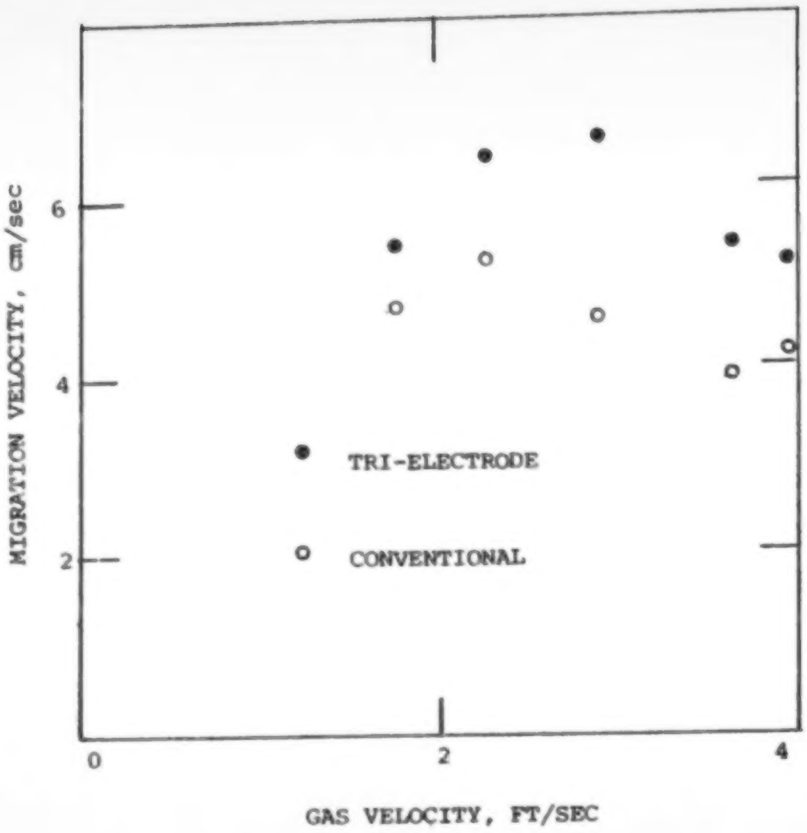

Fig. 8. Calculated migration velocity from pilot tests

COLLECTION OF FLY ASH WITH HIGH ELECTRICAL RESISTIVITY ELECTROSTATIC PRECIPITATOR PRECEDED BY THE EPA-SoRI PRECHARGER

by

L. E. Sparks, G. H. Ramsey and B. E. Daniel
U. S. Environmental Protection Agency
Industrial Environmental Research Laboratory
Particulate Technology Branch
Research Triangle Park, N. C. 27711

INTRODUCTION

It is well known that dust with high electrical resistivity is difficult to collect in electrostatic precipitators (ESP). The difficulty is primarily due to poor particle charging. This poor particle charging is not because particles having high electrical resistivity are intrinsically difficult to charge, but because back corona (which results from deposition of material on the collection electrode) produces a bipolar ion field. When ions of both positive and negative polarity are present in the charging region, the competing effects of the two plus low values of electric field produce low electrical charge on particles.

EPA has contracted with Southern Research Institute (SoRI) to develop a novel ESP consisting of a precharger and a downstream collector. The precharger has been built. The downstream collector is still being designed. The experiments described in this paper were designed to demonstrate the effectiveness of the precharger and to provide information needed to design the downstream collector. The data presented here are the first published data demonstrating the effect of the EPA/SoRI precharger on particle collection in an ESP.

CONCLUSIONS

Although the ESP was not the optimum downstream collector, particle collection by the precharger/ESP combination was excellent. With a specific collector area (SCA) of 29.2 $m^2/m^3/s$ (128 $ft^2/10^3$ acfm) the particulate emissions from the ESP without precharger were 2.5 times the particulate emissions from the precharger/ESP combination when collecting a dust with electrical resistivity greater than 10^{12} ohm-cm. The particulate emissions from the ESP alone were 15 times the particulate emissions from the combination when collecting a dust with electrical resistivity of about 10^{10} ohm-cm. The graded penetration (penetration versus particle diameter) curves show results consistent with those of the mass emission tests.

It appears that the precharger more than doubles the effective SCA of the ESP. Initial capital cost estimates indicate that the precharger will cost about a third to half the cost of one conventional electrical section. A conventional electrical section might increase the SCA of a small ESP, such as used for high sulfur coal, by as much as 33 percent and the SCA of a large ESP, such as used for low sulfur coal, by no more than 17 percent. Thus, the cost effectiveness of the precharger appears to be excellent.

The data were used to estimate the SCA needed to meet an emission standard of 13 ng/J (0.03 lb/10^6 Btu) when collecting fly ash with electrical resistivity of about 10^{12} ohm-cm. The estimated SCA is 70 $m^2/m^3/s$ (355 $ft^2/10^3$ acfm) which compares with an estimated SCA of at least 180 $m^2/m^3/s$ (930 $ft^2/10^3$ acfm) for a conventional ESP.

Pilot scale ($\sim$ 0.5 m^3/s) and prototype scale ($\sim$ 14 m^3/s) field tests plus more pilot plant tests are planned to confirm these initial results.

THE EPA/SoRI PRECHARGER

The EPA/SoRI precharger has been fully described by Pontius and Sparks (1978) and Pontius et al. (1978). The basic concept is presented in the following paragraphs quoted from Pontius et al. (1978).

"In research sponsored by the Particulate Technology Branch of the Industrial Environmental Research Laboratory, Environmental Protection Agency, Research Triangle Park, North Carolina, Southern Research Institute has devised and investigated the performance of a three-electrode system for controlling the effects of back corona in a particle precharger. In this device two of the three electrodes are the conventional corona discharge and passive electrodes. The third is a screen electrode placed near the passive electrode. Separate power supplies are provided for the corona discharge and screen electrodes. The passive electrode is set at ground potential.

"The general principle of operation is based on the use of the screen electrode as a sink for ions generated at the passive electrode as a result of back corona effects. Consider, for example, a two electrode system where the corona discharge electrode is at a high negative potential with respect to the grounded passive electrode. Now, locate an equipotential surface near the passive electrode and insert a conducting screen coincident with that equipotential surface. If the screen voltage is set equal to the original potential on the surface the electric field will be practically undisturbed in comparison with the original field. Only the non-zero thickness of the wires in the screen will cause very localized modifications to the field. A corona current originating at the discharge electrode will be distributed such that a fraction of the total equal to the ratio of open area to total surface of the screen will reach the passive electrode. The remainder of the current will be intercepted by the screen.

"Now, if the potential on the screen electrode is made more negative the field near the screen will become distorted in such a way that negative ions from the discharge electrode will be repelled from the screen wires and forced toward the open area, through which they can proceed to the plate. If we introduce high resistivity particulate material into the system, deposition will occur on both the plate and the screen electrodes. Since negative ions from the discharge electrode are being repelled by the screen, it must have a lower current density than the plate, and hence corona from the screen electrode would probably not occur. If back corona occurs, the positive ions from the passive electrode would be attracted to the screen electrode, where many would be captured and removed from the system. If most of the positive ions resulting from back corona can be captured by the screen electrode, the ion field between the screen and the discharge electrode would be essentially unipolar."

Pontius and Sparks (1978) and Pontius et al. (1978) presented data showing the effectiveness of the precharger in charging particles--but did not present data on particle collection in a device preceded by the precharger.

EXPERIMENTAL APPARATUS

The experiments were conducted in a one-lane pilot plant ESP located in EPA's Industrial Environmental Research Laboratory, Research Triangle Park, N.C.

The ESP was operated with plate-to-plate spacing of 22.9 cm (9 in.). The discharge electrodes were selected to maximize the electric field for a given current density. Several different discharge electrode geometries were tried including: screen electrodes, 0.318 cm diameter wire, 2.54 cm apart;, 0.635 diameter wires, 5.08 cm apart; and 0.635 cm diameter wires, 2.54 cm apart. Once the discharge electrode wires became dirty they all gave essentially the same voltage current (V-I) curves. A set of typical dirty wire/dirty plate V-I curves is shown in Figure 1.

The precharger was installed in the inlet duct to the ESP. The precharger was a two-lane precharger with plate-to-plate spacing of about 13 cm (5 in.). Each lane had a single discharge electrode.

Sampling was conducted using sampling ports located after the precharger and before the ESP, and at the ESP outlet. Mass samples were collected using an out-of-stack filter. Impactor sampling was conducted using Meteorology Research, Inc. cascade impactors. The cascade impactors were calibrated by personnel of EPA/Industrial Environmental Research Laboratory's Particulate Technology Branch (PATB), using the procedure described by Calvert et al. (1976).

The dust used in these experiments was a fly ash which was injected into the ESP through two sand blast guns. The particle size distribution of the resuspended fly ash was approximately log-normal with a geometric mass mean physical diameter of about 8.5 μm and a geometric standard deviation of about 3. The resistivity of this fly ash is about 10^{12} ohm-cm at 150°C when no steam is injected and 10^{10} ohm-cm at 20°C. Steam injection at 150°C reduced the resistivity to about 5×10^{11} ohm-

All data were reduced using TI-59 programmable calculator programs reported by Sparks (1978).

RESULTS

The average graded penetration curve for the high resistivity fly ash ($\sim 10^{12}$ ohm-cm) for both precharger-off and precharger-on is shown in Figure 2. These graded penetration curves were used to calculate effective migration velocities, $w_e(d_i)$, for various particle diameters.

$$w_e(d_i) = \ln Pt(d_i)/(A/V) \qquad (1)$$

where $Pt(d_i)$ is the penetration of particles with diameter d_i, and
A/V is the SCA.

The effective migration velocities are plotted in Figure 3.

The graded penetration curves indicate that rapping reentrainment may be a problem. The penetration of large particles is higher than expected and is probably due to reentrainment. An optimized downstream collector should minimize the rapping reentrainment problem.

The graded penetration curve for the low resistivity case is shown in Figure 4.

DESIGN TO MEET NSPS

The effective migration velocity curves can be used to estimate the SCA required give a given penetration or a given emission such as required to meet New Source Performance Standards (NSPS). The overall penetration can be estimated from

$$Pt_o = \sum_{i=1}^{\infty} \exp\left[f_i\ (A/V)\ w_e\ (d_i)\right] \qquad (2)$$

where f_i is the fraction of the total mass at the inlet with diameter d_i,
$w_e(d_i)$ is the effective migration velocity of particles with diameter d_i,
and A/V is the SCA.

Equation (2) was solved for a typical fly ash size distribution, various values of SCA, and $w_e(d_i)$ taken from Figure 3. The particle size distribution was assumed to be log-normal with d_g = 20 μm and σ_q = 4.5. The results of these calculations are shown in Table 1. Based on these calculations it appears that an SCA of 70 $m^2/m^3/s$ (355 $ft^2/10^3$ acfm) may be adequate to meet the proposed NSPS of 13 ng/J (0.03 $lb/10^6$ Btu). This is less than half the SCA required for a conventional ESP.

REFERENCES

Calvert, S., C. Lake, and R. Parker (1976), "Cascade Impactor Calibration Guidelines," EPA-600/2-76-118 (NTIS PB 252-656/AS), April 1976.

Pontius, D. H. and L. E. Sparks (1978), "A Novel Device for Charging High Resistivity Dust,", J. Air Poll. Control Assoc. 28, 698.

Pontius, D. H., P. V. Bush, and L. E. Sparks (1978), "A New Precharger for Two Stage Electrostatic Precipitation of High Resistivity Dust." In Symposium on the Transfer and Utilization of Particulate Control Technology: Volume I. Electrostatic Precipitators, EPA-600/7-79-044a, February 1979.

Sparks, L. E. (1978), "Cascade Impactor Data Reduction with SR-52 and TI-59 Programmable Calculators," EPA-600/7-78-226 (NTIS PB 290 710), November 1978.

Table 1. ESTIMATED OVERALL PENETRATION FOR VARIOUS SCA IN NOVEL ESP COLLECTING FLY ASH WITH HIGH RESISTIVITY

SCA			
$m^2/m^3/s$	$(ft^2/10^3$ acfm)	Pt_o	E%
25	(127)	0.087	91.30
40	(203)	0.031	96.9
50	(254)	0.016	98.4
60	(304)	0.0083	99.17
70	(355)	0.0044	99.56
75	(381)	0.0032	99.68
80	(406)	0.0023	99.77

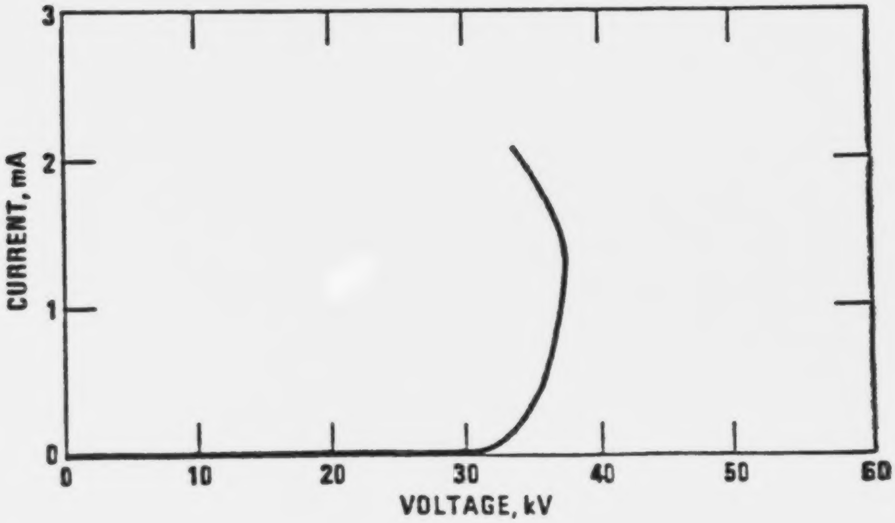

Figure 1. Typical dirty-wire/dirty-plate V-I curves for high resistivity case.

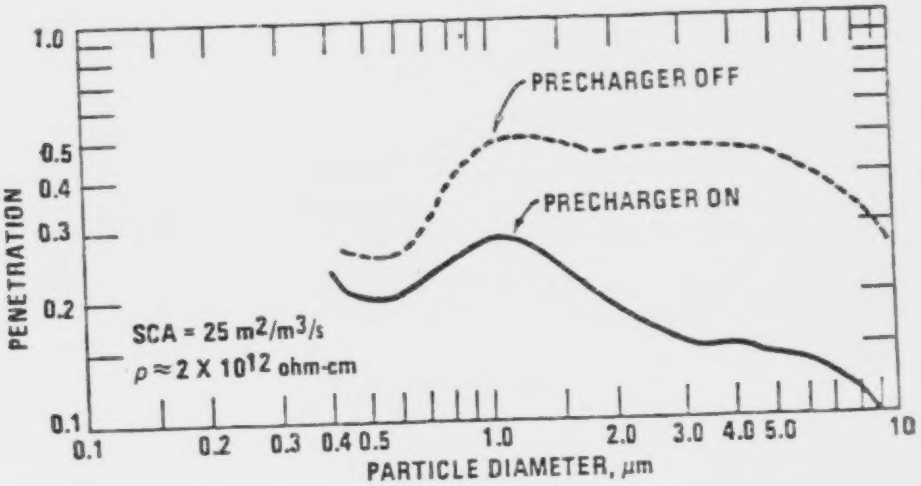

Figure 2. Graded penetration curves for high resistivity runs.

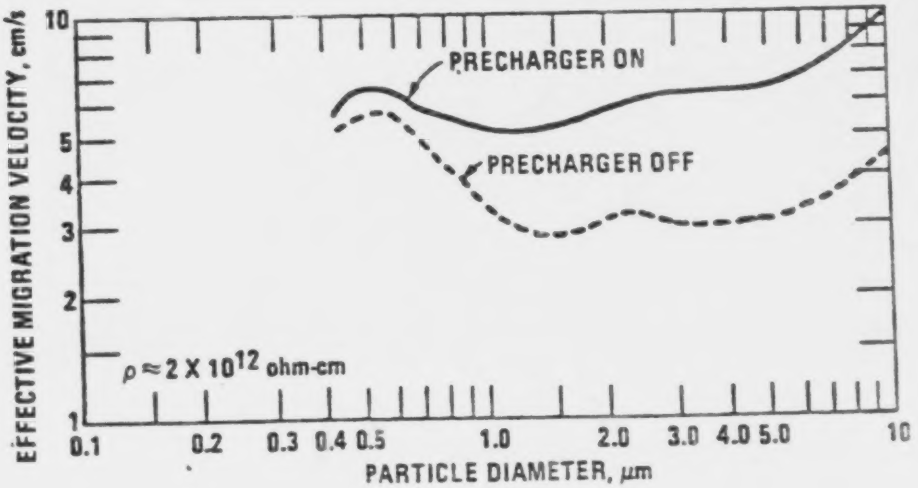

Figure 3. Effective migration velocity versus particle diameter for high resistivity runs.

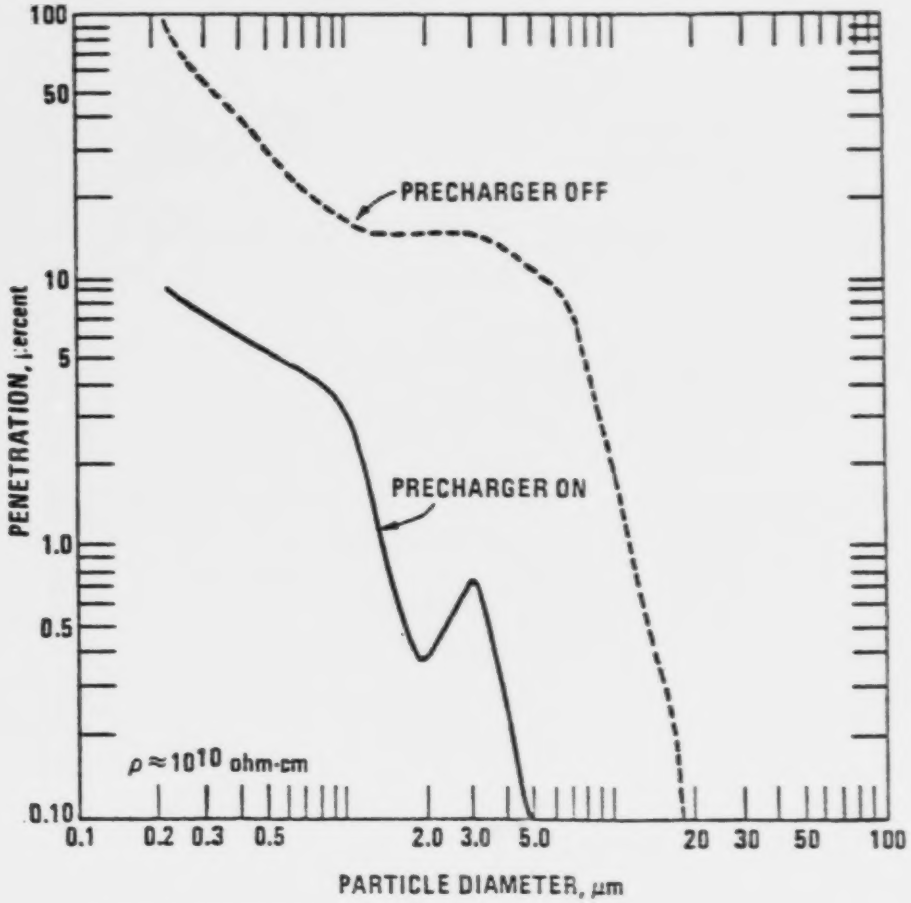

Figure 4. Graded penetration curves for low resistivity runs.

PILOT PLANT/FULL SCALE EP SYSTEM DESIGN AND PERFORMANCE ON A BOF APPLICATION

By:
Douglas Ruth, P.E.
United McGill Corporation
Columbus, Ohio 43216
And:
David Shilton
CF & I Steel Corporation
Pueblo, Colorado 81002

ABSTRACT

An ESP pilot plant study was done on emissions from a BOF process which is cyclic with very high and low gas volumes, temperature and grain loadings. Data collected were EP performance vs. gas velocity, and collection area. Also measured was particle size distribution, dust resistivity, and grain loading vs. opacity at the EP outlet. From this data, a full size EP system was designed and installed. Recent performance tests indicate the data agrees well with the initial pilot plant study. Emissions have been reduced from 11 grs/scf to less than .033 grs/scf and opacity to 20% or less.

INTRODUCTION

The BOF shop where these tests were done, CF & I, Pueblo Colorado, is operated with two (2) 90 metric ton vessels, with one vessel active at any given time; the other vessel concurrently undergoing a reline. A precipitator system installed would accordingly be designed to handle the emission from one active vessel. Specifically, the volume to the precipitator would be 300,000 acfm at 350°F, with moistures between 10 to 30%. This shop utilizes an open hood concept with a spark box cooling chamber immediately after the vessel. This system removes the bulk of the heavy solids and is directed with a separate clarifier - lagoon water treatment system.

The emission from a BOF furnace is cyclic, with high grain loading for a period of twenty minutes, then a quiescent period lasting 20 minutes. After the first 20 minute period, oxygen lance reblows may be necessary to satisfy metalurgical requirements on the steel being melted. The highest grain loadings are usually associated with reblows. Scrap iron is poured into the converter, which is filled with molten iron, then oxygen lanced. This process takes about 20 minutes, and it is during this time that the outlet flue volume, gas temperature and particulate emissions increase markedly. During this blow period, emissions go from essentially zero to around 11 gr/scf, the temperature goes from 175°F to near 400°F, and the gas volume increases to it's maximum value of about 300,000 acfm. The particulate emission is primarily Fe_2O_3, 90% of which is below 10 micron in size, with 10% of these below 1 micron. The dust resistivity at flue gas conditions is about 10^{10} ohm-cm. It was the desire of CF & I to reduce these emissions to .033 grs/scf and not to exceed a visual stack opacity of 20%. For these requirements, United McGill designed and installed an electrostatic precipitator system.

PILOT PLANT STUDY

One of the best possible ways to specify the design and size of a full size electrostatic precipitator system is to do a pilot plant study on the site where it is to be used. This is so the actual stack emissions to be collected are specifically characterized and actual operating data are obtained with a unit exactly like the full scale system, only reduced in size. This was done at CF & I during April 1976 by United McGill Corporation, using one of their Mobile EPs and testing laboratories. This Mobile is a completely self-contained EP system, which has three (3) fields, each of which has its own TR set and voltage control, rapper system, hopper, and rotary valve. Also included are the fan, duct work, outlet stack, evaporative cooler, control panel and inlet/outlet testing ports including opacity transmissometers. Each field uses the McGill needle/plate design, with needles on the leading and trailing edges of the discharge plates, which are held at a positive potential of about 25 KV. The Mobile EP cross-sectional area is 25 ft^2, and the fan is capable of pulling 8000 cfm at temperatures up to 800°F. The entire EP system is mounted on a trailer for ease of transportation. It can usually be set up and be operating in eight (8) hours. The accompanying laboratory trailer is fully equipped for performing the standard EPA stack tests, gas analysis by infared spectrophotometry, and some chemical analysis.

At CF & I, the Mobile EP was connected to a breech in the existing downcomer from the process by a 85 ft long by 20 inch diameter insulated duct. Figure 1 shows the Mobile EP at this installation. Figure 2 is another view of the installation.

Emission collection performance of the pilot EP was done only during the blow or reblow part of the BOF cycle, since this is the period of maximum emission. A crew from CF & I tested at a point before the EP inlet using the W.P.-50 apparatus, while a simultaneous EP outlet test was done by a United McGill crew, using EPA Method 5. An observer was located in the BOF shop who gave signals to the test crews at the beginning of a cycle. Within one minute, the equipment would be readied and a portion of a test completed during the 20 minutes blow cycle. The EP inlet test could only last 8 minutes due to the high grain loading. The outlet tests were done for 2 blow/reblow cycles, but with testing halted during the quiet cycle. Figure 3 shows the EP outlet during a blow cycle with all fields de-energized. Figure 4 shows the outlet with one field on, Figure 5 shows 2 fields on and Figure 6 with all three fields energized. The white plume at this point is merely water condensation. Figure 7 and 8 show that indeed the EP collects the dust.

The primary data to be obtained were that of optimum EP flow-through velocity, specific collection area, and rapping timing. Operation temperature is more or less fixed by the process, which was 360°F during the periods of heavy emission, so no attempt was made to change this, except to insulate the duct. Also of interest, was the chemical make up of the dust, dust resistivity, particle size, and opacity measurements.

The EP velocity was varied by changing the volume flow with a damper control on the fan section and was varied between 1.5 to 3.0 ft/sec. The specific collection area was also varied in this manner, and also by de-energizing one or two fields from 400 to 800 ft^2 per 1000 acfm. From this data, graphs were generated showing the relation between outlet grain loading EP flow-through velocity, and specific collection area. From this, one could then determine the full size EP design.

Figure 9 shows the result of a dust resistivity measurement vs. temperature and moisture. Figure 10 shows a typical particle size distribution, a correlation between grain loading and opacity was done, with results shown in Figure 12, for a 48 inch diameter stack.

EP DESIGN

From a graph relating EP gas velocity and outlet grain loading, obtained from the pilot testing, the cross-sectional area of the full size unit was chosen. Also taken into account was the particle size, especially in regards to re-entrainment. This influenced the choice in the number of fields required, as well as the velocity. As for plate area or total collection area, the following procedure was used. A curve of the form

$$\text{outlet} = e^{-(a \times \text{SCA} + b)}$$

was fit to the data by means of regression analysis, ie., least square fit.

This technique finds values for the fitting parameters a, b. Once these are determined, one can calculate the required SCA needed to achieve the desired outlet grain loading, providing the operating conditions for the EP, such as inlet loading, temperature and moisture, are in the range that they were during the pilot testing. It was assumed that this would be so since the process would not be expected to change. The equation is only a fitting technique and no physical meaning is given to it, it just happens to fit this type of data. It might be argued that it is a modified Deutsch - Anderson equation, however, one could find more argument against this than for it.

As mentioned, the basic EP size was determined by the EP velocity/gas volume relation, which in this case, dictated a 1800 ft^2 chamber. The total collection surface area required determined by the above technique, was found to be about 238,000 ft^2 to treat 300,00 acfm of gas. This would yield a predicted outlet grain loading of .033 grs/scf. For these requirements, it was decided that a McGill Model 5-600x4 EP would be the best choice. This consists of 4 chambers, each 600 ft^2 in cross-sectional area, each with five fields, and each with about 79,000 ft^2 of collection area. Four, rather than the necessary three units was chosen so that there would be 3 active units and one standby. Using three units for 300,000 cfm of gas at 360°F and 11 grs/scf inlet loading gives an average EP flow through velocity of 2.7 fps, an SCA of 790 for an expected outlet of .033 grs/scf and 20% or less visual opacity. The EP's are paired, and each pair share the same TR set on the first field. Fields 2, 3 and 4, 5 on each EP have their own TR set. These were designed to operate at 25 KV at 500 ma each.

Since each of the four precipitators is the same, flow modeling was done on only one unit. A 1/[illegible]6 scale model was constructed of plexiglas. The velocity pressure was set the same in the model as would be found in the full size system (Euler Modeling) and a velocity profile measured across the face of the model. The standard technique of fitting turning vanes and perforated plates to provide an even flow distribution was used. The final configuration installed was diagonal grid of channel pieces with a 6" opening, followed by a perforated plate and then a set of splitter vanes.

Another design consideration was dust handling. Each row of EP hoppers are connected by a screw conveyor. These in turn empty into a pnuematic conveyor to a dust silo. Dust from the silo is pelletized and carried away by rail car. This hopper dust has a bulk density of around 60 lbs/ft^3. One third of the dust from the process is quite heavy, near 140 lbs/ft^3. For this, a single dropout chamber was built before the EP system inlet. This dust is also conveyed to the silo for pelletizing and subsequent re-use.

One final concern was that of possible explosion due to the high CO levels possible. In light of this, a CO monitoring system was designed to de-energize the fields. This reduces the possibility of a spark induced explosion in the EP.

FABRICATION AND INSTALLATION

The unique McGill design allows for a modular construction; that is, each EP is made up of one or more of five standard modules. These individual modules are manufactured complete before shipping, including plates, side skins, and rapper boxes where required. The top structures, hoppers and transitions are also shop produced and shipped ready for installation. In this particular case, the 600 model is made of 4-150 ft^2 modules, stacked 2 x 2, each field. Therefore, each of the four EP's is a 5 x 4 array of modules for a total of 80 modules to make up the system. Field erection then consists only of pouring the foundation, setting up the support structure and hoppers and then lifting the modules in place. Top structures and transitions are then installed.

Finally the wiring, piping, insulation and siding is installed. Using this method, the quality of the final product is higher, because most of the EP is shop produced and assembled, under controlled supervision. This means that the quality of the installation is not totally in the hands of a contractor who may not have the necessary experience in areas where critical assembly is needed. This is especially true in the case of plate alignment.

FULL SCALE SYSTEM PERFORMANCE

Colorado regulations require that the full system emission be less than 40 lbs/hr, and less than 20% opacity. The three unit system operation easily meets the process weight requirement. Figure 12 shows a comparison between the pilot plant data and the full system performance data. As can be seen, the agreement between the two sets of data is good.

With three of the four units in operation, there are occasional excursions above 20% opacity. Most typically there readings over 20% opacity are brief and associated with commencement of the blow or reblows. These puffs are indigenous to the BOF process and well controlled with all four units operating.

OPERATION AND MAINTENANCE

All four EP's were installed and operating within two years after the pilot plant study. The biggest operating problem with the system has been associated with the high density dust transporting system; evidenced by plugging in the line or defective gate valves. Periodic cleaning of all the transporters is needed to maintain continuity of dust removal.

It was also found necessary to attend to the "automatic" pelletizer full time, due to the required water feed adjustments. However, one eight hour shift can pelletize dust from a 24 hour collection period. It is also necessary to blow off the ledges between modules with compressed air once every shift, due to the high buildup in this area.

The biggest problem area with EP operation seems to be failure of the insulators in the rapper boxes, especially in colder weather. A re-piping of the purge air system has reduced this problem somewhat.

SUMMARY

The pilot plant testing and subsequent data has provided for a successful full size EP design and installation for this BOF application. The problems unique to this process were solved at the early stage of the pilot plant program when design changes were easily made. As a result, the required emission level and opacity is within that allowed by state regulation with no major problems in day to day operation.

Reproduced from
best available copy.

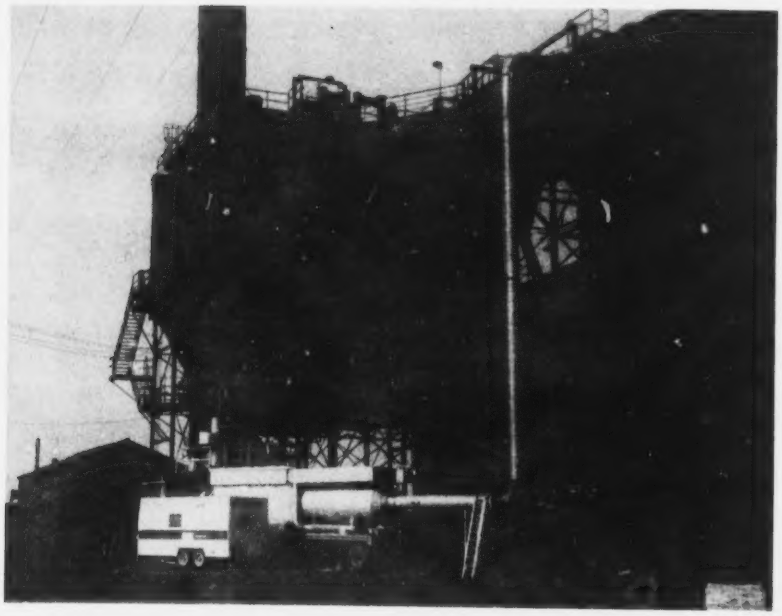

Figure 1 - Pilot Plant installation at BOF plant

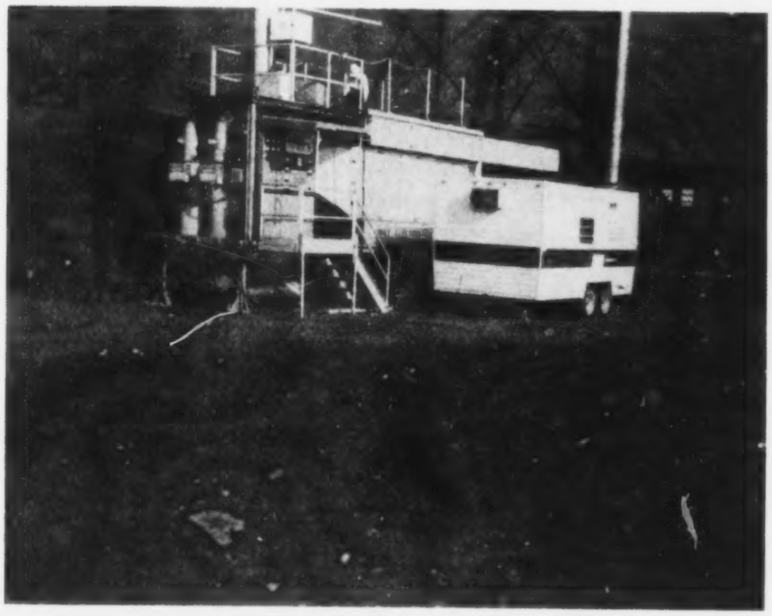

Figure 2 - Another view of Mobile EP at BOF site

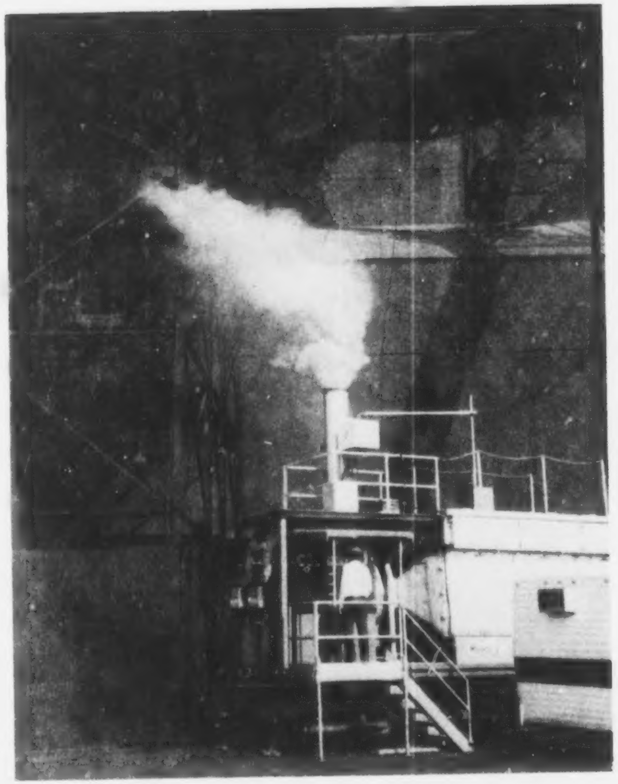

Mobile EP outlet with all
fields off during blow cycle

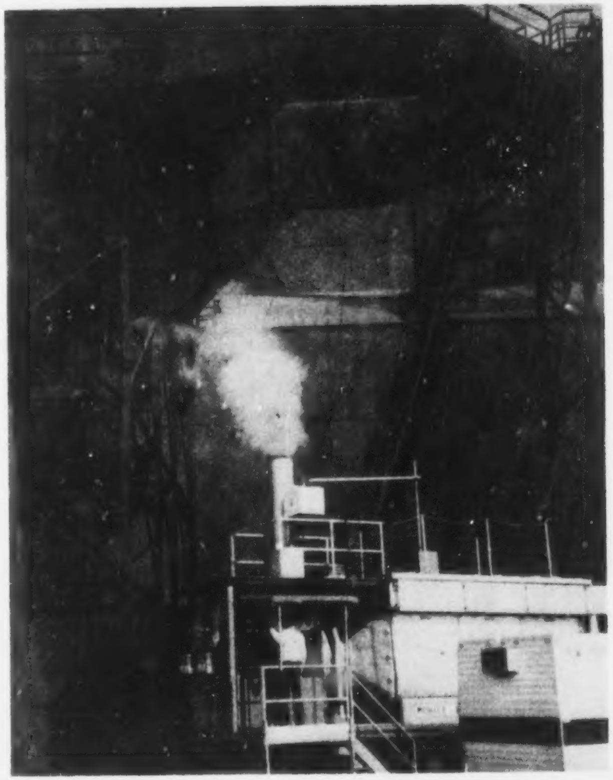

Figure 4 - Mobile EP outlet with one field on

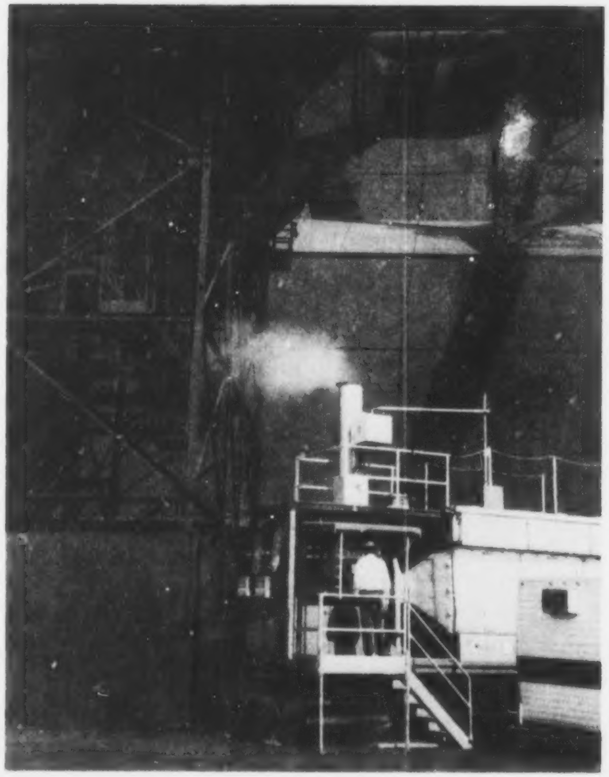

Figure 5 - Mobile EP outlet with 2 fields

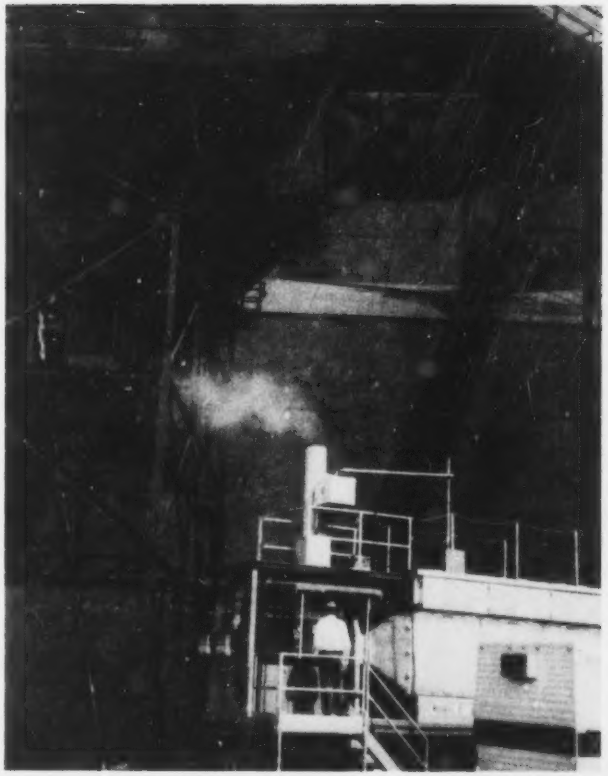

Figure 6 - Mobile EP outlet with 3 fields

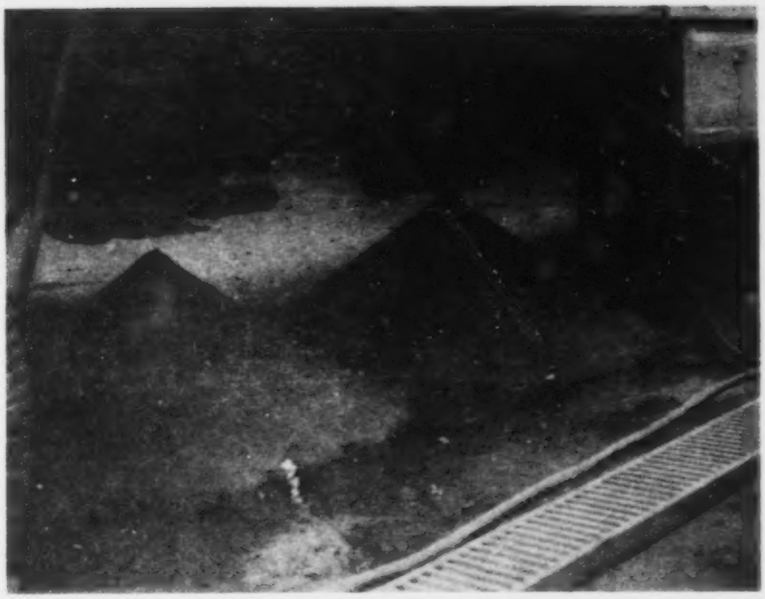

Figure 7 - Mobile EP hopper outlet

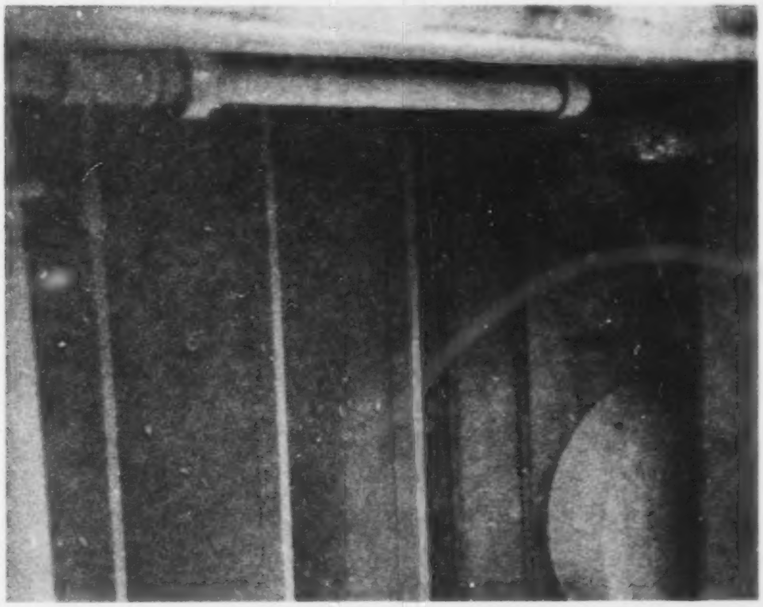

Figure 8 - Mobile EP plates with BOF

FIGURE 9, BOF DUST RESISTIVITY

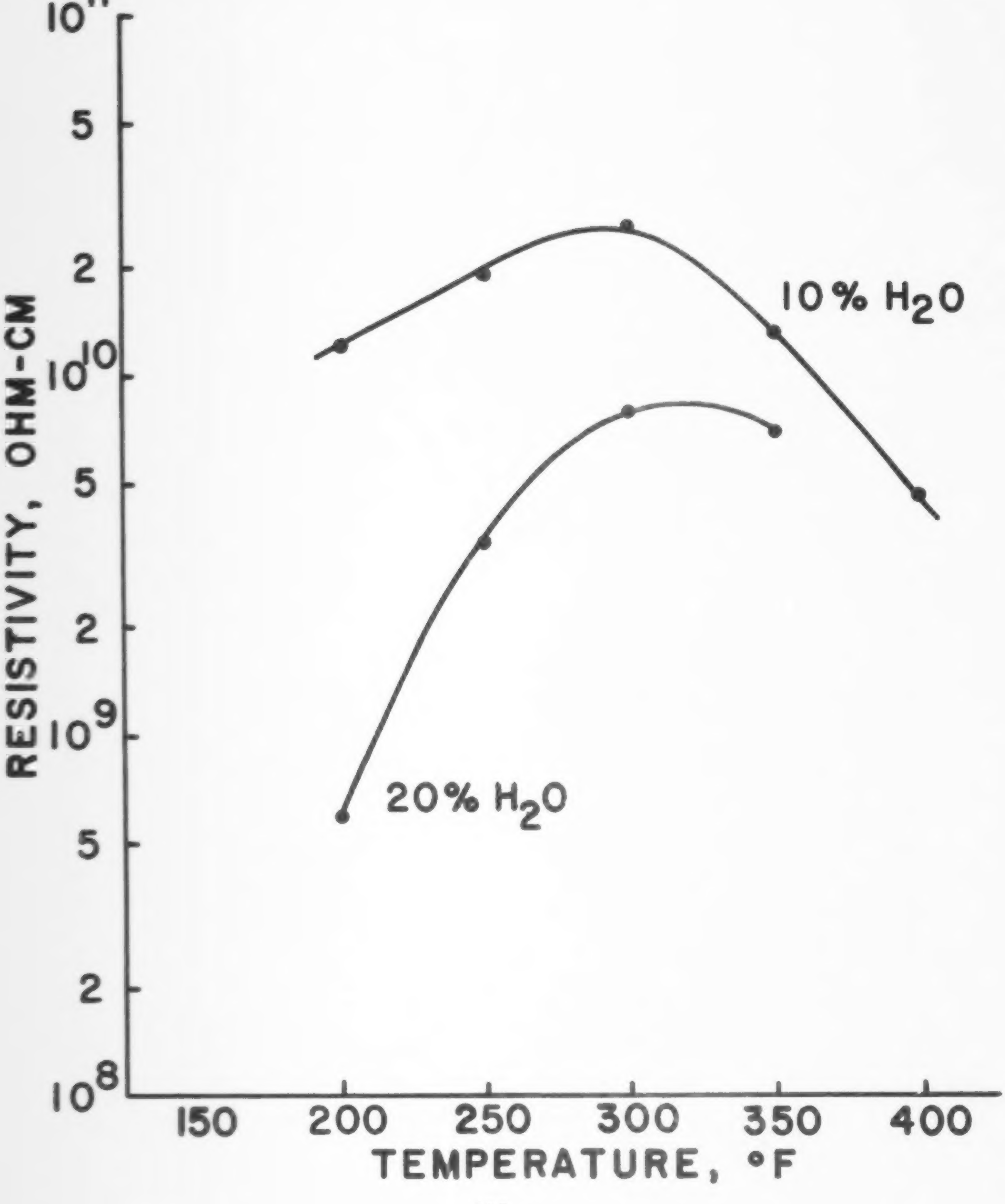

FIGURE 10, PARTICLE SIZE DISTRIBUTION

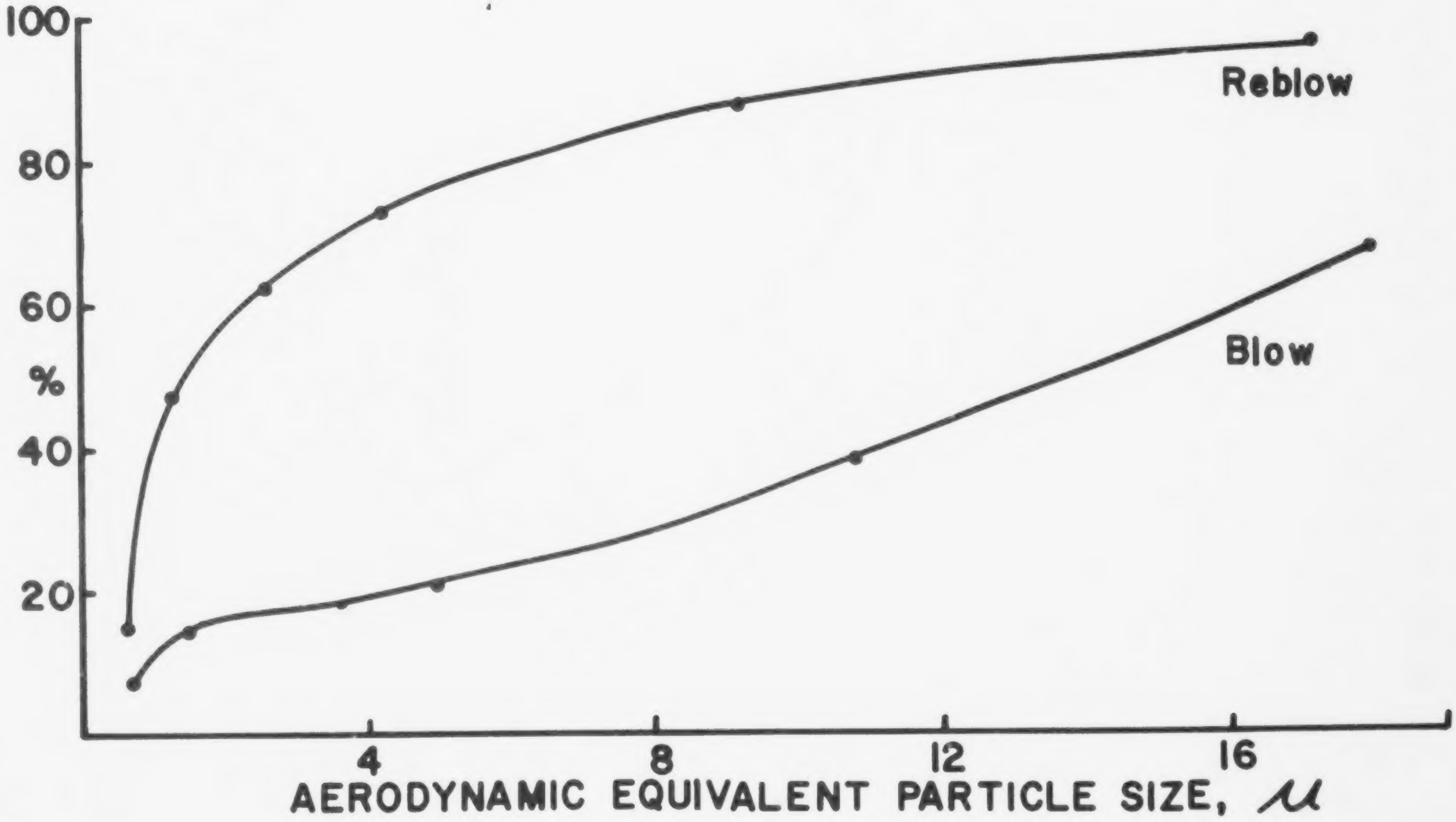

FIGURE 11, OPACITY vs ESP OUTLET

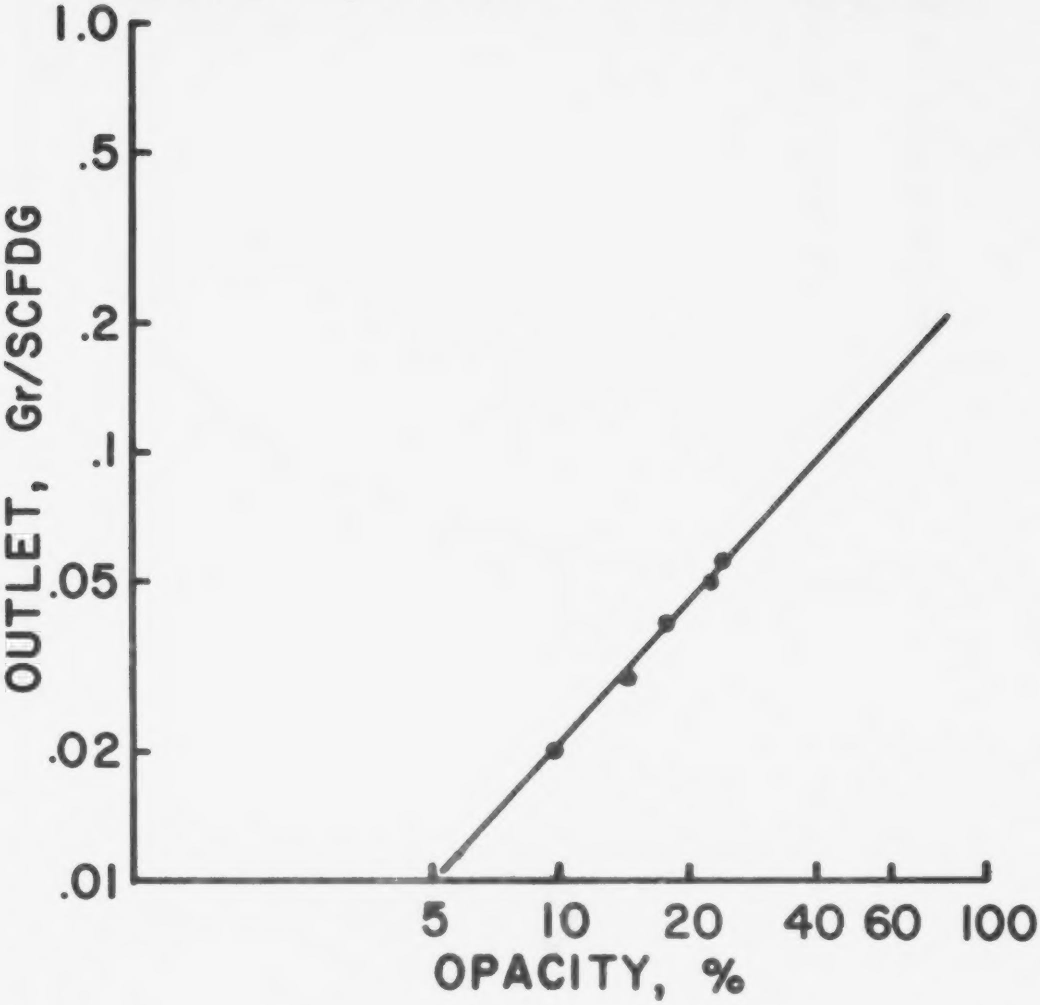

FIGURE 12

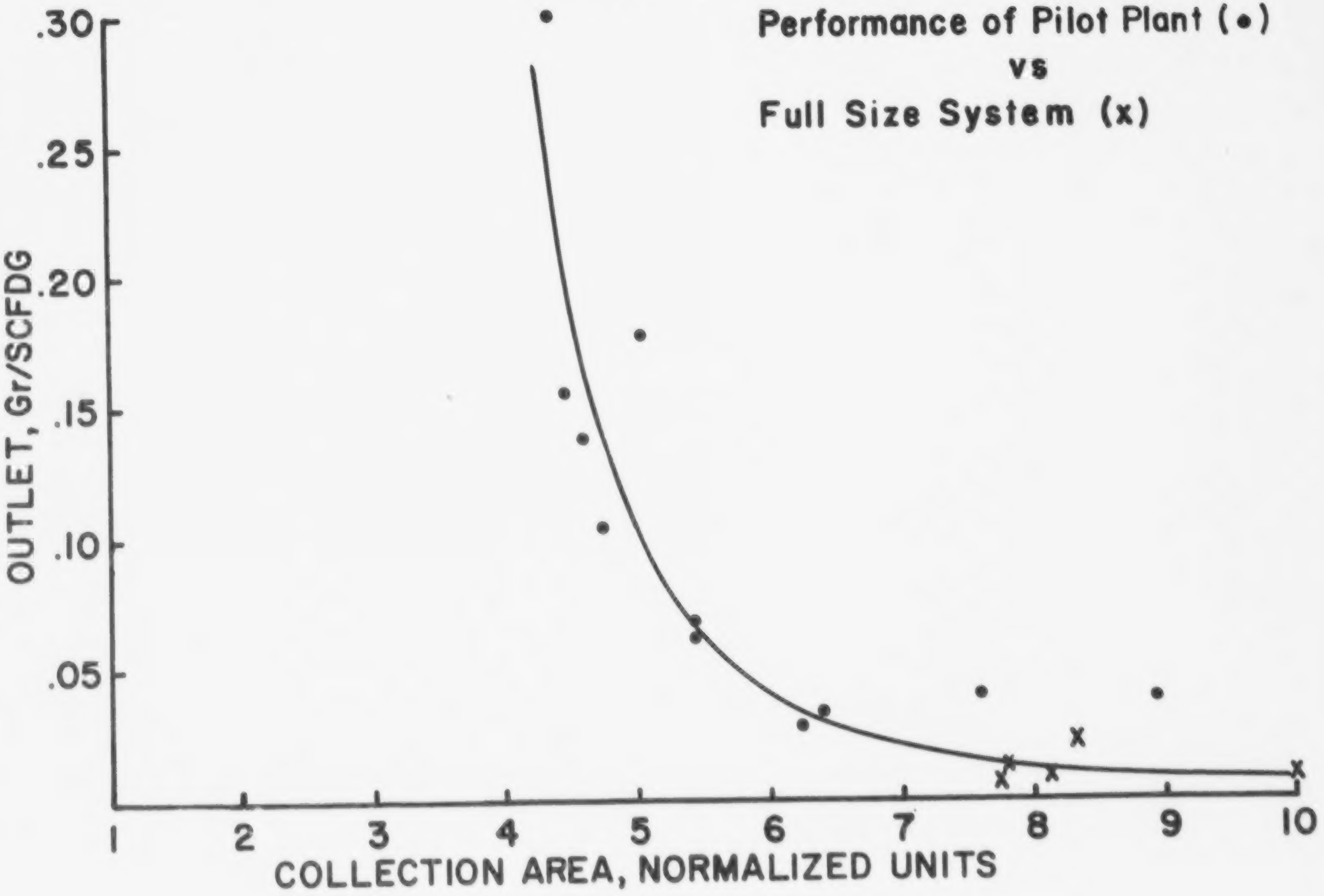

Performance of Pilot Plant (●)
vs
Full Size System (x)

THE SELECTION AND OPERATION OF A NEW PRECIPITATOR SYSTEM ON AN EXISTING BASIC OXYGEN FURNACE

By:

Douglas Ruth, P.E.
United Mc Gill Corporation
2400 Fairwood Avenue
Columbus, Ohio 43216
And:
David Shilton
CF&I Steel Corporation
P. O. Box 316
Pueblo, Colorado 81002

ABSTRACT

The selection of a new precipitator installation on an existing basic oxygen furnace facility is discussed. The selection process began with a search of technical alternatives and ultimately was based on a mobile unit test unit program. The completed precipitator system was then tested after initial operation. Performance data and operating practices are then summarized.

THE SELECTION AND OPERATION OF A NEW PRECIPITATOR SYSTEM ON AN EXISTING BASIC OXYGEN FURNACE

SEARCH AND SELECTION

The original precipitator was installed as part of the Basic Oxygen Furnace installation completed in the summer of 1961. At that time, performance on precipitators, or for that matter, any other air pollution control device, was not predicated on opacities, but on efficiencies or outlet grain loadings. A satisfactory level of particulate emissions on a pounds-per-hour basis was usually established between the purchaser and the supplier of the air pollution control device. The precipitator supplied with the original Basic Oxygen Steel Shop in 1961 was commensurate with the air pollution control regulations then in force or anticipated.

CF&I operates a two 90 metric ton vessel BOF shop with one vessel active at any given time; the other vessel concurrently undergoing a reline. The precipitator system installed was accordingly designed to handle the emissions from one active vessel. Specifically, the volume to the precipitator was rated at 300,000 ACFM at 350° F. with moisture levels varying between 10 to 30%. CF&I's BOF shop utilizes an open hood concept with a "spark box" cooling chamber immediately after the vessel. This system removes much of the heavy solids which are then directed to a clarifier-lagoon water treatment system. It should be noted that a spark box or a somewhat similar pre-treatment device would be included in a majority of air pollution control systems installed on the existing BOF. The original precipitator system was designed with an efficiency of 97.5%. This efficiency was established between the incoming emissions to the precipitator, but after the spark box, and the emissions emanating from the stack.

This two-chamber three field precipitator was first tested in October, 1962. Results of that test indicated an operating efficiency of 97.26% with volumes near 300,000 ACFM at 350° F. Although not at the design criteria, it was acceptable at that time, due to the difficulty in verifying all of any of the idiosyncrasies which may have been evident during the testing. It is worth noting that opacity considerations were not of primary importance during this era of air pollution control.

During the first ten years of operation of the original precipitators, trends became apparent. The principal problem was severe corrosion of the collecting plates primarily near their lower connection point. Complete replacement of most of the internal components was necessary approximately every three years. An early problem with severe corrosion and subsequent breakage of the emitter electrode wires was substantially solved by the use of Carpenter 20 wiring to replace the original 316 stainless; however, during the periodic repair periods, plates, wires, and frames were all replaced. The danger of explosions with high levels of CO was not only realized, but actual explosions did occur. Most of the explosions were quite minor and only on rare occasions was more than a few minutes of production time lost. Another major drawback of the original precipitators was the two-chambered limitation. Shutting down one half of the precipitator to work on the remaining chamber resulted in excessive stack emissions. Additionally, with only an insulated dividing wall, the shut down chamber took a long time to cool down sufficiently for workmen to enter. A gradual deterioration of the precipitator was evident after the first ten years of operation.

The advent of the Colorado State Regulation I, with a stringent 20% opacity limitation on any given stack reading, made it necessary to re-evaluate the performance of the BOF precipitator. Opacity observations on the BOF precipitator stack were initiated on a routine basis in 1974. Observations indicated compliance with the 20% limit a great deal of the time in cool or cold damp weather, but readings above 20% opacity in hot, dry conditions. The affect of ambient conditions on the precipitator was immense - a phenomenon which we have never fully understood.

In order to appraise the operating conditions of the precipitator, an efficiency test was performed in August 1974. Testing was performed at the inlet to the precipitators and the existing stack. Dust sampling commenced at the start of the oxygen blow and included any reblows which occur. Usually, the oxygen blow would last 19 to 21 minutes with reblows 30 seconds to 2 minutes. Test data was fractionated to various parts of the cycle and averages also developed for the whole process. These tests indicated an average efficiency of 97.5%, actually higher than the original tests in 1962; a maximum inlet grain loading of 11 GR/SCFD, an average inlet grain loading of 7 GR/SCFD, and an average outlet loading of .1261 GR/SCFD. The maximum inlet grain loadings were usually associated with reblows. Stack opacities observed during these tests averaged 68%. The measured volume of gas entering the precipitator thru the ductwork had decreased to 212,000 ACFM at 350° F., indicative of leaks which had accumulated in the precipitator system during 13 years of operation. The calculated emission of 55 lbs./heat with over 10,000 heats per year established an operating level of 300 tons per year of emissions. Assuming 1.3 heats per hour, this translated to approximately 72 lb./hr. of emissions. The Colorado Process Weight Regulation allowed for 40 lb./hr. Subsequent tests in 1975, even after one-half of the precipitator was rebuilt, indicated emission levels near the 300 ton-per-year level. The actual search and selection of a system of the BOF primary emission source now had its design criteria established; performance at less than 20% opacity at any time and a process weight level below 40 lb./hr. of emissions at the inlet conditions established.

It should be noted that the 20% opacity requirement is stated "at any time". Colorado opacity regulations do not allow averaging of opacity readings; any instantaneous reading over 20% opacity is technically a violation. Hence, our design requirements could actually be described as a clear stack during normal operation with a 20% opacity limit for non-optimum performance during a reblow.

CF&I virtually accepted the fact that upgrading the existing precipitators electrically would not meet the more stringent requirements. The limitation of collection surface area would remain with the two chambered, three-field precipitator. A closed-hood, non-combustion system had been discussed several years earlier, but was prohibitively difficult to install in an existing BOF shop, and the merits of its installation from an air pollution control standpoint were rather dubious. The scope of inquiries for new or additional equipment was narrowed down to baghouses, scrubbers, and precipitators.

Baghouses were discussed but never seriously considered due to the burn up potential caused by the wide variation of temperatures inherent with the BOF. Any baghouse would need a complex conditioning tower ahead of it to relieve moisture problems and to protect it from high temperature excursions.

Two options remained; scrubbers and precipitators. The trend in 1975 and still today was to install scrubbers on BOF shops. Considerably more than half of the BOF shops in North America use scrubbers for primary control. Preliminary proposals on a scrubber installation at the CF&I shop were extremely expensive; in retrospect, approximately double that of the ultimate precipitator installation. Outside of the initial capital cost, scrubbers were obviously considerably more energy intensive than precipitators, due to the high horsepower requirements of higher operating pressure differentials. The Pueblo Plant's water system and future discharge permit conditions also could have been affected with the addition of a water-based, solid-waste removal system associated with a scrubber. The most attractive features of a scrubber system were the non-explosive nature of its operation with carbon monoxide and the ability of a scrubber to operate under the many wide process changes which accompany a basic oxygen furnace operation. CF&I then sought precipitator equipment which could reduce the disadvantages of scrubbers and mitigate precipitator maladies.

Several precipitator alternatives were sought by CF&I. Consideration was given to adding one or two more precipitators to the existing unit so as to permit maintenance on one unit and comply with the control regulations with the residual operating units. All designs of precipitators were initially considered: rigid frame (European design), wire-weight, stiff electrode, and various other electrode configurations. Consideration was given to rebuild the existing precipitators with new internals of a different manufacturer. Many of the precipitator vendors did not wish to guarantee a system with their internal components in another manufacturer's 15-year-old unit. With all the alternatives being evaluated, the underlying principle of the modifications to be made was to meet the opacity and process weight requirements with one unit (precipitator) off line.

Through the course of evaluating precipitator proposals, the ultimate efficiency and control needed to satisfy the opacity requirement became questionable. Installations on BOF shops in Europe and Great Britain were visited, as well as other industrial operations in the United States. It was observed that the German BOF installation did not need to satisfy any opacity requirements, only a concentration allowance of .07 GR/SCFD. A British Steel Operation needed to satisfy an outlet emission of .05 GR/SCFD. Opacity vs. Grain Loading tests done on the existing CF&I BOF precipitator in December 1974 did not conclusively provide a means to verify the actual grain loading corresponding to 20% opacity. Because the levels of performance on the BOF's operating overseas did not show any visible emissions, it was thought that a grain loading below those reported GR/SCFD would conservatively satisfy a 20% opacity requirement. Additionally, manufacturers who were members of the International Gas Cleaning Institute (IGCI) were reluctant to guarantee any precipitator system to an opacity proviso. Consequently, the number of proposals received which did accept this opacity guarantee was limited and those which did decreased the outlet option to .033 GR/SCFD in order to comply with the opacity limit.

In order to verify the actual size of the precipitator system which was required to meet the grain loading and opacity limits, the United McGill mobile EP unit was operated on a slip stream at the CF&I BOF plant in April 1976. Results from the mobile test unit agreed quite favorably with the previously discussed test data. This data provided the basis of the design of the precipitator units with sufficient capacity to meet the desired performance and maintenance levels. It also provided data to alleviate some of the problems with precipitators on BOF's, such as carbon monoxide levels and the unit size needed to handle process variations.

In the final analysis, it was the United McGill Corporation, with the supportive data from their mobile EP unit, who provided CF&I with an economically attractive proposal [four (4) completely separate five (5) field precipitator units as ultimately constructed], which would guarantee opacity limits below 20% and satisfy process weight limitations. These conditions were to be maintained with three of the four units operating, thus allowing one unit down for maintenance while the system was on line.

FULL SCALE TESTING

Units 1 and 2 were initially placed on line in late July 1977. After a short period of trial operation, the old precipitator inlet duct system was removed in August 1977. Stack appearance of the new two unit system was much improved over the old system.

It was decided to stack test the two units to gauge the performance with only two units operating against both the past performance of the original precipitator and future performance of the complete new precipitator. The units were tested in October 1977. The volume and temperature of the gas were found to be very close to design conditions, 300,000 ACFM at 350° F. Outlet particulate loadings were tested at .073 GR/DSCF, approximately double the expected design value of .033 GR/DSCF for three unit operation.

The 300 ton per year level of emissions which was previously discussed in the interim had become a state approved variance level of operating performance. Since the construction format of the United McGill precipitator system called for the demolition of the existing precipitators, it became obvious that half of the new McGill precipitator system would meet the variance level. In fact, emissions for the first two units out of the four total were calculated at 171 tons per year, slightly over half as much as the 300 ton per year variance level.

The second two EP units were placed in service in early March 1978. After final checkout and trouble shooting, the complete precipitator system was tested during the week of April 10, 1978. Since the system contained four units and any three units were to operate and perform to design specifications, all combinations of three EP operation plus four EP operation were tested. Inlet and outlet points were tested simultaneously. The inlet ports were located in the 8 ft. diameter downcomer duct after the "Y" junction to accomodate either vessel operating. The outlet ports were on the main stack at the 90 foot level on the 110 foot high, 10 foot diameter stack.

The test results of April 1978 indicated that all combinations of three unit operation operated well below the process weight allowance of 40 lbs./hr. Maximum grain loadings to the precipitator system were previously estimated at 11 GR/DSCF. An average value of 7 GR/DSCF had also been determined during mobile EP testing and prior experience with the old precipitator. The initial performance tests bore out both of these concentration levels.

Performance guarantees on the United McGill precipitators specified that with three unit operation outlet grain loadings would be .033 GR/DSCF; with four unit operation .022 GR/DSCF. All four combinations of three unit operation readily met the .033 GR/DSCF criteria. The four unit operation was less than one half the guaranteed outlet of .022 GR/DSCF.

Using the design maximum inlet grain loading of 11 GR/DSCF and design outlet grain loading of .033 GR/DSCF, the efficiency of the system would then be 99.7%; 99.8% with .022 GR/DSCF outlet grain loading. The performance tests showed that these efficiencies indeed were obtained with three unit operation (99.7%) and four unit operation (99.8%). Although the inlet concentrations were not as great as expected, the outlet concentrations were also appropriately lower to achieve the design efficiencies.

It should be noted that average moisture levels for these tests were above the 15% minimum desired. With the temperatures at the inlet to the precipitator also staying somewhat above 350° F, the resistivity condition during the test was such that near optimum precipitation was achieved.

A follow up test run about a year later, May 24, 1979, with four (4) units operating, showed the same high level of performance with an efficiency of 99.81% based on actual test data, flow and grain loadings, and an outlet grain loading of .019 GR/DSCF. This test covered the full blowing time of four heats including six reblows. Opacity observations made during each of the heats averaged less than one (1) and no readings were over 20%.

For the sake of clarity, efficiency measurements were based on inlet concentrations before the drop out chamber and outlet concentrations measured in the stack. It is impossible to measure dust concentrations after the drop out chamber just ahead of the precipitators due to duct restrictions. Therefore, efficiencies should be referred to as system efficiencies and not precipitator efficiencies.

Opacity levels as read by both an in-stack transmissometer and by certified smoke readers (including State and local air pollution control personnel) during the performance tests in April 1978 indicated that they were maintained below 20% with four unit operation. A few short duration excursions slightly above 20% opacity were observed with three unit operation, generally associated with initial blowing of oxygen and reblows of oxygen.

Several inspections by State and local air pollution control personnel have been made since April 1978 and compliance with the Colorado opacity code has been maintained.

OPERATION AND MAINTENANCE

As stated previously, four unit operation of the precipitator system began shortly before March 1, 1978. Units 1 and 2 had been operating since July 1977. No major operating problems were encountered with these two units from July 1977 to March 1978. The first two precipitator units had been subject to overloading in order to handle total gas and dust volume during this period, thus the lack of operating problems was very gratifying.

Upon initiation of the four unit operation, the A.V.C.'s (Automatic Voltage Controllers) inappropriate installation resulted in overheating and some of the wiring was destroyed. A decrease in efficiency was noted by way of the precipitator stack appearance. After the A.V.C. wiring was corrected, stack appearance improved dramatically with four unit operation of the system. One A.V.C. unit was later replaced in November 1978; however, overall experience with the A.V.C. operation since the initial problem period has been quite satisfactory.

The most persistent operating problem with the precipitator system since April 1978 has been associated with the high density pneumatic dust transporting system. Almost weekly problems on any one of the transporter lines has been evidenced and usually associated with plugging in the line or a defective gate valve. Gate valves have been replaced in some of the transporters. Periodic cleaning of all the transporters is needed to maintain continuity of dust removal. Another problem which was encountered and essentially solved was periodic malfunctions of the compressed air dryer supplying the transporter system. In general, preventive maintenance based on experience has alleviated major problems with the transporter system and its overall operation has been satisfactory.

A pelletizer was installed underneath the dust storage silo in mid April 1978 to further assure total dust control in the system including fugitive emissions associated with dust handling. Initial operation of the pelletizer involved adjustment to the water feed rates which determine the size of the balls formed by the pelletizer. Although the pelletizer system was designed for automatic operation to start when a high level was reached in the dust silo and to stop at a low dust level, it has not been possible to leave the pelletizer unattended. The dust level probes have not worked reliably and frequent adjustments are required on the spray water. Usually eight (8) hours of semi-attended operation on one shift is sufficient to pelletize all of the dust collected in 24 hours. The 6000 ACFM baghouse system associated with the pelletizer and silo has required some bag replacement. It presently appears that annual bag replacement will be necessary. As with the transporters, periodic plugging of the silo has been noted but not serious enough to jeopardize the operation of the pelletizer during attended operation.

The EP units proper have not experienced any problems with intrinsic hardware. Most notably, the emitting electrode plates and collecting plates have not become distorted to cause chronic shorts or arcing. Accordingly, no emitter spikes or plates have needed replacement. It has, however, been necessary to use compressed air through a permanent piping system to blow dust off ledges between modules, blowing each field at each level once every shift to avoid dust buildup which can cause a ground.

The complete four unit system operated during the winter season of 1978-1979. January 1979 was the coldest January in Pueblo on record, and also for Pueblo, one of the wettest. A marked increase in insulator failures was noted in the rapper boxes during this past winter, especially around January. A "Catch 22" appears to be evident in this particular case in that increased ambient air into the rapper boxes tends to induce moisture on the insulators but maintains air flow through the boxes to keep internal components clean; if the boxes are completely sealed, moisture and the effects of ambient air are kept out but dust accumulation in the boxes tends to increase drastically resulting in excessive insulator failure and limit switch failure due to high temperatures. The changing ambient conditions due to the seasons dictates that some equilibrium condition must be established to prevent the chronic rapper insulator failures which have proliferated this past winter. Piping to the rapper boxes has been revised to more efficiently clean them and purge air holes have been enlarged to accomodate more air. The insulators located in the High Voltage energizing system have had no failures. These insulators are enclosed in heated compartments in the penthouse section of the EPs and operate without fan generated purge air.

Air leaks have been noted through the seals in the pneumatic cylinders. All four units have had the air seals replaced in these cylinders. The cylinder air leakage has not been evident since these replacements.

One of the major drawbacks of the installation of a precipitator system on a Basic Oxygen Furnace is the potential of explosions inherent with the combination of high voltage and moderate amounts of carbon monoxide in the presence of oxygen. An explosion occurred in May 1978 in the EP system. However, because explosion doors were designed into the system, the doors opened and no structural damage was suffered by the precipitators. CF&I's BOF primary gas cleaning system has two CO monitors; one (the original) near the operating pulpit and the new monitor on the downcomer just upstream of the inlet sampling location. Both monitors are arranged to stop the production process and shut off the precipitator upon sensing high CO. The pulpit monitor analyzes a sample of gas withdrawn from the duct, but the downcomer monitor senses directly through the 8 ft. diameter duct, reading the CO content in a fraction of a second. If the CO should exceed 14 percent at either analyzer, the power to the precipitator fields shuts off to prevent ignition of an explosion. Simultaneously, at the BOF vessel, the oxygen blow stops and the lance raises. The explosion in May 1978 reached reactive levels below the set points of the monitors which are set at 14%. Improved sampling and calibration techniques are being investigated by CF&I on the CO monitor located on the downcomer.

Closely associated with the CO hazard is the operation of the main I.D. fans. The fan inlet dampers are operated hydraulically by a current control system to maintain a pre-set amperage to the fan motor. When the duct system is cold after a BOF down day, the normal current control can result in insufficient draft. It has been found desirable to hold a higher amperage during the first three heats after startup. Tests were conducted in February 1979 to determine what amperage levels and fan louvre settings were needed after start up to maintain sufficient draft to nullify CO buildup. It was determined that the fan motors do indeed have sufficient power to maintain the 4" H_2O draft necessary during start up and that the amperage levels may need changing during various climatic changes. As with the rapper insulators, the CO and air flow relationship is subject to cold weather idiosyncrasies and will have to be monitored.

PERFORMANCE

As mentioned before in the discussion involving initial performance tests, the four unit EP system has satisfied the design specifications. System performance accomodates the "instantaneous" 20% opacity limits with four units operating. Since it is the intent of CF&I to operate with four units whenever possible, the Colorado Opacity Regulation of 20% is satisfied virtually continuously. Three unit system operation easily meets process weight requirements (again, refer to initial performance tests). However, as the initial performance tests indicated, occasional excursions above 20% opacity may occur with three unit operation. Most typically, these readings over 20% opacity are very brief and associated with commencement of the blow or reblows. These puffs are indigenous of the BOF process and well controlled with four units operating. Three unit operation is limited to the extent possible; however, on occasion one unit has been shut down. Reasons for such shut downs have been plugged hoppers, plugged screws, or broken insulators. The durations of the shut downs usually have been less than one day. A preventive maintenance program was instituted in March 1979 which involves the isolation of one precipitator from the active gas system for one 8-hour period per week. As initially discussed, this was one of the maintenance features that was designed into the precipitator system.

The most repetitive performance malady with the precipitator system has been with high CO tripping off power to the units. In the past, there has been one or two instances of these cutoffs most every month. As previously discussed, knowledge obtained from fan amp changes and improved calibration and maintenance of the CO monitor system should alleviate such power outages on the precipitators.

Daily operation of the system with four unit operation indicates no visible emissions during any stage of the process. Performance of the four unit system appears to be at least equivalent to that of a high energy scrubber.

CONTROL OF FINE PARTICLE EMISSIONS WITH WET ELECTROSTATIC PRECIPITATION

By:

Steven A. Jaasund
Fluid-Ionic Systems
a division of Envirotech Corporation
2525 East Magnolia
Phoenix, Arizona 85034

This paper presents the results, both pilot and full-scale, of experience with the application of wet electrostatic precipitation technology for the control of fine particle emissions from industrial processes. Performance data involving the collection of such difficult-to-clean emissions as sulfuric acid mist and recovery boiler salt fume are presented. The measured wet precipitator performance parameters (e.g., SCA, effective migration velocity) are compared to those reported in literature for dry precipitators operating on equivalent processes. Particular emphasis is directed toward examining wet electrostatic precipitator performance levels in controlling very high concentrations of submicron fume with the accompanying problem of space charge corona quenching. Relationships between these performance data and specific wet precipitator operating parameters such as operating voltage and current density are also examined.

CONTROL OF FINE PARTICLE EMISSIONS WITH WET ELECTROSTATIC PRECIPITATION

INTRODUCTION

Considerable attention has been focused recently on the harmful effects of airborne particles less than two microns in diameter. Particles in this size range have been shown to have a high potential to cause lung damage, both directly and with adsorbed gases. Also, these particles are known to be a chief cause of visibility degradation in polluted areas. As a consequence, the emphasis in applied and basic research concerning particulate emission control has been directed toward the development of more efficient means for collecting these fine particles.

Electrostatic precipitation is known to be among the most promising means of achieving high fine particle collection efficiencies. To date, the great majority of the research on the collection of fine particles by electrostatic precipitation has been concerned with the collection of fly ash from the combustion of coal for power generation. The exclusive attention given to fly ash collection with dry electrostatic precipitators (ESPs) is unfortunate because:

- Dry ESP technology is often limited in applicability when collection of particulate matter other than fly ash is required; e.g., condensible materials cannot be collected in a dry ESP.
- Conventional dry ESP technology is limited by inherent flaws and nonidealities in design; e.g., rapping/reentrainment losses and high resistivity dusts often make the attainment of very low outlet loadings impossible.

The wet electrostatic precipitator (WESP) can be an effective means of overcoming most of the design deficiencies of dry ESPs so that the maximum potential for fine particulate collection may be achieved. It is the object of this paper to present selected WESP operating and performance data in order to illustrate the potential of the wet electrostatic precipitation process to reduce fine particle emissions to very low levels. To this end, the following text will:

- report actual operating and performance data collected at both full and pilot-scale WESP installations operating on fine particle emission sources,

- compare the performance of the individual WESP facilities with the performance of other conventional technologies reported for similar applications, and
- explore the operating factors which affect WESP performance.

Specifically, performance data gathered for WESP applications on the following fine particle emission sources and categories will be discussed:

- Mineral wool cupola
- Sintering windboxes
- SO_3 hydration (sulfuric acid mist)
- Sulfite recovery boilers
- Phosphorus furnace
- Chemical incinerators

DESCRIPTION OF WET PRECIPITATION PROCESS

The wet precipitation process is fundamentally the same as the dry precipitation process. The distinguishing feature of the wet precipitation process is that the particles are collected on a liquid medium which then acts as both a collecting surface and a removal medium. In dry precipitators, the collection function is performed by a grounded metal surface and removal of collected material is achieved by mechanical impact. The simple change from dry collection with mechanical rapping to collection and removal in a liquid medium frees the wet process from some of the problems associated with the dry process. That is, with the wet process:

- resistivity of the collected material is not a performance-influencing factor,
- rapping and reentrainment losses are avoided, and
- condensible emissions are readily collected.

Of course, the use of a flushing medium, usually water, can introduce new considerations and problems to the application of the electrostatic precipitation process. The principal problems introduced are:

- increased corrosion potential
- need for water treatment.

The embodiment of the wet precipitation process has taken many forms since the first WESP was conceived. WESP designs employing continuous and intermittent flushing, either with sprays or overflow weirs, have been tried on a wide variety of applications with varying degrees of success. The specific performance and operating data presented in this paper were all gathered at operating installations of the HYDRO-PRECIPITROL™ wet electrostatic precipitator.

The HYDRO-PRECIPITROL is a continuously-irrigated, concentric-cylinder wet electrostatic precipitator with integral prescrubber and gas distribution system. As shown in Figure 1, hot dirty gas enters tangentially at the bottom where a bank of hydraulic spray nozzles cool the entering gases and provide some degree of large particulate removal. The tangentially spinning gas next passes upward through gas straightening vanes which remove the tangential component of the gas velocity and render the flow profile essentially uniform across the entire cross section. The cooled, partially-cleaned gases next enter a series of annular electrostatic zones; these are made up of seven concentric collection cylinders, with six concentric high-voltage, expanded-metal discharge electrode cages suspended from above and located equidistant between the cylinders. The discharge electrode cage assembly is supported by a centrally located insulator as shown. As the gas passes up into the zone between the discharge electrode and the wall of a collecting cylinder, the particles are charged by a high-voltage corona discharge and driven to the collecting cylinder by the high-voltage field. Each collection cylinder is continuously irrigated from above by circular liquor distribution pipes mounted on top of each cylinder. The distribution pipes employ a unique overflow design of 1/2-inch vertical nipples mounted four inches apart around the circumference of each distributor. This arrangement provides a smooth, contiguous film of liquor flowing over all collecting surfaces. This water distribution system is essentially nonplugging due to the large discharge orifice size employed; it also is insensitive to the leveling difficulties encountered with weir-type water distributors. With the exception of the discharge electrodes, the entire device is constructed of corrosion-resistant, fiberglass-reinforced plastic (FRP). The discharge electrodes are made of metals suitable for the corrosion potential of the applications; e.g., high-grade alloys, such as Hastelloy C-276, may be specified for very corrosive gas streams.

The HYDRO-PRECIPITROL design described above offers the following operating features which help maximize the collection of fine particles:

- excellent gas flow distribution (RMS deviations of less than 10% from the mean velocity are achievable),
- smooth irrigating film to minimize electric field disturbances and increase operating voltage, and
- no sneakage due to the vertical/concentric design.

In fact, a careful scrutiny of the design features show that this design eliminates all of the nonidealities occurring in other precipitator designs, both wet and dry. The following data show that the HYDRO-PRECIPITROL is able to achieve performance levels on fine particulate applications significantly higher than reported for any other available precipitation technology.

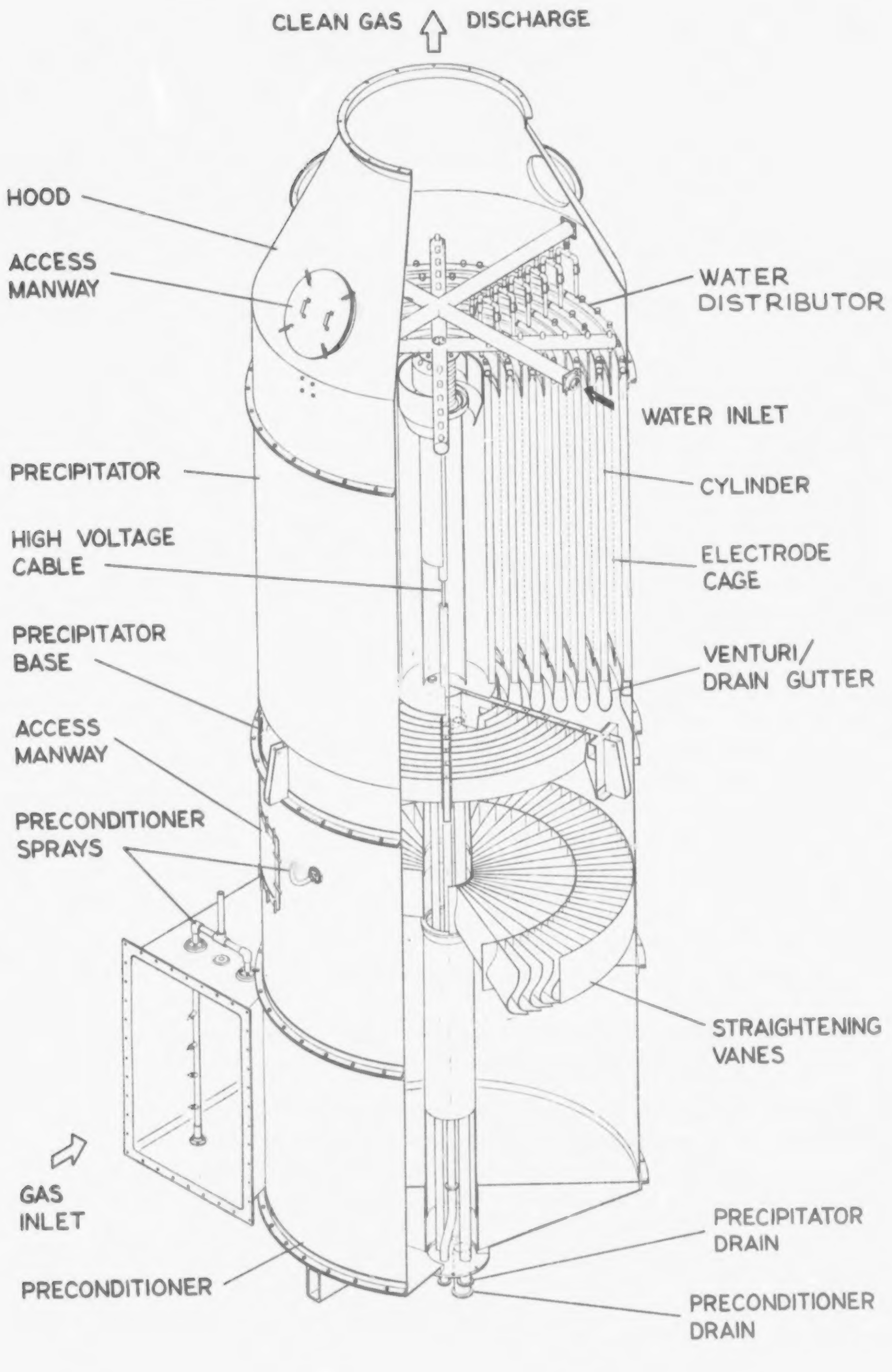

Figure 1 "HYDRO-PRECIPITROL" wet electrostatic precipitator.

FINE PARTICLE COLLECTION RESULTS

Fluid-Ionic Systems, a division of Ervirotech Corporation, has been manufacturing and marketing the HYDRO-PRECIPITROL wet electrostatic precipitator since 1974. Since then, WESP operating and performance data has been acquired on 62 different pilot and full-scale applications. Some of the test programs at these applications have been extensive, lasting over a year and involving up to 100 individual stack tests. Also, many of these applications have involved the collection of high concentrations of particles less than two microns in diameter. The following data are selected from the application experience with the HYDRO-PRECIPITROL specifically to illustrate the capability of the WESP to collect fine particles. As a point of reference, performance parameters will be given in terms of the Deutch equation,

$$\text{EFFICIENCY} = 1 - \text{EXP}\left(\frac{-AW}{Q}\right)$$

where

$$\text{EFFICIENCY} = \frac{\text{Inlet - Outlet}}{\text{Inlet}}$$

A = Collecting surface (adjacent to discharge electrodes)

Q = Area volumetric gas flow rate (at saturated conditions)

W = Effective migration velocity

Performance parameters were calculated from test data obtained with various sampling techniques; i.e., in-stack filter, EPA Method No. 5, and EPA Method No. 8. Other than acid mists, condensible concentrations measured were not included in the calculation of performance parameters.

Mineral Wool Cupola

A pilot test program was conducted at a Bethlehem Steel Corporation Mineral Wool Plant to demonstrate the capability of the WESP to effectively clean the top gas emissions from two hot-blast, slag-melting cupola furnaces. The particulate emissions from the cupola consisted chiefly of silica, alkali, and elemental sulfur fume. Particle size analyses of the aerosol showed that 80% was less than 1.0 micron in diameter. Prior pilot testing with a high energy scrubber showed that the emission was exceptionally hard to clean; i.e., over 80 inches W.G. pressure drop was reouired to reduce the concentration to 0.04 grains/SCFD, the state outlet criterion.

The results of the pilot testing demonstrated the ability of the WESP to achieve extremely low outlet loadings. During the final phase of testing, a series of eight inlet/outlet efficiency tests were conducted. The inlet and outlet particulate loadings averaged 1.08 grams/NM^3 (0.470 grains/SCFD) and 0.005 grams/NM^3 (0.002 grains/SCFD) respectively. The specific collection area and the migration velocity averaged 30 M^2/M^3/second (153 ft^2/1000 ACFM) and 18 cm/second respectively. Field strengths of 5 kv/cm and current densities of 5 na/cm^2 were measured for these tests.

Sintering Plants

Bethlehem Steel also tested the WESP at two sintering plants for the control of windbox emissions. A pilot test program was conducted at the Lackawanna Sintering Plant, and a subsequent full-scale demonstration test was conducted at the Johnstown Sintering Plant. The results of these test programs have been reported by Mazer et. al. (1976)[1].

No specific size distributions are available for either WESP application. However, it is known that sintering windbox emissions usually present an extremely difficult gas cleaning task due to both high concentrations of fine particles and the high dust resistivity often encountered. In a recently published report, Szabo and Gerstle (1978)[2] state that specific collection areas in excess of 80 M^2/M^3/second (400 ft^2/1000 ACFM) may be required to achieve 99% efficiency on windbox emissions with dry ESPs.

The data obtained at Johnstown and Lackawanna may be compared to performance curves also reported by Szabo and Gerstle for dry ESPs operating on windbox emissions. This comparison, shown on Figure 2, illustrates the dramatic increase in precipitator performance that can be achieved by switching from conventional dry technology to a well-designed wet system. It is noteworthy that the data reported in Figure 2 for a dry precipitator are for operation on the raw windbox emissions, while the WESP data reported are for emissions that had been treated by cyclones (Lackawanna) or an existing precipitator (Johnstown). Hence, the dry precipitator performance curves are for an inherently easier gas cleaning situation. It should also be noted that the WESP efficiency includes the scrubbing effect of the sprays at the gas inlet. These sprays undoubtedly perform a significant scrubbing function on any coarse particulate entering the WESP. Unfortunately, because of the WESP geometry, it is nearly impossible to quantify this effect by field testing.

Sulfuric Acid Mist

The release of anhydrous SO_3 into a humid environment is known to form an extremely fine sulfuric acid mist aerosol. La Mer et. al. (1950)[3] showed that sulfuric acid mist aerosols formed in this manner had mass mean diameters which ranged from 0.1 to 0.4 microns and occurred in very narrow size ranges.

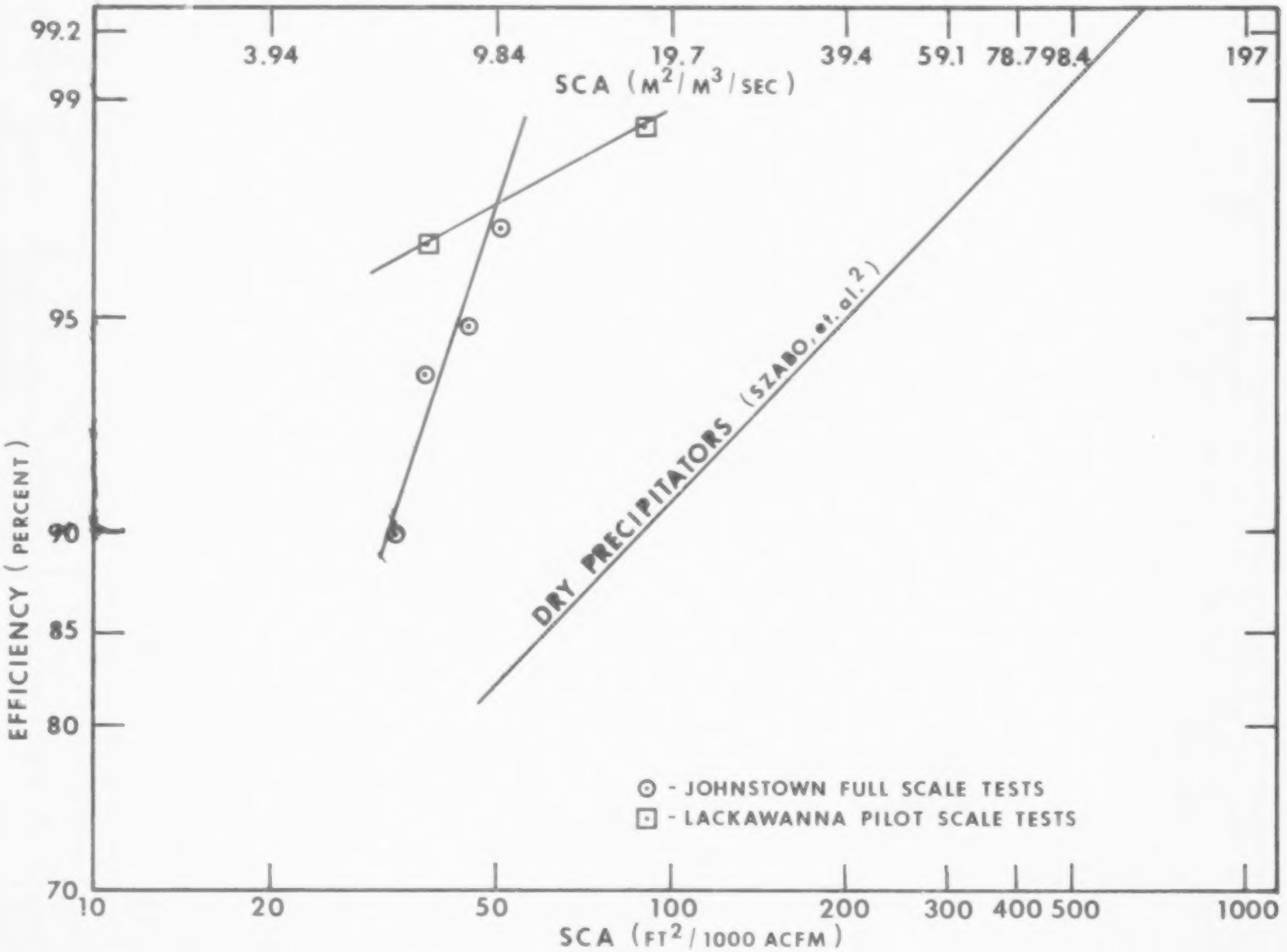

Figure 2 Dry and wet precipitator performance on sinter windbox emissions.

During a 1978 EPA sponsored pilot-scale evaluation of the HYDRO-PRECIPITROL as an SO_2 removal device, tests were conducted on the WESP to quantify its ability to capture sulfuric acid mist. The test aerosol was formed as described above--anhydrous SO_3 was continuously bled into a warm (49°C, 120°F) saturated stream of simulated boiler flue gas to form approximately 0.39 grams/NM^3 (0.17 grains/SCFD) of sulfuric acid mist. The gas stream, laden with acid mist, was then passed through the WESP pilot plant. Inlet/outlet testing was conducted according to the specifications of EPA Method No. 8. To quantify the effect of voltage on precipitator performance, the operating voltage was deliberately varied from test to test. The results of the efficiency tests showing the effect of voltage variations are plotted in Figure 3.

Sulfite Recovery Boiler

In the sulfite pulping process, the recovery boiler flue gas is scrubbed in a series of spray and packed absorption towers for the recovery of SO_2 necessary to the pulping process. At facilities where saltwater- borne logs are processed, the gases exiting the absorption towers are often contaminated with heavy concentrations of submicron salt fume and require further particulate removal steps. Figure 4 illustrates the extremely fine nature of the aerosol encountered at two such operations.

To identify the technology necessary to reduce the fine particle emission problem at these two pulp mills, pilot scale WESP performance evaluations were conducted. At one of these mills a full-scale WESP was subsequently installed and evaluated. The results of all three test programs, shown below in Table 1, clearly demonstrated the capability of the WESP to effectively abate this fine particulate emission.

TABLE 1

WESP PERFORMANCE PARAMETERS ON
SULFITE RECOVERY BOILER EMISSIONS

	COLLECTION EFFICIENCY (%)	MIGRATION VELOCITY (cm/sec)	SPECIFIC COLLECTION AREA M^2/M^3/sec and (FT^2/1000CFM)	FIELD STRENGTH (kv/cm)	CURRENT DENSITY (na/cm^2)
Plant 1 Pilot	96.1	21.3	15.3 & (78)	7.3	--
Plant 1 Full Scale	94.3	22.0	13.4 & (68)	4.3	3.3
Plant 2 Pilot	97.2	25.0	14.6 & (74)	5.8	--

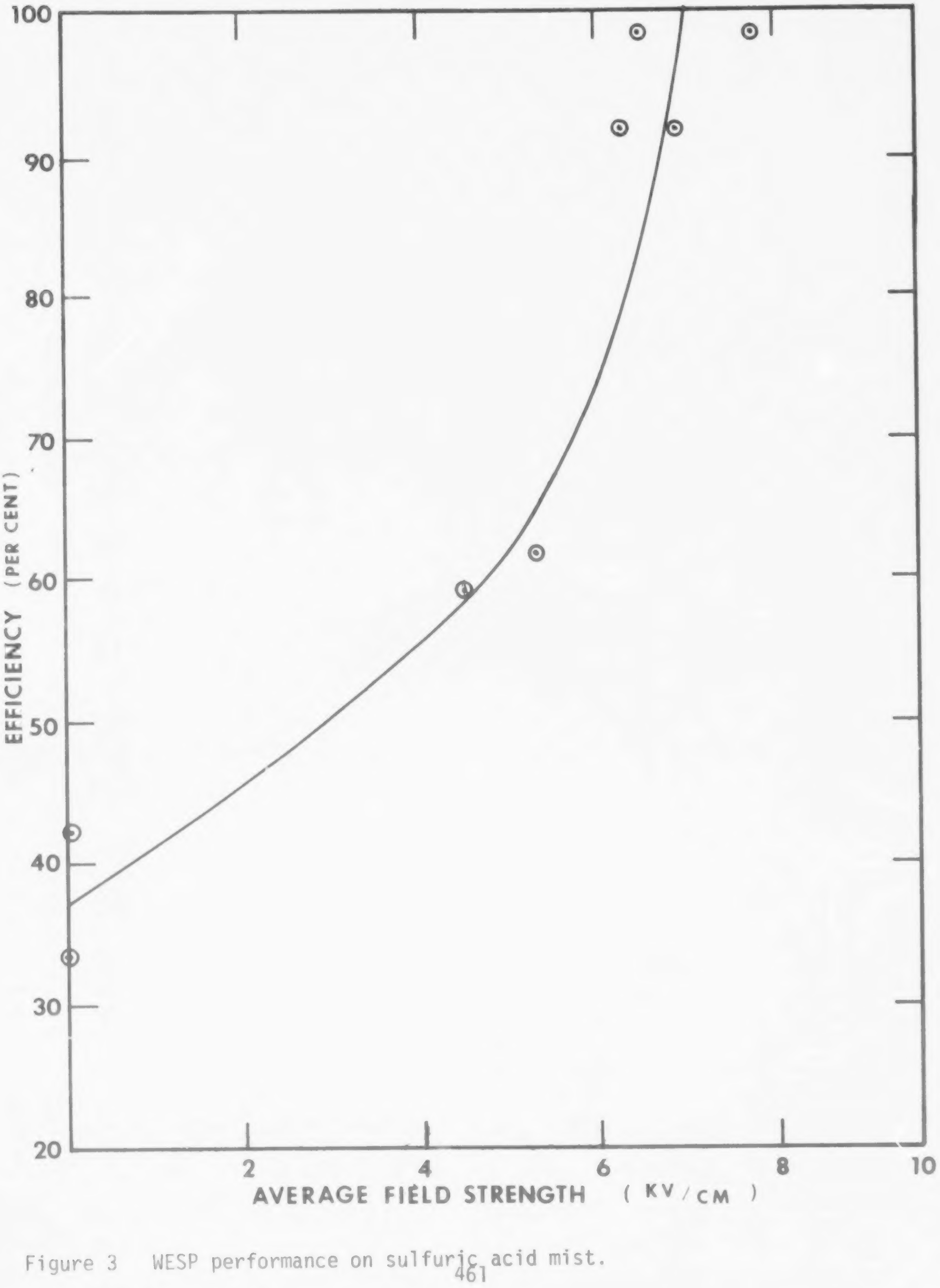

Figure 3 WESP performance on sulfuric acid mist.

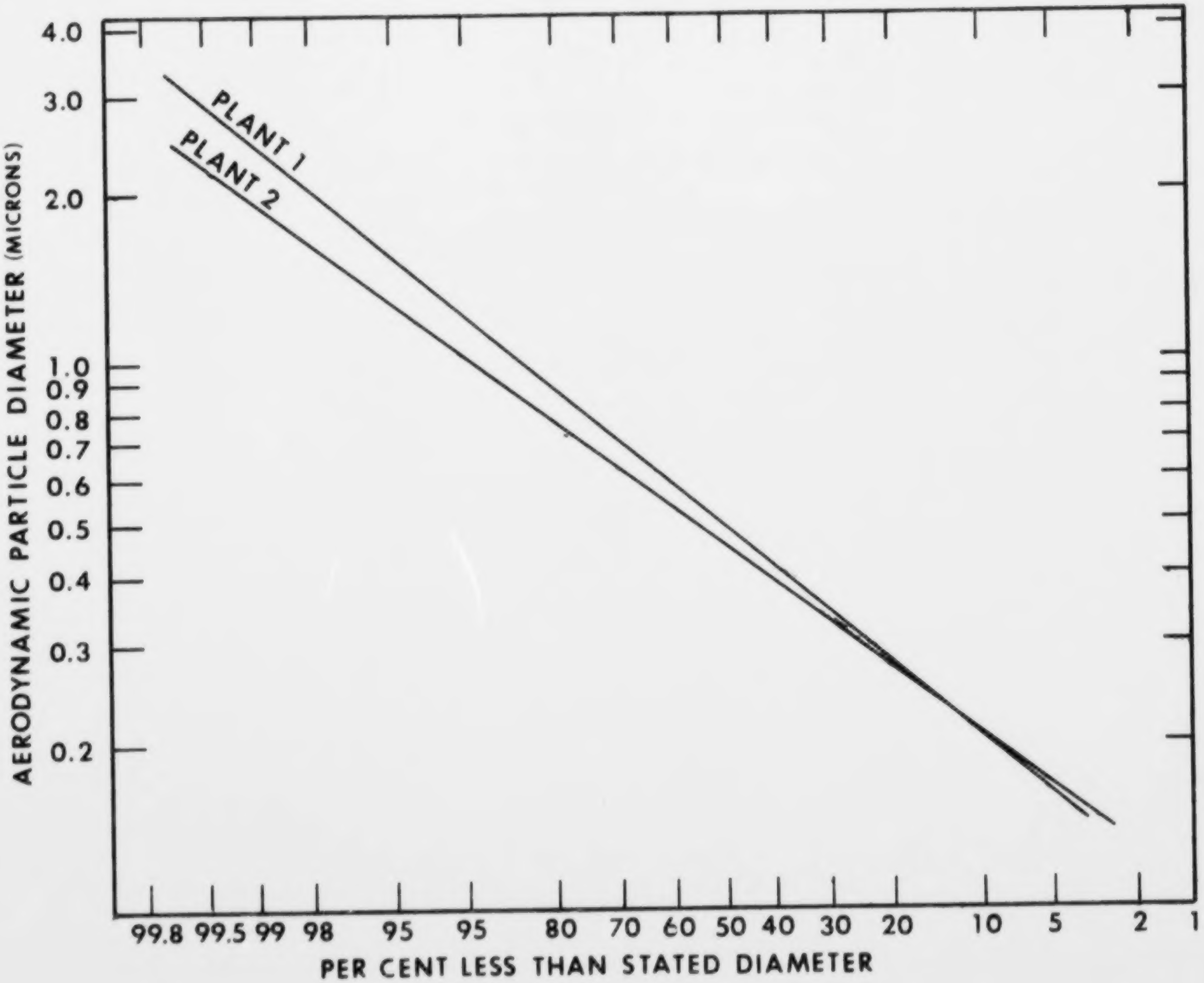

Figure 4 Sulfite recovery boiler salt fume size distributions.

It is noteworthy that the full-scale WESP performs effectively despite an extremely low current density.

Phosphorus Furnace

The formation of P_2O_5 and related compounds from the rapid oxidation of elemental phosphorus is known to result in an extremely fine aerosol. An observable measure of this fineness is the dense white smoke which results from the combustion of phosphorus. Pilot tests on such emissions from the tapping hole of a phosphorus furnace again demonstrated the capability of the WESP to achieve high efficiencies on submicron particles. A summary of the results of the 22 pilot tests conducted is shown below in Table 2.

TABLE 2

WESP PERFORMANCE ON P_2O_5 AEROSOL

Average effective migration velocity	- 22.3 cm/second
Average specific collection area	- 8.1 M^2/M^3/second - (41.2 ft^2/1000 ACFM)
Average P_2O_5 removal efficiency	- 84%
Particle size distribution	- Greater than 90% by weight below 1.0 micron in diameter

Chemical Incinerators

The incineration of liquid and solid waste chemicals results in the generation of varying concentrations of submicron particulate matter. The concentration of submicron material is often extremely high when waste compounds containing certain noncombustible constituents (e.g., sodium, calcium, or potassium) are being burned.

The WESP was pilot tested on two chemical incinerators and later installed for full-scale duty on one. Both of these incinerators burn waste chemicals and generate high concentrations of fine particles due to the presence of noncombustible constituents in the wastes. A summary of the results of the pilot tests at both facilities, plus corresponding aerosol size distribution information, is given in Table 3.

The high inlet loads encountered at chemical incinerators are of particular concern in the application of single field precipitators, such as the HYDRO-PRECIPITROL, because of the problem of space-charge corona quenching. The phenomenon of severe corona quenching, illustrated in Figure 5, results when very high concentrations of fine aerosol enter a precipitator and become charged to the polarity of the discharge electrode. The resultant "space charge" of the aerosol has the effect of reducing the electric field at the discharge electrode which, in turn, reduces the corona current density. By contrast, the space charge increases the field at the collection surface. Since the theoretical migration velocity is a function of both the particle charging conditions at the electrode and the precipitating field, it is not apparent whether space charge actually increases or decreases precipitator migration velocities.

TABLE 3

PILOT WESP PERFORMANCE
AT CHEMICAL INCINERATORS

	COLLECTION EFFICIENCY (%)	EFFECTIVE MIGRATION (cm/sec)	SPECIFIC COLLECTION AREA M^2/M^3/sec and (FT^2/1000CFM)	FIELD STRENGTH (kv/cm)	CURRENT DENSITY (na/cm^2)
Plant 1	99.5	39.4	13.4 & (68.3)	--	--
Plant 2	93.2	13.2	20.3 & (103.3)	5.6	59.1

SIZE DISTRIBUTION

	% LESS THAN 1.0 MICRON	MASS MEAN DIAMETER (MICRONS)
Plant 1	90	--
Plant 2	92	0.67

The full-scale WESP performance data gathered at the chemical incinerator installation, shown in Figure 6, points to the possibility that the increase in the precipitating field more than compensates for the loss of particle-charging field and current density. However, as there are no data or calculations to further support such a conclusion, we must reserve judgment as to the actual cause of this interesting relationship. It should be noted, however, that the increase in migration velocity should not be attributed to an increase in average particle size with increasing inlet load. The full-scale WESP was installed downstream of a medium-energy venturi scrubber which, by nature, tends to yield a relatively uniform outlet particle size distribution regardless of large changes in the inlet distribution.

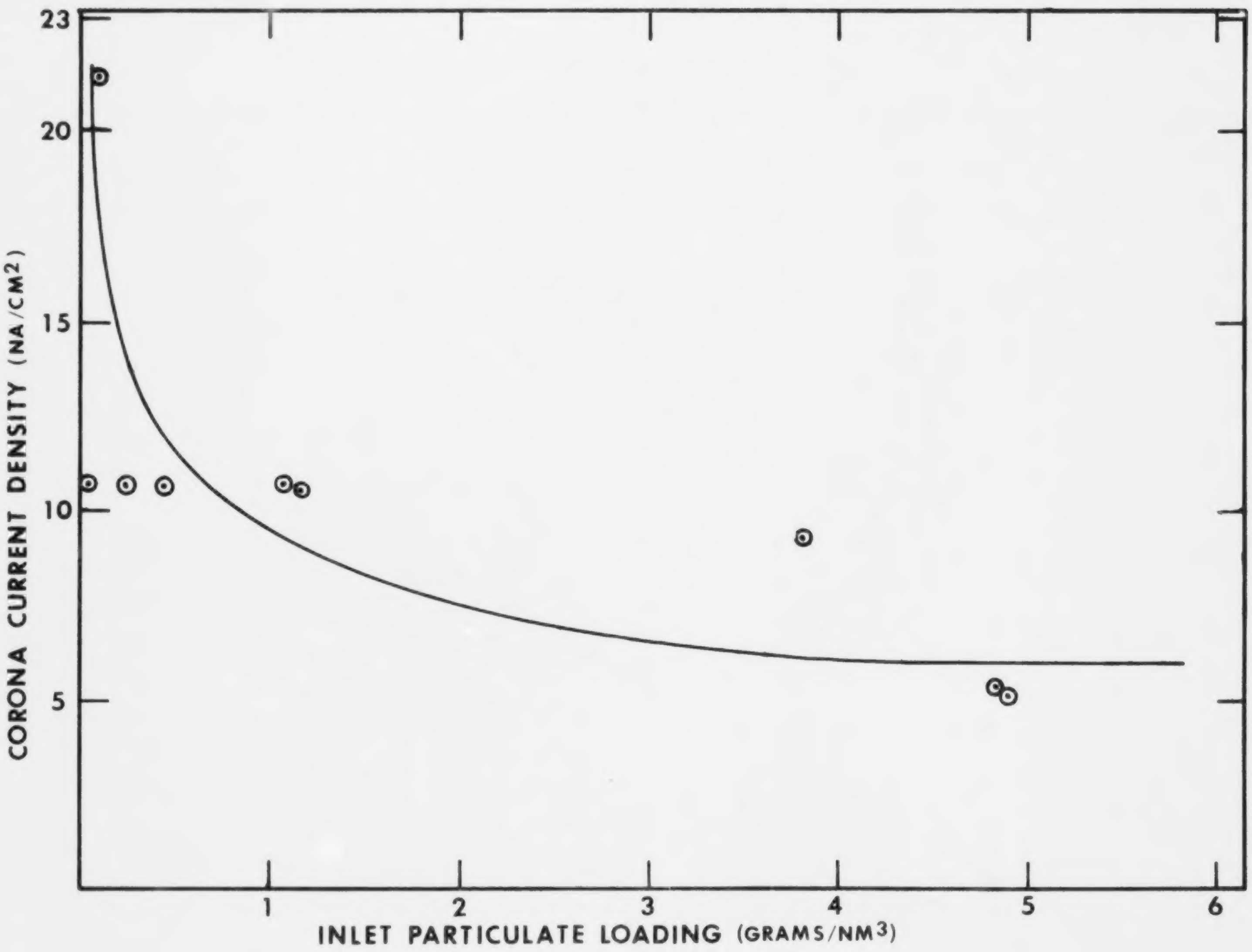

Figure 5 Effect of particulate loading on corona current - chemical incinerator.

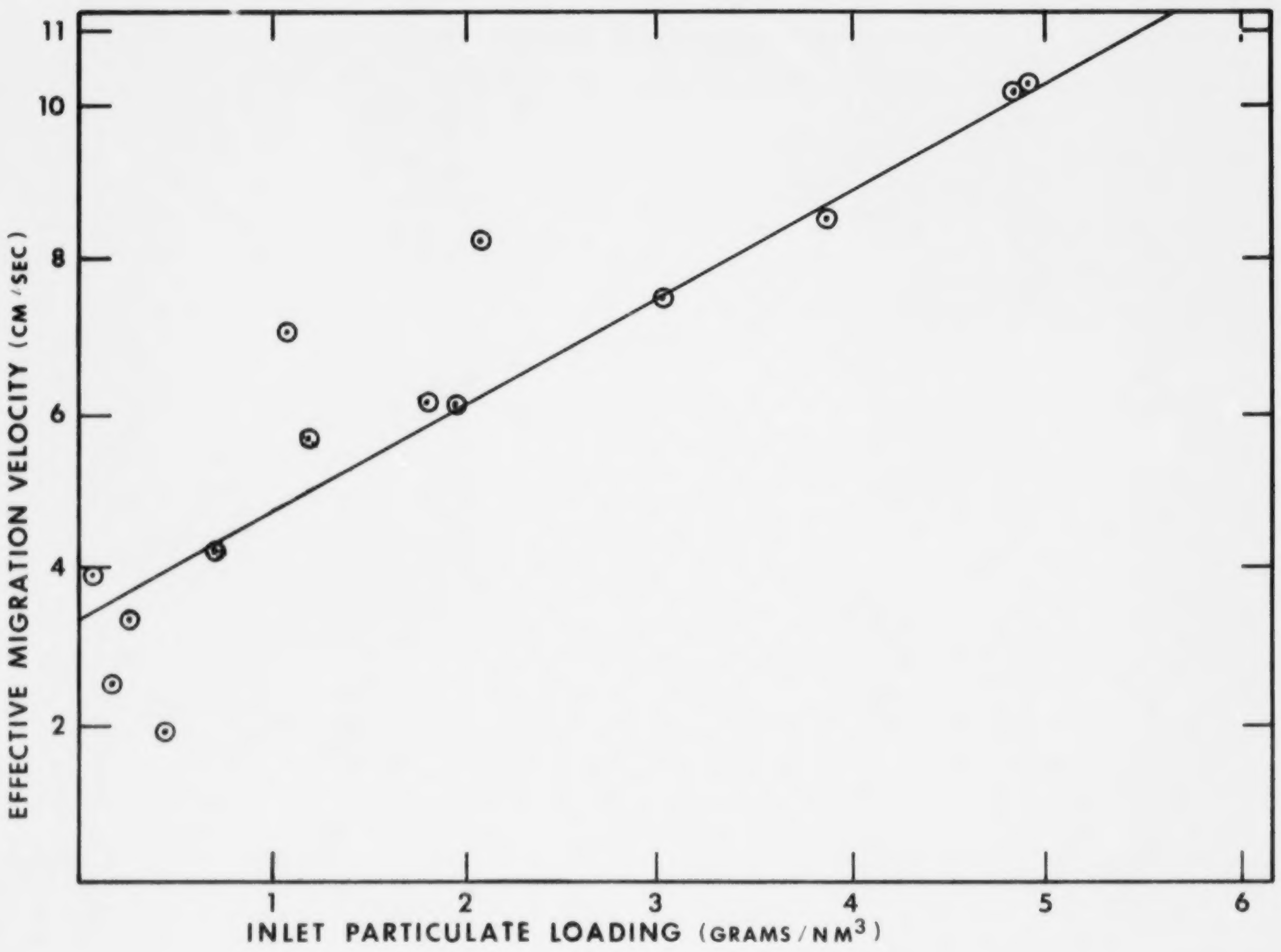

Figure 6 Effect of particulate loading on WESP effective migration velocity.

CONCLUSIONS

The data presented in this paper clearly demonstrate the ability of the wet electrostatic precipitation process to attain very high performance levels when operating on high concentrations of fine particles. The data also demonstrate the dependence of WESP performance on operating voltage, but refute the notion that very high inlet concentrations necessarily have a limiting effect on performance due to space charge corona quenching.

REFERENCES

1. Mazer, M. R., S. T. Herman, and S. A. Jaasund. Adaptation of Wet Electrostatic Precipitators for Control of Sinter Plant Windbox Emissions (presented at the annual meeting of the Air Pollution Control Association, Toronto, Ontario, June 1976, paper #77-6.1).

2. Szabo, M. S. and R. W. Gerstle. Operation and Maintenance of Particulate Control Devices on Selected Steel and Ferroalloy Processes, PEDCO ENVIRONMENTAL CORPORATION, Cincinnati, Ohio, March 1978, PD 282256.

3. La Mer, V., E. Inn, and I. Wilson. Journal of Colloid Science. 5;471, 1950.

TUBULAR ELECTROSTATIC PRECIPITATORS
OF TWO-STAGE DESIGN

By:
Harish S. Surati
Michael R. Beltran
and
Isaac Raigorodsky
Beltran Associates, Inc.
Syosset, New York 11791

ABSTRACT

Although the "two stage" electrostatic precipitator concept was first developed in 1910, until recently most of their use was confined to in-plant air cleaning. In the last decade, plate type designs have been modified to make them suitable for industrial applications involving organic emissions, most notably in Asphalt saturating, Plastic curing, Food processing, Printing, Textile finishing and Heat treating industries. However, plate type designs are inadequate in applications where very high loading and/or high particulate content are involved.

Tubular design with wider spacing and higher voltages incorporates best features of both the single stage and two stage type precipitators. These units have been used in Molybdenum roasting, Zirconium Calcining, Ammonia scrubbing of oxides of sulfur, Meat broiling, Foundry exhaust, etc.

The paper discusses design parameters, field test data, and operating data on these units. Comparisons with single-stage type precipitators are made wherever applicable. Advantages and disadvantages of two stage precipitators are also discussed.

TUBULAR ELECTROSTATIC PRECIPITATORS
OF TWO-STAGE DESIGN

INTRODUCTION

The two-stage electrostatic precipitator concept was first conceived and patented by Schmidt in 1910. Unlike the single-stage or Cottrel type precipitator, the two-stage precipitator has separate ionizing and collecting sections. Although the first commercial use of the two-stage precipitator design was reported in 1937, applications were limited to air cleaning in offices, bars and hospitals. In the past fifteen years design modifications have enabled the plate type two-stage precipitator to be used in various industrial applications. The use of two-stage precipitators for hydrocarbon emission control has gained wide popularity. The two-stage units have virtually replaced thermal incinerators for emission control in textile, rubber, vinyl, asphalt, carpet, printing, grain drying and food industries. A detailed discussion of the use of two-stage precipitators in various applications can be found in other publications of the authors.[1,2,3]

Theory and experiment both indicate that particle charging takes place very rapidly, as compared to their separation from the gas stream. Moreover, the charging process requires a nonuniform field, whereas a uniformly high field is required for the most efficient separation of the particles from the air stream. Both these facts indicate the need for separate ionizing and collecting sections. The treatment time for the industrial single-stage type unit varies from 1 to 10 seconds. Thus, long residence times are needed for the separation and subsequent collection of the particles from the gas stream. Saturation charging can be achieved in 0.01 seconds or less for most industrial applications encountered. Consequently, in single-stage precipitators the corona power is wasted over the major portion of the ionizing electrode. Figure 1 shows a typical arrangement of tubular precipitators, both single-stage and two-stage design. Table 1 gives some typical comparison figures for single-stage precipitators and tubular precipitators of two-stage design.

The tubular single-stage units have a large grounded cylinder known as the collecting electrode and, coaxial with it, a high potential wire called the discharge electrode. In the two-stage design the precipitator consists of a short ionizing section followed by a comparatively longer collecting section. The discharge electrode is in the form of a rod or tube with a sharp needle at the end and is centered in the tube. Various tube geometries have been utilized over the years, the most common being the round and hexagonal. The hexagonal shape is more space efficient than the round shape. The square configuration shown in Figure 1 is a slight variation of the hexagonal shape and was chosen because of manufacturing ease. The corona is generated on the needle when high voltage is applied to the discharge electrode. The whole length of the rod then acts as a nondischarging electrode still providing the electric field. This arrangement provides a nonuniform electric field in the ionizing section and a uniform electric field in the collecting section.

THEORETICAL ASPECTS

The electrostatic precipitation phenomenon can be divided into three main categories:
(1) Ionization or particle charging
(2) Collection of the charged particles
(3) Removal of the collected particles

Ionization Mechanism:

When electrical potential is applied to the discharge electrode (the rod and the needle assembly) located in the center of the grounded tube (collecting electrode), an electric field is created that varies from a high strength near the sharp needle point to a low strength near the grounded electrode. When the potential difference between the discharge electrode and the collecting electrode reaches the "critical corona voltage", local ionization of the air stream surrounding the needle occurs and an onset of blue corona can be observed on the needle point tip. As the potential is increased, the corona glow increases in strength and volume. In some cases when sufficiently high voltages are applied to the thin needle, a corona sheath can be observed on the whole shank of the needle. Such corona was observed with the present design at 40kv using 1/16" diameter needle. The corona was observed to be of the inverted umbrella shape, with the needle as the shaft of the umbrella. When the applied potential reaches sparkover voltage, complete ionization of the air stream occurs, resulting in a short circuit.

With the discharge electrode at the negative potential, which is the usual arrangement in most industrial applications, positive ions generated are attracted to the needle and negative ions to the grounded tube. Although an equal number of positive and negative ions are generated in the corona region, 99 percent of the gas space between the needle and the tube is filled with only negative ions. This forms a space charge of high opposing voltage which limits the corona current.

Particle charging occurs by way of two known mechanisms: (a) field charging, wherein particles are charged in the corona region by the bombardment of negative ions moving toward the grounded tube in the applied field, and (b) diffusion charging which occurs because of the random motion of the particles themselves. The diffusion charging mechanism is relatively insignificant for particles above 1 micron in diameter. Sub-micron particles have significant random motion and, hence, the diffusion charging mechanism is important to achieve the saturation charge. Typical charge values are 300 electron charges for one micron and 30,000 electron charges for 10 micron particles. This saturation charge is achieved in less than .01 seconds. In tubular two-stage design, an ionization residence time of between .02 to .05 seconds is desirable. In conventional single-stage design, a charging time of between 5 to 10 seconds is provided. This results in wasted corona power. In practice, power requirements for single-stage precipitators are much greater than indicated by theoretical calculations because only a small fraction of the power is used to transport the particles. The theoretical energy requirements may be approached in practice for two-stage designs. The two-stage design requires less than one-third of the power of the single-stage design for equal efficiency.

Various tube and discharge electrode geometries have been tried in the past. The relation between the collection efficiency and the corona current is very unclear. It does not conform to any set trends. Ionization produced by a sharp needle point was found to have the most efficient utilization of the corona current. These findings are presented in graphical form in Figure 2. An extensive research program is underway to determine the effect of tube geometry and discharge electrode spacings. It is believed that more than one discharge point in the horizontal plane produces overlapping corona fields. The overlapped region would have markedly decreased concentration of negative ions, resulting in decreased overall efficiency. Addition of the electrical discharge points in the direction of the airflow was found to marginally increase the efficiency.

Collection Mechanism:

The particles charged in the corona region surrounding the needle enter the collecting section. The collecting section is composed of a large positive (grounded) tube and a nondischarging rod at a high negative potential. The particles are repelled by the rod and attracted by the tube wall. The particles are accelerated toward the collecting electrode by the Coloumb force and this motion is resisted by inertial and viscous forces. Since, for fine particles inertial forces are insignificant, the particle attains a velocity determined by the equilibrium between the Coloumb and Stokes forces. This velocity is known as the migration or drift velocity. The typical drift velocity in the tubular two-stage type precipitator ranges between 0.3 to 0.7 ft/sec for submicron particles. It is a function of collecting field strength, gas medium, gas temperature and pressure, and the nature and size of the particles.

In tubular precipitators of both single-stage and two-stage design, the most critical cross-section is that at which the discharge electrode enters the collecting electrode. In this plane the electric field is highly concentrated and is distorted by edge effects. In order to avoid sparkover in this region, various methods have been tried, the most notable being the "necking down" of the electrode at that point. Structural and mechanical considerations limit the amount of necking that can be employed.

Extensive work done by Dr. Masuda in Japan has shown that particle migration velocity in the tubular precipitator increases with increase in interelectrode spacing. A variety of explanations have been offered, most of them involving a redistribution of the electric field. In this explanation, if the current is held constant as the interelectrode space increases, the total space charge in the gap also increases. The space charge, being of the same polarity as the discharge electrode, more effectively shields the discharge electrode from the tube. Thus, the field is reduced near the discharge electrode and, in compensation, is raised near the grounded electrode. The intensified field near the wall is more effective in charging particles.

Removal Mechanism:

Tubular precipitators are mainly used as mist precipitators and, hence, do not have reentrainment problems if the precipitator throughput velocity is kept below 7-8 ft/sec. If the collected material is not very viscous, it drains by gravity. Most of the industrial applications where two-stage tubular precipitators are used have saturated exhaust streams, and the high moisture content provides continuous flushing of the collecting surface.

Precipitator Efficiency:

The exponential Deutsch-Anderson equation is extensively used in practice for the design of the single-stage precipitators. Field experience has shown that, with little modification, the same equation can also be applied to two-stage precipitator design. The more refined expression developed by Penny (1937) for the two-stage precipitator is not used in industry.[4]

In its simplest form, the Deutsch-Anderson equation is given as:

$$\text{Eff} = 1 - \exp\left(-A/Vw\right) \qquad (1)$$

The collecting electrode area, A, and volumetric flow rate, V, are calculated from the known geometry. The drift velocity, w, is generally determined from data collected on similar applications.

From Figure 3 for duct precipitators,

$$\frac{A}{V} = \frac{2Lh}{2Shv} = \frac{L}{Sv} \qquad (2)$$

So,

$$\text{Eff}_{DP} = 1 - \exp\left(-Lw/Sv\right) \qquad (3)$$

From Figure 3, for tubular precipitators, (single-stage design)

$$\frac{A}{V} = \frac{2\pi RL}{\pi R^2 v} = \frac{2L}{Rv} \qquad (4)$$

Also from Figure 3, for tubular precipitators, (two-stage design)

$$\frac{A}{V} = \frac{4(2RL)}{4R^2 v} = \frac{2L}{Rv} \qquad (5)$$

Therefore,

$$\text{Eff}_{TP} = 1 - \exp\left(-2Lw/R\right) \qquad (6)$$

Comparison of Equations (3) and (6) indicates:

(i). For a given efficiency a tubular precipitator may be operated at twice the gas velocity of a duct precipitator of equal electrode length and interelectrode spacing.

(ii). For a given gas flow (volumetric flow rate) efficiency of the duct precipitator is independent of duct spacing.

(iii). For a given volumetric flow rate, efficiency of a tubular precipitator increases with increase in tube diameter.[6]

DESIGN ASPECTS

Polarity:

Electrical energization is the single most important design consideration in the two-stage precipitator design. The two-stage precipitator developed by Penny used positive polarity to reduce the amount of ozone produced. This practice is still continued in air cleaning units. However, units designed for industrial duty use negative ionization to achieve higher sparkover voltages. The fouling of the discharge electrode is less, in the case of negative ionization, compared to positive ionization.

Voltage Waveform:

Unfiltered voltage waveforms are generally used in the single-stage design, both plate and tube type. Unfiltered waveforms allow for higher peak operating voltages and reduced intensity of sparks. The plate type two-stage units generally use filtered or low ripple waveforms. Although the particle approaches a higher final value for the unfiltered waveforms, the effective charging time constantly increases. This is because the particle accepts a charge only during the time interval in which the applied electric field, in the vicinity of the particle, exceeds the self field from the charged particle.

Two-stage tubular precipitators are operated at comparatively high voltages compared to its plate type counterpart and, hence, it is not appropriate to lable them as "low voltage" precipitators, the name commonly used for the plate type units of two-stage design. The high potential and a short ionization zone make it virtually mandatory to use sophisticated silicone controlled rectifier (SCR) automatic controllers to keep the operating voltage at the maximum. The capacitance of the tubes themselves is used to smooth the waveform. The use of a three-phase power supply with Saturable Core Reactor (SR) is also under investigation. The typical power supply for the tubular units have ratings of about 10KVA and, hence, the use of external capacitors to reduce the ripple is not advisable. The intensity of a spark, in such a case, would be deleterious to the tube material.

The shift in phase angle, or more appropriately the conduction angle, because of the space charge effect, can also alter the shape of the waveform significantly. Space charge occurs with a medium concentration of fine fumes or with a heavy concentration of large particles. The particles being charged to the same polarity tend to reduce the electric field at the discharge electrode and, in some cases involving very high concentration, may reduce the potential to the incipient corona starting voltage. The corona current is then reduced by a factor of 100 or more. Incorporation of a variable inductance or a resistor in the primary circuit is necessary to reduce the effect of the phase angle shift.

Sectionalization:

Sectionalization of electrical energy is a very important consideration in the design of a precipitator. The expression for sparkover voltage for negative discharge electrodes energized by a single power supply is given by:

$$V_{s,n} = V_{s,1} - C \ln n \quad (7)$$

The reduction in voltage, Cln n, is because: (i) The instantaneous potential of all parallel-connected discharge electrodes is set by the reduced potential of whichever electrode in the system is experiencing sparkover at that moment and, (ii) The greater the total discharge electrode length in the section, the higher is the probability of the occurrence of conditions which tend to lower the sparkover potential. This problem can be circumvented, partially, by introducing adequate resistance in each leg of the parallel-connected discharge electrodes. The other obvious solution is to reduce the number of discharge electrodes energized by a single power supply. The economic considerations preclude a high degree of sectionalization in spite of its obvious advantage. Tubular units generally use one power supply per 20,000 CFM per pass. Several sections in series are necessary where high current suppression conditions due to space charge is observed.

Velocity Distribution:

Velocity through the precipitator is the only flow parameter involved in the Deutsch equation. The Deutsch equation assumes plug flow velocity distribution. In practice, however, this condition is very difficult to achieve. Nonuniform gas flow can affect the precipitator performance by scouring the plates in the localized regions of high gas velocity and by reducing performance due to the exponential relation between efficiency and the gas flow. Poor gas flow can decrease the precipitator efficiency as much as 20 to 30%. For single-stage units, 1/10 or 1/16 scale model studies are usual. Such expensive studies are rarely undertaken for the two-stage units. IGCI gas flow quality criteria or their equivalent are generally required in the single-stage units. Although such requirements are not included in the specifications for two-stage units, well engineered two-stage system designs generally adhere to them. Two-stage units are smaller in size and do not have much internal structural framework to disturb the air flow quality. Various air distribution devices are used in the two-stage units. A well engineered equipment layout can also materially contribute to the efficient air flow distribution in the precipitator.

INDUSTRIAL APPLICATIONS

Two-stage design tubular electrostatic precipitators are ideally suited for the control of the sub-micron organic mist and inorganic acid mist emissions. High collection efficiency in sub-micron particulate size range and the lightweight compact design make the two-stage tubular precipitator ideal for such applications.

Organic emission occurs when high boiling point organic compounds volatilize and evaporate in any part of an industrial process. Organic impurities are generally found with most of the ores. More organic matter is introduced during floatation operation. Lubrication oils, cutting oils, mineral oils, etc., are also sources of organic matters. When materials containing organic compounds are roasted, calcined, sintered, or reduced at high temperatures, organic emissions occur. When the fumes come in contact with cold outside air, the hydrocarbons condense to form fine aerosol. Condensation phenomena produces sub-micron size particles. Very fine mist is also produced during gas phase chemical reaction where the product of reaction has very low vapor pressure at the reaction temperature and, hence, condenses from the gas stream. The reaction of sulfur trioxide and water vapor to form sub-micron sulfuric acid mist is probably the best example of fine mist formation during gas phase reaction.

The sub-micron particle size range is optimum for scattering the light, hence, a very small weight fraction produces highly visible plume. Moreover, these fine particles can also bypass the body's respiratory filters and penetrate deeply into the lungs. Because of their high surface area, some fine particles have been identified as transport vehicles for gaseous pollutants, both absorbed and reacted and, hence, can produce synergistic effects deleterious to human health.[5]

Typical Applications:

Tubular two-stage type units have been tried in several industrial applications involving very tough corrosion problems. A special conductive fiberglass resin was developed to combat the problem. This eliminates the need for, and also the problems associated with, maintaining water film on the collecting electrode. The tubular design lends itself easily to various types of materials of construction.

Molybdenum Roaster:

Molybdenum disulfide is oxidized in the multilevel hearth furnace to Molybdenum trioxide and sulfur dioxide. The exhaust is first passed through a baghouse and then through a lead-lined quench scrubber. The two-stage tubular unit treats the exhaust stream before venting it to the atmosphere. The exhaust stream entering the precipitator contains organic compounds and sulphuric acid mist with some oxides of molybdenum, sellenium and mercury. Chlorides and trace amounts of fluorides are also present in the air stream. Tantalum is the only metal that could be used as material of construction. Fiberglass reinforced plastic (FRP) with synthetic fiber veil on the inside surface proved to have excellent corrosion resistant characteristics in this service also. Collection efficiency in excess of 99 percent was obtained.

Pulp and Paper Industry:

Recovery of spent sulfite liquor is widespread in the pulp and paper industry. The spent sulfite liquors are burnt to recover the sulfur values. The scrubbing of the oxides of sulfur is accomplished by the use of ammonium, sodium, calcium or magnesium base liquors. A significant amount of fine particulate matter is generated during this absorbing operation. The exhaust plume from the scrubber is thus highly visible. The particle size is extremely fine, between 0.1 to 0.5 microns in diameter. The particles are partially insoluble and, hence, plug the fiber bed type devices used to control these emissions. Moreover, considerable energy is spent to overcome the gradually increasing pressure drop through the fiber bed. Unavailability of suitable and economical materials of construction hindered the use of electrostatics in these applications. The conductive FRP construction was tested for corrosion resistance in this service. No measurable signs of corrosion were observed after a few months of tests. Collection efficiencies in excess of 98 percent were obtained under the entire range of process conditions. Throughput velocities of 6 to 7 fps were found to be optimum. The collection efficiency was measured by EPA method 5 and also by a forward light scattering photometer. Excellent agreement was found between these two measurements. Although the inlet particulate concentration of 0.6 grain/CF is not heavy enough to cause current suppression, the secondary current was reduced by a factor of three when exhaust gases were passed through the precipitator. This is believed to have been caused by extremely fine particle size (.1-.5 micron) and enormous moisture loading (saturated stream at 160°F). Additional fogging was not required to keep the unit clean.

Zirconium Calcining:

Zirconium and Hafnium are used in the nuclear industry for the full rod casings. These metals are immune to corrosion attack from most of the chemicals and can withstand very high temperature. Neutrons pass through Zirconium, whereas they are absorbed in Hafnium. Thus the nuclear reaction can be controlled by use of Zirconium and Hafnium tubes. Zirconium and Hafnium are mined as Zircon sand. The ore is chlorinated, selectively precipitated, passed through separation operation, chlorinated again, and then reduced. The exhaust from the calciner contains Zirconium oxide, Hafnium oxide, a trace amount of elemental sulfur, some chlorides and sulfuric acid mist, and sulfur dioxide. The exhaust gases are highly corrosive to most of the metals. Zirconium or FRP are acceptable materials of construction. The exhaust is first treated in a soda ash packed bed scrubber to reduce oxides of sulfur. The tubular two-stage precipitator is used to remove fine particulates and acid mist. Severe current suppression is observed because of high moisture loading. The collected liquor washes off the tubes as it drains making the unit self-cleaning.

Metal Industry:

Primary and secondary metal production usually involves smelting of the ore in a reduction furnace. Sulfur oxides generated during this operation have to be treated before they can be vented to the atmosphere. Sulfur dioxide concentration in most of the smelter gases varies from 6 to 14 percent. The contact process for the manufacturing of sulfuric acid requires 7 to 14 percent concentration of sulfur dioxide for the most efficient conversion to sulfur trioxide. The smelter gases are thus ideal for a sulfuric acid production. However, metal oxide impurities and acid mist from the exhaust stream has to be removed to prevent black acid formation. Tubular precipitators are ideal for this application. Wet electrostatic tubular lead precipitators have been used most extensively for this application. FRP tubulars are less costly, easier to construct and maintain, and are equally corrosion resistant. A very high collection efficiency can be obtained with a two-stage tubular design. The tubular two-stage unit can also be used to control the emission from the interpass tower or the final absorber tower in the contact acid plant train using spent acid as the source of sulfur. FRP construction is not good if more than 50 percent concentrated acid is being handled. ASTM 316 steel or carpenter-20 alloy might be required for such applications.

The tubular two-stage units can also be used to control emissions from sinter plants, forging, casting, foundry exhaust, meat broiling exhaust, scarfing operations, etc.

CONCLUSION

Tubular precipitators of two-stage design have a very high collection efficiency in a sub-micron region. The compactness and ease of manufacture of these units make them ideally suitable for corrosive acid mist applications involving particulate emissions. New and different applications for the two-stage tubular units are numerous and are vigorously being explored. Increased use of these units in applications having high resistivity problems is also envisaged.

REFERENCES

1. Surati, H. S. Two-Stage Precipitator for Hydrocarbon Emission Control. IEEE-IAS Annual Meeting, Chicago, 1976. pp 340-345
2. Surati, H. S., and M. R. Beltran. Heat Recovery On Organic Electrostatic Precipitators. Annual Industrial Air Pollution Control Seminar, 1976. pp 5-1-5-10
3. Beltran, M. R. Smoke Abatement for the Carpet Industry. Carpet and Rug Industry, May 1973. pp 30-34
4. Penny, G. W. A New Electrostatic Precipitator. Elect. Eng., January 1937. pp 159-163
5. Harrington, R. E. JAPCA, vol. 24 pp 927-931
6. White, H. J. Industrial Electrostatic Precipitations. Addison-Wesley Publishing Company, Inc., 1963. pp 180
7. Hall, H. J. Technical Report HAR79-218.

TABLE-1 TYPICAL OPERATING DATA[7]

	Single-Stage	Two-Stage
Ionizing field, KV/in.	13.3	16.67
Collecting field, KV/in.	13.3	25
Tube dimension	9 in Ø	3x3 in. square
Current consumption MA/1000 CFM	15-30	5-10
Power consumption, watts/1000 CFM	400	125
SCA, ft^2/1000 CFM gross	400	100
Treatment time, sec.	4-10	1-2

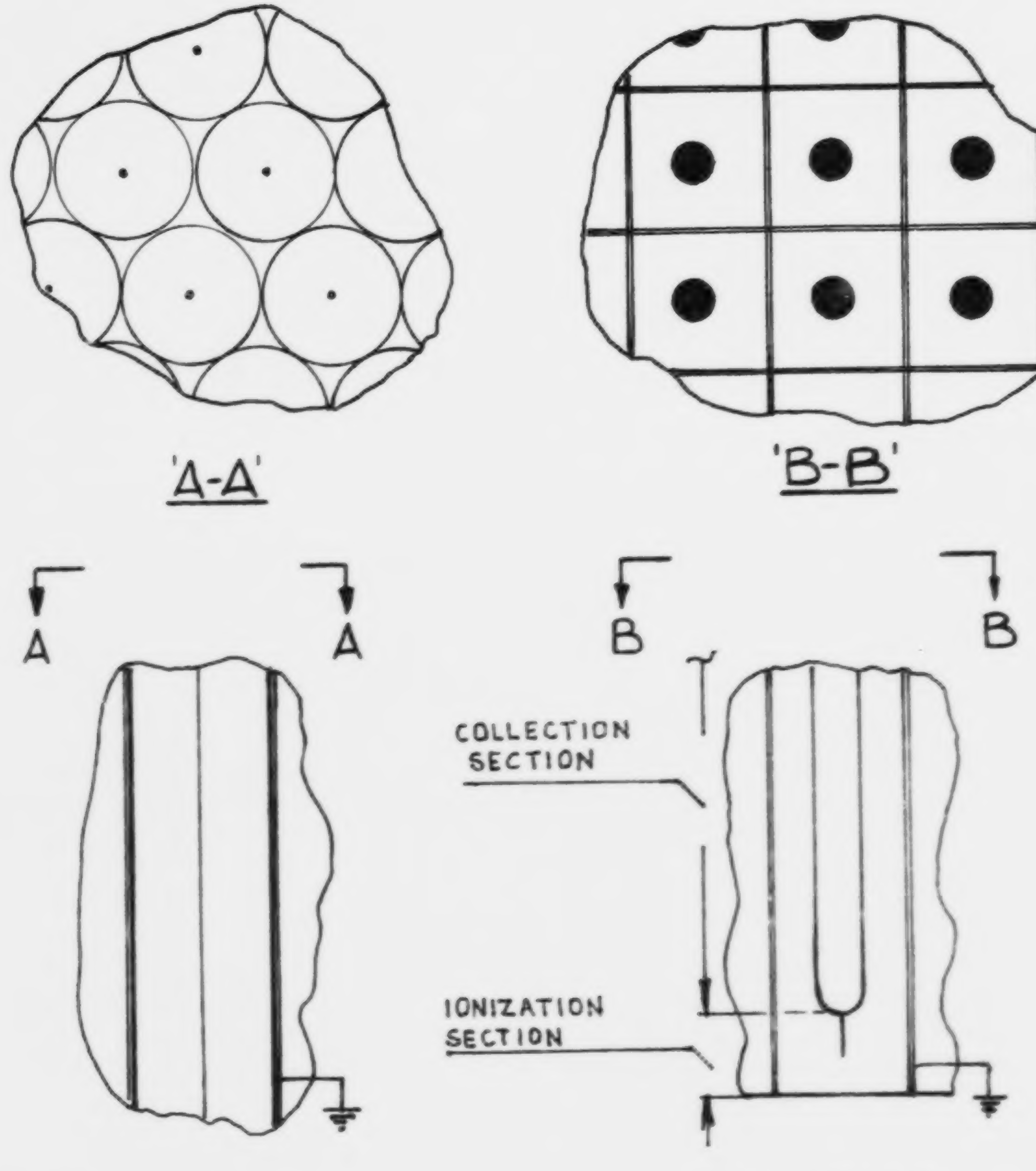
'A-A'
'B-B'
A
A
B
B
COLLECTION SECTION
IONIZATION SECTION
SINGLE STAGE
TWO STAGE

FIG. 1

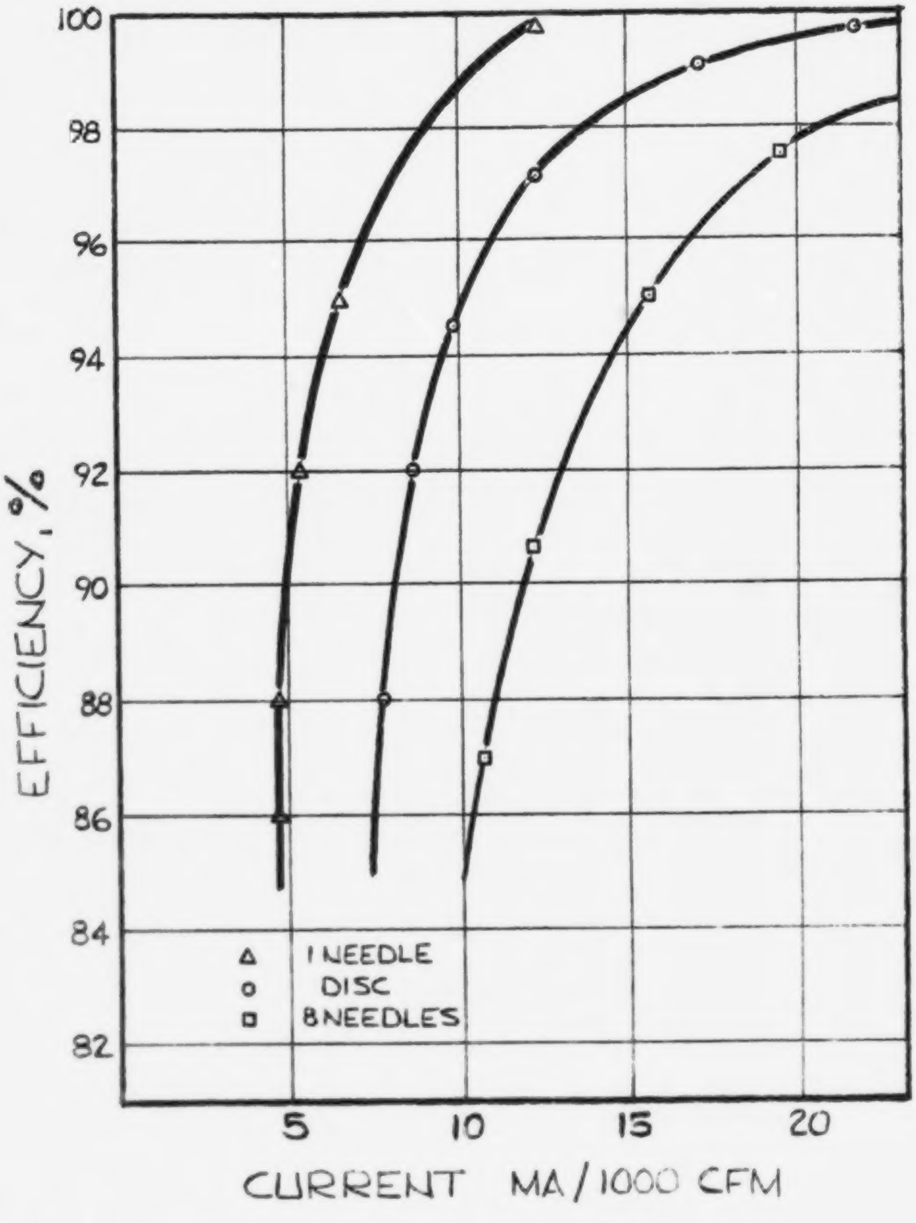

100
98
96
94
92
90
88
86
84
82
EFFICIENCY, %
5
10
15
20
CURRENT MA/1000 CFM
△ 1 NEEDLE
○ DISC
□ 8 NEEDLES

FIG. 2

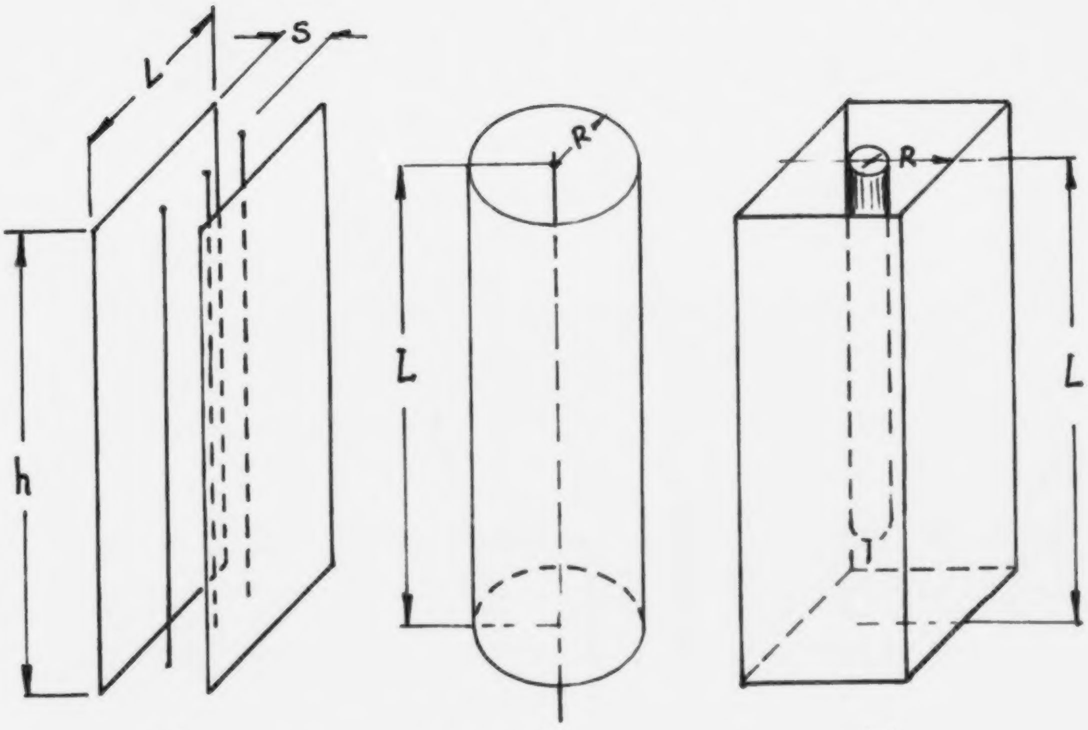

(a) (b) (c)

(a) Single-Stage Duct Precipitator

(b) Single-Stage Tubular Precipitator

(c) Two-Stage Tubular Precipitator

FIG.3

PRESENT STATUS OF WIDE-SPACING TYPE PRECIPITATOR IN JAPAN

By:
Senichi Masuda
Department of Electrical Engineering
Faculty of Engineering, University of Tokyo
7-3-1, Hongo, Bunkyo-ku, Tokyo, Japan 113

ABSTRACT

The wide-spacing type electrostatic Precipitator (WESP) has aquired an established position in Japan in the recent decade, and 160 WESPs had been installed until the end of 1978 by 10 manufacturers in almost all the application fields. The collection performance remains unchanged with increasing duct spacing up to ca. 400 - 600 mm or more at a constant precipitator volume, so far as the applied voltage be raised correspondingly. As a result, WESP results in a substantial reduction of installation cost in case of a large gas volume, amounting to 15 - 20 % under the most favourable conditions. Moreover, the stability in operation is largely increased, so that the initial high collection performance can be maintained. The maintenance work becomes also much easier. WESP-design can be applicable also in the wet ESPs and the novel type ESPs recently developed.

PRESENT STATUS OF WIDE-SPACING TYPE PRECIPITATOR IN JAPAN

1. INTRODUCTION

The wide-spacing type electrostatic precipitator (WESP) using a duct spacing of 400 - 600 mm or more, substantially larger than the conventional spacing of ca. 250 mm, represents one of the largest technical impact occured in the recent decade in the field of ESP. In Japan 160 WESPs had been installed until the end of 1978, and now WESP has aquired an established position. In the case of high performance precipitators, common under the present severe emission standard, the collection efficiency remains almost unchanged even if the duct spacing, D, is increased from its conventional value of D = 250 - 300 mm up to a large value of D = 400 - 600 mm or more, so far as the applied voltage be raised correspondingly. This effect, hard to understand from the classical Deutschian concept, should be refered to as the "WESP-effect". At any rate WESP produces a large economical advantage over the conventional spacing ESP in the case of medium or large gas volume. Moreover, the stability in operation is largely increased, and the the maintenance work becomes much easier. WESP-design can also be successfully applied in the wet ESPs and the novel type ESPs recently developed.

WESP in Japan has originated from two different sources: one being Nippon Kai Heavy Industries Co., Ltd, and another being Nihon Kogei Co., Ltd. Nippon Kai started the commercialization of WESP with the license of R.F. and D.O. Heinrich. Its first WESP was installed for a cement clinker cooler in October 1971, and showed a spectacular performance with no visible stack emission (Figure 1). Nihon Kogei started from a completely different design, using a large horizontal grounded duct with more than 2 m in diameter as a collecting electrode and a very fine horizontal wire with less than 0.3 mm in diameter spanned along the duct axis as a discharge electrode. The voltage to be applied was 200 kV.

The advantages of WESP, both economical and technical, have been widely recognized by the process operators and manufacturers, and 160 WESPs had been installed until the end of 1978 by 10 manufacturers in Japan, as shown in Table 1. In this paper is described the present status of WESPs in Japan.

2. THEORETICAL EXPLANATIONS AND EXPERIMENTAL RESULTS

The WESP-effect caused a big controversy on the Deutschian concept of precipitation itself. The dust migration velocity, w, in the Deutsch equation has long been considered as a process parameter specific to each gas and dust condition and independent of D. However, the existence of WESP-effect requires the migration velocity, w , to rise proportionally with D. Many theories have been presented to explain this effect, whereas a number of experiments performed to examine this effect in more details.

Heinrich proposed recently a theoretical explanation based on the classical Deutsch equation and the approximate expressions of corona field intensity (Heinrich (1978)[1]). According to this theory, w could rise proportionally with D, provided the total corona current be kept unchanged.

T. Misaka et. al. made thorough experimental investigations on the test WESPs in air at NTP using fly ash samples and changing D from 250 to 750 mm with the inter-wire spacing kept constant (Misaka et. al. (1978)[2]). The applied voltage, U, was changed proportionally with D so that the average inter-electrode field intensity, Ea = U/D, could be kept constant at Ea = 4.0 and 3.2 kV/cm. In this case, the average current density per unit collection area, i, remained almost constant independent of D. The solid curves in Figure 2 represent the magnitudes of w derived from the collection efficiencies at these two Ea-values and plotted against D. w shows a rise slightly less than proportional to D. They further measured the space distribution of field intensity, E, inside the corona space using the dynamic probe method. The magnitude of E at the surface of collecting electrode, Es, increased with D even though Ea was kept unchanged, evidently due to the space-charge effect. Misaka et. al. explained the WESP-effect from this phenomenon, considering the collection process of very fine particles to be govererned by their Coulombic transport in the boundary layer region. If the values of Es measured at different Ds are used for E in the expression of the migration velocity, $w = k \cdot E^2$, the dotted curves in Figure 2 are obtained, where the constant c was derived from the data at D = 250 mm. The ageement between the solid and dotted curves is quite satisfactory, providing some support to their explanation.

S. Matts presented a different explanation, considering the fact that the WESP-effect appears only in the case of very high collection efficiency, say 99 %, where the reentrainment loss plays a major role in collection performance (Matts (1978)[3]). This loss will be lowered in WESPs because of the decreased number of collection plates.

P. Cooperman presented a non-Deutschian expression for the collection efficiency assuming the existence of reverse transport of dust particles due to turbulent diffusion (Cooperman (1976)[4]). He pointed out that the WESP-effect could be derived from this new expression.

O. Gűpner, H. Lau, R. Aureille et. al., and St. Nibeleanu also presented the experimental results supporting the existence of the WESP-effect under suitable conditions (Gupner (1976)[5]), (Lau (1969)[6]), (Aureille and Blanchot (1971)[7]), (Nibeleanu (1979)[8]).

The author and his co-workers carried out the field tests of wet WESP at a dry-process cement rotary kiln (Ago et. al. (1975)[9]). The applicable voltage at D = 250 mm was considerably low at U = 40 kV/cm (Ea = 3.2 kV) owing to a large sparking tendency. This was due to the Taylor cones of water appearing at the lower edges of the collection plates. By doubling the duct spacing to D = 500 mm, the operation became completely stable, and U = 100 kV could be applied without any sparking, resulting in the increase in Ea up to 4 kV/cm. The magnitude of w could be more than doubled (2.16 times) by doubling D at Ea unchanged (3.2 kV/cm). By increasing Ea up to 4.0 kV/cm, the further rise in w (2.51 times) could be obtained. In addition, the savings of irrigation water and its treatment system were quite substantial.

Noso et. al. carried out recently the thorough field tests on WESPs (Noso et. al. (1978)[10]). Two large series of tests were performed: one using a large test precipitator located at the research station, and the other using a pilot plant located at a cement mill. In the first series of test, where the sample dusts were injected into the oil-burned gas, the electrical characteristics and collection performance were measured at D = 250 - 800 mm under different corona current density, i, and inlet dust loading, Ci. The sparking voltage, V_{sp} showed a linear rise with increasing D in air load condition. Whereas, in dust load condition, V_{sp} at a very large duct spacing D = 800 mm showed a substantial drop at C_i beyond $7 g/Nm^3$ owing to excessive sparking caused by the space-charge effect. Figure 3 indicates the effect of i on w, where w is normalized by its value at i = $0.4 mA/m^2$, $w_{i=0.4}$, and reduced to D = 250 mm as

$$w^* = (w/w_{i=0.4})/(D/250). \qquad (1)$$

The value i = $0.4 mA/Nm^3$ is considered as the current threshold beyond which a satisfactory collection performance can be expected under the normal operating conditions. The curves of w^* coincide well each other, and rise with i up to a certain value. The more than proportional rise of w with D can be seen from this figure, which tendency is enhanced with the increase in i, but becomes saturated at i = $0.6 mA/m^2$ owing to the increased sparking. The optimum current density lies in the gange of 0.4 - $0.6 mA/m^2$ independent of D. Figure 4 shows the effect of C_i on w^*, where the magnitude of w at $C_i = 5 g/Nm^3$, $w_{Ci=0.5}$, is used instead of $w_{i=0.4}$ for normalization in Equation (1). w^* at D = 250 mm continues to increase with C_i, whereas that for WESP shows the saturation in its increase beyond $C_i = 5 g/m^3$. Figure 5 indicates the effect of D on w^* at different C_i-values, where w at D = 250 mm, $w_{D=250}$, is used for normalization. Again, the more than proportional WESP-effect is shown to exist in the low

C_i range below 5 g/Nm^3, which, however, becomes saturated at D = 600 mm. Noso et. al. came to the conclusion that the optimum value of D in view of both stability in electrical operation and collection performance seemed to lie in the range of D = 400 - 600 mm, and that the minimum overall cost calculated from the economical assessment also coincides with the same duct spacing range. In the second series of test the duct spacing was set at both D = 250 mm and D = 400 mm, and the effects of gas velocity, v, and C_i on w^* were investigated. Figures 6 and 7 show the results obtained. The effect of v is the same for both D = 250 mm and D = 400 mm. The effect of C_i is also the same except for the very high range of C_i beyond 60 g/Nm^3. From these and many other results, Noso et. al. concluded that the design data obtained at the conventional spacing ESP could be well transfered to WESP through the concept of normalized migration velocity.

Finally, R. Ito and K. Takimoto presented recently a method of estimating the collection efficiency of WESP from the data of the conventional spacing ESP and dust to be collected (Ito and Takimoto (1977)[11]). They expressed the fractional loss out of WESP as

$$Ft = 1 - y = (h(d_i) - h(d_{i+1})) \cdot \exp(-w(D,d_i).f) \qquad (2)$$

where y = fractional collection efficiency, d_i = i-th diameter of particle, $h(d_i)$ = dust cummulative mass fraction above d_i, $w(D,d_i)$ = dust migration velocity for d_i at D, and f = specific collection area. If the magnitude of $w(D,d_i)$ is proportional to D, it can be expressed, using its value at the conventional spacing ESP with D = 250 mm, $w_{D=250}(d_i)$, as follows:

$$w(D,d_i) = (D/250) \cdot w_{D=250}(d_i) \qquad (3)$$

Hence, if $w_{D=250}(d_i)$ is known from the data of the conventional spacing ESP and $h(d_i)$ measured for the dust to be collected, the overall collection performance can be immediately calculated from Equation (2). Ito and Takimoto confirmed that this procedure could provide a satisfactory estimation for performance of WESP.

3. CHARACTERSITIC FEATURES OF WIDE-SPACING PRECIPITATOR

From the field experiences thus far obtained, the characteristic features of WESP can be summarized as follows:

(1) The technically optimum value of duct spacing lies usually in the range of D = 400 - 600 mm. The corresponding voltage is 80 - 150 kV.

(2) The increase in D at a constant precipitator volume produce the cost reductions in the discharge and collecting ellectrodes, rapping elements, construction members and ground, whereas it causes, through the rise of voltage needed, the cost increases in

the power pack, insulators, bushings etc. It also causes the increase in dead space owing to the large gas gap needed for insulation and, therefore, the quantity of heated cleaning air to be purged into the insulator boxes. The magnitude of D providing the maximum economical advantage, therefore, depends largely on the precipitator size. In case of small sized ESPs, the weight of cost increase due to increased voltage becomes dominant, so that the economical advantage of WESP appears only in the medium or large sized ESPs with a gas volume beyond, say, 1,000 m^3/min. The cost reduction by 15 - 20 % can be obtained in large precipitators under most favorable conditions. The economically optimum value of duct spacing lies in the range of D = 400 - 600 mm, which coincides with the technically optimum value cited above.

(3) WESP has a large stability in operation owing to much less sparking tendency. This is because the relative variation of the inter-electrode gap due to deformatios of electrode and construction members as well as irregular dust deposit becomes largely diminished. A high voltage and, therefore, a high collection performance at the start of operation can be maintained during its entire period.

(4) Ease in the maintenance work enabled by the increased gap is its another large technical merit (see Figure 8; D = 640 mm)).

(5) The davantages of WESP are preserved also in the case of wet precipitators. In this case, the stability in operation becomes much more pronounced. In addition, the quantity of irrigation water needed and the capacity of the water treatment system are reduced. The lowering of gas temperature is decreased owing to reduced contact area to water film..

(6) WESP-design is especially suited to the Roof-Monted--Type precipitator, because of its reduced total weight.

(7) WESP is more sensitive to the dust space-charge effect causing the reduction or quenching of corona current and excessive sparking especially in the inlet field. This is because the space-charge effect is a size effect to be enhanced by the increase in D. Among two factors enhancing this effect, the high inlet dust loading and the fine dust particle size, the latter proved to have much more detriorating effect, because the fine particles cannot be quickly collected and remain suspended for much longer time. Therefore, when the very fine dust or mist with a considerable mass loading is encountered, the decrease of D or use of the conventional duct spacing value becomes imperative. On the contrary, no reduction of D is needed in the case of a large mass loading of coase dust.

(8) The effect of back discharge on the performance of WESP is one of the most controversial problems. Back discharge is observed to occur also in WESPs collecting high resistivity

dusts, and the size of WESP has to be more or less increased accordingly. In case of the sinter main dust of steel plants with ca. 10^{13} ohm-cm resistivity, an excellent collection performance could be obtained by the WESPs having a considerably large size, whereas, in case of very high resistive low sulphur fly ash, somewhat pessimistic prospect is suggested by the tests so far made. Anyway, the economical advantage of WESP seems to become more or less diminished in the case of high resistivity applications.

5. DESIGN OF WIDE-SPACING TYPE PRECIPITATORS

WESP is mostly constructed in the vertical plate design identical to the conventional ESP (Figure 1). However, the horizontal and vertical cylinder geometries, both single and multiple, are also used in a few special cases. Figure 9 illustrates the multiple horizontal duct construction named "ESCS (House Type)" (Electrostatic Space Cleaner - Super) which has a house-like cross-section and a very large duct spacing at D = 1,200 - 1,800 mm (Masuda (1978)[12]). It has been developed by Nippon Steel Corporation with the license of Nihon Kogei, and preserve well its original design. The House-Type ESCS, although showed an excellent collection performance for very high resistive dusts from the ore sinter machine, proved to be fairly expensive. As a result, it has been modified now to the ordinary vertical plate construction named "ESCS (Straight-Type)". Figure 10 shows the photograph of a huge Straight-Type ESCS (30,000 m^3/min) installed at a sinter machine of Nippon Steel (Wakamatsu Works; sinter main gas). The typical data of ESCS are given in Table 2. The vertical multiple duct construction, as shown in Figure 11 is also used in the case of medium gas volume.

The high voltage power pack is mostly mounted on the top of WESP, and the conduit type connection is used for feeding of current at beyond 150 kV. In case of lower voltage, the high voltage cable is also used for feeding. The voltage in the range of 80 - 150 kV is preferably used in most of the applications at D = 400 - 600 mm because of the reasons previously described. The use of voltage as high as 200 kV is now restricted to a few special applications with D beyond this range.

The magnitude of D used in WESP differs considerably from one manufacturer to another. Some manufacturer uses D = 500 mm as a standard design in all of the fields, and uses D = 400 mm only in the case when the space-charge effect is substantial. Another manufacturer uses a narrower duct spacing at the inlet field, considering the space-charge effect, and D = 400 - 800 mm in the outlet field: D = 400 - 500 mm for smaller gas volume to lower the cost of power pack, D = 600 - 700 mm for larger gas volume to lower the electrode and construction costs, and D = 800 mm in the high resistivity applications.

The estimation of the necessary specific collection area, f, can be made from the data in the conventional spacing ESPs using the methods already described.

6. APPLICATION FIELDS OF WIDE-SPACING TYPE PRECIPITATORS

The application fields of WESP cover almost all the areas where the conventional spacing ESPs, both dry and wet, have been used (see Table 1), such as:

(1) Cement industry: rotary kiln, clinker cooler, clinker mill and dryer.

(2) Steel industry: sinter machine, sinter cooler, electric furnace, basic oxygen furnace and open hearth furnace.

(3) Metal and mining industry: melting furnace, smelter furnace, holding furnace, sinter-machine, sinter-cooler, electric furnace, casting furnace, rotary kiln and sulphuric acid plant.

(4) Chemical plant: sulfuric acid plant, spray dryer and incinerator.

(5) Glass industry: glass melting furnace.

(6) Oil refinery: FCC plant.

(7) Electric power industry: oil-fired boiler, coal-fired boiler and desulfurization plant.

(8) City gas supplier: coke oven and coke mixing room.

(9) Firebrick industry: baking furnace.

(10) Municipal incinerator plant.

(13) Automobile tunnel.

WESP-design have also been successfully applied in the novel types of precipitators recently developed, including:

(a) Hybrid-Type ESP (Onoda Cement Mfg. Co., Ltd.): A small wet field is located after one or two dry fields in a common casing to prevent the rapping loss (Masuda et. al. (1976)[13]). The wide duct spacing are used in both the wet and dry fields.

(b) Bias-Controlled Pulse Charging ESP (IHI Heavy Industries Co., Ltd.): A very large duct spacing at D = 600 mm is used in the tri-electrode fields (Masuda (1978)[14]).

(c) CEEP-Type ESP (Nippon Kai Heavy Industries, Co., Ltd.): The collecting electrodes consist of the water-cooled square pipes and comprize the mechanical scrapers moving vertically to remove dust deposit (Figures 12 and 13). The very high resitive dust from FCC process of an oil refinery plant is collected effectively, and the heat recovered from the cooling water is used for preheating of boiler feed water. This economical gain amounts to more than 32,000 $/year. The second CEEP has started its operation recently at a cement rotary kiln.

(d) Roof-Mounted-Type ESP (Sumitomo Heavy Industries Co., Ltd.; Sumitomo Metal Mining Co., Ltd.; Hitachi Plant Engineering & Construction Co., Ltd.): See (Nomura and Sakai (1977)[15]) and (Ito and Takimoto (1978)[11]).

(e) RCCES-Type ESP (Rotary Cylindrical Collecting Electrode with Scraper) (Koyo Iron Works & Construction Co., Ltd.): A large rotary cylinder with 1.5 - 2.0 m in diameter and 10 - 20 m in length serves as a collecting electrode, and a number of long needles (40 cm in length) planted radially on the center rod serve as the discharge electrodes (Isahaya (1978)[16]) (Figure 14). A chain scraper is attached on the entire length of the bottom of the cylinder (Figure 15). The rotation of the cylinder brings the deposit on its inner wall to its bottom position where the deposit is mechanically removed. The applied voltage is 200 kV. The very viscous or sticky tar fume (50 - 300 Englar degree) can be effectively collected.

7. CONCLUSION

WESP has aquired an established position now in Japan, and is expected to be more widely accepted in future. From the experiences of WESPs, amounting to 160 in number at the end of 1978, the following conclusions are derived:

(1) WESP can be used in almost all the applications of the conventional spacing dry and wet ESPs.

(2) The optimum duct spacing lies in the range of 400 - 600 mm depending upon the gas volume, emission level required, and concentration and resistivity of dust to be collected.

(3) The voltage of 80 - 150 kV is preferably used in most of the applications. The use of a higher voltage as 200 kV is restricted in a few application where a very large duct spacing is needed.

(4) Its economical advantage appears only in the medium or large sized precipitators with the gas volume beyond, say, 1,000 m^3/min, and it becomes more pronounced with increasing size. The cost reduction to be obtained amounts to 15 - 20 % under the most favorable conditions.

(5) WESP has an excellent stability in operation, so that its

high initial performance can be maintained throughout the whole operation period. WESP also has an advantage of ease in maintenance work.

(6) WESP is affected by the dust space-charge much more sensitively than the conventional spacing ESP. The very fine particles with a considerable mass loading causes the most detrimental space-charge effect, so that the use of the smaller duct spacing is imperative in this case.

(7) The economical advantage of WESP is likely to be diminished in the case of high resistivity applications.

(8) The design of WESP can be made from the data obtained in the conventional spacing ESP.

(9) WESP-design can also be successfully applied in the novel type ESPs.

REFERENCES

1. Heinrich, D.O. Der grosse Gassenabstand im Elektrofilterbau. Staub-Reinhaltung der Luft, 38 (11): 446-451 (November, 1978).

2. Misaka, T., K. Sugimoto and H. Yamada. Electric Field Strength and Collection Efficiency of Electrostatic Precipitators Having Wide Collection Pitches. Proc. CSIRO Conf. on Electrostatic Precipitation (Leura, N.S.W., Australia), Paper No. 11 (August, 1978).

3. Matts, S. Some Experiments with Increased Electrode Spacing. Proc. CSIRO Conf. on Electrostatic Precipitation (Leura, N.S.W., Australia), Paper No. 13 (August, 1978).

4. Cooperman, P. Non-Deutschian Phenomenon in Electrostatic Precipitation. APCA 69th Annual Meeting (Portland, Oregon), Paper No. 76-42.2 (June/July, 1976).

5. Güpner, O. Einflüsse auf die Wanderungsgeschwindigkeit, nachgewiesen mit einem Versuchselektrofilter. Dissertation, Univ. of Essen (1976).

6. Lau, H. Mit Wechselspannung betriebene Elektrofilter. Staub-Reinhaltung der Luft, 29 (8): 311-314 (August, 1969).

7. Aureille, R. and P. Blanchot. Experimentelle Untersuchungen des Einflusses verschiedener Parameter auf den Wirkungsgrad

eines Elektrofilters. Staub-Reinhaltung der Luft, 31 (9):371-375 (September, 1971).

8. Nibeleanu, St. Der Einfluss des Gassenabstandes auf den Entstaubungsgrad von Elektrofiltern bei Stäuben mit hohem Widerstand. Staub-Reinhaltung der Luft, 39 (2): 41-44 (February, 1979).

9. Ago, S., T. Itoh, H. Saito, N. Furuya and S. Masuda. Use of Large Electrode Spacing in A Wet-Type Electrostatic Precipitator. Proc. 1975 Annual Conf. of Inst. Elect. Engrs. Japan, Paper No. 921 (1975).

10. Noso, S., Y. Nishimura, S. Yokawa, S. Koosaki, T. Tomita, K. Hayashi, A. Tanaka, T. Noda, M. Mieno, S. Kuroki and M. Uragami. Research on Dry-Type Electrostatic Precipitator. Technical Journal of Sumitomo Heavy Industries Co., Ltd., 26 (28): 65-74 (December, 1978) (Japanese).

11. Ito, R. and K. Takimoto. Wide Spacing EP Is Available in Cleaning Exhaust Gases from Industrial Sources. Proc. 1978 EPA-Sumposium on Transfer and Utilization of Particulate Control Technology (Denver, Colorado), 1: 297-305 (July, 1978).

12. Masuda, S. Electrostatic Precipitation in Japanese Steel Industries. Proc. 1978 EPA-Symposium on Transfer and Utilization of Particulate Control Technology (Denver, Colorado), 2: 309-318 (July, 1978).

13. Masuda, S., S. Ago, T. Itoh, H. Saito and N. Furuya. Hybrid-Type Electrostatic Precipitator. APCA 69th Annual Meeting (Portland, Oregon), Paper No. 76-42.1 (June/July, 1976).

14. Masuda, S. Novel Electrode Construction for Pulse Charging. Proc. 1978 EPA-Symposium on Transfer and Utilization of Particulate Control Technology (Denver, Colorado), 1: 241-251 (Junly, 1978).

15. Nomura, T. and M. Sakai. Roof-Mounted Electrostatic Precipitator for Blast Furnace. Proceedings of Inst. Electrostatics Japan, 1 (2): 82-87 (July, 1977).

16. Isahaya, F. and K. Ishida. Development of New Electrostatic Precipitator Using Rotary Cylinder Collecting Electrode, Attaching Rotary Chain Scraper. Proc. CSIRO Conf. on Electrostatic Precipitation (Leura, N.S.W., Australia), Paper No. 20 (August, 1978).

TABLE 1. STATUS OF WIDE-SPACING TYPE ESP IN JAPAN
(160 units in total at the end of Dec. 1979 ; $D > 300$ mm)

Manufacturer	Number	Application Field
1. Nippon Kai Heavy Heavy Industries Co., Ltd.	65	cement rotary kiln, cement clinker cooler, glass melt, furnace, FCC process in oil refinery plant, incinerator plant, desulfurization plant for oil burning boiler, and sinter main gas in steel plant.
2. Sumitomo Metal & Mining Co., Ltd.	64	sinter cooler, electric furnace, sulfuric acid plant, roof-mounted type ESP for electric furnace, cement plant, incinerator plant.
3. Nippon Steel Corporation	11	sinter main gas in steel plant (large gas volume).
4. Onoda Engineering Co., Ltd.	6	cement rotary kiln, cement clinker cooler, Hybrid-type ESP for cement Lepol-kiln.
5. Mitsubishi Heavy Industries	2	FCC process in oil refinery plant, Hot-ESP for low-sulfur-coal burning boiler (power plant).
6. Hitachi Plant Engineering & Construction Co., Ltd.	2	incinerator plant, roof-mounted type ESP for electric furnace.
7. Koyo Iron Works & Construction Co., Ltd.	2	tar fume from baking furnace (rotary drum type ESP).
8. Sumitomo Heavy Industries Co., Ltd.	6	cement rotary kiln, sinter cooler in steel plant
9. Chiyoda Plant Engineering & Construction Corporation	1	roof-mounted type ESP for convertor.
10. Nihon Cement Mfg. Co., Ltd.	1	cement clinker cooler.

TABLE 2. RECORDS OF ESCS-TYPE ESP INSTALLED IN NIPPON STEEL CORPORATION (at Sinter Main Gas)

Specification	House Type	Straight Type	Straight Type
Gas Flow Rate (m^3/min)	19,200	30,000	26,000
Gas Temperature (°C)	Normal 130	Normal 150, Max.200	130-150, Max.250
Gas Pressure (mm H_2O)	±100	-2,200	±100
Ci (g/Nm^3)	0.3	0.5	0.35
Co (g/Nm^3)	< 0.05	< 0.05	< 0.05

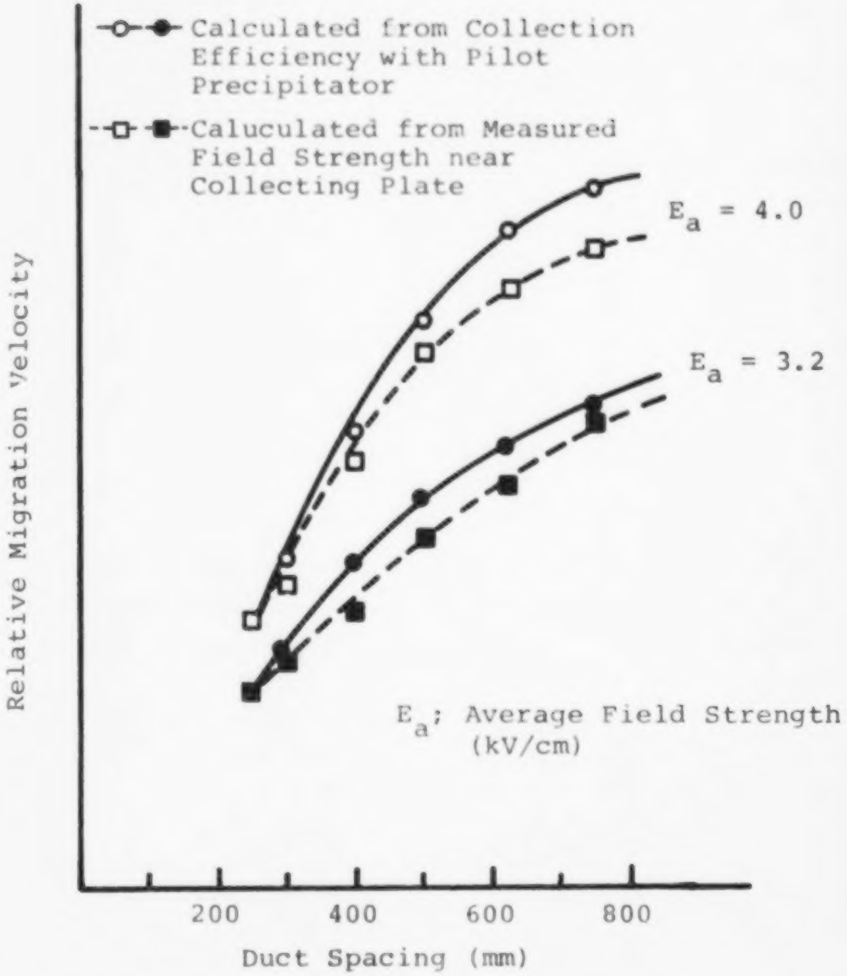

Figure 2 Relative dust migration velocity vs. duct spacing (Misaka et.al.)

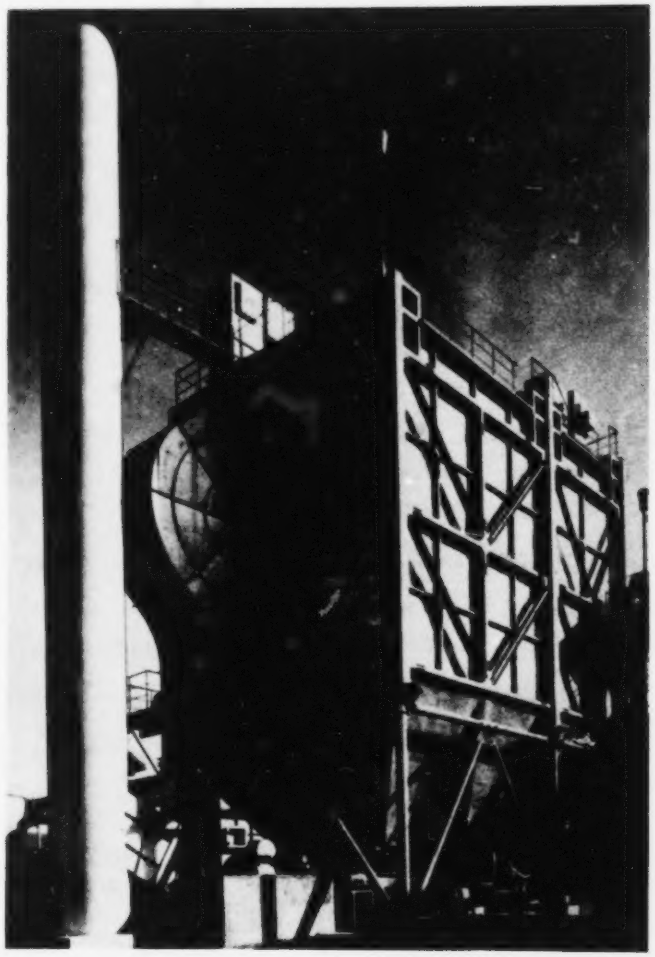

Figure 1 Wide-Spacing precipitator in operation (cement clinker cooler; 2,300 m^3/min, 150 °C)

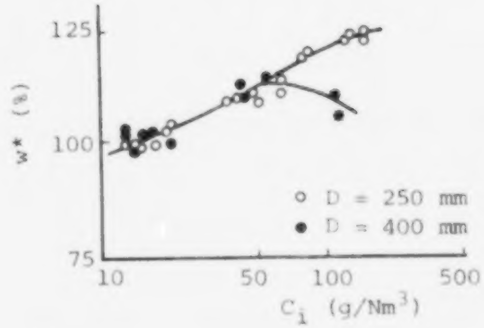

Figure 7 Effect of inlet dust loading C_i on w*

(Noso et. al. test series II)

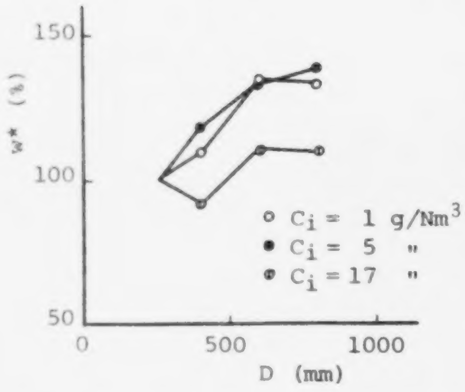

Figure 5 Effect of duct spacing D on w*

(Noso et. al.; test series I)

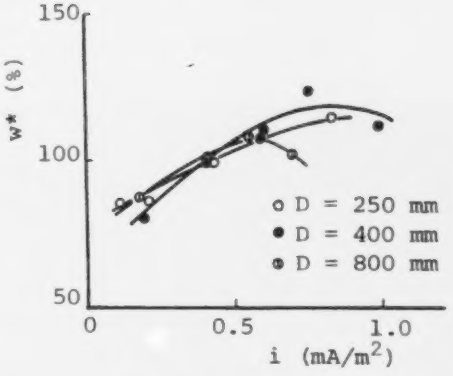

Figure 3 Effect of current density i on w*

(Noso et. al.; test series I)

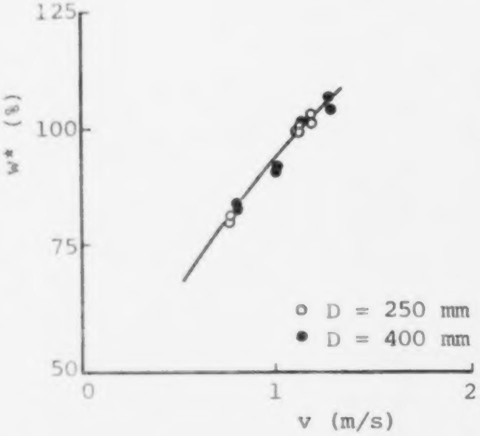

Figure 6 Effect of gas velocity v on w*

(Noso et. al.; test series II)

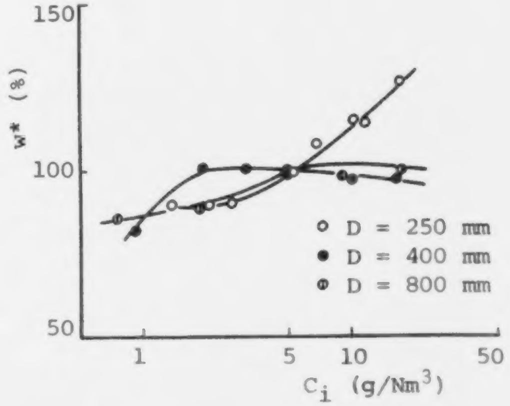

Figure 4 Effect of inlet dust loading C_i on w*

(Noso et. al.; test series I)

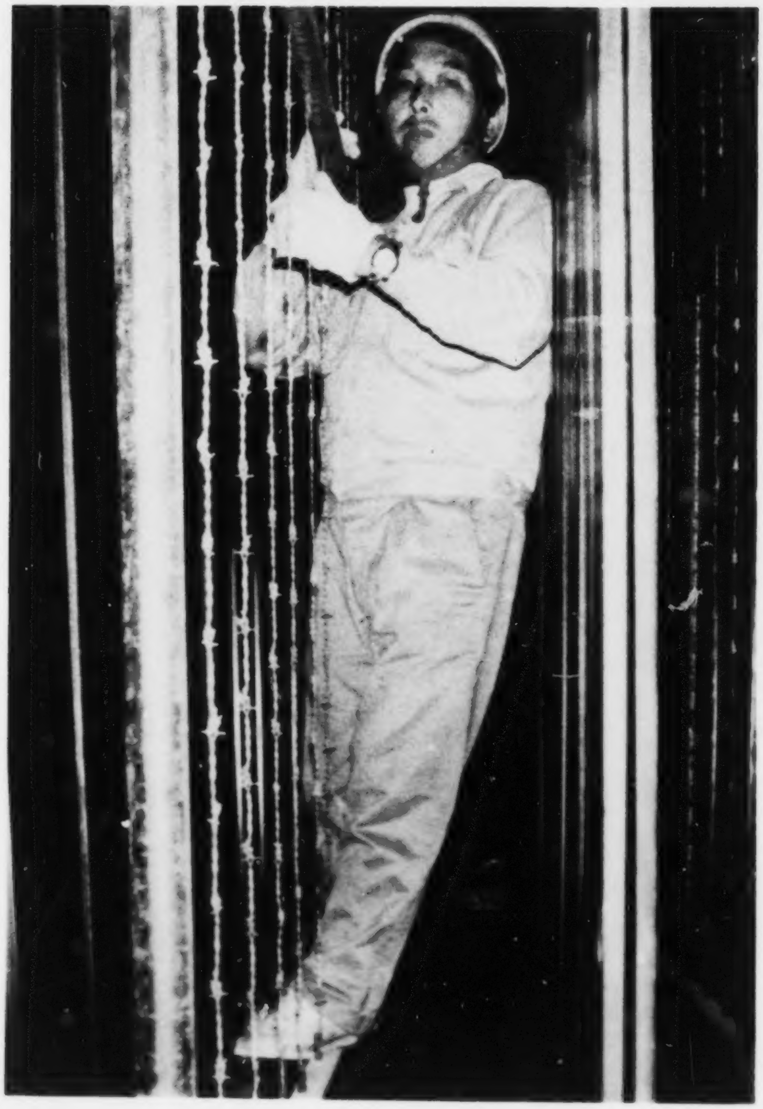

Figure 8 Collection field of WESP
(D = 640 mm ; by the courtesy of
Nippon Kai Heavy Ind.,Co.,Ltd.)

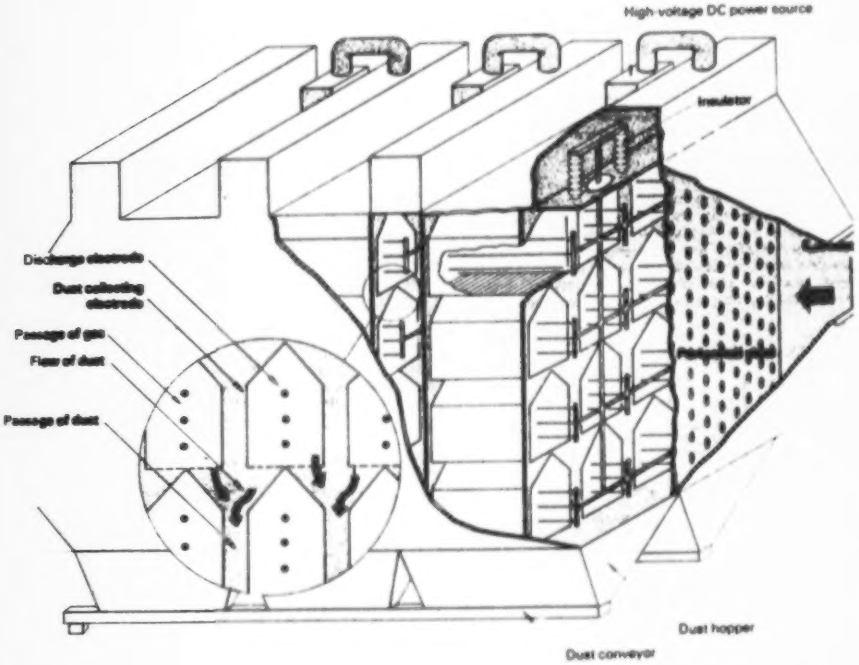

Figure 9
House-Type ESCS (Nippon Steel Corp.)

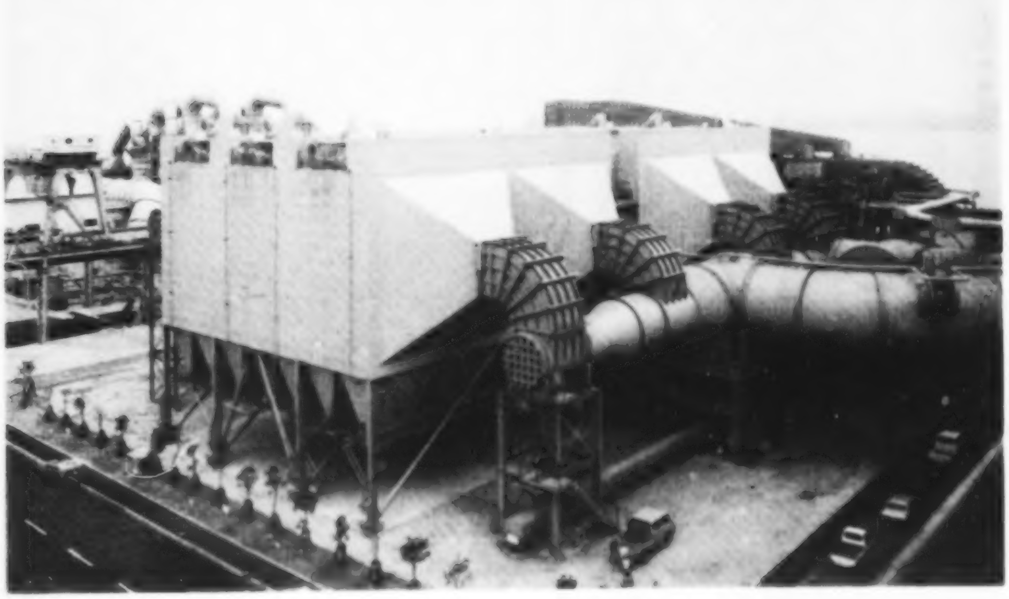

Figure 10. Straight-Type ESCS (Nippon Steel Corp., Wakamatsu Works; Sinter main gas; 30,000 m^3/min; 150°C; $Ci = 500$ mg/Nm^3; $C_o < 50$ mg/Nm^3)

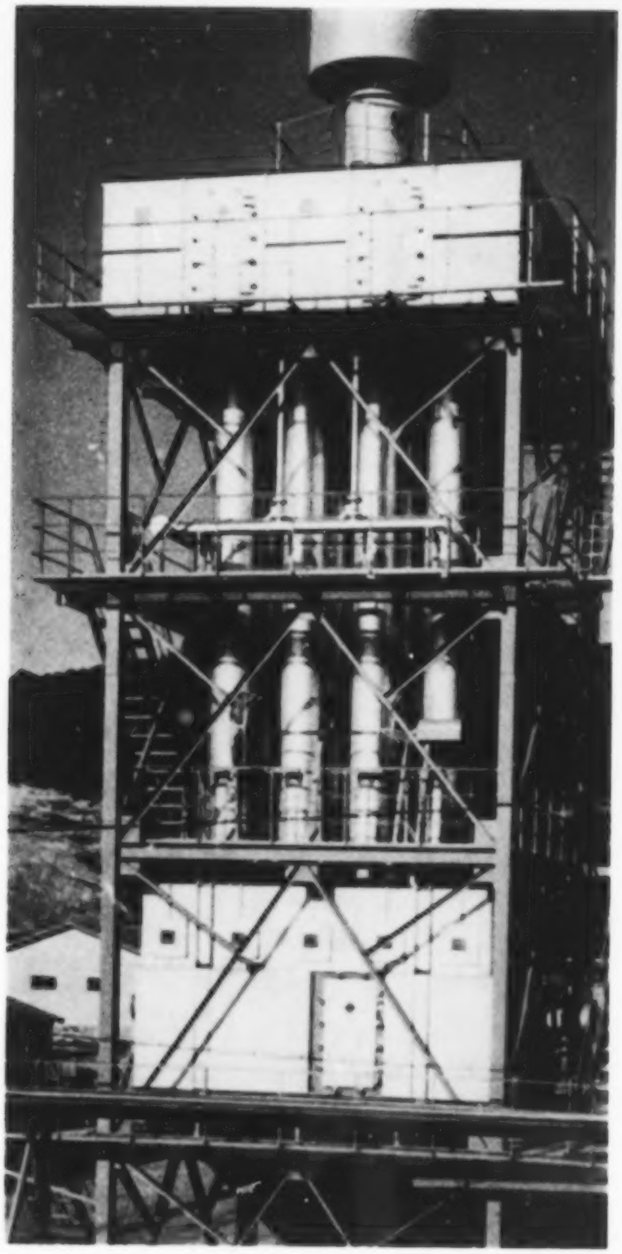

Figure 11 Vertical-Duct Type WESP
(Sumitomo Metal Mining Co., Ltd.)

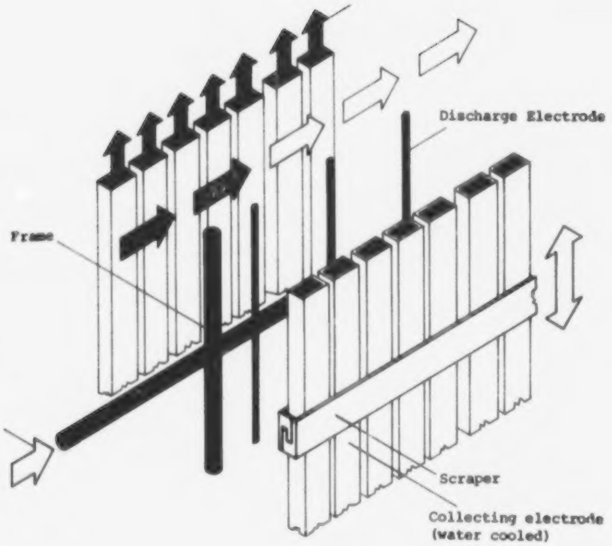

Figure 12 CEEP - Type WESP with water-cooled collecting electrodes and mechanical scrapers
(Nipponkai Heavy Ind., Co., Ltd.)

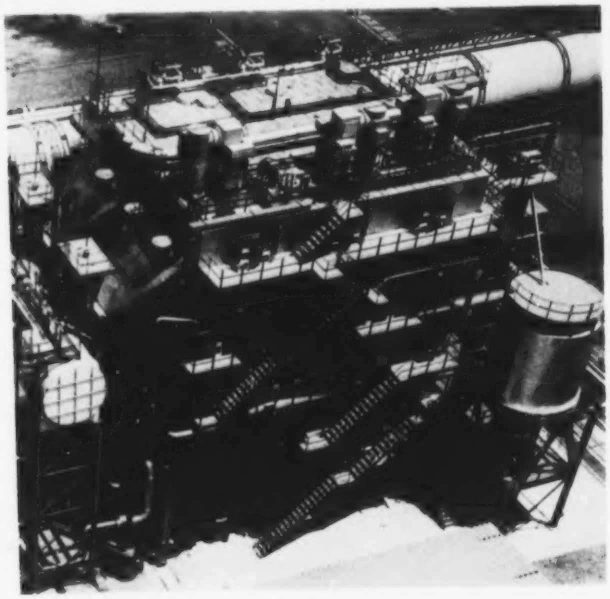

Figure 13 CEEP - Type WESP at FCC-Plant
(Idemitsu oil Co., Ltd., Chiba Refinery; 3,570 m^3/min;
gas temp. = 180 - 185 °C; outlet gas temp. = 160 - 165 °C;
C_i = 90 mg /Nm^3, C_o = 43 mg/Nm^3)

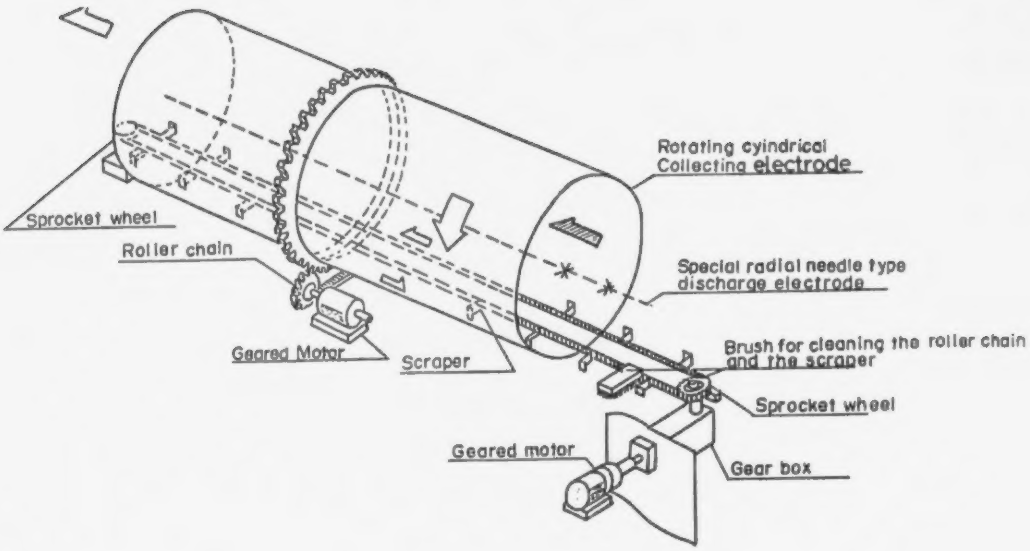

Figure 14 RCCES - Type WESP with a large rotating cylinder and chain scraper
(Koyo Iron Works & Construction Co., Ltd.)

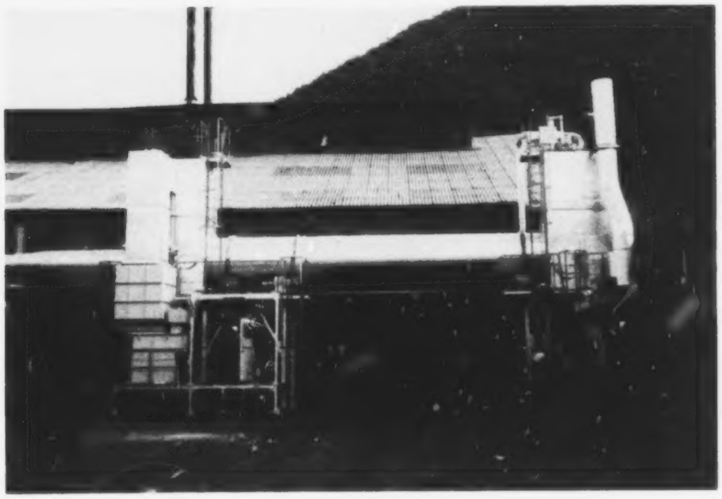

Figure 15 RCCES - Type WESP at firebrick baking furnace
(Shinagawa White Firebrick Co., Ltd: 200 m^3/min; 20 - 30 °C; tar fume; $C_i = 30 - 50$ mg/Nm^3; $C_o = 2.4 - 4.0$ mg/Nm^3)

LOW FREQUENCY SONIC CLEANING APPLIED TO ELECTROSTATIC PRECIPITATORS

By:

Stewart B. Smith
Inspiration Consolidated Copper, Inc.
Inspiration, Arizona

Joseph A. Schwartz
KVB, Inc.
17332 Irvine Blvd.
Tustin, California 92680

ABSTRACT

Inspiration Consolidated Copper was the first company in the United States to apply low frequency horns to an electrostatic precipitator. These low frequency acoustic devices (horns) have successfully demonstrated the ability to solve many of the dust collection problems associated with the operation of electrostatic precipitators. The type of problem addressed includes: inlet distribution plate clogging, hopper clogging and bridging, bridging between collector plates and structure, and build-up on wires.

While these horns have been widely used in Europe since 1969, they were only recently introduced in the United States by KVB.

Dust particles clinging to surfaces are dislodged by sound wave vibrational energy (145 dB, 250 Hz). The wave pressure fluidizes particles by breaking their bond with other particles and the surfaces to which they cling. Once "fluidized," particles will flow from surfaces by gravity or gas stream pressure.

Noise levels outside the precipitator are well below OSHA regulations.

Prior to use of the horns the electric furnace precipitator Number 4 was shut down for cleaning every four to seven days. With three KVB horns installed, the precipitator operated for six weeks before a mechanical problem caused a shut-down. Inspiration has since installed horns on two precipitators, a cyclone, and a converter gas cooler.

This paper describes the installation, operation, and economics of the Inspiration Consolidated Copper application.

LOW FREQUENCY SONIC CLEANING APPLIED TO ELECTROSTATIC PRECIPITATORS

INTRODUCTION

Inspiration Consolidated Copper Company (ICC) was the first company in the United States to solve some very serious precipitator dust collection problems by installing special purpose, low frequency, high energy acoustic horns. Faced with such severe dust problems that a precipitator had to be shut down and cleaned after less than a week of operation, ICC decided to proceed with an evaluation program in the summer of 1978. The results, as described below, have been extremely satisfactory, with benefits extending beyond the precipitator to include improvements in emission controls, acid plant operations, and mineral recovery. Economic savings in precipitator cleaning alone provided a payback period of about two months.

THE PROBLEM

The copper smelting process employed at ICC, as shown in Figure 1, produces approximately 80 tons of dust per day from the electric smelting furnace. Flue gas from the electric furnace passes first through a cyclone, where about 65 tons per day are collected, then through an electrostatic precipitator, and finally goes to the sulfuric acid plant. In less than a week's operation the precipitator would experience one or more of these problems.

- Inlet distribution plate clogging of 60% or more
- Dust build-up of two to three feet in the cat-walks between fields
- Dust build-up on wire electrodes and collector plates of one to two inches
- Bridging between collector plates and structure
- Bridging between hoppers and structure

Not only did this require frequent precipitator shut-downs for cleaning, but the reduced efficiency of the precipitator--a drop from 95% to less than 50% in less than a week--adversely affected the sulphuric acid plant. Dust overloads tended to clog the acid plant converter catalyst beds, necessitating shut-downs for cleaning every four to six months. Also adversely affected by the reduced precipitator efficiency was the recovery of copper and other minerals from the dust lost downstream.

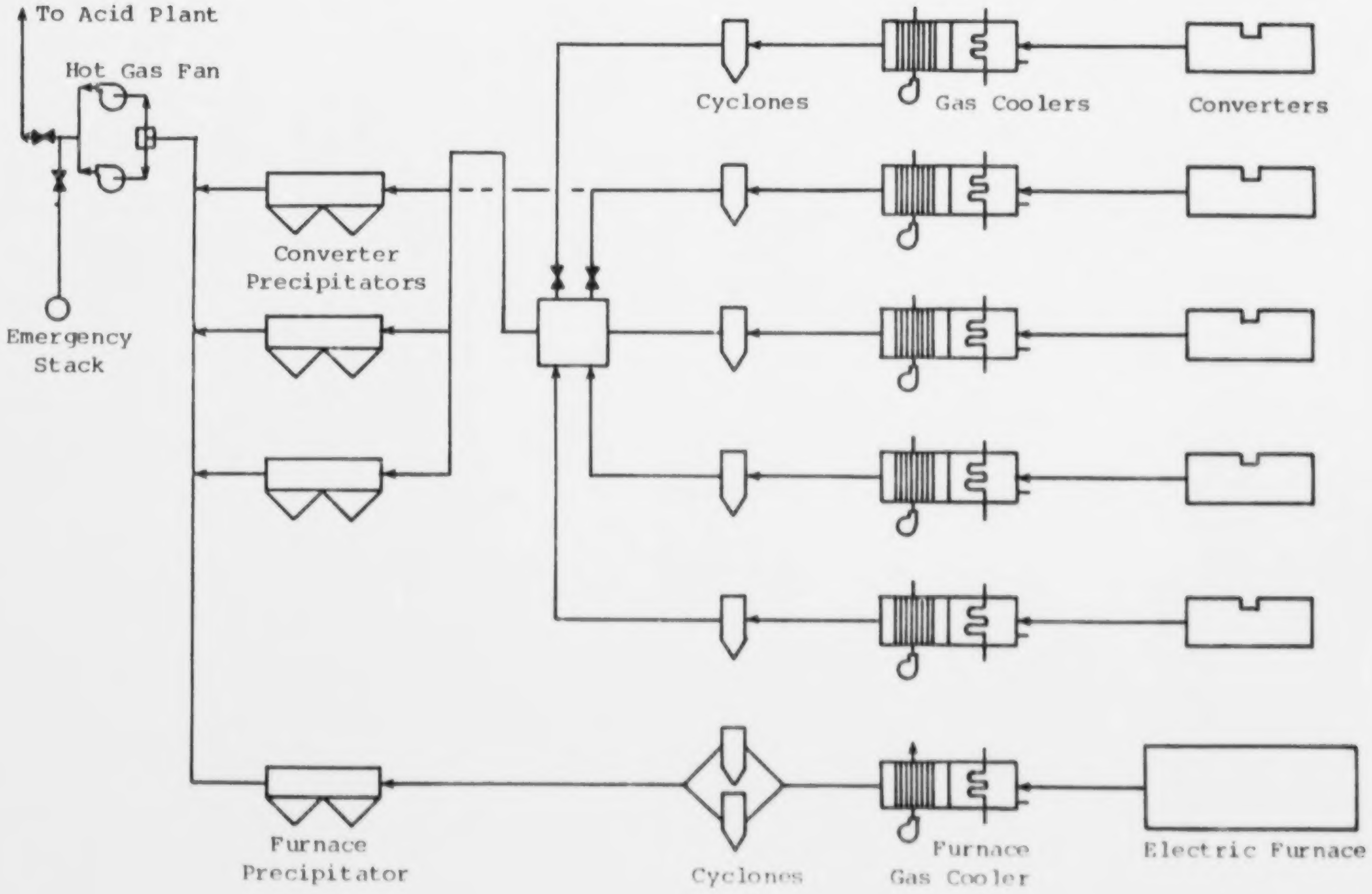

Figure 1. Inspiration Consolidated Copper Process.

On the average, it took 15 work shifts--about one week--to cool the hot precipitator down, get inside and clean out the dust, and put the unit back into service. In addition to being time-consuming and costly, the nature of the cleaning operation was particularly distasteful.

PRECIPITATOR DESIGN CHARACTERISTICS

The Number 4 precipitator at ICC consists of three nine-foot fields separated by one foot wide cat-walks. Each field had 30 collector plates with nine inch spacing between plates. Each plate is 20 feet high. The inlet distribution plate measures about 22 feet by 20 feet.

The gas flow is about 24,000 SCFM at a temperature of 750 to 800°F (399 to 427°C) and contains 4% SO_2 with a dew point of 430 °F (221°C).

KVB HORN DESCRIPTION

Figure 2 is a picture of the KVB horn. They are low frequency, high energy acoustic devices--250 Hz and 145 dB. The bell is made of cast stainless steel and is good for temperatures of 1900°F (1040°C). There is only one moving part--a titanium diaphragm.

The horns operate on compressed gas--at ICC compressed air--in the 75 to 100 psi range. Plant air is satisfactory and instrument air is not required. Air consumption during insonations is 40 to 80 SCFM. They are turned on and off by actuating a 110 volt solenoid valve. In operation this valve is controlled by an automatic electric timer. The solenoids may be located remote from the horn.

Each horn weighs 55 pounds and measures about two feet in length and one foot in diameter at the mount of the bell. The bell is bolted to the housing to facilitate installation. Diaphragms--which should last six months to one year--are replaced by simply unbolting the back of the diaphragm housing. In operation the diaphragm is cooled by a continuous air flow of three to five SCFM.

Soot and other particles clinging to surfaces are dislodged by sound wave vibrational energy. The wave pressure fluidizes particles by breaking their bond with other particles and the surfaces to which they cling. Once "fluidized," particles will flow from surfaces by gravity or gas stream pressure.

The "fluidizing" effect is compounded in an enclosed space where large, solid surfaces reflect sound waves, creating a homogeneous vibrational energy field.

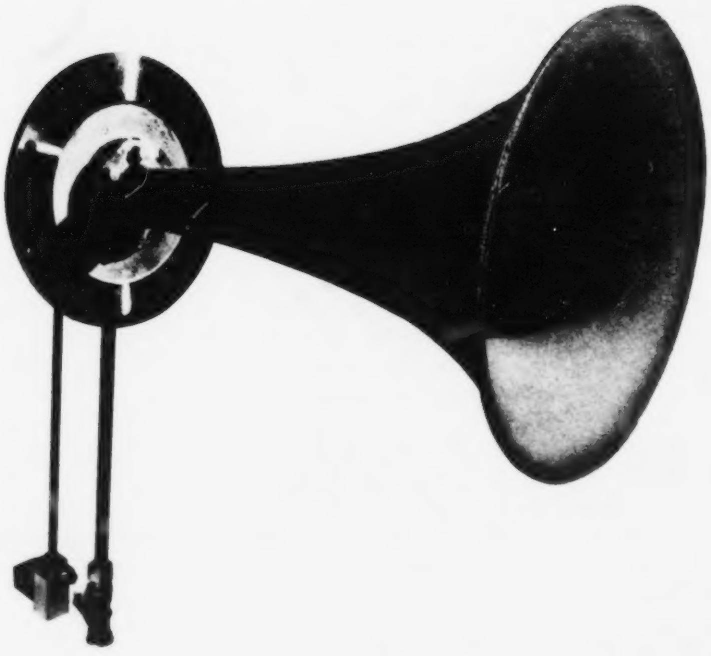

Figure 2. KVB horn.

HORN INSTALLATION

In July 1978, three KVB horns were installed in precipitator Number 4 as shown in Figure 3--one in the side of the inlet plenum, and one in each cat-walk on opposite sides of the unit. Total installation time, including electrical and pneumatic supply lines, is estimated at 40 hours.

All three horns are insonated simultaneously for 25 seconds every 25 minutes. Outside noise levels are well below OSHA regulations. During insonations, the outside noise level is affected by sound coming through the wall of the precipitator, by air coming out the solenoid valve exhaust, and by sound coming through the back of the horn. A sheet metal box filled with about three inches of rockwool insulation was built around each horn housing. The solenoid valve exhausts to the atmosphere without any muffler. Noise levels five feet from the precipitator measured about 90 dBA.

OSHA permissible noise exposures are shown below. Note that the limit for one half hour per day is 110 dBA--25 seconds every 25 minutes results in a daily insonation time of less than 30 minutes.

Duration Per Day Hours	Sound Level dBA Slow Response
8	90
4	95
2	100
1	105
1/2	110

RESULTS

The overall results of utilizing the KVB low frequency acoustic horns were very satisfactory and produced several significant benefits to Inspiration Consolidated Copper including:

- An increase in precipitator running time
- A reduction in the time required to clean the precipitator
- An increase in the ratio of running time to cleaning time from one to one to six to one
- An increase in operating time of the acid plant prior to screening the converter catalyst bed
- A significant labor cost saving

With three KVB horns installed, precipitator Number 4 operated for six weeks before a mechanical breakdown caused a shut-down. In fact, since installation of the horns, factors other than dust build-up, i.e. mechanical and electrical problems, now dictate the length of service of the precipitator.

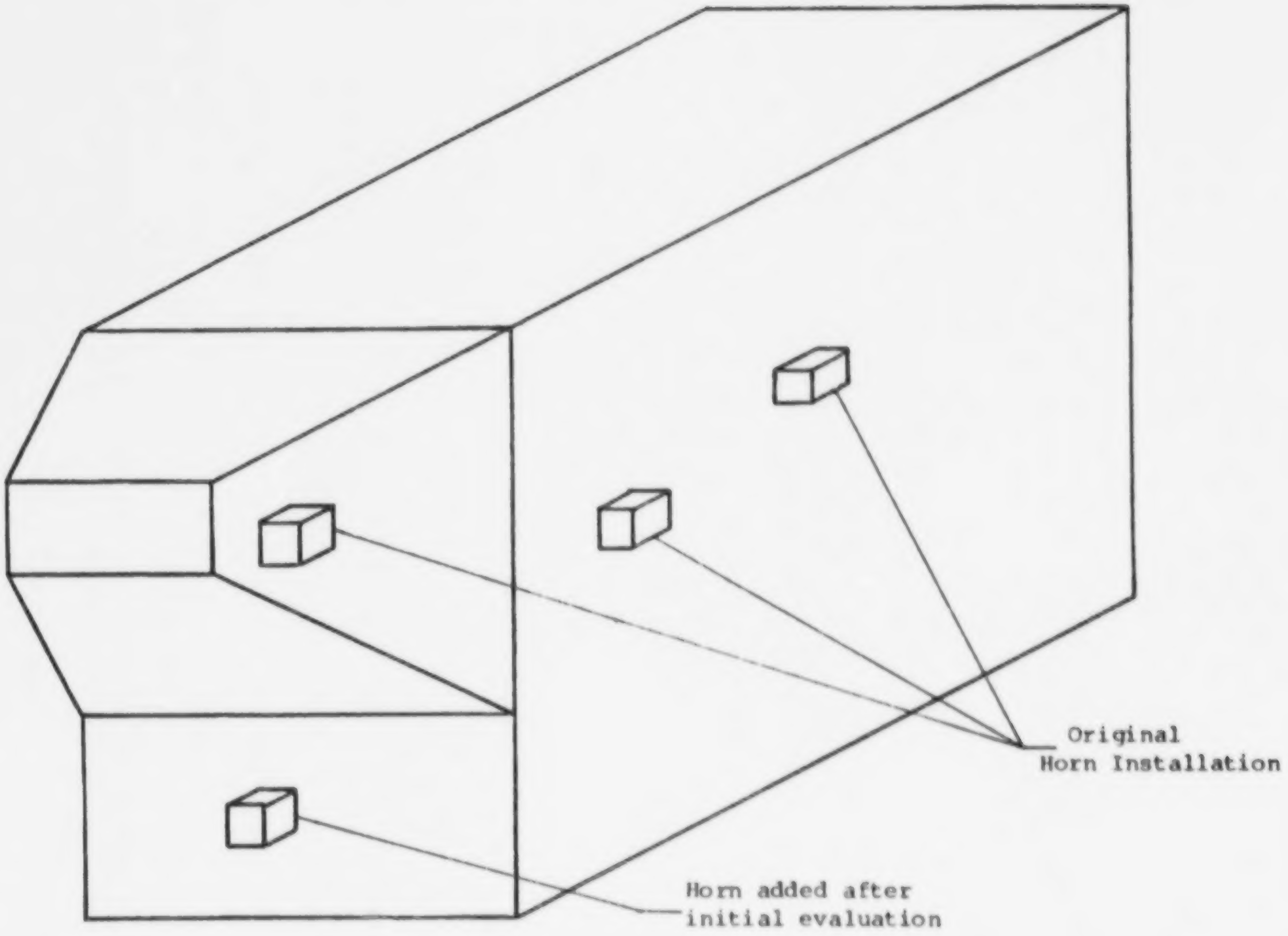

Figure 3. Horn installation precipitator No. 4

Before installation of the horns, the operating time for the precipitator equaled the cleaning time, on the average, about 15 shifts. After the horns, continuous precipitator operating time (not counting problems unrelated to the horns) jumped to 30 shifts, while clean-up time dropped to five shifts. This, alone, is a labor cost saving of $4,260.

The acid plant converter catalyst bed can now be operated up to eight months prior to shut-down for screening, compared with four to six months before the horns were being used.

Another interesting result was obtained. During a one month period, the precipitator was operated without any power on one of the fields. After shut-down visual inspection of this section showed it to be as clean as the other fields.

A fourth horn was subsequently added to deal with the dust build-up occurring on the field-wire weight bottle guideways. This build-up was allowing the bottles to hang up, thereby creating slack in the wire electrodes, a condition leading to electrical shorts. The fourth horn was located at the level of the bottles and was successful in eliminating the dust build-up (Figure 3).

Cyclone Application

ICC was also experiencing severe clogging problems with the cyclone handling flue gas between the electric furnace and precipitator. The dust is fairly sticky and would build up on the cyclone walls and then slough off due to its own weight. This would plug the one foot diameter dust collection duct on the order of once or twice per week. Three mechanical vibrators had been installed on the cyclone without producing a material improvement.

In December 1978 ICC installed a horn in the top of the cyclone as shown in Figure 4. The operating cycle was ten seconds on every minute. The horn successfully solved this problem and to date they have not experienced a plugging situation.

The result is a more efficient cyclone and a significant reduction in the manpower associated with dust removal and handling.

CONCLUSIONS

The use of low frequency, high energy acoustic horns significantly reduced dust collection problems at Inspiration Consolidated Copper. Three horns installed on the electric furnace precipitator extended the operating period between shut-downs for cleaning from less than one week to about six weeks. In fact, since installation of the horns, factors other than dust build-up, i.e. mechanical and electrical problems, now dictate the length of service of the precipitator. A horn was also successfully used in a cyclone to prevent frequent clogging.

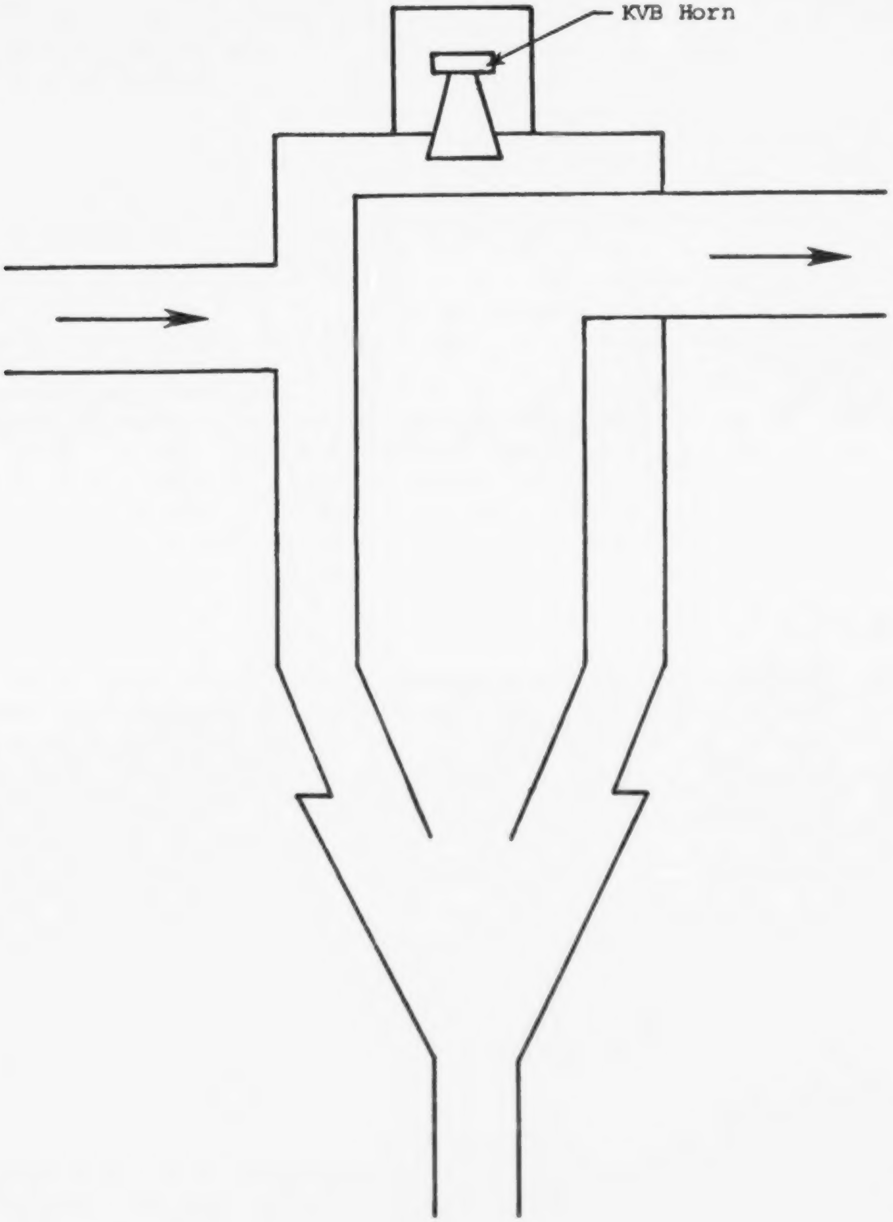

Figure 4. Cyclone installation.

ADDENDUM

ANALYSIS OF ACOUSTIC WAVE EFFECTS ON FINE PARTICULATE MATERIALS

To put the nature of the acoustic field into perspective we should note that at a point where the intensity is 145 decibels, the local pressure fluctuation is of the order of one $\mathrm{lb/ft}^2$. At the conditions of a precipitator this corresponds to a local air velocity fluctuation of about 0.5 ft/sec., and when this velocity acts upon a particle of approximately one micron radius, the particle experiences an acceleration on the order of 2500 g. These forces are usually intense enough to fluidize a lightly packed particulate volume or remove particles that are lightly bound to surfaces. In this section we shall carry out an approximate calculation that will disclose some of the mechanisms of the acoustic-particle interactions and illustrate how we may expect the results to scale when particle size is varied.

The first problem relates to the penetration of the acoustic cone into a lightly packed volume of particles such as might be encountered at various locations of the precipitator. Only these particles will be initially fluidized if the local acoustic velocities are sufficient to accelerate the particles to perhaps 50 g. Thus the rate of attenuation of the acoustic velocity below the surface of the particulate volume is the quantity which we shall require to estimate the depth of fluidization.

To analyze this, consider a particulate volume

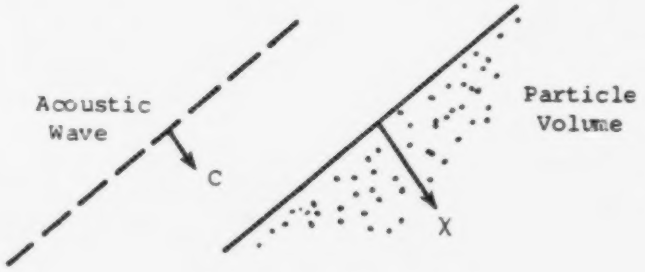

that may be considered one-dimensional with x measuring the distance below the surface. A beam of plane waves moves with acoustic velocity c toward the surface, and this beam may be represented analytically as

$$\frac{P'}{\gamma P_o} = \frac{u}{c} = Pe^{i(\omega t - kx)}$$

where P' and u are the acoustic pressure and velocity fluctuations, Po and c are the reference (atmospheric) pressure and acoustic velocity respectively, P is the magnitude of the wave, ω is the angular frequency (= $2\eta \times 250$ for present application) and the wave number $K = \omega/c$ for the wave before it enters the particle pile. Within the particle volume, the air motions are acted upon by the resistance of the particles. In the present instance, this force may be represented roughly by the Stokes interaction between moving gas and stationary particles. It may be shown that this force is

$$Fp = (n)\ (6\eta\ \sigma\mu)\ (u)$$

where n is the number of particles per unit volume having a radius σ, μ is the gas viscosity, and u is the local gas velocity. This results in an acoustic equation that can be represented as

$$\frac{\partial^2 u}{\sigma t^2} - c^2 \frac{\partial^2 n}{\partial x^2} + \frac{\kappa p}{\tau} \frac{u}{\partial t} = 0$$

where κp is the ratio of particle mass to air mass in the volume and

$$\tau \equiv \frac{m}{\eta\sigma\mu}$$

is the "relaxation time" of the particles where m is the mass of a single particle. For usual solid particles of one micron radius, $\tau \sim 10^{-4}$ seconds. The relaxation time scales as the square of the particle radius. The particle leading κp is of the order 10^2 and hence the parameter $(\kappa p/\omega t)$, which enters the solution of the acoustic problem within the particle pack, is quite large. The approximate solution, valid for our range of interest, is then

$$\frac{U}{c} \overset{\sim}{=} Pe^{iwt} \cdot e^{-i \frac{w}{c} \sqrt{\frac{\kappa p}{2\omega t}}\, x} \cdot e^{- \frac{w}{c} \sqrt{\frac{\kappa p}{\omega t}}\, x}$$

which matches appropriately with the impinging wave at $x = 0$. The attenuation within the pack is given by the last factor, which may also be written

$$e^{- \frac{2\pi}{\lambda} \sqrt{\frac{\kappa p}{\omega T}}\, x}$$

where λ is the acoustic wave length in free air. The value of $\breve{x}$, the depth at which the acoustic velocity has dropped to e^{-1} of its initial value, is

$$\frac{x}{\lambda} = \frac{1}{2\pi} \sqrt{\frac{\omega t}{\kappa p}}$$

and thus increases with particle size for a given pack loading κp and frequency. For one micron particle and particle loading of 10^2 and other quantity appropriate to our problem, $\tilde{x}$ is approximately 0.5 inches. This would indicate that the acoustic field would fluidize the external layers at any time of its operation.

To obtain a better estimate of this fluidization depth we may note that the acceleration experienced by any one particle is

$$u \cdot \frac{6\eta\rho\mu}{m} = \frac{u}{\tau}$$

when us is the local gas velocity. Therefore $u/g\tau$ is the acceleration in gravitational units which, if we set to 50 as a requirement for fluidization, gives

$$\frac{u}{c} = 50 \left(\frac{g\tau}{c}\right)$$

as the minimum effective velocity. Therefore,

$$50 \left(\frac{g\tau}{c}\right) = e^{-2\pi\sqrt{\frac{\kappa p}{\omega\tau}} \cdot \frac{x^*}{\lambda}}$$

gives the actual depth of fluidization x^* as

$$x^* = \lambda \frac{1}{2\pi} \sqrt{\frac{\omega\tau}{\kappa p}} \; \ln \left(\frac{c}{50\ g\tau}\right)$$

which differs from the previous result by the logarithmic factor. For our previous example, this factor is 8.97 so that the actual fluidization depth is nearly five inches. The scaling of this value with particle size, gas conditions and particle material is now more complex but is evident from the above relation.

AUTHOR INDEX

AUTHOR NAME	PAGE
Ariman, T.	III-222
Bacchetti, J. A.	I-529
Bernstein, S.	II-125
Bibbo, P. P.	II-219
Bickelhaupt, R. E.	I-154
Blackwood, T. R.	IV-312
Bloomfield, D. P.	III-145
Brackbill, E. A.	III-472
Brines, H. G.	I-351
Brookman, E. T.	IV-274
Brown, J. T. (Jr.)	III-439
Buchanan, W. J.	II-168
Burckle, J. O.	III-484
Bush, J. R.	IV-154
Carlsson, B.	III-260
Carr, R. C.	I-35, III-270
Chang, C. M.	II-314
Chapman, R. A.	I-1
Chmielewski, R.	III-1
Cooper, D. W.	III-127
Cowen, S. J.	IV-424
Cowherd, C. (Jr.)	IV-240
Czuchra, P. A.	III-104
Darby, K.	I-15
Daugherty, D. P.	IV-182

AUTHOR NAME	PAGE
Dennis, R.	I-494
Dietz, P. W.	III-429
Donovan, R. P.	I-476
Drehmel, D. C.	IV-170
Durham, M. D.	IV-368
Dybdahl, A. W.	IV-443
Ellenbecker, M. J.	III-171, III-190
Engelbrecht, H. L.	II-279
Ensor, D.S.	III-39
Ernst, M.	IV-30, IV-42
Eschbach, E. J.	II-114
Evans, J. S.	IV-252
Fasiska, E. J.	IV-486
Faulkner, M. G.	IV-508
Fedarko, W.	IV-64
Ferrigan, J. J.	I-170
Finney, W. C.	II-391
Furlong, D. A.	I-425
Garrett, N. E.	IV-524
Gastler, J. H.	IV-291
Gavin, J. H.	III-81
Giles, W. B.	IV-387
Gooch, J. P.	I-132
Gooding, C. H.	III-404
Grace, D. S.	III-289
Guiffre, J. T.	I-80

AUTHOR NAME	PAGE
Hall, F. D.	III-25
Hardison, L. C.	III-382
Hoenig, S. A.	IV-201
Hudson, J. A.	I-263
Iinoya, K.	III-237
Isoda, T.	III-16
Jaasund, S. A.	II-452
Kalinowski, T. W.	III-363
Kallio, G. A.	III-344
Kearns, M. T.	III-61
Kelly, D. S.	I-100
Kinsey, J. S.	III-95
Kolber, A. R.	I-224
Ladd, K. L.	I-317
Lamb, G. E.R.	III-209
Lane, W. R.	I-410
Langan, W. T.	I-117, II-256
Larson, R. C.	III-448
Leonard, G.	II-146
Lipscomb, W. O.	I-453
Malani, S.	I-570
Marcotte, W. R.	I-372
Martin, J. R.	I-591
Masuda, S.	II-65, II-334, II-483
McCain, J. D.	IV-496
McDonald, J. R.	II-93

AUTHOR NAME	PAGE
Mitchell, D. A.	III-162
Modla, J. C.	II-399
Mosley, R. B.	II-45
Mycock, J. C.	I-432
Neundorfer, M.	II-189
Nixon, D.	I-513
Noll, C. G.	II-374
Nunn, M.	II-369
Ondov, J. M.	IV-454
Ostop, R. L.	I-342
Parker, R.	IV-1
Patch, R. W.	IV-136
Patterson, R. G.	IV-84
Pearson, G. L.	I-359
Pedersen, G. C.	III-416
Petersen, H. H.	II-352
Pilat, M. J.	I-561
Potter, E. C.	I-184
Ranade, M. B.	I-538
Raymond, R. K.	II-173
Rinard, G.	II-31, IV-127
Roehr, J. D.	II-208
Rolschau, D. W.	III-251
Ruth, D.	II-427, II-441
Samuel, E. A.	II-1
Schliesser, S. P.	I-56

AUTHOR NAME	PAGE
Self, S. A.	III-309
Severance, R. L.	IV-321
Shale, C. C.	I-390
Smit, W.	I-297
Smith, S. B.	II-502
Spafford, R. B.	I-202
Sparks, L. E.	II-417, IV-411
Stenby, E. W.	I-243
Stock, W. E.	IV-333
Surati, H.	II-469
Szabo, M. F.	III-508
Tendulkar, S. P.	IV-338
Tennyson, R. P.	III-117
Tsao, K. C.	IV-14
Umberger, J. H.	II-296
VanOsdell, D. W.	II-74
VanValkenburg, E. S.	IV-351
Wang, J. C.F.	IV-396
Weber, E.	IV-98
Wybenga, F. A.	II-242
Yung, S.	IV-217